materials

Special Issue Reprint

Sustainability in Asphalt, Concrete and Pavement Materials

Design, Performance, and Characterization

Edited by
Wentao Wang and Linbing Wang

mdpi.com/journal/materials

MDPI

Sustainability in Asphalt, Concrete and Pavement Materials: Design, Performance, and Characterization

Sustainability in Asphalt, Concrete and Pavement Materials: Design, Performance, and Characterization

Guest Editors

Wentao Wang
Linbing Wang

MDPI

Basel • Beijing • Wuhan • Barcelona • Belgrade • Novi Sad • Cluj • Manchester

Guest Editors
Wentao Wang
National Center for Materials Service Safety
University of Science and Technology Beijing
Beijing
China

Linbing Wang
School of Environmental
Civil Agricultural and
Mechanical Engineering
University of Georgia
Athens
USA

Editorial Office
MDPI AG
Grosspeteranlage 5
4052 Basel, Switzerland

This is a reprint of the Special Issue, published open access by the journal *Materials* (ISSN 1996-1944), freely accessible at: https://www.mdpi.com/journal/materials/special_issues/33MB0725Y9.

For citation purposes, cite each article independently as indicated on the article page online and as indicated below:

Lastname, A.A.; Lastname, B.B. Article Title. *Journal Name* **Year**, *Volume Number*, Page Range.

ISBN 978-3-7258-9127-6 (Hbk)
ISBN 978-3-7258-9128-3 (PDF)
https://doi.org/10.3390/books978-3-7258-9128-3

© 2026 by the authors. Articles in this reprint are Open Access and distributed under the Creative Commons Attribution (CC BY) license. The reprint as a whole is distributed by MDPI under the terms and conditions of the Creative Commons Attribution-NonCommercial-NoDerivs (CC BY-NC-ND) license (https://creativecommons.org/licenses/by-nc-nd/4.0/).

Contents

About the Editors . . . . . **vii**

Wentao Wang and Linbing Wang
Sustainability in Asphalt, Concrete and Other Pavement Materials: Design, Performance, and Characterization
Reprinted from: *Materials* **2026**, *19*, 1890, https://doi.org/10.3390/ma19091890 . . . . . **1**

Yu Chen, Tingting Huang, Xuqing Wen, Kai Zhang and Zhengang Li
Experimental Investigation of Water Vapor Concentration on Fracture Properties of Asphalt Concrete
Reprinted from: *Materials* **2024**, *17*, 3289, https://doi.org/10.3390/ma17133289 . . . . . **6**

Xiangyu Jiang, Wen Xu, Yixing Chen and Jiaqi Li
Design and Microwave Absorption Performance Study of SiC-Fe_3O_4 Emulsified Asphalt Mixture
Reprinted from: *Materials* **2024**, *17*, 3935, https://doi.org/10.3390/ma17163935 . . . . . **20**

Sheng Xu, Wen Xu, Yixing Chen, Jiaqi Li and Yueguang Li
Enhancement of Microwave Heating Technology for Emulsified Asphalt Mixtures Using SiC-Fe_3O_4 Composite Material
Reprinted from: *Materials* **2024**, *17*, 4572, https://doi.org/10.3390/ma17184572 . . . . . **53**

Jun Nie, Kai Zhang, Xiangyang Fan, Yixuan Zhang, Guoxu Wei, Xiangyong Yu and Wen Xu
Study on the Mechanical Properties of Modified Sludge Soil Based on an SM-C Modifier
Reprinted from: *Materials* **2025**, *18*, 483, https://doi.org/10.3390/ ma18030483 . . . . . **79**

Zeyu Geng, Weixiao Yu, Min Jiang and Yinghao Miao
Comparison of Microwave Sensitivity and Performance of Asphalt Mastic with Various Steel Slag Powders
Reprinted from: *Materials* **2025**, *18*, 1348, https://doi.org/10.3390/ma18061348 . . . . . **96**

Duanyi Wang, Chuanxi Luo, Meng Fu, Wenting Zhang and Wenjie Xie
Study on Non-Destructive Testing Method of Existing Asphalt Pavement Based on the Principle of Geostatistics
Reprinted from: *Materials* **2025**, *18*, 1848, https://doi.org/10.3390/ma18081848 . . . . . **114**

Weixiao Yu, Yun Li, Zhipeng Liang, Jiaxi Wu, Sudi Wang and Yinghao Miao
Laboratory Investigation of Packing Characteristics and Mechanical Performance of Aggregate Blend
Reprinted from: *Materials* **2025**, *18*, 1953, https://doi.org/10.3390/ma18091953 . . . . . **132**

Yang Lv, Boyu Zhao, Jie Zhu, Chenhao He, Yunlu Ge, Yuanshuai Wu, et al.
The Preparation and Properties of Ultra-High-Performance Concrete with Aeolian Sand: A Lab Study on the Effect of the Curing Method
Reprinted from: *Materials* **2025**, *18*, 2031, https://doi.org/10.3390/ma18092031 . . . . . **148**

Mingshi Liang, Liqiang Jiang and Jianguang He
Seismic Response Mitigation of Reinforced-Concrete High-Speed Railway Bridges with Hierarchical Curved Steel Dampers
Reprinted from: *Materials* **2025**, *18*, 2120, https://doi.org/10.3390/ma18092120 . . . . . **166**

Sudi Wang, Jianxia Wang, Jie Wang, Jian Xu, Yinghao Miao, Qing Ma, et al.
Characterization of Force Distribution and Force Chain Topology in Asphalt Mixtures Using the Discrete Element Method
Reprinted from: *Materials* **2025**, *18*, 2347, https://doi.org/10.3390/ma18102347 . . . . . **182**

Guokai Li, Min Wang, Kezhen Yan and Xiaojin Song
Study on the Self-Healing Performance of Polyurethane/Graphene Oxide-Modified Asphalt Based on Dynamic Disulfide Bonds
Reprinted from: *Materials* **2025**, *18*, 2549, https://doi.org/10.3390/ma18112549 . . . . . **209**

Kai Zhang, Xuwen Zhong, Xukun Huang, Weihua Wan, Hai Zhou and Bin Liu
Micromodification Mechanism and High-Temperature Rheological Properties of Activated Rubber/Styrene–Butadiene–Styrene Compound-Modified Asphalt
Reprinted from: *Materials* **2025**, *18*, 2643, https://doi.org/10.3390/ma18112643 . . . . . **230**

Besma Belaidi, Abderraouf Messai, Cherif Belebchouche, Mourad Boutlikht, Kamel Hebbache, Abdellah Douadi and Laura Moretti
Physical, Mechanical, and Durability Performance of Olive Pomace Ash in Eco-Friendly Mortars
Reprinted from: *Materials* **2025**, *18*, 2667, https://doi.org/10.3390/ma18112667 . . . . . **248**

Sakariyau Babatunde Abdulkadir, Qiusong Chen, Erol Yilmaz and Daolin Wang
Comparative and Meta-Analysis Evaluation of Non-Destructive Testing Methods for Strength Assessment of Cemented Paste Backfill: Implications for Sustainable Pavement and Concrete Materials
Reprinted from: *Materials* **2025**, *18*, 2888, https://doi.org/10.3390/ma18122888 . . . . . **265**

Zhaojun Hou, Hui Liu, Jianchuan Cheng, Qifeng Zhang and Zheng Tong
Permittivity Measurement in Multi-Phase Heterogeneous Concrete Using Evidential Regression Deep Network and High-Frequency Electromagnetic Waves
Reprinted from: *Materials* **2025**, *18*, 3766, https://doi.org/10.3390/ma18163766 . . . . . **289**

Gulzar Hussain Jatoi, Giuseppe Loprencipe and Laura Moretti
Comparative Review of Marshall and Superpave Mix Designs: Enhancing Asphalt Performance with Polymers
Reprinted from: *Materials* **2025**, *18*, 4273, https://doi.org/10.3390/ma18184273 . . . . . **314**

Hande Varol Morova and Cengiz Özel
Experimental Investigation of Polymer-Modified Bituminous Stone Mastic Asphalt Mixtures Containing Cellulose Acetate Recycled from Cigarette Butts
Reprinted from: *Materials* **2025**, *18*, 5340, https://doi.org/10.3390/ma18235340 . . . . . **332**

Wentao Wang, Yue Yang, Mengxue Xu, Xiangrui Han, Yinghao Miao and Linbing Wang
Characterization of Viscoelastic Performance and VOC Emission of Warm-Mixed SBS Asphalt Binder Under Different Dosages of Warm-Mixed Additive
Reprinted from: *Materials* **2026**, *19*, 485, https://doi.org/10.3390/ma19030485 . . . . . **358**

Hao Huang, Yanfei Zhu, Kun Zhou, Yue Xiao and Liantong Mo
Evaluation of the Crushing Characteristics of Slate Coarse Aggregate Used for Asphalt Mixture
Reprinted from: *Materials* **2026**, *19*, 503, https://doi.org/10.3390/ma19030503 . . . . . **375**

Wentao Wang, Hua Rong, Yinghao Miao and Linbing Wang
Evaluation of Moisture Damage in Asphalt Mixtures Under Dynamic Water Pressure Using 3D Laser Scanning
Reprinted from: *Materials* **2026**, *19*, 1514, https://doi.org/10.3390/ma19081514 . . . . . **399**

About the Editors

Wentao Wang

Wentao Wang is an associate research fellow at the National Center for Materials Service Safety (NCMS) at the University of Science and Technology Beijing (USTB). He obtained his B.S. and M.S. degrees from Wuhan University of Technology, and Ph.D. degree from the USTB. He conducted post-doctoral research for two years at the USTB. His research interests include, but are not limited to, moisture damage to asphalt mixture, the service performance of asphalt pavement in a multi-physics coupling environment using numerical simulation and accelerated pavement testing technology, and corrosion damage and service safety evaluation on urban reinforced concrete drainage pipeline. Dr. Wang has led three research projects funded by the Beijing Natural Science Foundation, the China Postdoctoral Science Foundation, and the Fundamental Research Funds for the Central Universities, and he has participated in five national and provincial scientific research projects. He has been awarded two national and provincial awards. Dr. Wang has published 28 SCI/EI academic articles and authorized 14 invention patents. Dr. Wang serves as a reviewer for academic journals such as *Construction and Building Materials*, *International Journal of Pavement Research and Technology*, and multiple MDPI journals.

Linbing Wang

Linbing Wang is a professor in civil engineering materials and transportation infrastructure at the University of Georgia. He is the founding chair of the Committee on Mechanics of Pavements, the former Chair of the Nanomechanics and Micromechanics Committee, a Fellow of ASCE, and a Fellow of the Engineering Mechanics Institute of ASCE. Dr. Wang has led more than 80 research projects funded by NSF, NCHRP, FHWA, DoD, DoA, DoTs, MOST and CNSF. His research centers on smart, resilient and sustainable transportation infrastructures. Specific foci of his research include multiscale characterization, modeling and simulation; smart and sustainable technologies; energy harvesting and sensor development; laser interferometry for material characterization and pavement assessment; innovative infrastructure assessment and performance predictions; high-performance and multifunctional materials; smart and resilient infrastructures; pavement testing and mechanistic pavement design; infrastructure preservation and management; and IoT sensor network for structural health monitoring and safety. Dr. Wang has served as a member of committees for TRB and ASCE and panels for NCHRP and NSF. He is the author of Mechanics of Asphalt, Microstructure and Micromechanics, McGraw Hill, and the author/co-author of more than 360 journal and proceeding publications. Dr. Wang has organized/co-organized a number of international workshops, symposiums, and conferences and hosted visiting students and faculty members from universities in China and Europe .

materials

MDPI

Editorial

Sustainability in Asphalt, Concrete and Other Pavement Materials: Design, Performance, and Characterization

Wentao Wang [1] and Linbing Wang [2,*]

[1] National Center for Materials Service Safety, University of Science and Technology Beijing, Beijing 100083, China; wentaowang@ustb.edu.cn
[2] The Sensing and Perception Lab, School of Environmental, Civil, Agricultural and Mechanical Engineering, University of Georgia, Athens, GA 30602, USA
* Correspondence: linbing.wang@uga.edu

1. Background and Scope

With the continuous growth of global infrastructure construction and increasing environmental pressures [1–4], the field of road engineering and construction materials is undergoing a profound green transformation. Asphalt, concrete, and various pavement materials consume substantial natural resources and emit significant greenhouse gases during production, construction, and service [5–7]. There is an urgent need to promote sustainable technologies through material design, performance evaluation, and functional characterization [8–10]. This Special Issue, "Sustainability in Asphalt, Concrete and Pavement Materials: Design, Performance, and Characterization," aims to present the latest research findings in sustainable pavement materials, covering areas such as material modification, waste valorization, low-carbon cementitious systems, performance prediction, and advanced characterization methods.

A total of 20 high-quality papers, all rigorously peer-reviewed, are included in this Special Issue. The research topics involve warm-mix asphalt technology, the recycling of cigarette butts for fiber reuse, the materialization of industrial/agricultural by-products such as steel slag and olive ash, the evaluation of strength and durability of cement-based materials, and advanced characterization techniques. These studies not only demonstrate the important role of materials science in sustainable transportation infrastructure but also provide a scientific basis for engineering design, standard formulation, and policy orientation.

2. Overview of Research Progress

Based on an analysis of all 20 papers published in this Special Issue, the research can be broadly categorized into the following key thematic areas.

(1) **Microwave Heating and Curing Technologies for Asphalt Mixtures**: Xu et al. [Contribution 1] and Jiang et al. [Contribution 2] developed SiC–Fe_3O_4 composites to enhance microwave absorption in emulsified asphalt mixtures. The optimal conditions (4% composite with 1:1 SiC–Fe_3O_4 ratio, 600–1000 W microwave power) significantly accelerated curing and improved early strength without compromising road performance.

(2) **Sustainable Binders and Supplementary Cementitious Materials**: Belaidi et al. [Contribution 3] systematically investigated the effects of olive pomace ash as a partial cement replacement on workability, mechanical properties, and freeze–thaw durability, identifying 20% as the optimal replacement rate. Wang et al. [Contribution 4]

systematically investigated the influence of warm-mix additive dosage on the viscoelastic properties and VOC emissions of SBS-modified asphalt binder. They found that 0.4–0.5% additive can significantly reduce construction temperature and harmful gas emissions without compromising pavement performance. Huang et al. [Contribution 5] demonstrated that slate coarse aggregates exhibit crushing values (9.2%) lower than basalt and limestone, with excellent water and heat resistance, confirming their viability as sustainable alternatives in aggregate-scarce regions.

(3) **Non-Destructive Testing and Performance Characterization**: Wang et al. [Contribution 6] employed 3D laser scanning technology to quantitatively evaluate the evolution of surface roughness in asphalt mixtures under dynamic water pressure, revealing the coupled damage mechanism of fine aggregate matrix (FAM) stripping and aggregate degradation. Hou et al. [Contribution 7] proposed an evidential regression deep network for permittivity measurement in heterogeneous concrete. The method quantified both aleatory and epistemic uncertainties, achieving a mean square error of 7.50% on 1500 samples. Abdulkadir et al. [Contribution 8] systematically compared the reliability of three non-destructive testing methods (ultrasonic pulse velocity, electrical resistivity, and acoustic emission) for strength prediction of cemented paste backfill through a meta-analysis and proposed a multi-parameter fusion prediction model.

(4) **Mechanical Behavior and Durability of Innovative Pavement Materials**: Chen et al. [5] investigated water vapor effects on asphalt concrete fracture resistance. Increasing relative humidity from 2% to 100% reduced tensile strength by 34.8% on average; genetic expression programming models captured the coupled effects of humidity and temperature with $R^2 > 0.94$. Jatoi et al. [Contribution 9] compared Marshall and Superpave mix designs. Superpave mixtures exhibited superior rutting resistance, fatigue life, and moisture damage mitigation, especially when combined with polymer-modified binders and rejuvenators. Varol Morova et al. [Contribution 10] used recycled cigarette butt-derived cellulose acetate fibers in SMA mixtures. At 0.3–0.4% fiber content, the recycled fibers achieved comparable performance to commercial cellulose fibers with 6–8% cost savings. Li et al. [Contribution 11] developed polyurethane/graphene oxide (PU/GO) composites for self-healing asphalt. The composite (1.6% GO) doubled PU tensile strength and achieved 100% ductility self-healing after 15 min infrared exposure. Yu et al. [Contribution 12] and Wang et al. [Contribution 13] studied aggregate packing characteristics and force chain networks using the discrete element method. SMA mixtures exhibited superior skeleton structures, and strong correlations ($R^2 > 0.7$) were found between packing and mechanical performance. Zhang et al. [Contribution 14] compared activated versus conventional rubber in SBS-modified asphalt. Activated rubber formed a uniform micro particle network, increasing complex modulus by 417.16%. Nie et al. [Contribution 15] and Lv et al. [Contribution 16] explored sustainable concrete formulations using modified sludge soil and aeolian sand, respectively. Both studies demonstrated that locally available waste materials can be engineered to meet structural requirements. Additional contributions addressed seismic response mitigation of railway bridges [Contribution 17], non-destructive testing of existing pavements using geostatistics [Contribution 18], and comparative analysis of steel slag powders in asphalt mastic [Contribution 19].

3. Future Outlook

Although this Special Issue covers several important research directions in sustainable materials, several areas warrant further exploration:

https://doi.org/10.3390/ma19091890

(1) **Synergistic Utilization of Multi-Source Solid Wastes**: Future research should focus on the combined effects of various industrial/agricultural solid wastes in pavement materials and develop integrated design methods based on performance, cost, and environmental impact.
(2) **High-Performance Warm and Cold Mix Technologies**: Further reduction in construction temperatures should be pursued while simultaneously enhancing the long-term durability and aging resistance of asphalt mixtures.
(3) **Non-Destructive Testing and Intelligent Monitoring**: Real-time monitoring systems integrating multi-physics signals (ultrasonics, resistivity, acoustics, imaging) should be developed and combined with digital twins and Internet of Things technologies.
(4) **Life Cycle Assessment**: The carbon emissions and resource consumption of sustainable pavement materials should be systematically quantified across raw material acquisition, construction, maintenance, and end-of-life stages to support green certification and carbon trading initiatives.

We believe that the research studies presented in this Special Issue will serve as a valuable reference for researchers, engineers, and policymakers in the fields of road engineering and construction materials, and will contribute to the development of greener, more durable, and intelligent infrastructure.

Acknowledgments: We would like to express our sincere gratitude to all the authors for their valuable contributions, the reviewers for their rigorous assessments, and the editorial team of the journal for their professional support throughout the publication process.

Conflicts of Interest: The authors declare no conflicts of interest.

List of Contributions:

1. Xu, S.; Xu, W.; Chen, Y.; Li, J.; Li, Y. Enhancement of Microwave Heating Technology for Emulsified Asphalt Mixtures Using SiC-Fe_3O_4 Composite Material. *Materials* **2024**, *17*, 4572. https://doi.org/10.3390/ma17184572.
2. Jiang, X.; Xu, W.; Chen, Y.; Li, J. Design and Microwave Absorption Performance Study of SiC-Fe3O4 Emulsified Asphalt Mixture. *Materials* **2024**, *17*, 3935. https://doi.org/10.3390/ma17163935.
3. Belaidi, B.; Messai, A.; Belebchouche, C.; Boutlikht, M.; Hebbache, K.; Douadi, A.; Moretti, L. Physical, Mechanical, and Durability Performance of Olive Pomace Ash in Eco-Friendly Mortars. *Materials* **2025**, *18*, 2667. https://doi.org/10.3390/ma18112667.
4. Wang, W.; Yang, Y.; Xu, M.; Han, X.; Miao, Y.; Wang, L. Characterization of Viscoelastic Performance and VOC Emission of Warm-Mixed SBS Asphalt Binder Under Different Dosages of Warm-Mixed Additive. *Materials* **2026**, *19*, 485. https://doi.org/10.3390/ma19030485.
5. Huang, H.; Zhu, Y.; Zhou, K.; Xiao, Y.; Mo, L. Evaluation of the Crushing Characteristics of Slate Coarse Aggregate Used for Asphalt Mixture. *Materials* **2026**, *19*, 503. https://doi.org/10.3390/ma19030503.
6. Wang, W.; Rong, H.; Miao, Y.; Wang, L. Evaluation of Moisture Damage in Asphalt Mixtures Under Dynamic Water Pressure Using 3D Laser Scanning. *Materials* **2026**, *19*, 1514. https://doi.org/10.3390/ma19081514.
7. Hou, Z.; Liu, H.; Cheng, J.; Zhang, Q.; Tong, Z. Permittivity Measurement in Multi-Phase Heterogeneous Concrete Using Evidential Regression Deep Network and High-Frequency Electromagnetic Waves. *Materials* **2025**, *18*, 3766. https://doi.org/10.3390/ma18163766.
8. Abdulkadir, S.B.; Chen, Q.; Yilmaz, E.; Wang, D. Comparative and Meta-Analysis Evaluation of Non-Destructive Testing Methods for Strength Assessment of Cemented Paste Backfill: Implications for Sustainable Pavement and Concrete Materials. *Materials* **2025**, *18*, 2888. https://doi.org/10.3390/ma18122888.

9. Jatoi, G.H.; Loprencipe, G.; Moretti, L. Comparative Review of Marshall and Superpave Mix Designs: Enhancing Asphalt Performance with Polymers. *Materials* **2025**, *18*, 4273. https://doi.org/10.3390/ma18184273.
10. Varol Morova, H.; Özel, C. Experimental Investigation of Polymer-Modified Bituminous Stone Mastic Asphalt Mixtures Containing Cellulose Acetate Recycled from Cigarette Butts. *Materials* **2025**, *18*, 5340. https://doi.org/10.3390/ma18235340.
11. Li, G.; Wang, M.; Yan, K.; Song, X. Study on the Self-Healing Performance of Polyurethane/Graphene Oxide-Modified Asphalt Based on Dynamic Disulfide Bonds. *Materials* **2025**, *18*, 2549. https://doi.org/10.3390/ma18112549.
12. Yu, W.; Li, Y.; Liang, Z.; Wu, J.; Wang, S.; Miao, Y. Laboratory Investigation of Packing Characteristics and Mechanical Performance of Aggregate Blend. *Materials* **2025**, *18*, 1953. https://doi.org/10.3390/ma18091953.
13. Wang, S.; Wang, J.; Wang, J.; Xu, J.; Miao, Y.; Ma, Q.; Wang, L.; Liu, T. Characterization of Force Distribution and Force Chain Topology in Asphalt Mixtures Using the Discrete Element Method. *Materials* **2025**, *18*, 2347. https://doi.org/10.3390/ma18102347.
14. Zhang, K.; Zhong, X.; Huang, X.; Wan, W.; Zhou, H.; Liu, B. Micromodification Mechanism and High-Temperature Rheological Properties of Activated Rubber/Styrene–Butadiene–Styrene Compound-Modified Asphalt. *Materials* **2025**, *18*, 2643. https://doi.org/10.3390/ma18112643.
15. Nie, J.; Zhang, K.; Fan, X.; Zhang, Y.; Wei, G.; Yu, X.; Xu, W. Study on the Mechanical Properties of Modified Sludge Soil Based on an SM-C Modifier. *Materials* **2025**, *18*, 483. https://doi.org/10.3390/ma18030483.
16. Lv, Y.; Zhao, B.; Zhu, J.; He, C.; Ge, Y.; Wu, Y.; Zhu, Y.; Dan, J.; Zhou, Y.; Li, X. The Preparation and Properties of Ultra-High-Performance Concrete with Aeolian Sand: A Lab Study on the Effect of the Curing Method. *Materials* **2025**, *18*, 2031. https://doi.org/10.3390/ma18092031.
17. Liang, M.; Jiang, L.; He, J. Seismic Response Mitigation of Reinforced-Concrete High-Speed Railway Bridges with Hierarchical Curved Steel Dampers. *Materials* **2025**, *18*, 2120. https://doi.org/10.3390/ma18092120.
18. Wang, D.; Luo, C.; Fu, M.; Zhang, W.; Xie, W. Study on Non-Destructive Testing Method of Existing Asphalt Pavement Based on the Principle of Geostatistics. *Materials* **2025**, *18*, 1848. https://doi.org/10.3390/ma18081848.
19. Geng, Z.; Yu, W.; Jiang, M.; Miao, Y. Comparison of Microwave Sensitivity and Performance of Asphalt Mastic with Various Steel Slag Powders. *Materials* **2025**, *18*, 1348. https://doi.org/10.3390/ma18061348.

References

1. Miao, Y.; Sheng, J.; Ye, J. An Assessment of the Impact of Temperature Rise Due to Climate Change on Asphalt Pavement in China. *Sustainability* **2022**, *14*, 9044. [CrossRef]
2. Mehrara, A.; Khodaii, A. A review of state of the art on stripping phenomenon in asphalt concrete. *Constr. Build. Mater.* **2013**, *38*, 423–442. [CrossRef]
3. Wang, W.; Wang, L.; Xiong, H.; Luo, R. A review and perspective for research on moisture damage in asphalt pavement induced by dynamic pore water pressure. *Constr. Build. Mater.* **2019**, *204*, 631–642. [CrossRef]
4. Tan, Y.; Li, G.; Shan, L.; Lv, H.; Meng, A. Research progress of bitumen microstructures and components. *J. Traffic Transp. Eng.* **2020**, *20*, 1–17.
5. Chen, Y.; Huang, T.; Wen, X.; Zhang, K.; Li, Z. Experimental Investigation of Water Vapor Concentration on Fracture Properties of Asphalt Concrete. *Materials* **2024**, *17*, 3289. [CrossRef] [PubMed]
6. Gong, Z.; Miao, Y.; Lantieri, C. Review of Research on Tire–Pavement Contact Behavior. *Coatings* **2024**, *14*, 157. [CrossRef]
7. Caro, S.; Castillo, D.; Masad, E. Incorporating the heterogeneity of asphalt mixtures in flexible pavements subjected to moisture diffusion. *Int. J. Pavement Eng.* **2015**, *16*, 432–444. [CrossRef]
8. Xue, Q.; Liu, L. Hydraulic-stress coupling effects on dynamic behavior of asphalt pavement structure material. *Constr. Build. Mater.* **2013**, *43*, 31–36. [CrossRef]

9. Luo, R.; Huang, T.; Zhang, D.; Lytton, R.L. Water vapor diffusion in asphalt mixtures under different relative humidity differentials. *Constr. Build. Mater.* **2017**, *136*, 126–138. [CrossRef]
10. Kringos, N.; Scarpas, T.; Kasbergen, C.; Selvadurai, P. Modelling of combined physical-mechanical moisture-induced damage in asphaltic mixes, part 1: Governing processes and formulations. *Int. J. Pavement Eng.* **2008**, *9*, 115–128. [CrossRef]

Disclaimer/Publisher's Note: The statements, opinions and data contained in all publications are solely those of the individual author(s) and contributor(s) and not of MDPI and/or the editor(s). MDPI and/or the editor(s) disclaim responsibility for any injury to people or property resulting from any ideas, methods, instructions or products referred to in the content.

https://doi.org/10.3390/ma19091890

materials

MDPI

Article

Experimental Investigation of Water Vapor Concentration on Fracture Properties of Asphalt Concrete

Yu Chen [1], Tingting Huang [1], Xuqing Wen [2,*], Kai Zhang [3] and Zhengang Li [1,4]

[1] School of Transportation and Logistics Engineering, Wuhan University of Technology, Hubei Highway Engineering Research Center, Wuhan 430063, China; yu.chen@whut.edu.cn (Y.C.); huangtingting@whut.edu.cn (T.H.)
[2] Jiangxi Provincial Communications Investment Group Co., Ltd. Project Construction Management Company, Nanchang 330200, China
[3] Jiangxi Transportation Institute Co., Ltd., 809 Jinsha Avenue, Nanchang 330200, China
[4] Wuhan Dongxihu District Transportation Bureau, Wuhan 430040, China
* Correspondence: sanmao44510@163.com

Abstract: The effect of moisture on the fracture resistance of asphalt concrete is a significant concern in pavement engineering. To investigate the effect of the water vapor concentration on the fracture properties of asphalt concrete, this study first designed a humidity conditioning program at the relative humidity (*RH*) levels of 2%, 50%, 80%, and 100% for the three types of asphalt concrete mixtures (AC-13C, AC-20C, and AC-25C).The finite element model was developed to simulate the water vapor diffusion and determine the duration of the conditioning period. The semi-circular bending (SCB) test was then performed at varying temperatures of 5 °C, 15 °C, and 25 °C to evaluate the fracture energy and tensile strength of the humidity-conditioned specimens. The test results showed that the increasing temperature and the *RH* levels resulted in a lower peak load but greater displacement of the mixtures. Both the fracture energy and tensile strength tended to diminish with the rising temperature. It was also found that moisture had a significant effect on the tensile strength and fracture energy of asphalt concrete. Specifically, as the *RH* level increased from 2% to 100% (i.e., the water vapor concentration rose from 0.35 g/m^3 to 17.27 g/m^3), the tensile strength of the three types of mixtures was reduced by 34.84% on average, which revealed that the water vapor led to the loss of adhesion and cohesion within the mixture. The genetic expression programming (GEP) model was developed to quantify the effect of water vapor concentrations and temperature on the fracture indices.

Keywords: asphalt concrete; water vapor concentration; relative humidity; fracture energy; tensile strength; semi-circular bending (SCB) test

1. Introduction

Moisture has a crucial impact on the performance and durability of asphalt concrete. Moisture infiltration into the asphalt concrete mixture can weaken the adhesion between aggregates and bitumen and lead to stripping, which is often referred to as moisture damage [1]. Forms of water in the pavement structure mainly exist as liquid and water vapor. Existing studies have found that water vapor is easier to diffuse or accumulate in the air void of asphalt concrete compared to liquid [2,3]. In this way, water vapor is regarded as the primary moisture form that affects the performance of asphalt concrete. Since water vapor infiltration can cause the separation of the bitumen and aggregates, it also has an effect on crack initiation and propagation in asphalt concrete. Therefore, it is imperative to study the effect of water vapor on the fracture resistance of asphalt concrete.

To study the influence of water vapor, humidity conditioning is required to ensure that the asphalt concrete mixture is conditioned at varying water vapor concentrations. Existing studies have mainly focused on the moisture susceptibility of the asphalt concrete mixture

using methods such as the boiling test [4], freeze–dry cycles [5,6], the vacuum saturation method [7], and so forth [8]. Compared to moisture conditioning, humidity conditioning, which controls the water vapor concentration and humidity level, is more complex and requires more sophisticated devices.

Some existing studies have attempted different methods to achieve controlled relative humidity (*RH*) levels. Hossain and Tarefder [9] utilized an aqueous solution of potassium acetate (CH_3COOK), potassium carbonate (K_2CO_3), and sodium chloride (NaCl) in enclosed desiccators to create a constant *RH* level of 25%, 49%, and 71%, respectively, for shear pull-off test specimens by following the ASTM E104 standard [10]. Tong et al. utilized a desiccant and distilled water in a vacuum desiccator to achieve the *RH* level of 0% and 100%, respectively [11]. The controlled *RH* level by a saturated salt solution requires sophisticated devices to maintain sealability and stable ambient temperature. Cheng et al. utilized a universal sorption device to measure the amount of water vapor absorbed in the mastic [12] while Xi et al. employed an environmental chamber to maintain a steady water vapor environment for humidity conditioning [13].

To study the effect of moisture on asphalt concrete, previous studies commonly conducted performance tests and compared the performance parameters of the asphalt mixture before and after moisture conditioning. Lytton et al. conducted a dynamic mechanical analysis (DMA) test to evaluate the rate of damage accumulation and found that moisture damage resistance was related to bond energy calculation [14]. Lee et al. performed a dynamic modulus test to evaluate the moisture susceptibility of the asphalt mixture [15] while Wang et al. performed a uniaxial penetration strength test to assess moisture sensitivity based on dynamic water environmental conditioning [16]. Akentuna et al. evaluated the effectiveness of different laboratory mechanical tests such as the loaded wheel tracking test, modified Lottman, and semi-circular bending test to study the moisture sensitivity of asphalt mixtures [17].

Fracture resistance is one of the most significant properties of asphalt concrete. The evaluation of its crack resistance relies on various fracture indices, which are divided into mechanical parameters and energy index (e.g., fracture energy), based on the different laboratory tests. Previous studies primarily focused on the effect of temperature, loading mode (e.g., loading rate), specimen geometry, and mixture composition on the fracture resistance of asphalt mixtures [18,19]. For instance, Li et al. conducted the semi-circular bending (SCB) test to evaluate the fracture resistance of the six types of asphalt mixtures with different binder types, binder modifiers, aggregate type, air voids, loading rate, initial notch length, and low-temperature level [20].

Some researchers have increasingly focused on the effect of moisture on the fracture resistance of the asphalt mixture. Specifically, the effect of moisture on the fracture resistance of asphalt concrete was investigated using moisture conditioning methods such as water baths, freeze–thaw cycles, and saline solutions. Karimi et al. performed moisture conditioning in a water bath and moisture damage at different levels on the specimens and conducted the SCB test to evaluate the effect of moisture and freeze–thaw damage on the fracture properties [21]. Fakhri and Ahmadi considered two aging levels and the freeze–thaw cycles on the asphalt mixture fabricated with reclaimed asphalt pavement (RAP) and coarse steel slag aggregate (SSA) and conducted the SCB test to investigate the fracture resistance [22]. Zhang et al. utilized chloride solutions to perform dry–wet cycles on the asphalt mixture and then conducted the splitting test to study the impact of different salty and moisture conditions on the mechanical properties of the mixtures [23].

However, there are limited studies considering humidity conditioning to control the water vapor concentration and its effect on the fracture resistance of asphalt concrete. Therefore, there is a need to explore the impact of humidity conditioning on asphalt concrete mixtures, as the water vapor diffuses and accumulates more easily in mixtures compared to liquid water, resulting in different severities of moisture damage.

Therefore, this study aimed to investigate the effect of water vapor concentration on the fracture properties of the asphalt concrete mixtures. The asphalt concrete specimens

were humidity-conditioned at various *RH* levels of 2%, 50%, 80%, and 100% in the form of water vapor, and the SCB test was then conducted to assess the fracture properties of the humidity-conditioned specimens.

2. Materials and Methods

2.1. Materials

The asphalt binders used in this study were styrene-butadiene-styrene (SBS)-modified asphalt and neat 70# binder. To ensure that the asphalt concrete mixture meets the standard specification, binder tests were conducted in accordance with the Chinese specification JTG E20-2011 [24] to obtain the properties (or technical indices) of the two types of binder such as penetration, ductility, softening point, and density. Moreover, the thin film oven test (TFOT) was conducted to evaluate the durability and aging characteristics of the binder by simulating the short-term aging of the binder. These binder test results met the technical index requirements in Chinese specification JTG F40-2004 [25]. Tables 1 and 2 present the binder test results for the SBS-modified binder and neat 70# binder, respectively.

Table 1. Test properties of the SBS-modified binder.

Properties		Unit	Test Value	Specification
Penetration (25 °C, 5 s, 100 g)		0.1 mm	55.0	40~60
Ductility (5 °C, 5 cm/min)		cm	27.0	≥20
Softening point ($T_{R\&B}$)		°C	76	≥75
Density		g/cm^3	1.03	-
TFOT	Loss in mass	%	0.10	≤±1.0
	Reduction penetration (25 °C)	%	71.0	≥65
	Ductility (5 °C, 5 cm/min)	cm	17.0	≥15

Table 2. Test properties of the neat 70# binder.

Properties		Unit	Test Value	Specification
Penetration (25 °C, 5 s, 100 g)		0.1 mm	68.0	60~80
Ductility (5 °C, 5 cm/min)		cm	36.0	≥20
Softening point ($T_{R\&B}$)		°C	47.0	≥46
Density		g/cm^3	1.04	-
TFOT residue	Loss in mass	%	0.03	≤±0.8
	Reduction penetration (25 °C)	%	75.0	≥61
	Ductility (10 °C, 5 cm/min)	cm	15.0	≥6

2.2. Sample Preparation

The test sample was prepared for humidity conditioning and then the semi-circular bending (SCB) test. Two typical types of aggregates including limestone and diabase were used for the preparation of the test sample. Three dense-graded asphalt concrete mixtures of AC-13C, AC-20C, and AC-25C were considered in this study based on the sponsored project. The AC-13C mixture used the SBS-modified asphalt and diabase, the AC-20C mixture used the SBS-modified asphalt and limestone, and the AC-25C mixture used the neat 70# asphalt and limestone. The aggregate gradation of the three types of asphalt concrete mixture is shown in Figure 1. The Marshall mix design of the three types of asphalt concrete mixture was conducted by following Chinese specification JTG E20-2011 [24] to determine the optimal asphalt content. The standard Marshall specimens based on the optimized aggregate gradation as shown in Figure 1 were fabricated for the Marshall stability test and volumetric mix design. The test results of the Marshall stability test and volumetric properties of the asphalt concrete mixtures met the requirements in Chinese specification JTG F40-2004 [25], as presented in Table 3. The optimal asphalt contents of

the three asphalt concrete mixtures were obtained as 4.8%, 4.5, and 3.9%, respectively, as shown in Table 3.

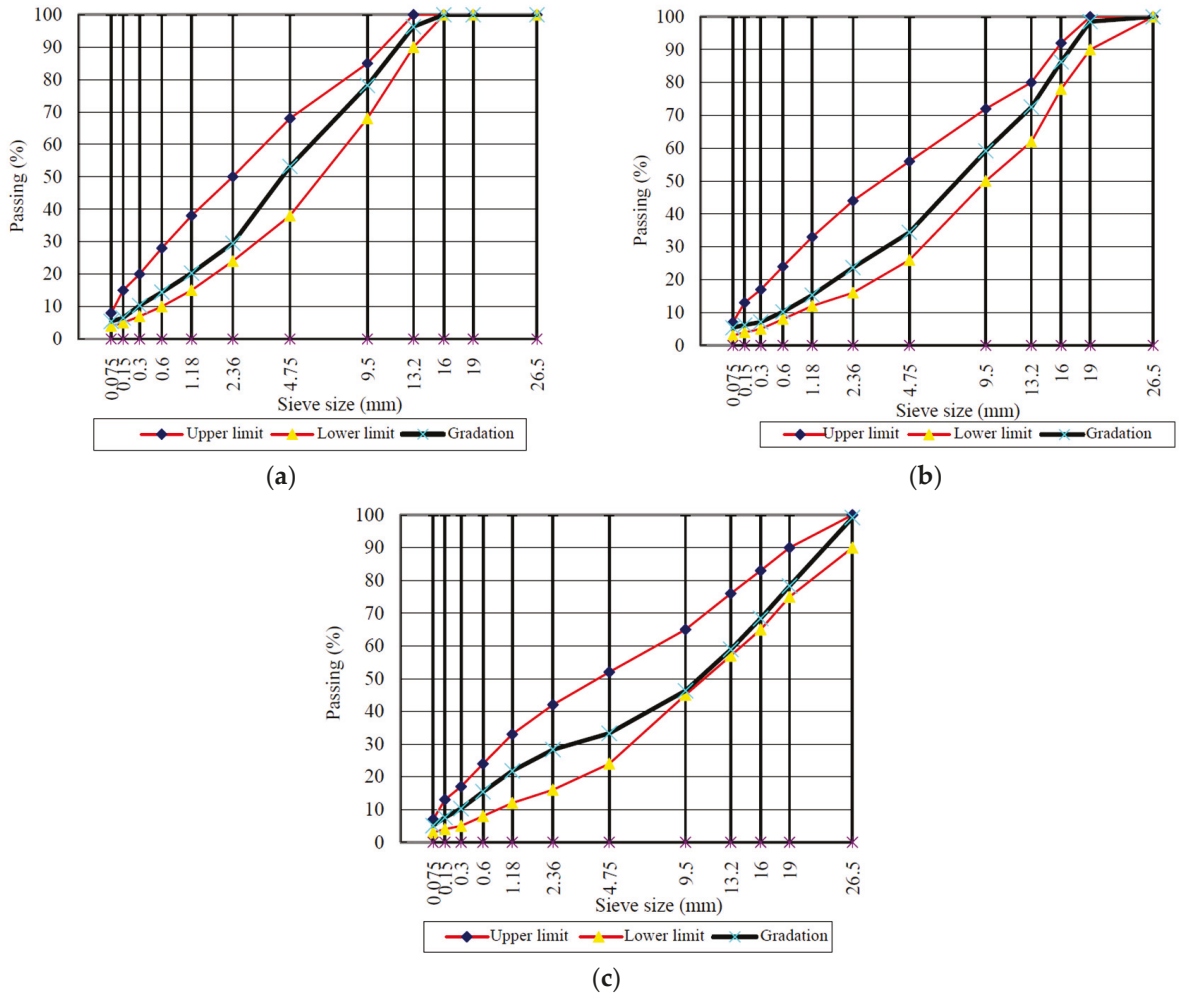

Figure 1. Aggregate gradation for (**a**) AC-13; (**b**) AC-20C; (**c**) AC-25C mixture.

Table 3. Marshall stability test results.

Mixture Properties	AC-13C		AC-20C		AC-25C	
	Value	Specification	Value	Specification	Value	Specification
Optimal asphalt content	4.8	—	4.5	—	3.9	—
Bulk specific gravity (g/cm^3)	2.412	—	2.457	—	2.492	—
Maximum specific gravity (g/cm^3)	2.694	—	2.571	—	2.586	—
Air void (V_a)/%	4.0	3~5	4.4	4~6	5.2	4~6
Air void in mineral aggregate (VMA)/%	14.6	≥14	14.0	≥13	12.1	≥12
Air void filled with asphalt (VFA)/%	71.3	65~75	68.4	65~75	69.7	65~75
Marshall Stability/kN	18.2	≥8	14.7	≥8	11.5	≥8
Flow value/0.1 mm	29.54	15~50	38.4	15~50	25.5	15~50

Based on the aggregate gradation and optimal asphalt content, the test specimens were compacted with a Superpave Gyratory Compactor (SGC) to obtain a cylinder sample with a diameter of 150 mm and a height of 180 mm. For the center of the cylinder samples, cylinder slices with a diameter of 150 mm and a thickness of 50 mm were obtained and then cut into two identical "halves" as the SCB test specimens. The specimens had a notch cut in the middle as the pre-existing cracking. The notch length and width were selected as 10 mm and 1 mm, respectively. Specifically, the SCB specimen with and without a notch was fabricated to obtain the fracture energy and tensile strength, respectively [26]. The

preparation procedure of the specimen for the SCB test is depicted in Figure 2. In order to reduce the measurement error, three parallel samples were fabricated for each test condition of temperature, water vapor concentration, and mixture type, etc. In total, we prepared 216 SCB test specimens to ensure the reliability of our test results.

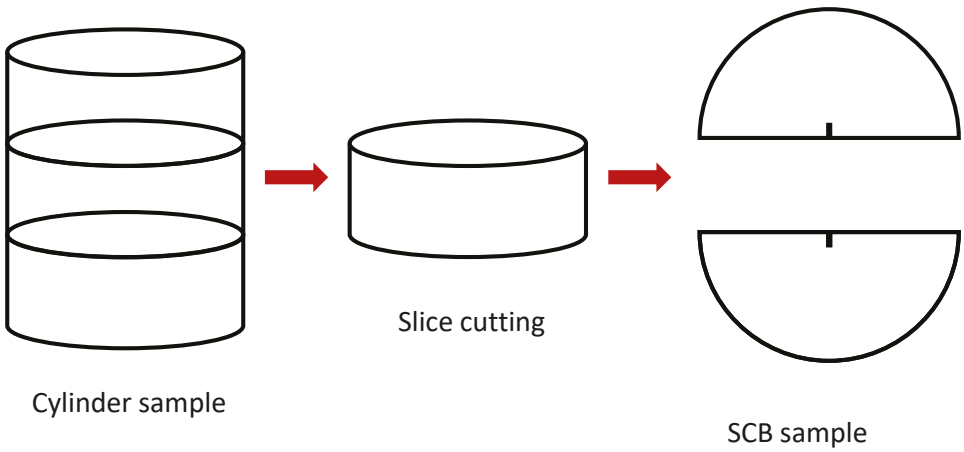

Figure 2. Sample preparation procedure for the SCB test.

2.3. Humidity Conditioning Program

In order to investigate the effect of water vapor concentration on the fracture behavior of asphalt concrete, the humidity conditioning program for the SCB test specimen was performed. Relative humidity (*RH*) is most widely used to represent humidity conditioning and refers to the percentage value of water pressure in the air and the saturated water pressure at the same temperature. The *RH* and water vapor concentration can be converted from the ideal gas law formula:

$$RH = \frac{RT}{P_T m_{H_2O}} \cdot C \tag{1}$$

where *RH* is the relative humidity, %; *R* is the general gas constant, 8.314 J/mol·K; *T* is the Kelvin temperature, K; m_{H_2O} is the molar mass of water, 18.015 g/mol; P_T is the saturated water vapor pressure, 2336.33 Pa at 20 °C; *C* is the water vapor concentration, g/m^3.

To cover a wide range of realistic environmental conditions, this study selected the *RH* levels of 2%, 50%, 80%, and 100% at a temperature of 20 °C as the humidity curing condition. At the *RH* level of 2%, asphalt concrete is subjected to the dry condition, while at the *RH* level of 100%, it is subjected to the saturation condition. A humidity chamber and vacuum drying oven were used for humidity conditioning under different *RH* levels, as shown in Figure 3. To reach the *RH* level of 2%, the negative pressure environment in the humidity chamber was made by pumping out air, and the dry desiccant of phosphorus pentoxide (P_2O_5) power was placed into the open glass container to absorb the water in the humidity chamber. Since the dry desiccant cannot fully absorb the water vapor, the *RH* level was maintained at an *RH* level of 2%, which is why the level was selected as the dry condition.

The humidity conditioning program designed in this study requires both the *RH* levels and the humidity curing period, which refers to the duration of time during which asphalt concrete specimens are conditioned at the specific *RH* level to reach moisture equilibrium within the specimens. To determine the humidity curing period, the finite element model was built to simulate the water vapor distribution in asphalt concrete and determine the period required to achieve the specified water vapor concentration. The initial water vapor distribution and boundary condition were defined, and the water vapor diffusion was simulated, as referenced in [27]. Figure 4 shows the three stages of water vapor diffusion. The difference in water vapor concentration between the boundary and interior of the

virtual specimen led to the continuous diffusion of water vapor from the boundary to the center until the equilibrium was reached. Based on the simulation results and to avoid influencing factors such as aging, the humidity curing period of 4 months was chosen for the SCB test specimens.

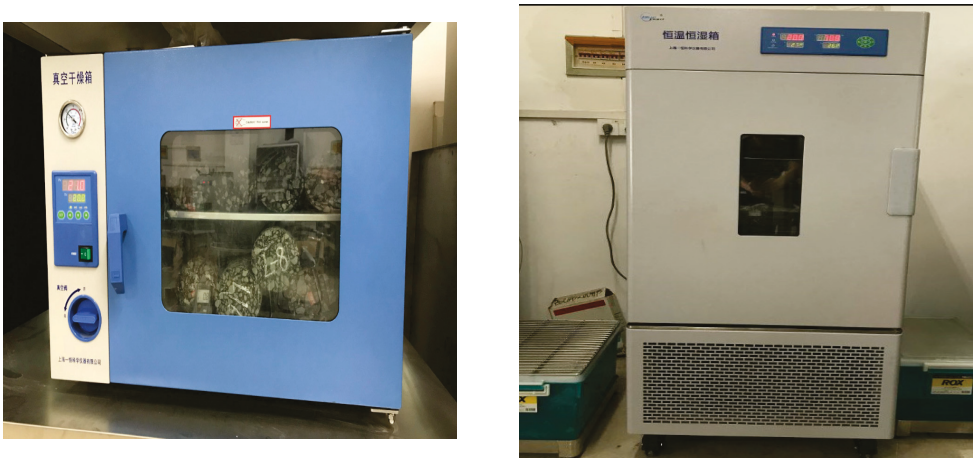

(**a**) (**b**)

Figure 3. Humidity conditioning apparatus for different *RH* levels: (**a**) vacuum drying oven; (**b**) constant temperature and humidity chamber.

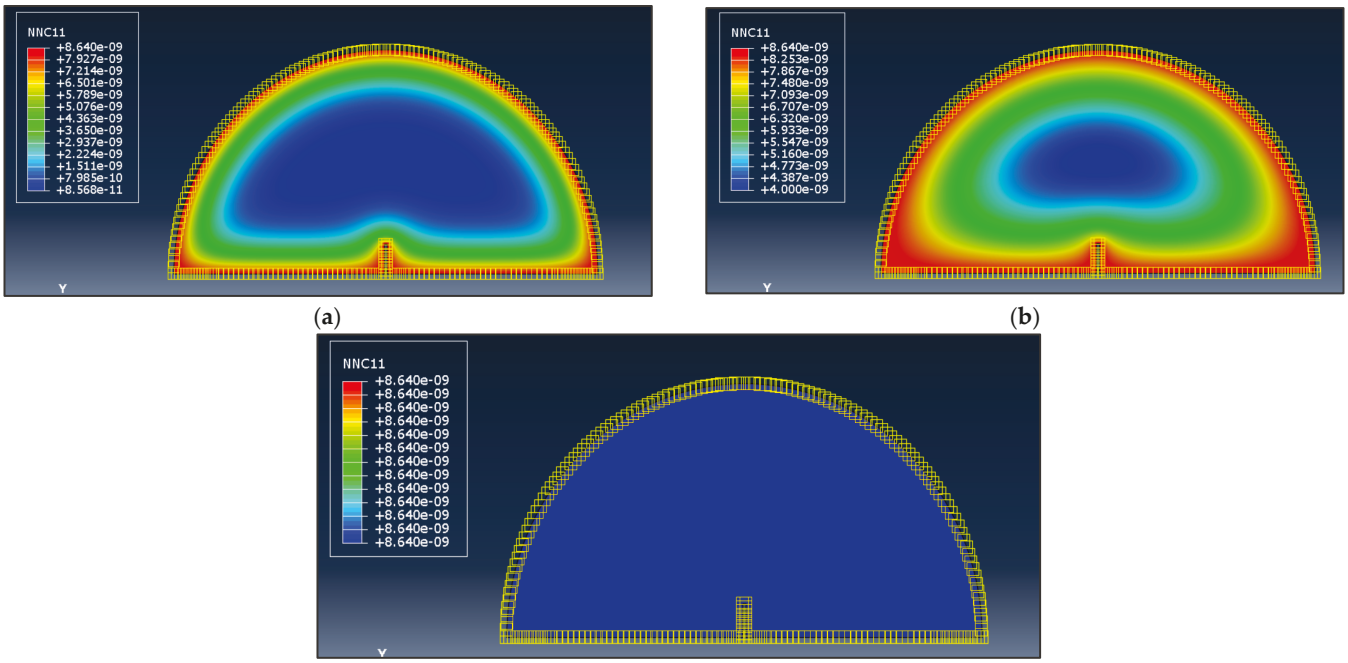

(**a**) (**b**)

(**c**)

Figure 4. Water vapor diffusion in the simulation for (**a**) early stage; (**b**) middle stage; (**c**) final stage.

2.4. Semi-Circular Bending Test

The SCB test was conducted to evaluate the fracture properties of the asphalt concrete mixtures under different humidity and temperature conditions. The SCB specimens were subjected to the temperatures of 5 °C, 15 °C, and 25 °C. The load was applied at the constant displacement rate of 2 mm/min. The SCB test setup and procedure followed the AASHTO TP105-13 protocol. The SCB test was set up as shown in Figure 5. The SCB test specimen was supported at two rollers and loaded at a single roller in the middle of the specimen. The length of the support roller for the SCB test was defined as the fraction of the test specimen diameter (D). A typical value of length is approximately 0.8D (i.e., 120 mm) [28].

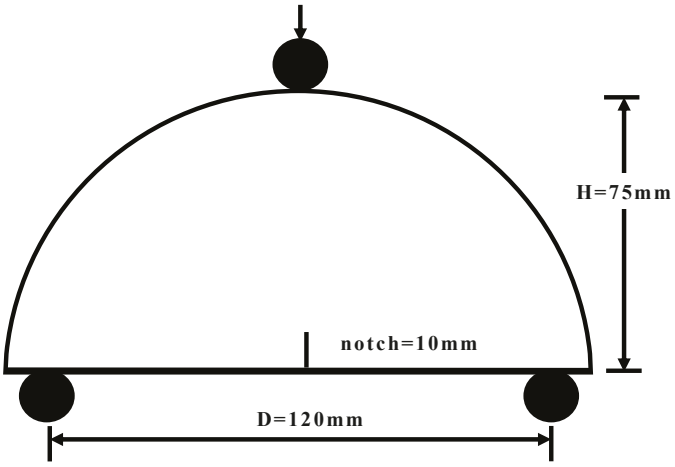

Figure 5. The SCB test configuration.

To maintain the *RH* level during the SCB test, the dry agent of P_2O_5 power was placed into the environment chamber to absorb water vapor for the *RH* level of 2%. A humidifier was installed in the environment chamber to maintain the stable humidity levels for the *RH* levels of 50%, 80%, and 100%.

In this study, the SCB test under different *RH* levels was conducted to evaluate the fracture resistance and tensile strength of asphalt concrete and investigate the water vapor concentration (or the *RH* level) on the fracture behavior of the asphalt mixture. The fracture energy is used to characterize the crack resistance of asphalt concrete. In the SCB test, the fracture energy indicates the energy required for the crack propagation. The area under the load–displacement curve is the fracture work for asphalt concrete completely fractured. The fracture energy is calculated as the ratio of the fracture work to the effective fracture area, as shown in Equation (2).

$$G_f = \frac{W_f}{A_{act}} \tag{2}$$

where G_f is the fracture energy, mJ/mm^2; W_f is the fracture work; A_{act} is the effective fracture area, $A_{act} = (r - c) \times t$; r is the specimen radius, mm; c is the notch length, mm; t is the specimen thickness, mm.

Tensile strength is another crucial indicator of the crack resistance of asphalt concrete. The crack initiates and propagates when the tensile stress exceeds the tensile strength. According to the literature [29], the tensile strength can be obtained by the SCB test using the specimen without a notch. Tensile strength refers to the maximum tensile stress calculated at the center bottom of the SCB specimen by the following:

$$\sigma_t = \frac{3PL}{2th^2} = \frac{6PL}{tD^2} \tag{3}$$

where σ_t is the tensile strength, MPa; P is the peak load, N; L is the length of support roller, mm; h is the height of the specimen, mm; t is the specimen thickness, mm; D is the specimen diameter, mm.

3. Results and Discussion

3.1. Load–Displacement Curve

Figure 6 shows the load–displacement curve under different *RH* and temperature levels for AC-13C. It was found that the curve showed the viscoelastic behavior of the specimen at an intermediate temperature (5 °C~15 °C). With the increase in loading time at the constant displacement rate, the load on the SCB specimen gradually increased and the notched crack continued to propagate with the accumulation of the fracture work. When the load reached the peak value, the SCB specimen became unstable, which led the notched

crack to rapidly propagate upward. The load decreased significantly after the peak, which indicates that the SCB specimen had fractured and could not sustain the substantial loading.

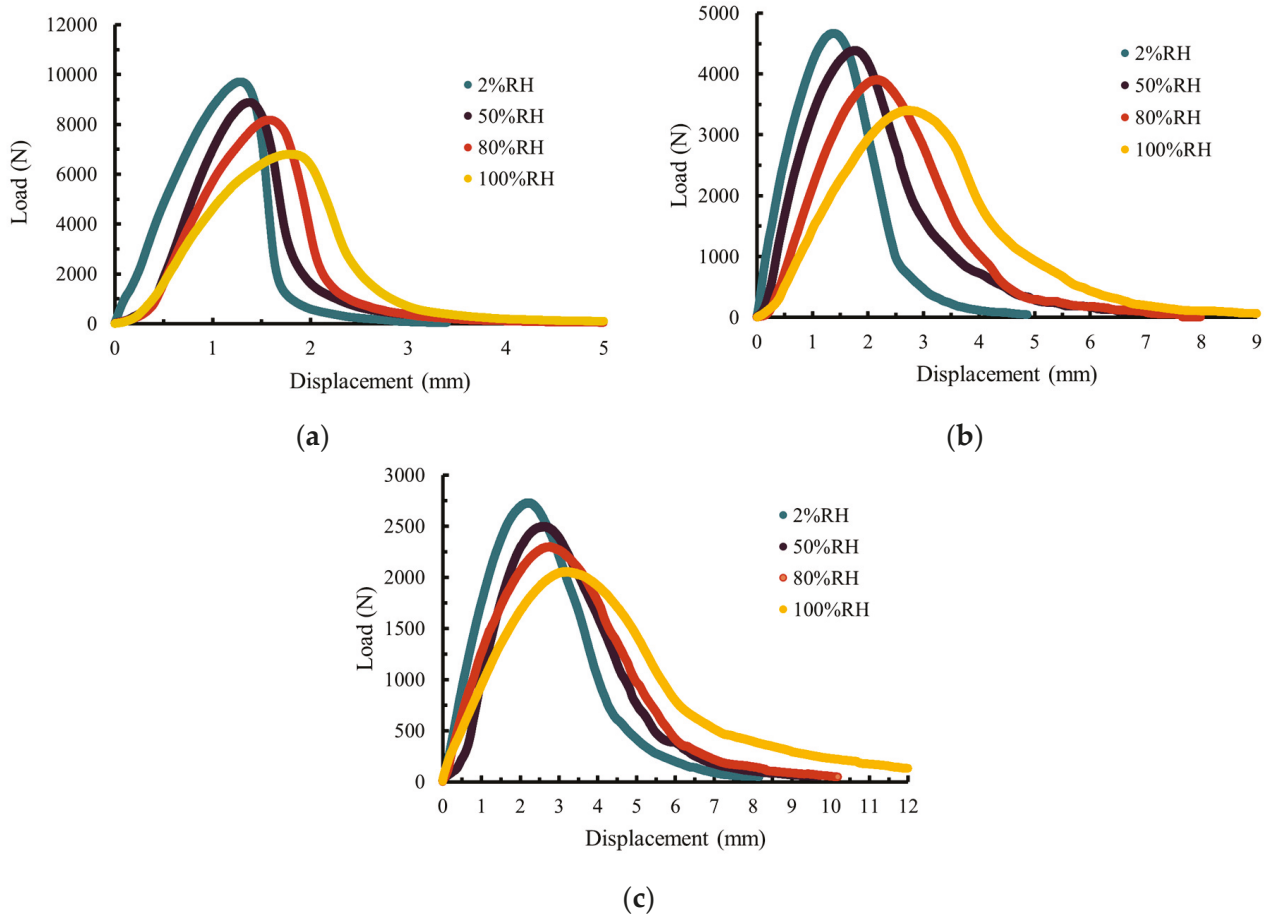

Figure 6. Load–displacement curve at different test temperatures for AC-13C at temperature of (**a**) 5 °C; (**b**) 15 °C; (**c**) 25 °C.

Figure 6 also shows that as the temperature increased, the peak load of the asphalt concrete mixture decreased, while the maximum displacement increased correspondingly, which indicates that the high temperature can reduce the bearing capacity of the asphalt concrete mixture. At the temperature of 5 °C, the load–displacement curve after the peak load dropped steeply, which indicates a decrease in the viscous deformation of the specimen. At the temperatures of 15 °C and 15 °C, the curve after the peak load dropped gradually and showed good toughness.

Moreover, Figure 6 shows that as the water vapor concentration (or the *RH* level) increased, the peak load of the asphalt concrete mixture showed a downward trend, which indicates that the high water vapor concentration can lead to a decrease in the bearing capacity of the mixture. The maximum displacement increased correspondingly with the rising temperature, which indicates that under a sufficient humidity curing period, the specimen becomes softer and more ductile.

3.2. Fracture Energy

At the intermediate temperature, the mixture behavior is governed by the viscoelastic fracture mechanics. Fracture energy can be used to characterize the crack resistance of the mixture. Figure 7 shows that the fracture energy had a downward trend as the temperature increased for the three types of mixtures. The AC-13C mixture had the highest fracture

energy and showed the best toughness due to it using the SBS-modified asphalt and had a higher asphalt content to withstand larger deformation.

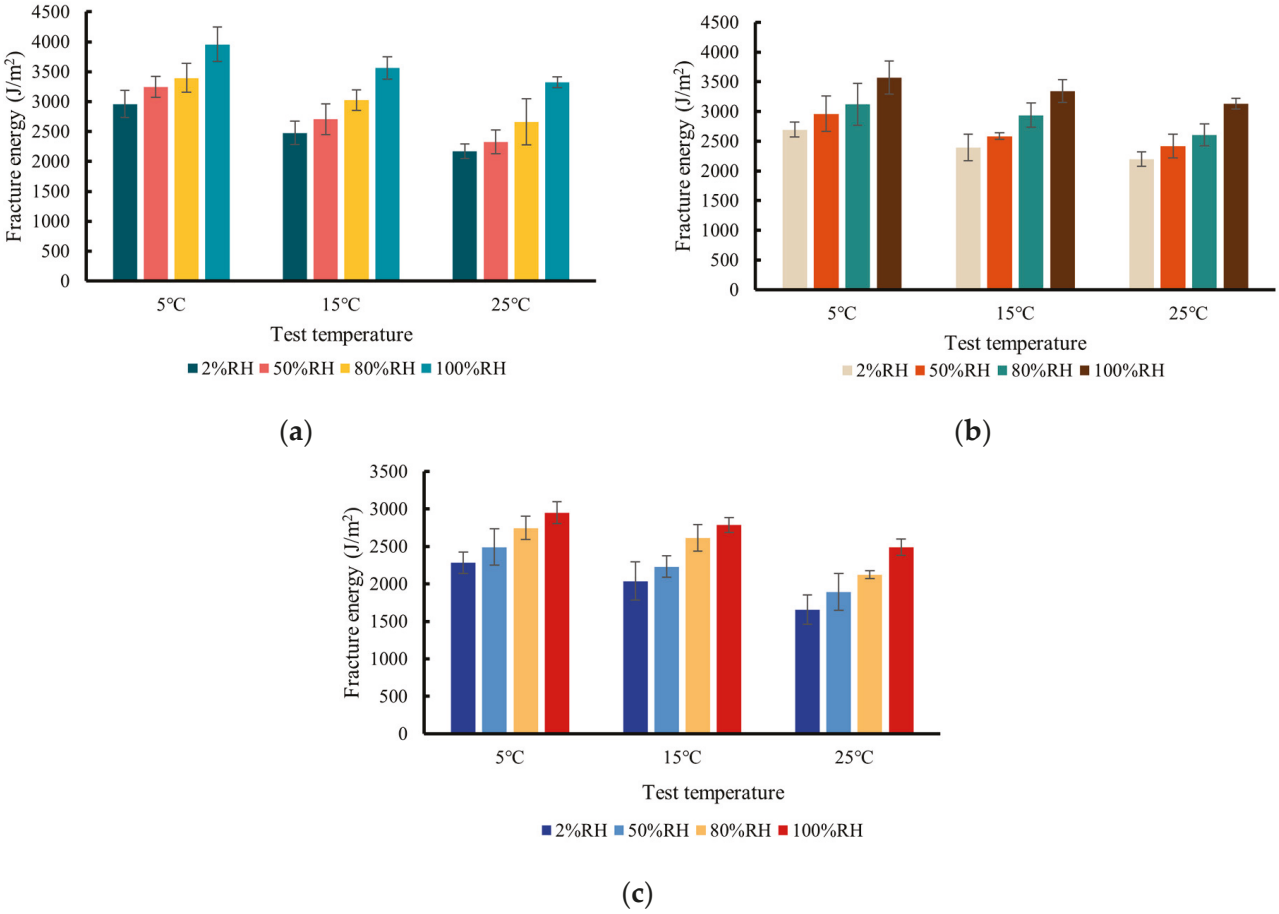

Figure 7. Fracture energy vs. test temperature at different *RH* levels for (**a**) AC-13; (**b**) AC-20C; (**c**) AC-25C mixture.

It was observed from Figure 7 that as the *RH* level (or the water vapor concentration) increased, the fracture energy of the three types of mixtures increased, which seems counter-intuitive. This is because, as noted in Figure 6, that the elevated *RH* level increased the ductility of the asphalt concrete mixture, which possibly led to a larger fracture energy. Another reason is that the water vapor may alter the internal pore pressure of the mixture and help to distribute the stress during loading.

3.3. Tensile Strength

Tensile strength is one of the significant parameters in which to evaluate the fracture properties of the asphalt concrete mixture. Figure 8 shows the tensile strength obtained by Equation (3) at varying temperatures and *RH* levels (or water vapor concentration). It is known that the tensile strength is primarily influenced by the peak load and the specimen dimension. It was noted in Figure 8 that the tensile strength showed a downward trend, which is consistent with the peak load. As the temperature increased, the tensile strength of the three types of mixtures declined, which indicates that the adhesion of the aggregate–asphalt interface dropped with higher temperature.

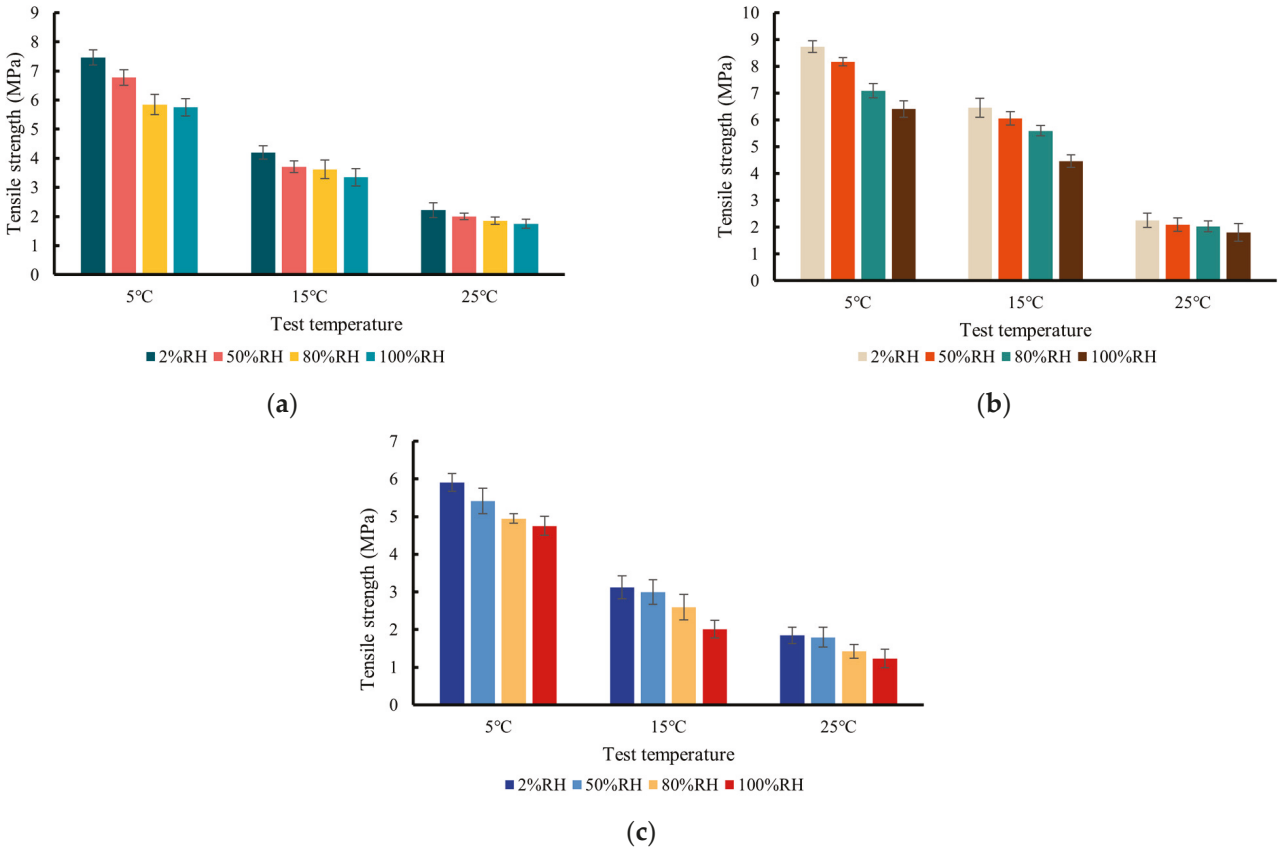

Figure 8. Tensile strength vs. test temperature at different *RH* levels for (**a**) AC-13; (**b**) AC-20C; (**c**) AC-25C mixture.

Figure 8 also shows that as the *RH* level rose from 2% to 100% (i.e., the water vapor concentration rose from 0.35 g/m^3 to 17.27 g/m^3), the tensile strength of the three types of mixtures was reduced by 34.84% on average. This shows that the water vapor resulted in the loss of adhesion and cohesion within the mixture.

3.4. Regression Analysis

This study correlated the water vapor concentration and temperature with the fracture indices to quantify their effects on the fracture resistance of asphalt concrete. The fracture indices including the fracture energy and tensile strength were calculated from the SCB tests. The genetic expression programming (GEP) model was adopted to perform this correlation due to its advantages in regression analysis with small datasets.

The GEP is an evolutionary algorithm to develop models without pre-defined expression and can evolve the form of the expression itself along with its parameters [30]. The structure of the GEP model includes chromosome and expression trees. The chromosome is composed of genes coded as a fixed-length string such as "0123456+−*$d_1d_2d_3d_4$". Chromosomes can be translated into expression trees and evolved by gene operators such as mutation (*), subtraction (−), and recombination (+), from one generation to the next. The mathematical expression is developed and optimized via evolution. The expression is composed of different variables (i.e., "d_1", "d_2", "d_3", and "d_4") and operators (i.e., "+", "−", and "*"). Figure 9 depicts the schematic diagram of the GEP model structures.

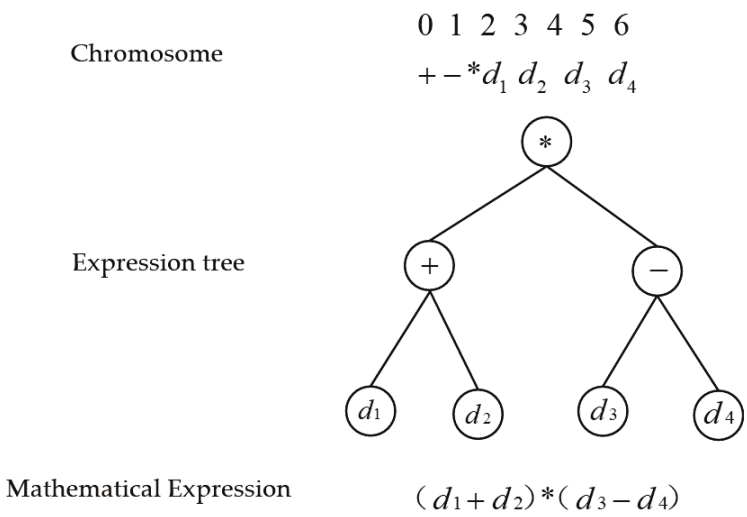

Figure 9. Schematic diagram of the GEP model structure.

The GEP model was developed to quantify the effect of water vapor concentration and temperature on the fracture properties of asphalt concrete. The performance of the GEP model was evaluated by using the root relative square error (RRSE) and R-squared, as calculated below:

$$\text{RRSE} = \sqrt{\frac{\sum_{i=1}^{n} (y_i - \hat{y}_i)^2}{\sum_{i=1}^{n} (y_i - \overline{y})^2}} \tag{4}$$

$$R^2 = 1 - \frac{\sum_{i=1}^{n} (y_i - \hat{y}_i)^2}{\sum_{i=1}^{n} (y_i - \overline{y})^2} \tag{5}$$

where R^2 is the coefficient of determination; y_i is the i-th tested value; $\hat{y}_i$ is the i-th predicted value or fitted value; $\overline{y}$ is the mean value of tested values; n is the total number of tested values. Both the RRSE and R-squared value are model metrics used to evaluate model performance. The R-squared value commonly falls into the range between 0 and 1. The R-squared value close to 1 means more accurate model prediction performance. The lower the RRSE value, the better the model's predictive power.

Table 4 presents the mathematical expressions derived from the GEP model based on the SCB test results for the fracture energy and (y_1) tensile strength (y_2) where x_1 and x_2 refer to the temperature (°C) and water vapor concentration (g/m^3), respectively. It can be seen from Table 4 that the R-squared values for the GEP models across the three types of mixtures exceeded 0.94, which means that the GEP models showed good agreement with the fracture energy and tensile strength obtained from the SCB test. Therefore, the GEP models are applicable for different mixture types (AC-13C, AC-20C, and AC-25C), but may not extend to other types of materials due to variations in binder type, aggregate characteristics, and mixture compositions.

Table 4. GEP model results for fracture indices.

Mixture Type	Fracture Index	Expression	R^2	*RRSE*
AC-13C	Fracture energy	$y_1 = 0.88{x_1}^2 - 67.19x_1 + 4.65{x_2}^2 - 15.81x_2 + 3204.96$	0.9821	0.0488
	Tensile strength	$y_2 = 0.005{x_1}^2 - 0.371x_1 - 0.058x_2 + 8.799$	0.9431	0.0317
AC-20C	Fracture energy	$y_1 = -0.54{x_1}^2 - 16.85x_1 + 3.93{x_2}^2 - 2.53x_2 + 2592.53$	0.9842	0.0465
	Tensile strength	$y_2 = -0.008{x_1}^2 - 0.032x_1 - 0.006{x_2}^2 + 0.015x_2 + 8.672$	0.9560	0.0414
AC-25C	Fracture energy	$y_1 = -1.64{x_1}^2 + 17.13x_1 + 2.44{x_2}^2 + 7.57x_2 + 2117.36$	0.9798	0.0394
	Tensile strength	$y_2 = 0.007{x_1}^2 - 0.404x_1 - 0.003{x_2}^2 + 0.001x_2 + 7.545$	0.9491	0.0271

4. Conclusions

In this study, the SCB test was performed to investigate the effect of the water vapor concentration (or the *RH* level) on the fracture properties of asphalt concrete. Three types of mixtures (AC-13C, AC-20C, and AC-25C) were utilized. The mixtures were humidity conditioned at varying *RH* levels of 2%, 50%, 80%, and 100% prior to the SCB test. The two significant parameters, that is, the fracture energy and tensile strength, were obtained to characterize the fracture properties of the mixtures. Based on the SCB test results, the main findings of this study can be drawn as follows:

- The humidity conditioning program was designed for the SCB specimens to study the impact of the *RH* levels of 2%, 50%, 80%, and 100% at 20 °C. The duration of the humidity curing period was determined by the finite element model, which simulated the water vapor diffusion until the equilibrium was reached.
- The load–displacement curve shows that the increase in *RH* level from 2% to 100% or the elevated temperature from 5 °C to 25 °C decreased the peak load but increased the displacement of the mixtures, which implies that the water vapor or higher temperature reduced the bearing capacity of mixture but improved the mixture toughness.
- The fracture energy showed a downward trend as the temperature increased for the three types of mixtures. Specifically, the AC-13C mixture had the highest fracture energy and showed the best toughness due to its use of the SBS-modified asphalt and higher asphalt content. Therefore, the use modified binders such as SBS-modified asphalt is recommended to enhance the durability of asphalt concrete, especially in regions with high humidity and temperature variations.
- With the rising *RH* levels, the fracture energy of the three types of mixtures increased since the water vapor enhanced the ductility of the mixture to some extent. Another reason is that the water vapor may alter the internal pore pressure of the mixture and help distribute the stress during loading.
- The tensile strength of the three types of mixtures declined with the increase in temperature, which indicates a reduction in the adhesion of the aggregate–asphalt interface with the higher temperature.
- As the *RH* level rose from 2% to 100% (i.e., the water vapor concentration rose from 0.35 g/m^3 to 17.27 g/m^3), the tensile strength of the three types of mixtures was reduced by 34.84% on average, which revealed that the water vapor led to the loss of adhesion and cohesion within the mixture.
- The GEP models were developed to quantify the effect of the water vapor concentration and temperature on the fracture indices. The R-squared values for the GEP models across the three types of mixtures were above 0.94, which indicates a good agreement between the GEP models and the fracture energy and tensile strength obtained from the SCB test.

The investigation in this study was restricted to the asphalt concrete mixtures with the SBS-modified binder and neat 70# binder. In future work, more binder types such as the modified binder with an anti-stripping additive will be utilized for humidity conditions and the SCB test. Moreover, the SCB tests will conducted on a wide variety of mixture types to enrich the data for the GEP model, thereby making it applicable to a broader range of mixtures.

Author Contributions: Conceptualization, Y.C. and X.W.; Methodology, Y.C., T.H., K.Z. and Z.L.; Investigation, Z.L.; Validation, Z.L; Writing—original draft preparation, Y.C.; Writing—review and editing, X.W., T.H. and K.Z.; Funding acquisition, X.W. and K.Z. All authors have read and agreed to the published version of the manuscript.

Funding: This work was financially supported by the Science and Technology Project of Jiangxi Provincial Department of Transportation of China (Project No. 2021C0008) and the Ganpo Talents Support Program High-Level and High-Skill Leading Talents Cultivation Project. This work was also supported by the Fundamental Research Funds for the Central University of China (WUT: 21302008).

Institutional Review Board Statement: Not applicable.

Informed Consent Statement: Not applicable.

Data Availability Statement: All data, models, and codes generated or used in this study are included in the submitted manuscript.

Conflicts of Interest: Authors Xuqing Wen, Kai Zhang, and Zhengang Li were employed by the Jiangxi Provincial Communications Investment Group Co. Ltd. Project Construction Management Company, Jiangxi Transportation Institute Co., Ltd. and Wuhan Dongxihu District Transportation Bureau, respectively. The remaining authors declare that the research was conducted in the absence of any commercial or financial relationships that could be construed as a potential conflict of interest.

References

1. Luo, R.; Liu, Z.; Huang, T.; Tu, C. Water vapor passing through asphalt mixtures under different relative humidity differentials. *Constr. Build. Mater.* **2018**, *165*, 920–930. [CrossRef]
2. Kassem, E.; Masad, E.; Lytton, R.; Bulut, R. Measurements of the moisture diffusion coefficient of asphalt mixtures and its relationship to mixture composition. *Int. J. Pavement Eng.* **2009**, *10*, 389–399. [CrossRef]
3. Arambula, E.; Caro, S.; Masad, E. Experimental measurement and numerical simulation of water vapor diffusion through asphalt pavement materials. *J. Mater. Civ. Eng.* **2010**, *22*, 588–598. [CrossRef]
4. Kennedy, T.W.; Roberts, F.L.; Lee, K.W. *Evaluation of Moisture Effects on Asphalt Concrete Mixtures*; Transportation Research Board: Washington, DC, USA, 1983.
5. Kim, Y.-R.; Zhang, J.; Ban, H. Moisture damage characterization of warm-mix asphalt mixtures based on laboratory-field evaluation. *Constr. Build. Mater.* **2012**, *31*, 204–211. [CrossRef]
6. *ASTM D4867*; Standard Test Method for Effect of Moisture on Asphalt Concrete Paving Mixtures. ASTM: West Conshohocken, PA, USA, 2006.
7. Airey, G.; Collop, A.; Zoorob, S.; Elliott, R. The influence of aggregate, filler and bitumen on asphalt mixture moisture damage. *Constr. Build. Mater.* **2008**, *22*, 2015–2024. [CrossRef]
8. Varveri, A.; Avgerinopoulos, S.; Scarpas, A. Experimental evaluation of long-and short-term moisture damage characteristics of asphalt mixtures. *Road Mater. Pavement Des.* **2016**, *17*, 168–186. [CrossRef]
9. Hossain, M.I.; Tarefder, R.A. Behavior of asphalt mastic films under laboratory controlled humidity conditions. *Constr. Build. Mater.* **2015**, *78*, 8–17. [CrossRef]
10. *ASTM E104-20a*; Standard Practice for Maintaining Constant Relative Humidity by Means of Aqueous Solutions. ASTM: West Conshohocken, PA, USA, 2012.
11. Tong, Y.; Luo, R.; Lytton, R.L. Moisture and aging damage evaluation of asphalt mixtures using the repeated direct tensional test method. *Int. J. Pavement Eng.* **2015**, *16*, 397–410. [CrossRef]
12. Cheng, D.; Little, D.N.; Lytton, R.L.; Holste, J.C. Moisture damage evaluation of asphalt mixtures by considering both moisture diffusion and repeated-load conditions. *Transp. Res. Rec.* **2003**, *1832*, 42–49. [CrossRef]
13. Xi, L.; Luo, R.; Liu, H. Evaluating the influence of humidity on asphalt mixture performance by the flow number test. *Constr. Build. Mater.* **2021**, *284*, 122754. [CrossRef]
14. Lytton, R.L.; Masad, E.A.; Zollinger, C.; Bulut, R.; Little, D.N. *Measurements of Surface Energy and Its Relationship to Moisture Damage*; Texas Transportation Institute, Texas A&M University: College Station, TX, USA, 2005.
15. Lee, J.; Moon, S.-J.; Im, J.; Yang, S. Evaluation of moisture susceptibility of asphalt mixtures using dynamic modulus. *J. Test. Eval.* **2017**, *45*, 1280–1288. [CrossRef]
16. Wang, W.; Wang, L.; Yan, G.; Zhou, B. Evaluation on moisture sensitivity of asphalt mixture induced by dynamic pore water pressure. *Int. J. Pavement Res. Technol.* **2020**, *13*, 489–496. [CrossRef]
17. Akentuna, M.; Liu, J.; Mohammad, L.N.; Sachdeva, S.; Cooper, S.B., III; Cooper, S.B., Jr. Moisture Susceptibility of Asphalt Mixtures: Conditioning and Testing Protocols. *Transp. Res. Rec.* **2023**, 03611981221147214. [CrossRef]
18. Kim, M.; Mohammad, L.N.; Elseifi, M.A. Characterization of fracture properties of asphalt mixtures as measured by semicircular bend test and indirect tension test. *Transp. Res. Rec.* **2012**, *2296*, 115–124. [CrossRef]
19. Kuruppu, M.D.; Chong, K.P. Fracture toughness testing of brittle materials using semi-circular bend (SCB) specimen. *Eng. Fract. Mech.* **2012**, *91*, 133–150. [CrossRef]
20. Li, X.-J.; Marasteanu, M. Using semi circular bending test to evaluate low temperature fracture resistance for asphalt concrete. *Exp. Mech.* **2010**, *50*, 867–876. [CrossRef]
21. Karimi, M.M.; Dehaghi, E.A.; Behnood, A. A fracture-based approach to characterize long-term performance of asphalt mixes under moisture and freeze-thaw conditions. *Eng. Fract. Mech.* **2021**, *241*, 107418. [CrossRef]
22. Fakhri, M.; Ahmadi, A. Evaluation of fracture resistance of asphalt mixes involving steel slag and RAP: Susceptibility to aging level and freeze and thaw cycles. *Constr. Build. Mater.* **2017**, *157*, 748–756. [CrossRef]
23. Zhang, K.; Li, W.; Han, F. Performance deterioration mechanism and improvement techniques of asphalt mixture in salty and humid environment. *Constr. Build. Mater.* **2019**, *208*, 749–757. [CrossRef]

24. *JTG E20-2011*; Standard Test Methods of Bitumen and Bituminous Mixtures for Highway Engineering. Ministry of Transportation: Beijing, China, 2011.
25. *JTG F40-2004*; Technical Specification for Construction of Highway Asphalt Pavements. Ministry of Transportation Highway Research Institute: Beijing, China, 2004.
26. Marín-Uribe, C.R.; Restrepo-Tamayo, L.M. Experimental study of the tensile strength of hot asphalt mixtures measured with indirect tensile and semi-circular bending tests. *Constr. Build. Mater.* **2022**, *339*, 127651. [CrossRef]
27. Tu, C.; Luo, R.; Huang, T. Numerical Simulation of Moisture Diffusion in the Microstructure of Asphalt Mixtures. *Materials* **2023**, *16*, 2504. [CrossRef] [PubMed]
28. *EN 12697-44*; Czech Standardization Agency. Bituminous Mixtures-Test Methods for Hot Mix Asphalt Part 44: Crack Propagation by Semi-Circular Bending Test. BSI: London, UK, 2019.
29. Huang, L.; Cao, K.; Zeng, M. Evaluation of semicircular bending test for determining tensile strength and stiffness modulus of asphalt mixtures. *J. Test. Eval.* **2009**, *37*, 122–128. [CrossRef]
30. Ferreira, C. *Gene Expression Programming: Mathematical Modeling by An Artificial Intelligence*; Springer: Berlin/Heidelberg, Germany, 2006; Volume 21.

Disclaimer/Publisher's Note: The statements, opinions and data contained in all publications are solely those of the individual author(s) and contributor(s) and not of MDPI and/or the editor(s). MDPI and/or the editor(s) disclaim responsibility for any injury to people or property resulting from any ideas, methods, instructions or products referred to in the content.

materials

MDPI

Article

Design and Microwave Absorption Performance Study of SiC-Fe_3O_4 Emulsified Asphalt Mixture

Xiangyu Jiang, Wen Xu *, Yixing Chen and Jiaqi Li

School of Transportation and Logistics Engineering, Wuhan University of Technology, Wuhan 430063, China
* Correspondence: wenxu@whut.edu.cn; Tel.: +86-15926241294

Abstract: To address the challenges of slow curing speed and suboptimal microwave absorption during the paving of cold-mixed and cold-laid asphalt mixtures, this study introduces SiC-Fe_3O_4 composite material (SF) into emulsified asphalt mixtures to enhance microwave absorption and accelerate curing via microwave heating. Initially, based on the maximum density curve theory, an appropriate mineral aggregate gradation was designed, and the optimal ratio of emulsified asphalt mixture was determined through mixing tests, cohesion tests, wet wheel wear tests, and load wheel sand adhesion tests. Subsequently, the influence of SF content on the mixing performance of emulsified asphalt mixtures was analyzed through mixing and consistency tests. Finally, the microwave absorption performance of the mixture was evaluated by designing microwave heating tests under different conditions, using temperature indicators and quality indicators. The experimental results indicate that when SF content ranges from 0% to 4%, the mixing performance of the emulsified asphalt mixture meets specification requirements. The dosage of SF, SF composite ratio, and microwave power significantly impact microwave absorption performance, whereas environmental temperature has a relatively minor effect. The optimal mix ratio for the emulsified asphalt mixture is mineral aggregate:modified emulsified asphalt:water:cement = 100:12.8:6:1. The ideal SF dosage is 4%, with an optimal SiC to Fe_3O_4 composite ratio of 1:1, and a suitable microwave power range of 600–1000 W.

Keywords: emulsified asphalt mixture; SiC-Fe_3O_4 composite material; mix proportion design; microwave absorption performance; microwave curing

1. Introduction

Among various grades of highways, asphalt pavement is currently the most extensively used high-grade pavement in China. With the gradual increase in the proportion of road maintenance in the field of road engineering, various road maintenance methods have also been developed. Among these methods, emulsified asphalt mixture is an important material. However, there exists a contradiction between "slow cracking during construction" and "fast setting during molding" in the application of emulsified asphalt [1]. To address this issue, the advantages of microwave heating, which is fast, uniform, and selective, can be utilized to heat emulsified asphalt mixtures [2]. Ordinary emulsified asphalt mixtures have a relatively poor microwave absorption ability [3]. The temperature rise rate after microwave heating is slow, and the water evaporation rate is also relatively slow, which affects the microwave heating curing speed of the mixture.

Based on the relatively poor microwave absorption performance of existing materials in emulsified asphalt mixtures, adding microwave-absorbing materials to improve the microwave absorption performance of the mixture is considered, thereby increasing the microwave curing speed of emulsified asphalt mixtures. Microwave-absorbing materials can be divided into two categories based on their loss mechanisms: electrical loss-type microwave-absorbing materials [4] and magnetic loss-type microwave-absorbing materials [5]. Electrical loss-type microwave-absorbing materials convert the electrical energy of microwaves into thermal energy through electrical loss, while magnetic loss-type

microwave-absorbing materials convert the magnetic energy of microwaves into thermal energy through magnetic loss. Both types of materials can be used separately to improve the microwave absorption performance of emulsified asphalt mixtures. Since microwaves are a type of electromagnetic wave that contains both electrical and magnetic energy, the single loss mechanism of single-phase materials cannot fully utilize the electromagnetic energy in microwaves. Therefore, it is necessary to find a microwave-absorbing material that can simultaneously utilize both electrical and magnetic energy.

Wan et al. [6] found through experiments that the main effective components in steel slag that absorb microwaves are iron and Fe_3O_4. When Fe_3O_4 powder is mixed with mineral powder and steel slag powder of the same quality and size, the temperature rise and heat generated by Fe_3O_4 powder are significantly higher than those by iron powder. In samples where both coexist, their contributions to microwave heating are independent, with Fe_3O_4 playing a dominant role.

Chen et al. [7] studied the microwave absorption properties of SiC and boron-doped SiC. The results indicated that boron-doped SiC exhibits greater microwave absorption performance in the frequency range of 2–18 GHz compared to SiC. At 14 GHz and a material thickness of 1.5 mm, the maximum microwave reflection loss is −37.94 dB.

Liu et al. [8] proposed that a composite material composed of SiC, an electric loss-type microwave-absorbing material, and Fe_3O_4, a magnetic loss-type microwave-absorbing material, can significantly enhance the microwave absorption performance of asphalt mixtures. To improve the efficiency of microwave deicing, researchers designed control specimens of microwave-enhanced functional layer asphalt concrete and asphalt concrete without the microwave-enhanced functional layer. It was found that the microwave-enhanced functional layer significantly improves the microwave heating efficiency and deicing efficiency of asphalt concrete. Through a series of experiments, the optimal ratio of SiC to Fe_3O_4 was determined to be 3:1.

Additionally, the research by Liu and Zhao et al. [9–12] has shown that traditional methods may lead to serious environmental pollution and energy consumption. The microwave heating technology for SF emulsified asphalt mixtures has high microwave energy utilization and is environmentally friendly, and has been widely studied. The research by Li et al. [13] has also demonstrated the excellent microwave absorption capability of Fe_3O_4. Microwave heating is currently considered to be the most promising clean energy technology for deicing asphalt pavements.

SiC-Fe_3O_4 composite material is a material that combines the characteristics of SiC and Fe_3O_4, with potential applications in various fields, including supercapacitors, electromagnetic wave absorption, and thermal management materials. When considering the use of this composite material and its microwave curing method, it is very important to ensure compliance with relevant regulations and safety standards. In articles such as "Microwave heating and deicing efficiency for asphalt concrete with SiC–Fe_3O_4 microwave enhanced functional layer" [14] and "Microwave absorption enhancement of asphalt concrete with SiC-Fe_3O_4 mixtures modifier" [8], the application of SF in the field of microwave heating of asphalt mixture is mentioned. Research, including the aforementioned articles, shows that the application of SF microwave heating technology is of great significance for extending the service life of road surfaces, reducing maintenance costs, and maintaining environmental protection.

Various microwave-absorbing materials have been proposed, including steel slag, steel wire fiber, carbon fiber, steel wool fiber, iron powder, natural magnetite powder, SiC, Fe_3O_4, and SiC-Fe_3O_4 binary composite materials. These materials have been studied for their enhancement effects on the microwave absorption performance of asphalt mixtures. Microwave heating technology has been applied in road surface repair, deicing, and curing. A performance comparison of these materials is presented in Table 1.

Based on the current research status both domestically and internationally, this article aims to enhance the microwave absorption performance of emulsified asphalt mixture. A composite material (SF) consisting of the electric loss-type microwave absorption material

SiC and the magnetic loss-type microwave absorption material Fe_3O_4 is introduced to investigate the microwave absorption performance of emulsified asphalt mixture doped with SF (SF-EAM).

Firstly, the technical performance of various raw materials for emulsified asphalt mixture is evaluated. Secondly, based on the commonly used MS-3 gradation for micro-surface applications, a gradation design is carried out according to the maximum density curve theory. The ratio of the emulsified asphalt mixture is determined through mixing tests, cohesion tests, wet wheel wear tests, and load wheel sand adhesion tests. Subsequently, the influence of SF on the mixing performance of the emulsified asphalt mixture is studied through mixing performance tests, and the reasonable range of SF dosage is determined. Finally, microwave heating experiments are designed with different SF dosages, SF composite ratios, environmental temperatures, and microwave powers. The effects of these factors on the microwave absorption performance of SF-EAM are studied using temperature and quality indicators.

This article employs various methods such as theoretical research and indoor experiments to study the microwave absorption performance of the SiC-Fe_3O_4 emulsified asphalt mixture. The technical route is illustrated in Figure 1.

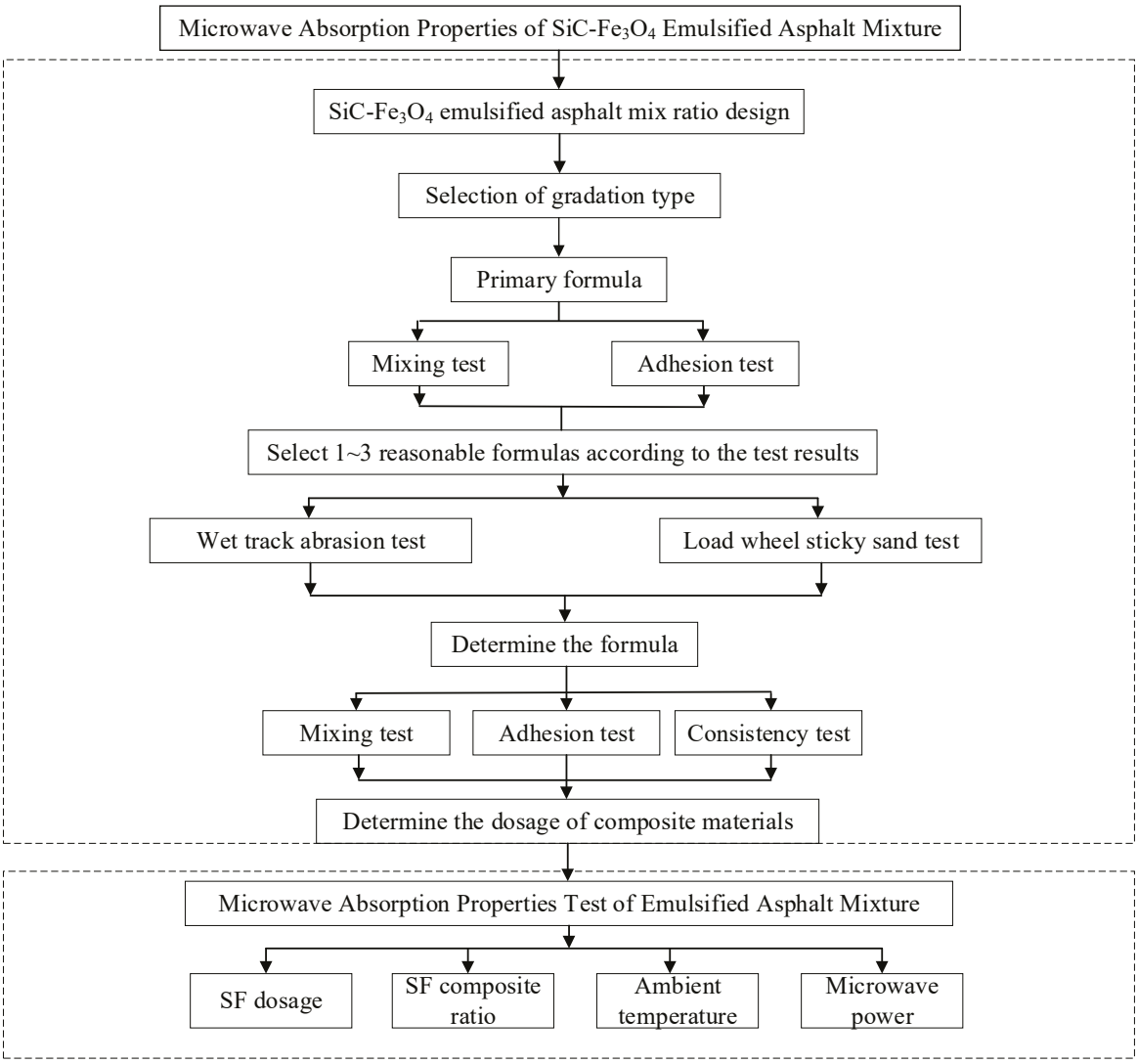

Figure 1. Technical roadmap.

Table 1. Characteristics of various microwave-absorbing materials.

Specimen	Characteristics of Absorbing Materials	Deficiency	Reference
Steel fiber	Electric Loss Type, Magnetic Loss Type	High costs and technical requirements	Yang et al. [15]
Sulfurous iron ore slag	Magnetic Loss Type	High technical requirements	Zhang et al. [16]
Carbon fiber	Electric Loss Type	High costs	Wang et al. [17]
Steel slag	Magnetic Loss Type	Complex composition of steel slag	Wang [18]
Natural magnetite	Magnetic Loss Type	Thermal efficiency is related to the grade of Fe_3O_4	Guan et al. [19]
Fe_3O_4	Magnetic Loss Type	Easy to reunite, high technical requirements	Guo et al. [20]
Boron-doped SiC	Electric Loss Type	High technical requirements	Chen et al. [7]
SiC-Fe_3O_4	Electric Loss Type, Magnetic Loss Type	High costs	Liu Xiaoming [21]

2. Materials and Methods

2.1. Materials and Preparation

The materials used in this study include modified emulsified asphalt, mineral materials, mineral powder, cement, SiC, and Fe_3O_4.

2.1.1. Modified Emulsified Asphalt

The basic performance indicators of the modified emulsified asphalt (self-made) prepared in this study are shown in Table 2.

Table 2. Technical performance of modified emulsified asphalt.

Test Item		Unit	Standard Specifications [22]	Test Result	Test Method
Remainder on sieve (1.18 mm sieve)		%	≤0.1	0.05	T0652
Electric charge		/	Positively charged cation	Positively charged cation	T0653
Engler viscosity E_{25}		/	3~30	18	T0622
Asphalt standard viscosity C_{25}		s	12~60	35	T0621
Evaporation residue content		%	≥60	65	T0651
Nature of evaporation residues	Penetration degree	0.1 mm	40~100	80	T0604
	Softening point	°C	≥53	66	T0606
	Ductility (5 °C)	cm	≥20	30	T0605
	Solubility	%	≥97.5	98	T0607
Storage stability	1 d	%	≤1	0.5	T0655
	5 d	%	≤5	2.5	

2.1.2. Mineral Materials

The coarse and fine aggregates (Mazhou Expressway Project Department, Jinzhou, China) used in this study are basalt aggregates. The basic performance indicators of these aggregates are presented in Table 3.

Table 3. Technical performance of mineral materials.

Specimen	Test Item	Unit	Standard Specifications [16]	Test Result	Test Method
Coarse aggregate	Crushing value	%	≤26	15	T0316
	LLA	%	≤28	20	T0317
	Polished stone value	BPN	≥42	50	T0321
	Sturdiness	%	≤12	7	T0314
	Flat and elongated particles	%	≤15	10	T0312
Fine aggregate	Sturdiness	%	≤12	6	T0340
Mineral	Sand equivalent	%	≥65	78	T0334

2.1.3. Mineral Powder and Cement

The basic performance indicators of mineral powder (Mazhou Expressway Project Department, Jinzhou, China) used in this study are shown in Table 4. The basic performance indicators of the ordinary Portland cement (Huaxin Cement Co., Ltd., Huangshi, China) used in this study are shown in Table 5.

Table 4. Technical performance of mineral powder.

Test Item	Unit	Standard Specifications [23]	Test Result	Test Method
Apparent relative density	t/m^3	≥2.50	2.8	T0352
Water content	%	≤1	0.8	T0103
Particle size range < 0.6 mm <0.15 mm <0.075 mm	% % %	100 90~100 75~100	100 98 92	T0351
Hydrophilicity	/	<1	0.8	T0353
Plasticity index	/	<4	3	T0354

Table 5. Technical properties of cement.

Test Item		Unit	Standard Specifications [24]	Test Result	Test Method
Setting time	Initial setting	min	≥45	132	T0505
	Final setting	min	≤600	270	
Compressive strength	3 d	MPa	≥17.0	20.4	T0553
	28 d	MPa	≥42.5	47.6	
Rupture strength	3 d	MPa	≥4.0	5.3	T0558
	28 d	MPa	≥7.0	8.2	
Thermal stability		/	Measurement records	Pass	T0505

2.1.4. Preparation of SiC and Fe_3O_4 Composite Materials

The SiC used in this study is high-purity silicon carbide powder produced by Nangong Yingtai Metal Materials Co., Ltd. (Xingtai, China). The SiC content in the silicon carbide powder is greater than 99%, and the appearance of the silicon carbide powder is shown in Figure 2a. The basic technical performance of SiC is evaluated according to the technical requirements for mineral powder, with the test results presented in Table 6.

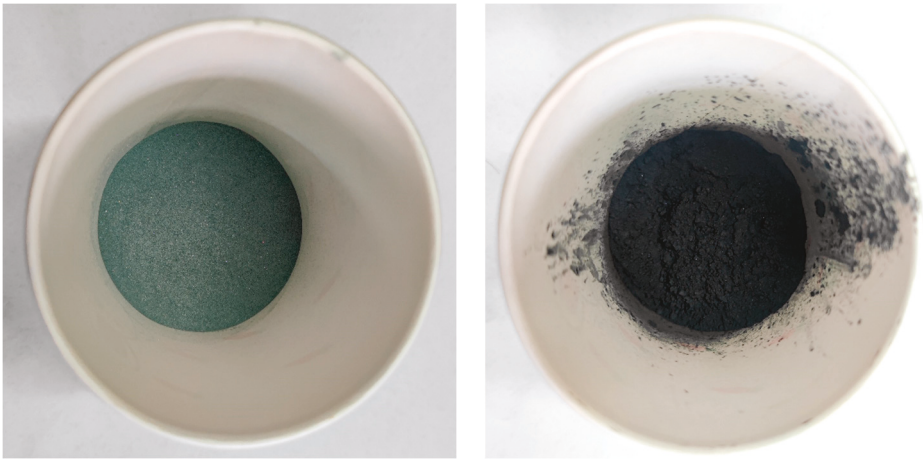

(**a**) (**b**)

Figure 2. Two types of added materials. (**a**) SiC powder; (**b**) Fe_3O_4 powder.

Table 6. Technical performance of SiC.

Test Item	Unit	Standard Specifications [23]	Test Result	Test Method
Apparent relative density	t/m^3	≥2.50	3.1	T0352
Water content	%	≤1	0.01	T0103
Particle size range < 0.6 mm <0.15 mm <0.075 mm	% % %	100 90~100 75~100	100 100 95	T0351
Hydrophilicity	/	<1	0.4	T0353
Plasticity index	/	<4	3	T0354

The Fe_3O_4 used in this study is high-purity iron oxide powder produced by Hebei Keze Metal Materials Co., Ltd. (Xingtai, China). The Fe_3O_4 content in the iron oxide powder is greater than 99%. The appearance of the iron oxide powder is shown in Figure 2b. The basic technical performance of Fe_3O_4 is evaluated according to the technical requirements for mineral materials, with the test results presented in Table 7.

Table 7. Technical performance of Fe_3O_4.

Test Item	Unit	Standard Specifications [23]	Test Result	Test Method
Apparent relative density	t/m^3	≥2.50	4.7	T0352
Water content	%	≤1	0.05	T0103
Particle size range < 0.6 mm <0.15 mm <0.075 mm	% % %	100 90~100 75~100	100 100 95	T0351
Hydrophilicity	/	<1	0.6	T0353
Plasticity index	/	<4	2.5	T0354

Based on the characteristics of the two materials having similar densities and no chemical reactions with each other [25,26], the method for preparing SiC-Fe_3O_4 composite materials from SiC and Fe_3O_4 in this study is as follows: a specified mass of SiC powder and Fe_3O_4 powder are mixed in a stirring cup, stirred thoroughly with a glass rod, and once the two materials are completely and evenly mixed, they are placed in a sealed bag for later use, as shown in Figure 3.

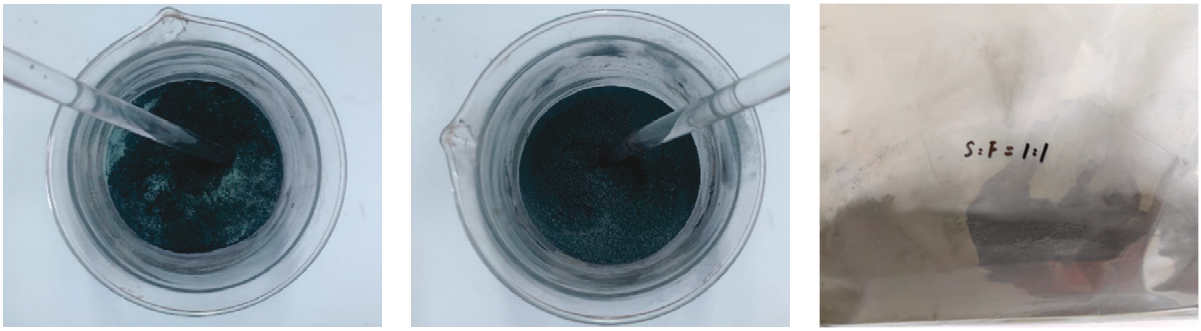

(**a**) (**b**) (**c**)

Figure 3. Preparation of SiC-Fe_3O_4 composite material. (**a**) Mix (**b**) thoroughly and evenly; (**c**) bag for temporary storage.

2.2. Test Methods

2.2.1. Mixing Test

The oil-to-stone ratio range specified in China's standards for MS-3 micro-surfacing is 6.0% to 8.5% [22]. Calculated based on a 60% evaporation residue content, the corresponding emulsified asphalt range is 10% to 14.2%. Based on this range, the initial selection of emulsified asphalt dosage in the mixing test is 13%, corresponding to an oil-to-stone ratio of 7.8%. Cement, used as a filler, has a small dosage and a relatively minor impact on the mix design of the emulsified asphalt mixture; thus, a commonly used dosage of 1% is adopted. The particle sizes of the added SiC and Fe_3O_4 materials are both less than 0.075 mm. In the mix design process, the role of SF is similar to that of mineral powder, and their influence on the initial mix ratio is not considered. The amount of water added is determined according to the consistency of the mixture. Since the asphalt emulsion contains some water, based on existing experiments, when the amount of modified emulsified asphalt is 13%, the range of added water should be 3% to 7%.

The mixing test procedure is shown in Figure 4, with the specific steps as follows:

1. Prepare a certain quantity of mineral materials, modified emulsified asphalt, cement, water, and other materials. Divide the test materials into 5 groups, pour the materials into the mixing cup one by one, and start timing.
2. Mix the mixture evenly. During the mixing test, when the mixture begins to thicken and feels strong in the hands, record the time at this moment. This time is the mixable time of the mixture. Record the mixing time for the 5 groups of emulsified asphalt mixtures in sequence, accurate to 1 s.

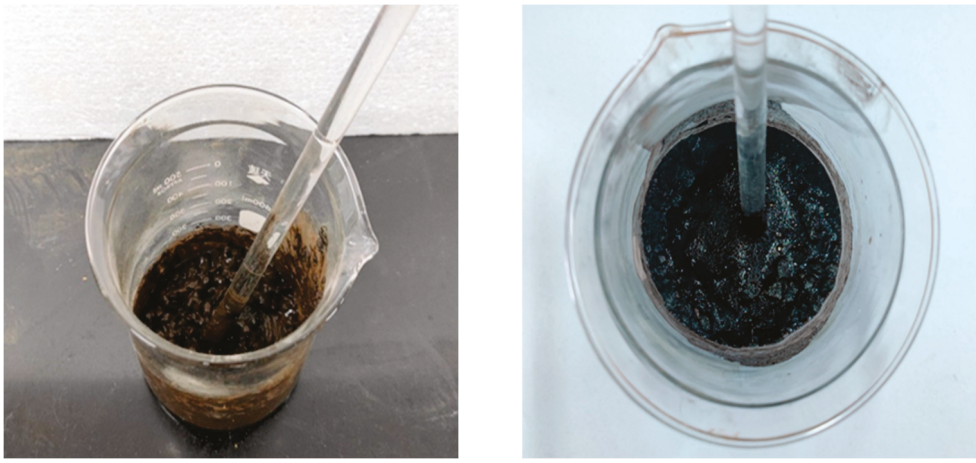

(**a**) (**b**)

Figure 4. Mixing test. (**a**) The state when the mixture begins to thicken; (**b**) when there is too much water added.

2.2.2. Cohesion Test

The cohesion tester (Changji Geological Instrument Co., Ltd., Shanghai, China) used in this study is shown in Figure 5. After determining the appropriate amount of added water for the emulsified asphalt mixture through mixing experiments, this amount was selected for the cohesion tests. A series of cohesion tests were conducted by fixing the quantities of other materials and only varying the amount of emulsified asphalt. The optimal amount of emulsified asphalt was selected based on the measured cohesion values and the failure state of the test specimens.

Figure 5. Cohesion Tester.

According to the Technical Guidelines for Micro-Surfacing and Slurry Seal [22] (hereinafter referred to as the "Guidelines"), the actual oil-to-stone ratio used for MS-3 grading is typically between 6.0% and 7.5% and should not exceed the specified limit of 8.5%. Therefore, based on a 60% evaporation residue content, the dosage range of modified emulsified asphalt was selected to be 10% to 14%, corresponding to an oil-to-stone ratio range of 6% to 8.4%. The dosage ratios of various materials used in the cohesion test are summarized in Table 8.

Table 8. Material usage ratio for cohesion test.

Specimen	Minerals	Water	Cement	Modified Emulsified Asphalt
Percentage of mineral mass	100%	1%	6%	10%, 11%, 12%, 13%, 14%

The specific steps for the cohesion test are as follows:

1. Prepare a certain quantity of mineral materials, modified emulsified asphalt, cement, water, and other materials. Group the test materials.
2. Mix the materials and prepare the test specimens, then demold and start timing. Measure the cohesion of the specimens after 30 min and 60 min of curing for the 5 groups, respectively, and record the failure state of the specimens.

2.2.3. Wet Wheel Wear Test

The wet wheel abrasion tester (Changji Geological Instrument Co., Ltd., Shanghai, China) used in this study is shown in Figure 6. The steps for conducting the wet wheel wear test are as follows:

1. Weigh the total mass of the oil felt and the test piece.
2. Place the prepared test piece and oil felt in a water bath at 25 °C for 1 h.
3. Install the sample in the tester and start the instrument.
4. After the test is completed, dry the oil felt and test piece to a constant weight and then weigh the total mass.

Figure 6. Wet Wheel Abrasion Tester.

The calculation method for the wear value is shown in Equation (1).

$$WTAT = (m_a - m_b)/A \tag{1}$$

where

$WTAT$ is the wear value of slurry mixture, g/m^2;
m_a is the weight of the specimen before wear, g;
m_b is the weight of the worn specimen, g;
A is the wear surface area of rubber hose with wear head, m^2.

2.2.4. Load Wheel Sand Adhesion Test

The load wheel sand adhesion tester (Changji Geological Instrument Co., Ltd., Shanghai, China) used in this study is shown in Figure 7. The steps for conducting the load wheel sand adhesion test are as follows:

1. Install the sample in the tester and start the instrument.
2. Roll the sample 1000 times at a frequency of 44 times per minute.
3. Dry and cool the sample, then weigh the mass (G_a).
4. Reinstall the sample, lay the preheated sand flat on the sample, and place the cover plate.
5. Roll the machine an additional 100 times, brush off the floating sand, and weigh the mass (G_b).

The calculation method for the adhesive sand quantity is shown in Equation (2).

$$LWT = (G_b - G_a)/A \tag{2}$$

where

LWT is the adhesive sand content of the emulsified asphalt, g/m^2;
A is the rolling area, m^2;
G_a is the mass of the specimen after 1000 rounds of rolling, g;
G_b is the quality of the specimen after 100 rounds of sanding and rolling, g.

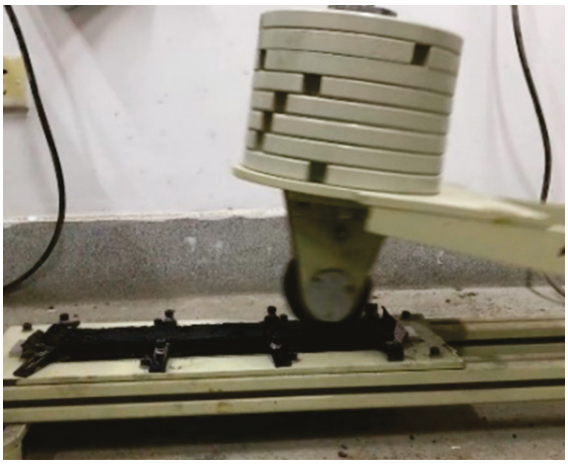

Figure 7. Load wheel sand adhesion tester.

2.2.5. Consistency Test

The consistency tester (Changji Geological Instrument Co., Ltd., Shanghai, China) used in this study is shown in Figure 8. The consistency test determines the consistency of the emulsified asphalt mixture, which can be affected by the addition of SF, altering the slurry state of the mixture. Both ASTM and ISSA specify that the viscosity of slurry mixtures should be within the range of 2–3 cm [22]. The viscosity of the emulsified asphalt mixtures with different mass fractions of SF is determined through viscosity tests, and the reasonable range of SF dosage is identified based on the viscosity specifications.

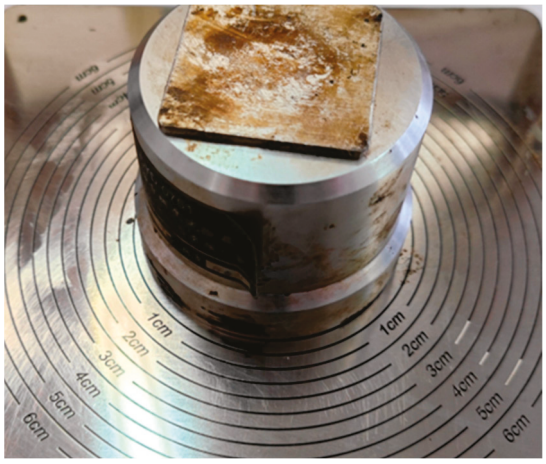

Figure 8. Consistency tester.

The specific steps for the consistency test are as follows:

1. The material preparation process is the same as in the mixing test. Pour the raw materials into the mixing pot in sequence and mix well. Then, pour the emulsified asphalt mixture into the cone of the consistency meter and cover it with a bottom plate with a scale.
2. Invert the cone and base plate together, then immediately lift the cone upwards to allow the mixture to collapse naturally.
3. Measure the distance between the edge and the central circular edge of the collapsed emulsified asphalt mixture, which is the consistency of the mixture. Measure the consistency of 6 sets of emulsified asphalt mixtures in sequence, accurate to 0.1 cm.

2.2.6. SF-EAM Microwave Absorption Performance Test

The appearance and interior of the microwave oven (Frigidaire, Zhongshan, China) used in this study are shown in Figure 9. The microwave oven's dimensions are 0.74 m in length, 0.40 m in width, and 0.44 m in height. The internal cavity size is 0.53 m in length, 0.36 m in width, and 0.25 m in height. The waveguide is located on the right side of the microwave oven, suitable for heating common emulsified asphalt mixture specimens. The maximum heating power of the microwave is 1000 W, with a frequency of 2.45 GHz, and the minimum accuracy of microwave heating time is 1 s. The standard curing box has a curing temperature range of 0–85 °C and a curing relative humidity range of 45–98%. The maximum range of the electronic balance is 1000 g, with a minimum accuracy of 0.001 g. Other instruments and equipment include mixing pots, mixing rods, glass cups, measuring cylinders, gloves, and wooden boards.

(**a**) (**b**)

Figure 9. Microwave oven. (**a**) Appearance; (**b**) internal structure.

The aggregate proportion of coarse and fine aggregates is approximately 89%, and the proportion of mineral powder is approximately 11%. Therefore, a total of 2225 g of coarse and fine aggregates, 225 g of mineral powder, 320 g of modified emulsified asphalt with an oil-to-stone ratio of 7.7%, 150 g of water, 25 g of cement, and 25 g of SiC powder and Fe_3O_4 powder with a particle size of 0.07 mm were weighed. These materials were divided into 5 groups. In each group, a certain mass of SiC powder and Fe_3O_4 powder were first combined to form SF, which then replaced some of the mineral powder.

All specimens were prepared in a laboratory at a specific ambient temperature and relative humidity of 75%, as follows:

1. First, mix the minerals, cement, and SF in each mixture and stir evenly. Then, add water to the mixture and mix well. Finally, add modified emulsified asphalt and stir for 30 s.
2. Divide the mixed emulsified asphalt mixture into two equal parts and pour them into two identical circular test molds to make two types of identical specimens. The inner diameter of the test mold is 80 mm, and the height is 20 mm. The two types of specimens are used for temperature testing and quality testing, respectively.
3. Compact and scrape the mixture to ensure a mass of 225 g for each specimen, then demold the specimen and place it in a 25 °C curing box for 10 min. Prepare 5 sets of specimens in sequence according to the above method, as shown in Figure 10.

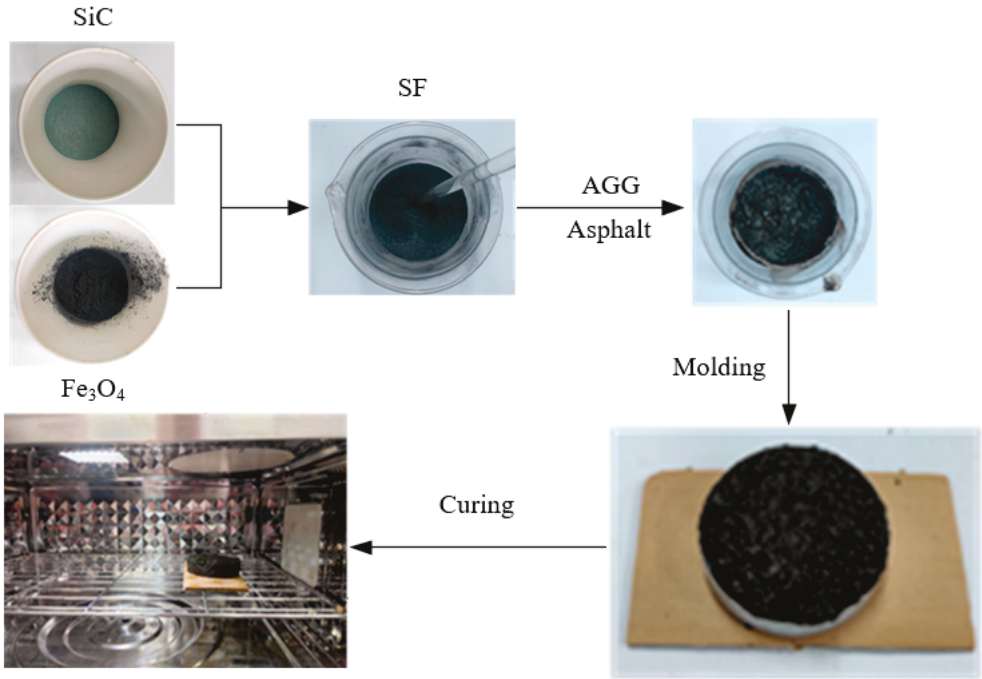

Figure 10. SF-EAM specimen preparation and heating process.

In the temperature-testing experiment, a specific microwave power and an initial temperature of the specimen are used. Three measuring points on the surface of the specimen are selected, and their surface temperatures are measured using an infrared thermometer (TASI, Suzhou, China). The average temperature of the three measuring points is calculated and recorded as the surface average temperature. The methodology is as follows: Place the specimens used for temperature testing in Group 1 in the microwave oven, turn on the microwave oven to heat for 140 s, and pause to measure the surface temperature of the specimens every 20 s, accurate to 0.1 °C. Heat and test 5 sets of specimens in sequence. The specimens before and after microwave heating are shown in Figure 11. The testing process of the temperature test is shown in Figure 12.

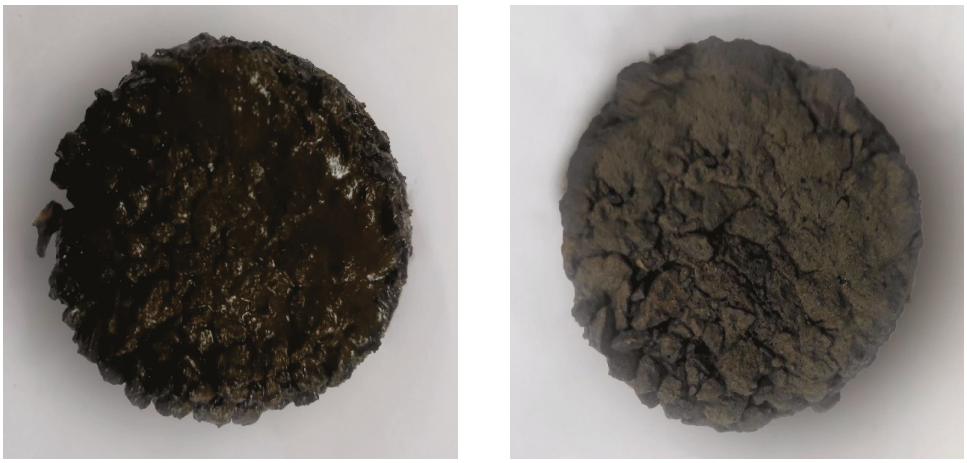

(**a**) (**b**)

Figure 11. Comparison of specimens before and after microwave heating. (**a**) Before heating; (**b**) after heating.

Figure 12. Temperature test.

For the quality testing experiment, a specific microwave power and initial temperature of the specimen are used. The methodology is as follows: Place the specimens used for quality testing in Group 1 in the microwave oven, turn on the microwave oven, and heat for 140 s. Measure the mass of the specimens every 20 s using an electronic balance, accurate to 0.1 g. Heat and test 5 sets of specimens in sequence, and the testing process for quality testing is shown in Figure 13.

Figure 13. Quality Testing.

3. Results and Discussion

3.1. Mix Proportion Design of SiC-Fe_3O_4 Emulsified Asphalt Mixture

In road maintenance engineering, emulsified asphalt mixture is often used in micro-surfacing technology, and the mix design of emulsified asphalt mixture is based on the "Guidelines" [22]. First, technical performance tests on raw materials are conducted. The type and range of aggregate gradation are determined based on road usage requirements, and the gradation curve is adjusted according to gradation design theory to design a suitable gradation. Next, based on existing experience in designing mix proportions, the amount of water added is determined through mixing tests, and the range of oil-to-stone ratio is determined through cohesion tests. One to three reasonable mix proportions are initially selected. Then, the optimal oil-to-stone ratio is determined through wet wheel wear tests and load wheel sand adhesion tests, and the final mix ratio of the mixture is determined. Finally, SF is used to replace some mineral powder, and the reasonable dosage range of SF is determined based on the mixing performance requirements of emulsified asphalt mixtures specified in the "Guidelines" [22] and through mixing tests and consistency tests.

3.1.1. Mix Proportion Design of Emulsified Asphalt Mixture

The emulsified asphalt mixture prepared in this study is mainly used in the maintenance engineering of high-grade pavements. The grading type should be MS-3 continuous grading. Additionally, considering that high-grade highway pavements need to have excellent anti-rutting performance, coarse aggregates should be selected for design.

According to Fuller's theory [27], when studying the relationship between the degree of overlap between grading curves and parabolic shapes and the compactness of their mixtures, it was found that the higher the degree of overlap, the greater the compactness of the mixture. The resulting Fuller formula is shown in Equation (3). Based on practical construction conditions, Taibo improved the Fuller formula and derived the Taibo formula, as shown in Equation (4). According to research by relevant scholars [27], when the value is small, the flowability of the emulsified asphalt mixture is good; in this study, it is set at 0.4.

$$P = 100 \times \sqrt{\frac{d}{D}} \tag{3}$$

$$P = 100 \times \left(\frac{d}{D}\right)^n \tag{4}$$

where

P is the percentage of aggregate passing, %;

d is the sieve size, mm;

D is the maximum particle size of the aggregate, mm;

n is the experimental index.

In summary, based on the MS-3 grading, this section calculates the grading pass rate using the Taibo formula with n = 0.4, and compares it with the median value of the MS-3 grading. The cumulative pass rate data of the two grading groups are shown in Table 9. According to the cumulative pass rate data of particle size distribution in Table 9, the pass rate between the sieve hole particle sizes of the two groups of gradations is calculated. The difference and variation amplitude of the pass rate between the two groups are compared, as shown in Table 10.

Table 9. Cumulative passing rate of each particle size.

Particle Size (mm)	9.5	4.75	2.36	1.18	0.6	0.3	0.15	0.075
Tebow equation n = 0.4	100	75.79	57.29	43.42	33.13	25.10	19.03	14.42
Median value of MS-3 grade	100	80	57.5	39	26.5	18.5	12.5	10

Table 10. Comparison of median data between calculated grading and MS-3 grading.

Particle Size Range (mm)	Passage Rate between Sieve Holes (%)		Difference (%)	Percentage of Difference (%)
	Tebow Equation n = 0.4	Median Value of MS-3 Grade		
4.75~9.5	24.21	20	−4.21	4.75~9.5
2.36~4.75	18.50	22.5	4.00	2.36~4.75
1.18~2.36	13.87	18.5	4.63	1.18~2.36
0.6~1.18	10.29	12.5	2.21	0.6~1.18
0.3~0.6	8.03	8	−0.03	0.3~0.6
0.15~0.3	6.07	6	−0.07	0.15~0.3
0.075~0.15	4.61	2.5	−2.11	0.075~0.15
Under 0.075	14.42	10	−4.42	Under 0.075

Based on the difference and ratio data calculated in Table 10, the following can be observed:

1. When the particle size range of the mixture is 4.75~9.5 mm, the pass rate of the median in the MS-3 grading is lower than that obtained by the Taibo formula at n = 0.4,

indicating that the proportion of large-sized coarse aggregates in the median of the MS-3 grading is relatively small.

2. When the particle size range of the mixture is 0.6~4.75 mm, the pass rate of the median in the MS-3 grading is greater than that obtained by the Taibo formula at n = 0.4 with accounting for a large proportion. Specifically, in the range of 1.18~2.36 mm, the difference accounts for 33%, indicating that the proportion of medium and small-sized coarse aggregates and large-sized fine aggregates in the median of the MS-3 grading is relatively high.
3. When the particle size range of the mixture is 0.075–0.6 mm, the pass rate of the median in the MS-3 grading is lower than that obtained by the Taibo formula at n = 0.4. Although the absolute difference is not significant, it accounts for a large proportion, especially in the range of 0.075–0.15 mm, where the difference accounts for as much as 46%, indicating that the proportion of small particle-sized fine aggregates in the median of the MS-3 grading is relatively small.

Based on the above requirements, the final grading A for this study was designed. The grading curve is depicted in Figure 14.

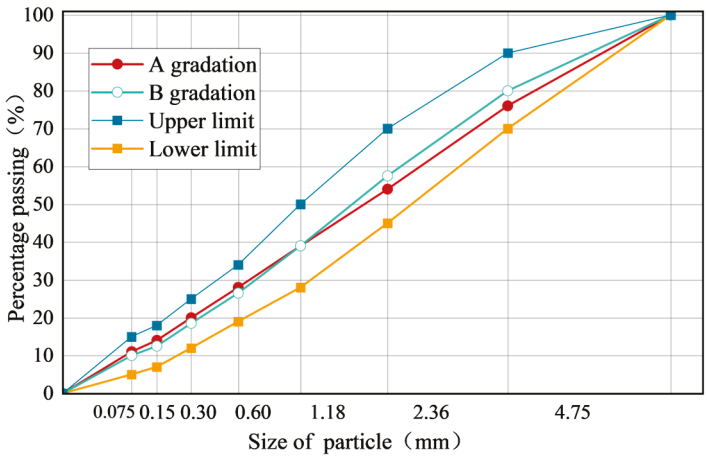

Figure 14. Grading curve.

After initially selecting two types of mineral aggregate gradations, and combining them with existing experience in emulsified asphalt mixture ratios for micro-surfacing, the dosage of emulsified asphalt, cement, and water is preliminarily selected. The range of commonly used materials for emulsified asphalt mixtures as specified in the "Guidelines" [22] is shown in Table 11. The mixing time and cohesion specifications for the mixing test and cohesion test are provided in Table 12.

Within the specified range of material usage, emulsified asphalt mixture specimens were prepared based on empirical mix proportions for mixing and cohesion tests. The amount of added water was determined through mixing tests, and the range of the oil-to-stone ratio was determined through cohesion tests. Based on the results of these tests, gradation was selected, and 1–3 reasonable mix proportions were preliminarily chosen.

Table 11. Range of common materials used in emulsified asphalt mixtures.

Test Item	Unit	MS-3
Thickness after regimen	mm	8~10
Mineral dosage	kg/m^2	10.0~22.0
Oil–stone ratio	%	6.0~8.5
Amount of cement, slaked lime (percentage of mineral mass)	%	0~3
Amount of water added (percentage of dry mineral mass)	%	Determined by the consistency of the mix

Table 12. Design indicators for mixing test and cohesion test.

Test Item		Standard Specifications [22]	Test Method
Mixable time (25 °C)		≥120 s	T0757
Adhesion test	30 min (Initial setting)	≥1.2 N·m	Adhesion test
	60 min (Open to traffic)	≥2.0 N·m	

The test results of the mixing test under two different gradations are shown in Figure 15.

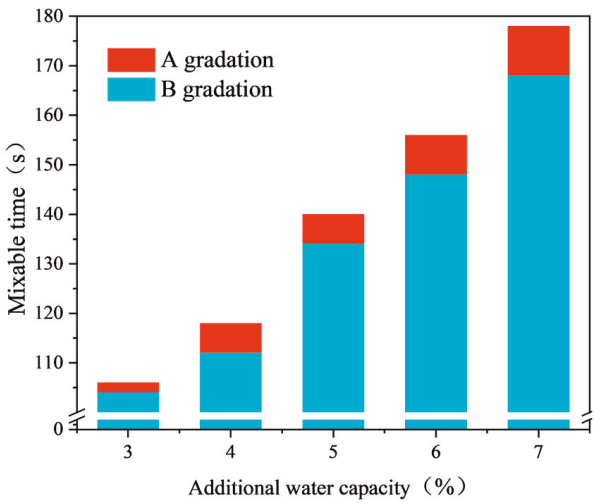

Figure 15. Mixing time corresponding to different added water amounts.

Based on the experimental data in Figure 15, the following observations were made:

- When the external water content is less than 4%, the mixing time of the emulsified asphalt mixture under both gradations is less than 120 s, which does not meet the specification requirements.
- When the external water content is greater than 5%, the mixing time exceeds 120 s, meeting the specification requirements.
- When the external water content reaches 7%, the surface of the emulsified asphalt mixture becomes relatively moist, with some flowing water, making it difficult to form a cohesive mixture.
- Under the same moisture content conditions, the mixing time for gradation A is higher than for gradation B, with an average increase of about 5%.

When the amount of external water is small, the fluidity of the emulsified asphalt mixture is insufficient, and the aggregate cannot be fully mixed with the emulsified asphalt. Conversely, when the amount of external water is too high, although the mixing performance improves, the emulsified asphalt mixture specimen system becomes loose and cannot be quickly formed during specimen preparation.

In Gradation B, the content of coarse aggregate is relatively low, while the proportion of fine aggregate is high. Due to the large specific surface area of the fine aggregate, more water from the asphalt emulsion is absorbed onto the aggregate surface during the wetting preparation stage. This process reduces the amount of free water in the mixing system, leading to a decrease in the fluidity of the mixture. Consequently, the mixing time for Gradation B is relatively short.

Considering the experimental results of the mixing tests under the two different gradations, it is proposed that the external water content for the emulsified asphalt mixture be set at 6%.

The test results of the cohesion test under two different gradations are shown in Figure 16. According to the experimental data in Figure 16, when the oil-to-stone ratio is 6%, the 30-min cohesion of the emulsified asphalt mixture under both gradations is less than 1.2 N·m, and the 60-min cohesion is less than 2.0 N·m, which does not meet the specification requirements. As the oil-to-stone ratio increases, the cohesion of both groups of mixtures also increases. When the oil-to-stone ratio exceeds 6.6%, the cohesion meets the specification requirements. However, when the oil-to-stone ratio reaches 8.4%, the cohesion of the mixture shows a decreasing trend.

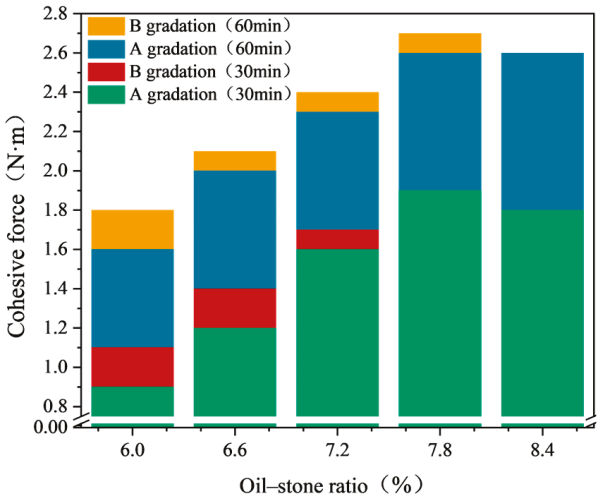

Figure 16. Cohesion force corresponding to different oil–stone ratios.

When the oil-to-stone ratio is small, the cohesion of the emulsified asphalt mixture with Gradation B is slightly higher than that with Gradation A. But when the oil-to-stone ratio exceeds 7.8%, the cohesion of the two groups of mixtures becomes close. When the oil-to-stone ratio is relatively small, there is insufficient emulsified asphalt in the mixture to bond with the aggregate, resulting in lower cohesion due to weak bonding between aggregate particles. As the emulsified asphalt content increases, the bonding between the emulsified asphalt and aggregate improves, leading to increased cohesion. When the emulsified asphalt content is too high, the amount of unbound asphalt in the system increases, causing the cohesion to decrease. Gradation B contains relatively fine aggregate with fewer voids in the mixture, resulting in a stronger overall bonding effect and higher cohesion.

Taking into account the test results of cohesion tests under the two different gradations, the proposed range for the oil-to-stone ratio in emulsified asphalt mixtures is 6.6% to 8.4%. Based on the results of the mixing test and cohesion test, it can be concluded that, under the premise that both sets of gradation test technical indicators meet the specification requirements, the gradation of the emulsified asphalt mixture applied to the micro-surfacingshould be selected as coarse type. Therefore, Gradation A is chosen as the final gradation for this study. The Preliminary proportions of emulsified asphalt mixtures and design indicators for wet wheel wear test and load wheel sand adhesion test as specified in the "Guidelines" [22] is shown in Tables 13 and 14.

Table 13. Preliminary proportions of emulsified asphalt mixtures.

Specimen	Minerals	Water	Cement	Modified Emulsified Asphalt
Percentage of mineral mass	100%	6%	1%	11%, 12%, 13%, 14%

Table 14. Design indicators for wet wheel wear test and load wheel sand adhesion test.

Item		Standard Specifications [22]	Test Method
Sand adhesion		≤450 g/m^2	T0755
Wet track abrasion value	Immersion in water for 1 h	≤540 g/m^2	Wet track abrasion value
	Immersion in water for 6 d	≤800 g/m^2	

The test results of the wet wheel wear test and load wheel sand adhesion test are shown in Figure 17. As illustrated in Figure 17, with the increase in the oil-to-stone ratio, the content of emulsified asphalt continues to rise. Consequently, the wet wheel wear curve decreases continuously, while the adhesion sand curve increases continuously. The two curves intersect in the graph, and the oil-to-stone ratio corresponding to this intersection point is the optimal oil-to-stone ratio.

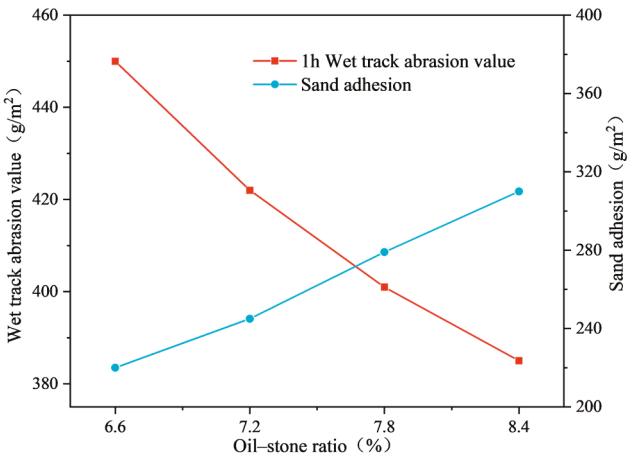

Figure 17. Relationship curve between wear value, adhesive sand content, and oil–stone ratio.

The intersection point in the figure indicates an oil-to-stone ratio of approximately 7.7%. The corresponding 1-h wet wheel wear value is 405 g/m^2, which is lower than the specification requirement of 540 g/m^2. The corresponding load wheel adhesion sand amount is 275 g/m^2, which is less than the specification requirement of 450 g/m^2. Both indicators meet the specification requirements. Therefore, the final oil-to-stone ratio of the emulsified asphalt mixture was determined to be 7.7%, corresponding to a modified emulsified asphalt dosage of 12.8%.

In summary, the final ratio of the emulsified asphalt mixture is determined as follows: mineral aggregate:modified emulsified asphalt:water:cement = 100:12.8:6:1, with Grade A used for the mineral aggregate.

3.1.2. Content Range of SiC-Fe_3O_4 Composite Materials

By conducting mixing and consistency tests, the mixing performance of the emulsified asphalt mixture mixed with SF (SiC-Fe_3O_4 composite materials) was studied. The reasonable dosage range of composite materials was determined based on the test results. The mixing time and consistency requirements specified in the guidelines are shown in Table 15.

Table 15. Design indicators for mixing test and consistency test.

Test Item	Standard Specifications [22]	Test Method
Mixable time	≥120 s	T0757
Consistency	2~3 cm	T0751

The optimal ratio of emulsified asphalt mixture determined earlier is mineral aggregate:modified emulsified asphalt:water:cement = 100:12.8:6:1. The particle size of the SiC and Fe_3O_4 materials used to replace the mineral powder is mostly concentrated in the range of 0.06~0.075 mm. The MS-3 graded emulsified asphalt mixture specifies a range of 5%~15% for mineral materials with a particle size below 0.075 mm [22]. Therefore, in the mixing performance test of the emulsified asphalt mixture, the initial range of SF dosage is set at 0~5%. Due to the small difference in particle size between the two materials, the influence of the SF composite ratio on mixing performance can be ignored. Therefore, in the mixing performance test, the SF composite ratio is set at 1:1. Additionally, environmental conditions significantly impact the mixing performance of emulsified asphalt mixtures. To minimize the influence of environmental factors, the mixing performance tests of the mixture were completed in a windless laboratory environment with a temperature of 25 °C and relative humidity of 75%.

After the mixing test, the mixing time of emulsified asphalt mixtures with different SF contents is shown in Figure 18. According to the experimental data in Figure 18, when the SF content is within the range of 0% to 5%, the mixing time of the emulsified asphalt mixture is greater than 120 s, meeting the specification requirements. When the SF content is 1%, the mixing time is the same as that of the mixture without SF. When the SF content is within the range of 1% to 5%, the mixing time increases continuously with the increase in SF content. When the SF content reaches 5%, the mixing time is 165 s, an increase of 9 s compared to the absence of SF.

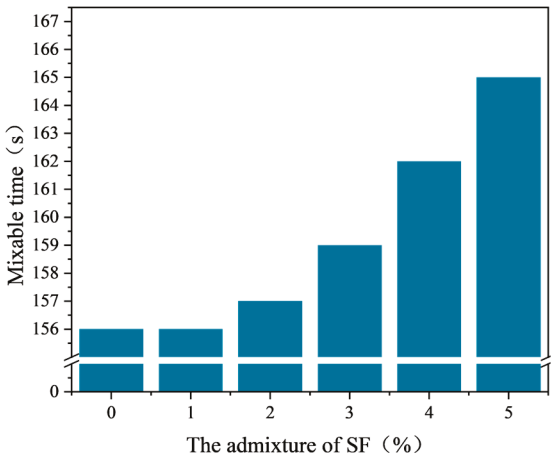

Figure 18. Mixing time of emulsified asphalt mixture with different SF content.

The particle size range of SF is mostly distributed around 0.06~0.075 mm, while the particle size of the replaced mineral powder is widely distributed between 0~0.075 mm. At low dosages, a small amount of SF will not affect the gradation of the mixture significantly, so its impact on the mixing time is also relatively small. As the SF content increases, the content of coarse particles in the emulsified asphalt mixture also increases. Coarse SF particles have a smaller specific surface area than fine particles in the mineral aggregate, reducing the ability of particles to adsorb water. As a result, the amount of free water increases, leading to a longer mixing time. Additionally, SF particles are mostly uniformly distributed with fewer pores than mineral powder particles, resulting in lower water absorption and longer mixing time.

After the viscosity experiment, the viscosity of emulsified asphalt mixtures with different SF contents was obtained as shown in Figure 19. According to the experimental data in Figure 19, when the SF content is within the range of 0% to 4%, the viscosity of the emulsified asphalt mixture is within the range of 2–3 cm, meeting the specification requirements. When the SF content is within the range of 0% to 5%, the viscosity gradually increases with the increase in SF content. When the SF content reaches 5%, the viscosity

is 3.2 cm, an increase of 1 cm compared to the absence of SF, which does not meet the specification requirements.

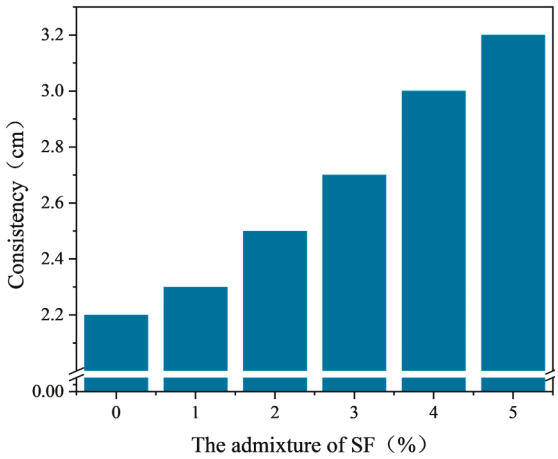

Figure 19. Consistency of emulsified asphalt mixture with different SF content.

In emulsified asphalt mixtures, the content of coarse particles increases with the gradual increase in SF content. As a result, the total specific surface area of the mineral material decreases, reducing the amount of water that can be adsorbed by the mineral material. Consequently, the amount of free water increases, improving the overall flowability of the emulsified asphalt mixture and increasing the viscosity. However, excessive free water makes the viscosity of the emulsified asphalt mixture too high, deteriorating the mixing performance and failing to meet the specification requirements.

From the results of the mixing and consistency tests, it can be concluded that although adding SF can improve the microwave absorption performance of the emulsified asphalt mixture, a larger dosage affects the mixing performance and greatly increases the economic cost. Therefore, the reasonable dosage range of SF in this study is 0% to 4%.

3.2. Microwave Absorption Performance Test of Emulsified Asphalt Mixture

3.2.1. Evaluation Indicators for Microwave Absorption Performance

1. Temperature change (Δ_T)

According to the theory of heat transfer, when there is a temperature difference between different objects or within the same object, energy transfer occurs through the collision of molecules, atoms, and electrons inside the object. When microwaves are used to heat an emulsified asphalt mixture, the temperature change is the most intuitive reflection of the mixture's energy absorption. After absorbing microwaves, the temperature of the mixture increases, and the more microwave energy is absorbed, the greater the temperature change. Therefore, the temperature change in the mixture can be used to represent its microwave absorption performance. The calculation method for temperature change (Δ_T) is shown in Equation (5).

$$\Delta_T = T_2 - T_1 \tag{5}$$

where

Δ_T is temperature change, °C;
T_1 is the temperature of the mixture before microwave heating, °C;
T_2 is the temperature of the mixture after microwave heating, °C.

2. Temperature rise rate (VT)

When the mixture contains different microwave-absorbing materials, microwave heating will increase its temperature. In this case, the temperature change alone is not sufficient to fully reflect the magnitude of the microwave absorption performance. The rate of temperature rise is also needed to reflect the microwave absorption performance. When

microwave-absorbing material is added to the emulsified asphalt mixture, a greater rate of temperature increase compared to when it is not added indicates that this material can improve the microwave absorption performance of the mixture. The calculation method for the temperature rise rate (VT) is shown in Equation (6).

$$V_T = \frac{\Delta_T}{t} \tag{6}$$

where

V_T is the temperature rise rate, °C/s;

t is the heating time, s.

The rate of temperature rise can be divided into two situations:

Linear Temperature Rise: When microwave heating causes the temperature of the mixture to change linearly with the heating time, the temperature rises linearly as the heating time increases. In this case, the slope of the temperature vs. time curve can reflect the rate of temperature increase.

Non-linear Temperature Rise: When microwave heating results in a non-linear relationship between the temperature of the mixture and the heating time, the temperature does not rise linearly as the heating time increases, and the slope of the curve changes continuously during the heating process. In this scenario, Equation (6) can be used to reflect the average temperature rise rate throughout the heating process.

3. The rate of increase in temperature rise rate (ω)

When an emulsified asphalt mixture contains microwave-absorbing materials of the same type but in different dosages, the temperature change caused by microwave heating may not be significantly different, and the rate of temperature increase may also be minimal. In this case, the rate of increase in the temperature rise rate can be used to reflect the change in microwave absorption performance. The calculation method for the increase rate of the temperature rise rate (ω) is shown in Equation (7).

$$\omega = \frac{V_{T2} - V_{T1}}{V_{T1}} \tag{7}$$

where:

ω is the rate of increase in temperature rise rate, %;

V_{T1} is the rate of temperature increase before the increase, °C/s;

V_{T2} is the rate of temperature increase after enlargement, °C/s.

4. Quality change (Δ_m)

When the emulsified asphalt mixture is heated by microwaves, it absorbs the microwave energy, causing its temperature to rise. As the temperature increases, the water in the system will gradually evaporate. When the internal temperature of the mixture exceeds 100 °C, a significant amount of water will evaporate. The demulsification process of emulsified asphalt involves the adhesion of asphalt particles to aggregates and the subsequent evaporation of water from the emulsified asphalt. Therefore, the change in mass of the emulsified asphalt mixture before and after heating can reflect the evaporation of water in the mixture. The stronger the microwave absorption ability of the emulsified asphalt mixture, the faster the evaporation rate of water in the mixture, and the greater the mass change in the mixture before and after heating, corresponding to a faster demulsification speed of the emulsified asphalt. The calculation method for the quality change quantity (Δ_m) is shown in Equation (8).

$$\Delta_m = m_2 - m_1 \tag{8}$$

where

Δ_m is the quality change quantity, g;

m_1 is the mass of the mixture before microwave heating, g;

m_2 is the mass of the mixture after microwave heating, g.

5. Quality reduction rate (V_m)

The rate of quality reduction can reflect the speed of mass reduction in the emulsified asphalt mixture during the heating process. The calculation method for the rate of mass reduction (V_m) is shown in Equation (9).

$$V_m = \frac{\Delta_m}{t} \tag{9}$$

where V_m is the quality reduction rate, g/s.

3.2.2. Analysis of the Effect of SF Content on the Microwave Absorption Performance of SF-EAM

The average temperature variation curve of SF-EAM (silicon carbide-ferrite emulsified asphalt mixture) under microwave heating with different SF doping levels is shown in Figure 20. The relationship between the temperature rise rate and SF doping level is shown in Figure 21.

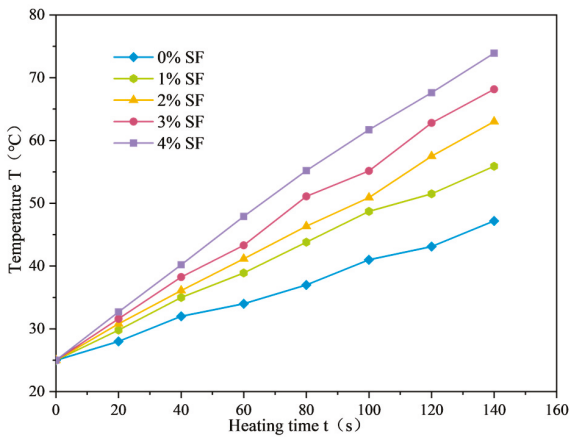

Figure 20. Temperature variation curve of SF-EAM (SF content).

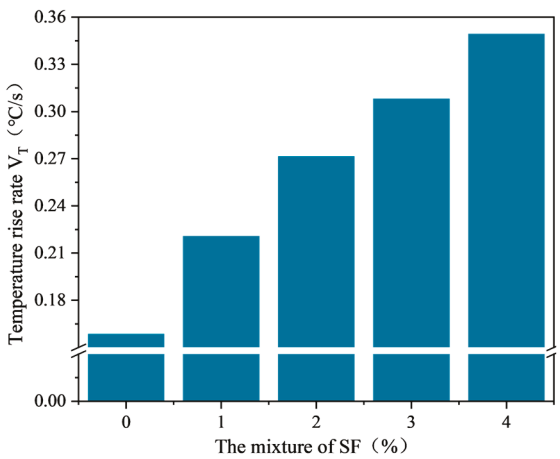

Figure 21. Relationship between temperature rise rate and SF content.

From Figures 20 and 21, it can be seen that when the initial temperature is 25 °C, the microwave power is 200 W, and the SF ratio is 1:1, heating the emulsified asphalt mixture specimen with 0~4% SF for 140 s results in the surface temperature of the SF-EAM specimen continuously increasing with the duration of microwave radiation, showing a roughly linear relationship. As the SF content increases, the rate of temperature rise gradually increases. The increase in temperature rise rate is particularly significant when 1% SF is

added. When 1%, 2%, 3%, and 4% SF were added, the increase rates of temperature rise rate were 39.0%, 70.4%, 93.7%, and 119.5%, respectively, compared to the absence of SF.

According to the thermal equilibrium conditions of the object, Equation (10) can be derived. Assuming that the microwave can be uniformly radiated to both the inside and outside of the specimen and that the electric field generated by the microwave is a uniform electric field, the electromagnetic parameters of the SF-EAM specimen remain unchanged, and the microwave absorption power of the specimen is constant. The maximum temperature of the specimen after 140 s of heating is 73.9 °C, with a temperature change that is not significant. During this process, the evaporation rate of water is slow, so the specimen can be regarded as an object with uniform and unchanged material properties throughout the entire heating process. Additionally, the thickness of the prepared specimen is relatively thin, allowing simultaneous heating of both the inside and outside, so internal heat transfer can be ignored. The divergence of heat flux density is zero, and the heat capacity of the specimen is constant. By substituting the above conditions into Equation (10) and solving the differential equation, Equation (11) can be obtained.

$$divq = P - C\frac{\partial T}{\partial t} \tag{10}$$

where

q is the heat flux density, J/(m^2·s)

P is the absorption power of an object to microwaves, W/m^3;

C is the heat capacity, J/°C;

T is the temperature, °C;

t is the time, s.

$$\frac{T}{t} = k \tag{11}$$

With the increase in SF content, the electromagnetic parameters of the emulsified asphalt mixture gradually increase, enhancing the microwave absorption performance of the mixture system. As a result, more microwaves can be absorbed in the same amount of time, causing the temperature rise rate to continue increasing. When SF is not added, the primary microwave-absorbing material in the mixture system is water. With the addition of 1% SF, both water and SF become the primary microwave-absorbing materials. The addition of SF significantly increases the electromagnetic parameters of the mixture, resulting in a substantial increase in the temperature rise rate.

The mass variation curves of SF-EAM under microwave heating with different SF dosages are shown in Figure 22. When the initial temperature is 25 °C, the microwave power is 1000 W, and the SF ratio is 1:1, and heating the emulsified asphalt mixture specimen with 0%~4% SF for 140 s causes the mass of the SF-EAM specimen to decrease continuously, showing a nonlinear relationship with the increase in microwave radiation time.

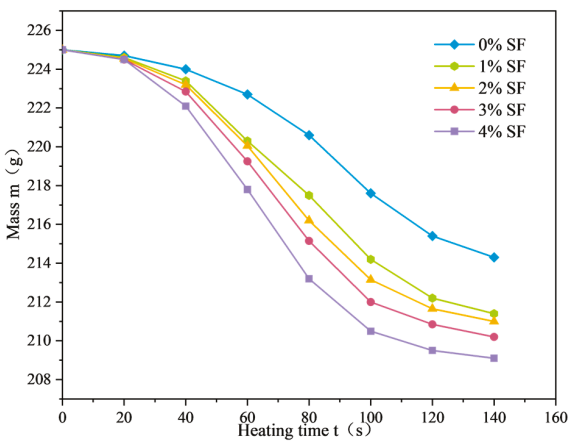

Figure 22. Quality change curve of SF-EAM (SF content).

According to the pattern of the quality change curve, the process of quality reduction can be divided into three stages. The time separation node between the first and second stages is denoted as node A, and the time separation node between the second and third stages is denoted as node B, as shown in Figure 23.

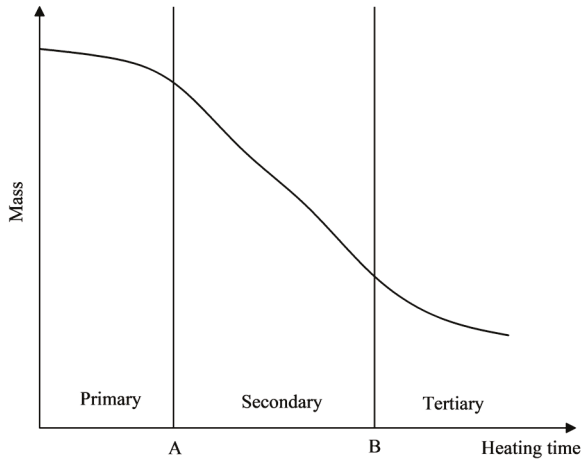

Figure 23. Curve of quality change law.

The slope of the first stage curve is relatively small, and the rate of mass reduction (V_m) of the emulsified asphalt mixture specimen is low, with a small magnitude of mass reduction.

The slope of the second stage curve increases, and the rate of decrease in specimen mass (V_m) increases.

The third stage curve tends to flatten out, and the rate of decrease in specimen mass (V_m) decreases again, while the specimen mass remains stable and unchanged.

With the increase in SF content, the mass change (Δ_m) of SF-EAM specimens continues to increase, the mass reduction rate (V_m) gradually increases, and nodes A and B continue to advance. When adding 1%, 2%, 3%, and 4% SF, the mass change increased by 27.1%, 30.8%, 38.3%, and 48.6%, respectively, compared to not adding SF.

The stages of the quality change process are described as follows:

Heat Accumulation Stage: During this stage, the microwave begins to irradiate the specimen. The internal temperature of the specimen rapidly increases, and the mixture remains at a relatively low temperature. The water evaporation rate is slow, and the rate of mass reduction (V_m) of the specimen is low.

Rapid Evaporation Stage: During this stage, the specimen continuously absorbs microwaves, and the internal temperature reaches the boiling point of water. A large amount of water evaporates outward from the mixture, increasing the rate of mass reduction (V_m).

Quality Stability Stage: During this stage, although the internal temperature of the specimen is high, the water in the mixture is eventually consumed, and the mass of the specimen stabilizes.

As the SF content increases, the temperature rise rate (V_T) of SF-EAM specimens increases, accelerating the water evaporation rate. Consequently, the mass reduction rate (V_m) continues to increase, with nodes A and B advancing continuously. The mass change in the specimen (Δ_m) also increases with the increase in SF content. According to the results of temperature and quality testing, the optimal dosage of SF is 4%.

3.2.3. Analysis of the Influence of SF Composite Ratio on the Microwave Absorption Performance of SF-EAM

The average temperature variation curve of SF-EAM microwave-heated surfaces with different SF ratios is shown in Figure 24, and the relationship between temperature rise rate and SF composite ratio is shown in Figure 25.

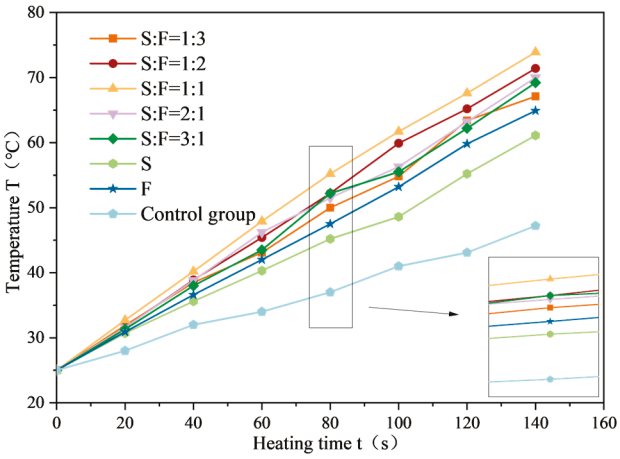

Figure 24. Temperature variation curve of SF-EAM (SF composite ratio).

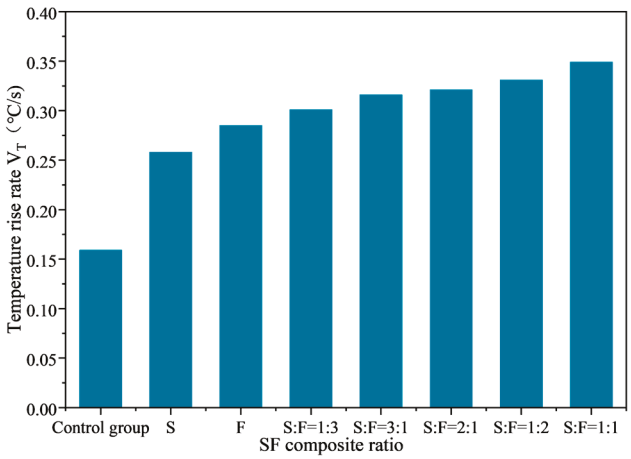

Figure 25. Relationship between temperature rise rate and SF composite ratio.

From Figures 24 and 25, it can be seen that when the initial temperature is 25 °C and the microwave power is 200 W, heating the emulsified asphalt mixture specimen with 4% SF for 140 s results in a significantly increased temperature rise rate (V_T) compared to the control group without microwave-absorbing material. The temperature rise rate (V_T) of the emulsified asphalt mixture specimen with either SiC or Fe_3O_4 single-phase material added is significantly increased, and the temperature rise rate (V_T) of the emulsified asphalt mixture specimen with SF added is greater than that of the mixture with single-phase material added (V_T).

When different proportions of SF are added, the temperature rise rates (V_T) from small to large are as follows:

S:F = 1:3, S:F = 3:1, S:F = 2:1, S:F = 1:2, S:F = 1:1.

Among these, the temperature rise rate (V_T) of emulsified asphalt mixture specimens with an SF ratio of S = 1:1 increased by 35.5% compared to the addition of SiC alone and increased by 22.6% compared to the addition of Fe_3O_4 alone.

These results indicate that a balanced composite ratio of SiC and Fe_3O_4 (1:1) provides the most effective microwave absorption performance, significantly enhancing the temperature rise rate of the emulsified asphalt mixture compared to single-phase materials.

Compared to doping SiC or Fe_3O_4 separately, doping SF can simultaneously leverage the electrical and magnetic loss mechanisms in the material, fully utilizing the electromagnetic energy in the microwave. Therefore, the microwave absorption effect of composite materials is better than that of single-phase materials. Under the above five composite ratios, the electromagnetic parameters of SF gradually increase, enhancing the

microwave absorption performance of SF-EAM, and the temperature rise rate (V_T) will also gradually increase.

The mass variation curves of SF-EAM under microwave heating with different SF ratios are shown in Figure 26. As illustrated, when the initial temperature is 25 °C and the microwave power is 1000 W, heating the emulsified asphalt mixture specimen with 4% SF for 140 s results in the highest temperature rise rate (V_T) at a composite ratio of S:F = 1:1. The mass change (Δ_m) is also the largest, with nodes A and B showing the most significant advance. Although the timing of node A and node B in the quality change curve varies at different ratios, there is a trend towards consistency in the final quality of emulsified asphalt mixture specimens at three ratios: S:F = 2:1, S:F = 1:2, and S:F = 1:1. According to the results of temperature testing and quality testing, among the various composite ratios set in this study, the microwave absorption performance of SF-EAM is optimal when the composite ratio of SiC to Fe_3O_4 is 1:1.

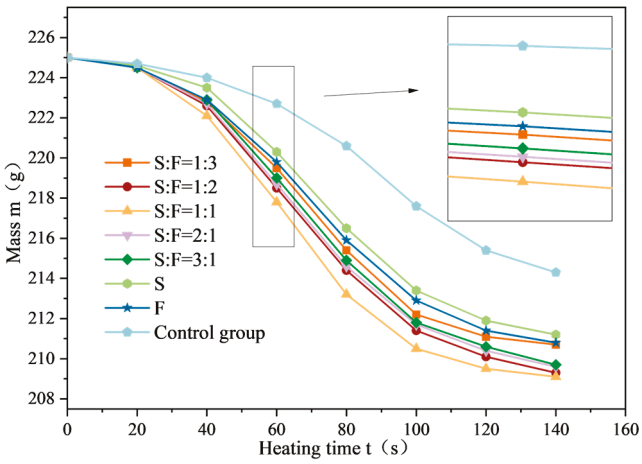

Figure 26. Quality change curve of SF-EAM (SF composite ratio).

3.2.4. Analysis of the Influence of Environmental Temperature on the Microwave Absorption Performance of SF-EAM

The average surface temperature variation curve of SF-EAM heated by microwave at different ambient temperatures is shown in Figure 27, and the relationship between the temperature rise rate (V_T) and ambient temperature is shown in Figure 28.

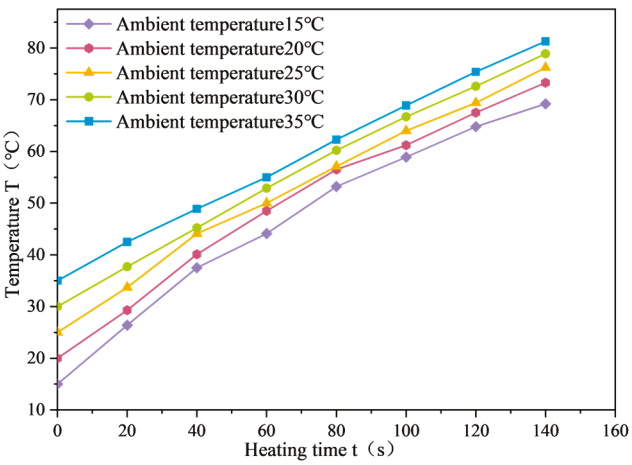

Figure 27. Temperature variation curves of SF-EAM under different ambient temperatures.

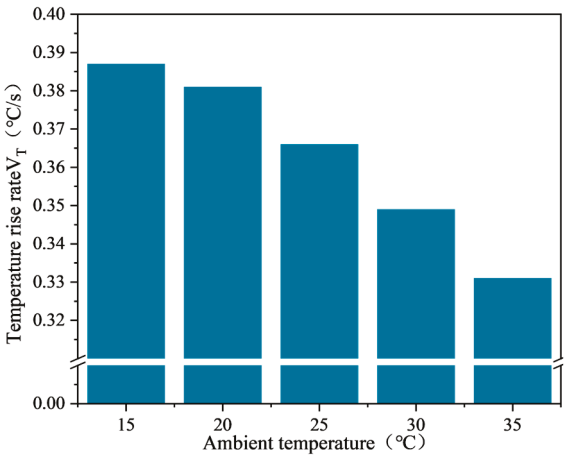

Figure 28. Relationship between temperature rise rate and ambient temperature.

According to Figures 27 and 28, when the ambient temperature changes, heating the emulsified asphalt mixture specimen with 4% SF (S:F = 1:1) for 140 s results in a linear relationship between the average surface temperature (T) and heating time (t) of the emulsified asphalt mixture specimen at different ambient temperatures. As the ambient temperature continues to rise, the rate of temperature increase of emulsified asphalt mixture specimens decreases. When the ambient temperature is 15 °C, the rate of temperature increase (V_T) is 0.387 °C/s, and when the ambient temperature is 35 °C, the rate of temperature increase is 0.331 °C/s, a decrease of 14.5% compared to 15 °C.

These results indicate that higher ambient temperatures negatively impact the microwave absorption performance of the SF-EAM, leading to a lower rate of temperature increase.

The absorption power of an object to microwaves (P) is related to the microwave operating frequency (f) and microwave electric field strength (E), and is independent of the ambient temperature (T). Therefore, while ambient temperature does impact the microwave absorption performance of SF-EAM, the degree of influence is minimal. The rate of temperature increase (V_T) of SF-EAM varies at different temperatures due to the principles of heat transfer, where the larger the temperature difference between two media, the faster the transfer speed. When preparing the specimen, the lower the ambient temperature, the greater the temperature difference between the specimen and the air in the microwave field, leading to a faster heat transfer rate and a quicker temperature rise rate (V_T) of the specimen. Hence, the rate of temperature increase (V_T) at this time cannot be used as an indicator to evaluate the microwave absorption performance of SF-EAM.

The mass change curve of SF-EAM under microwave heating at different ambient temperatures is shown in Figure 29. From Figure 29, it can be seen that when the ambient temperature changes, heating the emulsified asphalt mixture specimen with 4% SF (S:F = 1:1) for 140 s results in greater mass change (Δ_m) at higher ambient temperatures, with node A appearing earlier in the mass change process. This indicates that the higher the ambient temperature, the better the microwave absorption performance of SF-EAM.

The conclusion drawn from the quality test results contrasts with that of the temperature test results because ambient temperature affects the water evaporation rate of the emulsified asphalt mixture and thus its quality change (Δ_m). Therefore, at this time, the quality change (Δ_m) cannot be used as an indicator to evaluate the microwave absorption performance of SF-EAM. According to the results of temperature and quality testing experiments, it can be concluded that while ambient temperature affects the temperature rise rate (V_T) and mass change (Δ_m) of SF-EAM, it has little effect on the microwave absorption performance of SF-EAM.

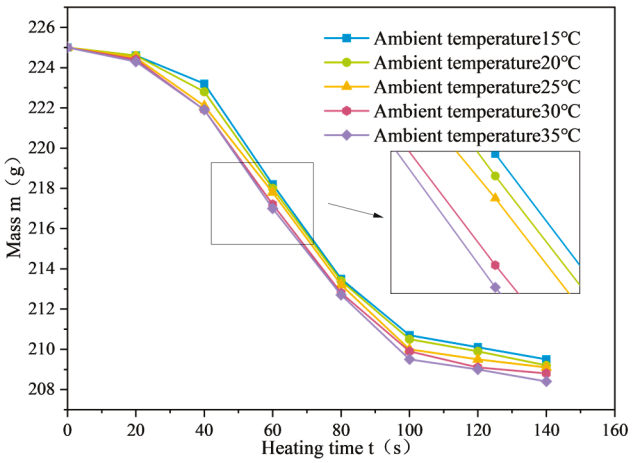

Figure 29. Mass change curve of SF-EAM at different ambient temperatures.

Based on the data obtained from the experiments, the microwave absorption efficiency remains essentially unchanged with temperature variations, indicating that the microwave absorption efficiency is constant, and the impact of ambient temperature on microwave absorption performance is negligible. Although an increase in temperature can directly affect the degree of curing by influencing the evaporation of water, ambient temperature is a factor that is difficult to alter, and its economic significance in practical applications is not high. Therefore, this paper does not delve into the exploration of the impact of ambient temperature on microwave absorption performance.

3.2.5. Analysis of the Influence of Microwave Power on the Microwave Absorption Performance of SF-EAM

The average surface temperature variation curve of SF-EAM under microwave heating at different powers is shown in Figure 30. It can be seen that at an initial temperature of 25 °C, the surface temperature (T) of the emulsified asphalt mixture specimen mixed with 4% SF (S:F= 1:1) varies linearly with the heating time (t) when heated for 140 s at 200 W. When the microwave power is 400–1000 W, the temperature (T) and heating time (t) exhibit a nonlinear relationship. The surface temperature growth trend of the specimen can be divided into three stages. The time separation node between the first and second stages is denoted as node C, and the time separation node between the second and third stages is denoted as node D, as shown in Figure 31.

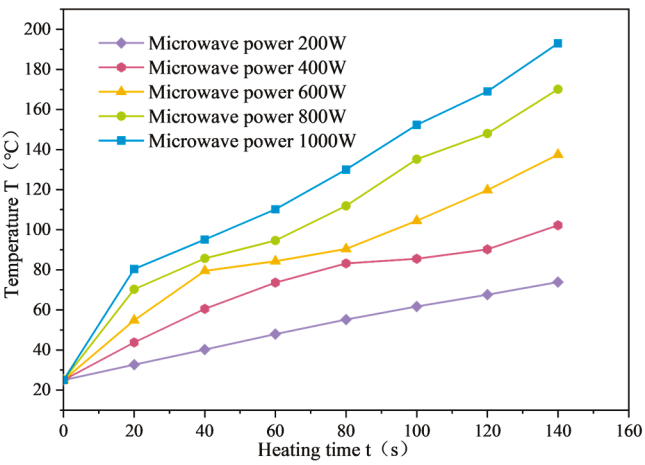

Figure 30. Temperature variation curve of SF-EAM under different powers.

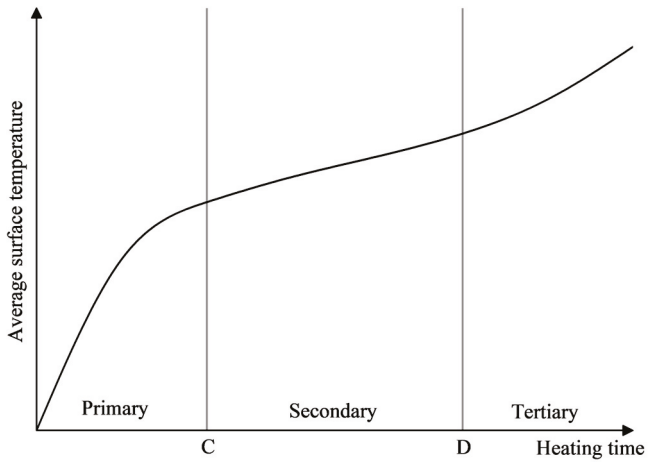

Figure 31. Surface average temperature variation curve.

In these stages:

The slope of the first-stage curve is the largest, and the rate of temperature rise (V_T) is the highest.

The second-stage curve is gentle, and the rate of temperature rise (V_T) is relatively small.

The slope of the third stage increases again but not as steeply as the first stage, and the rate of temperature rise (V_T) increases again.

As the microwave power increases, the rate of temperature rise (V_T) of emulsified asphalt mixture specimens continues to increase. When the microwave power is 200 W, 400 W, 600 W, 800 W, and 1000 W, the temperature change (Δ_T) of the specimen heated for 140 s is 48.9 °C, 77.2 °C, 112.5 °C, 145.1 °C, and 168 °C, respectively.

The relationship between the average temperature rise rate and microwave power is shown in Figure 32. According to Figure 32, the rate of average temperature rise is roughly proportional to microwave power. There are differences in the duration of the three stages of temperature changes in SF-EAM under different powers. As microwave power continues to increase, the rate of temperature rise (V_T) of emulsified asphalt mixture specimens in the three stages also increases. That is, the higher the microwave power, the shorter the duration of the first and second stages, and the earlier the C and D node times.

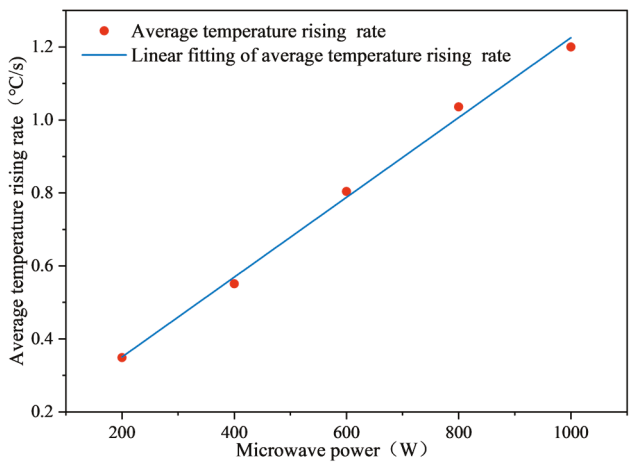

Figure 32. Relationship between average temperature rise rate and microwave power.

When the microwave power is 200 W, the temperature of the emulsified asphalt mixture specimen uniformly increases after heating for 140 s, indicating that the first 140 s are in the first stage. For microwave powers of 400 W, 600 W, 800 W, and 1000 W, the duration of the first stage is about 70 s, 50 s, 30 s, and 20 s, respectively, and the duration of the second stage is about 40 s, 35 s, 30 s, and 25 s, respectively.

The temperature variation in emulsified asphalt mixture specimens during microwave heating is closely related to the moisture content in the mixture. The process can be divided into three distinct stages:

Initial Heating Stage: During this stage, the water and SF (SiC-Fe_3O_4) in the emulsified asphalt mixture absorb microwaves together, resulting in a rapid increase in the specimen's temperature.

Temperature Stabilization Stage: At this stage, the temperature rises above 100 °C, reaching the boiling point of water. A large amount of water evaporates in the mixture system, and the evaporation of water takes away most of the heat. This leads to a relatively slow rate of temperature increase (V_T).

Secondary Heating Stage: In this stage, the water in the emulsified asphalt mixture has almost completely evaporated. The heat carried away by the evaporation of water is not sufficient to prevent the temperature from rising. However, since only SF and a small amount of water absorb microwaves during this stage, the rate of temperature rise (V_T) is lower than in the initial heating stage.

The formula for electric power is shown in Equation (12), and the formula for electric field strength is shown in Equation (13).

$$P_a = \frac{U^2}{R} \tag{12}$$

where

P_a is the microwave power, W;

U is the potential difference between two points in an electric field, V;

R is the resistance, Ω.

$$E = \frac{U}{d} \tag{13}$$

where

E is the electric field strength, V/m;

d is the distance between two points in an electric field, m.

$$V_T \propto P_\mathrm{a} \tag{14}$$

When the microwave power increases, the electric field strength (E) generated by electromagnetic waves also increases. According to Equations (12) and (13), assuming that the electric field generated by a microwave with a fixed frequency is a uniform electric field, and the distance between the resistance R and the electric field (d) remains constant, the square of the electric field strength (E) in the microwave is proportional to the microwave power P. Thus, it can be concluded that the absorption power (P_a) of the emulsified asphalt mixture specimen to microwaves is proportional to the microwave power (P). Based on the previous conclusions, it can also be concluded that the average temperature rise rate (V_T) of the specimen is roughly proportional to the microwave power (P), as shown in Equation (14).

The mass change curve of SF-EAM under microwave heating at different powers is shown in Figure 33. As illustrated, at an initial temperature of 25 °C, the emulsified asphalt mixture specimens with 4% SF (S:F= 1:1) were heated for 140 s at different powers. With the continuous increase in microwave power, the mass change (Δ_m) of the emulsified asphalt mixture specimens also increased.

When the microwave power was 200 W, 400 W, 600 W, 800 W, and 1000 W, the mass change (Δ_m) of the specimens heated for 140 s was 3.1 g, 7.1 g, 13.9 g, 15.5 g, and 15.9 g, respectively. The quality change trend of emulsified asphalt mixture specimens heated for 140 s varies slightly under different powers:

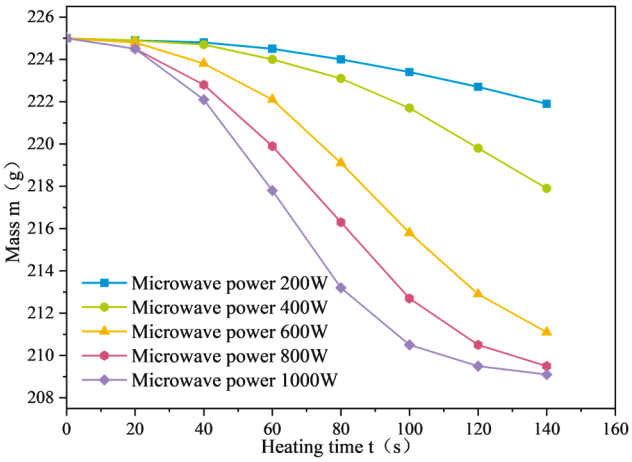

Figure 33. Mass change curve of SF-EAM at different powers.

At 200 W, the mass of the emulsified asphalt mixture specimens slowly decreases.

At 400 W, the rate of mass reduction of the specimen slightly increases, but the trend remains consistent with that at 200 W power.

At powers exceeding 600 W, the rate of mass reduction of the specimen increases significantly and begins to show a trend of "three stages".

When the microwave power is low, the internal temperature of the emulsified asphalt mixture specimen heated for 140 s does not reach 100 °C, resulting in a slow water evaporation rate and a small mass change (Δ_m). When the microwave power is high, the quality change in the emulsified asphalt mixture specimens corresponds to the average surface temperature change.

The stages of the process are as follows:

Heat Accumulation Stage: The temperature rise rate (V_T) is high, but the mass decrease rate (V_m) is low.

Rapid Evaporation Stage: The temperature rise rate (V_T) decreases while the mass decrease rate (V_m) increases rapidly.

Mass Stabilization Stage: The temperature continues to rise, but the mass remains basically unchanged.

Based on Figures 23 and 31, the corresponding relationship between the temperature change process and the mass change process is shown in Figure 34. When heating SF-EAM with high power, the temperature and mass changes of SF-EAM are closely related to the moisture content in the material:

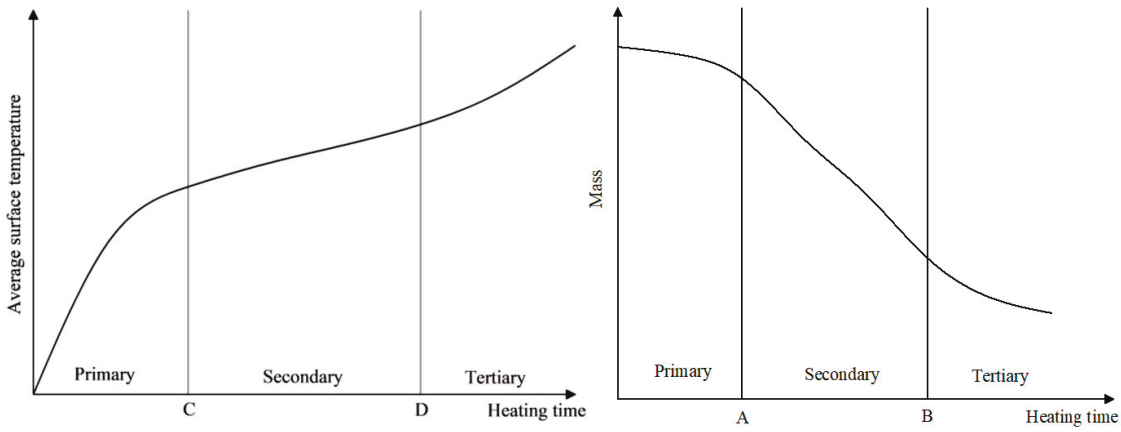

Figure 34. Corresponding relationship between temperature change and mass change.

First Stage: The temperature rapidly increases while the mass remains almost unchanged.

Second Stage: The temperature exceeds the boiling point, and the mass rapidly decreases.

Third Stage: Water evaporation is completed, and the temperature continues to rise.

The second stage, where water evaporation occurs, is the microwave heating curing stage of SF-EAM. The microwave absorption performance of SF-EAM determines the development speed of the first two stages. The better the microwave absorption performance, the faster the development speed of these stages.

Comprehensive temperature and quality testing results indicate that when the microwave power exceeds 600 W, both the temperature and quality of SF-EAM undergo significant changes. Under the same conditions, higher microwave power results in better microwave absorption performance of SF-EAM. However, excessive microwave power can cause the temperature rise rate of SF-EAM to be too fast, making it difficult to control the microwave heating time and leading to resource waste.

Recommendation: This study recommends a microwave heating power range of 600–1000 W to optimize the microwave absorption performance of SF-EAM without causing excessive temperature rise rates and resource waste.

4. Conclusions

This article investigates the microwave absorption properties of SiC-Fe_3O_4 emulsified asphalt mixture (SF-EAM), and the main research conclusions are as follows:

(1) Gradation and Ratio Design: Based on the median value of MS-3 gradation, Gradation A was designed using the theory of the maximum density curve. Based on performance tests at the micro-surface, the ratio of each component of the emulsified asphalt mixture was determined as follows: mineral aggregate:modified emulsified asphalt:water:cement = 100:12.8:6:1.

(2) Effect of SF Addition on Mixing Performance: The addition of SF affects the mixing performance of the emulsified asphalt mixture. As the SF content increases, the mixing time and viscosity of the emulsified asphalt mixture also increase. The optimal dosage range of SF, obtained through mixing performance tests, is 0% to 4%.

(3) Microwave Absorption Performance: When the SF content is in the range of 0% to 4%, higher content results in better microwave absorption performance of SF-EAM. The optimal dosage of SF is 4%. When the composite ratio of SF is S:F = 1:1, the microwave absorption performance of SF-EAM is best.

(4) Influence of Environmental Temperature and Microwave Power: The environmental temperature has a minimal effect on the microwave absorption performance of the emulsified asphalt mixture. In contrast, microwave power has a significant impact. The higher the microwave power, the better the microwave absorption performance of SF-EAM. Considering both heating efficiency and economic factors, the recommended range of microwave power in this study is 600–1000 W.

Author Contributions: Conceptualization, X.J.; formal analysis, W.X.; methodology, W.X.; investigation, X.J. and Y.C.; writing—original draft preparation, X.J., Y.C. and J.L.; writing—review and editing, X.J., Y.C. and J.L.; supervision, W.X.; project administration, W.X.; funding acquisition, X.J. and W.X. All authors have read and agreed to the published version of the manuscript.

Funding: This research was supported by the Science and Technology Project of Jiangxi Provincial Transportation Department (2023H0026).

Institutional Review Board Statement: Not applicable.

Informed Consent Statement: Not applicable.

Data Availability Statement: The original contributions presented in the study are included in the article, further inquiries can be directed to the corresponding author.

Conflicts of Interest: The authors declare no conflicts of interest.

References

1. Xu, W.; Luo, R. Evaluation of interaction between emulsified asphalt and mineral powder using rheology. *Constr. Build. Mater.* **2022**, *318*, 125990. [CrossRef]
2. Xiao, Q.; Huang, K.M.; Shi, H.X. Microwave Hyperpolarization Effect—An Orthogonal Incoherent Microwave Field Heating Study. *J. Phys. Chem. B.* **2024**, *128*, 1963–1974. [CrossRef] [PubMed]
3. Wei, Y.F.; Huo, J.Y.; Wang, Z.J.; Guo, J.T. Microwave Heating Characteristics of Emulsified Asphalt Repair Materials Incorporated with Steel Slag. *Adv. Mater.* **2020**, *1*, 1–12. [CrossRef]
4. Xu, W.; Guan, Y.H.; Shah, Y.I.; Luo, R.; Xu, Z.Q. Study on curing characteristics of cold-mixed and cold-laid asphalt mixture based on electrical properties. *Constr. Build. Mater.* **2022**, *330*, 127223. [CrossRef]
5. Samuel, D.; Cinzia, B.; Vasiliki, T.; Fausto, F. Magnetic Losses in Soft Ferrites. *Magnetochemistry* **2022**, *8*, 60. [CrossRef]
6. Wan, J.M.; Wu, S.P.; Xiao, Y.Y.; Chen, Z.W.; Zhang, D. Study on the effective composition of steel slag for asphalt mixture induction heating purpose. *Constr. Build. Mater.* **2018**, *178*, 542–550. [CrossRef]
7. Chen, J.H.; Liu, M.; Yang, T.; Zhai, F.M.; Hou, X.M.; Chou, K.C. Improved microwave absorption performance of modified SiC in the 2–18 GHz frequency range. *Crystengcomm* **2017**, *19*, 519–527. [CrossRef]
8. Liu, X.M.; Zhao, Y.; Wei, Z.Q. Microwave absorption enhancement of asphalt concrete with SiC-Fe_3O_4 mixtures modifier. *Constr. Build. Mater.* **2020**, *254*, 119209. [CrossRef]
9. Liu, X.M.; Wei, Z.Q.; Zhao, Y.; Yan, D.X. Improving the Electromagnetic Properties of Bitumen Using SiC-Fe_3O_4 Composites. *J. Mate. Civ. Eng.* **2021**, *33*, 04021326. [CrossRef]
10. Liu, X.M.; Zhao, Y.; Yan, D.X.; Feng, Y. An Environmentally Friendly Asphalt Concrete Containing SiC Aggregate for Microwave Heating Deicing. *J. Mater. Civ. Eng.* **2023**, *35*, 1–13. [CrossRef]
11. Zhao, Y.; Liu, X.M.; Zhang, X.H. Experimental and Analytical Study on Heating and Road Performance of Asphalt Mixture with Silicon Carbide and Ferroferric Oxide Composite Structure Layer. *Case Stud. Constr. Mater.* **2023**, *19*, 2214–5095. [CrossRef]
12. Zhao, Y.; Liu, X.M.; Wei, D.M. Asphalt mixture with nucleus-shell structural microwave enhanced aggregate: Structure design, preparation and performance. *Case Stud. Constr. Mater.* **2023**, *19*, 2214–5095. [CrossRef]
13. Li, C.; Wu, S.P.; Chen, Z.W.; Shu, B.A.; Li, Y.Y.; Xiao, Y.; Liu, Q.T. Synthesis of Fe3O4-decorated Mg-Al layered double hydroxides magnetic nanosheets to improve anti-ultraviolet aging and microwave absorption properties used in asphalt materials. *Constr. Build. Mater.* **2019**, *220*, 320–328. [CrossRef]
14. Liu, X.M.; Zhao, Y.; Liu, W.Z.; Yan, D.X. Microwave heating and deicing efficiency for asphalt concrete with SiC-Fe3O4 microwave enhanced functional layer. *J. Cleaner Prod.* **2022**, *332*, 130111. [CrossRef]
15. Yang, F.; Li, K.H.; Xiong, R.; Guan, B.W.; Zhao, H. Investigation on Deicing Property of Steel Wool Fiber-Reinforced Asphalt Mixture by Induction Heating. *Adv. Mater.* **2020**, *1*, 5250628. [CrossRef]
16. Zhang, J.F.; Yan, Y.; Hu, Z.H.; Fan, X.Z.; Zheng, Y. Utilization of low-grade pyrite cinder for synthesis of microwave heating ceramics and their microwave deicing performance in dense-graded asphalt mixtures. *J. Cleaner Prod.* **2018**, *170*, 486–495. [CrossRef]
17. Wang, Z.J.; Gao, J.; Ai, T.; Zhao, P. Laboratory Investigation on Microwave Deicing Function of Micro Surfacing Asphalt Mixtures Reinforced by Carbon Fiber. *J. Test. Eval.* **2014**, *42*, 498–507. [CrossRef]
18. Wang, H.P.; Zhang, Y.; Zhang, Y.; Feng, S.F.; Lu, G.Y.; Cao, L.T. Laboratory and Numerical Investigation of Microwave Heating Properties of Asphalt Mixture. *Materials* **2019**, *12*, 146. [CrossRef] [PubMed]
19. Guan, B.W.; Yang, T.; Xiong, R.; Wang, Y.W. Electromagnetic Wave Absorbing Properties of Asphalt Mixture with Natural Magnetite Powder. *J. Build. Mater.* **2016**, *19*, 6. [CrossRef]
20. Guo, H.Y.; Wang, Z.J.; Huo, J.Y.; Wang, X.F.; Liu, Z.R.; Li, G. Microwave heating improvement of asphalt mixtures through optimizing layer thickness of magnetite and limestone aggregates. *J. Clean. Prod.* **2020**, *273*, 123090. [CrossRef]
21. Liu, X.M.; Wei, Z.Q.; Zhao, Y. Simulation and experimental study on heating efficiency of microwave-enhanced asphalt concrete with binary composites. *Civ. Eng.* **2021**, *54*, 116–123.
22. *JTG.T F40-02-2005*; Technical Guidelines for Micro-Surfacing and Slurry Seal. China Communications Press: Beijing, China, 2006.
23. *JTG F40–2004*; Technical Specification for Construction of Highway Asphalt Pavements. China Communications Press: Beijing, China, 2004.
24. *JTG/T F30-2014*; Technical Guidelines for Construction of Highway Cement Concrete Pavements. China Communications Press: Beijing, China, 2014.
25. Chen, R.Y.; Zhu, H.P.; Li, S.S. Fabrication of SiC reticulated porous ceramics with dense struts by in-situ generation of SiC. *J. Eur. Ceram. Soc.* **2024**, *44*, 635–642. [CrossRef]
26. Liu, R.S.; Wu, D.A.; Yu, X.; Zhou, N.F.; Liu, D.; Wang, L.C.; Xu, Z.Y.; Gong, H.Y.; Zhao, T.Y.; Sun, J.R.; et al. Improved magnetic properties of self-composite SrFe12O19 powder prepared by Fe_3O_4 nanoparticles. *Arab. J. Chem.* **2022**, *15*, 104071. [CrossRef]
27. Xu, W.; Shah, Y.I.; Cheng, Z.; Li, Y.C.; Zhang, K.; Yu, X.Q. Laboratory design and evaluation of a functional color micro-surfacing with synthetic resin-based binder. *Road Mater. Pavement Des.* **2022**, *24*, 2343–2362. [CrossRef]

Disclaimer/Publisher's Note: The statements, opinions and data contained in all publications are solely those of the individual author(s) and contributor(s) and not of MDPI and/or the editor(s). MDPI and/or the editor(s) disclaim responsibility for any injury to people or property resulting from any ideas, methods, instructions or products referred to in the content.

materials

MDPI

Article

Enhancement of Microwave Heating Technology for Emulsified Asphalt Mixtures Using SiC-Fe_3O_4 Composite Material

Sheng Xu, Wen Xu, Yixing Chen, Jiaqi Li and Yueguang Li *

School of Transportation and Logistics Engineering, Wuhan University of Technology, Wuhan 430063, China
* Correspondence: monlit2008@163.com; Tel.: +86-186-0271-9183

Abstract: The application of microwave heating technology can significantly enhance the water evaporation rate of emulsified asphalt mixtures post paving. To improve the microwave absorption and curing performance of these mixtures, SiC-Fe_3O_4 composite material (SF) was incorporated. This addition aims to enhance the microwave absorption efficiency and accelerate the curing process of emulsified asphalt mixtures under microwave heating. This study begins with an analysis of the microwave absorption principles pertinent to emulsified asphalt mixtures. Subsequently, the microwave heating temperature fields of ordinary emulsified asphalt mixture (EAM), SiC emulsified asphalt mixture (S-EAM), Fe_3O_4 emulsified asphalt mixture (F-EAM), and SiC-Fe_3O_4 emulsified asphalt mixture (SF-EAM) were simulated using COMSOL Multiphysics finite element software (COMSOL 6.2). The early strength variations in SF-EAM under different microwave heating durations were then examined through adhesion tests, leading to the proposal of a microwave heat curing process for SF-EAM. Finally, the wear resistance, water damage resistance, rutting resistance, and skid resistance of SF-EAM post-microwave curing were evaluated through wet wheel wear tests, wheel track deformation tests, and road friction coefficient tests. The results indicate that the optimal microwave heating time is 90 s, with the microwave absorption performance of the materials ranked as follows: EAM, S-EAM, F-EAM, and SF-EAM, from lowest to highest. The road performance of SF-EAM complies with specification requirements, and its wear resistance, water damage resistance, and rutting resistance are notably improved after microwave heating.

Keywords: emulsified asphalt mixture; SiC-Fe_3O_4 composite material; microwave absorption performance; microwave curing performance

1. Introduction

With the continuous improvement of the national highway network, various levels and types of highways have been constructed and opened to traffic, leading to a saturation in China's highway construction. Consequently, the focus has shifted from construction to maintenance. Among various road maintenance methods, emulsified asphalt mixture (EAM) plays a crucial role. It is commonly used in maintenance techniques such as slurry sealing, micro-surfacing, the cold patching of road surfaces, and asphalt cold recycling technology. The development of road maintenance and construction technology based on emulsified asphalt mixture can save energy, and at the same time, the construction technology without heating raw materials can reduce the emission of toxic gasses, which is in line with the strategic requirements of energy conservation and environmental protection in today's world [1]. However, a contradiction exists between "construction slow cracking" and "molding fast setting" in the application of emulsified asphalt. During construction, emulsified asphalt and mineral aggregate require time for thorough mixing, and the mixture needs time to be spread on the pavement. During this process, the mixture must maintain fluidity [2]. Once spread, it is necessary to quickly evaporate the moisture and solidify the mixture to enable quick traffic opening [3]. Therefore, in-depth research is required

to address the challenges of rapid solidification and the formation of emulsified asphalt mixtures post mixing and paving.

The solidification process of emulsified asphalt mixtures involves breaking the emulsion, solidifying the mixture, and achieving a certain strength. Klaila et al. first proposed the concept of microwave demulsification in 1984, successfully conducting feasibility experiments using microwaves to dehydrate crude oil [4]. Later, Fang et al. suggested that microwave radiation could break oil–water solid emulsions, achieving faster separation than gravity settling and conventional heating methods [5]. Abdurrahman et al. found that microwave radiation is a dielectric heating technique characterized by penetration, rapid, uniform, and selective heating, making it suitable for emulsion-breaking processes [6]. Thus, applying microwave heating technology to demulsify emulsified asphalt and solidify the mixture is feasible.

The inherent microwave absorption performance of the original materials in emulsified asphalt mixtures is relatively poor. Enhancing the mixture's microwave absorption by adding microwave absorbing materials can increase the microwave curing speed. Microwave absorbing materials can be categorized based on their loss mechanisms into electrical loss type and magnetic loss type [7] materials.

Guan et al. noted that Fe_3O_4 in natural magnetite powder exhibits good electromagnetic properties. Replacing mineral powder with magnetite in asphalt mixtures can improve microwave absorption [8]. Chen et al. studied the microwave absorption properties of SiC and boron-doped SiC, finding that boron-doped SiC shows superior microwave absorption performance in the 2–18 GHz frequency range. At 14 GHz and a material thickness of 1.5 mm, the maximum microwave reflection loss is −37.94 dB [9]. Liu et al. proposed that a composite material comprising SiC (an electrical loss-type material) and Fe_3O_4 (a magnetic loss-type material) can significantly enhance the microwave absorption performance of asphalt mixtures [10]. Consequently, SiC can be used as a standalone microwave absorbing material or combined with other materials for improved performance.

Additionally, incorporating SiC into asphalt mixtures can improve their road performance. Sun et al. mentioned that nano SiC has excellent thermal conductivity and oxidation resistance at high temperatures. Experiments showed that adding 100 nm nano SiC at 6% content maximizes asphalt aging resistance and improves water damage resistance [11]. Wang et al. compared the early road performance of cold recycled emulsified asphalt mixtures treated at room temperature, in an oven, and microwaved. They used environmental scanning electron microscopy and optical microscopy to study the morphology and emulsion-breaking behavior. Gray relational analysis was employed to compare the influence of microwave radiation time on the early road performance of cold recycled emulsified asphalt mixtures [12].

Dai et al. analyzed the early strength and road performance of cold recycled emulsified asphalt mixtures heated by microwave, finding microwave heating effective in enhancing early strength. Based on experimental results, a heating power of 800 W and a microwave heating time of 15 min were recommended. The study demonstrated that microwave heat curing rapidly increases early strength, making it superior to room temperature and oven curing [13].

Wang et al. studied the influence of the microwave heating time, power, water–cement ratio, and asphalt–cement ratio on the early strength of cement–asphalt lotion mixtures. They concluded that the total microwave energy is composed of power and radiation time, and higher total microwave energy results in higher surface temperature [14]. However, excessively long microwave radiation times can reduce mixture strength, necessitating a balanced approach to improve early strength.

Although prior research has primarily focused on strength and road performance concerning microwave emulsion breaking and curing, few studies have emphasized incorporating microwave absorbing materials to enhance absorption performance. Few have explored enhancing microwave absorption performance through both electrical and magnetic losses simultaneously. This study employed theoretical research, numerical

simulation, and laboratory experiments to investigate the microwave absorption and curing performance of SiC-Fe_3O_4 emulsified asphalt mixtures, aiming to apply improved microwave heating technology in practical engineering.

The aim of this study was to improve the microwave absorption and curing performance of emulsified asphalt mixtures. This research started by analyzing the microwave absorption performance of each component material in emulsified asphalt mixtures, leading to the introduction of the microwave absorbing material SF. Subsequently, COMSOL Multiphysics finite element software was used to simulate the microwave heating temperature field of different emulsified asphalt mixtures, evaluating the microwave absorption performance through temperature field changes. Early strength variations in SF-EAM under different microwave heating times were studied through adhesion tests to determine a reasonable microwave heating time and propose a curing method. Finally, the wear resistance, water damage resistance, rutting resistance, and skid resistance of SF-EAM cured by microwave heating were evaluated using wet wheel wear tests, wheel track deformation tests, and road friction coefficient tests. The technical roadmap is shown in Figure 1.

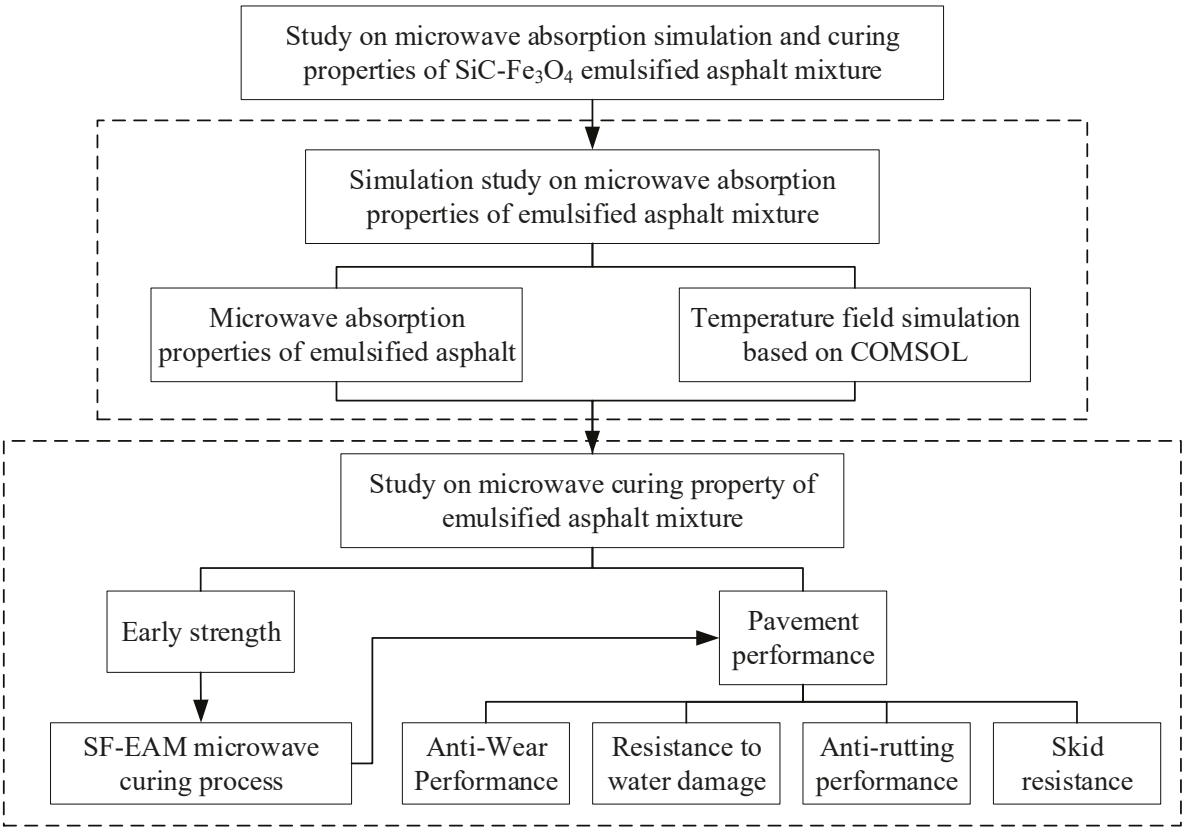

Figure 1. Technical roadmap.

2. Materials and Methods

2.1. Materials

2.1.1. Modified Emulsified Asphalt

The emulsified asphalt mixture prepared in this study had to meet the performance requirements for micro-surfacing according to the technical requirements outlined in the "Guidelines for Micro Surfacing and Slurry Seal Technology" [15] (hereinafter referred to as the "Guidelines") and the test method referred to the "Standard Test Methods of Bitumen and Bituminous Mixtures for Highway Engineering" [16]. The main technical indicators are presented in Table 1.

Table 1. Technical performance of modified emulsified asphalt.

Test Item		Unit	Standard Specifications	Test Result	Test Method
Percentage of sieve residue		%	≤0.1	0.05	T0652
charge		/	Positive charge of cation	Positive charge of cation	T0653
Evaporative residue content		%	≥60	65	T0651
evaporative residue properties	penetration	0.1 mm	40~100	80	T0604
	softening point	°C	≥53	66	T0606
	ductility	cm	≥20	30	T0605
	solubility (Trifluoroethylene)	%	≥97.5	98	T0607
storage stability	1d	%	≤1	0.5	T0655
	5d	%	≤5	2.5	

2.1.2. Mineral Materials

The coarse and fine aggregates used in this study were ordinary basalt aggregates and the test method referred to the "Test Methods of Aggregates for Highway Engineering" [17]. The main technical indicators are shown in Table 2.

Table 2. Technical performance of mineral materials.

Material	Test Item	Unit	Standard Specifications [15]	Test Result	Test Method
coarse aggregate	Stone crushing value	%	≤26	15	T0316
	Los Angeles attrition loss	%	≤28	20	T0317
	Stone polish value	BPN	≥42	50	T0321
	ruggedness	%	≤12	7	T0314
fine aggregate	Ruggedness	%	≤12	6	T0340
mineral aggregate	Equivalent of sand	%	≥65	78	T0334

2.1.3. Filler

The first type of filler used in this study was ordinary mineral powder. The test methods used are referred to as the "Test Methods of Aggregates for Highway Engineering" and "Test Methods of Soils for Highway Engineering" [17,18]. According to the technical requirements for mineral powder outlined in the "Technical Specification for Construction of Highway Asphalt Pavement" [19], the main technical indicators are presented in Table 3.

Table 3. Technical performance of mineral powder.

Test Item	Unit	Standard Specifications [19]	Test Result	Test Method
Apparent relative density	t/m^3	≥2.50	2.8	T0352
Water content	%	≤1	0.8	T0103
Particle size range < 0.6 mm	%	100	100	T0351
<0.15 mm	%	90~100	98	
<0.075 mm	%	75~100	92	
Coefficient of water affinity	/	<1	0.8	T0353
Index of plasticity	/	<4	3	T0354

The second type of filler used in this study was ordinary Portland cement. The test method used is referred to as the "Testing Methods of Cement and Concrete for Highway Engineering" [20] According to the technical requirements for cement specified in the "Technical Rules for Construction of Highway Cement Concrete Pavement" [21], the main technical indicators are presented in Table 4.

Table 4. Technical properties of cement.

Test Item		Unit	Standard Specifications [21]	Test Result	Test Method
setting time	initial setting	min	≥45	132	T0505
	final setting	min	≤600	270	
compressive strength	3 d	MPa	≥17.0	20.4	T0553
	28 d	MPa	≥42.5	47.6	
flexural strength	3 d	MPa	≥4.0	5.3	T0558
	28 d	MPa	≥7.0	8.2	

2.1.4. Additive Materials

The SiC used in this study was high-purity silicon carbide powder produced by Nan gong Yingtai Metal Materials Co., Ltd. (Xingtai, China). The SiC content in the silicon carbide powder exceeded 99%. The primary function of SiC is to enhance the microwave absorption performance of the emulsified asphalt mixture by improving its electrical loss characteristics. The test method used is referred to as the "Test Methods of Aggregates for Highway Engineering" and "Test Methods of Soils for Highway Engineering" [17,18]. The basic technical performance of SiC was evaluated according to the technical requirements for mineral powder, and the test results are shown in Table 5.

Table 5. Technical performance of SiC.

Test Item	Unit	Standard Specifications [19]	Test Result	Test Method
Apparent relative density	t/m^3	≥2.50	3.1	T0352
Water content	%	≤1	0.01	T0103
Particle size range < 0.6 mm	%	100	100	
<0.15 mm	%	90~100	100	T0351
<0.075 mm	%	75~100	95	
Coefficient of water affinity	/	<1	0.4	T0353
Index of plasticity	/	<4	3	T0354

The Fe_3O_4 used in this study was high-purity ferric oxide powder produced by Hebei Keze Metal Materials Co., Ltd. (Xingtai, China). The Fe_3O_4 content in the ferric oxide powder exceeded 99%. The primary function of Fe_3O_4 is to enhance the microwave absorption performance of the emulsified asphalt mixture by improving its magnetic loss characteristics. The basic technical performance of Fe_3O_4 was evaluated according to the technical requirements for mineral materials, and the test results are shown in Table 6.

Table 6. Technical performance of Fe_3O_4.

Test Item	Unit	Standard Specifications [19]	Test Result	Test Method
Apparent relative density	t/m^3	≥2.50	4.7	T0352
Water content	%	≤1	0.05	T0103
Particle size range < 0.6 mm	%	100	100	
<0.15 mm	%	90~100	100	T0351
<0.075 mm	%	75~100	95	
Coefficient of water affinity	/	<1	0.6	T0353
Index of plasticity	/	<4	2.5	T0354

Based on the characteristics of two materials with similar densities and no chemical reactions with each other [22,23], the method for preparing SiC-Fe_3O_4 composite materials from SiC and Fe_3O_4 in this study involved mixing a specified mass of SiC powder and Fe_3O_4 powder in a stirring cup, stirring with a glass rod until the two materials were completely and evenly mixed, and then placing them into a sealed bag for later use.

2.1.5. Grading

This study used the commonly applied MS-3 gradation for micro-surfacing, with the range shown in Figure 2. Through moderately adjusting the pass rate of the mixture through each particle size sieve, the gradation curve of the designed mixture was made to closely align with the gradation curve obtained using the Taylor formula when $n = 0.4$. Ultimately, gradation A of this study was designed [24]. The scope is shown in Figure 2.

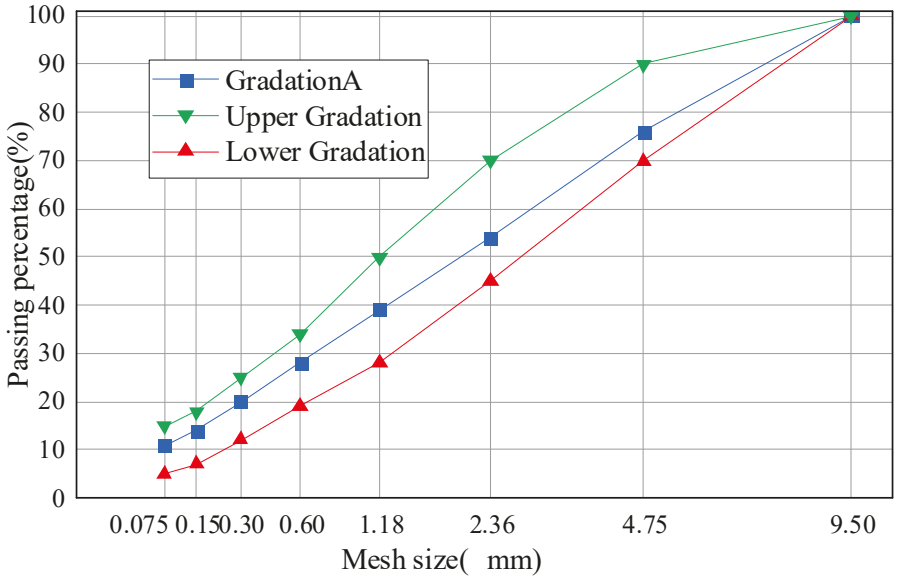

Figure 2. Grading curve.

2.2. Experimental Equipment and Methods

2.2.1. Microwave Heating Equipment and Principle

The microwave heating equipment used in this study was a large multifunctional microwave oven, model FPBM3077RFA. The appearance and interior are shown in Figure 3, and the internal structure diagram is shown in Figure 4. The waveguide is located on the right side of the microwave oven, which is suitable for the microwave heating of common emulsified asphalt mixture specimens. The maximum heating power of the microwave is 1000 W, with a frequency of 2.45 GHz, and the minimum accuracy of the microwave heating time is 1 s. The standard curing box is a constant temperature and humidity box, model LHS-100CL. The curing temperature range of the standard curing box is 0–85 °C, and the curing relative humidity range is 45–98%.

(**a**) Appearance (**b**) Internal structure

Figure 3. (**a**) Appearance and (**b**) interior of microwave oven (model FPBM3077RFA).

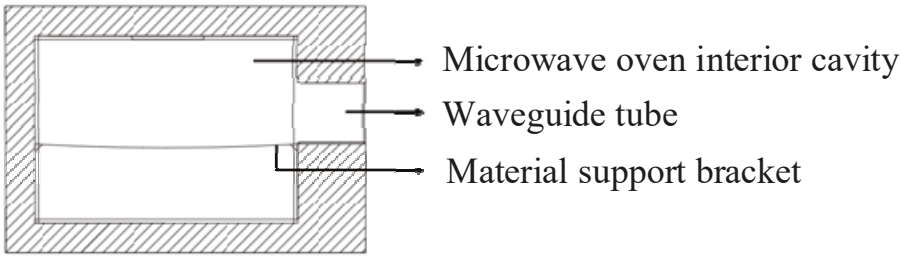

Figure 4. Internal structure diagram of microwave oven.

Changes in current or charge within a charged system can induce variations in the electromagnetic field. A changing electric field generates a changing magnetic field, and vice versa. These alternating electric and magnetic fields continuously propagate in the form of waves, known as electromagnetic waves. Each type of electromagnetic wave possesses a specific frequency, defined as the number of periodic changes in the electromagnetic field per unit time. Microwaves are a type of electromagnetic wave with a frequency range of 300 MHz to 300 GHz and a wavelength range of 1 mm to 1 m, categorized into three bands: decimeter wave, centimeter wave, and millimeter wave [25].

When microwaves encounter different materials during transmission, various phenomena occur, primarily reflection, penetration, and absorption. These phenomena are influenced by factors such as the dielectric constant and electromagnetic loss coefficient of the materials. Based on the microwave reflection, transmission, and absorption characteristics of different materials, commonly used materials are categorized into conductors, insulators, dielectrics, and magnetic compounds.

Under the influence of electromagnetic fields generated by microwaves, media can convert electromagnetic energy into thermal energy. The efficiency of media in absorbing microwaves is related to their complex permittivity and complex permeability, generally represented by Equations (1) and (2) [26].

$$\varepsilon = \varepsilon' - j\varepsilon'' = \varepsilon_0\varepsilon_r = \varepsilon_0(\varepsilon_r' - \varepsilon_r'') \tag{1}$$

where ε is the dielectric constant of the material, F/m; ε_0 is the permittivity of vacuum, with a value of $8.854 \times 10^{-128.854}$; ε_r is the relative permittivity of the material; ε_r' is the real part of the relative permittivity; ε_r'' is the imaginary part of the relative permittivity; and j is the imaginary unit.

$$\mu = \mu' - j\mu'' = \mu_0\mu_r = \mu_0(\mu_r' - j\mu_r'') \tag{2}$$

where μ is the complex permeability of the material, H/m; μ_0 is the permeability of vacuum, with a value of $4\pi \times 10^{-7}$ H/m; μ_r is the relative permeability of the material; μ_r' is the real part of the relative permeability; and μ_r'' is the imaginary part of the relative permeability. The power absorbed by the material from the microwave is given by Equations (3) and (4) [27].

$$P = 0.556\, fE^2\varepsilon_r \tan\delta \times 10^{-12} \tag{3}$$

where P is the power absorbed per unit volume of the material, W/cm^3; f is the operating frequency of the microwave, Hz; E is the magnitude of the electric field, W/cm; and δ is the loss angle of the material.

$$\tan\delta = \tan\delta_E + \tan\delta_M = \frac{\varepsilon''}{\varepsilon'} + \frac{\mu''}{\mu'} \tag{4}$$

where δ_E is the electric loss angle of the material, and δ_M is the magnetic loss angle of the material.

According to Equations (3) and (4), it can be seen that the absorption power of materials for microwaves is influenced by two factors: internal and external. Among them, the

working frequency f and electric field strength E of the microwave are external factors that depend on the properties of the microwave field. The higher the working frequency and electric field strength, the greater the absorption power of the microwave. The relative dielectric constant (ε_r) and loss angle (δ) of the material are internal factors that depend on the properties of the material. Specifically, ε'' and μ' are the real parts of the dielectric constant and magnetic permeability, respectively, characterizing the energy storage capacity of the material, such as electrical energy and magnetic energy. The imaginary parts ε'' and μ'' represent the material's loss factor, reflecting the dielectric material's ability to dissipate electromagnetic waves.

A good material for microwave absorption not only needs to exhibit strong microwave loss capabilities but also needs to allow microwaves to penetrate the material as much as possible, minimizing reflection at the material interface. The reflection loss is given by Equations (5) and (6). The smaller the reflection loss and microwave reflectivity when microwaves enter the material, the better the microwave absorption performance of the material [28].

$$R_L = 20\lg\left|\frac{Z_{in} - Z_0}{Z_{in} + Z_0}\right| \tag{5}$$

where R_L is the reflection loss, in dB; Z_{in} is the impedance of the microwave in free space, in ohms (Ω); and Z_0 is the impedance at the interface between free space and the material, in ohms (Ω).

$$Z_{in} = Z_0\sqrt{\frac{\mu}{\varepsilon}}\tanh[j(2\pi ft/c)\sqrt{\mu\varepsilon}] \tag{6}$$

where c is the speed of light, in m/s; f is the operating frequency of the microwave, in Hz; and t is the thickness of the material, in meters (m).

According to Equation (3), to increase microwave absorption power, the electric field strength E or microwave frequency (f) can be increased, and the relative dielectric constant (ε_r) or loss angle (δ) of the material can also be improved by changing its properties. However, the electric field strength cannot be increased indefinitely, as high electric field strength can lead to electrode breakdown [25], which is not conducive to heating materials. In addition, blindly increasing the frequency is also ineffective because when electromagnetic waves penetrate into the medium, some of the energy will be consumed and converted into heat energy, causing the electric field strength to decay according to a certain law.

The distance from the surface at which the microwave energy decreases to its original maximum value is defined as the penetration depth. When the dielectric loss factor (D) of the material is small, the penetration depth (D) can be expressed by Equation (7) [29].

$$D = \frac{\lambda\sqrt{\varepsilon'}}{2\pi\varepsilon''} \tag{7}$$

where D is the penetration depth of the microwave, in cm, and λ is the wavelength of the microwave, in cm.

According to Equation (7), the microwave penetration depth (D) and microwave wavelength (λ) are of the same order of magnitude. The wavelength range of microwaves is usually 1 mm to 1 m, allowing most materials to be uniformly heated by microwaves. When using higher frequency electromagnetic waves to heat materials, the wavelength of the electromagnetic waves becomes shorter. Although high-frequency electromagnetic fields can increase the absorption power of the medium, the short wavelength and small penetration depth of the waves prevent comprehensive and uniform heating.

Therefore, altering the composition of the mixture and improving the electromagnetic parameter properties of the material are effective ways to enhance the microwave absorption power of the material.

2.2.2. Cohesion Test

This section evaluates the early strength of emulsified asphalt mixtures through cohesion tests. Under the same conditions, the adhesive strength and molding state of SF-EAM specimens cured by heating with different microwave times may vary. When the microwave heating time is insufficient, the strength of the emulsified asphalt mixture cannot meet the standard specifications. Conversely, when the microwave heating time is too long, the asphalt in the emulsified asphalt mixture will overheat and age, affecting the strength. Therefore, by designing the adhesion test of SF-EAM, its reasonable microwave heating time can be determined. After the SF-EAM adhesive strength test specimen is formed, it needs to be microwave-heated and cured before testing the adhesive strength. Therefore, this section includes some adjustments and modifications to the cohesion test steps specified in the standards. The specific test steps are as follows:

1. Prepare a specific quantity of mineral materials, modified emulsified asphalt, cement, water, SiC, Fe_3O_4, and other materials. Prepare SiC-Fe_3O_4 emulsified asphalt mixture (SF-EAM) specimens and ordinary emulsified asphalt mixture (EAM) specimens without composite materials. Set EAM as the control group. The SF content in SF-EAM is 4%, and the composite ratio of the two materials is SiC = 1:1.
2. Prepare standard specimens for adhesive strength testing according to the specifications. Divide the demolded specimens into 6 groups and place them in a laboratory environment at room temperature for 10 min. Then, place them in a microwave oven with a power of 1000 W for 0 s, 30 s, 60 s, 90 s, 120 s, and 150 s. After heating, remove the specimens and place them at room temperature for 20 min (for 30 min adhesive strength testing) or 50 min (for 60 min adhesive strength testing). The curing methods for each group of specimens are shown in Table 7.

Table 7. Curing methods and curing time for each group of specimens.

Item	Thirty-Minute Adhesive Strength		Sixty-Minute Adhesive Strength	
	Microwave Heating Time (s)	Total Maintenance Time at Room Temperature (min)	Microwave Heating Time (s)	Total Maintenance Time at Room Temperature (min)
1	0	30	0	60
2	30	30	30	60
3	60	30	60	60
4	90	30	90	60
5	120	30	120	60
6	150	30	150	60

3. Place the cured specimen on the testing platform of the cohesion tester and measure the cohesion according to the specifications, with an accuracy of 0.1 N·m.
4. Repeat steps (1) to (3) to test the adhesion of EAM and SF-EAM under different microwave exposure times, as shown in Figure 5.

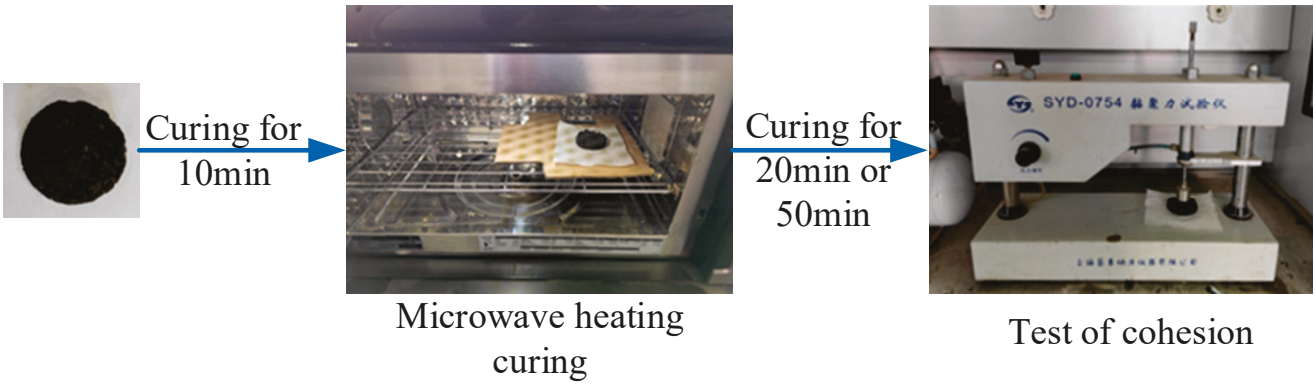

Figure 5. Adhesion test after microwave heat curing.

2.2.3. Microwave Heat Curing Process of SF-EAM

This section proposes the microwave heat curing process for SF-EAM, which uses microwave heating technology to heat and cure emulsified asphalt mixture specimens, thereby improving the early strength of newly mixed and formed specimens. The specific steps are as follows:

1. Prepare raw materials according to the ratio of mineral aggregate–emulsified asphalt–water–cement = 100:12.8:6:1 [24]. The mineral aggregate consists of coarse aggregate, fine aggregate, and mineral powder, with coarse and fine aggregates accounting for 89% and mineral powder accounting for 11%. The grading of each component is shown in Figure 2.
2. Mix SiC and Fe_3O_4 evenly in a 1:1 ratio to produce SF, and replace 4% of the mineral powder by mass with SF.
3. First, mix the aggregate, mineral powder, SF, and cement at room temperature. Then, add water to the mixture, and finally, add emulsified asphalt and stir evenly. The total mixing time should not exceed 60 s.
4. Pour the mixed emulsified asphalt mixture into the test mold, lightly compact, and scrape it flat.
5. Demold the specimen, and then place it in the laboratory at room temperature for 10 min for curing. Finally, place it in a microwave oven and heat it with a microwave power of 600–1000 W to cure. During heating, adjust the microwave power according to different specimens to ensure that the maximum surface temperature of the specimen does not exceed 150 °C.
6. Remove the heated specimen and continue with subsequent tests according to the standard specifications.

2.2.4. Wet Wheel Wear Test

This section evaluates the wear resistance and water damage resistance of SF-EAM through wet wheel wear tests after 1 h and 6 days of water immersion. Wear and tear refer to the phenomenon where the road surface is gradually damaged due to repeated friction caused by loads during use. The maintenance pavement made of emulsified asphalt mixture as a raw material usually has high wear resistance, which is generally determined by the material properties and maintenance methods of the pavement. Firstly, SF-EAM contains two types of doping materials, SiC and Fe_3O_4, which can affect the gradation of the mixture and thus affect the wear resistance of SF-EAM. Secondly, the specimens cured by microwave heating have stronger adhesion between materials, which also affects the wear resistance of SF-EAM. Two sets of control tests were established:

1. The first set includes EAM and SF-EAM specimens subjected to indoor curing, with EAM specimens as the control group.
2. The second set includes SF-EAM specimens subjected to both indoor curing and microwave heat curing, with indoor-cured SF-EAM specimens as the control group.

The wet wheel wear test procedure is illustrated in Figures 6 and 7. During the test, measure the combined mass of the oil felt and the specimen (m_a) before testing. Place the prepared specimen and oil felt in a 25 °C water bath for either 1 h or 6 days, and then install the specimen and operate the instrument. After the test, measure the total mass of the dried oil felt and specimen (m_b). The wear value is calculated using Equation (8):

$$WTAT = (m_a - m_b)/A \tag{8}$$

where $WTAT$ is the wear value of the slurry mixture, g/m^2; m_a is the mass of the specimen before wear, g; m_b is the mass of the specimen after wear, g; and A is the wear area of the abrasion head rubber tube, m^2.

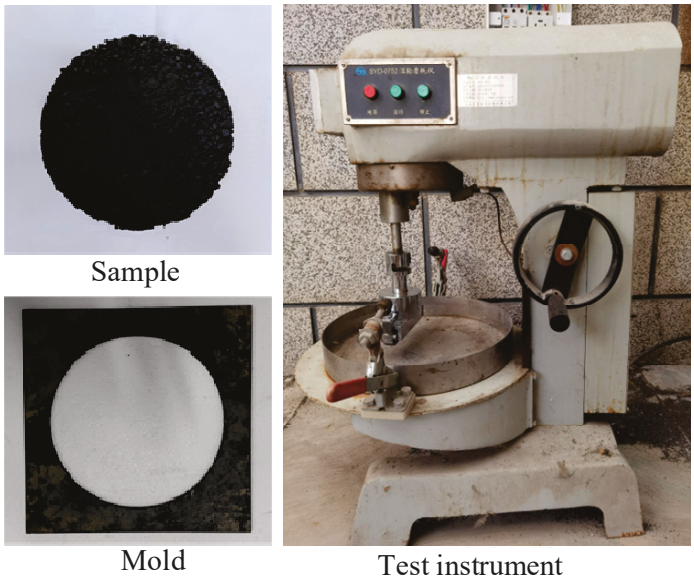

Figure 6. Wet wheel wear test set up.

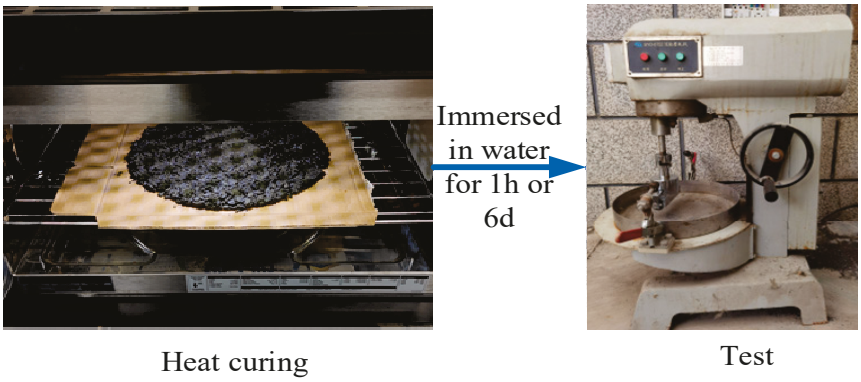

Figure 7. Wet wheel abrasion test after microwave heat curing.

2.2.5. Rutting Deformation Test

This section evaluates the anti-rutting performance of SF-EAM through wheel track deformation tests. Rutting is a permanent deformation that occurs under the combined effects of repeated driving loads and high temperatures, manifested as longitudinal strip-shaped grooves along the driving wheel tracks. Asphalt mixture has viscoelastic properties, and when subjected to repeated vehicle loads under high-temperature conditions, ruts may form due to the insufficient high-temperature stability of asphalt. As mentioned in the previous research, the microwave heat curing method can enhance the early strength of SF-EAM, and therefore, microwave heating will have a certain impact on the anti-rutting performance of SF-EAM. Two control experiments were set up:

1. The first group consisted of EAM and SF-EAM specimens after indoor curing, with EAM specimens as the control group.
2. The second group underwent experiments on SF-EAM after indoor curing and microwave heat curing, with indoor-cured SF-EAM specimens as the control group.

Complete the wheel track deformation test according to the standard procedures, as shown in Figure 8. After the experiment is completed, calculate the width deformation rate using Equation (9):

$$PLD = (L_b - L_a) \times 100/L_a \tag{9}$$

where PLD is the deformation rate per unit width of the specimen, %; L_a is the initial width of the specimen before the test, mm; and L_b is the width of the specimen after rolling, mm.

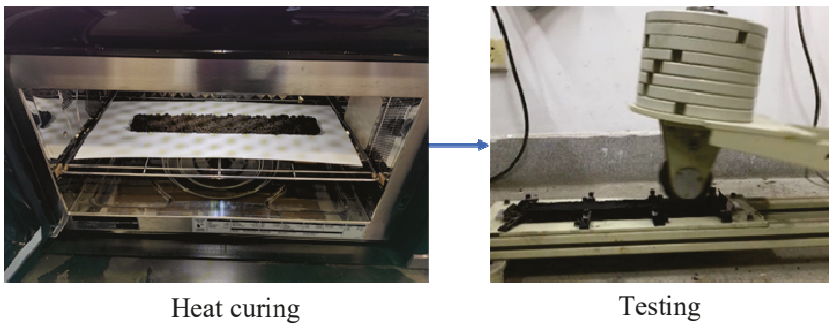

Figure 8. Wheel track deformation test after microwave heating and curing.

2.2.6. Road Friction Coefficient Test

This section evaluates the anti-skid performance of SF-EAM through road friction coefficient testing. Asphalt pavement should have sufficient anti-skid performance to ensure that vehicles can travel safely at high speeds under the most unfavorable conditions, and its anti-skid performance should not quickly decrease under external factors. The surface structure of the road itself is the main provider of anti-skid performance, and the addition of SF can cause slight differences in the surface structure of SF-EAM. Therefore, it is necessary to study the anti-skid performance of SF-EAM. Two control experiments were set up:

1. The first group consisted of EAM and SF-EAM specimens after indoor curing, with EAM specimens as the control group.
2. The second group underwent experiments on SF-EAM after indoor curing and microwave heat curing, with indoor-cured SF-EAM specimens as the control group.

Remove the cured specimen, fix it on both sides with thick steel plates, and clean the surface with a brush. Place the pendulum at the measuring point and set it to zero. Fix the pendulum on the right cantilever. Press the switch after spraying water on the test piece to make it scratch on the test piece. Repeat the operation to record data and note the surface temperature of the measuring point. The experimental process is shown in Figure 9. After the experiment is completed, correct the swing value for temperature according to Equation (10). The temperature correction values are shown in Table 8.

$$BPN_{20} = BPN_T + \Delta BPN \tag{10}$$

where BPN_{20} is the swing value converted to the standard temperature of 20 °C; BPN_T is the swing value measured at the pavement temperature; and ΔBPN is the temperature correction value, obtained from Table 8.

(**a**) Pendulum friction tester (**b**) Testing process

Figure 9. Road friction coefficient test.

Table 8. Temperature correction values.

Temperature (°C)	0	5	10	15	20	25	30	35	40
Temperature correction value ΔBPN	−6	−4	−3	−1	0	+2	+3	+5	+7

3. Simulation Study on Microwave Absorption Performance of Emulsified Asphalt Mixture

3.1. Microwave Absorption Performance of Emulsified Asphalt Mixture

When using microwave heating to heat materials, it is essential for the material to contain a medium that can absorb microwaves. To quickly heat the emulsified asphalt mixture under microwave radiation, the mixture must include a microwave-absorbing medium. According to Equation (3), under the same external conditions, the microwave absorption performance of the emulsified asphalt mixture is related to its relative dielectric constant (ε_r) and loss tangent value (tanδ). Emulsified asphalt mixture, as a composite medium, typically contains more than 80% mineral aggregate, 5–10% water, 4–8% petroleum asphalt, less than 10% mineral powder, and other additives. The dielectric constant and loss tangent values of common emulsified asphalt mixture materials are shown in Table 9 [30].

Table 9. Dielectric constant and loss tangent of emulsified asphalt mixture materials.

Material		T/°C	f/MHz	ε_r	tanδ
Water		25	300	77.5	0.016
		25	3000	76.7	0.157
Pure asphalt		26	3000	2.5	0.001
Aggregate material diorite		20	2450	5.6~7	0.018~0.036
Asphalt mixture	Containing diorite	20	2450	5.8	0.034
	Containing limestone	20	2450	6.7	0.015
	Containing quartz	20	2450	4.0	0.006

According to Table 9, the electromagnetic parameters of each component in the emulsified asphalt mixture are relatively low. Among them, the dielectric constant and loss tangent of pure asphalt are relatively small, indicating that it does not significantly absorb microwaves. The microwave absorption performance of aggregates is also similar to that of asphalt and is generally related to the metal mineral composition they contain, making the absorption performance unstable. The electromagnetic parameters of water are relatively high, providing good microwave absorption performance. However, the proportion of water in the emulsified asphalt mixture is small, resulting in an overall insignificant temperature rise during microwave heating.

Therefore, adding a high-performance microwave-absorbing material to the mixture, which can effectively absorb and attenuate incident electromagnetic waves, converting electromagnetic energy into thermal energy, can better leverage the advantages of microwave heating. According to the research of Chen et al. [9], SiC is an excellent electrical loss-type microwave-absorbing material with good impedance matching characteristics [31]. Fe_3O_4 is an excellent magnetic loss absorbing material with stronger microwave absorption performance than iron powder [32]. The electromagnetic parameters of SiC [33] and Fe_3O_4 [34] are shown in Table 10.

Table 10. Electromagnetic parameters of several microwave absorbing materials.

Material	Electromagnetic Parameters (at 2.45 GHz Frequency)			
	ε'	ε''	μ'	μ''
SiC	42~45	7~10	1.2~1.25	0~0.1
Fe_3O_4	12~13	0.1~0.2	2.5~3	1.3~1.5

According to Table 10, the imaginary part of the dielectric constant (ε'') of SiC is very large, while the imaginary part of the magnetic permeability (μ'') is almost zero. From Equation (4), it can be seen that the larger the imaginary part, the higher the electromagnetic loss. Therefore, SiC can effectively utilize the electrical energy in electromagnetic waves, whereas its ability to absorb and utilize magnetic energy is relatively weak. The properties of Fe_3O_4 are exactly the opposite of SiC. Both SiC and Fe_3O_4 can serve as excellent microwave-absorbing materials to enhance the microwave absorption performance of emulsified asphalt mixtures. However, since microwaves contain both electrical and magnetic energy, the loss mechanism of a single material cannot fully utilize the electromagnetic energy in microwaves.

Liu et al. [10] found that the reflection loss of the SiC-Fe_3O_4 composite material, composed of SiC and Fe_3O_4 in a certain proportion, is lower than that of single SiC or Fe_3O_4. Lower reflection loss allows more microwaves to penetrate into the interior of the material. Therefore, this study considered utilizing the different microwave loss mechanisms of the two materials simultaneously by introducing the SiC-Fe_3O_4 composite material and incorporating it into the emulsified asphalt mixture to improve the microwave absorption performance of the mixture.

3.2. Simulation of Microwave Heating Temperature Field for Emulsified Asphalt Mixture

3.2.1. Constitutive Relationship between Microwave Field and Temperature Field

The electromagnetic field theory for the microwave heating of emulsified asphalt mixture involves solving Maxwell's equations, which can be expressed in partial differential form, as shown in Equations (11) and (12).

Maxwell's equations in differential form are as follows:

$$\nabla \cdot D = \rho \tag{11}$$

$$\nabla \cdot B = 0 \tag{12}$$

$$\nabla \times E = -\frac{\partial B}{\partial t} \tag{13}$$

$$\nabla \times H = J + \frac{\partial D}{\partial t} \tag{14}$$

where D is the electric displacement vector, C/m^2; ρ is the charge density, C/m^3; B is the magnetic flux density vector, T; E is the electric field vector, N/C; H is the magnetic field vector, A/m; and J is the current density, A/m^2.

In order to better apply Maxwell's equations, it is necessary to obtain constitutive relationships that describe the macroscopic behavior of matter under field influence. In assuming that emulsified asphalt mixture is an isotropic linear material, its constitutive equation can be formulated as shown in Equations (15)–(17):

$$J = \sigma E \tag{15}$$

$$D = \varepsilon E \tag{16}$$

$$B = \mu H \tag{17}$$

where σ is the electrical conductivity of the material, S/m; ε is the permittivity of the material, F/m; and μ is the permeability of the material, H/m.

The formula for a Fourier transform is shown in Equation (15). According to the Fourier transform, the time domain in Maxwell's equations is transformed into the frequency domain, as shown in Equation (18):

$$f(\omega) = \int x(t)e^{-j\omega t}dt \tag{18}$$

$$\frac{\partial}{\partial t} \sim j\omega \tag{19}$$

According to Equations (18) and (19), the Helmholtz equation in the frequency domain can be derived from the Maxwell equations. The Helmholtz equation is an important control equation for electromagnetic waves when using COMSOL to solve microwave heating problems, as shown in Equation (20), where the expression for k_0 is shown in Equation (21):

$$\nabla \times \mu_r^{-1}(\nabla \times E) - k_0^2(\varepsilon_r - j\frac{\sigma}{\omega\varepsilon_0})E = 0 \tag{20}$$

$$k_0^2 = \omega^2\mu_0\varepsilon_0 \tag{21}$$

where μ_0 is vacuum permeability, H/m; ε_0 is the vacuum dielectric constant, F/m; μ_r is the relative magnetic permeability; and ε_r is the relative dielectric constant.

Microwave heating emulsified asphalt mixture generally transfers heat through thermal conduction. According to the theory of thermal conduction, the temperature distribution of emulsified asphalt mixture at various spatial points at any time is the temperature field distribution of the object.

The heat conduction problem of microwave heating of emulsified asphalt mixture can be expressed by the heat transfer equation, expressed in partial differential form as Equation (22). The heat transfer equation is an important control equation for solid heat transfer when using COMSOL to solve microwave heating problems.

$$\rho C_P \frac{\partial T}{\partial t} + \rho C_P u \cdot \nabla T + \nabla \cdot (-k\nabla T) = Q + Q_{ted} \tag{22}$$

where ρ is the density of heated substance, kg/m^3; C_P is the constant pressure heat capacity, J/(kg·K); T is temperature, °C; k is thermal conductivity, W/(m·K); and Q is the heat source, J/(m^2·s).

3.2.2. Simulation Model of Microwave Heating Emulsified Asphalt Mixture

The coupling of multiple physical fields is generally divided into strong coupling and weak coupling. Weak coupling refers to the relatively weak mutual influence between physical fields, while strong coupling refers to the very intense mutual influence between physical fields [35]. The microwave heating problem of emulsified asphalt mixture specimens is a strong coupling problem between the electromagnetic wave field and the temperature field. The calculation process of the strong coupling problem model is very complex, and in the modeling process, it is necessary to simplify the complex problem to save computational costs. Therefore, this section makes the following assumptions about electromagnetic fields, temperature fields, materials, and geometric models:

1. During microwave heating, the thermal parameters such as heat capacity and electromagnetic parameters, such as the dielectric constant of emulsified asphalt mixture specimens, remain constant.
2. The influence of the internal electromagnetic field of emulsified asphalt mixture specimens is ignored.
3. After the microwave is absorbed by the emulsified asphalt mixture specimen, the microwave energy is completely converted into thermal energy.
4. The material inside the emulsified asphalt mixture specimen is homogeneous and isotropic.
5. The interior of the microwave oven is homogeneous and smooth, and does not absorb microwaves. Other materials inside the microwave oven do not absorb microwaves except for the specimen.

In the subsequent microwave heating test, the emulsified asphalt mixture specimen was placed on a wooden thin plate. Due to the small volume of the wooden board and the low microwave dissipation of the wooden material, this part of the structure was ignored in the modeling process. The microwave oven cavity and waveguide are both rectangular prisms, with the dimensions of the microwave oven cavity being 0.53 m in length, 0.36

m in width, and 0.25 m in height. Regardless of the cavity thickness, the dimensions of the waveguide are 0.08 m in length, 0.12 m in width, and 0.11 m in height. The emulsified asphalt mixture specimen is cylindrical with a radius of 0.04 m and a height of 0.02 m. The specimen was placed at the rectangular waveguide mouth of a microwave oven and remained in a fixed position during the microwave heating process. The geometric models of the microwave oven, waveguide, and specimen are shown in Figure 10.

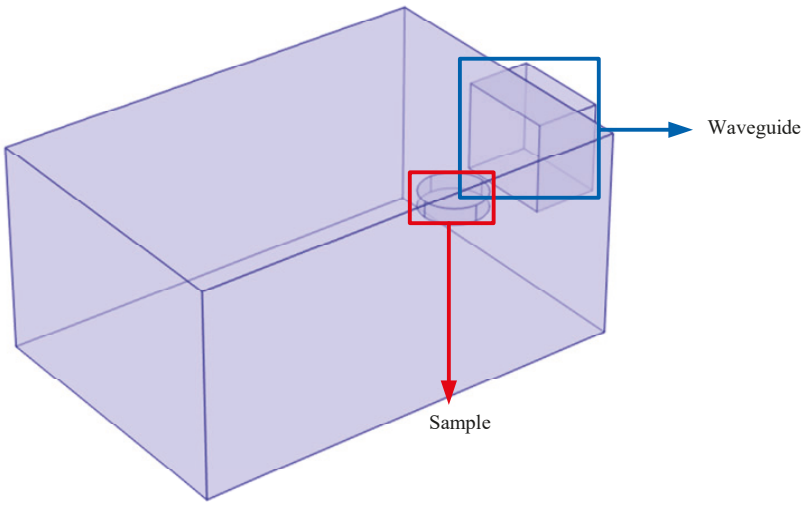

Figure 10. Geometric model of microwave oven and specimen.

The microwave cavity was filled with air. Considering that the imaginary part of the dielectric constant of air is very small, it was assumed in the simulation that its imaginary part was 0, and the power loss caused by it was ignored. The surface resistance of the stainless-steel cavity is relatively small, and the electromagnetic loss of the cavity can be ignored. Therefore, it was assumed that there was no heat source or heat conduction in the area other than the emulsified asphalt mixture specimen during the heating process. There were four types of emulsified asphalt mixture specimens in this simulation: EAM, S-EAM (emulsified asphalt mixture mixed with SiC), F-EAM (emulsified asphalt mixture mixed with Fe_3O_4), and SF-EAM. Their electromagnetic and thermal parameters are shown in Tables 11 and 12, respectively.

Table 11. Electromagnetic parameters of four emulsified asphalt mixtures.

Specimen	Conductivity (S/m)	ε'	ε''	μ'	μ''
EAM	8×10^{-7}	6	0.25	1	0
S-EAM	8×10^{-7}	6.34	0.33	1	0
F-EAM	8×10^{-7}	6.05	0.28	1.21	0.04
SF-EAM	8×10^{-7}	6.45	0.38	1.25	0.05

Table 12. Thermal parameters of four emulsified asphalt mixtures.

Specimen	Density ρ (kg/m^3)	Thermal Conductivity k (W/(m·K))	Thermal Conductivity C_P (J/(kg·K))
EAM	2500	1.5	800
S-EAM	2500	1.5	800
F-EAM	2500	1.5	800
SF-EAM	2500	1.5	800

Define the waveguide and microwave cavity as impedance boundary conditions. The port boundary condition is used to define the boundary of microwave power entering the

model. A heat flux boundary condition was set on the surface of the air in the microwave cavity in contact with the emulsified asphalt mixture specimen, and a universal value of 10 W/(m^2·°C) was selected for the heat transfer coefficient [36]. The microwave power of the microwave oven was 200 W, and the microwave frequency was 2.45 GHz. Based on the existing microwave heating experience and actual laboratory conditions, the temperature of emulsified asphalt mixture specimens and air was set to 25 °C, and the microwave heating time was set to 120 s.

The mesh partitioning process is a crucial step in verifying the finite element model and establishing the reliability of the software, model, and computational results. Under electromagnetic waves at a frequency of 2.45 GHz, Liu et al. proposed a grid size calculation method [37], as shown in Equation (23):

$$l = \frac{\lambda}{6\sqrt{\varepsilon'}} \tag{23}$$

where l is the grid size, mm; λ is the wavelength of microwaves, mm; and ε' is the real part of the complex dielectric constant of a material.

To accelerate the convergence of the simulation model and reduce unnecessary computation time, the main research object, emulsified asphalt mixture specimens, will be divided into extremely refined grids, while other areas will be divided into ordinary grids. The grid division of the specimens and other areas is shown in Figure 11. The number of grid cells in the emulsified asphalt mixture specimen after partitioning is 1571, and the number of grid cells in other parts is 9466. The minimum unit length (l_{min}) of the emulsified asphalt mixture specimen grid partitioning is 1.22×10^{-4} m, and the maximum unit length (l_{max}) is 0.0122 m, which conforms to Equation (23).

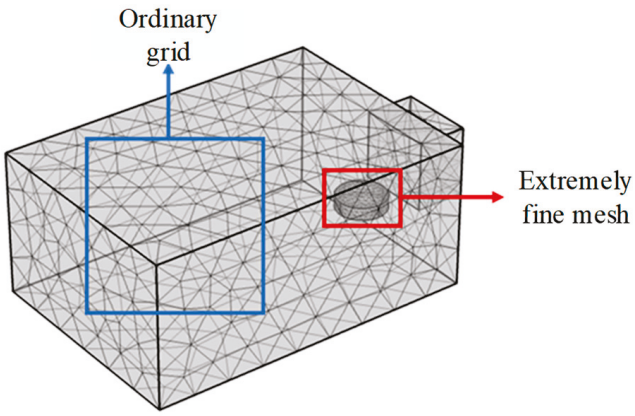

Figure 11. Grid division of microwave oven and specimen.

3.2.3. Simulation Results of Microwave Heating Emulsified Asphalt Mixture

A simulation model for the microwave heating of emulsified asphalt mixture was established under the conditions of a microwave power of 200 W and a microwave frequency of 2.45 GHz. The temperature field distribution of four types of emulsified asphalt mixture specimens—EAM, S-EAM, F-EAM, and SF-EAM—after microwave heating was simulated. The influence of external materials on the temperature field change in emulsified asphalt mixture during microwave heating was studied, and the microwave absorption performances of different emulsified asphalt mixtures were compared. The simulation results are shown in Figure 12. The initial temperature of the specimen before heating was 25 °C, and the highest and lowest temperatures of the specimen after heating are shown in Table 13.

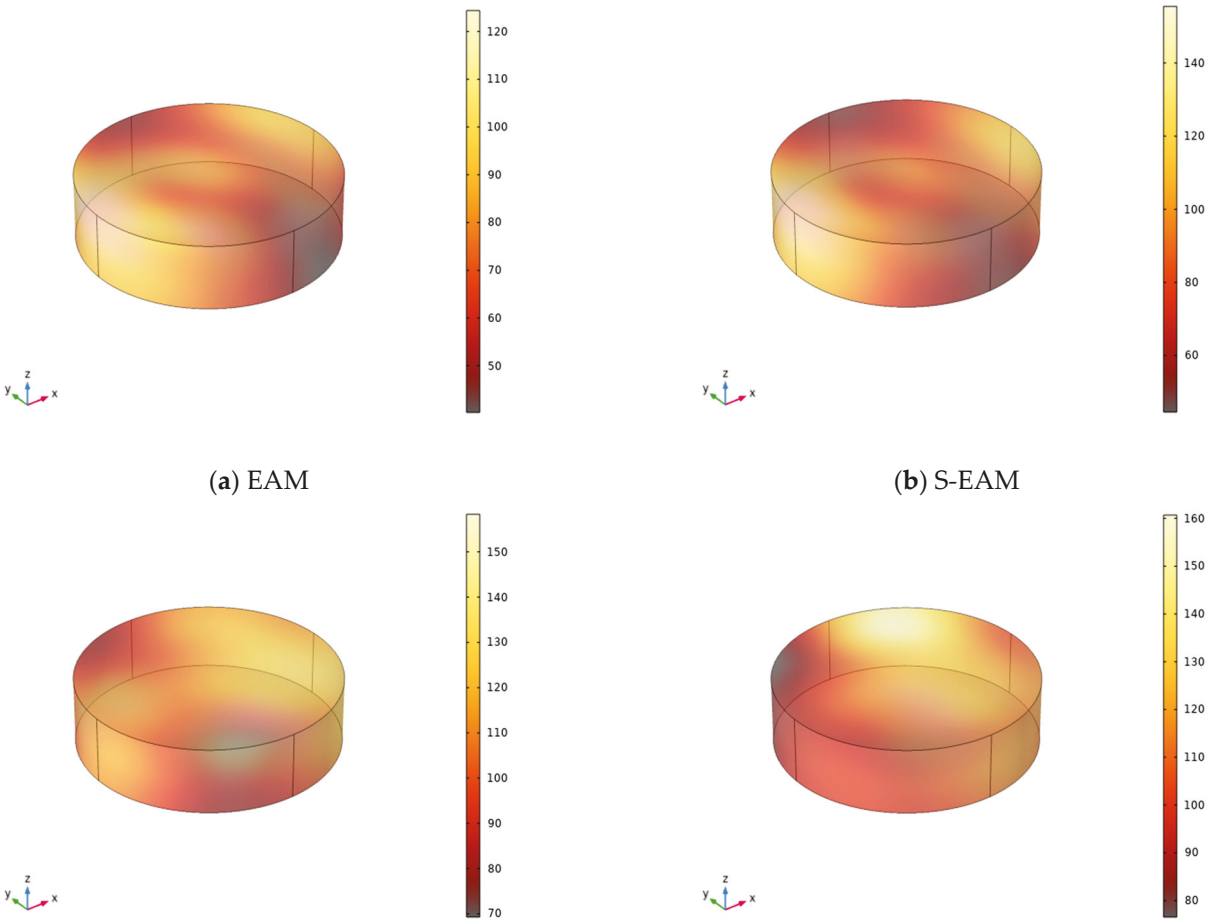

(**a**) EAM (**b**) S-EAM

(**c**) F-EAM (**d**) SF-EAM

Figure 12. Temperature distribution of four materials after 120 s of microwave heating.

Table 13. Temperature of four materials heating for 120 s.

Type	EAM	S-EAM	F-EAM	SF-EAM
Minimum temperature (°C)	40	50	69	77
Maximum temperature (°C)	124	155	158	165
Maximum temperature difference (°C)	84	105	89	88

In Figure 12, the dark areas represent low-temperature regions, while the bright areas represent high-temperature regions. According to the data in Table 13 and the color comparison in Figure 12, it can be seen that after 120 s of microwave heating, the temperatures of all four emulsified asphalt mixtures increased. The temperature in most areas of EAM and S-EAM increased significantly, but the dark areas are also larger, with large temperature differences and uneven heating. The bright color areas of F-EAM and SF-EAM have a larger distribution range and more uniform heating. Among them, SF-EAM has the largest proportion of bright color areas and the greatest temperature rise.

According to Table 13, a schematic of the temperature changes in different emulsified asphalt mixtures was drawn, as shown in Figure 13. The calculation method for temperature change is shown in Equation (24);

$$\Delta T = T_{max} - T_0 \tag{24}$$

where ΔT is the temperature variation, °C; T_{max} is the maximum temperature, °C; and T_0 is the initial temperature, °C.

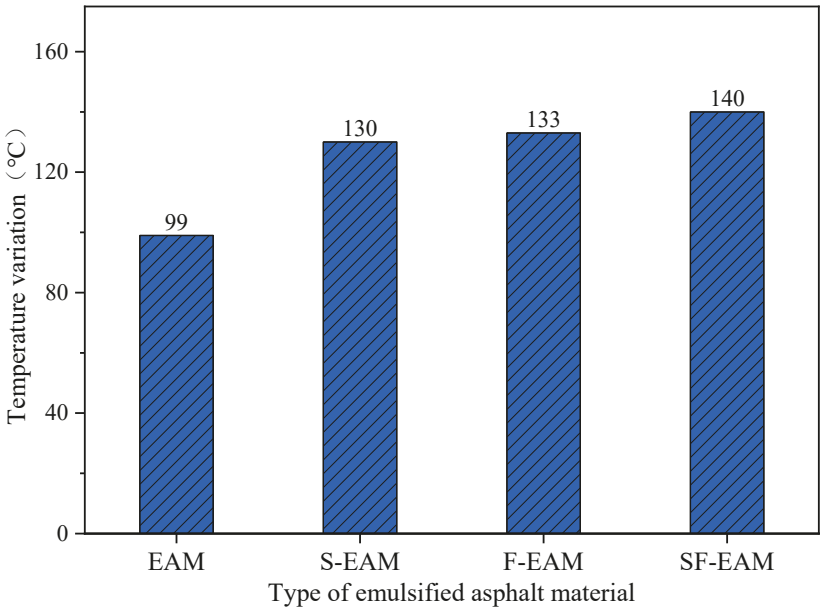

Figure 13. Temperature variation in different emulsified asphalt mixtures.

According to Table 13 and Figure 13, the temperatures of the four emulsified asphalt mixtures significantly increased after microwave heating. The temperature increases range from small to large as follows: EAM, S-EAM, F-EAM, and SF-EAM. The maximum temperature increases are 396%, 520%, 532%, and 560%, respectively. Compared to EAM, the temperature changes in S-EAM, F-EAM, and SF-EAM increased by 31%, 34%, and 41%, respectively. The maximum temperature differences in the four emulsified asphalt mixtures from small to large are EAM, SF-EAM, F-EAM, and S-EAM, but the maximum temperature differences are not significantly different.

When microwave heating emulsified asphalt mixtures of different compositions, the temperature increases. Among them, the temperature increase in emulsified asphalt mixtures mixed with SiC, Fe_3O_4, and SF is greater than that of ordinary emulsified asphalt mixtures, indicating that the addition of SiC and Fe_3O_4 can improve the microwave absorption performance of emulsified asphalt mixtures. The temperature increases in the emulsified asphalt mixture mixed with SF is the largest, and the microwave heating is more uniform, indicating that the improvement in microwave absorption performance by adding SF is more significant than adding a single material.

In summary, the microwave absorption performance of the material depends on the electric loss and magnetic loss characteristics of the material itself, and is related to the material's relative dielectric constant (ε_r) and loss tangent value (tanδ). In the emulsified asphalt mixture, the electromagnetic parameters of each component material are relatively small, so its microwave absorption performance is poor. The real and imaginary parts of SiC permittivity are larger, and the real and imaginary parts of Fe_3O_4 permeability are larger. The SiC-Fe_3O_4 composite can improve the microwave absorption performance of emulsified asphalt mixture. Therefore, further research is needed on the curing performance of emulsified asphalt mixtures through microwave heating tests.

4. Results and Discussion of Microwave Curing Performance Test

4.1. Cohesion Test

The adhesion test results of EAM and SF-EAM are shown in Table 14.

Table 14. Cohesion force under different microwave heating times.

Specimen	Thirty-Minute Cohesion (N·m)		Sixty-Minute Cohesion (N·m)	
	EAM	SF-EAM	EAM	SF-EAM
1	1.8	1.7	2.5	2.4
2	1.8	1.9	2.6	2.6
3	1.9	2.2	2.7	2.8
4	2.1	2.5	2.8	2.9
5	2.3	2.4	2.8	2.7
6	2.2	2.2	2.7	2.5

According to Table 14, the variation curves of the 30 min and 60 min cohesion of EAM and SF-EAM are plotted with different microwave heating times, as shown in Figures 14 and 15.

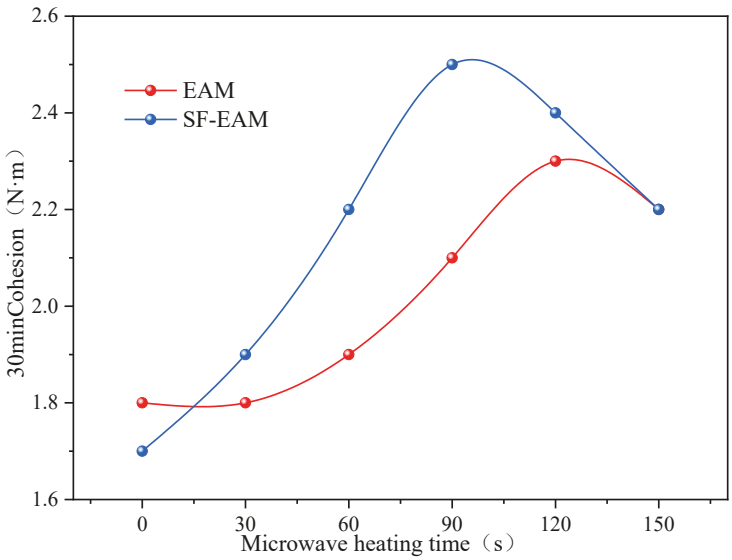

Figure 14. Thirty-minute cohesion of EAM and SF-EAM under different microwave heating times.

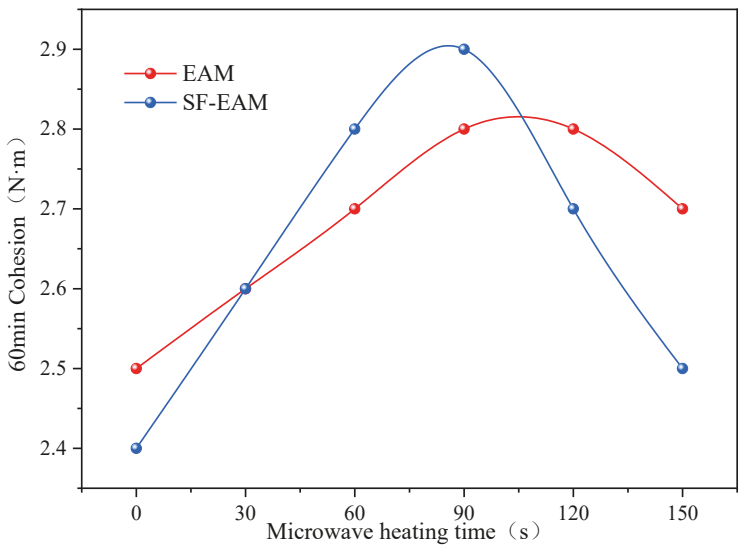

Figure 15. Sixty-minute cohesion of EAM and SF-EAM under different microwave heating times.

From Figures 14 and 15, it can be seen that as the microwave heating time increases; the 30 min cohesion of EAM and SF-EAM shows an initial increase followed by a decrease. The 30 min cohesion of EAM reaches its maximum value of 2.3 N·m after 120 s of microwave

heating, while the 30 min cohesion of SF-EAM reaches its maximum value of 2.5 N·m after 90 s of microwave heating, indicating that the maximum 30 min cohesion of SF-EAM is greater and requires a shorter microwave heating time to reach its maximum value. As the microwave heating time increases, the 60 min cohesion of EAM and SF-EAM also shows an initial increase followed by a decrease. The 60 min cohesion of EAM reaches its maximum value of 2.8 N·m after 90 s of microwave heating, while the 60 min cohesion of SF-EAM reaches its maximum value of 2.9 N·m after 90 s of microwave heating, indicating that the 60 min cohesion of SF-EAM is even greater.

After microwave heating treatment, the internal temperatures of EAM and SF-EAM continuously increase with the increase in heating time. At high temperatures, the rate of water evaporation accelerates, and the specimens can be quickly cured and formed to a certain strength. Therefore, under the same total curing time, the longer the microwave heating time, the higher the strength of the specimens. However, the temperature of the emulsified asphalt mixture should not be too high. When the temperature exceeds 150 °C, the asphalt will gradually age due to high temperature. At this time, some of the light asphalt oil adhered to the aggregate will gradually evaporate, and the adhesion between asphalt and aggregate will deteriorate, resulting in a decrease in the strength of the emulsified asphalt mixture. Therefore, when the microwave heating time exceeds 120 s, both the 30 min and 60 min cohesion of SF-EAM will decrease.

Comparing EAM and SF-EAM emulsified asphalt mixtures, SF-EAM has a better ratio of mineral aggregate in EAM. Therefore, when cured directly without microwave heating, EAM has a greater cohesion force. However, SF-EAM contains microwave absorbing material SF, which has better microwave absorption performance than EAM. Therefore, after the same heating treatment time, SF-EAM absorbs more heat, increases temperature faster, evaporates moisture faster, heats and solidifies faster, and increases adhesion faster. Therefore, the time required for SF-EAM to reach its maximum cohesion is shorter. Correspondingly, the rate at which the cohesion of SF-EAM decreases is also faster than that of EAM.

According to Table 14, the comparison curves of the 30 min and 60 min cohesion of SF-EAM under different microwave heating times are drawn, as shown in Figure 16.

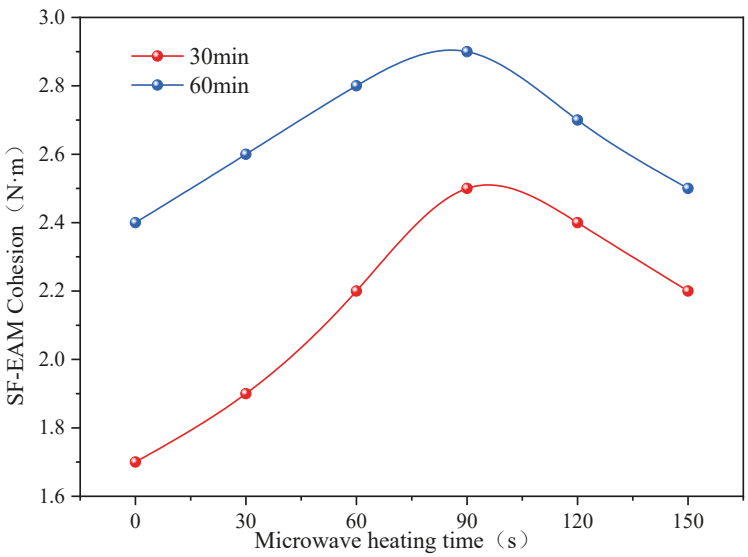

Figure 16. Cohesion force of SF-EAM under different microwave heating times.

As shown in Figure 16, with the continuous increase in microwave heating time, the difference between the 30 min and 60 min cohesion of SF-EAM becomes smaller and smaller. Therefore, it can be concluded that the 30 min cohesion increase rate of SF-EAM after microwave heating is faster than the 60 min cohesion increase rate.

In comparing the 30 min and 60 min cohesion of SF-EAM, microwave heating has a greater impact on the 30 min cohesion of SF-EAM, resulting in a faster increase in the 30 min cohesion of SF-EAM. Microwave heating enhances the strength of emulsified asphalt mixture by accelerating the evaporation of water. When the total curing time increases from 30 min to 60 min, the water evaporation effect generated by microwave heating will be reduced. As the curing time gradually increases, the strength of SF-EAM cured by microwave heating will gradually approach that of SF-EAM cured by conventional curing, which also reflects that microwave heating has a greater impact on the early strength of SF-EAM.

Based on the adhesive strength test results of EAM and SF-EAM, microwave heating for a certain period of time can improve the early strength of both materials, but the improvement in SF-EAM is greater, indicating that the microwave heat curing performance of SF-EAM is better than that of EAM. When SF-EAM is microwave heated for 90 s, its 30 min and 60 min cohesion can reach their maximum values. At this time, the early strength of the emulsified asphalt mixture is relatively high. Therefore, the recommended microwave heating time for SF-EAM in this study is 90 s.

4.2. Wear Resistance Performance Test

The indoor curing process of EAM and SF-EAM was carried out in accordance with the standard specifications, and the microwave heat curing process referred to the previous text. After the experiment, calculate the 1 h wet wheel wear value of the emulsified asphalt mixture according to Equation (8), and the results are shown in Table 15.

Table 15. Test results of 1 h wet wheel wear test after immersion in water.

Specimen	Heat Curing Method	One-Hour Wear Value (g/m^2)		
		First Value	Second Value	Average Value
EAM	Direct drying	402.2	399.5	400.9
SF-EAM	Direct drying	420.7	421.2	421.0
SF-EAM	Microwave heating	401.0	398.3	399.7

According to Table 15, the 1 h wet wheel wear values of EAM and SF-EAM with different maintenance methods were all less than 540 g/m^2, meeting the specification requirements. When both specimens are subjected to direct drying and heat curing, the wear value of SF-EAM is greater than that of EAM. When the curing method of SF-EAM specimens involves microwave heating, the wear value is lower than that of direct drying. The smaller the 1 h wear value, the smaller the wear loss of the emulsified asphalt mixture specimen, and the better the abrasion resistance of the specimen. Therefore, although the wear resistance of EAM under direct drying curing is better than that of SF-EAM, microwave heat curing can improve the wear resistance of SF-EAM. The anti-wear performance of SF-EAM after microwave heating is better than that of EAM.

Therefore, compared to EAM, SF-EAM contains 4% SF. The adhesion between SF and asphalt is not as good as that between mineral powder and asphalt. The overall compatibility of EAM is better than that of SF-EAM, resulting in less wear when subjected to external forces. However, after microwave heating and curing, the early strength of SF-EAM is improved, and the hard surface can better resist the wear of the wear head, thus enhancing its wear resistance.

4.3. Water Damage Resistance Performance Test

Water damage is usually caused by asphalt pavement damage in rainy areas in the south or during periods of freeze–thaw cycles in the north. Under the combined action of vehicles and loads, moisture gradually accumulates at the interface between asphalt and aggregate, causing the adhesion between asphalt and aggregate to gradually weaken over

time. Like abrasion resistance, water damage resistance is also determined by the material properties and maintenance methods of the road surface.

This study evaluated the water damage resistance of SF-EAM through a 6-day wet wheel wear test. The experimental group setting method, specimen preparation and curing process, and microwave heat curing process refer to the previous text. After the experiment, calculate the 6-day wet wheel wear value of emulsified asphalt mixture according to Equation (8), and the results are shown in Table 16.

Table 16. Test results of wet wheel wear test after immersion in water for 6 days.

Specimen	Heat Curing Method	Six-Day Abrasion Value (g/m^2)		
		First Value	Second Value	Average Value
EAM	Direct drying	644.5	628.8	636.7
SF-EAM	Direct drying	687.2	695.0	691.1
SF-EAM	Microwave heating	645.5	641.1	643.3

According to Table 16, the 6-day wet wheel wear values of EAM and SF-EAM with different maintenance methods were all less than 800 g/m^2, meeting the regulatory requirements. When both specimens are subjected to direct drying and heat curing, the wear value of SF-EAM is greater than that of EAM. When the curing method of SF-EAM specimens involves microwave heating, the wear value is lower than that of direct drying. The smaller the 6-day wear value, the smaller the wear loss of the emulsified asphalt mixture specimen after immersion, and the better the water damage resistance of the specimen. Therefore, although the water damage resistance of EAM under direct drying curing is better than that of SF-EAM, microwave heat curing can enhance the water damage resistance of SF-EAM. The water damage resistance of SF-EAM after microwave heating is similar to that of EAM.

4.4. Anti-Rutting Performance

The experimental results are shown in Table 17.

Table 17. Test results of wheel track deformation test.

Specimen	Heat Curing Method	Width Deformation Rate (%)		
		First Value	Second Value	Average Value
EAM	Direct drying	3.95	4.01	3.98
SF-EAM	Direct drying	4.22	4.41	4.32
SF-EAM	Microwave heating	4.15	4.26	4.21

According to Table 17, the width deformation rate of EAM and SF-EAM with different maintenance methods is less than 5%, meeting the requirements of the specifications. When both specimens are cured by direct drying, the width deformation rate of SF-EAM is greater than that of EAM. When the curing method of SF-EAM specimens involves microwave heating, the width deformation rate is smaller than that of direct drying. The smaller the width deformation rate, the smaller the rutting of the emulsified asphalt mixture under the load wheel gauge, and the better the anti-rutting performance of the specimen. Therefore, although the anti-rutting performance of EAM under direct drying curing is better than that of SF-EAM, microwave heat curing can improve the anti-rutting performance of SF-EAM. The anti-rutting performance of SF-EAM after microwave heating is slightly lower than that of EAM.

The particle size ratio of SF-EAM to EAM is coarser because the particle size of SF is coarser than the particle size of the mineral powder it replaces. Although a coarser grading generally has better anti-rutting performance, the coarse particles of SF-EAM are limited to the part below 0.075 mm in size, and the content of these coarse particles is very small, which has little effect on improving the anti-rutting performance. On the

contrary, the particle size distribution of mineral powder in EAM is more uniform, making EAM denser than SF-EAM. Therefore, when directly dried, EAM has better anti-rutting performance. However, after microwave heating, the surface free asphalt of SF-EAM decreases, so microwave heating can improve the anti-rutting performance of SF-EAM.

4.5. Anti-Slip Performance Test

Due to the temperature being 25 °C during testing, the correction value for the swing value was taken as +2. The statistical test results after correction are shown in Table 18.

Table 18. Test results of road friction coefficient test.

Specimen	Heat Curing Method	Actual Measured Swing Value (BPN_T)				Convert the Swing Value (BPN_{20})
		First Value	Second Value	Third Value	Average Value	
EAM	Direct drying	66.5	66.1	66.9	66.5	69
SF-EAM	Direct drying	65.2	67.1	66.4	66.2	68
SF-EAM	Microwave heating	66.0	66.1	65.8	66.0	68

According to Table 18, the conversion values (BPN_{20}) of EAM and SF-EAM for different maintenance methods are all greater than 45, meeting the regulatory requirements. The difference in swing values between EAM and SF-EAM is not significant, and there is no significant difference in swing values between SF-EAM after microwave heating and after direct drying. Microwave heating has little effect on the anti-skid performance of SF-EAM.

The coarse and fine aggregate components of EAM and SF-EAM are identical, with differences only in the particles with a size of 0.075 mm or less. This fraction of the mineral material has little effect on the friction coefficient, resulting in similar swing values for EAM and SF-EAM. Although microwave heating can reduce the surface moisture content of SF-EAM, the swing value test involves spraying water on the surface of the specimen, and the surface moisture reduction from microwave heating can be largely ignored. Therefore, microwave heating has little effect on the swing value test results of SF-EAM.

5. Conclusions

This study investigated the microwave absorption simulation and curing performance of SiC-Fe_3O_4 emulsified asphalt mixture (SF-EAM). The main research conclusions are as follows:

- The SiC-Fe_3O_4 composite material (SF) formed by mixing SiC and Fe_3O_4 can improve the material's relative dielectric constant (ε_r) and loss tangent value (tanδ), thereby enhancing the microwave absorption performance of emulsified asphalt mixtures.
- The numerical simulation results from COMSOL show that compared to EAM, the temperature changes in S-EAM, F-EAM, and SF-EAM increased by 31%, 34%, and 41%, respectively. Therefore, the microwave absorption performance improvement effect of the SiC-Fe_3O_4 composite material is more significant than that of a single material.
- As the microwave heating time increases, the adhesion of SF-EAM first increases and then decreases. When microwave heating is 90 s, the 30 min and 60 min cohesion force of SF-EAM reach the maximum values of 2.5 N·m and 2.8 N·m, respectively. Therefore, the recommended microwave heating time for SF-EAM in this study is 90 s.
- After microwave heating and curing, the 1 h wet wheel wear value is 399.7 g/m^2, the 6-day wet wheel wear value is 643.3 g/m^2, the wheel track deformation rate is 4.21%, and the swing value of SF-EAM is 68°, which all meet the specifications. Therefore, microwave heating can not only improve the early strength of SF-EAM but also ensure that its road performance, such as wear resistance, water damage resistance, rutting resistance, and skid resistance, meets the requirements of the specifications.

- The particle size range of SiC and Fe_3O_4 used in this paper is 0.07~0.075 mm, and the influence of materials with other particle sizes on the microwave absorption performance of emulsified asphalt mixture was not considered. Therefore, further research is needed for materials with other particle sizes.

Author Contributions: Conceptualization, S.X.; Formal analysis, W.X. and Y.L.; Methodology, W.X. and Y.L.; Investigation, S.X. and Y.C.; Writing—original draft preparation, S.X., Y.C. and J.L.; writing—review and editing, S.X., Y.C. and J.L.; supervision, W.X.; project administration, W.X.; funding acquisition, S.X. and W.X. All authors have read and agreed to the published version of the manuscript.

Funding: This research was supported by National College Students' Innovation and Entrepreneurship Training Program (S202310497187) and the Science and Technology Project of Jiangxi Provincial Transportation Department (2023H0026).

Institutional Review Board Statement: Not applicable.

Informed Consent Statement: Not applicable.

Data Availability Statement: The original contributions presented in the study are included in the article, further inquiries can be directed to the corresponding author.

Conflicts of Interest: The authors declare no conflicts of interest.

References

1. Xu, W.; Shah, Y.I.; Cheng, Z.; Li, Y.C.; Zhang, K.; Yu, X.Q. Laboratory design and evaluation of a functional color micro-surfacing with synthetic resin-based binder. *Road Mater. Pavement Des.* **2023**, *24*, 2343–2362. [CrossRef]
2. Xu, W.; Guan, Y.H.; Shah, Y.I.; Luo, R.; Xu, Z.Q. Study on curing characteristics of cold-mixed and cold-laid asphalt mixture based on electrical properties. *Constr. Build. Mater.* **2022**, *330*, 127223. [CrossRef]
3. Xu, W.; Luo, R. Evaluation of interaction between emulsified asphalt and mineral powder using rheology. *Constr. Build. Mater.* **2022**, *318*, 125990. [CrossRef]
4. Wolf, N. Use of Microwave Radiation in Separating Emulsions and Dispersions of Hydrocarbons and Water. Patent US4582629A, 29 December 1986.
5. Fang, C.; Chang, B.; Lai, P. Microwave demulsification. *Chem. Eng. Commun.* **1988**, *73*, 227–239. [CrossRef]
6. Abdurahman, N.H.; Yunus, R.M.; Azhari, N.H.; Said, N.; Hassan, Z. The potential of microwave heating in separating water-in-oil (w/o) emulsions. *Energy Procedia* **2017**, *138*, 1023–1028. [CrossRef]
7. Xu, P.X.; Zhang, D.R.; Miao, Y.; Sani, B.M.; Zhang, K. Development and characterization of a novel steel slag-based composite. *Constr. Build. Mater.* **2022**, *341*, 127769. [CrossRef]
8. Guan, B.W.; Yang, T.; Xiong, R. Electromagnetic wave absorbing properties of asphalt mixture with natural magnetite powder. *J. Build. Mater.* **2016**, *19*, 198–203. [CrossRef]
9. Chen, J.; Liu, M.; Yang, T. Improved microwave absorption performance of modified SiC in the 2–18 GHz frequency range. *CrystEngComm* **2016**, *19*, 519–527. [CrossRef]
10. Liu, X.; Zhao, Y.; Wei, Z. Microwave absorption enhancement of asphalt concrete with SiC-Fe_3O_4 mixtures modifier. *Constr. Build. Mater.* **2020**, *254*, 119209. [CrossRef]
11. Sun, J. Experimental Study on Performance of SiC Nano-Modified Asphalt and Its Mixture. Master's Thesis, Changsha University of Science and Technology, Changsha, China, 2017.
12. Wang, Z.; Dai, N.; Wang, X.; Wang, Z.J.; Dai, N.; Wang, X.F.; Li, G.; Guo, H.Y. Early-stage Road property improvements of cold recycled asphalt emulsion mixture with microwave technology. *J. Clean. Prod.* **2020**, *263*, 121451. [CrossRef]
13. Dai, N. Study on Early Strength Mechanism of Microwave Curing Cold Recycled Emulsified Asphalt Mixture. Master's Thesis, Chang'an University, Xi'an, China, 2020.
14. Wang, Z.J.; Dai, N.; Wang, X.F. Laboratory investigation on effects of microwave heating on early strength of cement bitumen emulsion mixture. *Constr. Build. Mater.* **2020**, *236*, 117439. [CrossRef]
15. Ministry of Transport Highway Science Research Institute. *Guidelines for Micro Surfacing and Slurry Seal Technology*; People's Transportation Press: Beijing, China, 2006.
16. *JTG E20-2011*; Ministry of Transport of the People's Republic of China. Standard Test Methods of Bitumen and Bituminous Mixtures for Highway Engineering. People's Transportation Press: Beijing, China, 2011.
17. *JTG E42-2005*; Ministry of Transport of the People's Republic of China. Test Methods of Aggregates for Highway Engineering. People's Transportation Press: Beijing, China, 2005.
18. *JTG 3430-2020*; Ministry of Transport of the People's Republic of China. Test Methods of Soils for Highway Engineering. People's Transportation Press: Beijing, China, 2020.

19. *JTG F40-2004*; Ministry of Transport of the People's Republic of China. Technical Specifications for Construction of Highway Asphalt Pavements. People's Transportation Press: Beijing, China, 2004.
20. *JTG 3420-2020*; Ministry of Transport of the People's Republic of China. Testing Methods of Cement and Concrete for Highway Engineering. People's Transportation Press: Beijing, China, 2020.
21. *JTG/T F30-2014*; Ministry of Transport of the People's Republic of China. Technical Rules for Construction of Highway Cement Concrete Pavements. People's Transportation Press: Beijing, China, 2014.
22. Yang, H.T.; Huang, X.Z. *SiC Fiber and Ceramic Composites*; Central South University Press: Changsha, China, 2020.
23. Wei, S.C.; Liang, Y.; Wang, Y.J. *Graphene/Ferromagnetic Particle Composite Wave-Absorbing Materials*; Science Press: Beijing, China, 2021.
24. Li, Y.G.; Chen, Y.X.; Li, J.Q.; Xu, W.; Zeng, S.H. Experimental study on microwave absorption performance of SiC-Fe_3O_4 emulsified asphalt mixture. *J. Wuhan Univ. Technol.* **2024**, *46*, 81–88.
25. Liu, W. Study on the Mechanism of Microwave Absorption Enhancement and Repair of Asphalt Mixtures. Master's Thesis, Southeast University, Nanjing, China, 2018.
26. Yang, C. Key Technologies for Measuring Complex Permittivity and Complex Permeability in Microwave and THz Bands. Ph.D. Thesis, Tianjin University, Tianjin, China, 2020. [CrossRef]
27. Zhang, T.Q.; Cui, X.K.; Zhang, Z.T. Principle, characteristics and technical superiority of microwave heating. *Road Mach. Constr. Mech.* **2008**, *7*, 10–14.
28. Gao, J.; Zhang, Z.W.; Han, Z.Q.; Sha, A.M.; Jiang, W. A review of electromagnetic wave absorbing materials used in microwave deicing pavement. *Mater. Rev.* **2016**, *30*, 87–95.
29. Nieftagodien, R. Suitability of Microwave Application to Heat Reclaimed Asphalt and Crushed Aggregates as an Energy Efficient Method in the Production of Half Warm Mix. Master's Thesis, Stellenbosch University, Stellenbosch, South Africa, 2013.
30. Wang, W. Utilization of High-Speed Microwave Heating Technology and Equipment on Bituminous Pavement Maintenance. Master's Thesis, Changsha University of Science and Technology, Changsha, China, 2007.
31. Yang, G.D.; Kang, Y.; Meng, Q.J. Progress in development of microwave absorbing materials. *Appl. Chem. Ind.* **2010**, *39*, 6. [CrossRef]
32. Wan, J.M.; Wu, S.P.; Xiao, Y.; Chen, Z.W.; Zhang, D. Study on the effective composition of steel slag for asphalt mixture induction heating purpose. *Constr. Build. Mater.* **2018**, *178*, 542–550. [CrossRef]
33. Li, R. Research on application of silicon carbide (SiC) materials in particle accelerator. *Mod. Inf. Technol.* **2021**, *5*, 165–168. [CrossRef]
34. Jia, K.; Zhao, R.; Zhong, J.C.; Liu, X.B. Preparation and microwave absorption properties of loose nanoscale Fe_3O_4 spheres. *J. Magn. Magn. Mater.* **2010**, *322*, 2167–2171. [CrossRef]
35. Gan, W. Multi-Physical Field Study of Solid-State Source Microwave Oven. Master's Thesis, University of Electronic Science and Technology of China, Chengdu, China, 2019.
36. Tong, C.H.; Lund, D.B. Microwave heating of baked dough products with simultaneous heat and moisture transfer. *J. Food Eng.* **1993**, *19*, 319–339. [CrossRef]
37. Liu, S.; Fukuoka, M.; Sakai, N. A finite element model for simulating temperature distributions in rotating food during microwave heating. *J. Food Eng.* **2013**, *115*, 49–62. [CrossRef]

Disclaimer/Publisher's Note: The statements, opinions and data contained in all publications are solely those of the individual author(s) and contributor(s) and not of MDPI and/or the editor(s). MDPI and/or the editor(s) disclaim responsibility for any injury to people or property resulting from any ideas, methods, instructions or products referred to in the content.

materials

MDPI

Article

Study on the Mechanical Properties of Modified Sludge Soil Based on an SM-C Modifier

Jun Nie [1], Kai Zhang [2,3], Xiangyang Fan [2,3], Yixuan Zhang [4], Guoxu Wei [4], Xiangyong Yu [4] and Wen Xu [4,*]

[1] Nanchang Expressway Co., Ltd., Nanchang 330009, China
[2] Jiangxi Transportation Institute Co., Ltd., Nanchang 330200, China
[3] Road Material and Structure Engineering Technology Research Center of Jiangxi Provincial, Nanchang 330200, China
[4] School of Transportation and Logistics Engineering, Wuhan University of Technology, Wuhan 430063, China
* Correspondence: wenxu@whut.edu.cn; Tel.: +86-159-2624-1294

Abstract

The purpose of this study is to solve the problem of the harmless treatment of dredged silt and soil extraction during road construction in lake areas. The silt in the project area is used as the research material to evaluate its engineering applicability as an improved filling material for the roadbed of the lake's surrounding road. Through indoor pretreatment and a series of mechanical performance tests, including compaction tests, unconfined compressive strength tests (UCS), bearing ratio tests (CBR), triaxial compression tests (CU consolidated undrained), and consolidation tests, we obtained key mechanical parameters of modified sludge soil, such as maximum dry density, optimal moisture content, unconfined compressive strength, bearing ratio, shear strength, and compression characteristics. The research results show that with the increase in modifier dosage, the optimal moisture content of modified sludge soil increases, the maximum dry density decreases, and its compressive strength and shear strength significantly improve. The CBR value also meets the technical requirements of each layer of the roadbed. Specifically, after 7 days of curing, the compaction degree of 10% modified sludge soil can exceed 96%, the unconfined compressive strength reaches 0.819 MPa, the CBR value reaches 17.5, the cohesion measured by triaxial tests is 78 kPa, the internal friction angle is 27°, and it exhibits low compressibility. These findings provide new solutions for environmentally friendly treatment, resource utilization, and road engineering in river and lake sediments.

Keywords: modified sludge soil; mechanical properties; roadbed filling; triaxial test

1. Introduction

With the rapid development of China's transportation network and the continuous increase in highway mileage and network density, the construction of transportation infrastructure in complex geological areas is increasing, bringing a series of technical challenges to road engineering [1].

In situations where the regional environment is complex and the special soil condition standards for road filling are difficult to meet, it is crucial to effectively handle and utilize local filling resources with poor performance in order to reduce road construction costs and alleviate material shortages. Among these special soils, silt and similar soils are particularly common, which usually have characteristics such as high compressibility, large porosity, high natural moisture content, and low shear strength [2]. Due to these characteristics, silt and silty soil cannot be directly used for engineering construction and

must undergo modified solidification treatment. The interdisciplinary research between environmental science and civil engineering provides a new approach for the treatment and improvement of these special soils. This article investigates how to convert waste sludge into valuable geopolymer materials for road construction and explores the process of converting waste sludge into geopolymers, which may involve chemical reactions that react to the silicon aluminum components in sludge with alkaline solutions to generate geopolymers [3]. This study is based on the Luhu Environmental Remediation and Cultural Tourism Comprehensive Development Project in Jiangxia District, Wuhan City. The silt in the project area was selected as the research object, and the engineering applicability and mechanical properties of modified silt soil as a filling material for the road subgrade around the lake were systematically studied. The research results provide innovative ideas for the environmentally friendly treatment and resource utilization of river and lake sediments, as well as road engineering construction in the lake area, which is in line with the concept of sustainable development and has significant economic and social benefits.

Many researchers at home and abroad use multiple curing agent components to prepare composite curing agents and determine the curing agent formula using orthogonal experimental methods. Mud modified soil is used as roadbed filling material to verify its mechanical properties. The testing methods include a compaction test, unconfined compressive strength test, CBR test, shear strength test, and a compression test [4–8]. The main conclusions are as follows: (1) Compaction characteristics—different curing agents represent different mechanisms of action, so the compaction characteristics of modified soil also vary. The use of sulfur fixing ash and lime-modified sludge reduces the maximum dry density, increases the maximum moisture content, and requires greater compaction effort. (2) Compressive strength—the research content mainly includes the effect of intensity enhancement and influencing factors. Zhang Rongjun [9] proposed through experiments that moisture content and cement dosage have independent effects on each other, and obtained a strength prediction formula for low cement dosage. Other influencing factors include curing temperature [10], water cement ratio [11], minimum dosage [12], curing age, and the synergistic modification of other additives [13]. The influence of each factor on compressive strength was obtained through experiments, and the strength was predicted through empirical formulas. (3) As a requirement indicator in the specification, CBR mainly obtains influencing factors through experiments [14], including compaction degree, curing age, and curing agent. (4) Shear strength—the main analysis focuses on the stress–strain relationship and the variation law of failure strain, with shear strength parameters as the main detection indicators. Wang Dongxing [15] replaced cement low-calcium fly ash with lime low-calcium fly ash in the same proportion, and the stress–strain relationship of the specimen changed from plasticity to brittleness, with a significant reduction in failure strain. The effect of different material curing agents was compared at 360 days of strength. (5) Compression performance [16–18]—the compression performance of modified soil is evaluated based on the compression modulus and compression coefficient, and the effects of dosage, initial moisture content, and curing age on the compression performance are evaluated. Different compression models are used to represent its compression characteristics. Li et al. [19] studied the use of industrial by-products such as fly ash, soda ash residue, and flue gas desulfurization gypsum (FGD gypsum) combined with lime to improve the mechanical and microstructural properties of excavated soil, reduce the use of lime, and enhance the engineering performance of soil.

Based on the current research status at home and abroad, this article takes the Luhu silt in Jiangxia District, Wuhan City as the research object, modifies the collected silt soil samples based on an SM-C modifier, and conducts mechanical property tests on the modified sludge soil. By conducting compaction tests, unconfined compressive strength

tests, CBR tests, triaxial tests, and consolidation tests, the changes in the mechanical properties of modified sludge soil materials under the influence of factors such as modifier dosage, curing age, compaction degree, and initial moisture content were studied. The main issues addressed in this study include the specific effects of SM-C amendments on the mechanical properties of silt soil, optimal dosage, and performance under different environmental conditions.

2. Materials and Methods

2.1. Materials

The soil sample was taken from Luhu Lake in Jiangxia District, Wuhan. The sampling point was close to the planned route of the scenic area road, and 3–4 sampling sites were selected with a sampling depth of about 1.0 m. The soil sample is gray-brown in color. The main physical property indexes of the soil sample are as follows: initial water content is 60 ± 5, wet density is 1.686 g·cm^{-3}, dry density is 1.038 g·cm^{-3}, specific gravity is 2.71, pore ratio is 1.62, plastic limit is 26%, liquid limit is 48.7%, and plastic index is 25%.

The modifier used in the experiment is an SM-C-type modifier from Guangzhou Zhengyuan Environmental Engineering Co., Ltd. (Guangzhou, China), and the product is in solid powder form. The modifier is composed of a certain proportion of various oxide components, mixed and reacted at a high temperature of 1200 °C. SM-C modifier is mostly used for sludge treatment. By treating the sludge with the inorganic composite material of ferrosilicon aluminum in the modifier, it overcomes the technical defect of the traditional curing agent, which can only increase the solid content in the mixture; it thoroughly modifies the sludge from the aspect of physical and chemical properties, breaks the colloidal structure of the mud, and converts the sludge into engineering raw materials with high engineering performance, which can be used as subgrade fillers. The modified soil can prevent secondary slime.

2.2. Compaction Test

This study used heavy compaction and wet sampling techniques to systematically investigate the effect of modifier dosage ranging from 4% to 15% on the compaction characteristics of modified sludge soil. In the experiment, six different mixing ratios of 0% (i.e., plain soil), 4%, 8%, 10%, 12%, and 15% were selected.

For plain soil samples, we first air dried them at a temperature not exceeding 80 °C, until the moisture content drops to near the plastic limit. Then, five samples with different moisture contents were prepared for compaction tests in increments of 2% each. For modified sludge soil, mixing and indoor curing are required first to achieve a moisture content close to the plastic limit, and the moisture content is also distributed with a difference of 2%.

The instruments used in the compaction test are shown in Figure 1, including the compaction device and automatic film release device. The inner diameter of the specimen is 10cm and the height is 12.7 cm. After compaction is completed, we first weighed the mass of the specimen and then cut a soil sample from the center of the specimen to determine the moisture content. The wet density of the compacted soil sample can be calculated by comparing the quality difference between the compacted specimen and the compacted cylinder. Based on the data of the moisture content sample, we calculated the dry density of the soil sample. These data provide an important basis for analyzing the compaction characteristics of modified sludge soil and its variation with dosage.

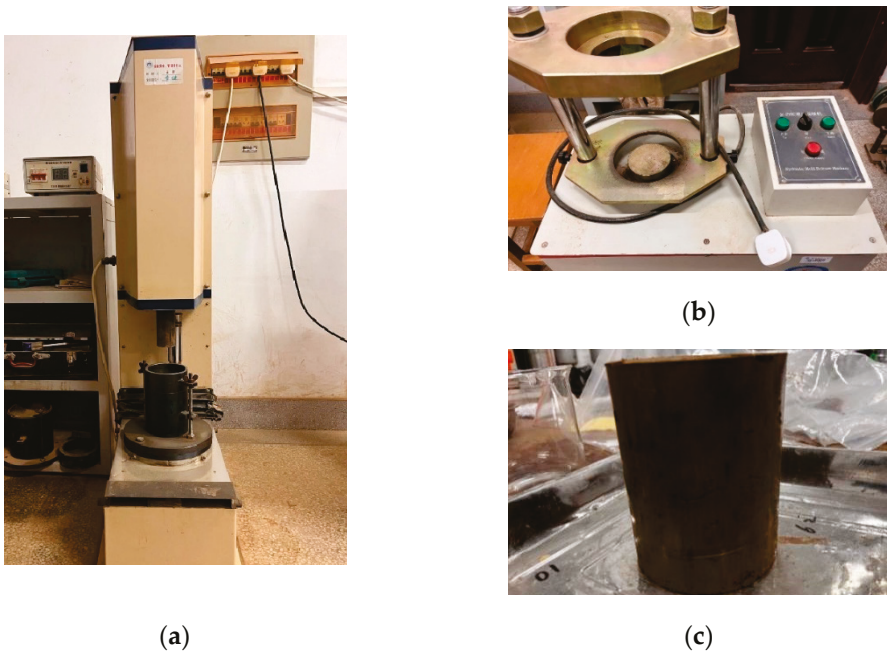

(**a**) (**b**) (**c**)

Figure 1. Compaction test instrument and specimen: (**a**) electric compaction device; (**b**) automatic film release device; (**c**) specimen.

2.3. Unconfined Compressive Strength Test

2.3.1. Design of Experimental Parameters for Modifier Dosage

This study designed three key experimental parameters in detail, including the dosage of modifier, initial moisture content, and curing age, to explore their effects on the unconfined compressive strength of modified sludge soil.

The dosage of modifier: The reaction between the modifier and certain components in the sludge is the key to strength formation, so the dosage is the main influencing factor. This experiment set dosages of 0%, 4%, 8%, 10%, 12%, and 15% to reveal the relationship between dosage and strength. Choosing a larger dosage is to explore the relationship between dosage and strength in indoor experiments. In practical engineering, the appropriate dosage should be selected according to specific requirements.

Initial moisture content: Even if the specimen is prepared according to the optimal moisture content, the initial moisture content still has an impact on the modified soil. This experiment set initial moisture contents of 50%, 65%, and 80% to separately study their effects on the properties of modified soil, while maintaining a constant dry soil mass.

Maintenance parameters: It is expected that the compressive strength of modified sludge soil will increase with the increase in maintenance age. This experiment selected curing ages of 1 day, 3 days, 7 days, 14 days, and 28 days to study the strength development of specimens in the early, middle, and stable stages of curing. Considering that the hydration reaction has already started in the pretreatment, a curing period of 1 day has been added to study the formation of initial strength. The maintenance conditions are set as indoor standard maintenance, with a temperature of 20 °C and humidity controlled at 90 ± 5% RH, slightly lower than outdoor summer temperatures, to simulate the effects of humidity and temperature on later strength.

2.3.2. Experimental Plan Design

This study used two methods to prepare test specimens to evaluate the effects of modifier dosage and initial moisture content on the unconfined compressive strength of modified sludge soil.

Option 1: Without considering changes in initial moisture content, set the initial moisture content to 65% and conduct 5 different age periods (1 day, 3 days, 7 days, 14 days, and 28 days) of testing on specimens with 5 different levels of modifier dosage. Each specimen is subjected to two parallel tests, with a total of 10 specimens prepared. The test results are taken as the average of the two tests. Therefore, a total of 50 sets of specimens need to be prepared for 5 levels of modifier dosage.

Option 2: Investigate the effect of initial moisture content on later strength by conducting 28 day curing tests on specimens with 5 different dosage levels at three different initial moisture contents (50%, 65%, and 80%), and preparing a total of 20 sets of specimens.

Taking into account both options, the total number of specimens for unconfined compressive strength testing is 70. The sample size is 3.91 cm × 8 cm, and the compaction degree was set to 95%. The material used for the soil sample was calculated based on the compaction degree and maximum dry density. The unconfined compressive strength test was prepared using the compression method, as shown in Figure 2a. The instrument used is a universal press, as shown in Figure 2b. The diameter of the pressure head is slightly larger than the specimen, and the sensor range is 30 kN, used to read longitudinal pressure. The displacement range was 30 mm, and a dial gauge was used for reading. The specimens were cured in a standard curing room, with temperature and humidity set to 20 °C and 90 ± 5% RH, respectively. The appearance of the specimen is shown in Figure 3a, and the curing box is shown in Figure 3b.

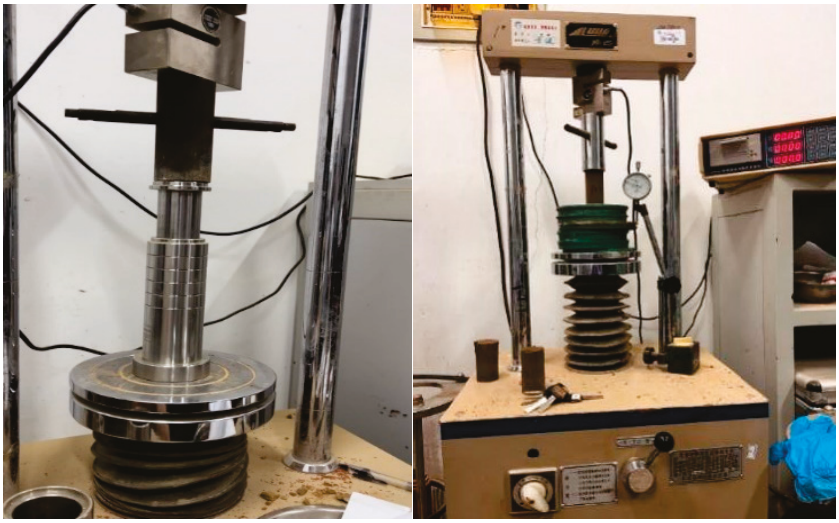

(**a**) (**b**)

Figure 2. Sample preparation and unconfined compressive strength test: (**a**) preparation of specimen; (**b**) unconfined compression strength test.

(**a**) (**b**)

Figure 3. Preparation and curing of test specimen: (**a**) specimen; (**b**) curing process.

2.4. CBR Test

This study thoroughly investigated the effects of modifier dosage and compaction degree on the CBR value of modified sludge soil through CBR experiments. The test piece adopts a large compaction cylinder with an inner diameter of 152 mm and a height of 170mm, prepared by a heavy-duty compaction method. The compaction degree was set at three levels, 92%, 94%, and 96%, and the modifier dosage was selected at four levels, 4%, 8%, 10%, and 12%. The soil sample used was air-dried soil sieved through a 5 mm sieve, and each specimen underwent three parallel tests, totaling 36 sets of specimens.

The experiment uses a pavement material strength meter, which was divided into two stages: immersion and penetration. During the immersion stage, the specimen was not demolded after compaction. The filter paper, porous plate, and load plate were placed in sequence, and a dial gauge was installed. The immersion time was 96 h. In the penetration test, a 7.5 kN force measuring ring was used, and penetration was carried out at a speed of 1mm/min. The vertical pressure was read by the sensor, and the displacement data on both sides were obtained through a dial gauge. The experimental process is detailed in Figure 4.

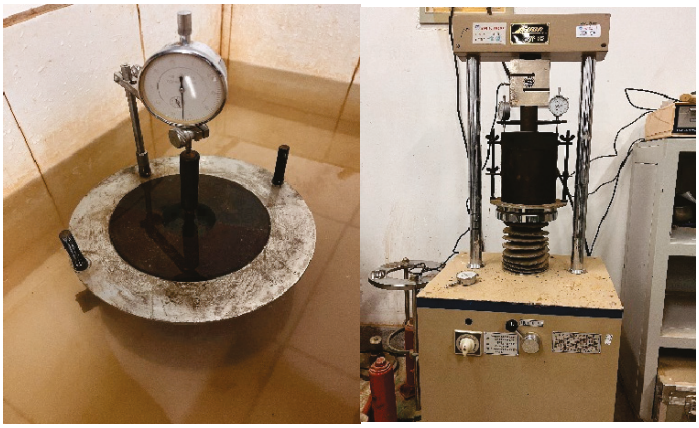

(**a**) (**b**)

Figure 4. Schematic diagram of CBR test process: (**a**) immersion in water; (**b**) penetration test.

2.5. Triaxial Test

This study used consolidated undrained triaxial tests to analyze the stress–strain curve, failure mode, and shear strength parameters of modified sludge soil. The experiment used a strain gauge triaxial apparatus produced by Nanjing Soil Instrument Factory, as shown in Figure 5. The specimen preparation used the compactor shown in Figure 6, with a diameter of 39.1 mm and a height of 80 mm. The experiment selected 3 and 7 days as the curing age, and all specimens were subjected to saturation treatment. After reaching the curing age, the specimen was wrapped in a thin film and placed in a saturator for saturation using the suction method.

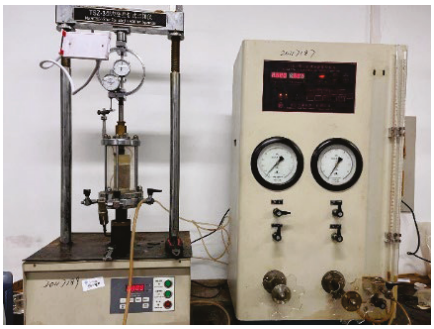

Figure 5. Triaxial testing instrument.

Figure 6. Triaxial specimens.

2.6. Consolidation Test

This article evaluates the compressive performance of modified sludge soil through standard consolidation tests, based on Terzaghi's unidirectional consolidation theory, with a stability standard of settlement less than 0.01 mm within 1 h. The goal is to obtain indicators such as the compression coefficient, compression modulus, compression index, and consolidation coefficient, and analyze the effects of compaction degree, modifier dosage, and curing age on compression performance.

The specimens were prepared by the compression method, and the amount was calculated based on the compaction degree. They were cured in a standard curing environment until the specified age, as shown in Figure 7. Vacuum saturation was performed before the test. After installing the specimen, the consolidation instrument was adjusted to zero under preloading cell pressure, and the inner ring dial gauge was immediately loaded once it was greater than zero. The first level load was 50 kPa, and then the settlement rate and consolidation coefficient were measured according to the specifications. After 24 h of consolidation and stability, 100 kPa, 200 kPa, and 400 kPa loads were applied sequentially. The process is detailed in Figure 8. The number of specimens was 14, with dosages of 4%, 8%, 10%, 12%, and 15%. The compaction degrees for the 10% dosage were 92%, 94%, and 96%, respectively. The curing ages are 3 days and 7 days, respectively. The main consolidation performance indicators include the following: initial porosity (e_0), unit settlement (S_i), compression coefficient within a certain load range (a_v), compression modulus (E_s) within a certain load range, volumetric compression modulus (m_v), and compression index (C_c).

Figure 7. Curing of consolidation test specimens.

Figure 8. Consolidation test.

3. Results and Discussion

3.1. Results and Analysis of Compaction Test

At least five samples were selected for each dosage in the compaction test, and sufficient compaction data were distributed on both sides of the maximum dry density to obtain the compaction curve shown in Figure 9. The compaction parameters of modified sludge soil samples were obtained through curve fitting. The existing fitting methods mainly include the numerical method and curve fitting method. Comparison shows that using a cubic curve to fit the compaction curve is the closest, and higher frequency results in overfitting between the curve and the data. The compaction test data were fitted to obtain the optimal moisture content and maximum dry density, as shown in Table 1. The variation in maximum dry density and optimal moisture content with dosage is shown in Figure 9.

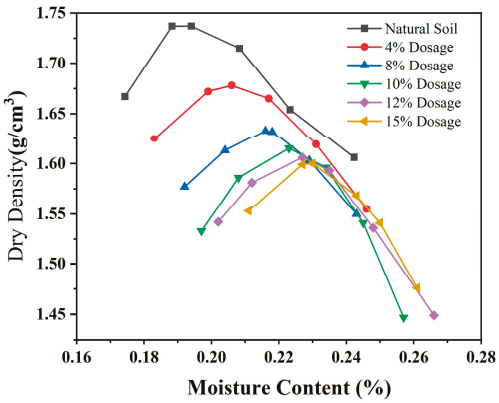

Figure 9. Compaction curve of modified sludge soil.

Table 1. Specific compaction parameters of modified sludge soil.

Modifier Content (%)	0	4	8	10	12	15
OWC (%)	19.4	20.6	21.6	22.3	22.7	23
MDD (g/cm^3)	1.737	1.678	1.633	1.615	1.606	1.600

(1) The variation law of compaction curve with dosage

From Figure 9, it can be seen that when the moisture content is below the optimal value, the dry density increases with the increase in moisture content because the water film acts as a lubricant. After exceeding the optimal moisture content, the dry density decreases because the water film offsets the compaction work. The compaction curve of the modified sludge soil exhibits a unimodal characteristic. With the increase in modifier, the compaction curve shifts to the right, and the shape becomes gentle on the left and steep on the right. Compared with untreated soil, modified sludge soil has a narrower range of moisture content changes, reduced plasticity, and increased sensitivity to moisture content. This may be due to the aggregation of small particles into larger ones, which increases frictional resistance, while the water film bonding weakens, requiring a higher moisture content for lubrication.

(2) The variation law of maximum dry density with the dosage of modifier

As shown in Figure 10, with the increase in modifier dosage, the maximum dry density of modified sludge soil decreases. For example, when the dosage is 15%, the maximum dry density decreases from 1.737 g/cm^3 to 1.600 g/cm^3. This is because the active minerals in the modifier react with the sludge to form a lightweight and bulky crystal structure,

causing small particles to agglomerate into larger particles and form aggregates, thereby reducing compaction performance.

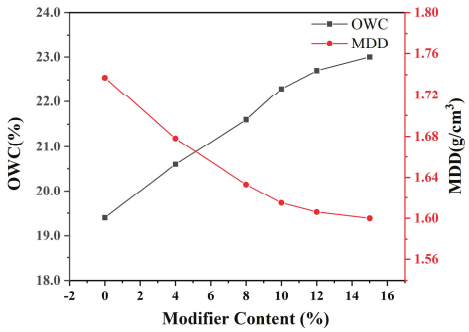

Figure 10. Maximum dry density, optimal moisture content vs. modifier content.

(3) The variation law of optimal moisture content with the dosage of modifier

From the compaction curve in Figure 10, it can be seen that the optimal moisture content of modified sludge soil increases with the increase in modifier dosage. Within the range of pure soil to 15% content, the optimal moisture content increases from 19.4% to 23.0%, with the growth rate initially fast and then slow, and the increase slows down after 10% content. This indicates that the modifier causes soil particles to aggregate, increasing the water and work required for compaction, as the modifier reduces the water film on the surface of the clay particles and requires more water lubrication.

3.2. Results and Analysis of Unconfined Compressive Strength Test

The compressive strength is shown in Table 2, and Figure 11 is used to analyze the variation in the compressive strength of modified sludge soil with the increase in modifier dosage during different curing ages.

Table 2. Results of Specific compaction parameters of modified sludge soil.

Curing Age	Unconfined Compressive Strength Value (MPa)				
	4%	8%	10%	12%	15%
1d	0.490	0.516	0.543	0.646	0.592
3d	0.586	0.645	0.675	0.770	0.714
7d	0.664	0.775	0.819	0.898	0.843
14d	0.709	0.861	0.888	0.963	0.904
28d	0.746	0.891	0.922	0.983	0.926

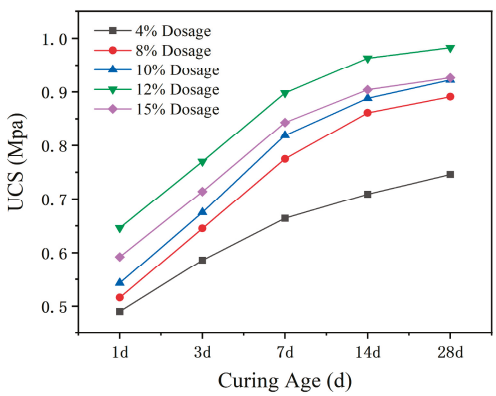

Figure 11. Unconfined compressive strength vs. modifier dosage.

From Figure 11, the following can be seen:

(1) The dosage of modifier significantly improved the unconfined compressive strength of modified sludge soil. For example, the 1-day compressive strength of 12% modified sludge soil is 0.676 MPa, which is 37.9% higher than that of 0.49 MPa with 4% content. This improvement is similar in the 7 day and 14 day maintenance periods. Overall, the compressive strength of modified sludge soil is significantly increased compared to silt plain soil.

(2) SM-C type modifier can significantly improve the compressive strength of modified sludge soil when the dosage is less than 12%, but after exceeding 12%, the strength growth slows down or even decreases. This may be due to excessive hydration products blocking the pores, hindering further hydration reactions, and an uneven distribution of modifiers in the sludge. Therefore, it is necessary to determine the optimal dosage through indoor testing to avoid a decrease in strength.

Figure 12 shows the effect of different initial moisture contents on the unconfined compressive strength and modifier dosage of modified sludge soil over a 28 day curing period. Due to differences in the mineral composition and the formation environment of sludge, the initial moisture content varies greatly. Usually, the higher the initial moisture content, the more modifier dosage is required to achieve optimal results.

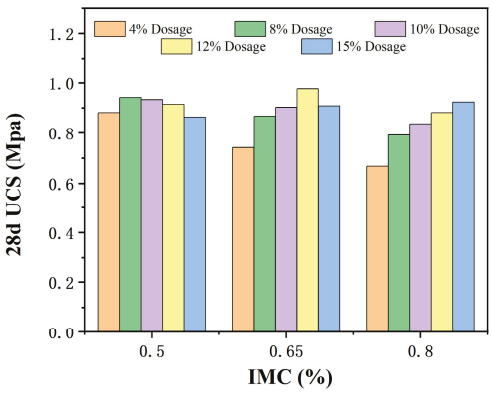

Figure 12. Modifier dosage vs. 28 day UCS value.

At a fixed dosage of modifier, the initial strength of modified sludge soil with low initial moisture content is higher. However, at the optimal dosage, the strength of different initial moisture contents tends to be consistent. This is because the dosage of the modifier is calculated based on the dry soil mass, and the strength mainly depends on the chemical reaction between the modifier and the silt components. At the optimal dosage, the reaction is sufficient, and the strength improvement is similar.

3.3. Results and Analysis of CBR Test

The CBR test data are shown in Table 3, and Figure 13 is used to analyze the variation in CBR with the change in modifier dosage under different compaction degrees. Referring to the results of the unconfined compressive strength test, the initial moisture content is set at 65%. Within 7 days of curing, the strength has basically formed. Therefore, 7 days are selected as the curing age for the CBR test.

Table 3. CBR test results of modified sludge soil.

Degree of Compaction	CBR Value			
	4%	8%	10%	12%
92%	5.5	9.7	11.8	10.4
94%	7.4	11.9	14.5	13.2
96%	9.1	16.4	17.5	16.7

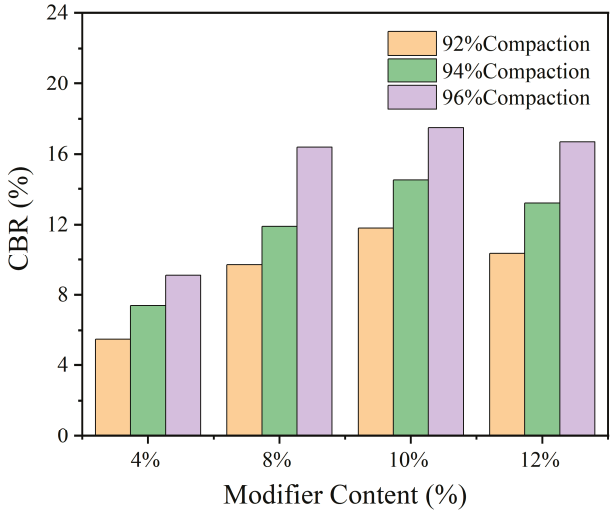

Figure 13. Modifier dosage vs. CBR value.

From Table 3 and Figure 13, the following can be concluded: The CBR value of modified sludge soil significantly increased within 7 days, and increased rapidly and then slowly with the dosage of modifier, reaching its peak at 10% dosage. Afterwards, due to an uneven distribution of modifiers, the CBR value decreased. The CBR value also increases with the increase in compaction degree. For roads in low traffic scenic areas, the modified sludge soil treated with SM-C modifier can meet the technical requirements, and the effect of compaction degree on the improvement of the CBR value is more significant under high dosage.

3.4. Results and Analysis of Triaxial Test

3.4.1. Analysis of Test Results

The range of variation in dosage from 4% to 12%, and the difference in the principal stress of the specimens under different confining pressure conditions are shown in Table 4. The maximum principal stress difference is taken as the peak stress in the stress–strain relationship, and the strain softening relationship without peak stress is taken as the stress difference corresponding to a strain value of 15%. According to the data in the table, the dosage of modifier significantly improves the shear strength of the silt soil sample.

Table 4. Difference in principal stress of triaxial specimens under different confining pressures (kPa).

Confining Pressure (kPa)	Principal Stress Difference (kPa)			
	4%	8%	10%	12%
50	88.13	170.01	226.33	273.96
100	124.87	237.87	303.67	394.45
150	172.02	297.96	374.00	476.36

The shear strength parameters of the modified sludge soil are calculated by taking the common tangent of the Mohr circle. Under three different confining pressure conditions, corresponding to three Mohr circles, the diameter of the Mohr circle is the corresponding difference in principal stress. The calculated shear strength parameters of the soil sample are shown in Table 5. From the data in the table, it can be seen that with the increase in dosage, the internal friction angle and cohesion of the modified sludge soil are significantly improved, and the improvement rate shows a trend of first fast and then slow. When the dosage is below 10%, the internal friction angle increases significantly, mainly manifested by the agglomeration of small soil particles into larger particles, and more obvious interlocking

between soil particles. When the dosage is high, the cohesion increases significantly, manifested microscopically as the bonding effect of hydration products.

Table 5. Shear Strength Parameters of Sludge Modified Soil.

4%		8%		10%		12%	
φ (°)	c (kPa)	φ (°)	c (kPa)	φ (°)	c (kPa)	φ (°)	c (kPa)
17	18	24	41	27	78	30	91

3.4.2. Stress–Strain Analysis

Figure 14 shows three basic types of stress–strain relationships: strain hardening type, ideal elastoplastic type, and strain softening type. These types are closely related to the stress state and internal structure of the specimen, influenced by factors such as the amount of modifier and confining pressure. At the same dosage, as the confining pressure increases, the specimen tends towards the strain hardening type; under the same confining pressure, as the dosage increases, the specimen tends towards the strain softening type.

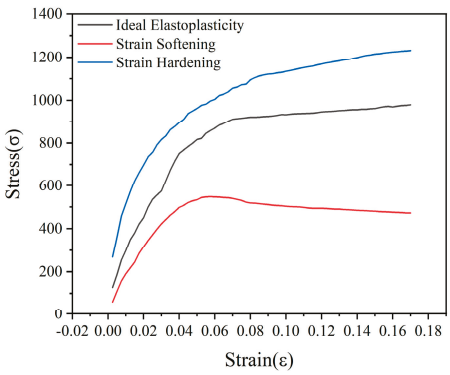

Figure 14. Basic types of stress–strain relationships in consolidation undrained test.

Figure 15 shows the stress–strain behavior of consolidated undrained specimens under different dosages of modifiers. In the initial stage, the stress–strain relationship is approximately linear, and the specimen undergoes elastic deformation; subsequently, plastic strain appeared, with a non-linear relationship, and the specimen yielded; finally, the stress growth slows down, the specimen hardens, and the stress stabilizes. When the dosage of modifier increases, the transition point from elasticity to yield of the specimen shifts to the left, and the maximum difference in principal stress increases, indicating that the increase in dosage enhances the shear strength of the specimen.

The 4% modified sludge soil specimen has more pores and less hydration reaction, resulting in low stress and large plastic strain, which may cause mudification in areas with low compaction. The specimens with a dosage of 8% to 12% are close to the optimal dosage, which improves the shear strength, fills the pores with hydration products, enhances the cohesion between soil particles, and forms a stable soil skeleton support.

Figure 16 shows that under low confining pressure, the stress–strain relationship of modified sludge soil changes from the hardening type to the softening type, while under high confining pressure, it tends towards the weak hardening or elastoplastic type. This is because the hydration products generated by the modifier bind the soil particles and fill the pores, enhancing friction. As the confining pressure increases, high content soil can produce sufficient hydration products, which not only bond and fill but also provide skeleton support, leading to brittle failure; low content soil, on the other hand, maintains plastic failure.

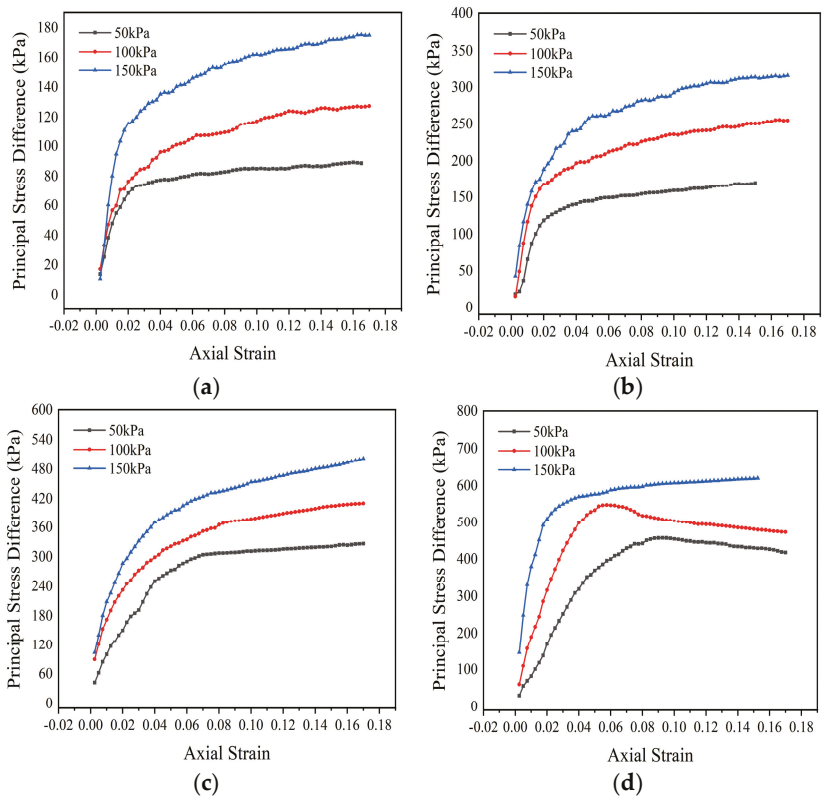

Figure 15. Modifier dosage vs. stress–strain relationship (consolidation undrained test): (**a**) 4%; (**b**) 8%; (**c**) 10%; (**d**) 12%.

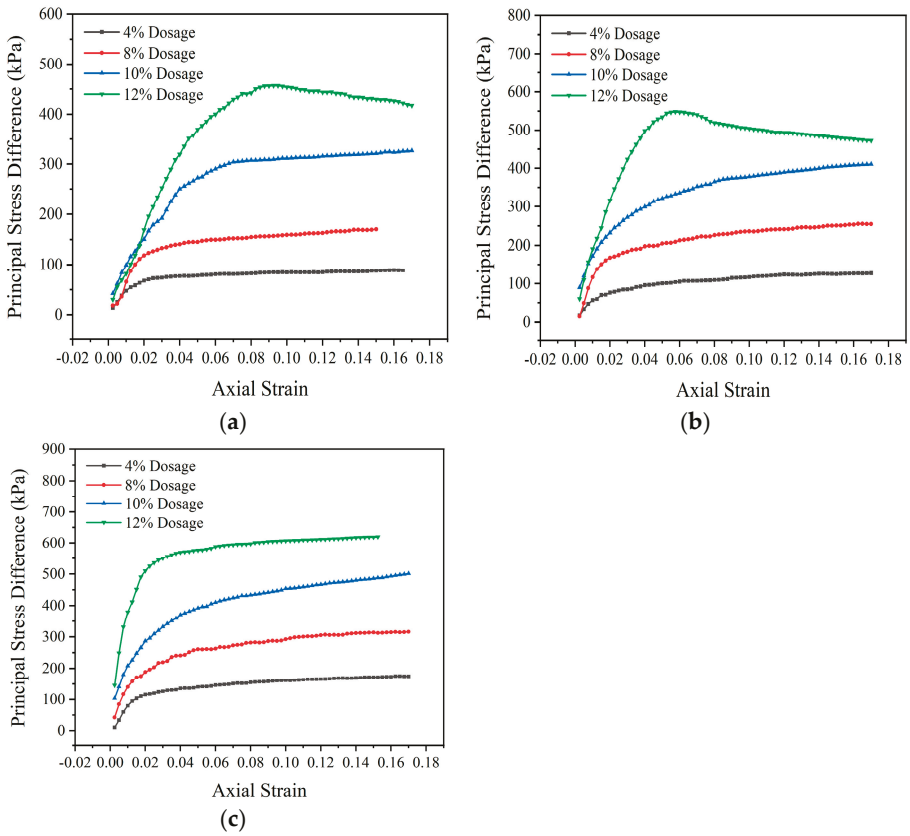

Figure 16. Stress–strain relationship of specimens under different confining pressures: (**a**) 50 kPa; (**b**) 100 kPa; (**c**) 150 kPa.

3.5. Subsection

The compression modulus and compression coefficient are both parameters that describe the compression performance of soil. The compression coefficient is defined as the slope of the tangent line of a certain pressure segment on the e-p curve obtained from the compression test, and the compression modulus is defined as the ratio of stress to strain under the complete confinement condition of the consolidation test. The compression modulus values vary greatly in different load intervals, so the compression modulus is taken as the vertical pressure range of 100 kPa~200 kPa. The same vertical pressure is convenient for comparing the compression performance. According to the specifications, the compression coefficient and compression modulus were calculated, and the test results are shown in Table 6.

Table 6. Compressive coefficient and modulus of modified sludge soil.

Curing Age	$a_{1\text{-}2}$ (MPa^{-1})					$Es_{1\text{-}2}$ (MPa)				
	4%	8%	10%	12%	15%	4%	8%	10%	12%	15%
3 d	0.586	0.645	0.675	0.770	0.714	0.586	0.645	0.675	0.770	0.714
7 d	0.746	0.891	0.922	0.983	0.926	0.746	0.891	0.922	0.983	0.926

Table 6 shows that the compressibility of modified sludge soil decreases with different amounts of modifiers, manifested as a decrease in compression coefficient and an increase in compression modulus. Compared with the original silt, the compression coefficient of the modified soil is lower than 0.5 MPa^{-1}, indicating that it has transformed from a highly compressible soil to a moderately compressible soil. When the dosage is 4%, the compressibility is still high because there are many pores in the soil and the skeleton is not sufficient to resist compression. As the dosage increases, the compression performance improves because hydration products fill the pores, form a skeleton, and enhance the anti-compression ability.

From Figure 17, it can be analyzed that with the increase in modifier dosage, the compression coefficient of modified sludge soil decreases sharply, and the decrease slows down after the dosage reaches 10%, indicating a turning point. Under pressures ranging from 100 kPa to 200 kPa, the compression deformation of the specimens decreases, indicating that the main consolidation stage is nearing completion. The compression coefficients of the specimens with 12% and 15% dosages are similar. When the dosage is between 4% and 10%, the compression coefficient decreases linearly, indicating a rapid improvement in the anti-compression performance. The increase in maintenance age also improves the compression coefficient as the continuous hydration reaction generates products that fill the pores, reduce moisture, further reduce compression deformation, and enhance compression performance.

Figure 18 shows that the compression coefficient of modified sludge soil decreases with increasing compaction degree. The addition of modifiers quickly enhances the strength and initial compressive resistance of modified sludge soil. But as the curing age increases, the hydration reaction slows down, and the compression deformation of low-pressure solid specimens is large, while the compression performance of high-pressure solid specimens is improved more significantly due to a denser skeleton.

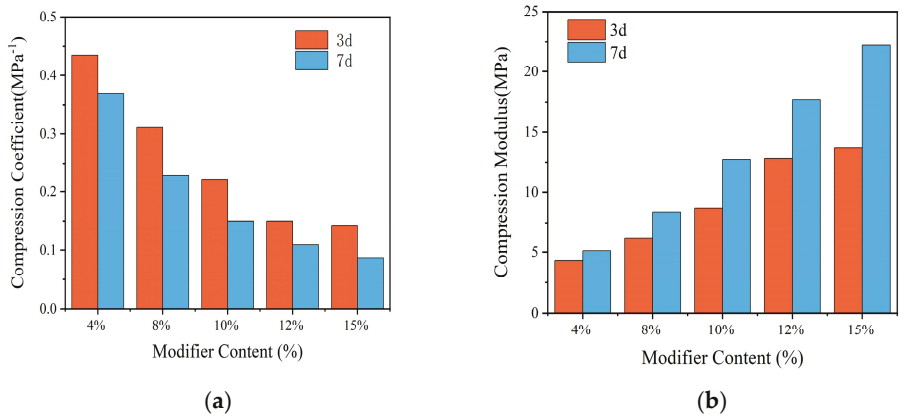

(**a**) (**b**)

Figure 17. Modifier dosage vs. compressive properties: (**a**) the influence on compression coefficient; (**b**) the influence on compression modulus.

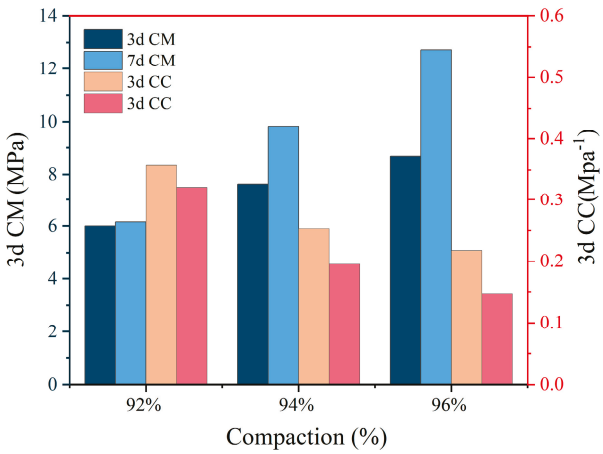

Figure 18. Compaction degree vs. compression performance.

4. Conclusions

This article uses indoor experiments to study the mechanical properties of modified sludge soil, and the main research conclusions are as follows:

(1) The compaction test of modified sludge soil shows that increasing the dosage of modifier will increase the optimal moisture content, reduce the maximum dry density, and cause soil particles to aggregate, increasing the required compaction work.

(2) The unconfined compressive strength test shows that with the increase in modifier dosage and age, the compressive strength first increases rapidly and then slowly, and there is an optimal dosage, beyond which the strength decreases.

(3) According to the CBR test of modified sludge soil, as the dosage and compaction degree increase, the CBR of modified sludge soil significantly improves. When the dosage reaches 8%, it exceeds the minimum specification requirement for CBR. The dosage is the main influencing factor of CBR, and when the dosage is high, the impact of the compaction degree on the CBR of modified sludge soil increases.

(4) According to the triaxial test, the internal friction angle and cohesion of modified sludge soil increase with the increase in dosage. The main failure mode of triaxial testing is plastic failure, and the stress–strain relationship mainly presents as the strain hardening type. With the increase in dosage, the strain hardening type transforms into the strain softening type.

(5) According to the consolidation test of modified sludge soil, with the increase in dosage and curing age, the compression coefficient of modified sludge soil decreases, and

the compression modulus increases. At high dosage, the specimen basically shows low compressibility, and the overall compression energy absorption is significantly improved.

(6) Considering that the mechanical properties of improved sludge soil vary over time, future research can focus on long-term performance evaluation, including durability, aging effects, and stability under different environmental conditions.

Author Contributions: Conceptualization, W.X. and K.Z.; methodology, J.N. and X.F.; validation, Y.Z., G.W. and X.Y.; formal analysis, W.X. and J.N.; investigation, Y.Z.; resources, K.Z.; data curation, W.X.; writing—original draft preparation, W.X.; writing—review and editing, W.X.; visualization, Y.Z. and G.W.; supervision, W.X.; project administration, K.Z. and X.Y.; funding acquisition, K.Z. and J.N. All authors have read and agreed to the published version of the manuscript.

Funding: This research was funded by the Jiangxi Province Natural Science Foundation (Grant No. 20212BAB214042) and the National Innovation and Entrepreneurship Training Program for College Students (S202410497275).

Institutional Review Board Statement: Not applicable.

Informed Consent Statement: Not applicable.

Data Availability Statement: The original contributions presented in the study are included in the article. Further inquiries can be directed to the corresponding author.

Conflicts of Interest: Jun Nie was employed by Nanchang Expressway Co., Ltd. Kai Zhang and Xiangyang Fan were employed by Jiangxi Transportation Institute Co., Ltd. The remaining authors declare that the research was conducted in the absence of any commercial or financial relationships that could be construed as a potential conflict of interest.

References

1. Editorial Board of China Journal of Highway and Transport. A Review of Academic Research on Roadbed Engineering in China. *China J. Highw. Transp.* **2021**, *34*, 1–49.
2. Zhou, S.; Zhang, R.; Xiao, Y.; Li, B.; Zeng, Z. Review on Improvement Methods and Principles of Special Soil. *J. Chang. Univ. Sci. Technol.* **2024**, *21*, 21–34.
3. Zhong, W.L.; Sun, Y.H.; Zhao, X.; Fan, L.F. Study on Synthesis and Water Stability of Geopolymer Pavement Base Material Using Waste Sludge. *J. Clean. Prod.* **2024**, *445*, 141331. [CrossRef]
4. Arabani, M.; Shalchian, M.M.; Rahimabadi, M.M. The Influence of Rice Fiber and Nanoclay on Mechanical Properties and Mechanisms of Clayey Soil Stabilization. *Constr. Build. Mater.* **2023**, *407*, 133542. [CrossRef]
5. Meena, S.K.; Sahu, R.; Ayothiraman, R. Utilization of Waste Wheat Straw Fibers for Improving the Strength Characteristics of Clay. *J. Nat. Fibers* **2021**, *18*, 1404–1418. [CrossRef]
6. Baldin, C.R.B.; Kawanami, M.Y.; Costa, W.G.S.; Bordignon, V.R.; da Luz, C.C.; dos Santos Izzo, R.L. Mechanical Properties of a Clay Soil Reinforced with Rice Husk under Drained and Undrained Conditions. *J. Rock Mech. Geotech. Eng.* **2023**, *15*, 2676–2686. [CrossRef]
7. Qian, B.; Yu, W.; Lv, B.; Kang, H.; Shu, L.; Li, N.; Wang, W. Mechanical Properties and Micro Mechanism of Nano-Clay-Modified Soil Cement Reinforced by Recycled Sand. *Sustainability* **2021**, *13*, 7758. [CrossRef]
8. Haeri, S.M.; Valishzadeh, A. Evaluation of Using Different Nanomaterials to Stabilize the Collapsible Loessial Soil. *Int. J. Civ. Eng.* **2021**, *19*, 583–594. [CrossRef]
9. Zhang, R.; Zheng, S.; Zheng, J. Study on the Strength Characteristics of Cement-Stabilized High Water Content Clay. *J. Huazhong Univ. Sci. Technol. Nat. Sci. Ed.* **2015**, *43*, 101–106.
10. Zheng, S. Experimental Study on the Strength Influencing Factors of Low Cement Content Stabilization of High Water Content Sludge. Master's Thesis, Huazhong University of Science and Technology, Wuhan, China, 2015.
11. Wang, W.; Yuan, F.; Jiang, J.; Cai, G. Strength Characteristics and Prediction Model of Solidified Sludge with High Water Content from Reclamation Projects. *Chin. J. Undergr. Space Eng.* **2021**, *17*, 461–467.
12. Ding, J.; Liu, T.; Cao, Y.; Yang, R. Unconfined Compressive Strength Tests and Strength Prediction of Solidified Dredged Sludge with High Water Content. *Chin. J. Geotech. Eng.* **2013**, *35*, 55–60.
13. Huang, L.; Wang, H.; Tan, Y.; Wu, J.; Zuo, Q. Study on the Long-Term Strength Development and Prediction Model of Solidified Sludge Soil. *J. Wuhan Univ. Technol.* **2016**, *38*, 70–75.

14. He, J.; Lv, X.; Zhu, Y. The Effect of Curing Temperature on the Strength Properties of Alkali Slag-Cement Sludge. *Adv. Sci. Technol. Water Resour.* **2023**, *43*, 58–65.
15. Wang, D.; Xu, W. Experimental Study on Long-Term Strength and Deformation Characteristics of Solidified Sludge. *J. Cent. South Univ. Nat. Sci.* **2013**, *44*, 332–339.
16. Huang, Y.; Zhu, W.; Zhou, X.; Zhang, C. Experimental Study on Compressive Characteristics of Solidified Sludge. *Rock Soil Mech.* **2012**, *33*, 2923–2928.
17. Xu, W.; Luo, R. Evaluation of interaction between emulsified asphalt and mineral powder using rheology. *Constr. Build. Mater.* **2022**, *318*, 125990. [CrossRef]
18. Xu, W.; Guan, Y.H.; Shah, Y.I.; Luo, R.; Xu, Z.Q. Study on curing characteristics of cold-mixed and cold-laid asphalt mixture based on electrical properties. *Constr. Build. Mater.* **2022**, *330*, 127223. [CrossRef]
19. Li, C.; Wang, S.; Ding, J.; Zhang, S.; Gao, M. Mechanical and microstructural properties of lime-treated excavated soil improved with different industry by-products. *Constr. Build. Mater.* **2024**, *318*, 125990. [CrossRef]

Disclaimer/Publisher's Note: The statements, opinions and data contained in all publications are solely those of the individual author(s) and contributor(s) and not of MDPI and/or the editor(s). MDPI and/or the editor(s) disclaim responsibility for any injury to people or property resulting from any ideas, methods, instructions or products referred to in the content.

materials

MDPI

Article

Comparison of Microwave Sensitivity and Performance of Asphalt Mastic with Various Steel Slag Powders

Zeyu Geng [1], Weixiao Yu [1], Min Jiang [2] and Yinghao Miao [1,*]

[1] National Center for Materials Service Safety, University of Science and Technology Beijing, Beijing 100083, China; m202221253@xs.ustb.edu.cn (Z.G.); yuweixiao@xs.ustb.edu.cn (W.Y.)
[2] School of Metallurgical and Ecological Engineering, University of Science and Technology Beijing, Beijing 100083, China; jiangmin@ustb.edu.cn
* Correspondence: miaoyinghao@ustb.edu.cn

Abstract

Steel slag is a common solid waste, but it has good microwave absorbing ability. The poor microwave sensitivity of asphalt mixture limits the development of microwave maintenance for asphalt pavement. Therefore, it is significant to apply steel slag to asphalt pavement. This study analyzes the difference in the microwave sensitivity and performance between the asphalt mastics with blast furnace slag powder (BFSP), converter slag powder (CSP), refined slag powder (RSP), and limestone powder (LP). First, the chemical composition of BFSP, CSP, RSP, and LP is analyzed by X-ray diffractometer (XRD) and X-ray fluorescence (XRF) tests. Then, the micromorphology characteristics of the asphalt mastic with BFSP, that with CSP, that with RSP, and that with LP are studied using atomic force microscope (AFM) tests. Finally, the rheological properties of the four asphalt mastics are investigated through dynamic shear rheometer (DSR) and bending beam rheometer (BBR) tests. The results show that steel slag powder can effectively improve the microwave sensitivity of asphalt mastic. RSP and CSP can improve the anti-deformation ability of asphalt mastic. In addition, steel slag powders have an adverse effect on the low-temperature cracking resistance of asphalt mastic, but the creep strength and creep rate of asphalt mastic with steel slag powder are within a reasonable range. In general, steel slag powder as filler has great application potential in road engineering. However, it has a certain influence on the performance of asphalt mastic. It is necessary to carry out targeted selection in practical engineering.

Keywords: road engineering; resource recovery; electromagnetic properties; microwave heating; rheological properties

1. Introduction

Steel slag is a solid waste in the production process of iron and steel. According to the treatment technology, it can be divided into blast furnace slag (BFS), converter slag (CS), refining slag (RS), and so on. BFS is the solid waste discharged during the smelting of pig iron in the blast furnace, CS is the main production of steelmaking, and RS is the solid waste in the secondary metallurgical process. The treatment method of steel slag has the disadvantages of the incomplete separation between slag and iron and the low grade of recovered scrap [1,2]. Approximately 12–20 tons of steel slags are manufactured when 100 tons of steels are produced [3,4]. The China Statistical Yearbook 2022 shows that about 1.035 billion tons of crude steel are produced in 2022, which means that about

155–207 million tons of steel slags are generated. A large amount of steel slag is piled up, not only occupying a large space but also producing lots of environment-polluted dust. Therefore, it is necessary to explore the utilization method of steel slags as resources to reduce environmental pollution.

Due to the unique morphological characteristics and physical properties, steel slag has been widely used in the performance optimization research of asphalt mixtures. The surface pores of steel slag can enhance the adhesion between steel slag and asphalt through adsorption, which improves resistance to external loads [5]. Compared with conventional aggregates, steel slag aggregates have a lower wear rate, higher initial angularity, and better wear resistance [6]. These characteristics can improve the skeleton quality and the low-temperature crack resistance of asphalt mixtures [7,8]. However, steel slag has volume instability. The f-CaO and f-MgO in steel slag undergo hydration reactions with water, causing the steel slag to expand in a humid environment and the asphalt mixture to crack [9].

To eliminate the volume expansion problem of steel slag asphalt mixtures, Wu et al. [10] and Chen et al. [11] used steel slag powder as the filler. The results showed that asphalt mixtures with steel slag powder not only have good volume stability but also excellent performance in terms of rutting resistance. Based on the high correlation between the performance of asphalt mastic and that of asphalt mixtures, some researchers have evaluated the rheological properties of various steel slag powder asphalt mastics. Lagos-Varas et al. [12] studied the rheological properties of asphalt mastics with hydrated ladle slag (i.e., refining slag) at different dosages and found that a filler-to-asphalt ratio of 0.75 has the best improvement effect on the rheological properties of the asphalt mastic. Li et al. [13] indicated that alkaline oxygen furnace slag (i.e., converter slag) powder was a potential substitute for limestone powder, and the alkaline oxygen furnace slag powder obtained by grinding steel slag with a size of 0–9.5 mm had the best modification effect on asphalt. Wang et al. [14] found that both thin-film oven aging and ultraviolet aging can increase the stiffness and fatigue life of the asphalt mastic, and the fatigue life of the alkaline oxygen furnace slag asphalt mastic after ultraviolet aging was better than that of the limestone powder asphalt mastic. It can be seen that steel slag powder is a potential substitute for limestone mineral powder.

Microwave heating technology is an economical and environmentally friendly way of in-situ rehabilitation [15], which enables in-situ heat recovery, repair of crack damage in asphalt pavements, and de-icing of pavements during winter maintenance operations [16]. It has high requirements for the microwave sensitivity of materials [17]. The poor microwave absorption performance of asphalt mixture limits the development of microwave heating technology in road engineering [18,19]. Steel slag contains abundant metal oxides, resulting in good microwave-absorbing properties. Chen et al. [20] studied the temperature distribution characteristics of steel slag aggregate asphalt mixtures under microwave heating and found that the average heating rates of the surface and interior of steel slag porous asphalt concrete were higher than those of basalt porous asphalt concrete. Liu et al. [21] showed that the microwave heating uniformity of asphalt mixtures was best when the percentage of steel slag in the aggregate was less than 75%, but multiple microwave heating cycles led to an increase in the proportion of large and oversized voids within the mixtures, which caused the decrease in the durability. In contrast, Wang et al. [22] found that microwave heating was effective in rehabilitating steel slag asphalt mixtures of dense-graded and interrupted-graded mixtures by restoring the porosity level to the initial state. Luo et al. [23] found that the thermal field distribution of asphalt mixtures was the most uniform at 2.45 GHz, but local overheating still occurred. Wang et al. [24] found that alkaline oxide furnace slag filler had excellent electromagnetic properties and was able to improve the

microwave heating efficiency of asphalt mastic, which was suitable for the construction of functional pavements with microwave rapid repair performance. In summary, steel slag aggregate performs well in improving the microwave heating efficiency of asphalt mixtures but can adversely affect the heated asphalt mixtures. Steel slag powder not only improves the performance of asphalt mastic but also enhances the microwave sensitivity of asphalt mastic.

However, based on the different steelmaking processes and raw materials, there are differences in the chemical and physical properties of different steel slags, so it is necessary to compare and analyze the effect of different steel slag powders on the road performance and microwave sensitivity of asphalt mastic. In this study, BFSP, CSP, and RSP are used as research objects, and their chemical compositions and electromagnetic properties are compared to explore their microwave sensitivity enhancement effects on asphalt. Meanwhile, the effect of road performance of asphalt mastics with different steel slag powders is analyzed.

2. Materials and Methods

2.1. Materials

2.1.1. Steel Slag and Limestone Powders

BFSP, CSP, and RSP used in this study were supplied by Zenith Steel Group Co., Ltd. (Changzhou, China), and LP was supplied by Beijing Municipal Road & Bridge Building Material Group Co., Ltd. (Beijing, China). BFSP, CSP, and RSP were selected as fillers to prepare microwave sensitivity-enhanced asphalt mastic, and LP was selected as filler to prepare common asphalt mastic to be used as the control group. The preparation process of steel slag fillers was as follows: (1) crushing the large-sized steel slags into small particles by a press machine, (2) grinding the small steel slag particles into powders using the planetary ball mill, and (3) sieving the steel slag powders using a 0.075 mm sieve. Figure 1 depicts the preparation process of three steel slag fillers. The technical properties of steel slag and limestone fillers (apparent density, hydrophilic coefficient, and heat invariability) were measured according to Chinese Technical Specification Test Methods of Aggregates for Highway Engineering (JTG 3432-2024 [25]), as shown in Table 1. As can be seen from Table 1, the hydrophilic coefficient of CSP was larger than 1, indicating that CSP was more likely to swell in water. The hydrophilic coefficients of BFSP, RSP, and LP were smaller than 1, indicating that they had a stronger affinity to asphalt than water.

Figure 1. Preparation process of three steel slag fillers.

Table 1. Technical properties of steel slag and limestone fillers.

Technical Indexes	BFSP	CSP	RSP	LP
Apparent density (g/cm^3)	3.023	3.203	3.651	2.807
Hydrophilic coefficient	0.85	1.06	0.74	0.81
Heat invariability		No color change		

2.1.2. Asphalt

Xinhai 70# asphalt was selected in this study. Its technical indicators are listed in Table 2.

Table 2. Technical indicators of Xinhai 70# asphalt.

Technical Indexes	Unit	70# Asphalt
Penetration (25 °C, 5 s, 100 g)	0.1 mm	67
Penetration Index (PI)	/	−0.37
Ductility (10 °C)	cm	34
Ductility (15 °C)	cm	>100
Softening Point (TR&B)	°C	48.0
Solubility	%	99.84
Flash Point	°C	268
Density (15 °C)	g/cm^3	1.036

2.2. Preparation of Asphalt Mastics with Different Fillers

All fillers were dried in an oven for 24 h at 105 °C before preparing asphalt mastic. The mass ratio of limestone filler to asphalt was 1:1, and that of each steel slag filler to asphalt, as shown in Table 3, was determined by replacing limestone filler with an equal volume of steel slag filler. The asphalt and filler were stirred for 45 min with the speed of 2500 r/min using a digital high-speed mixer at 135–150 °C. During the mixing process, the filler was added into asphalt multiple times. Figure 2 describes the preparation process of asphalt mastic. For convenience, 70-LP was employed to represent the asphalt mastic with limestone filler, and the same pattern was used to denote the asphalt mastics with steel slag fillers.

Table 3. Mass ratio of each steel slag filler to asphalt in asphalt mastic.

Fillers	LP	BFSP	CSP	RSP
Mass ratio	1.000:1	1.077:1	1.141:1	1.301:1

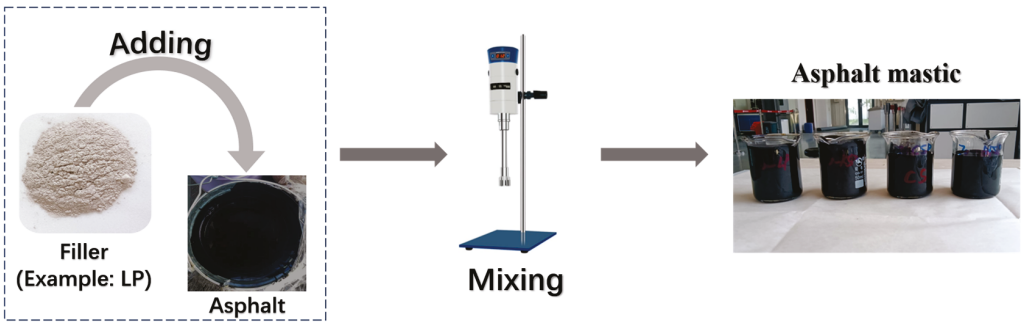

Figure 2. Preparation process of asphalt mastic.

2.3. Test Methods for Properties of Steel Slag and Limestone Powders

The electromagnetic performance of steel slag and limestone powders is closely related to their chemical composition, and it determines the microwave sensitivity of corresponding asphalt mastics.

The difference in the chemical composition between BFSP, CSP, RSP, and LP contributes to understanding the microwave sensitivity-enhanced mechanism of steel slag powders. Therefore, the X-Ray Diffractometer (XRD, D8 Advance, Bruker, Rheinstetten, Germany)test. X-Ray Fluorescence (XRF, Zetium, Malvern Panalytical, Malvern, UK) text, and electromagnetic performance tests were conducted on steel slag and limestone powders.

2.3.1. XRD Test

An XRD test was conducted on steel slag and limestone powders to analyze the internal material parameters such as the number of atoms in the crystal lattice and crystal size. Analyses were performed using Cu targets and reflection patterns. Samples were prepared using the tablet method. The diffraction angle was 5–90°, the scan frequency was 2°/min, the scan step was 0.02°, and the angular accuracy was 0.0001°.

2.3.2. XRF Test

An XRF test was conducted on steel slag and limestone powders adopting the press-flake method to quantitatively analyze the oxide composition. The samples were prepared by the tablet method. The elements were analyzed in the range of 9F to 92U.

2.3.3. Electromagnetic Performance Test

The electromagnetic parameters of BFSP, CSP, RSP, and LP were measured using a Vector Network Analyzer through the coaxial method in the frequency range of 2 GHz to 18 GHz to evaluate the microwave absorption ability of four fillers. The weight ratio of filler to paraffin wax is 4:1. The inner diameter, external diameter, and height of the coaxial ring were 3.04 mm, 7 mm, and 2 mm, respectively.

2.4. Test Methods for Performance of Asphalt Mastics

The microwave heating tests were conducted on 70-BFSP, 70-RSP, 70-CSP, and 70-LP to determine the microwave sensitivity improvement in asphalt mastics by steel slag powders. The steel slag powders can be used as fillers under the condition that the performances of asphalt mastics meet requirements, so dynamic shear rheometer (DSR) and bending beam rheometer (BBR) tests are conducted to understand the performances of asphalt mastic. The atomic force microscope (AFM) test is carried out to explain the influence mechanism of steel slag powder on the performance of asphalt mastic.

2.4.1. Microwave Heating Test

A microwave heating test was carried out using an FCMCR-3C type microwave reactor to analyze the microwave sensitivity of the asphalt mastics with different fillers. The initial temperature and volume of each asphalt mastic were, respectively, 25 °C and 25 mL. The heating frequency of the microwave reactor was 2.45 GHz, and its output power was 300 W. The heating time was 5 min. The temperature of asphalt mastic was recorded per second using a Teflon-coated Pt100 platinum resistance temperature sensor (Kerui Instrument Co., Gongyi, China).

2.4.2. DSR Test

The Smart Pave 102 type DSR equipment was applied in this study to investigate the high-temperature rheological properties of asphalt mastic. The frequency sweep test was conducted in strain-controlled mode to evaluate the viscoelasticity and anti-rutting performance of different asphalt mastics. The sweep frequency range was from 0.01 to 100 rad/s, and the sweep temperature was, respectively, 15 °C, 25 °C, 35 °C, 45 °C, 55 °C, 65 °C, and 75 °C.

The multiple stress creep recovery (MSCR) test was carried out to assess the permanent deformation resistance of different asphalt mastics. According to AASHTO T350-19 [26], two constant stresses of 0.1 kPa and 3.2 kPa and the temperature of 60 °C were selected.

2.4.3. BBR Test

The BBR test was performed according to AASHTO T313-19 [27] to evaluate the low-temperature stiffness and stress relaxation characteristics of asphalt mastics with different fillers. The test was conducted under 980 mN for 240 s. The test temperature was −12 °C.

2.4.4. AFM Test

An AFM test was carried out at the test temperature of 25 °C using a Dimension Icon AFM device to intuitively observe the difference in the microstructure between asphalt mastics with different fillers. The surface morphology of asphalt mastic is acquired by the Peak Force QNM model with a scanning range of 20 μm × 20 μm.

3. Properties of Steel Slag and Limestone Powders

3.1. Chemical Composition

The chemical compositions of LP, BFSP, CSP, and RSP are analyzed to understand the influence mechanism of steel slag and limestone powders on the microwave sensitivity of asphalt mastic. Figure 3 depicts the phase compositions of the four powders. As can be seen, the peak intensities of the phases of the four powders are pronounced, indicating they have a high purity degree. The primary mineral phase of LP is calcium carbonate and dolomite, that of BFSP is akermanite–gehlenite, that of CSP is calcium aluminum. RSP is mainly composed of iron oxide and calcite.

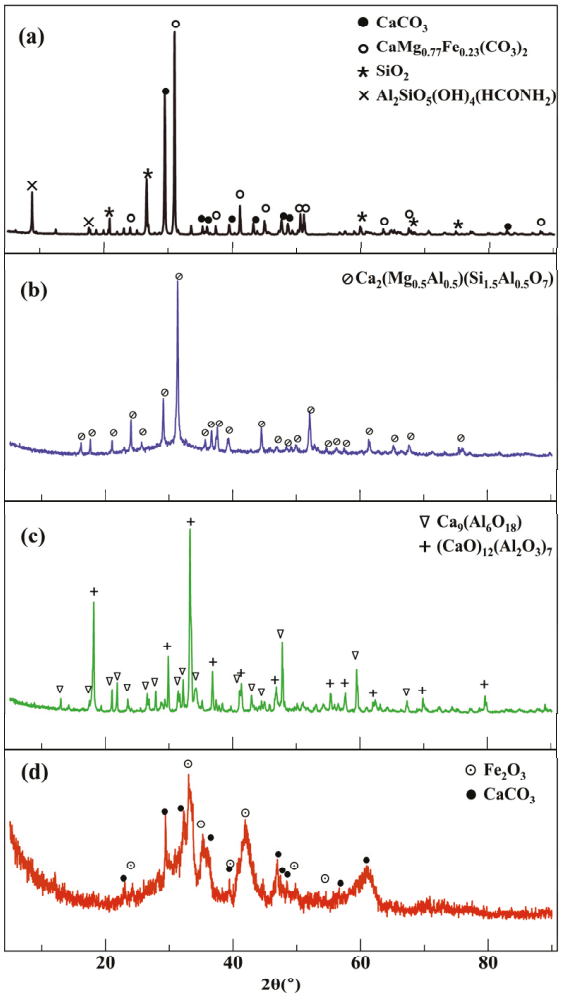

Figure 3. XRD test results of different powders: (**a**) LP, (**b**) BFSP, (**c**) CSP, and (**d**) RSP.

Table 4 shows the chemical composition of LP, RSP, CSP, and BFSP. It can be seen that the content of CaO is highest and that of Fe_2O_3 is smallest in LP. BFSP contains a high content of SiO_2 and CaO and a low content of Fe_2O_3. CSP is mainly composed of CaO and Al_2O_3. The chemical compositions of RSP mainly are CaO, Fe_2O_3, and SiO_2. The XRF characterization also further verifies the reliability of the XRD results.

Table 4. Chemical compositions of different powders.

Filler Type	CaO	MgO	SiO_2	Al_2O_3	Fe_2O_3	MnO
LP	59.77%	17.87%	14.85%	4.34%	1.43%	0.06%
BFSP	32.12%	11.91%	33.18%	18.64%	0.57%	0.41%
CSP	58.21%	2.43%	2.67%	30.75%	0.94%	0.07%
RSP	38.82%	6.02%	14.88%	2.85%	26.01%	5.20%

3.2. Microwave Absorption Property

The microwave absorption ability is related to the electromagnetic parameters of materials, which include relative complex permittivity ($\varepsilon_r = \varepsilon' - j\varepsilon''$) and relative magnetic permeability ($\mu_r = \mu' - j\mu''$). The real parts ε' and μ' denote the microwave energy storage capacity of materials. The imaginary parts ε'' and μ'' reflect the microwave energy loss ability of materials. Figure 4 presents the electromagnetic parameters of LP, BFSP, CSP, and RSP. As can be seen, with the increase in frequency, ε' remains basically unchanged, ε'' shows a rising tendency, and μ' and μ'' show a downward trend. CSP and RSP have higher values of ε' and ε'' compared with LP and BFSP. RSP has the largest values of μ' and μ''. In a low-frequency range (2–8 GHz), the μ' and μ'' of CSP are higher than those of LP and BFSP. In a high-frequency range (12–18 GHz), there is no significant difference in the μ' and μ'' between CSP, LP, and BFSP. The above results show that RSP is a dielectric and magnetic loss microwave-absorbing material. CSP is a dielectric loss microwave absorbing material. BFSP has better dielectric loss capability. LP has worse electromagnetic performance. Steel slag powders are more sensitive to microwave radiation than LP.

The principle of microwave absorption is to convert the microwave energy into thermal energy through a physical mechanism and the dissipation of the motion. Magnetic and dielectric losses are two main microwave energy conversion mechanisms, which are, respectively, denoted as the angular tangent of the dielectric loss ($\tan\delta_\varepsilon = \varepsilon''/\varepsilon'$) and the angular tangent of the magnetic loss ($\tan\delta_\mu = \mu''/\mu'$). Higher loss angle tangent represents that the material could convert microwave energy into more thermal energy through the corresponding loss mechanism. Therefore, the loss angle tangent ($\tan\delta$) is closely related to microwave absorption ability, which can be calculated by Equation (1). The larger the loss angle tangent, the better the microwave absorption ability.

$$\tan\delta = \tan\delta_\varepsilon + \tan\delta_\mu \tag{1}$$

Figure 5 depicts $\tan\delta_\varepsilon$ and $\tan\delta_\mu$ of LP, BFSP, CSP, and RSP. As can be seen, with the increase in frequency, $\tan\delta_\varepsilon$ of four fillers shows a rising tendency, and $\tan\delta_\mu$ of four fillers shows a downward trend. RSP has higher values of $\tan\delta_\varepsilon$ and $\tan\delta_\mu$. CSP has a higher value of $\tan\delta_\varepsilon$ and a lower value of $\tan\delta_\mu$. Both $\tan\delta_\varepsilon$ and $\tan\delta_\mu$ of LP and BFSP are relatively small. The above results show that the synergistic effect of dielectric and magnetic loss of RSP is best in the four fillers, indicating that RSP has the strongest ability to convert the microwave energy into thermal energy. CSP has a good dielectric loss ability, but its magnetic loss ability is poor. Both LP and BFSP have worse dielectric and magnetic loss properties. However, the dielectric loss ability of BFSP is higher than that of LP in the low-frequency range.

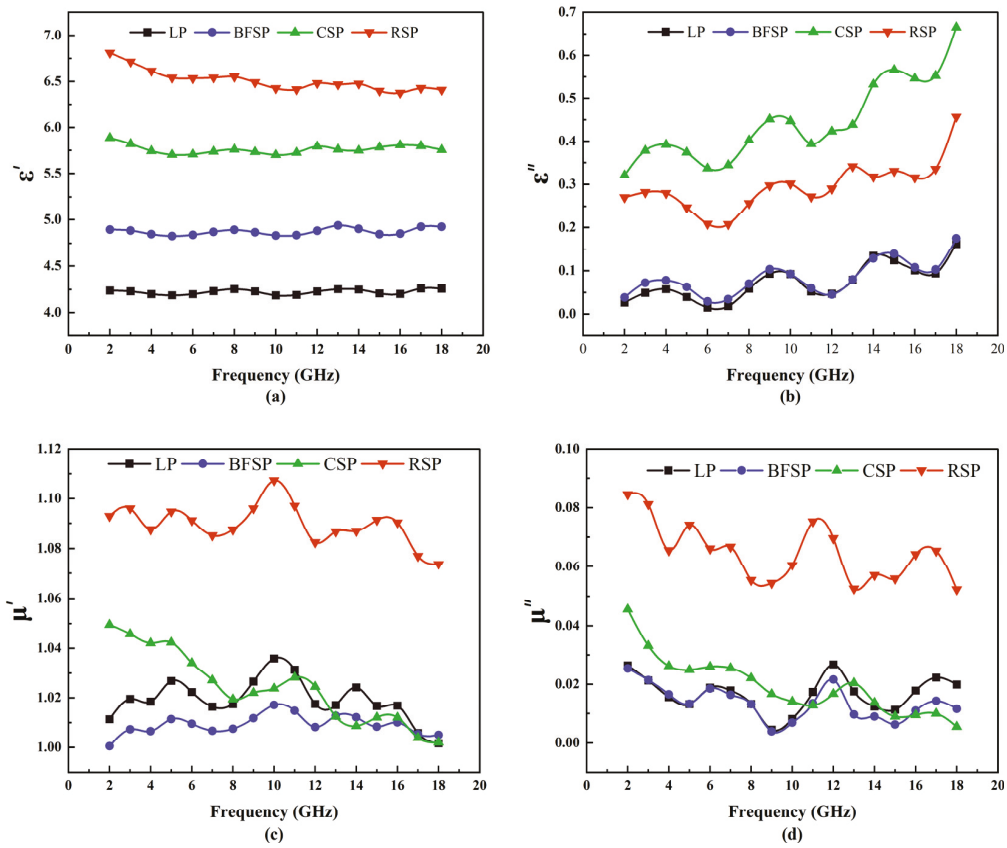

Figure 4. Electromagnetic parameters of four fillers: (**a**) ε', (**b**) ε'', (**c**) μ', and (**d**) μ''.

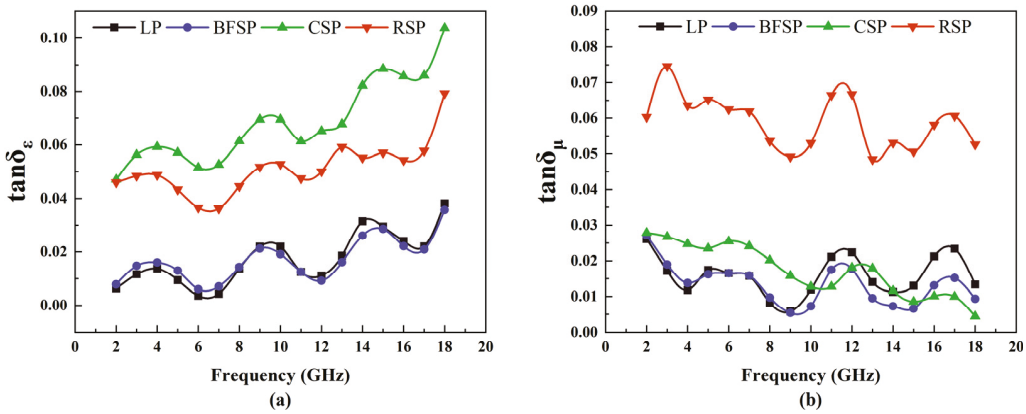

Figure 5. Magnetic and dielectric losses of four fillers: (**a**) $\tan\delta_\varepsilon$ and (**b**) $\tan\delta_\mu$.

Figure 6 shows the microwave absorption ability of LP, BFSP, CSP, and RSP. As can be seen, RSP has the strongest microwave absorption performance, followed by CSP. The microwave absorption ability of BFSP is better than that of LP at 2–8 GHz, while the result is opposite at 10–18 GHz. This is because the magnetic material Fe_2O_3 plays a leading role in the microwave absorption ability, and its content in RSP is far higher than that in the other three fillers. In addition, the dielectric material Al_2O_3 also has a certain influence on the microwave absorption ability, and its content in the fillers follows the order of CSP > BFSP > LP.

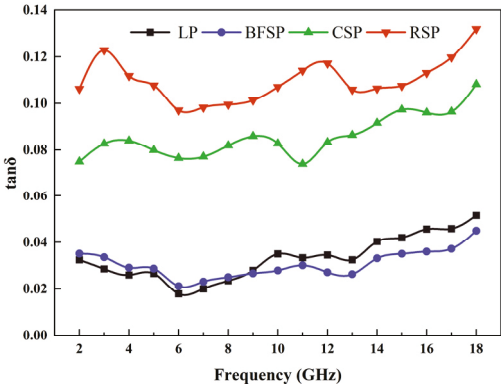

Figure 6. Loss angle tangent of fillers.

4. Microwave Sensitivity of Asphalt Mastics with Different Fillers

4.1. Heating Curve

Figure 7 describes the heating curves of asphalt mastics with different fillers. It can be seen that the temperature of each asphalt mastic gradually rises as microwave heating time increases. After microwave heating for 300 s, the temperature of 70-LP, 70-BFSP, 70-CSP, and 70-RSP reaches 38 °C, 69 °C, 130 °C, and 172 °C, respectively. Under the same heating time, the temperature of the asphalt mastic with steel slag filler is higher than that of asphalt mastic with limestone filler, indicating that the addition of steel slag powder achieves a large amount of heat formation in a short time and improves the microwave sensitivity of asphalt mastic. RSP has the best effect to enhance the microwave absorption of asphalt mastic, followed by CSP and BFSP.

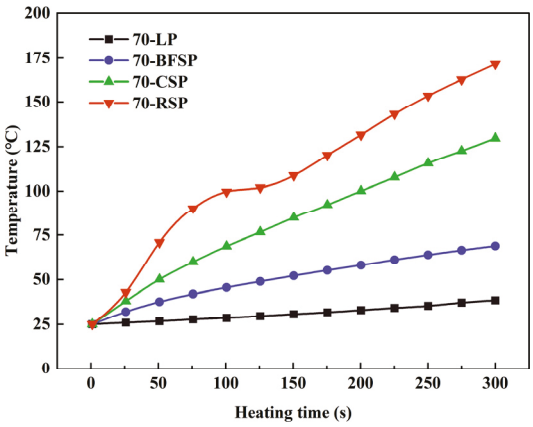

Figure 7. Heating curves of asphalt mastics with different fillers.

The heating curves are fitted to understand the relationship between temperature and microwave heating time for asphalt mastics. Table 5 lists the fitting results. As can be seen, there is a good linear relation between the heating time and temperature, with correlation coefficients of above 0.96. The slopes of fitting equations for asphalt mastics with different fillers follow the order of 70-RSP > 70-CSP > 70-BFSP > 70-LP.

Table 5. The fitting results of heating curves.

Asphalt Mastics	Fitting Equation	R^2
70-LP	$y = 0.043x + 24.54$	0.9898
70-BFSP	$y = 0.137x + 30.38$	0.9820
70-CSP	$y = 0.336x + 32.52$	0.9925
70-RSP	$y = 0.441x + 44.35$	0.9628

4.2. Heating Rate

The ratio of the temperature difference between 0 s and 300 s to the heating time is defined as the heating rate to analyze the response effect of asphalt mastics with different fillers to microwave heating. Figure 8 depicts the heating rate of each asphalt mastic. It can be seen that the microwave heating rate of asphalt mastics follows the order of 70-RSP > 70-CSP > 70-BFSP > 70-LP. The heating rate of 70-BFSP, 70-CSP, and 70-RSP is, respectively, 3.02, 6.51, and 9.80 times that of 70-LP. The results further proved that the addition of steel slag powder effectively improves the microwave absorption ability of asphalt mastics.

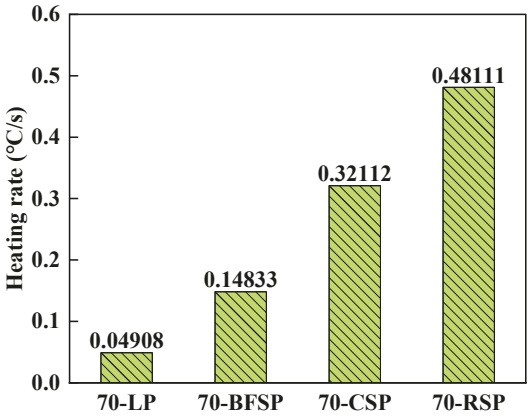

Figure 8. Heating rate of asphalt mastics with different fillers.

Figure 9 shows the correlation between the electromagnetic property of fillers and the heating rate of corresponding asphalt mastics at 2.45 GHz. As can be seen, there is a good linear relationship between the electromagnetic property of fillers and the microwave sensitivity of corresponding asphalt mastics, with correlation coefficients of above 0.96.

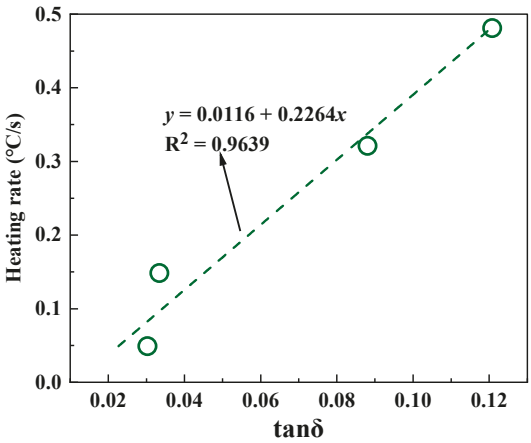

Figure 9. Correlation between the electromagnetic property of fillers and the heating rate of corresponding asphalt mastics.

5. Performance of Asphalt Mastics with Different Fillers

The above results show that the addition of steel slag powder can effectively improve the microwave sensitivity of asphalt mastics. However, for realizing its application on the microwave maintenance of asphalt pavement, the performance of asphalt mastic with steel slag filler needs to be further investigated.

5.1. Viscoelastic Characteristics

According to the frequency sweep test, the complex shear modulus (G*) and phase angle (δ) are two important parameters evaluating the viscoelastic characteristics of asphalt mastics. The composite shear modulus is the ratio of the maximum shear stress to the corresponding shear strain. It reflects the ability to resist the deformation of asphalt mastic. The phase angle is the ratio of the loss modulus to the storage modulus, and it indicates the components of viscosity and elasticity of asphalt mastic. The larger the storage modulus, the better the ability to recover from deformation. The larger the loss modulus, the better the ability to resist deformation. Therefore, the asphalt mastic with the smaller phase angle has better elastic properties. According to the frequency sweep results and time-temperature superposition principle, the master curves of complex shear modulus and phase angle at the reference temperature of 35 °C are constructed based on the CAM model to analyze the viscoelasticity of asphalt mastics, as shown in Figures 10 and 11.

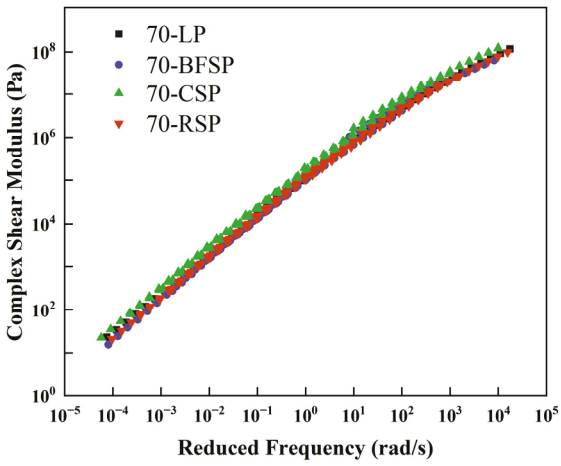

Figure 10. Master curves of complex shear modulus.

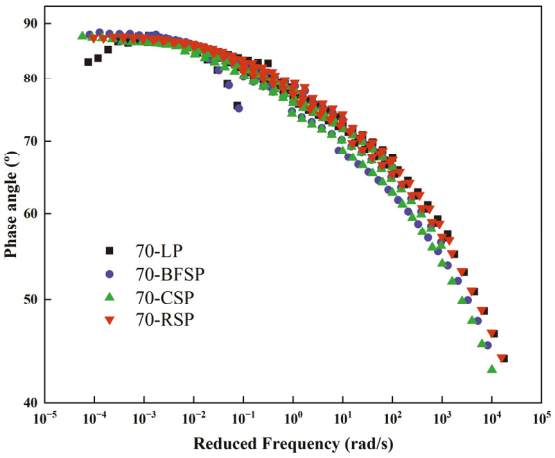

Figure 11. Master curves of phase angles.

As shown in Figure 10, there is no significant difference in the master curves of complex shear modulus between 70-LP, 70-BFSP, and 70-RSP, indicating that BFSP and RSP have little influence on the stiffness of asphalt mastic. Moreover, 70-CSP has the largest complex shear modulus, indicating that CSP improves the stiffness of asphalt mastic. As can be seen from Figure 11, in the frequency range of 10^{-3}–10^{-2} rad/s, there is no significant difference in the phase angles between 70-LP, 70-BFSP, 70-CSP, and 70-RSP. When the frequency is greater than 0.1 rad/s, 70-BFSP and 70-CSP have relatively small phase angles compared with 70-LP and 70-RSP. The above results indicated that RSP would not destroy the elastic

properties of asphalt mastic, and BFSP and CSP can improve the elastic properties of asphalt mastic.

5.2. Resistance to Rutting

The rutting factor (G*/sinδ) is a key indicator for assessing the rutting resistance of asphalt mastic. The larger the G*/sinδ, the stronger the resistance to rutting deformation. The loading frequency of the DSR test has a corresponding relationship with the travelling speed. The loading frequency of 5 Hz corresponds to a travelling speed of about 30–40 km/h, and that of 10 Hz corresponds to a travelling speed of about 60–65 km/h [28]. On urban roads, the travelling speed of vehicles is between about 30 km/h and 80 km/h. Therefore, the changes of G*/sinδ with temperature at 100 rad/s (16 Hz), 63.1 rad/s (10 Hz), and 25.1 rad/s (4 Hz) are analyzed, as shown in Figure 12. It can be seen that the 70-BFSP has the smallest G*/sinδ, indicating that BFSP decreases the rutting resistance of asphalt mastic. There is no significant difference in the G*/sinδ between 70-CSP, 70-RSP, and 70-LP, indicating that CSP and RSP have little effect on the rutting resistance of asphalt mastic.

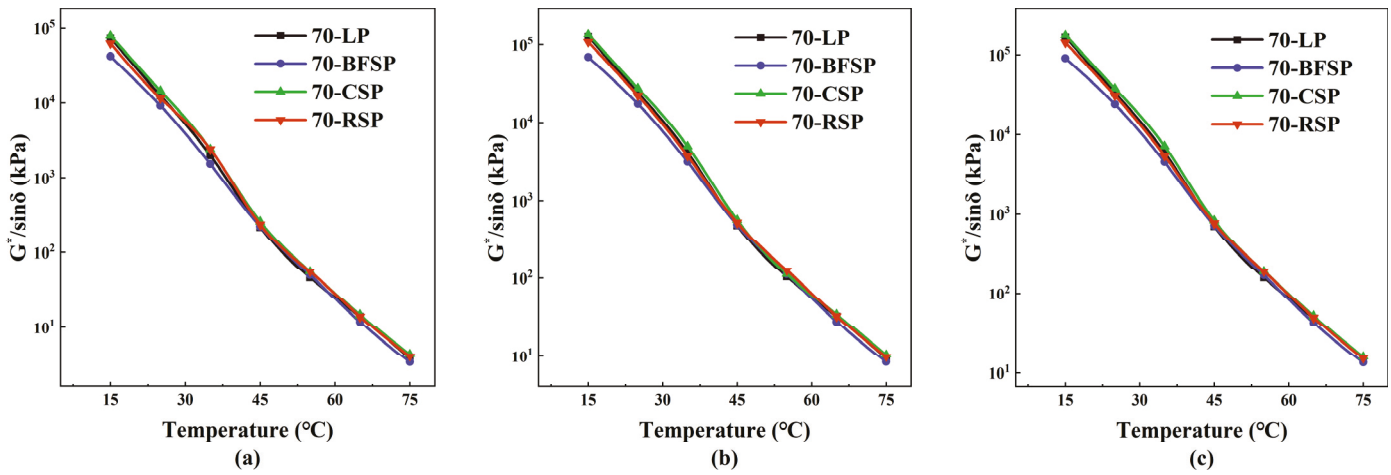

Figure 12. Change in G*/sinδ with temperature at different frequencies: (**a**) 25.1 rad/s, (**b**) 63.1 rad/s, and (**c**) 100 rad/s.

Based on the MSCR test, the creep recovery rate (R), the unrecoverable creep flexibility (J_{nr}), and the difference rate of unrecoverable creep flexibility ($J_{nr\text{-}diff}$) are also frequently used parameters evaluating the deformation resistance. The R reflects the resistance to elastic deformation capacity of asphalt mastic. The Jnr represents the cumulative strain of asphalt mastic. The Jnr-diff can respond to the stress sensitivity of asphalt mastic. Figures 13 and 14 depict the R and Jnr of asphalt mastics under the stress levels of 0.1 kPa and 3.2 kPa. As can be seen, both 70-CSP and 70-RSP have higher R and lower Jnr than 70-LP, indicating that CSP and RSP can improve the permanent deformation resistance of asphalt mastic. Both Jnr and R of 70-BFSP are larger than that of 70-LP, indicating that BFSP does not have a negative effect on the permanent deformation resistance of asphalt mastic. Figure 15 depicts the Jnr-diff of asphalt mastics under the stress levels of 0.1 kPa and 3.2 kPa. It can be seen that the Jnr-diff values of asphalt mastics follow the order of 70-BFSP > 70-CSP > 70-LP > 70-RSP. This indicates that 70-BFSP and 70-CSP have higher sensitivity to stress compared with 70-LP and 70-RSP, which may result in the greater deformation of 70-BFSP and 70-CSP under the repeated loading. In summary, BFSP, CSP, and RSP can improve the elasticity of asphalt mastic. CSP and RSP have a good inhibition effect on the permanent deformation of asphalt mastic. BFSP results in the higher sensitivity of asphalt mastic to stress, which has an influence on the resistance to the permanent deformation of asphalt mastic.

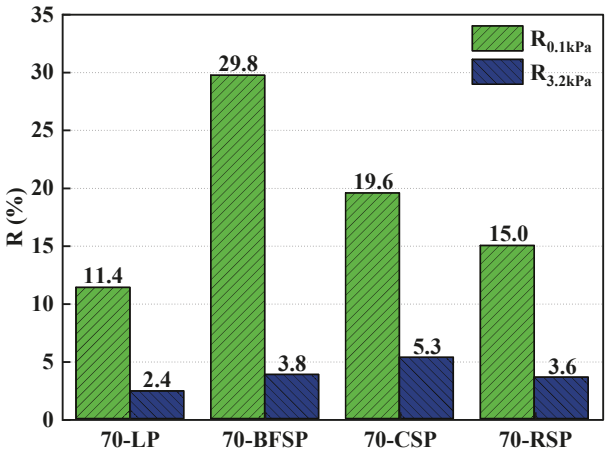

Figure 13. R values of asphalt mastics under the stress levels of 0.1 kPa and 3.2 kPa.

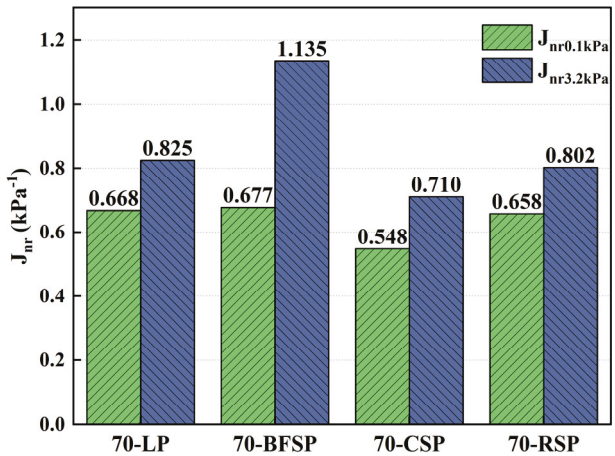

Figure 14. Jnr values of asphalt mastics under the stress levels of 0.1 kPa and 3.2 kPa.

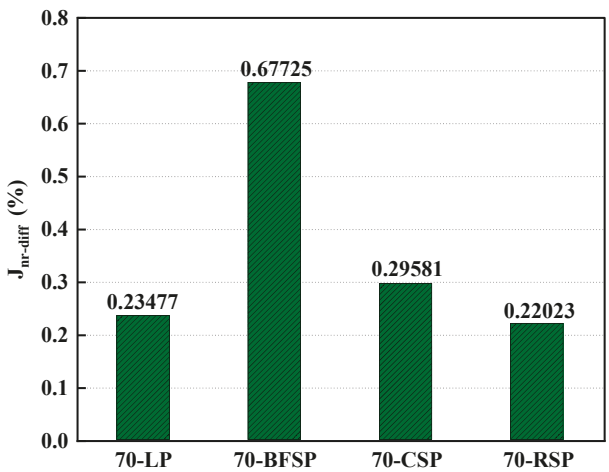

Figure 15. Jnr-diff values of asphalt mastics.

5.3. Low-Temperature Crack Resistance

In the BBR test, the creep strength (S) and creep rate (m) are used to evaluate the low-temperature performance. The asphalt mastic with lower S and higher m has better low-temperature cracking resistance. Figure 16 shows the results of S and m values obtained from the BBR tests. As can be seen, 70-LP has the smallest creep strength and the largest creep rate in all asphalt mastics, indicating that the steel slag powders have an adverse effect on the low-temperature cracking resistance of asphalt mastic. Moreover, 70-CSP has

the largest creep strength and the smallest creep rate, indicating it has the biggest influence on the low-temperature cracking resistance of asphalt mastic. The differences in the creep strength and creep rate between BFSP and LP are small, which illustrates that BFSP has little influence on the low-temperature cracking resistance of asphalt mastic.

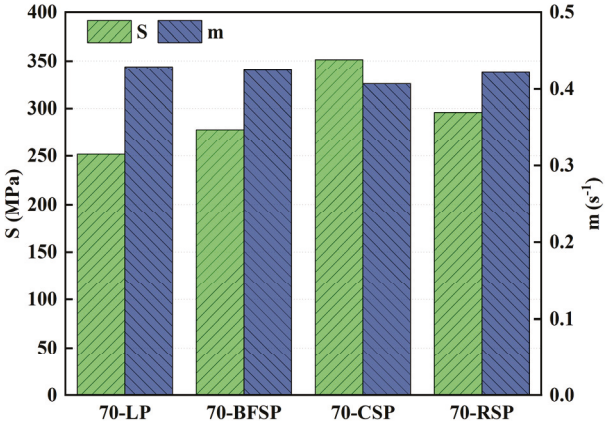

Figure 16. Creep strength and creep rate of each asphalt mastic.

In summary, steel slag powder can effectively improve the microwave sensitivity property of asphalt mastic, especially RSP and CSP, and it has little influence on the viscoelasticity and anti-deformation performance of asphalt mastic. Although the low-temperature performance of asphalt mastic with steel slag filler is inferior to that of 70-LP, its creep strength and creep rate are within a reasonable range. Therefore, it is feasible to use steel slag powder as filler for enhancing the microwave sensitivity of asphalt mastic.

6. Microscopic Mechanism of Steel Slag Powder Impacting Asphalt Mastic Performance

Figure 17 presents the schematic diagram of three phases of AFM images of asphalt mastics. As shown in this figure, the catana phase is a bee-like structure, the peri phase is the peripheral area of the bee-like structure, and the para phase is the adjacent area of the peri phase [29]. The para phase is the softest microdomain [30]. The more the para phase, the better the low-temperature performance. The bee-like structure represents the four components of asphalt. Asphalt mastic with high asphaltene and resin content has more bee-like structures. In the catana phase, the protruding white part is asphaltene, the yellow part is resins, the yellowish-brown part is aromatic, and the concave black part is saturate. The more the bee-like structures, the better the agglomeration degree of asphalt molecules, and thus the better the high-temperature performance.

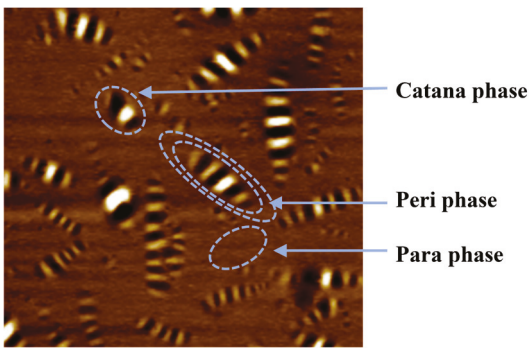

Figure 17. Schematic diagram of three phases of AFM image of asphalt mastic.

Figure 18 depicts the AFM images of 70-LP, TP-BFSP, 70-CSP, and 70-RSP. As can be seen, steel slag powders have a significant influence on the micromorphology of asphalt mastics. Furthermore, 70-LP and 70-BFSP have more para phase and fewer bee-like structures compared with 70-CSP and 70-RSP. This is the reason why they have better low-temperature performance and worse anti-deformation performance.

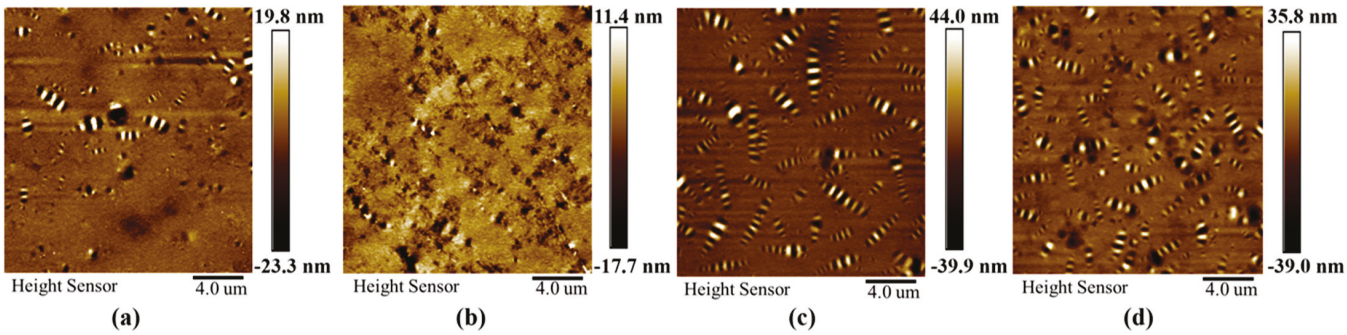

Figure 18. AFM images of asphalt mastic: (**a**) 70-LP, (**b**) 70-BFSP, (**c**) 70-CSP, and (**d**) 70-RSP.

The surface roughness index allows quantitative analysis for the information of the surface structure [31]. In this study, the mean roughness index (Ra) and the root mean square roughness index (Rq) are employed to evaluate the surface roughness of each asphalt mastic, which are calculated by Nanoscope Analysis software 3.00, according to Equations (2) and (3).

$$R_a = \frac{\sum(Z_i)}{N} \tag{2}$$

$$R_q = \sqrt{\frac{\sum(Z_i)^2}{N}} \tag{3}$$

where N is the number of selected data points within the range, and Z_i is the height measurement of a surface point relative to the microscope's operational state.

Figure 19 shows the results of two surface roughness indexes of 70-LP, 70-BFSP, 70-CSP, and 70-RSP. It can be seen that 70-CSP and 70-RSP have larger surface roughness compared with 70-LP and 70-BFSP. This indicates that 70-CSP and 70-RSP have better viscosity.

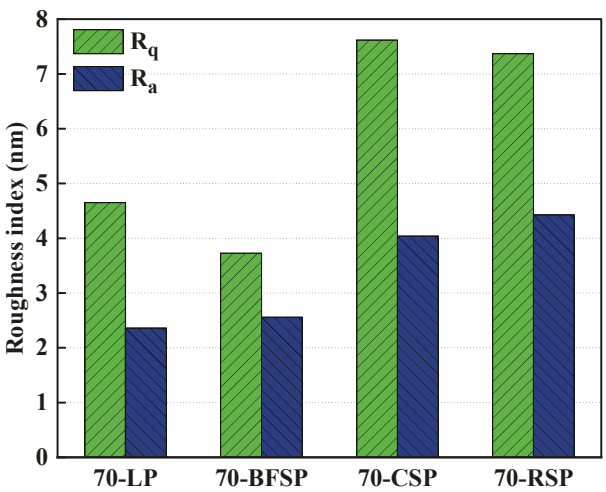

Figure 19. The surface roughness indexes of asphalt mastics.

7. Conclusions

This study analyzes the chemical composition of steel slag and limestone powders by XRD and XRF tests, evaluates the microwave absorption ability of steel slag and limestone

powders by electromagnetic performance tests, compares the microwave sensitivity and performance of the asphalt mastics with different steel slag powders and LP, and reveals the effect mechanism of steel slag powder on asphalt mastic performance. The main conclusions are as follows.

(1) The chemical compositions of BFSP, CSP, RSP, and LP are similar. RSP has the strongest ability to convert microwave energy into thermal energy. CSP has a good dielectric loss ability, but its magnetic loss ability is poor. Both LP and BFSP have worse dielectric and magnetic loss properties. However, the dielectric loss ability of BFSP is higher than that of LP in the low-frequency range.
(2) Steel slag powder can improve the microwave sensitivity of asphalt mastic, especially RSP and CSP. There is a good linear relationship between the electromagnetic property of fillers and the microwave sensitivity of corresponding asphalt mastics.
(3) BFSP and RSP have little influence on the stiffness of asphalt mastic, and CSP improves the stiffness of asphalt mastic. RSP would not destroy the elastic properties of asphalt mastic, while BFSP and CSP can improve the elastic properties of asphalt mastic.
(4) Steel slag powders have an adverse effect on the low-temperature cracking resistance of asphalt mastic, but the creep strength and creep rate of asphalt mastic with steel slag powder are within a reasonable range.

In summary, steel slag powder has great potential in improving the microwave sensitivity of asphalt mastic, which is of great significance in reducing environmental pollution and promoting the application of microwave heating technology in asphalt pavement maintenance. In addition, there are significant differences in the microwave sensitivity and performance between the asphalt mastics with different steel slag powders. Therefore, this study is of guiding significance for selecting suitable steel slag according to different road service conditions.

Author Contributions: Conceptualization, Y.M.; data curation, Z.G.; funding acquisition, Y.M.; methodology, Z.G., W.Y. and Y.M.; supervision, Y.M., W.Y. and M.J.; validation, W.Y. and M.J.; writing—original draft, Z.G.; writing—review and editing, W.Y., Y.M. and M.J. All authors have read and agreed to the published version of the manuscript.

Funding: This research received no external funding.

Institutional Review Board Statement: Not applicable.

Informed Consent Statement: Not applicable.

Data Availability Statement: The original contributions presented in this study are included in the article. Further inquiries can be directed to the corresponding author.

Conflicts of Interest: The authors declare no conflicts of interest.

Abbreviations

The following abbreviations are used in this manuscript:

BFSP	blast furnace slag powder
CSP	converter slag powder
RSP	refined slag powder
LP	limestone powder
XRD	X-ray diffractometer
XRF	X-ray fluorescence
AFM	atomic force microscope
DSR	dynamic shear rheometer
BBR	bending beam rheometer

BFS	blast furnace slag
CS	converter slag
RS	refined slag
MSCR	the multiple stress creep recovery
70-LP	asphalt mastic with limestone powder
70-BFSP	asphalt mastic with blast furnace slag powder
70-CSP	asphalt mastic with converter slag powder
70-RSP	asphalt mastic with refined slag powder
S	the creep strength
m	the creep rate (m)

References

1. Guo, J.; Bao, Y.; Wang, M. Steel slag in China: Treatment, recycling, and management. *Waste Manag.* **2018**, *78*, 318–330. [CrossRef] [PubMed]
2. Gao, W.; Zhou, W.; Lyu, X.; Liu, X.; Su, H.; Li, C.; Wang, H. Comprehensive utilization of steel slag: A review. *Powder Technol.* **2023**, *422*, 118449. [CrossRef]
3. Gao, D.; Wang, F.; Wang, Y.; Zeng, Y. Sustainable Utilization of Steel Slag from Traditional Industry and Agriculture to Catalysis. *Sustain. Sci.* **2020**, *12*, 9295. [CrossRef]
4. Yi, H.; Xu, G.; Cheng, H.; Wang, J.; Wan, Y.; Chen, H. An Overview of Utilization of Steel Slag. *Procedia Environ. Sci.* **2012**, *16*, 791–801. [CrossRef]
5. Xu, H.; Chen, A.; Wu, S.; Li, Y.; Li, J.; Zhu, Y.; Wu, J.; Zhou, Y.; Feng, J. Mechanism of asphalt concrete reinforced with industrially recycled steel slag from the perspectives of adhesion and skeleton. *Constr. Build. Mater.* **2024**, *424*, 135899. [CrossRef]
6. Wang, H.; Qian, J.; Zhang, H.; Nan, X.; Chen, G.; Li, X. Exploring skid resistance over time: Steel slag as a pavement aggregate—Comparative study and morphological analysis. *J. Clean. Prod.* **2024**, *464*, 142779. [CrossRef]
7. Wang, F.; Xiao, Y.; Cui, P.; Ma, T.; Liu, X.; Wang, F.; Zhang, L. Enhancement mechanism of asphalt mixture skeleton structures due to morphological characteristics of steel slag. *Constr. Build. Mater.* **2024**, *432*, 136703. [CrossRef]
8. Bai, X.; Wang, L. Study on mesoscopic model of low-temperature cracking of steel slag asphalt mixture based on random aggregate. *Constr. Build. Mater.* **2023**, *364*, 129974. [CrossRef]
9. Yüksel, İ. A review of steel slag usage in construction industry for sustainable development. *Environ. Dev. Sustain.* **2017**, *19*, 369–384. [CrossRef]
10. Wu, B.; Liu, L.; Feng, Y. Evaluation of steel slag powder as filler in hot-mix asphalt mixtures. *Adv. Civ. Eng. Mater.* **2018**, *7*, 64–72. [CrossRef]
11. Chen, Z.; Leng, Z.; Jiao, Y.; Xu, F.; Lin, J.; Wang, H.; Cai, J.; Zhu, L.; Zhang, Y.; Feng, N.; et al. Innovative use of industrially produced steel slag powders in asphalt mixture to replace mineral fillers. *J. Clean. Prod.* **2022**, *344*, 131124. [CrossRef]
12. Lagos-Varas, M.; Movilla-Quesada, D.; Raposeiras, A.C.; Castro-Fresno, D.; Vega-Zamanillo, Á.; Cumian-Benavides, M. Use of Hydrated Ladle Furnace Slag as a filler substitute in asphalt mastics: Rheological analysis of filler/bitumen interaction. *Constr. Build. Mater.* **2022**, *332*, 127370. [CrossRef]
13. Li, C.; Chen, Z.; Wu, S.; Li, B.; Xie, J.; Xiao, Y. Effects of steel slag fillers on the rheological properties of asphalt mastic. *Constr. Build. Mater.* **2017**, *145*, 383–391. [CrossRef]
14. Wang, R.; Xiong, Y.; Ma, X.; Guo, Y.; Yue, M.; Yue, J. Investigating the differences between steel slag and natural limestone in asphalt mixes in terms of microscopic mechanism, fatigue behavior and microwave-induced healing performance. *Constr. Build. Mater.* **2022**, *328*, 127107. [CrossRef]
15. Gallego, J.; del Val, M.A.; Contreras, V.; Páez, A. Heating asphalt mixtures with microwaves to promote self-healing. *Constr. Build. Mater.* **2013**, *42*, 1–4. [CrossRef]
16. Gulisano, F.; Gallego, J. Microwave heating of asphalt paving materials: Principles, current status and next steps. *Constr. Build. Mater.* **2021**, *278*, 121993. [CrossRef]
17. Lu, D.; Jiang, X.; Leng, Z. Sustainable microwave-heating healing asphalt concrete fabricated with waste microwave-sensitive fillers. *J. Clean. Prod.* **2024**, *434*, 140343. [CrossRef]
18. Miao, P.; Liu, W.; Wang, S. Improving microwave absorption efficiency of asphalt mixture by enriching Fe_3O_4 on the surface of steel slag particles. *Mater. Struct.* **2017**, *50*, 134. [CrossRef]
19. Wang, F.; Zhu, H.; Shu, B.; Li, Y.; Gu, D.; Gao, Y.; Chen, A.; Feng, J.; Wu, S.; Liu, Q.; et al. Microwave heating mechanism and self-healing performance of asphalt mixture with basalt and limestone aggregates. *Constr. Build. Mater.* **2022**, *342*, 127973. [CrossRef]

20. Chen, X.; Wan, B.; Wang, Y.; Dong, Q. Investigation on the temperature distribution characteristics of steel slag asphalt mixture under different microwave heating and cooling methods. *Constr. Build. Mater.* **2024**, *425*, 136004. [CrossRef]
21. Wang, A.; Guan, B.; Zhao, H.; He, Z.; Ding, D.; Gai, W. Microwave self-healing characteristics of the internal voids in steel slag asphalt mixture subjected to salt-freeze-thaw cycles. *Constr. Build. Mater.* **2024**, *449*, 138362. [CrossRef]
22. Liu, J.; Wang, Z.; Li, M.; Wang, X.; Wang, Z.; Zhang, T. Microwave heating uniformity, road performance and internal void characteristics of steel slag asphalt mixtures. *Constr. Build. Mater.* **2022**, *353*, 129155. [CrossRef]
23. Lou, B.; Sha, A.; Barbieri, D.M.; Liu, Z.; Zhang, F. Microwave heating properties of steel slag asphalt mixture using a coupled electromagnetic and heat transfer model. *Constr. Build. Mater.* **2021**, *291*, 123248. [CrossRef]
24. Wang, R.; Sha, T.; Xiong, Y.; Cai, Y.; Yue, J.; Wang, H. Potential contribution of steel slag fillers to asphalt mastic in terms of microwave heating efficiency, electromagnetic mechanisms and fatigue durability. *Int. J. Pavement Eng.* **2023**, *24*, 2240471. [CrossRef]
25. *JTG 3432-2024*; Test Methods of Aggregates for Highway Engineering. Ministry of Transport: Beijing, China, 2024.
26. *AASHTO T350-19*; Standard Method of Test for Multiple Stress Creep Recovery (MSCR) Test of Asphalt Binder Using a Dynamic Shear Rheometer (DSR). American Association of State Highway and Transportation Officials: Washington, DC, USA, 2019.
27. *AASHTO T313-19*; Standard Method of Test for Determining the Flexural Creep Stiffness of Asphalt Binder Using the Bending Beam Rheometer (BBR). American Association of State Highway and Transportation Officials: Washington, DC, USA, 2019.
28. Luo, M.; Chen, C.; Li, T. Experimental Study on the Influence of Temperature and Loading Frequency on Dynamic Modulus of Asphalt Mixture. *Open J. Transp. Technol.* **2019**, *8*, 312–320. [CrossRef]
29. Davis, D.; Castorena, C. Implications of physico–chemical interactions in asphalt mastics on asphalt microstructure. *Constr. Build. Mater.* **2015**, *94*, 83–89. [CrossRef]
30. Yang, Q.; Fan, Z.; Yang, X.; Hao, L.; Lu, G.; Fini, E.H.; Wang, D. Recycling waste fiber-reinforced polymer composites for low-carbon asphalt concrete: The effects of recycled glass fibers on the durability of bituminous composites. *J. Clean. Prod.* **2023**, *223*, 138692. [CrossRef]
31. Ma, X.; Wang, D.; Liu, S.; Jiang, J.; Kan, J.; Tu, M. Analysis of asphalt microscopic and force curves under water-temperature coupling with AFM. *Case Stud. Constr. Mater.* **2024**, *20*, e03071. [CrossRef]

Disclaimer/Publisher's Note: The statements, opinions and data contained in all publications are solely those of the individual author(s) and contributor(s) and not of MDPI and/or the editor(s). MDPI and/or the editor(s) disclaim responsibility for any injury to people or property resulting from any ideas, methods, instructions or products referred to in the content.

materials

MDPI

Article

Study on Non-Destructive Testing Method of Existing Asphalt Pavement Based on the Principle of Geostatistics

Duanyi Wang [1], Chuanxi Luo [1,2,*], Meng Fu [3], Wenting Zhang [2] and Wenjie Xie [2]

[1] School of Civil Engineering and Transportation, South China University of Technology, Guangzhou 510000, China
[2] Xiaoning Institute of Roadway Engineering, Guangzhou 510000, China
[3] Guangdong Communication Planning & Design Institute Group Co., Ltd., Guangzhou 510000, China
* Correspondence: luochuanxiyouyong@163.com; Tel.: +86-188-2518-1976

Abstract

In the context of the rapid advancement of reconstruction and expansion projects, there has been a significant increase in the demand for the inspection and evaluation of existing asphalt pavements. In order to enhance the efficiency and effectiveness of joint detection using 3D ground-penetrating radar and falling weight deflectometers, this study investigates non-destructive testing methods for existing asphalt pavements based on geostatistical correlation principles. The relationship between crack rate and deflection is analyzed using group average values. The characteristic sections division method based on the crack rate guideline was realized. Research on the prediction method for deflection using Kriging interpolation has been conducted. Research has revealed that there is a positive correlation between the crack rate and the deflection index. The principle of the singularity index can be employed to divide characteristic sections. The falling weight deflectometer is capable of conducting targeted testing in accordance with characteristic sections. Furthermore, the superior performance of Kriging interpolation in predicting deflection compared with linear interpolation has been demonstrated. According to the Kriging interpolation principle, the detection interval of slow lane deflection should not be more than 100 m. Kriging interpolation on one way lane of matrix data has the best effect, and it can predict deflection using a limited amount of slow lane and hard shoulder data. This facilitates analysis of the changing trend of the deflection index in cases where detection conditions are constrained. This method is of great significance for grasping the true performance status of the existing asphalt pavement structure.

Keywords: 3D GPR; FWD; geostatistics; deflection; crack rate

1. Introduction

As the number of reconstruction and expansion projects continues to increase, there is an increasing demand for the detection and assessment of in-service asphalt pavement. Non-destructive testing (NDT) techniques are being utilized extensively due to their rapid detection speed and minimal damage to the pavement [1,2]. The most commonly employed techniques are 3D ground-penetrating radar (3D GPR) and the falling weight deflectometer (FWD). The 3D GPR employs electromagnetic wave reflection signals to detect internal damage within the pavement structure, enabling the distinct identification of disorders such as cracks, looseness, and voids in the pavement structure [3–5]. The FWD applies an impact load to test the overall strength of the road surface structure. The combined application of

these two devices has been demonstrated to enhance the detection of existing problems in the pavement structure. However, several challenges have emerged during large-scale implementation, namely the discrepancy between spatial coverage and resolution. While 3D GPR can perform continuous scanning to acquire three-dimensional images, the FWD relies on fixed-point measurements. This discrepancy in the spatial sampling density may result in localised defect oversights. Secondly, FWD requires lane closure and is highly sensitive to road smoothness; in contrast, 3D GPR can perform detection without disrupting traffic. When conducting joint inspections, the time required to close the lanes must be balanced against the need for precision, which increases the complexity of the project.

3D GPR and FWD have been extensively utilized in the NDT evaluation of existing asphalt pavements. The Indiana Department of Transportation has utilized a systematic approach, incorporating FWD testing and 3D GPR data collection, to acquire critical insights into pavement performance characteristics. These characteristics are instrumental in determining project priorities and developing budgetary estimates for maintenance initiatives [6]. In the evaluation of flexible pavement, the 3D GPR is utilized to accurately measure the thickness of pavement structural layers and detect potential defects such as voids, delamination, and cracks. The FWD is employed to evaluate the overall load-bearing capacity and structural integrity of the road surface. The integration of the structural layer thickness data obtained from 3D GPR with the load-bearing capacity data from FWD facilitates a more comprehensive and precise assessment of the road surface condition [7,8]. The researchers utilized a 3D GPR to detect pavement thickness, and the FWD modulus inversion program employed the detected pavement thickness to enhance the accuracy of the results [6,8]. The FWD was utilized to analyze the bond between pavement layers and the strength of the structural layers, while the 3D GPR was employed to detect the type and size of the disease inside the pavement structure. The two devices were used in combination to assess the health of the pavement from different perspectives [7].

With the development of geostatistics, the statistical methods of geostatistics are gradually applied across the border in the civil engineering industry. The core of geostatistics lies in the modeling and prediction of spatially dependent data through methods such as spatial interpolation (Kriging), semi-variational function analysis, and spatial autocorrelation analysis [9]. In the field of tunnelling, Kriging interpolation plays a pivotal role in predicting and simulating grid models for various parameters. This ensures the reliability and representativeness of the tunnel design, thereby enhancing the efficiency and accuracy of the design process [10,11]. In geotechnical engineering, parameters such as soil bearing capacity, soil density and permeability coefficient are predicted using the Kriging method and semi-variational function method, especially in engineering design under complex geological conditions. The spatial variability of geomechanical parameters is analyzed through geostatistics, which effectively improves the reliability and validity of the indicators [12–15]. In the domain of structural engineering, the semi-variational function has been demonstrated to possess the capacity to quantify the spatial aggregation of crack length and density, thereby providing a quantitative foundation for the development of maintenance strategies [16–18]. In relation to materials, studies have demonstrated that by analyzing the spatial distribution of concrete surface roughness through the semi-variational function, the bonding performance between concrete layers of different ages can be predicted in order to optimise the construction process [19]. Furthermore, when analyzing the compressive strength of asphalt mixtures, the semi-variational function describes the spatial variation of the material's internal porosity or strength gradient, which can then be used to assess the structural reliability [19]. Geostatistics is the scientific discipline that studies the spatial variation and spatial structure of natural phenomena based on the theory of regionalized variables characterized by spatial distribution [20–22]. Conventional statistical research

is confined to the imputation of data, disregarding the spatial distribution of the sample. The research object must be a purely random variable, capable of repetition without limit, and the samples must be independent of each other. It should be noted that the geologic variables will vary depending on the geologic setting and are spatial. This methodological approach is particularly well-suited to the inference of spatial distribution in scenarios where data is limited, such as in the context of pavement inspection, where the health of an entire pavement is predicted from data obtained at a limited number of sampling points. However, at this stage, there are relatively few studies on the cross-border application of geostatistics and NDT of asphalt pavements.

With the increase of reconstruction and expansion projects, how to utilize existing asphalt pavement structure is a great issue faced by engineers and technicians, and how to efficiently and scientifically evaluate the service state of existing asphalt pavement is a problem that researchers must face directly. However, due to systematic differences, data density differences and other issues, researchers more often carry out joint analyses of independent data, and do not form good correlation relationships in the detection process. This paper utilizes the principle of geostatistics to carry out research on existing pavement inspection and evaluation methods based on 3D GPR guidelines, focusing on realizing the interactive inspection of 3D GPR and FWD during the inspection process, which improves the inspection efficiency, reduces the influence of the difference in data density between the two, and provides a new idea for the joint inspection of 3D GPR and FWD.

2. Research Methodology

In this paper, the Guangyun Expressway and the Yangmao Expressway in the Guangdong Province of China are used as the objects of analysis. Three-dimensional GPR is a 21-channel ground-coupled ground-penetrating radar system produced by 3D-Radar in Oslo, Norway. FWD is the Phonix PRI2100 system produced by Carl Bro in Grontmij, Denmark. The 3D GPR is used to detect the cracks of each structural layer and form the crack rate index of each layer, which is calculated as shown in Equation (1). The FWD is used for the detection of deflection index. Since deflection detection requires the use of point measurement, which is often time-consuming and requires the closure of traffic, the detection efficiency is very low; however, the crack rate can be obtained by 3D GPR detection, which does not require the closure of traffic and is more efficient [23–25]. Therefore, this paper proposes to utilize 3D GPR inspection to guide the characteristic road sections according to the crack rate index, then carry out targeted deflection strengthening inspections for the characteristic road sections, and finally extend the deflection inspection results through the principle of geostatistics to enhance the efficiency and effectiveness of the inspection of the in-service pavement structure of the reconstruction and expansion project.

$$\gamma = \frac{l_c}{Area} \times 100 \tag{1}$$

where γ is the crack rate, unit m/100 m^2; l_c is the length of the structural layer cracks in the section, unit m; and $Area$ is the section area, with a section size of 50 m $\times$ 3.75 m, unit m^2.

Firstly, an exploration and analysis of the relationship between crack rate and deflection of asphalt pavement under real traffic volume was conducted. In order to address the effect of spatial density inconsistency, the analysis method of grouped mean in geostatistics was adopted to study the correspondence. Subsequently, the principle of singularity was utilized to analyze the singularity of the crack rate index, and the segmentation method based on the crack rate index was investigated to identify the characteristic road sections with high and low crack rates. The subsequent stage of the research was to carry out the research of deflection detection method based on Kriging interpolation. This involved

analyzing the effect of Kriging interpolation of different dimensions of deflection data and the influence factors of the interpolation effect. In addition, the reasonable spacing of deflection detection by the principle of semi-variable function was analyzed. Finally, the NDT method of existing asphalt pavement based on 3D GPR guidelines was constructed.

3. Basic Relationship Between Cracking Rate and Deflection

The deflection index is a measure of the overall strength of the pavement structure, while the crack rate index of a single structural layer is indicative of the cracking state of that layer. To analyze the relationship between the deflection index and the crack rate index, the surface crack rate of the pavement surface, the crack rate of the bottom of the asphalt structural layer, and the bottom of the cement-stabilized gravel layer are accumulated to form the overall crack rate of the pavement structure, which is calculated as shown in Equation (2). The overall cracking rate and deflection correspondence pattern are illustrated in Figure 1.

$$\gamma_o = \gamma_s + \gamma_a + \gamma_c \tag{2}$$

where γ_o is the overall crack rate of the pavement structure; γ_s is the surface crack rate of the pavement surface; γ_a is the crack rate of the bottom of the asphalt structural layer; and γ_c is the bottom of the cement-stabilized gravel layer.

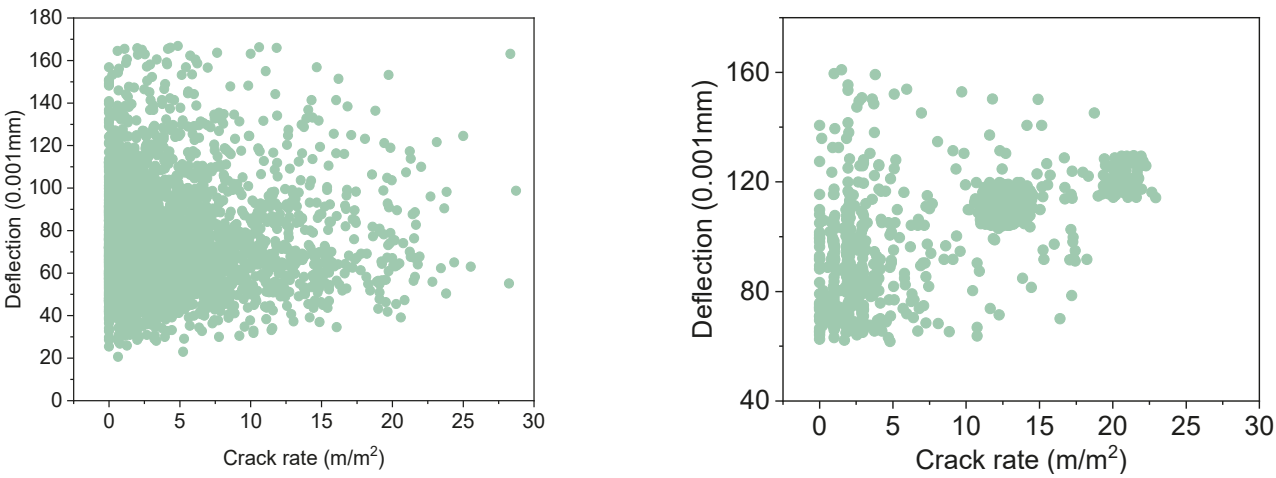

(**a**) Guangyun Expressway (**b**) Yangmao Expressway

Figure 1. Corresponding patterns of crack rate and deflection.

In accordance with the principles of damage mechanics, it is posited that an increase in crack rate corresponds to an increase in deflection. However, as illustrated in Figure 1, a clear correlation between these variables is not evident. The fundamental reason for this discrepancy lies in the nature of the indicators themselves. The crack rate is a regional indicator, whereas the deflection is a point indicator. In the same region, the crack rate indicator remains constant, while the deflection indicator undergoes changes when the detection location is altered. Consequently, the conventional modeling method is unable to effectively establish a model relationship between the crack rate and the deflection. In order to further analyze the correspondence between the crack rate and the deflection, the crack rate index is ranked. Geostatistical data analysis methods are used to calculate the average crack rate and the corresponding average deflection at different intervals. The correspondence between the two is characterized by analyzing the relationship between the average crack rate and the average deflection. It is imperative to acknowledge that disparate grouping spacings will invariably give rise to disparate relationship models. In order to further analyze the model effects established by different grouping spacings,

model analysis was performed for a variety of grouping spacings. The results are shown in Figure 2.

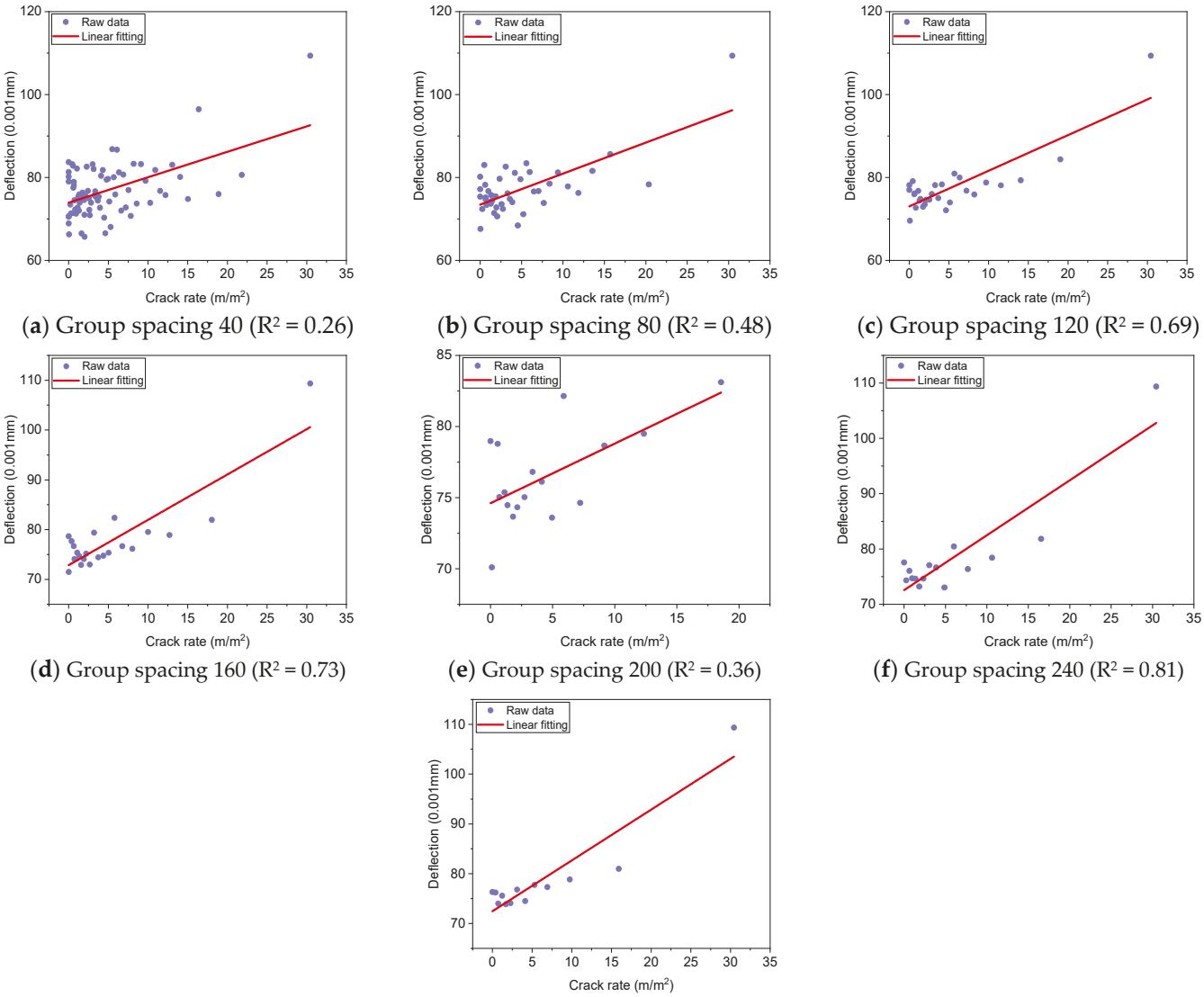

(**a**) Group spacing 40 (R^2 = 0.26) (**b**) Group spacing 80 (R^2 = 0.48) (**c**) Group spacing 120 (R^2 = 0.69)

(**d**) Group spacing 160 (R^2 = 0.73) (**e**) Group spacing 200 (R^2 = 0.36) (**f**) Group spacing 240 (R^2 = 0.81)

(**g**) Group spacing 280 (R^2 = 0.85)

Figure 2. Crack rate and deflection corresponding form—arithmetic mean value (Guangyun Expressway).

As illustrated in Figure 2, with the increase of the group spacing, R^2 values tend to increase. An evident correlation between crack rate and deflection emerges as group spacing is increased. The data demonstrate a positive relationship between deflection and crack rate, exhibiting a notable linear trend. Consequently, a linear model was employed for the fitting analysis, with multiples of 10 designated as the group spacing. The analysis was conducted for various group spacings, and the results are presented in Figures 3 and 4 and Table 1.

As illustrated in Figure 3 and Table 1, the intercept indicators of different subgroups demonstrate a high degree of similarity, with an average intercept value of 74 and a coefficient of variation of only 1%. However, the slope indicators demonstrate significant variations, with an average slope value of 0.60 and a coefficient of variation as high as 35%. The average value of the coefficient of determination R^2 is 0.48, and the coefficient of variation is 58%. The coefficient of determination R^2 indicator reveals that the fitting results vary considerably, and as a whole, they tend to increase with the increase of the

subgroup spacing. According to the fitting results, although there is a large variation in the slope, it can still reflect the positive correlation between crack rate and deflection, with the higher the crack rate, the greater the deflection. According to the fitting results of the coefficient of determination R^2, the data fitting effect is optimal when the group spacing is 280, the intercept is 72.5 and the slope is 1.02.

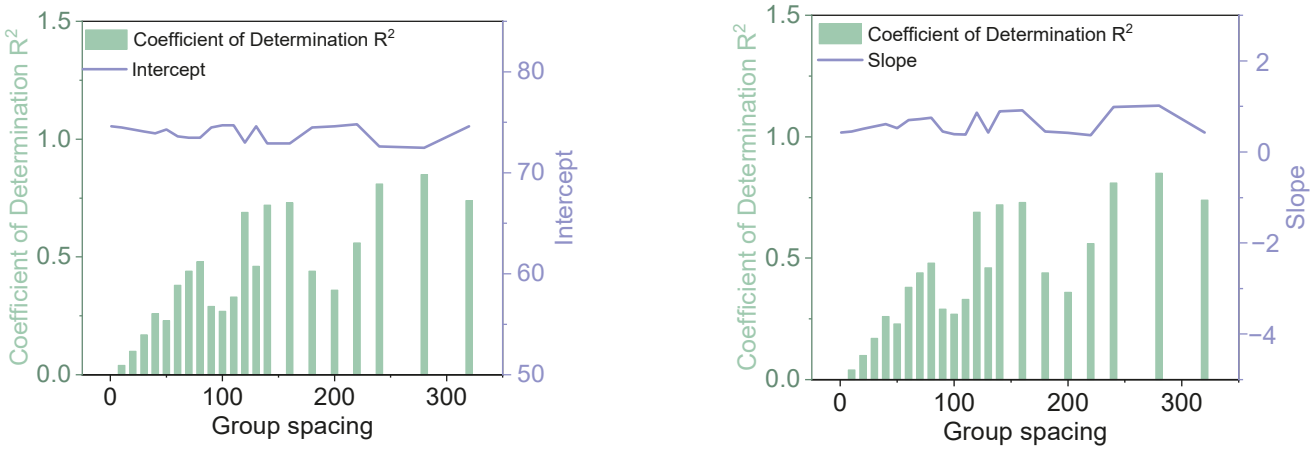

(**a**) Intercept (**b**) Slope

Figure 3. Fitting results of crack rate and deflection grouping (Guangyun Expressway).

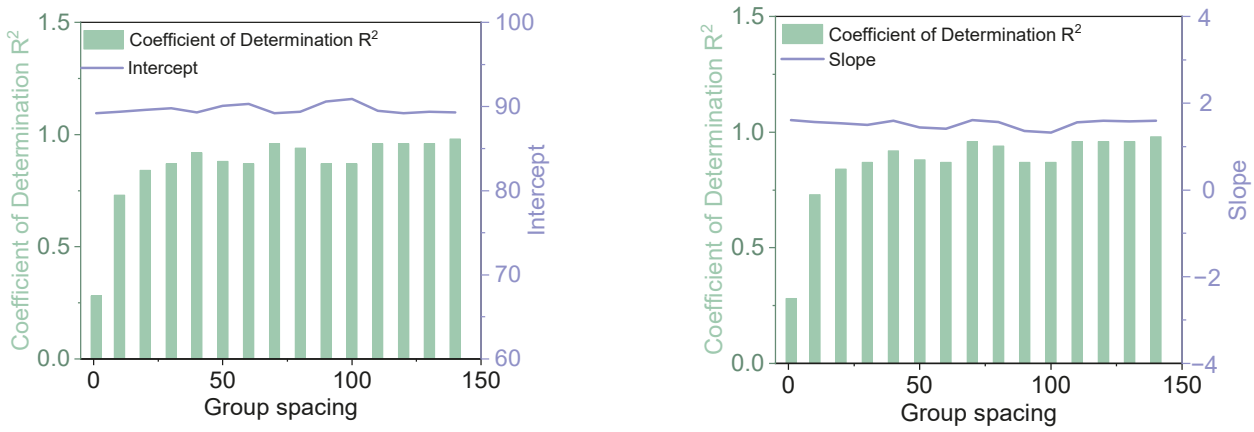

(**a**) Intercept (**b**) Slope

Figure 4. Fitting results of crack rate and deflection grouping (Yangmao Expressway).

Table 1. Fitted effect summary.

Expressway	Parameter	Intercept	Slope	Coefficient of Determination R^2
Guangyun	Mean	74.0	0.60	0.48
	Coefficient of variation	1%	35%	58%
Yangmao	Mean	89.7	1.52	0.9
	Coefficient of variation	1%	6%	19%

As can be seen from Figure 4 and Table 1, there are some differences between the fitting results of the Yangmao Expressway and the Guangyun Expressway. The fitting results of Yangmao Expressway are relatively stable, and its crack rate is also positively correlated with deflection. The data fitting effect is optimal when the group spacing is 140, the intercept is 89.3 and the slope is 1.60.

In summary, the correlation between the deflection and crack rate indicators of the two roads is positive, and the higher the crack rate, the higher the deflection. The slope of the Guangyun Expressway is 1.02, while the slope of Yangmao Expressway is 1.60, which is quite different. The main reason for this difference is that the pavement structures are different. The pavement structure of the Guangyun Expressway consists of a 22 cm asphalt structure layer and a 56 cm cement-stabilized gravel structure layer, while the pavement structure of the Yangmao Expressway consists of a 15 cm asphalt structure layer and a 56 cm cement-stabilized gravel structure layer. Both are typical semi-rigid asphalt pavement structures. Due to the subtropical region, low temperatures are relatively infrequent, and cracking of the pavement structure occurs mainly in the semi-rigid base layer during operation. Since the Guangyun Expressway has a thick asphalt structural layer, if the cement-stabilized gravel layer cracks, the strength of the road structure is more likely to be maintained by the thick asphalt structural layer. However, the strength of the road structure with a thin asphalt structural layer is more likely to be affected by the cracking of the cement-stabilized graded aggregate layer. Therefore, there will be some difference in the slopes of the fitting models of the two roads. However, it is clear that the cracking rate is positively correlated with the deflection index. Therefore, the statistical analysis of the crack rate can be used to characterize the deflection.

4. Characteristic Section Division Based on Crack Rate Guidelines

4.1. Singularity Analysis Algorithm

The basic principle of singularity was first proposed by Professor Cheng Qiuming during his geochemical research, which defined singularity as a phenomenon involving a huge release of energy or a large amount of matter formation in a very small time-space region [26–29]. The traditional density-area fractal model is given by Equation (3) [28,30].

$$\rho(\varepsilon) \simeq c\varepsilon^{\alpha-1} \tag{3}$$

where $\rho(\varepsilon)$ is the density parameter; α is the singularity index, which characterizes the degree of measure singularity; and c is the corresponding local coefficient.

Positive singularity ($\alpha < 1$) indicates that the cracking rate of the road section is relatively high; negative singularity ($\alpha > 1$) indicates that the cracking rate of the road section is relatively low; and no singularity ($\alpha \approx 1$) indicates that the cracking rate of the road section is relatively stable. The smaller the singularity index, the stronger the positive singularity, which can be used to directly spatially locate local abnormal areas and thereby identify the abnormality. The specific algorithm process is as follows:

(1) For any given spatial location, define the shape of the spatial window, with the window size increasing in sequence, such as $\varepsilon_{\min} = \varepsilon_1 < \varepsilon_2 < \cdots < \varepsilon_n = \varepsilon_{\max}$;
(2) Calculate the average crack rate $\rho(\varepsilon_i)$ in each window;
(3) In double logarithmic coordinates, take $\log(\varepsilon_i)$ as the horizontal axis and $\log \rho(\varepsilon_i)$ as the vertical axis, and perform a linear fit to the data to estimate the slope $\alpha - 1$ of the linear model;
(4) repeating steps (1)–(3) by moving the window series to other positions to obtain a map of the spatial distribution of the local singularity index.

4.2. Singularity Index Analysis

Based on the distribution pattern of singularity index in frequency, relevant researchers have proposed a singularity quantile analysis method for separating weak geochemical anomalies [29]. This method fits a normal distribution line, then sets a confidence interval for the residuals, and solves for the intersection points α_1 and α_2 of the singularity index

fitting curve and the confidence interval line to achieve anomaly threshold segmentation. This article utilizes a 99% confidence interval through the normal distribution to restrict the range of the singularity index. An additional polynomial curve is fitted by the singularity index, as demonstrated in Figure 5, represented in blue. Ultimately, the intersection point of the fitted curve with the confidence interval is resolved to ascertain the breakpoint of the singularity index, thereby identifying anomalous data.

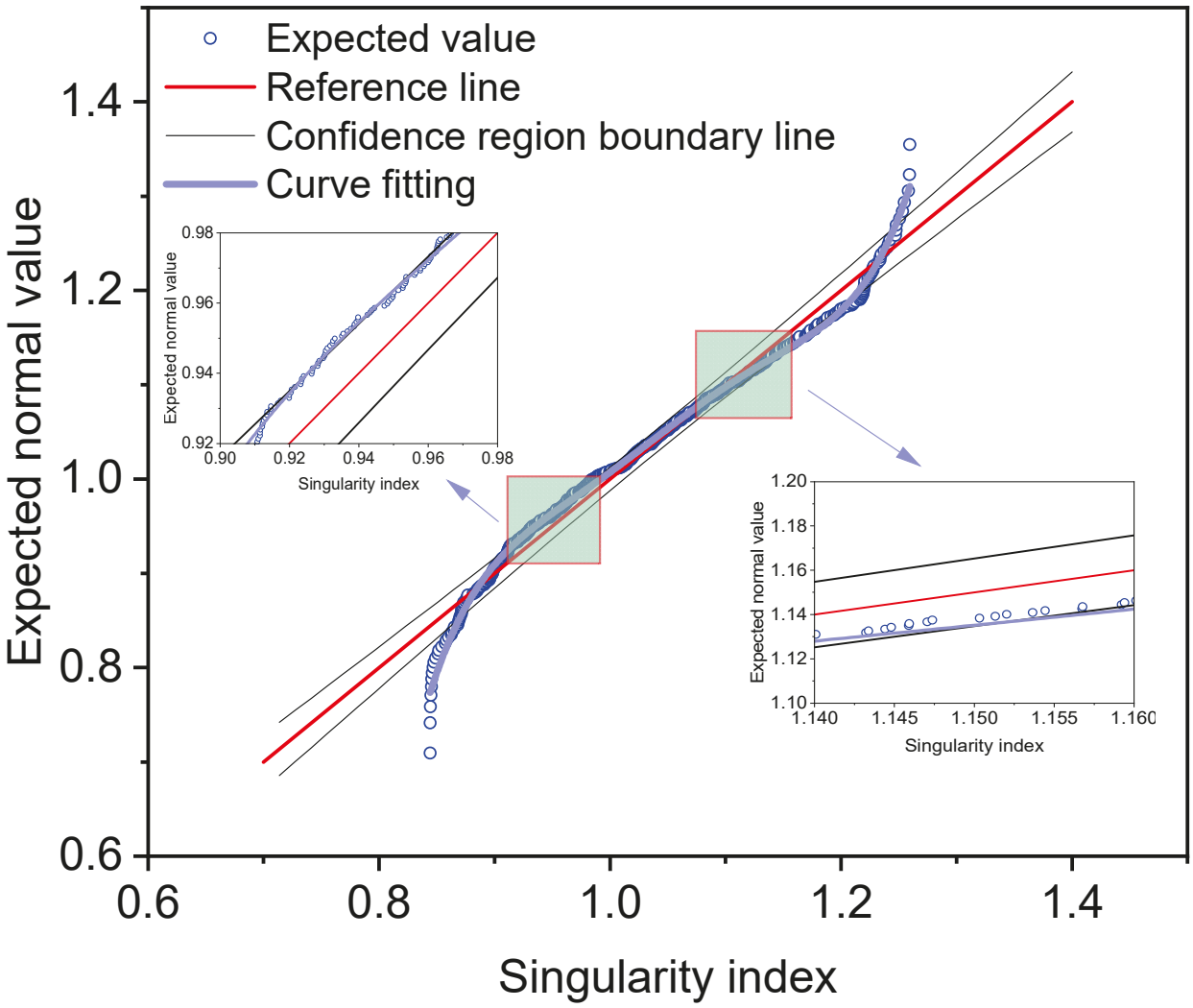

Figure 5. Singularity index analysis.

As illustrated in Figure 5, the intersection point solution indicates that when $\alpha > 1.15$ or $\alpha < 0.94$, the data is considered abnormal, exhibiting either a low crack rate or a high crack rate. To elucidate the impact of the singularity index, the singularity index and crack rate data are plotted for analysis, as depicted in Figure 6. To identify sections exhibiting a high crack rate, the data set with $\alpha < 0.94$ is highlighted in green. As demonstrated in Figure 6, the singularity index is more effective at identifying data points with a high crack rate. However, the distribution of these points is too diffuse, making it impractical to test all of the data for deflection, as this would require the interruption of traffic in the lane. Consequently, it is essential to further segment the characteristic data and select the most indicative segments based on the prevailing conditions.

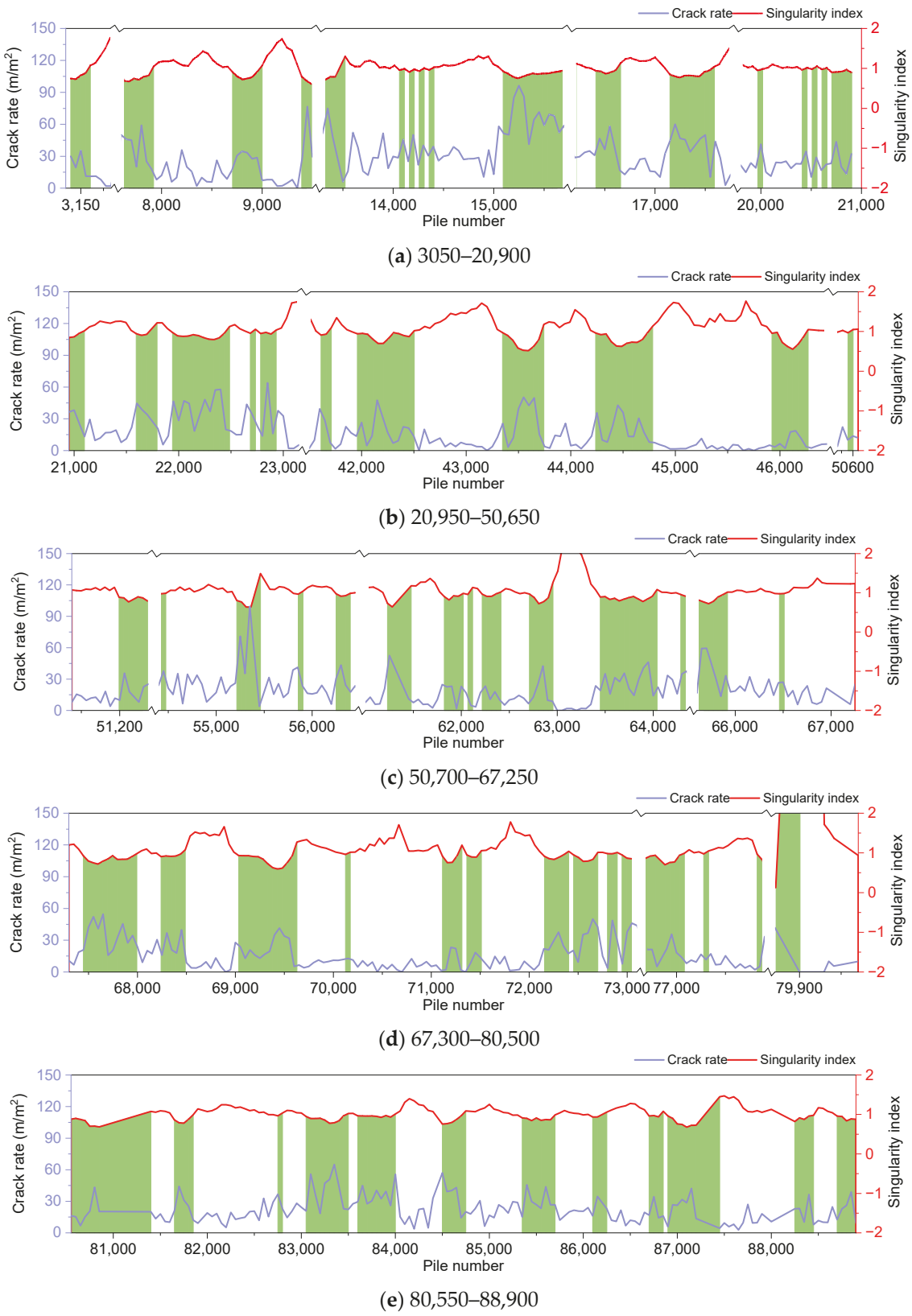

Figure 6. Corresponding relationship between the crack rate and the singularity index.

4.3. Characteristic Sections Division

Given that the maximum length of traffic control on highways is generally limited to 2 km, the length of the detection area is set to 2 km. The number of abnormal data in the detection area is calculated, and the calculation results are shown in Figure 7. Since the

length of the crack rate calculation area is 50 m, there are a total of 40 crack rate indicators in the detection area. When the detection area contains more than 20 (50%) abnormal data, the road section is designated as a characteristic section. As can be seen in Figure 7, 20,400–22,400, 62,050–64,050, 67,450–69,450, 71,150–73,150 and 82,750–84,750 are sections with high crack rates. Similarly, the sections with lower crack rates were analyzed and determined to be sections 13,750–15,700 and 43,750–45,750.

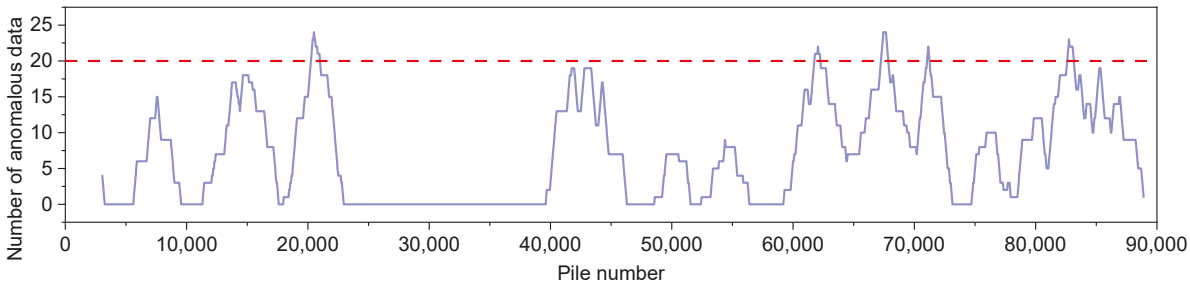

Figure 7. Number of abnormal data (the statistical area starts at the abscissa pile number and extends in the direction of increasing pile number for 2 km).

5. Deflection Detection Method Based on Kriging Interpolation

5.1. Analysis of the Interpolation Effect of Deflection Data in Different Dimensions

Kriging interpolation is a method based on the theory of variogram and structural analysis, which provides a linear unbiased optimal estimate of the values of regionalized variables within a finite region [31–33]. In order to analyze the interpolation effect of different dimensional deflection data, the difference in effect between Kriging interpolation and linear interpolation is compared and analyzed for data from a single-lane, one-way lanes, and two-way lanes.

(1) Single-lane data interpolation analysis

The data in the slow lane and the hard shoulder are used to make interpolation predictions, and the differences in the effects of Kriging interpolation and linear interpolation are compared. The spacing between the data points for the deflection data is 50 m. In order to analyze the prediction effects of Kriging interpolation at different spacings, the data is filtered into five prediction groups with spacings of 100 m, 200 m, 500 m, 1000 m, and 2000 m, and the remaining data is used as the validation group. The schematic diagram is shown in Figure 8. A prediction model is established using the prediction group, and interpolation prediction is performed on the data in the validation group. The interpolation effect of the two different methods is analyzed by comparing the difference between the actual data and the predicted data in the validation group. The results are shown in Figures 9 and 10.

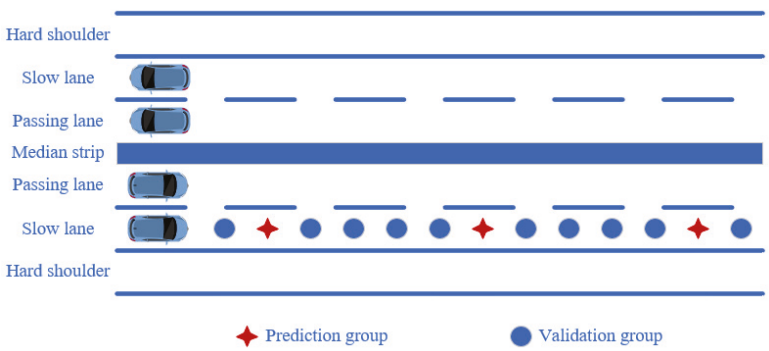

Figure 8. Schematic diagram for analysis of single-lane data.

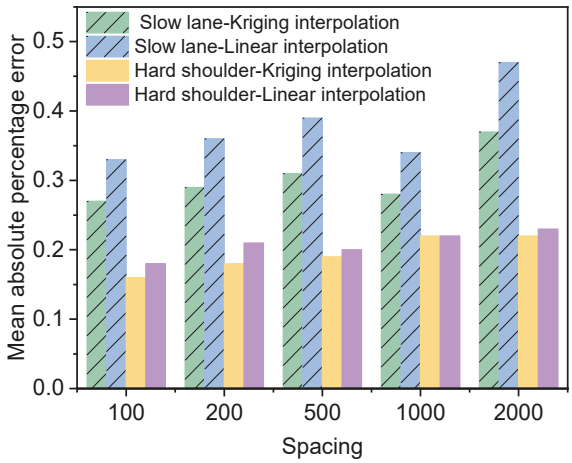

Figure 9. Effect of interpolation of one-lane data.

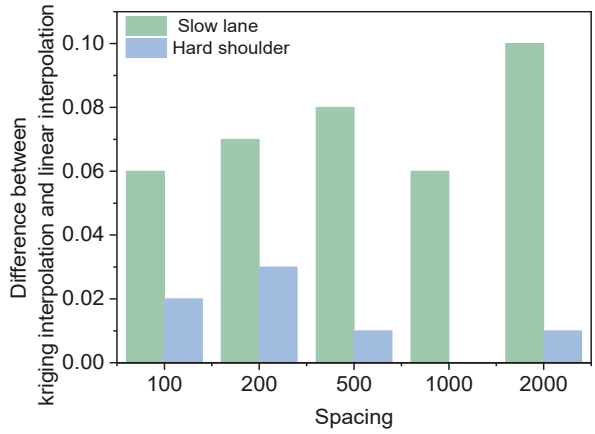

Figure 10. Difference between mean absolute percentage error of Kriging interpolation and linear interpolation.

As demonstrated in Figure 9, there are substantial discrepancies in the mean absolute percentage error of interpolation results in different lanes. The mean absolute percentage error of interpolation in the slow lane is notably higher than that in the hard shoulder, primarily due to the significantly higher coefficient of variation of the deflection in the slow lane compared to the hard shoulder. When data exhibits substantial variation, attaining a satisfactory interpolation outcome becomes challenging. The mean absolute percentage error of Kriging interpolation is consistently smaller than that of linear interpolation, thereby substantiating the superiority of the Kriging interpolation method. As the spacing of the data in the prediction group increases, the mean absolute percentage error of both Kriging and linear interpolation exhibit a tendency to increase. As illustrated in Figure 10, the difference between the mean absolute percentage error of Kriging interpolation and linear interpolation in the slow lane is greater than that in the hard shoulder, suggesting that the Kriging interpolation method may be more effective than the linear interpolation method when the sample data exhibits high variability.

(2) Multi-lane data interpolation analysis

In order to further analyze the effect of Kriging interpolation of multi-lane data, the data of the slow lane and hard shoulder are statistically analyzed. Due to certain deviations in the data correspondence during the actual detection process, in order to further reduce the impact of the correspondence, only the data from 63,000–83,000 are used for the analysis of multi-lane data. To facilitate a comprehensive comparison of the effects of analyzing data from a single-lane, one-way lanes, and two-way lanes, the data was filtered into four

prediction groups with intervals of 100 m, 200 m, 500 m, and 1000 m. The remaining data from the slow lane on the right were designated as the verification group. The schematic diagram is shown in Figure 11. The results of the interpolation are illustrated in Figure 12.

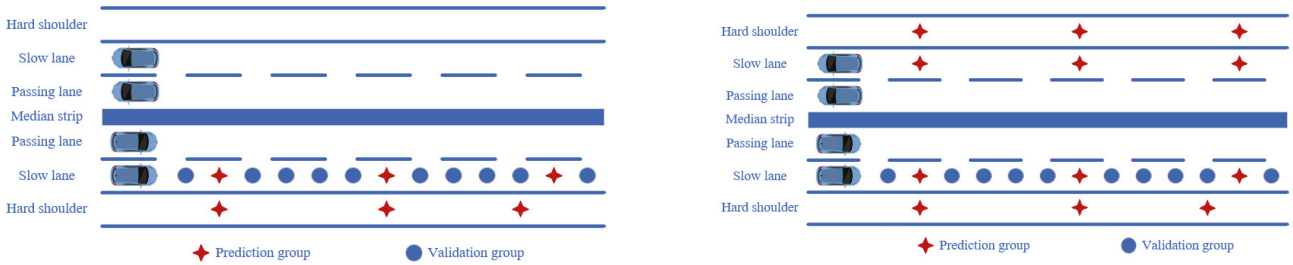

(**a**) Schematic diagram of one-way lanes (**b**) Schematic diagram of two-way lanes

Figure 11. Schematic diagram of data of different dimensions.

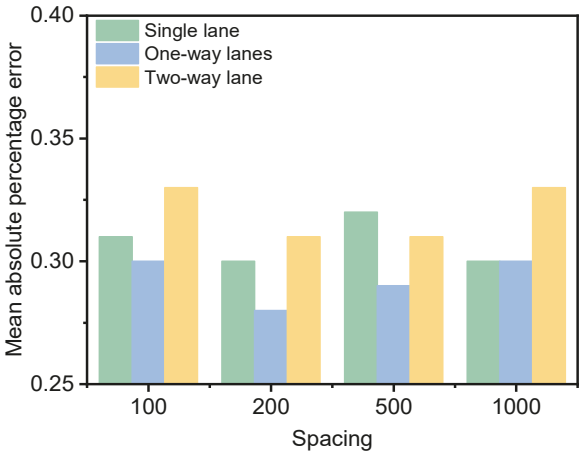

Figure 12. Interpolation results for data with different dimensions.

As can be seen from Figure 12, the Kriging interpolation effect is optimal for one-way lanes. The main reason for this is that the pavement structure layer of one-way lanes is constructed at the same time, and the loading effects of different lanes are relatively stable. The deflection indicators of different lanes have a relatively stable relationship and are relatively predictable. In addition, the predictive effect of the data matrix is inevitably better than that of a single lane, but the construction time of the road surface structure of a two-way lane is different, and the initial damage is inevitably inconsistent. The spatial relationship of the data is relatively weak, so using two-way lane data for Kriging interpolation is not the best choice.

5.2. The Impact of Data Variability on Kriging Interpolation

There is a significant difference in the mean absolute percentage error of the interpolation of the slow lane, hard shoulder, one-way lane and two-way lane Kriging. Even if the distance of the predicted group data is 100 m, the mean absolute percentage error of the slow lane interpolation reaches 0.26. However, the mean absolute percentage error of the hard shoulder interpolation is only 0.16, and there is a significant difference in the interpolation effect between the slow lane and the hard shoulder. In order to further analyze the main reasons for the differences, the coefficients of variation of the prediction group, the coefficients of variation of the validation group and the mean absolute percentage error of the interpolation results were analyzed in correspondence. The results are presented in Figure 13.

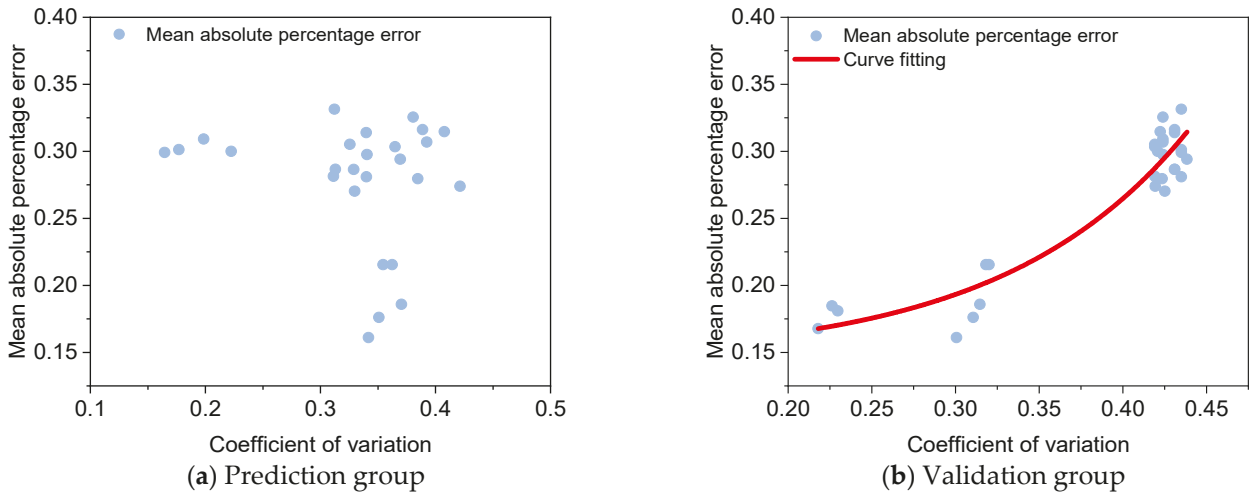

Figure 13. Coefficient of variation and Kriging interpolation mean absolute percentage error.

As can be seen from Figure 13, the coefficient of variation of the prediction group's data has no direct relationship with the effect of Kriging interpolation, but there is an obvious non-linear relationship between the coefficient of variation of the validation group and the effect of Kriging interpolation; the fitting model is shown in Equation (4), and the coefficient of determination R^2 reaches 0.89. In summary, it can be seen that the effect of Kriging interpolation and the variability phenomenon of the data itself are closely related. The Kriging interpolation method cannot predict the sudden variation phenomenon, but for continuous data, the variation can be effectively predicted. If the data itself varies more, the effect of Kriging interpolation will be greatly reduced.

$$\psi = 0.00324\, e^{\frac{X}{0.111}} + 0.145 \tag{4}$$

where ψ is the mean absolute percentage error of Kriging interpolation; X is the coefficient of variation of the validation group data.

5.3. Detection Spacing Analysis Based on Kriging Interpolation

The detection spacing that is too long may not reflect the deflection trend, while detection spacing that is too short will inevitably increase the test time. Therefore, how to reasonably determine the detection spacing for deflection is a key issue in the evaluation of old roads. Kriging interpolation minimises the prediction error mainly by fitting a semi-variogram function. The semi-variogram function is a continuous function used to describe spatial variation, reflecting the changing relationship between indicators and observations at different distances [34–37]. The specific formula is given in Equation (5), and a schematic diagram of the model is shown in Figure 14. Variable range (a) is the abscissa value when the value of the semi-variation function stabilises. If the detection spacing is within the variable range, the smaller the distance, the greater the spatial autocorrelation, and the greater the accuracy of the interpolation; if the detection spacing is greater than the variance, the regionalisation variable has no spatial autocorrelation, and the accuracy of the interpolation cannot be guaranteed. Therefore, the basic principle of interpolation can be used to determine a reasonable detection distance for deflection. The results of the semi-variogram fit to the deflection data on different expressways are shown in Table 2.

$$r(h) = \frac{1}{2N(h)} \sum_{i=1}^{N(h)} [Z(X_i) - Z(X_i + h)]^2 \tag{5}$$

where $r(h)$ is the semi-variogram function; h is the distance between sample points in the spatial domain, known as the step size; $N(h)$ is the number of sample points at a distance of h; and $Z(X_i)$ and $Z(X_i + h)$ are the measured values of the regionalized variable $Z(X)$ at the spatial positions X_i and $X_i + h$, respectively.

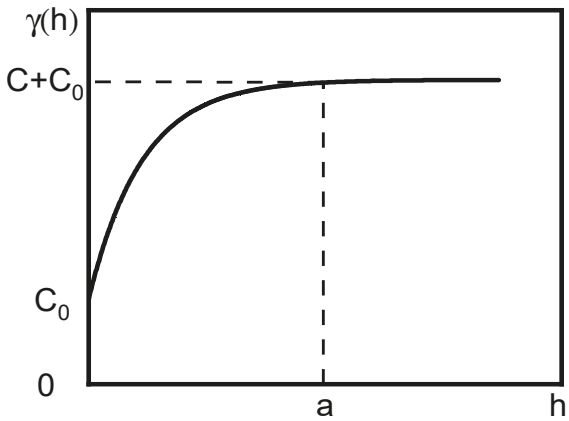

Figure 14. Semi-variogram model (C_0 is the block gold value; C_0+C is the abutment value; C is the partial abutment value; a is the variable range).

Table 2. Results of the fitting of the semi-variogram function to the deflection data.

Traffic Lane	Direction	Guangyun Expressway	Yangmao Expressway
Slow lane	Left	375	511
	Right	105	366
Hard shoulder	Left	2580	2668
	Right	1464	5590

Table 2 shows that the variable range of the slow lane, which is subjected to vehicle loads, is relatively small, while the variable range of the hard shoulder, which is not subjected to vehicle loads, is relatively large. According to the above statistical results, when performing deflection detection, if the aim is to obtain detailed deflection changes, the sampling interval for the deflection of the slow lane should not be greater than 100 m, and the sampling interval for the deflection of the hard shoulder should not be greater than 1400 m. Deflection data within the above intervals can be obtained by Kriging interpolation to further improve the efficiency of obtaining deflection data.

6. Non-Destructive Testing Method Based on the Principle of Geostatistics

In the case of expressways that are open to traffic, it is inevitable that deflection measurements on the slow lane will require lane closures. For reasons of safety, the traffic management department permits a one-time lane closure of 2 km, which consequently results in an inefficient testing process. However, for hard shoulders that are not open to traffic, testing can be carried out with safety protection vehicles. When there is a high risk of interrupting lane traffic, 3D GPR can be used to detect crack rate without interrupting traffic and identify characteristic road sections based on the rate of cracks. Deflection detection is carried out on characteristic road sections of the slow lane, while fixed interval deflection detection is carried out on the hard shoulder. The Kriging interpolation method is used to predict deflection analysis for the entire road section, which greatly reduces the risk of interrupting traffic while improving detection efficiency.

The analysis section is 62,000–74,000. According to the above characteristic section division results, the slow lane selects the characteristic section 62,050–64,050 with a high

crack rate as the deflection detection area, and the detection spacing is 50 m. In order to ensure the effectiveness of the slow lane Kriging interpolation, the entire hard shoulder is deflection detected with a spacing of 200 m. The above test data is used as the predicted group data. To verify the accuracy of the prediction results, deflection tests were carried out at intervals of 50 m along the remaining sections of the slow lane, and the test data was used as a verification group. The interpolation results are shown in Figure 15. The mean absolute error of the Kriging interpolation result is 22%. The interpolation result basically meets the needs of overall deflection analysis. As can be seen from Figure 15, the data points with large deviations in the Kriging interpolation results all appear in the area where the deflection results suddenly change, once again verifying the impact of the variability of the verification group data on the Kriging interpolation effect.

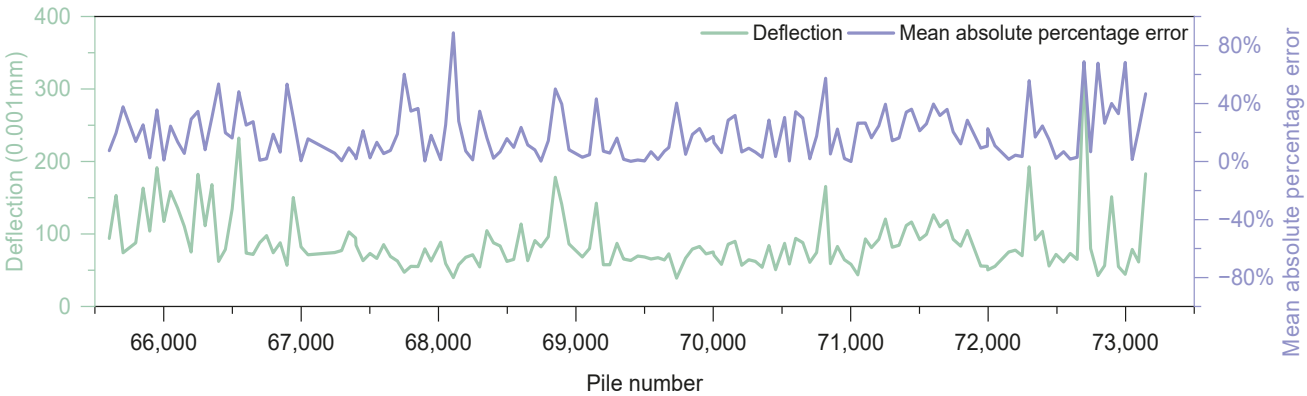

Figure 15. Validation group interpolation results.

7. Conclusions

The NDT method based on geostatistics mainly uses 3D GPR to detect the crack rate of the pavement structure layer and determines the characteristic sections by the crack rate. Targeted deflection testing is carried out for the characteristic sections, and Kriging interpolation technology is used to predict the remaining deflection data. This method can quickly and efficiently obtain the trend of deflection index changes in the whole area when the testing conditions are limited; at the same time, the deflection data of the whole area can also be obtained by Kriging interpolation. The research process led to the following conclusions.

(1) A positive correlation has been observed between the crack rate and the deflection index; however, the relationship model for different road surface structures varies. It has been demonstrated that the thickness of the asphalt mixture structure layer has a direct impact on the deflection, with greater thickness leading to a reduction in the effect of the crack rate on deflection.

(2) The singularity index principle has been demonstrated to be an effective method for identifying the characteristic data of the crack rate. Furthermore, the data analysis method that utilizes fixed intervals has been shown to identify characteristic sections with high or low crack rates.

(3) Kriging interpolation is more effective than linear interpolation for predicting deflection data. The interpolation effect is limited by the variation of the data being interpolated. Kriging interpolation is most effective when the original data is one-way lanes matrix.

(4) When the detection spacing is maintained within the variable range index, Kriging interpolation can predict deflection with a limited amount of deflection data. This

analysis can be used to examine the trend of deflection index changes when the detection conditions are limited.

Although the research and application of geostatistics have been carried out in this paper, there is no in-depth analysis on the interpolation prediction of deflection. The variation in the deflection value is also one of the reasons for the large deviation of Kriging interpolation. Further research is needed on how to further improve the effect of interpolation. The application of geostatistics principles to other non-destructive testing techniques is also the next step that needs to be expanded. At the same time, although the method of geostatistics is mainly applied to interpolation prediction, the application of the results after interpolation is not discussed, and the application of the data after interpolation can be further studied in the future.

Author Contributions: Conceptualization, D.W.; methodology, D.W.; software, W.Z.; validation, D.W. and M.F.; formal analysis, W.X.; investigation, W.Z.; resources, W.X.; data curation, W.Z.; writing—original draft preparation, D.W. and C.L.; writing—review and editing, D.W. and C.L.; visualization, C.L.; supervision, C.L.; project administration, D.W.; funding acquisition, M.F. All authors have read and agreed to the published version of the manuscript.

Funding: This research was funded by the Natural Science Fund of Guangdong Province, grant number 2019A1515011965, and Natural Science Foundation of China, grant number 51808228.

Institutional Review Board Statement: Not applicable.

Informed Consent Statement: Not applicable.

Data Availability Statement: The original contributions presented in this study are included in the article. Further inquiries can be directed to the corresponding author.

Acknowledgments: The authors gratefully acknowledge all those who have helped.

Conflicts of Interest: Chuanxi Luo, Wenting Zhang and Wenjie Xie were employed by the Xiaoning Institute of Roadway Engineering, Guangzhou 510000, China. Meng Fu was employed by the Guangdong Communication Planning & Design Institute Group Co., Ltd., Guangzhou 510000, China. The remaining author declare that the research was conducted in the absence of any commercial or financial relationships that could be construed as a potential conflict of interest.

References

1. Baltrušaitis, A.; Vaitkus, A.; Židanavičiūtė, J. Asphalt Pavement Compaction Control: Relevance of Laboratory and Non-Destructive Testing Methods of Density. *Balt. J. Road Bridg. Eng.* **2022**, *17*, 143–166. [CrossRef]
2. Ziari, H.; Behbahani, H.; Izadi, A.; Divandary, H. Field Evaluation of Nondestructive Tests in Measuring the Pavement Layers Density. *J. Appl. Sci.* **2010**, *10*, 3091–3097. [CrossRef]
3. Huang, Z.; Xu, G.; Zhang, X.; Zang, B.; Yu, H. Three-dimensional ground-penetrating radar-based feature point tensor voting for semi-rigid base asphalt pavement crack detection. *Dev. Built Environ.* **2025**, *21*, 100591. [CrossRef]
4. Liu, H.; Zheng, J.; Yu, J.; Xiong, C.; Li, W.; Deng, J. Clustering of Asphalt Pavement Maintenance Sections Based on 3D Ground-Penetrating Radar and Principal Component Techniques. *Buildings* **2023**, *13*, 1752. [CrossRef]
5. Zhu, H.; Wei, G.; Ma, D.; Yu, X.; Dong, C. Research on the detection and identification method of internal cracks in semi-rigid base asphalt pavement based on three-dimensional ground penetrating radar. *Measurement* **2025**, *244*, 116486. [CrossRef]
6. Marecos, V.; Fontul, S.; Solla, M.; Antunes, M.d.L. Transport infrastructures assessment using multiple GPR configurations and FWD. *MATEC Web Conf.* **2018**, *211*, 12005. [CrossRef]
7. Elseicy, A.; Alonso-Díaz, A.; Solla, M.; Rasol, M.; Santos-Assunçao, S. Combined Use of GPR and Other NDTs for Road Pavement Assessment: An Overview. *Remote Sens.* **2022**, *14*, 4336. [CrossRef]
8. Zhao, W.; Yang, Q.; Wu, W.; Liu, J. Improving the accuracy of pavement structural quality assessment by correcting numerical hypothetical model of modulus Back-Calculation through GPR. *Constr. Build. Mater.* **2022**, *333*, 127422. [CrossRef]
9. Oliveira, C.E.A.; Tinôco, I.d.F.F.; Damasceno, F.A.; de Oliveira, V.C.; Ferraz, G.A.e.S.; de Sousa, F.C.; Andrade, R.R.; Barbari, M. Mapping of the Thermal Microenvironment for Dairy Cows in an Open Compost-Bedded Pack Barn System with Positive-Pressure Ventilation. *Animals* **2022**, *12*, 2055. [CrossRef]

10. Chen, H.; Su, Y.; Wei, R.; Jiang, C. Spatial interpolation-based method for tunnel lighting quality assessment. In Proceedings of the International Conference on Smart Transportation and City Engineering (STCE 2023), Chongqing, China, 16–18 December 2023; Proceedings of SPIE, 2024; p. 13018D.
11. Luo, Y.; Chen, J.; Wang, M. Calculation method of tunnel portal temperature based on spatial interpolation theory. *China Railw. Sci.* **2010**, *31*, 42–46.
12. Huang, D.; Yao, Q.; Zhang, R. Krigings over space and time based on latent low-dimensional structures. *Sci. China Math.* **2021**, *64*, 823–848. [CrossRef]
13. Liu, J.; Liu, J.; Li, Z.; Hou, X.; Dai, G. Estimating CPT Parameters at Unsampled Locations Based on Kriging Interpolation Method. *Appl. Sci.* **2021**, *11*, 11264. [CrossRef]
14. Miao, C.; Wang, Y. Interpolation of non-stationary geo-data using Kriging with sparse representation of covariance function. *Comput. Geotech.* **2024**, *169*, 106183. [CrossRef]
15. Muhsin, D.; Shakir, R.R. Evaluation CPT based soil classification at particular locations using Kriging method. *AIP Conf. Proc.* **2024**, *2864*, 030022.
16. Gomez-Cardenas, C.; Sbartaï, Z.; Balayssac, J.; Garnier, V.; Breysse, D. New optimization algorithm for optimal spatial sampling during non-destructive testing of concrete structures. *Eng. Struct.* **2015**, *88*, 92–99. [CrossRef]
17. McLean, P.; Léger, P.; Tinawi, R. Post-processing of finite element stress fields using dual kriging based methods for structural analysis of concrete dams. *Finite Elements Anal. Des.* **2006**, *42*, 532–546. [CrossRef]
18. Wu, R.-J.; Xia, J.; Chen, K.-Y.; Chen, J.-J.; Liu, Q.-F.; Jin, W.-L. Spatiotemporal interpolation of surface chloride content for marine RC structures based on non-uniform spatiotemporal Kriging interpolation method. *Struct. Saf.* **2023**, *103*, 102329. [CrossRef]
19. Kozubal, J.; Wróblewski, R.; Muszyński, Z.; Wyjadłowski, M.; Stróżyk, J. Non-Deterministic Assessment of Surface Roughness as Bond Strength Parameters between Concrete Layers Cast at Different Ages. *Materials* **2020**, *13*, 2542. [CrossRef]
20. Hu, L.Y.; Chugunova, T. Multiple-point geostatistics for modeling subsurface heterogeneity: A comprehensive review. *Water Resour. Res.* **2008**, *44*, 2276–2283. [CrossRef]
21. Sun, H.-Q.; Li, L.; Gao, J.-Q. Simulation of Spatial Distribution of Urban Surface Water Quality by Geostatistics. In Proceedings of the International Conference on Information Technology for Manufacturing Systems (ITMS 2011), Shanghai, China, 7–8 May 2011.
22. Tartakovsky, D.M.; Wohlberg, B.; Guadagnini, A. Nearest-neighbor classification for facies delineation. *Water Resour. Res.* **2007**, *43*, W07201. [CrossRef]
23. Ling, J.; Qian, R. Critical Technical Problems of 3D GPR Road Cavity Detection Based on Vast Field Experiment Data Analysis. *J. Phys. Conf. Ser.* **2023**, *2651*, 012037. [CrossRef]
24. Liu, Z.; Wu, W.; Gu, X.; Li, S.; Wang, L.; Zhang, T. Application of Combining YOLO Models and 3D GPR Images in Road Detection and Maintenance. *Remote Sens.* **2021**, *13*, 1081. [CrossRef]
25. Zhang, B.; Cheng, H.; Zhong, Y.; Tao, X.; Li, G.; Xu, S. Automatic quantitative recognition method for vertical concealed cracks in asphalt pavement based on feature pixel points and 3D reconstructions. *Measurement* **2023**, *220*, 113296. [CrossRef]
26. Ali, K.; Cheng, Q.; Chen, Z. Multifractal power spectrum and singularity analysis for modelling stream sediment geochemical distribution patterns to identify anomalies related to gold mineralization in Yunnan Province, South China. *Geochem. Explor. Environ. Anal.* **2007**, *7*, 293–301. [CrossRef]
27. Cheng, Q. Multifractal interpolation method for spatial data with singularities. *J. South. Afr. Inst. Min. Met.* **2015**, *115*, 235–245. [CrossRef]
28. Cheng, Q.; Li, L.; Wang, L. Characterization of peak flow events with local singularity method. *Nonlinear Process. Geophys.* **2009**, *16*, 503–513. [CrossRef]
29. Liu, Y.; Zhou, K.; Cheng, Q. A new method for geochemical anomaly separation based on the distribution patterns of singularity indices. *Comput. Geosci.* **2017**, *105*, 139–147. [CrossRef]
30. Cheng, Q. Singularity theory and methods for mapping geochemical anomalies caused by buried sources and for predicting undiscovered mineral deposits in covered areas. *J. Geochem. Explor.* **2012**, *122*, 55–70. [CrossRef]
31. Asa, E.; Saafi, M.; Membah, J.; Billa, A. Comparison of Linear and Nonlinear Kriging Methods for Characterization and Interpolation of Soil Data. *J. Comput. Civ. Eng.* **2012**, *26*, 11–18. [CrossRef]
32. Lu, Y.; Wang, L.; Qiu, A.; Yong, C.; Zhao, Y.Y. Kriging interpolation method based on semi-supervised learning. *Comput. Eng. Appl.* **2018**, *54*, 265–270.
33. Nguyen, X.T.; Nguyen, B.T.; Do, K.P.; Bui, Q.H.; Nguyen, T.N.T.; Vuong, V.Q.; Le, T.H. Spatial Interpolation of Meteorologic Variables in Vietnam using the Kriging Method. *J. Inf. Process. Syst.* **2015**, *11*, 134–147.
34. Chen, H.; Fang, F.; Zhang, J.; Wang, Y.; Lu, J.; Cai, B.; Su, C. The spatial variability of tobacco's water-soluble total sugar content and soil fertility factor in tobacco planting fields in central Henan Province. *Proc. SPIE* **2024**, *12988*, 129880U.
35. Karp, F.H.S.; Adamchuk, V.; Dutilleul, P.; Melnitchouck, A. Comparative study of interpolation methods for low-density sampling. *Precis. Agric.* **2024**, *25*, 2776–2800. [CrossRef]

36. Yan, J.-X.; Li, J.-J.; Li, H.-J.; Zhang, Y.-H. Studies on spatial heterogeneity of soil respiration in a subalpine meadow. *Huan Jing Ke Xue Huanjing Kexue* **2013**, *34*, 3992–3999.
37. Zhao, Y.; Shi, H.; Miao, Q.; Yang, S.; Hu, Z.; Hou, C.; Yu, C.; Yan, Y. Analysis of Spatial and Temporal Variability and Coupling Relationship of Soil Water and Salt in Cultivated and Wasteland at Branch Canal Scale in the Hetao Irrigation District. *Agronomy* **2023**, *13*, 2367. [CrossRef]

Disclaimer/Publisher's Note: The statements, opinions and data contained in all publications are solely those of the individual author(s) and contributor(s) and not of MDPI and/or the editor(s). MDPI and/or the editor(s) disclaim responsibility for any injury to people or property resulting from any ideas, methods, instructions or products referred to in the content.

materials

MDPI

Article

Laboratory Investigation of Packing Characteristics and Mechanical Performance of Aggregate Blend

Weixiao Yu [1], Yun Li [2], Zhipeng Liang [2], Jiaxi Wu [1], Sudi Wang [3,*] and Yinghao Miao [1,*]

[1] National Center for Materials Service Safety, University of Science and Technology Beijing, Beijing 100083, China; yuweixiao@xs.ustb.edu.cn (W.Y.); wujiaxi94520@163.com (J.W.)
[2] Beijing Transportation Infrastructure Construction Project Management Center, Beijing 100053, China; liyun88930@foxmail.com (Y.L.); zhipengliang@126.com (Z.L.)
[3] Research Institute of Highway Ministry of Transport, Beijing 100088, China
* Correspondence: sd.wang@rioh.cn (S.W.); miaoyinghao@ustb.edu.cn (Y.M.)

Abstract

Aggregates are the main material forming the skeleton structure of asphalt mixtures and are of great importance to resist external load for asphalt pavement. This study analyzed the packing characteristics and mechanical performance of aggregate blend to provide a reference for improving the bearing capacity of asphalt mixtures. The single-size, two-size, and multi-size aggregate blends were chosen to conduct the laboratory packing and California bearing ratio (CBR) tests. Six particle sizes were selected to design the single-size aggregate blends. Six size combinations were included and various mass ratios were considered for each size combination in the two-size aggregate blends. The multi-size aggregate blends were designed through the gradually filling method according to stone matrix asphalt with a nominal maximum particle size (NMPS) of 16 mm (SMA16) and dense asphalt concrete with an NMPS of 26.5 mm (AC25). The packing characteristics of the blends were quantified by the air voids and the percentage of contribution to the packing volume (*PCPV*). The mechanical performance of the blends was analyzed by the CBR value. The relationship between packing characteristics and mechanical performance was explored by data fitting. The results showed that the particle size and the size ratio have an effect on the packing characteristics and mechanical performance of aggregate blend. The smaller the particle size, the larger the air void of the blend. The blends composed of larger particles have better load bearing capacity than those composed of smaller particles. The larger the particle size ratio, the greater the air void of the blend and the weaker the load bearing capacity. The particles smaller than 1.18 mm and those smaller than 0.3 mm in AC25 mainly play a role in filling the voids and have little contribution to the load bearing. There is a certain correlation between the packing characteristics and mechanical performance of aggregate blend.

Keywords: aggregate blend; packing characteristics; mechanical performance; California bearing ratio

1. Introduction

Aggregates are the main material forming the skeleton structure of asphalt mixture and resisting external load [1]. Aggregate packing characteristics have a significant influence on the skeleton structure and the anti-deformation ability of asphalt mixtures [2,3]. Enhancing the packing degree of aggregate particles contributes to improving the engineering properties of paving materials [4]. Asphalt mixture is a multiphase material composed

of coarse aggregates, fine aggregates, fillers, asphalt binders, and air voids. The volume parameters of asphalt mixtures are determined by the packed aggregates and usually applied to instruct the composition design [5]. Therefore, it is necessary to investigate the packing characteristics and mechanical performance of aggregate blend to provide a reference for improving the performance and optimizing the design method for asphalt mixture.

Traditional asphalt mixture gradation design is mainly based on the power function curve [6]. This method can achieve the densest packing and maximum density of aggregates, but it is unable to ensure the anti-rutting performance of asphalt mixtures. Several researchers attempted to conduct the design of aggregate blend by packing test and macroscopic volume parameters. The Bailey method concluded that the critical size of coarse aggregate and fine aggregate is 0.22 times of the nominal maximum aggregate size (NMAS) through the geometric packing model of spheres [7]. Weymouth [8] proposed particle interfering theory and developed the calculation method of aggregate gradation for cement concrete to improve workability. Kim et al. [9–11] proposed a dominant aggregate size range (DASR) model to evaluate the composition features of aggregate blends. The method suggested that the voids formed by DASR particles should be filled by small particles and asphalt mastics. Guarin [12] determined the voids between DASR particles based on particle packing theory and proposed an interference coefficient and interference particle size range. Miao et al. [13] defined the percentage of contribution to the packing volume (PCPV) index to quantify the packing function of particles in packed aggregate blend. They also analyzed the effect of particle size and morphology on packing characteristics of aggregates [14]. The results showed that the packing function of particles is decided by both particle size and the composition of particles with different sizes. In summary, the above research mainly conducts geometric model-based theoretical analysis, lacking attention to the laboratory performance of aggregate blends.

The digital image processing (DIP) technique provides another way to evaluate the packing characteristics of aggregate blend. Shi et al. [15] obtained the meso-structural evaluation indicators of coarse aggregate main skeleton and asphalt mortar interference by DIP technique. The results showed that the number of contact points and pore cells within the asphalt mixture increase, interference coefficient decreases, and skeleton rate increases gradually under the action of loads. Cai et al. [16] characterized the asphalt mixture skeleton under various cycles of compaction repetitions by coarse aggregate contact points, aggregate inclination, and some other indexes. Xing et al. [17] proposed a skeleton filling system evaluation method of asphalt mixture based on the compressible packing model and industrial computed tomography (CT). Wang et al. [18] found that gradation types have a significant impact on average contact number and internal structure index of asphalt mixtures. Sun et al. [19] evaluated the homogeneity of asphalt mixture based on a digital image processing technique and stereology theory. The results indicated that a decrease in the nominal maximum aggregate size and a finer aggregate gradation can improve the homogeneity of asphalt mixtures. Moreover, some other indicators describing aggregate contact can also be used to evaluate the packing characteristic, such as contact point number [20,21], co-ordination number [22], and the distribution of air voids [23]. In summary, it is feasible to analyze the packing characteristics using DIP technique. However, the method for obtaining the sectional image of asphalt mixture is complicated and costly. In addition, the analysis of packing characteristics is not comprehensive enough.

The discrete element method (DEM) is also usually used to study the packing characteristics of aggregate blend. Xing et al. [24] studied the skeleton filling system of asphalt mixture and found that the variation coefficient of contact force of asphalt mortar with low filling coefficient is larger and the localization phenomenon is more serious. Shen et al. [25] investigated the effect of particle size on the packing of aggregate particles based on DEM

method. The results showed that aggregate size distribution played a significant role in the packing characteristics, affecting both volumetrics and the contact characteristics of a packed structure. Chen et al. [26] analyzed the voids content of unbound aggregate blend under dry-rodded condition to evaluate the development of aggregate packing in porous asphalt mixture. Miao et al. [27] investigated the function of different-sized particles in packed aggregate blend using DEM method and found that the main function conversion particle size is 2.36 mm for SMA-16 and 4.75 mm for AC-25. Kusumawardani et al. [28] studied the packing conditions of unbound aggregate blends and porous asphalt mixture by nine aggregate gradations with variations in 2.36–4.75 mm and 6.3–9.5 mm fractions. The results showed that 6.3–9.5 mm aggregates have little influence on the aggregate packing structure, while 2.36–4.75 mm aggregates have obvious influence on it. In summary, many researchers mainly focus on the packing characteristics of aggregate blend and the factors affecting packing characteristics from macroscopic and mesoscopic views (macroscopic and mesoscopic views refer to the performance of mixtures and the features of aggregates in mixtures, respectively), which contributes to fully understanding the load transfer mechanism. However, little attention has been paid to the relationship between the packing characteristics and mechanical characteristics of aggregate blends.

The objective of this study is to analyze the effect of packing characteristics of aggregate blend on its mechanical performance. The single-size, two-size, and multi-size aggregate blends were selected to conduct the packing and California bearing ratio (CBR) tests. The packing characteristics of the blends were quantified by the air voids and the packing volume. The mechanical performance of the blends was analyzed by the CBR value. The relationship between packing characteristics and mechanical performance were explored by data fitting. This study can provide a reference for improving the performance and optimizing the design method for asphalt mixture.

2. Materials and Methods

2.1. Materials

The crushed stone, manufactured sand, and limestone mineral powder were, respectively, selected as coarse aggregates, fine aggregates, and filler to perform the laboratory tests. Figure 1 depicts the selected aggregates. The properties of different-sized aggregates and filler were determined according to the Chinese specification "Test Methods of Aggregate for Highway Engineering (JTG E42-2005)" [29], which is listed in Table 1. It should be noted that the Los Angeles abrasion of coarse aggregates is able to meet the requirements of the Chinese specification "Technical Specification for Construction of Highway Asphalt Pavements (JTG F40-2004)" [30] according to the report provided by the manufacturer, so the Los Angeles abrasion's range of the specification requirements (≤28%) is only presented in Table 1.

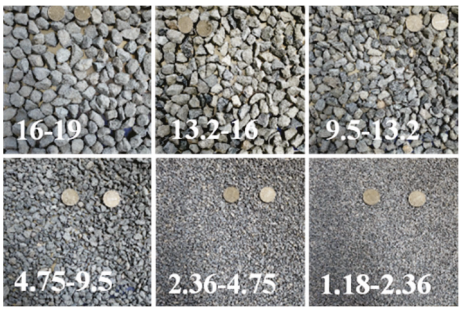

Figure 1. Aggregates with different sizes.

Table 1. Properties of aggregates and filler.

Size (mm)	Bulk Density (g/cm^3)	Los Angeles Abrasion	Water Absorption (%)	Hydrophilic Coefficient	Water Content (%)
26.5–31.5	2.854	≤28%	0.450	/	/
19–26.5	2.928		0.438	/	/
16–19	2.892		0.445	/	/
13.2–16	2.829		0.462	/	/
9.5–13.2	2.764		0.600	/	/
4.75–9.5	2.762		0.718	/	/
2.36–4.75	2.669	/	0.430	/	/
1.18–2.36	2.622	/	1.312	/	/
0.6–1.18	2.601	/	1.526	/	/
0.3–0.6	2.629	/	1.127	/	/
0.15–0.3	2.599	/	1.251	/	/
0.075–0.15	2.567	/	1.691	/	/
Filler	2.802	/	/	0.7	0.33

2.2. Aggregate Blends

The single-size, two-size, and multi-size aggregate blends were employed to conduct the investigation of packing characteristics and mechanical performance. Three parallel tests were performed for each aggregate blend, and the average value of test results was adopted. For the single-size aggregate blends, six sizes were involved. For the two-size aggregate blends, six size combinations were included and various mass ratios were considered for each size combination to understand the influence of aggregate composition, particle size, and size ratio. To explore the contribution of specific size particles to the packing and mechanical performance, the multi-size aggregate blends were designed through the gradually filling method based on the blend with specific gradation, which has been detailed described in the reference [13], and the composition ratios were determined according to two typical gradations, namely stone matrix asphalt with a nominal maximum particle size (NMPS) of 16 mm (SMA16) and dense asphalt concrete with an NMPS of 26.5 mm (AC25). The reasons for selecting AC25 are as follows: (1) AC25 gradation is commonly used on the lower surface or base course of asphalt pavement; (2) more multi-size aggregate blends can be designed according to the gradation with larger NMPS design, contributing to better analyzing the change in packing characteristic and mechanical performance in the gradually filling process of smaller particles. Figure 2 depicts the gradations of SMA16 and AC25 used in this study. Table 2 lists the information of the designed aggregate blends. Three parallel experiments were performed for each blend and the average values were taken for analysis. For convenience, the particles retained on s mm sieve but passing the s + 1 mm sieve are denoted as s mm particles. It should be noted that s + 1 is the smallest sieve size in the sieves larger than s mm. For example, if s is 2.36, s + 1 is 4.75. And 2.36 mm aggregates represent the particles retained on 2.36 mm sieve but passing the 4.75 mm sieve. A_s is used to represent the single-size blend composed of the particles with the size of s mm. a + b represents the two-size aggregate blend composed of a mm and b mm particles. $A_{s\text{-}M}$ is employed to represent the multi-size blend composed of particles with a size larger than s mm in SMA16 or AC25 gradation. A represents the aggregate blend with given gradation.

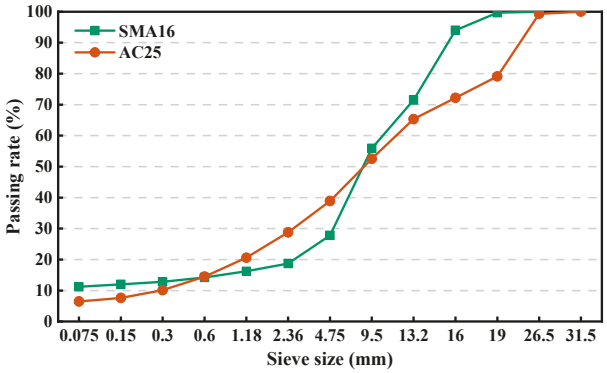

Figure 2. Gradation curves.

Table 2. The designed aggregate blends.

Aggregate Blend	Composition
Single-size	A_{16}, $A_{13.2}$, $A_{9.5}$, $A_{4.75}$, $A_{2.36}$, $A_{1.18}$
Two-size	16 + 4.75, 16 + 2.36, 16 + 1.18, 4.75 + 2.36, 4.75 + 1.18, 2.36 + 1.18 (The mass ratios of the smaller particles to larger particles are, respectively, 1:10, 2:10, 3:10, 4:10, 5:10, 6:10, 7:10, 8:10, 9:10, and 10:10, i.e., the mass percentages of the smaller particles are, respectively, 9.1%, 16.7%, 23.1%, 28.6%, 33.3%, 37.5%, 41.2%, 44.4%, 47.4%, and 50%)
Multi-size	$A_{9.5\text{-}M}$, $A_{4.75\text{-}M}$, $A_{2.36\text{-}M}$, $A_{1.18\text{-}M}$, $A_{0.6\text{-}M}$, $A_{0.3\text{-}M}$, $A_{0.15\text{-}M}$, $A_{0.075\text{-}M}$, A (The composition ratio of each blend was determined according to SMA16 and AC25)

2.3. Packing Test

The packing tests were performed in a cylinder with a height of 170 mm and a diameter of 152 mm by vibration method in accordance with the method of T0309-2005 in the technological specification "Test Methods of Aggregate for Highway Engineering (JTG E42-2005)" of China [29]. The mass of each sample is 3 kg. The vibration time for each aggregate blend is 2 min, the vibration frequency is 50 Hz, and the amplitude is 0.5 mm. For the single-size aggregate blends, the air void was used to evaluate the packing characteristics. For the two-size and multi-size aggregate blends, the air void, the percentage of contribution to the packing volume (PCPV), and the change in air void from $A_{(s+1)\text{-}M}$ to $A_{s\text{-}M}$ were selected to characterize the packed aggregates, which are defined as Equations (1–3), respectively [13].

$$V_a = \frac{V_B^{blend}}{V_P^{blend}} \tag{1}$$

$$PCPV_{s\text{-}M} = \frac{V_p^{s\text{-}M}}{V_p^A} \tag{2}$$

$$RV_s = V_a^{(s+1)\text{-}M} - V_a^{s\text{-}M} \tag{3}$$

where V_a is the air void of an aggregate blend; V_B^{blend} is the bulk volume of an aggregate blend; V_P^{blend} is the packing volume of an aggregate blend; $PCPV_{s\text{-}M}$ is the contribution of $A_{s\text{-}M}$ to the packing volume of A (for the two-size blend, $PCPV_{s\text{-}M}$ is the contribution of larger particles to the packing volume of a + b blend); $V_P^{s\text{-}M}$ is the packing volume of $A_{s\text{-}M}$ (for the two-size blend, $V_P^{s\text{-}M}$ is the packing volume of packed larger particles); V_P^A is the packing volume of A (for the two-size blend, V_P^A is the packing volume of a + b blend); RV_s is the change in air void after adding s mm particles in $A_{(s+1)\text{-}M}$ (for the two-size blend, RV_s is the change in air void after adding smaller particles in larger particles); $V_a^{(s+1)\text{-}M}$ is

the air void of $A_{(s+1)\text{-}M}$ (for the two-size blend, $V_a^{(s+1)\text{-}M}$ is the air void of packed larger particles); and $V_a^{s\text{-}M}$ is the air void of $A_{s\text{-}M}$ (for the two-size blend, $V_a^{s\text{-}M}$ is the air void of a + b blend).

The packing function of aggregate particles in a blend mainly includes skeleton building and air void filling. The addition of s mm particles into $A_{(s+1)\text{-}M}$ will cause the change in air void content of the blend, and the larger the decrease in the air void content, the better its air void filling function. Therefore, the RV_s can be used to quantify the air void filling contribution of s mm particles in a blend. The larger the RV_s, the stronger the air void filling function of s mm particles. Figure 3 depicts the relationships between $V_a^{(s+1)\text{-}M}$, $V_a^{s\text{-}M}$, $V_P^{(s+1)\text{-}M}$, and $V_P^{s\text{-}M}$.

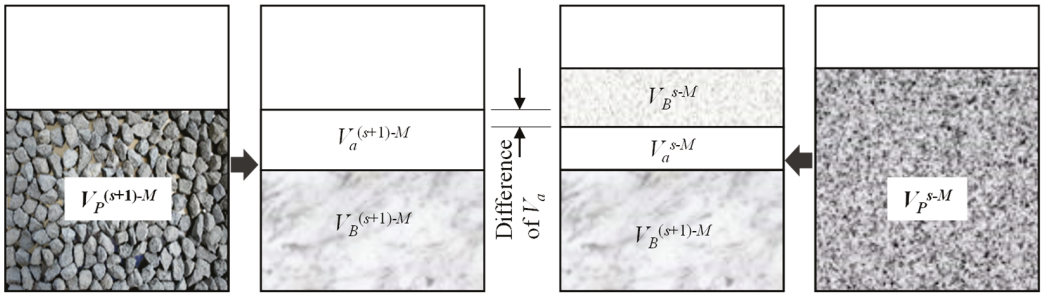

Figure 3. The relationships between $V_a^{(s+1)\text{-}M}$, $V_a^{s\text{-}M}$, $V_P^{(s+1)\text{-}M}$, and $V_P^{s\text{-}M}$.

2.4. California Bearing Ratio (CBR) Test

The California bearing ratio (CBR) test is a relatively easy and inexpensive test and has been widely used to characterize the bearing capacity of unbound granular materials in pavement structures [31–33]. Although the CBR value provides only a relative strength, it has been considered to provide a reasonable way to assess the material performance [34] and closely related to the stability of asphalt mixture [35]. Therefore, this study adopted the CBR test to assess the mechanical performance of aggregate blend according to Chinese technological specifications "Test Methods of soils for Highway Engineering (JTG 3430-2020)" [36]. The specific experimental steps are as follows: (1) making CBR specimens according to the vibration method in Section 2.3; (2) soaking the CBR specimens in water for 4 days to make them reach saturation; (3) penetrating into the specimen using a standard indenter with an area of 19.35 cm^2 of LD-127 pavement material strength tester (as shown in Figure 4) at a speed of 0.1 cm/min; and (4) recording the penetration force per 0.25 cm of penetration depth until it reaches 1.25 cm. The value of CBR is defined as the proportion of the unit pressure to the standard pressure at a certain penetration depth, as shown in Equation (4). The unit pressure is defined as the proportion of the penetration force to the area of the indenter. The standard pressure is the unit pressure of high-quality standard crushed stones, which is listed in Table 3. It should be noted that the CBR value is calculated at a penetration depth of 0.25 cm. However, if the CBR value at the penetration of 0.25 cm is less than that at the penetration of 0.5 cm, the latter should be used as the test result.

$$CBR = \frac{P}{P_i} \times 100\% \tag{4}$$

where P is the unit pressure of aggregate blend at a certain penetration depth, kPa; P_i is the standard pressure at the corresponding penetration depth, kPa.

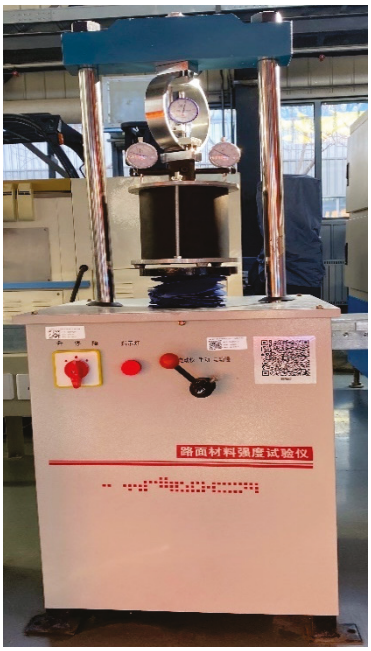

Figure 4. LD-127 pavement material strength tester.

Table 3. Standard pressure of CBR test.

Penetration depth (mm)	2.5	5.0	7.5	10.0	12.5
Standard pressure (MPa)	7.0	10.5	13.4	16.2	18.3

3. Results and Discussion

3.1. Packing Characteristics of Aggregate Blend

3.1.1. Single-Size Blends

Figure 5 depicts the air voids of single-size aggregate blends. As can be seen, the air void is between 36% and 40% for the single-size aggregate blend. The particle size has a significant effect on the air void of the blend. The smaller the particle size, the larger the air void of the single-size aggregate blend. This is because the larger aggregates are minimally affected by the surface force and their position can be adjusted more easily on the vibration table compared with the smaller aggregates.

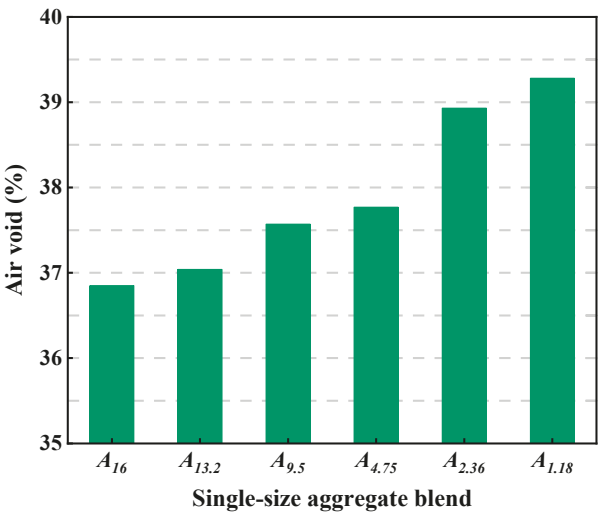

Figure 5. Air voids of single-size aggregate blends.

3.1.2. Two-Size Blends

Figure 6 depicts the air voids of two-size aggregate blends. As can be seen, with the increase in the mass percentage of smaller particles, the air voids of all two-size aggregate blends gradually decrease first and then keep stable, except 16 + 1.18. The air voids of 16 + 1.18 blends decrease first and then gradually increase with increase in 1.18 mm particles. Therefore, the addition of smaller particles in larger particles can reduce the air void of the blend. The air void of 16 + 4.75 is larger than that of 16 + 2.36 and 16 + 1.18, and the air void of 4.75 + 2.36 is greater than that of 4.75 + 1.18 at the same mass percentage of smaller particles. This indicates that particle size ratio has a significant effect on the packing characteristics of the blend. The larger the size ratio, the greater the air void of the blend at the same mass percentage of smaller particles and the faster the decrease in the air void with the increase in the mass percentage of smaller particles. In addition, the air voids of 16 + 4.75, 4.75 + 2.36, and 2.36 + 1.18 follow the order of 2.36 + 1.18 > 4.75 + 2.36 > 16 + 4.75, indicating that the particle size also has a significant effect on the air void of the blend. The smaller the particle size, the larger the air void of the blend.

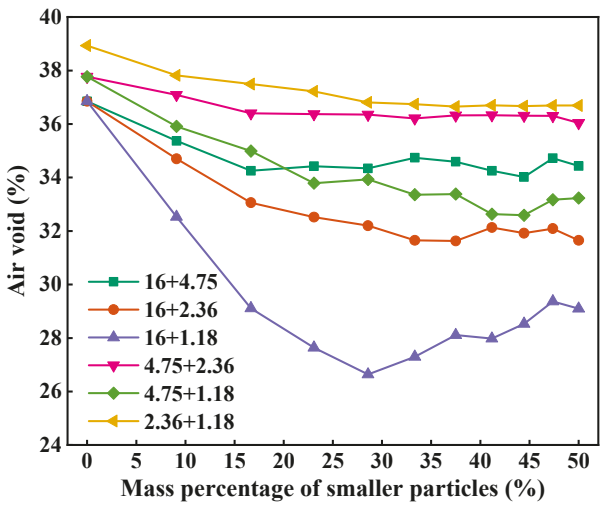

Figure 6. Air voids of two-size aggregate blends.

Figure 7 describes the contribution of the larger particles to packing volume in two-size aggregate blends. It can be seen that the PCPV of larger particles shows a decrease trend with the increasing mass percentage of smaller particles in two-size aggregate blend. At the same mass percentage of smaller particles, the PCPV of the larger particles in 16 + 1.18 blends is larger than that in other blends, and that in 16 + 4.75, 16 + 2.36, 4.75 + 2.36, 4.75 + 1.18, and 2.36 + 1.18 blends is almost equal. The difference in the PCPV of larger particles between 16 + 4.75, 16 + 2.36, 4.75 + 2.36, 4.75 + 1.18, and 2.36 + 1.18 blends is less than 3% and that between 16 + 1.18 and other blends is between 2% and 9%. Therefore, only when the particle size ratio is very high will it have an effect on the PCPV of larger particles.

Figure 8 depicts the RV_s of smaller particles in two-size aggregate blends. As can be seen, the RV_s of the smaller particles shows an increasing trend with the increase in the mass percentage. The RV_s of the smaller particles is greater than 0, indicating that the addition of smaller-sized particles in larger-sized particles can reduce the air voids of the blend. The RV_s of the smaller particles in 16 + 1.18 is larger than that in 16 + 2.36 and 16 + 4.75 at the same mass percentage, which indicates that, the larger the particle size ratio, the greater the air void filling contribution of smaller-sized particles in two-size blends, and the smaller the particle size ratio, the weaker the air void filling contribution of smaller-sized particles.

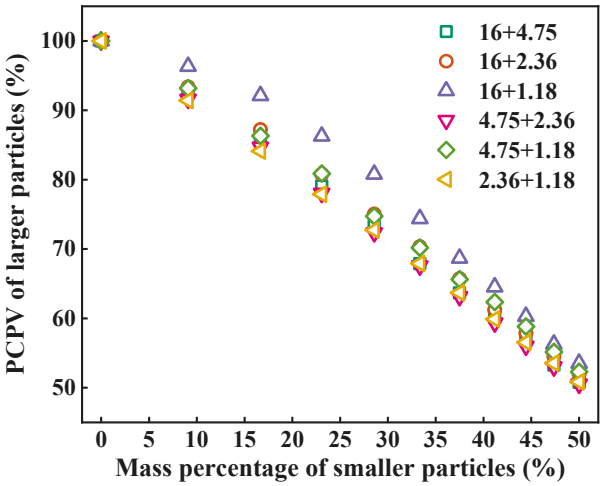

Figure 7. PCPV of larger particles in two-size aggregate blends.

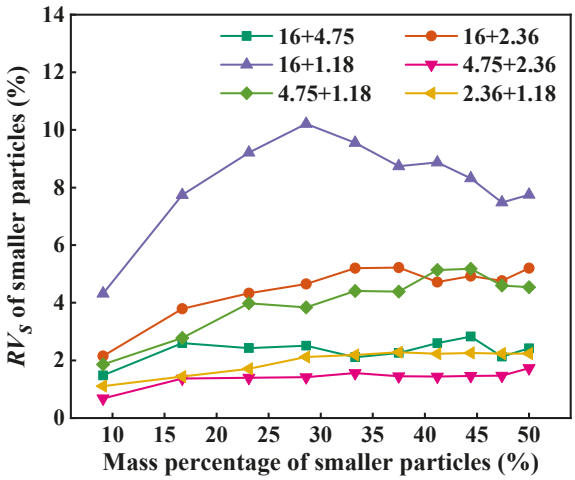

Figure 8. RV_s of smaller particles in two-size aggregate blends.

3.1.3. Multi-Size Blends

Figure 9 depicts the air void of multi-size aggregate blend. It can be seen that the air void of $A_{(s+1)\text{-}M}$ gradually decreases with the addition of *s* mm particles in it, indicating that the dense degree of the blend becomes better and the density of aggregate blend gradually increases. The designed $A_{s\text{-}M}$ according to SMA16 has larger air void than that according to AC25, which indicates that the composition ratio of particles with different sizes has a significant effect on the air void of the blend.

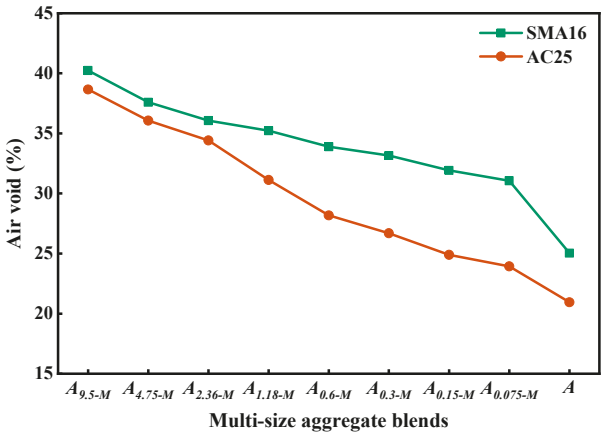

Figure 9. Air void of multi-size aggregate blend.

Figure 10 shows the contribution of $A_{s\text{-}M}$ to the packing volume of A. As can be seen, the change in $PCPV_{s\text{-}M}$ can be divided into two stages: increasing stages and steady stages. For the designed multi-size blends according to SMA16, the $PCPV_{s\text{-}M}$ will not change when gradually adding the particles with a size smaller than 1.18 mm into $A_{s\text{-}M}$. For the designed multi-size blends according to AC25, the $PCPV_{s\text{-}M}$ will not change when gradually adding the particles with a size smaller than 0.3 mm into $A_{s\text{-}M}$. This indicates that particles smaller than 1.18 mm fully fill the voids in SMA16 and thosesmaller than 0.3 mm fully fill the voids in AC25. The $PCPV_{s\text{-}M}$ in SMA-16 grows faster than that in AC25, indicating that the composition ratio of particles with different sizes has an effect on the PCPV of the blend. Moreover, the fillers mainly provide better adhesive behavior between aggregates and asphalt binders.

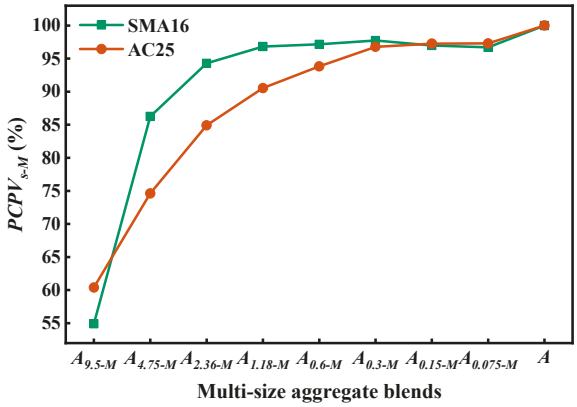

Figure 10. $PCPV_{s\text{-}M}$ of multi-size aggregate blend.

Figure 11 depicts the RV_s in multi-size aggregate blend. As can be seen, the smaller the particle, the larger the RV_s. This indicates that smaller particles have higher air void filling contribution. All the RV_s values are greater than 0, which indicates that all particles have air void filling contribution in the corresponding blend. In general, the RV_s in SMA16 is smaller than that in AC25. This indicates that the air voids of the designed multi-size blends according to AC25 decrease more quickly with the addition of smaller particles compared with that of the designed multi-size blends according to SMA16.

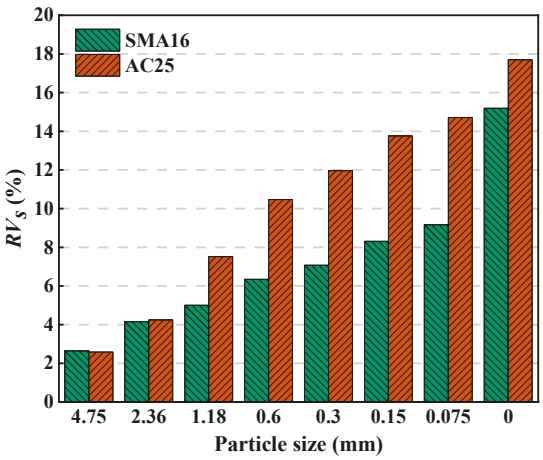

Figure 11. RV_s in multi-size aggregate blend.

3.2. Mechanical Performance of Aggregate Blend

3.2.1. Single-Size Blends

Figure 12 depicts the CBR of the single-size aggregate blend. As shown in Figure 9, the particle size has an obvious influence on the values of CBR. The larger the particle size,

the higher the values of CBR, indicting that larger particles have better bearing capacity and mechanical performance.

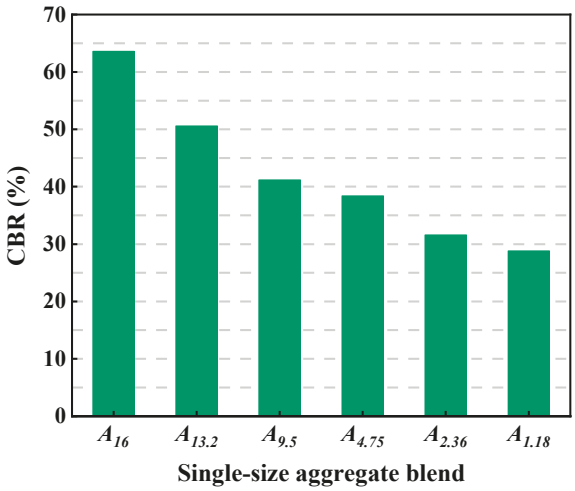

Figure 12. CBR of the single-size aggregate blend.

3.2.2. Two-Size Blends

Figure 13 describes the CBR value of two-size aggregate blend. As can be seen, with the increase in the mass percentage of smaller particles, the CBR value of the blend slightly increases first and then gradually decreases. This indicates that the mechanical performance and bearing capacity of the blend can be improved by properly increasing the smaller particles in larger particles. For the 16 + 1.18 and 16 + 2.36 blends, the CBR values are largest when the mass percentage of the smaller particles is 16.7%. For the 16 + 1.18, 16 + 2.36, and 16 + 4.75 blends, the CBR values decrease significantly when the mass percentage of smaller particles is more than 30%. This is because excessive smaller particles destroy the skeleton structure of larger particles, resulting in the reduction in the bearing capacity of the blend. In general, at the same mass percentage of smaller particles, the CBR values of 16 + 4.75, 16 + 2.36, and 16 + 1.18 blends follow the order of 16 + 4.75 > 16 + 2.36 > 16 + 1.18 and that of 4.75 + 2.36 is larger than that of 4.75 + 1.18. This indicates that size ratio has a significant effect on the mechanical performance of the blends and, the larger the particle size ratio, the weaker the load bearing capacity. The CBR value of 16 + 4.75 is greater than that of 4.75 + 2.36 and that of 2.36 + 1.18 is smallest, indicating that the blends composed of larger particles have better load bearing capacity than those composed of smaller particles.

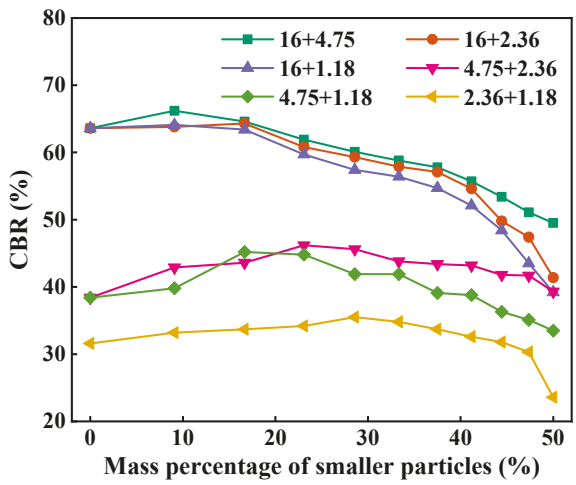

Figure 13. CBR of the two-size aggregate blend.

3.2.3. Multi-Size Blends

Figure 14 depicts the CBR value of the multi-size aggregate blend. It can be seen that the CBR values of the blends increase first and then keep stable with the addition of smaller particles. This indicates that the addition of smaller particles can improve the bearing capacity of mixtures and reduce the crushing of aggregates, which contributes to enhance the stability of asphalt mixtures. For the designed multi-size blends according to SMA16, the CBR will not change when adding particles with a size smaller than 1.18 mm into $A_{s\text{-}M}$. For the designed multi-size blends according to AC25, the CBR will not change when adding particles with a size smaller than 0.3 mm into $A_{s\text{-}M}$. The above results indicate that the particles smaller than 1.18 mm in SMA16 and those smaller than 0.3 mm in AC25 mainly play a role to fill the voids and have little contribution to the load bearing. The designed blends according to AC25 have a larger CBR compared with that according to SMA16, indicating that the load bearing capacity of AC25 is better than that of SMA16.

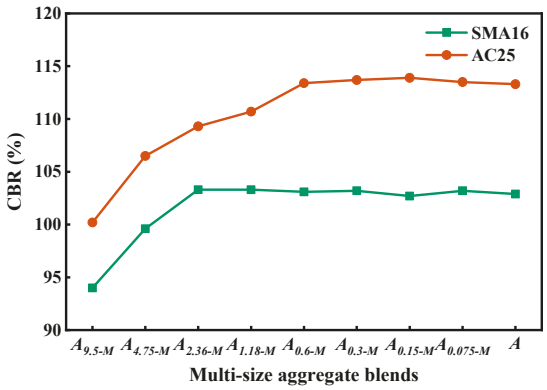

Figure 14. CBR of the multi-size aggregate blend.

3.3. Relationship Between Packing Characteristics and Mechanical Performance

3.3.1. Single-Size Blends

Figure 15 describes the relationship between the air void and CBR for the single-size aggregate blend. It can be seen that, for the single-size aggregate blend, the larger the air void, the smaller the CBR value, and the air void and CBR shows a significant quadratic relationship. Therefore, the air void of the blend has an effect on the mechanical performance.

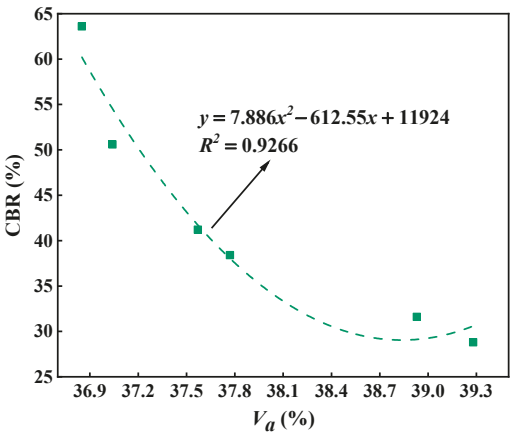

Figure 15. Relationship between the air void and CBR for the single-size aggregate blend.

3.3.2. Two-Size Blends

Figure 16 depicts the relationship between the air void and CBR for the two-size aggregate blend. As can be seen, for the two-size aggregate blend, there is no obvious correlation between the air void and CBR value.

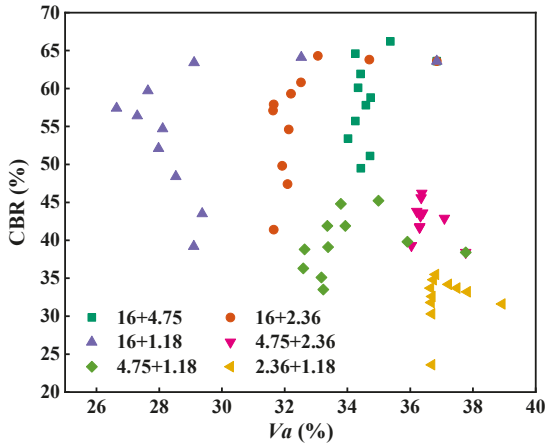

Figure 16. Relationship between the air void and CBR for the two-size aggregate blend.

Figure 17 depicts the relationship between the PCPV of larger particles and CBR for the two-size aggregate blend. Table 4 lists the curve fitting results of the PCPV of larger particles versus CBR value. As shown in Figure 17 and Table 4, the PCPV of larger particles and the CBR value show a quadratic relationship for all blends, and the correlation coefficients are larger than 0.9, except 2.36 + 1.18 blend. For 16 + 4.75, 16 + 2.36, and 16 + 1.18 blends, the higher the PCPV of larger particles, the larger the CBR value. For 4.75 + 2.36, 4.75 + 1.18, and 2.36 + 1.18 blends, the CBR value slightly increases first and then shows a downward trend with the increasing PCPV of larger particles.

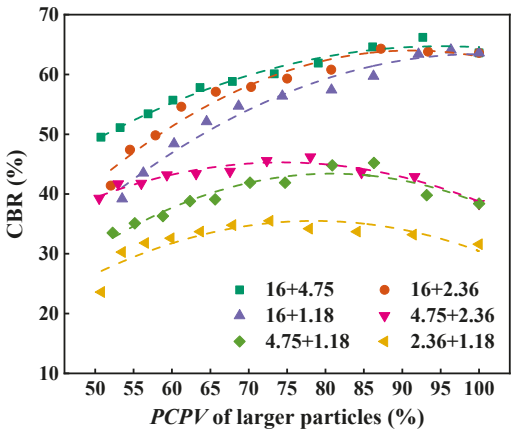

Figure 17. Relationship between the PCPV of larger particles and CBR for the two-size aggregate blend.

Table 4. Curve fitting results of the PCPV of larger particles versus CBR value.

Blend Type	Fitting Equations	R^2
16 + 4.75	$y = (-0.008 \pm 0.001)x^2 + (1.464 \pm 0.181)x - (4.933 \pm 6.52)$	0.98
16 + 2.36	$y = (-0.013 \pm 0.002)x^2 + (2.373 \pm 0.363)x - (44.25 \pm 13.24)$	0.96
16 + 1.18	$y = (-0.01 \pm 0.002)x^2 + (2.057 \pm 0.378)x - (39.57 \pm 14.02)$	0.97
4.75 + 2.36	$y = (-0.01 \pm 0.001)x^2 + (1.478 \pm 0.157)x - (9.673 \pm 5.64)$	0.92
4.75 + 1.18	$y = (-0.013 \pm 0.002)x^2 + (2.136 \pm 0.294)x - (42.89 \pm 10.76)$	0.91
2.36 + 1.18	$y = (-0.011 \pm 0.002)x^2 + (1.716 \pm 0.368)x - (31.86 \pm 13.26)$	0.77

Note: x and y represent the PCPV of larger particles and the CBR value of the corresponding aggregate blend, respectively.

3.3.3. Multi-Size Blends

Figure 18 describes the relationship between air void and CBR for the multi-size aggregate blend. As can be seen, for the designed multi-size aggregate blend according to SMA16 and AC25, the air void and CBR show a quadratic relationship, and the correlation

coefficients are larger than 0.85. In general, the larger the air void, the smaller the CBR value. This indicates that the air void has a significant influence on the mechanical performance of the multi-size blend. In addition, the CBR values of AC25 blends are larger than those of SMA16 blends. The reason for this is that there are more coarse aggregates in AC25 blends compared with SMA16 blends, which can provide stronger penetration strength for aggregate blends.

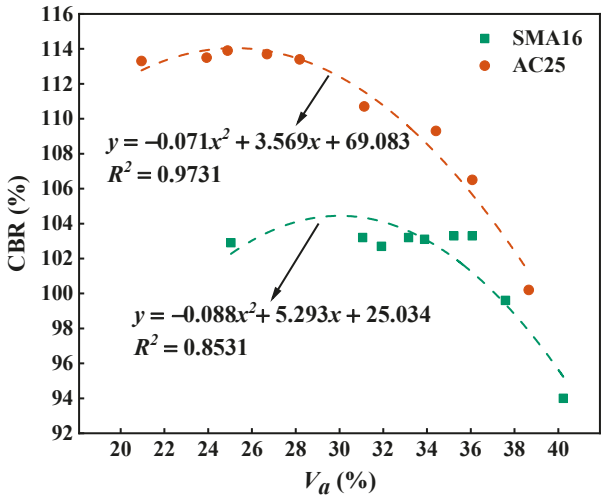

Figure 18. Relationship between $PCPV_{s\text{-}M}$ and CBR for the multi-size aggregate blend.

4. Conclusions

In this study, the single-size, two-size, and multi-size aggregate blends were selected to conduct the laboratory packing and CBR test. The packing characteristics and mechanical performance of aggregate blends were investigated. The relationships between the packing characteristics and mechanical performance were analyzed. The main conclusions are as follows:

(1) The particle size and the size ratio have an effect on the packing characteristics of aggregate blend. The smaller the particle size, the larger the air void of the blend. For the two-size blends, the larger the size ratio, the greater the air void of the blend and the faster the decrease in the air void with the increase in the mass percentage of smaller particles. The addition of smaller particles in larger particles can reduce the air void of the blend. The PCPV of larger particles shows a decrease trend with the increasing mass percentage of smaller particles in two-size aggregate blend.

(2) Particles smaller than 1.18 mm and those smaller than 0.3 mm in AC25 mainly play a role to fill the voids and have little contribution to the load bearing. The air voids of the designed multi-size blends according to AC25 decrease more quickly with the addition of smaller particles than those of the designed multi-size blends according to SMA16. For the multi-size blends, with the addition of smaller particles, the change in $PCPV_{s\text{-}M}$ can be divided into two stages: increasing stages and steady stages. The $PCPV_{s\text{-}M}$ in SMA-16 grows faster than that in AC25, indicating that the composition ratio of particles with different sizes has an effect on the PCPV of the blend.

(3) The blends composed of larger particles have better load bearing capacity than those composed of smaller particles. For the two-size blends, with the increase in the mass percentage of smaller particles, the CBR value of the blend slightly increases first and then gradually decreases, indicating that the mechanical performance and bearing capacity of the blend can be improved by properly increasing the smaller particles in larger particles. The larger the particle size ratio, the weaker the load bearing capacity. For the multi-size aggregate blend, the CBR values of the blends increases first and then keeps stable with

the addition of smaller particles. The designed blends according to AC25 have larger CBR compared with those according to SMA16, indicating that the load bearing capacity of AC25 is better than that of SMA16.

(4) For the single-size aggregate blend, the larger the air void, the smaller the CBR value, and the air void and CBR show a significant quadratic relationship. For the two-size aggregate blends, there is no obvious correlation between the air void and CBR value, but the PCPV of larger particles and CBR value show a quadratic relationship. For the designed multi-size aggregate blend according to SMA16 and AC25, the air void and CBR value show a quadratic relationship, and the $PCPV_{s\text{-}M}$ and the CBR value show a good linear relationship.

The significance of this study is in providing a reference to design and optimize gradations. Therefore, aggregate blends with various compositions were considered. This research presents preliminary findings about the mechanical properties and packing features of aggregate blend. In the future study, the mesoscopic mechanical and structural characteristics of asphalt mixture need to be further explored by DEM and DIP technique. Although the CBR value provides a reasonable way to assess the material performance, it is only a relative strength. In the future study, the dynamic triaxial test can be conducted to analyze the mechanical behavior of aggregate blends.

Author Contributions: Conceptualization, W.Y., S.W. and Y.M.; Methodology, W.Y., J.W., S.W. and Y.M.; Software, Z.L.; Validation, Y.L. and J.W.; Formal analysis, J.W.; Investigation, W.Y.; Resources, Y.L. and S.W.; Data curation, Z.L.; Writing—original draft, W.Y. and Y.L.; Writing—review & editing, W.Y., Z.L. and S.W.; Supervision, Y.M.; Funding acquisition, Y.M. All authors have read and agreed to the published version of the manuscript.

Funding: The research reported in this paper is funded by the National Natural Science Foundation of China (No. 51978048).

Institutional Review Board Statement: Not applicable.

Informed Consent Statement: Not applicable.

Data Availability Statement: The original contributions presented in this study are included in the article. Further inquiries can be directed to the corresponding authors.

Conflicts of Interest: The authors declare no conflict of interest.

References

1. Wang, S.; Miao, Y.; Wang, L. Effect of grain size composition on mechanical performance requirement for particles in aggregate blend based on photoelastic method. *Constr. Build. Mater.* **2023**, *363*, 129808. [CrossRef]
2. Zhu, J.; Ma, T.; Lin, Z.; Zhu, H. Effect of aggregate structure on load-carrying capacity and deformation resistance of porous asphalt concrete based on discrete-element modelling. *Int. J. Pavement Eng.* **2022**, *23*, 4023–4033. [CrossRef]
3. Miranda, H.M.B.; Batista, F.A.; de Lurdes Antunes, M.; Neves, J. Influence of laboratory aggregate compaction method on the particle packing of stone mastic asphalt. *Constr. Build. Mater.* **2020**, *259*, 119699. [CrossRef]
4. Roohi Sefidmazgi, N.; Bahia, H.U. Effect of compaction conditions on aggregate packing using 2-dimensional image analysis and the relation to performance of HMA. *Mater. Struct.* **2014**, *47*, 1313–1324. [CrossRef]
5. Pouranian, M.R.; Haddock, J.E. Determination of voids in the mineral aggregate and aggregate skeleton characteristics of asphalt mixtures using a linear-mixture packing model. *Constr. Build. Mater.* **2018**, *188*, 292–304. [CrossRef]
6. Fuller, W.B. *A Treatise on Concrete, Plain and Reinforced: Materials, Construction, and Design of Concrete and Reinforced Concrete*; Proportioning Concrete; Taylor, F.W., Thompson, S.E., Eds.; John Wiley & Sons: New York, NY, USA, 1906; pp. 183–215.
7. Vavrik, W.R.; Pine, W.J.; Huber, G. The bailey method of gradation evaluation: The influence of aggregate gradation and packing characteristics on voids in the mineral aggregate. *J. Assoc. Asph. Paving Technol.* **2001**, *70*, 132–175.
8. Weymouth, C.A.G. Effects of Particle Interference in Mortars and Concretes. *Rock Prod.* **1933**, *36*, 26–31.
9. Kim, S.; Guarin, A.; Roque, R.; Birgisson, B. Laboratory evaluation for rutting performance based on the DASR porosity of asphalt mixture. *Road Mater. Pavement Des.* **2008**, *9*, 421–440. [CrossRef]

10. Kim, S. Identification and Assessment of the Dominant Aggregate Size Range of Asphalt Mixture. *J. Assoc. Asph. Paving Technol.* **2012**, *75*, 479–486.
11. Kim, S.; Roque, R.; Birgisson, B.; Guarin, A. Porosity of the Dominant Aggregate Size Range to Evaluate Coarse Aggregate Structure of Asphalt Mixtures. *J. Mater. Civ. Eng.* **2009**, *21*, 32–39. [CrossRef]
12. Guarin, A.; Roque, R.; Kim, S.; Sirin, O. Disruption factor of asphalt mixtures. *Int. J. Pavement Eng.* **2013**, *14*, 472–485. [CrossRef]
13. Miao, Y.; Wang, S.; Guo, L.; Li, J. A method for quantifying the packing function of particles in packed aggregate blend. *Constr. Build. Mater.* **2018**, *188*, 607–614. [CrossRef]
14. Miao, Y.; Liu, X.; Hou, Y.; Li, J.; Wu, J.; Wang, L. Packing Characteristics of Aggregate with Consideration of Particle size and Morphology. *Appl. Sci.* **2019**, *9*, 869. [CrossRef]
15. Shi, L.; Wang, D.; Lin, P.; Sun, X.; Qin, X. Meso-structural evaluation of asphalt mixture based on pore cellular structure model. *Int. J. Pavement Eng.* **2022**, *23*, 2675–2688. [CrossRef]
16. Cai, X.; Wu, K.; Huang, W. Study on the optimal compaction effort of asphalt mixture based on the distribution of contact points of coarse aggregates. *Road Mater. Pavement Des.* **2021**, *22*, 1594–1615. [CrossRef]
17. Xing, C.; Liang, Z.; Tan, Y.; Wang, D.; Zhai, C. Skeleton Filling System Evaluation Method of Asphalt Mixture Based on Compressible Packing Model. *J. Transp. Eng. Part B Pavements* **2021**, *147*, 4021062. [CrossRef]
18. Wang, F.; Xiao, Y.; Cui, P.; Ma, T.; Kuang, D. Effect of aggregate morphologies and compaction methods on the skeleton structures in asphalt mixtures. *Constr. Build. Mater.* **2020**, *263*, 120220. [CrossRef]
19. Sun, P.; Zhang, K.; Han, S.; Liang, Z.; Kong, W.; Zhan, X. Method for the Evaluation of the Homogeneity of Asphalt Mixtures by 2-Dimensional Image Analysis. *Materials* **2022**, *15*, 4265. [CrossRef]
20. Cai, X.; Wang, D. Evaluation of rutting performance of asphalt mixture based on the granular media theory and aggregate contact characteristics. *Road Mater. Pavement Des.* **2013**, *14*, 325–340. [CrossRef]
21. Coenen, A.R.; Kutay, M.E.; Sefidmazgi, N.R.; Bahia, H.U. Aggregate structure characterisation of asphalt mixtures using two-dimensional image analysis. *Road Mater. Pavement Des.* **2012**, *13*, 433–454. [CrossRef]
22. Liu, J.; Chen, S.; Liu, Q.; Wang, Y.; Yu, B. Influence of steel slag incorporation on internal skeletal contact characteristics within asphalt mixture. *Constr. Build. Mater.* **2022**, *352*, 129073. [CrossRef]
23. Abdul Hassan, N.; Airey, G.D.; Hainin, M.R. Characterisation of micro-structural damage in asphalt mixtures using image analysis. *Constr. Build. Mater.* **2014**, *54*, 27–38. [CrossRef]
24. Xing, C.; Liu, B.; Sun, Z.; Tan, Y.; Liu, X.; Zhou, C. DEM-based stress transmission in asphalt mixture skeleton filling system. *Constr. Build. Mater.* **2022**, *351*, 128956. [CrossRef]
25. Shen, S.; Yu, H. Characterize packing of aggregate particles for paving materials: Particle size impact. *Constr. Build. Mater.* **2011**, *25*, 1362–1368. [CrossRef]
26. Chen, M.J.; Wong, Y.D. Evaluation of the development of aggregate packing in porous asphalt mixture using discrete element method simulation. *Road Mater. Pavement Des.* **2017**, *18*, 64–85. [CrossRef]
27. Miao, Y.; Yu, W.; Hou, Y.; Guo, L.; Wang, L. Investigating the Functions of Particles in Packed Aggregate Blend using a Discrete Element Method. *Materials* **2019**, *12*, 556. [CrossRef]
28. Kusumawardani, D.M.; Wong, Y.D. Evaluation of aggregate gradation on aggregate packing in porous asphalt mixture (PAM) by 3D numerical modelling and laboratory measurements. *Constr. Build. Mater.* **2020**, *246*, 118414. [CrossRef]
29. *JTG E42-2005*; Test Methods of Aggregate for Highway Engineering. China Communications Press: Beijing, China, 2005.
30. *JTG F40-2004*; Technical Specification for Construction of Highway Asphalt Pavements. China Communications Press: Beijing, China, 2005.
31. Salcedo Fontalvo, J.E.; Vega Araujo, D.L.; Ariza Polo, L.; Padilla Quiroz, J.; Castro Cabeza, A. Influence of Recycled Concrete Aggregates on the California Bearing Ratio (CBR) of Granular Sub-bases. *Arab. J. Sci. Eng.* **2023**, *48*, 14095–14104. [CrossRef]
32. Divinsky, M.; Ishai, I.; Livneh, M. Simplified Generalized California Bearing Ratio Pavement Design Equation. *Transp. Res. Rec.* **1996**, *1539*, 44–50. [CrossRef]
33. Yideti, T.F.; Birgisson, B.; Jelagin, D. Influence of aggregate packing structure on California bearing ratio values of unbound granular materials. *Road Mater. Pavement Des.* **2014**, *15*, 102–113. [CrossRef]
34. Sweere, G.T.H. *Unbound Granular Bases for Roads*; Delft University of Technology: Delft, The Netherlands, 1990.
35. Zhao, Y. *Composition Mechanism of Asphalt Mixtures*; Southeast University: Nanjing, China, 2005.
36. *JTG 3430-2020*; Test Methods of Soils for Highway Engineering. China Communications Press: Beijing, China, 2020.

Disclaimer/Publisher's Note: The statements, opinions and data contained in all publications are solely those of the individual author(s) and contributor(s) and not of MDPI and/or the editor(s). MDPI and/or the editor(s) disclaim responsibility for any injury to people or property resulting from any ideas, methods, instructions or products referred to in the content.

materials

MDPI

Article

The Preparation and Properties of Ultra-High-Performance Concrete with Aeolian Sand: A Lab Study on the Effect of the Curing Method

Yang Lv [1,2], Boyu Zhao [1], Jie Zhu [3], Chenhao He [1], Yunlu Ge [1], Yuanshuai Wu [1], Yanchao Zhu [2], Jianming Dan [4], Yang Zhou [4] and Xiangguo Li [1,4,*]

[1] State Key Laboratory of Silicate Materials for Architectures, Wuhan University of Technology, Wuhan 430070, China; yang.lv@whut.edu.cn (Y.L.); 331481@whut.edu.cn (B.Z.); hch@whut.edu.cn (C.H.); geyunlu0419@163.com (Y.G.); wuyuashuai@163.com (Y.W.)
[2] Hubei Key Laboratory of Polymer Materials, Hubei University, Wuhan 430070, China; zhuyc@hubu.edu.cn
[3] China Railway Electrification Bureau Group Co., Ltd., Beijing 100071, China; 15347075977@163.com
[4] State Key Laboratory Incubation Base for Green Processing of Chemical Engineering, School of Chemistry and Chemical Engineering, Shihezi University, Shihezi 832003, China; danjmxj@163.com (J.D.); zhougroup@shzu.edu.cn (Y.Z.)
* Correspondence: lxggroup@163.com

Abstract

The utilization of aeolian sand (AS) as a substitute for river sand (RS) in ultra-high-performance concrete (UHPC) offers a sustainable solution to address natural sand resource shortages while enhancing AS utilization. This study systematically evaluates the influence of AS content (0–100% RS replacement by mass) on the workability, mechanical properties, and microstructure of UHPC under different curing regimes. All mixtures incorporate 0.65% by volume of straight steel fibers to ensure adequate fiber reinforcement. The results reveal that the spherical morphology, smooth surface nature, and fine particle size of AS enhance the matrix fluidity and reduce the early autogenous shrinkage of UHPC. By employing steam curing at 90 °C for 2 d followed by standard curing for 7 d (M3), UHPC samples with a 60% and 80% AS substitution achieve a compressive strength of 132.4 MPa and 130.8 MPa, respectively; a flexural strength exceeding 18 MPa; a porosity below 10%; and a gel pore content exceeding 60%. The steel fiber reinforcement contributes significantly to the flexural performance, with the fiber–matrix interface quality maintained even at high AS replacement levels. These findings highlight the feasibility of AS as an alternative fine aggregate in UHPC.

Keywords: ultra-high-performance concrete (UHPC); aeolian sand; mechanical properties; microstructure

1. Introduction

Ultra-high-performance concrete (UHPC) has attracted considerable interest in the construction industry owing to its outstanding strength, toughness, and durability [1–3]. UHPC typically incorporates fine aggregates, a high cementitious content, and low water-to-binder ratios, which enables a dense microstructure via optimized particle packing [4]. However, the rapid depletion of natural river sand (RS) necessitates sustainable alternatives, such as aeolian sand (AS), to mitigate the ecological damage caused by excessive mining [5]. Aeolian sand, primarily composed of quartz with minor feldspar and mica, originates from

weathered sandstone and granite residues. Compared to RS, AS exhibits finer particle sizes (0.15–0.6 mm), a higher sphericity, and smoother surfaces [6,7].

Previous studies have explored the incorporation of AS in concrete. For workability, Al-Harthy et al. [8] and Amel et al. [9] observed a parabolic trend in slump with increasing AS content (20–60% optimal), attributing this to the spherical morphology of AS particles enhancing interparticle mobility. However, excessive AS (>60%) disrupts the aggregate gradation, increasing fine particle proportions and reducing slurry fluidity. Regarding the mechanical properties, Li et al. [10,11] demonstrated that moderate AS addition ($\leq$60%) reduces porosity and enhances matrix densification through filler effects and heterogeneous nucleation. Reactive SiO_2 in AS reacts with cementitious phases to form C-S-H/C-A-H gels, which bridge interfacial cracks and refine pore structures. Conversely, Luo et al. [12] emphasized that ultrafine AS particles (<175 μm) act as nucleation sites for hydration products, accelerating cement hydration. However, excessive AS weakens the interfacial transition zone (ITZ) by increasing harmful pores and microcracks, ultimately degrading strength. However, Al-Harthy et al. [4] and Seif et al. [13] obtained a different conclusion, noting that the compressive strength of concrete tends to decrease with the increase in the dosage of AS, which is due to the differences in the physical and chemical characteristics of AS in different regions. For example, the fineness modulus of AS from the Maowusu Desert region of China is much lower, its specific surface area is larger, its water absorption is higher, and its fluidity is poorer than that of the AS from West Asia and North Africa. This leads to a large difference in the properties of the concrete obtained from AS prepared with different physical and chemical characteristics.

The existing literature shows that AS can partially replace natural RS in concrete. However, the current substitution ratio of aggregates remains insufficient to effectively alleviate the shortage of natural RS resources. Additionally, conventional curing methods may degrade the performance of AS–concrete mixtures. Such degradation often manifests as reduced strength, compromised workability during construction, and diminished durability. These limitations make it difficult for AS–concrete to meet the practical requirements of structural engineering projects.

While AS demonstrates potential as a partial RS substitute, conventional curing methods often fail to optimize its performance in UHPC, resulting in inconsistent strength, durability, and workability. In response to the above issues, this study proposes an improved Andreas Andersen particle filling model to systematically evaluate the synergistic effects of the AS substitution rate (0–100%) and a multi-stage curing system (steam + standard curing) on UHPC performance. By combining thermogravimetric analysis, mercury intrusion porosimetry, and SEM, the mechanism of AS on hydration kinetics, pore evolution, and the fiber matrix interface is elucidated. This article aims to address the following key issues: (1) improving the substitution rate of AS while maintaining the mechanical properties of UHPC; (2) maintaining the dense microstructure of UHPC through gradation optimization under a high AS substitution rate; and (3) maintain the development of the basic performance of UHPC under a high AS substitution rate with the multi-stage curing system. The research results will provide basic theoretical support for the efficient utilization of AS resources, promote the transformation of UHPC towards low-carbon and low-cost directions, and have important practical significance for alleviating the shortage of natural sand and gravel resources and promoting the efficient utilization of local resources in desert areas.

2. Materials and Methods

2.1. Materials

This study adopts P O. 52.5 grade ordinary Portland cement provided by Shandong Qingyun Kangjing Building Materials Co., Ltd., in Dezhou, China. Polycarboxylate superplasticizer (SP) is used to regulate the workability of concrete. Commercial silica fume (SF) and blast furnace slag powder (Slag) are used as volcanic ash cementitious materials to partially replace cement. The silica fume is provided by Henan Zhengzhou New Materials Co., Ltd., (Zhengzhou, China). The blast furnace slag powder is the V800 ultrafine slag powder provided by Wuhan Huashen Intelligent Co., Ltd., (Wuhan, China). River sand with an original fineness modulus of 2.4 and a continuous particle size distribution is divided into two groups: one group is fine grain river sand with a particle size of 0–0.6 mm (RS 1), and the other group is coarse grain river sand with a particle size of 0.6–1.18 mm (RS 2). The particle size of AS is between 0 and 0.6 mm. The steel fibers used are long straight steel fibers (LSF) with a diameter of 0.2 mm, a length of 13 mm, and a tensile strength of 2929 MPa. Table 1 shows the chemical properties of the binder materials analyzed by X-ray fluorescence (XRF).

Table 1. Oxide composition of cement, slag, and silica fume/(mass %).

Substance	Cement	Slag	SF
CaO	62.05	38.80	1.25
SiO_2	21.94	32.27	94.44
Al_2O_3	5.82	16.17	0.35
Fe_2O_3	2.63	0.41	0.14
K_2O	0.67	0.56	0.37
Na_2O	0.19	0.46	0.19
SO_3	2.09	2.67	0.12
MgO	2.82	7.25	0.56
TiO_2	0.30	0.77	0.10
MnO	0.09	0.20	0.01
P_2O_5	0.06	-	0.39
Cl^-	0.10	0.03	0.05
Other	1.24	0.41	2.04

2.2. Experimental Methodology

2.2.1. Mixture Ratio Design

The modified model based on the Andreasen and Andersen equations proposed by Funk and Dinger is the most widely used for UHPC at present [14]. The modified Andreasen–Andersen (A&A) model is shown in Equation (1) [15,16].

$$P(D) = \frac{D^q - D_{min}^q}{D_{max}^q - D_{min}^q} \tag{1}$$

where P(D) denotes the total number of particles under the sieve (%); D denotes the current particle size (μm); D_{min} and D_{max} denote the minimum and maximum particle sizes of the particles (μm); and q is the distribution coefficient.

The modified Andreasen and Andersen infill model is now successfully applied in UHPC [17,18]. By adjusting the distribution coefficient q in Equation (1), it was possible to change the ratio and admixture between fine and coarse particles in the concrete particle system. The use of higher distribution coefficients ($q > 0.5$) led to an overall coarsening of the mixed particles, whereas lower distribution coefficients ($q < 0.23$) led to a particulate system enriched with more fine particles [19]. Brouwers [20] has demonstrated through

several experiments that a distribution coefficient q value in the range of 0–0.28 produces an optimal system of stacked particles, and Hunger [21] suggested that distribution coefficient values in the range of 0.22–0.25 should be used in SCC design. Therefore, the q value was fixed at 0.23 considering that a large number of fine particles were used for the preparation of UHPC.

In this study, the modified Andreasen and Andersen model was used as an objective function to optimize the overall particle size ratio of the concrete system. The optimization algorithm based on the least squares method (LSM) was employed to adjust the admixture amounts of individual materials in the mixture. This adjustment process was integrated with actual production applications, resulting in an improved particle size distribution and optimized UHPC mix ratios. Furthermore, the algorithm facilitated precise fitting to the target curve of the mixture, which was calculated using the modified Andreasen and Andersen model as referenced in Equation (2) [22]. RSS denotes the residual difference sum of squares; the smaller the value, the smaller the error between the actual stacking curve and the target curve.

$$\mathrm{RSS} = \Sigma_{i=1}^{n}\left(\mathrm{P_{mix}}\left(\mathrm{D_i^{i+1}}\right) - \mathrm{P_{tar}}\left(\mathrm{D_i^{i+1}}\right)\right)^2 \tag{2}$$

where $\mathrm{P_{mix}}$ is the composed mixture material and $\mathrm{P_{tar}}$ is the target gradation calculated according to Equation (1).

Based on the optimized particle filling model, the mixing ratio of the cementitious materials (cement, SF, and Slag) and the fine aggregate (RS 1, RS 2, and AS) particles was adjusted in conjunction with their particle size distributions so that the actual stacking state between the component particles of the designed UHPC was close to the most compact stacking state. The fits of UHPC formulated by replacing RS 1 with different proportions of AS in an equal mass with the same grain size distribution are shown in Table 2, and the stacking curves are shown in Figure 1. The results show that the particle gradation of AS in the same particle size range is not exactly the same as that of RS, but the actual stacking curves between the component particles are in good agreement with the target curves, which indicates that the stacking forms between the component particles of UHPC mixed with AS have not been significantly damaged, and the matrix is still in a state of compact stacking.

Table 2. Design of UHPC mix AS/(kg/m^3) proportions.

Group	Cement	SF	Slag	RS 2	RS 1	AS	Water	SP	LSF (Vol.%)
UHPC-1	774.7	166.0	166.0	169.3	959.6	0	210.3	22.1	0.65
UHPC-2	774.7	166.0	166.0	169.3	767.7	191.9	210.3	22.1	0.65
UHPC-3	774.7	166.0	166.0	169.3	575.7	383.8	210.3	22.1	0.65
UHPC-4	774.7	166.0	166.0	169.3	383.8	575.7	210.3	22.1	0.65
UHPC-5	774.7	166.0	166.0	169.3	191.9	767.7	210.3	22.1	0.65
UHPC-6	774.7	166.0	166.0	169.3	0	959.6	210.3	22.1	0.65

The mixture proportions for all UHPC formulations are presented in Table 2. The acronyms UHPC-1 through UHPC-6 represent six distinct concrete mixtures with varying AS replacement levels (0–100% of RS 1 by mass). Each mixture designation corresponds to a unique composition that was tested as a complete set of specimens for all experimental measurements. For each mixture (UHPC-1-UHPC-6), multiple specimens were prepared and tested under each curing regime to ensure the statistical reliability of the results. The number of replicates for each test is provided in the respective Experimental Methods sections.

Preliminary trials identified 60–80% AS substitution as critical thresholds where mechanical performance (e.g., compressive strength > 120 MPa) remained compliant with UHPC standards while maximizing AS utilization. Consequently, UHPC-4 (60% AS) and UHPC-5 (80% AS) were prioritized for microstructure and pore structure analysis to investigate the interplay between high AS content and optimized curing regimes.

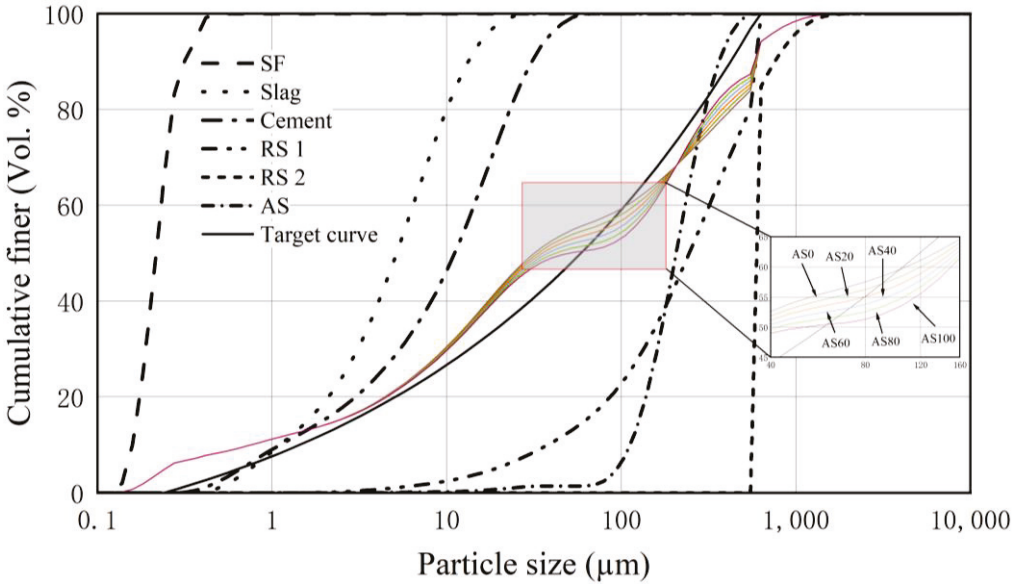

Figure 1. Particle accumulation curves of UHPC raw materials.

2.2.2. Mixing Procedures and Curing Methods

The mixing procedure, as shown in Figure 2, was followed for UHPC preparation. After mixing, the prepared UHPC specimens were cured using different curing conditions, namely: (1) M1: Standard curing (20 ± 2 °C, ≥95% RH, 28 d): This represented the baseline condition and allowed for comparison with conventional UHPC curing practices. The extended 28 d duration enabled the complete evaluation of long-term hydration and strength development under normal conditions. (2) M2: Steam curing (90 °C, ≥95% RH, 2 d): This accelerated curing regime was chosen because high-temperature steam curing is commonly used in precast UHPC production to achieve early-age strength. The 2 d duration represented the typical industrial practice for thermal activation. The temperature of 90 °C was selected as it optimally activated pozzolanic reactions without causing detrimental effects to the microstructure. (3) M3: Combined curing (steam, 90 °C, 2 d + standard curing 5 d): This hybrid approach was designed to evaluate the effects of continued hydration after initial steam curing. Practical scenarios where steam-cured elements experienced subsequent ambient conditions were simulated. The 7 d total duration allowed for the direct comparison with standard test ages while capturing the critical early-age development. The specific sample curing process diagram is shown in Figure 3. Table 3 shows the annotations and meanings of each acronym.

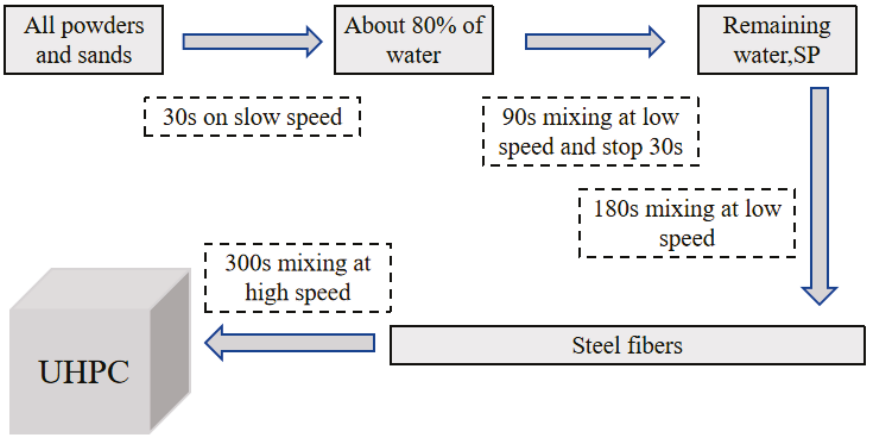

Figure 2. UHPC production process.

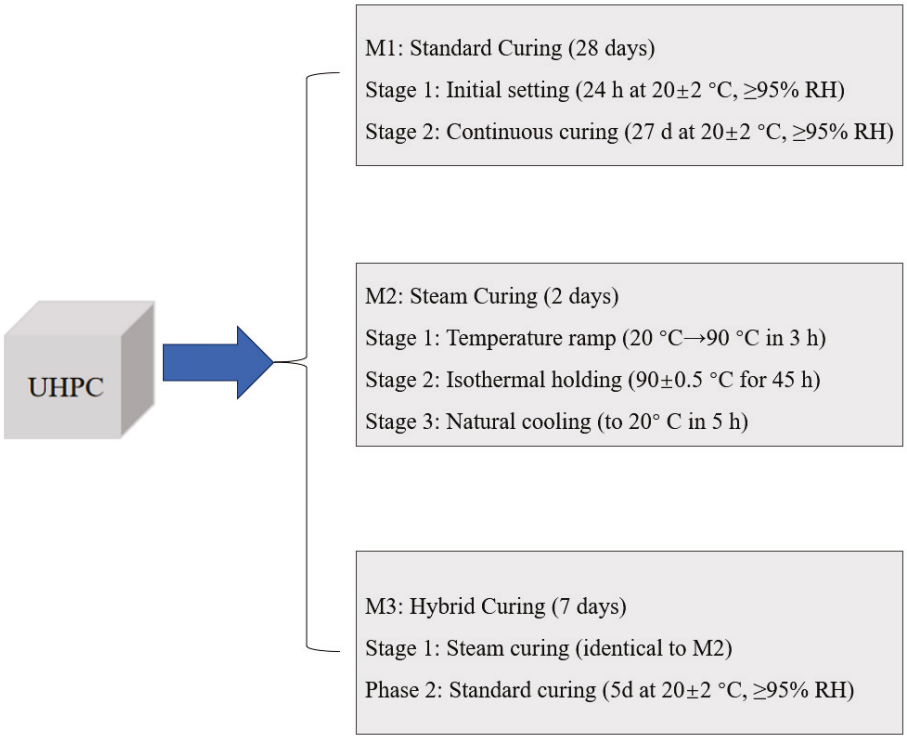

Figure 3. UHPC curing procedure flowchart.

Table 3. Abbreviation annotations and meanings.

Sample Code	AS Substitution Rate	Curing Regime	Description
UHPC-1–UHPC-6	0–100%	M1, M2, or M3	See Table 2 for mix proportions; curing regimes defined in Section 2.2.2
M1	N/A	Standard (20 °C, 28 d)	Control curing condition
M2	N/A	Steam (90 °C, 2 d)	High-temperature accelerated curing
M3	N/A	Steam (2 d) + standard curing (5 d)	Hybrid curing for optimized hydration

These regimes were selected based on preliminary studies and industry standards to provide comprehensive data on AS-UHPC behavior under different curing conditions relevant to both laboratory research and practical applications.

2.2.3. Fluidity

The flowability of fresh UHPC slurry was evaluated in accordance with the Chinese standard GB/T 2419-2005 [23]. The test procedure involved the following steps: (1) Mold

Preparation: Fresh slurry was poured into a truncated cone-shaped mold (top inner diameter: 70 mm; bottom inner diameter: 100 mm; height: 60 mm) in two successive layers. Each layer was compacted 15 and 10 times, respectively, using a standardized tamping rod. (2) Mold Removal: The mold was carefully lifted vertically upward to ensure minimal disturbance to the slurry. (3) Vibration and Measurement: The slurry underwent vibration for 25 s on a jump table. Subsequently, the maximum spread diameters along two mutually perpendicular directions were measured using a calibrated steel ruler. The flowability of UHPC was determined by averaging these two diameters.

2.2.4. Mechanical Properties

According to Chinese standard GB/T 50081-2019 [24] and T/CBMF 37-2018 [25], flexural test specimens and compressive test specimens were prepared separately according to the requirements, and flexural strength and compressive strength tests were conducted on UHPC specimens, respectively. An electro-hydraulic servo universal testing machine (YAW-3000) was used to test the compressive strength of UHPC specimens. Six standard specimens (sized 40 mm × 40 mm × 40 mm) were prepared for each mix proportion for compressive strength testing, and the arithmetic mean was taken as the representative value. A universal testing machine (UTM5105) was used for the three-point bending test. The flexural strength test adopted the three-point bending method, and three standard specimens (sized 40 mm × 40 mm × 160 mm) were prepared for each mix proportion. The arithmetic mean was taken as the representative value.

2.2.5. Autogenous Shrinkage

According to the testing requirements of ASTM C1698-2009 (2014) [26], non-contact displacement sensors were used to measure the early autogenous shrinkage of UHPC. The test conditions were set as follows: a maintenance environment temperature of (20 ± 2) °C and a relative humidity of (60 ± 5)%. The specific operation was as follows: The sample was prepared according to the reference mix ratio (excluding steel fibers), and a secondary vibration process was used (60 vertical vibrations and 60 horizontal vibrations) to fill the corrugated pipe. After measuring the initial length with a vernier caliper, the specimen was placed in the equilibrium position of the autogenous shrinkage tester, 5 min intervals were set for continuous monitoring, and finally, the autogenous shrinkage time curve was obtained.

2.2.6. Mercury Intrusion Porosimetry

The porosity of UHPC samples was measured using mercury intrusion porosimetry (MIP). The instrument adopted was the Auto Pore TV 9500 mercury intrusion porosimeter. After the compressive strength test, the central part of the test block was soaked in anhydrous ethanol for 7 d, and then dried in a 60 °C oven for 3 d. A block sample of about 3 g crushed to 2–3 mm was taken for testing, with a pore size testing range of 3 nm to 350 μm.

2.2.7. Thermogravimetry Analysis

Thermogravimetric (TG) analysis experiments were performed using a STA449F3 simultaneous thermal analyzer (Netzsch, Selb, Germany). The test parameters were set as follows: the furnace was fed with high-purity nitrogen as a protective gas, the starting temperature was 30 °C, and the temperature was increased to 1000 °C at a rate of 10 °C/min. Based on the synchronous thermal analysis curve (DSC-TG), the calcium hydroxide ($Ca(OH)_2$) in the hydration products of the samples was quantitatively characterized.

2.2.8. Scanning Electron Microscope

A model VEGA3 TESCAN (SEM) (Provided by China Taisiken Co., Ltd., Tianjin, China) was used to observe the microscopic morphology of the hydration products and the internal structure of UHPC at a working distance of 11–15 mm, a resolution of 50–400 um, and an accelerating voltage of 15 KV.

3. Results and Discussion

3.1. Fluidity

The flowability of fresh UHPC slurries with different AS replacement rates are shown in Figure 4. It can be seen that adding AS instead of river sand as a fine aggregate was beneficial for improving the flowability of fresh UHPC slurry. The flowability of fresh UHPC slurry showed a trend of first increasing and then decreasing with the increase in AS content. The flowability of the freshly mixed UHPC slurry in the blank group was 237 mm. When the replacement rates of AS in the experimental group were 20%, 40%, 60%, 80%, and 100%, the flowability of fresh UHPC slurry was 246 mm, 257 mm, 244 mm, 241 mm, and 242 mm, respectively. Compared with the blank group, the flowability increased by 3.8%, 8.4%, 3.0%, 1.7%, and 2.1%, respectively. When the AS content was 40%, the improvement in flowability of the fresh UHPC slurry was most significant.

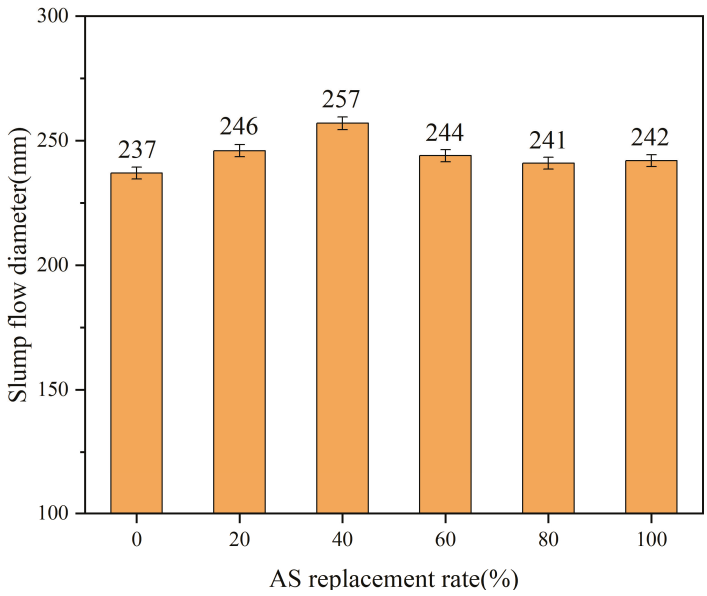

Figure 4. Fluidity of UHPC with different AS replacement rates.

This phenomenon can be attributed to the unique morphological characteristics of AS. Compared to RS 1, the AS particles exhibited higher sphericity and smoother surfaces, reducing interparticle friction and promoting a "balling effect" that enhanced slurry mobility. Furthermore, AS filled the macropores between RS 1 particles, liberating the entrapped slurry originally occupying smaller voids. This redistribution increased the effective slurry volume in the fresh mixture, thereby improving fluidity [6]. However, beyond 40% AS substitution, the gradation of fine aggregates became uneven, and the fineness modulus declined. At this threshold, AS particles no longer optimized packing efficiency, leading to reduced fluidity due to agglomeration and disrupted particle distribution.

3.2. Mechanical Properties

The flexural and compressive strengths of UHPC with varying AS replacement rates (0–100%) under standard curing (28 d) are illustrated in Figure 5. Both properties exhibited

a gradual decline with increasing AS content, contrasting with the trends observed in ordinary concrete. For conventional concrete, flexural and compressive strengths typically peak at intermediate AS substitution levels (e.g., 20–60%) due to AS's ability to fill the voids between coarse aggregates, optimizing gradation and enhancing densification [27,28]. However, in UHPC—composed predominantly of fine particles (RS and powders) without coarse aggregates—AS's filling effect is limited, resulting in monotonic strength reductions at higher substitution rates.

The effects of different curing regimes on the flexural and compressive strength of UHPC with different AS replacement rates are shown in Figure 6. The results showed that the flexural and compressive strengths of the test blocks under curing with steam at 90 °C showed a significant increase compared to those under standard curing. For example, in the group with 60% and 80% AS content, the flexural strengths were 12.7 MPa and 13.1 MPa, while the compressive strengths were 94.7 MPa and 92.9 MPa under the standard curing regime. The flexural strengths reached 14.6 MPa and 15.1 MPa, respectively, under the M2 regime, which were 14.9% and 15.3% higher compared to the M1 regime, and the compressive strengths were 113.7 MPa and 108.6 MPa, which were 20.1% and 16.9% higher than the M1 regime. In the M3 regime, the flexural strengths were 18.5 MPa and 17.7 MPa, which were 45.7% and 35.1% higher than the M1 regime, and the compressive strengths were 132.4 MPa and 130.8 MPa, respectively, which were 39.8% and 40.8% higher than the M1 regime. This enhancement stemmed from steam curing's activation of pozzolanic reactions. Silica fume (highly reactive amorphous SiO_2) reacts with $Ca(OH)_2$ from cement hydration to form an additional C-S-H gel, refining the pore structures and densifying the matrix [29]. Minor amorphous SiO_2 in AS further contributed to this reaction under elevated temperatures.

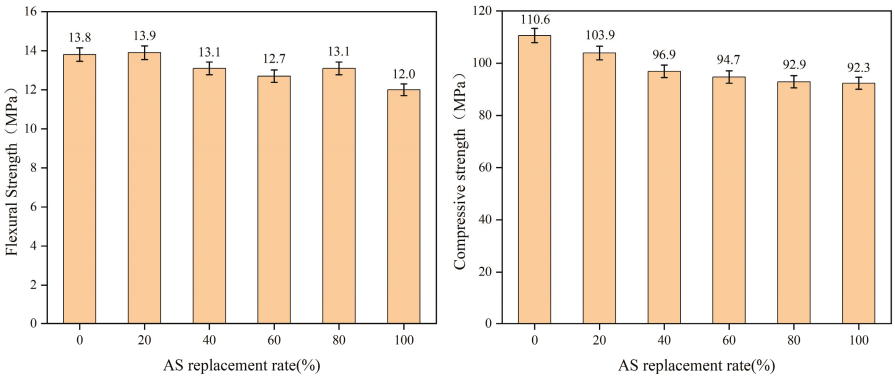

Figure 5. Compressive and flexural strength of UHPC with different AS replacement rates (standard curing for 28 d).

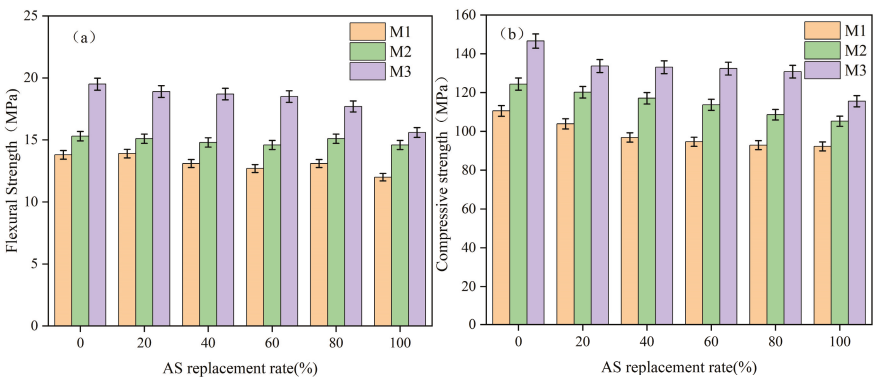

Figure 6. Mechanical properties of UHPC with different AS replacement rates: (**a**) flexural strength, (**b**) compressive strength.

While the highest strengths were achieved with 0% AS replacement, the 60–80% replacement samples still met UHPC strength requirements (>120 MPa compressive strength). This strength reduction was attributed to the following: (1) differences in the particle packing efficiency between AS and RS; (2) the higher water demand of AS particles; and (3) the slightly increased porosity with higher AS content. However, the optimized curing regime (M3) minimized these effects, demonstrating that high AS replacement is feasible with proper processing.

The significant performance differences between curing regimes (M1–M3) highlighted the critical importance of curing protocol selection for AS-UHPC. While standard curing (M1) produced adequate results, the combined steam + standard curing (M3) consistently yielded superior mechanical properties, suggesting that this approach may be optimal for practical applications where both early-age strength and long-term performance are important.

3.3. Autogenous Shrinkage

Figure 7 shows the trend of the autogenous shrinkage of UHPC with different AS content; all the data are the values of the autogenous shrinkage of UHPC after final setting. From the figure, it can be found that the autogenous shrinkage of UHPC is large, and is several times greater than the shrinkage value of ordinary concrete. At 12 h after final condensation, the autogenous shrinkage of UHPC was 4404, 2345, 2465, 2897, and 3795 μm/m when the content of AS was 0%, 20%, 40%, 60%, and 80%. The autogenous shrinkage showed a trend of first decreasing and then increasing with increasing AS content, and the shrinkage stabilized after 24 h. The shrinkage of UHPC primarily stemmed from capillary tension caused by self-drying during cement hydration. As the AS content increased, the specific surface area of particles per unit volume in UHPC rose significantly. This amplified the water demand for the hydration reaction and slowed the hydration rate. Additionally, a higher AS content refined the pore structures, further increasing capillary tension. Consequently, the internal free water diminished under these combined effects. With the reduced internal free moisture, when the cementitious material was hydrated, the material internal self-drying phenomenon occurred in advance, leading to the relative increase in autogenous shrinkage [19,30]. The non-linear relationship between AS content and shrinkage stemmed from competing mechanisms: at a low AS content (<40%), the spherical AS particles improved packing and reduced shrinkage. At higher contents, the increased surface area led to greater water demand and capillary tension.

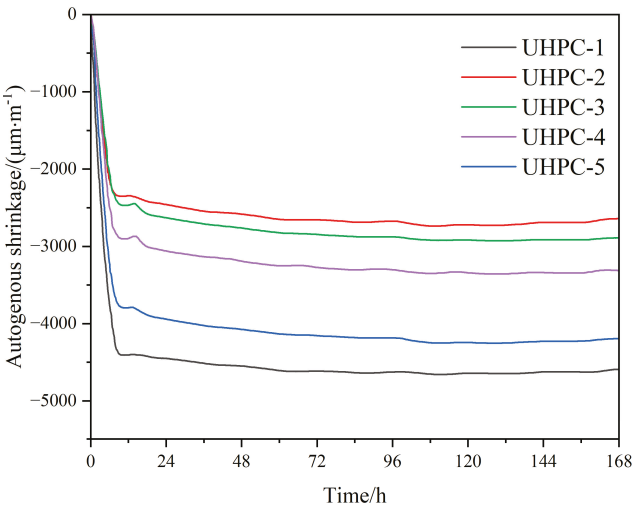

Figure 7. Effects of RS 1 replaced by AS on autogenous shrinkage of UHPC.

It is worth noting that the degree of autogenous shrinkage of UHPC containing AS was generally lower than that of UHPC without AS, which was due to the fact that with the increase in AS content, the gradation of aggregate particles gradually improved and the porosity decreased, which improved the cracking-resistant ability and volume stability of the matrix, and the autogenous shrinkage could be reduced by 13.83% to 34.22% when the content of AS ranged from 60% to 80%. This indicated that the degree of autogenous shrinkage of UHPC with a high AS content was also within the controllable range.

3.4. Pore Structure Analysis

The internal pore structure of cementitious materials can be categorized into four types according to the pore size: (0, 10) nm pores are gel pores, [10, 100] nm pores are small capillary pores, (100, 5000] nm pores are large capillary pores, and >5000 nm pores are large pores. Among them, the gel pores with a pore size of less than 10 nm can be regarded as harmless pores, and their influence on the concrete properties can be neglected. The small capillary pores with a pore size of 10–100 nm will significantly affect the properties of concrete materials. The large capillary pores with a pore size of more than 100 nm as well as the macropores are usually regarded as being harmful pores, which will have a serious impact on the mechanical properties and durability of concrete [31].

To evaluate the impact of high AS substitution on pore refinement, UHPC4 (60% AS) and UHPC5 (80% AS) were selected for detailed analysis, as these levels represented the optimal balance between AS utilization (>60%) and retained mechanical integrity under hybrid curing (M3). Table 4 shows the effect of no AS content and 60% and 80% AS content on the porosity of UHPC under different curing regimes. Figure 8 shows the effect of no AS content and 60% and 80% AS content on the pore volume distribution of UHPC under different curing regimes. From Table 4, it can be seen that with the increase in AS content, the porosity decreased. Compared to the M1 and M2 system, the overall porosity of the M3 system decreased. In the same curing system, with the increase in AS content and the gel pore content below 10 nm and above 100 nm, the large capillary pore and macroporous content decreased and increased.

Table 4. Porosity of UHPC.

Specimen	Porosity/%	Aperture Distribution/%			
		(0, 10) nm	[10, 100] nm	(100, 5000] nm	>5000 nm
M1-1	12.24	28	50	13	9
M1-4	13.72	27	47	17	9
M1-5	13.43	23	50	17	10
M2-1	12.15	54	16	15	15
M2-4	11.94	52	16	14	18
M2-5	10.24	52	16	15	17
M3-1	12.08	66	10	12	12
M3-4	10.87	61	13	12	14
M3-5	9.17	58	14	14	14

Note: M1: Standard curing (28 d); M2: Steam curing (2 d); M3: Steam (2 d) + standard curing (5 d). Numeric suffixes (e.g., −1, −4, −5) denote AS substitution rates (0%, 60%, 80%) as per Table 2.

A comprehensive analysis of Table 4 and Figure 8 shows that the main pore size distribution of UHPC under the M1 regime is concentrated to 100 nm and below, with small capillary pores dominating and a low gel pore content, so the compressive strength of UHPC under the M1 regime is lower, and the large number of small pores and the concentrated small capillary pores reduce the mechanical properties of the material. By accelerating the cement hydration process through steam curing, it can clearly be seen that a large number of small capillary pores under the M1 system are further refined, which leads

to the distribution of the main pore size of UHPC under the M2 system being concentrated to 10 nm and below, with the proportion of the total porosity accounting for about 50%, and by continuing to carry out curing, it is found that the content of gel pores under the M3 system is further increased, which leads to a significant increase in the compressive strength of UHPC under the M3 system compared to that of M2 and M1. Comparing Table 4 and Figure 8a–c, it can be found that the most available pore size of M1-4 and M1-5 decreases from 11.05 nm to 5.48 nm and 4.52 nm by steam curing, and after steam curing and continuing the standard curing, the most available pore size is further decreased to 5.16 nm and 3.62 nm, and the main pore size distribution is changed to gel pores, which indicates that the combination of steam and standard curing has a significant effect on the UHPC mechanical properties and durability performance [32].

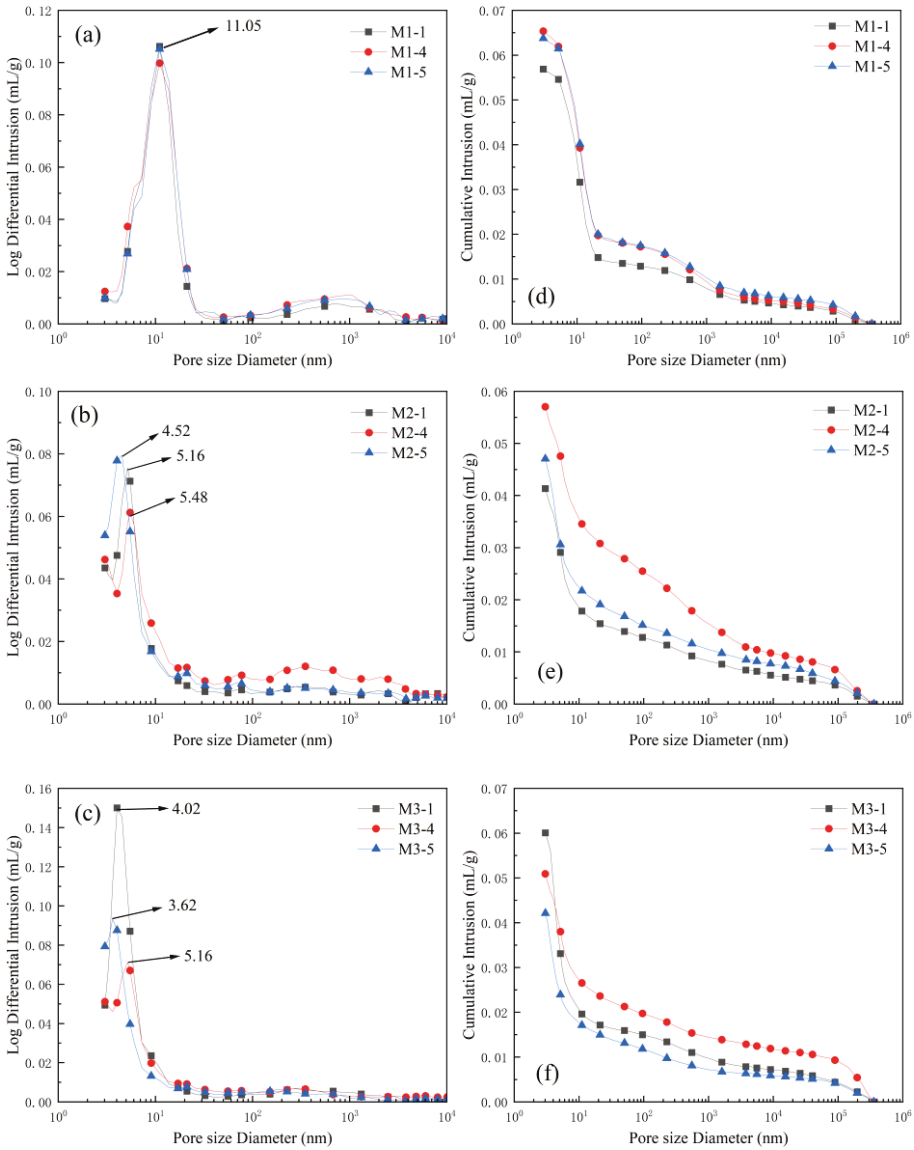

Figure 8. Analysis of pore structure of UHPC under different curing regimes (M1, M2, M3): differential pore volume (**a**–**c**); cumulative pore volume (**d**–**f**).

The main reasons for the above changes in pore structure are as follows: (1) The particle size of AS is smaller than the particle size of RS 1, and by replacing RS 1 with an equal mass, the porosity of the UHPC decreases. (2) The water–gel ratio used in the preparation of the UHPC is low, and with the increase in the content of the AS, the specific surface of the particles per unit volume of the UHPC increases dramatically, which leads to

an increase in the amount of water needed for the hydration reaction of the concrete, and so the hydration rate slows down and the concrete cannot be generated. More C-S-H gel fills the aggregate pores and refines the pore structure, resulting in a decrease in the gel pore content [33]. (3) Steam curing to accelerate the UHPC cement hydration process, and silica fume, which contains a large number of reactive SiO_2 and has a strong volcanic ash activity, in the process of the second hydration will generate more C-S-H gel to fill the pore space. This will further refine the pore structure, resulting in a substantial increase in the pore content of the gel, which in turn improves the mechanical properties and durability of UHPC [34,35].

3.5. TG-DTG Analysis

The thermogravimetric (TG) and derivative (DTG) curves of the three AS substitution rates of UHPC in the M1, M2, and M3 regimes are shown in Figure 9. From the graphs, it is initially concluded that the incorporation of AS leads to a reduction in the final residual mass. In the DTG curves, the mass loss at around 100 °C was caused by the evaporation of free water, and the mass loss at around 400 °C was caused by the dehydration of the C-S-H gel and $Ca(OH)_2$ crystals [36,37]. $Ca(OH)_2$ decomposed at around 420 °C, and based on the DTG curves, the temperature range at which the decomposition of $Ca(OH)_2$ occurred was considered to be from 380 to 450 °C. It was noteworthy that the $Ca(OH)_2$-induced mass loss peak at about 420 °C was significantly lower in the specimens after steam curing compared to the specimens after 28 d of standard curing.

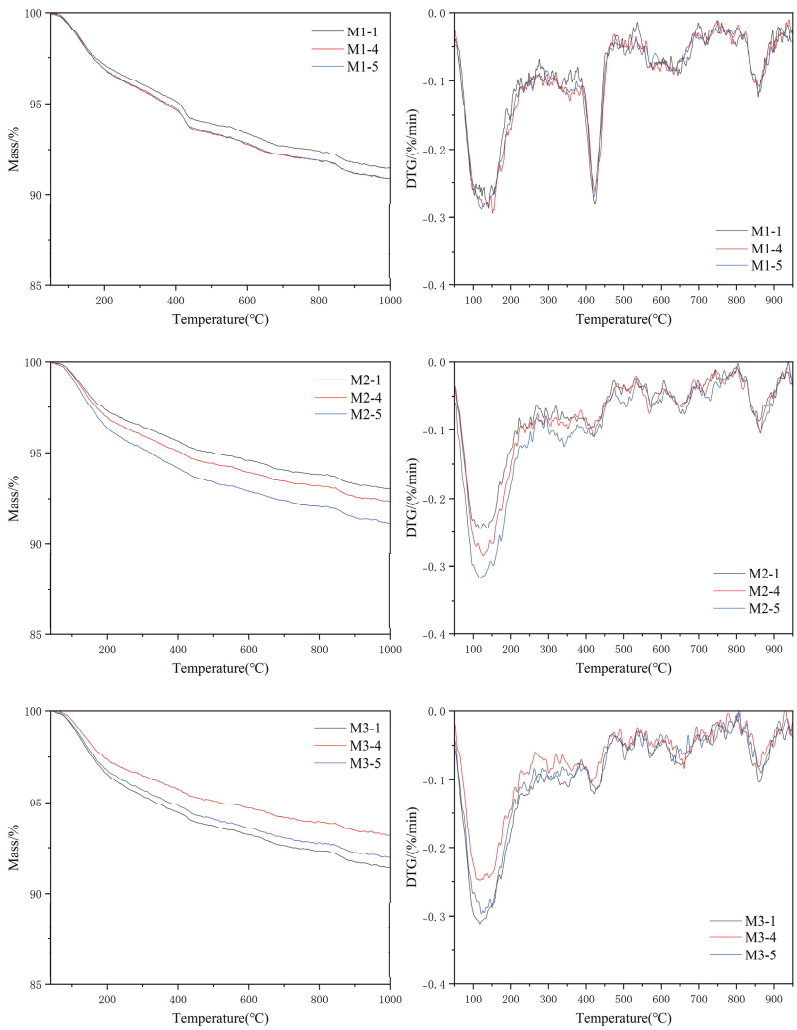

Figure 9. TG and DTG under M1 system, M2 system, and M3 system.

The $Ca(OH)_2$ content in each sample at each conditioning regime can be calculated according to the following formula, as shown in Equation (3):

$$W_{CH} = -\frac{M_{CH} m_{420}}{M_{H_2O} m_{800}} \tag{3}$$

where W_{CH} is the $Ca(OH)_2$ content, M_{CH} and M_{H_2O} are the molar mass of $Ca(OH)_2$ and water, and m_{420} and m_{800} are the mass loss at around 420 °C (380 °C to 450 °C) and the residual mass obtained at 800 °C.

The calculated $Ca(OH)_2$ contents of the UHPC samples with a 0%, 60%, and 80% replacement rate of AS in the M1 regime were 9.58%, 10.15%, and 9.91%, which suggests that AS does not have the property of promoting secondary hydration or participating in secondary hydration under the ambient conditions of standard curing. The mass loss in the interval from 105 °C to 540 °C was caused by the amount of non-evaporated water, which was 6.01%, 6.66%, and 6.54% for the three groups. Under the same curing regime and a fixed water content (Table 2), the incorporation of AS increased the amount of non-evaporated water. While total water remained constant, AS's higher specific surface area altered the distribution and availability of water within the matrix. The finer AS particles increased the interfacial area between the solids and water, enhancing water adsorption on particle surfaces and reducing free water mobility. This localized water retention prolonged the hydration kinetics, allowing for more water to participate in pozzolanic reactions over time, despite the fixed total water content. This mechanism improved the utilization of water for secondary hydration (e.g., SiO_2–$Ca(OH)_2$ reactions), thereby influencing the mechanical and durability properties [38,39].

The $Ca(OH)_2$ contents of UHPC samples with 0%, 60%, and 80% AS substitution rates under the M2 regime were 6.45%, 7.03%, and 8.59%. This indicates that steam curing at 90 °C significantly promotes the consumption of $Ca(OH)_2$ in the AS-UHPC. The $Ca(OH)_2$ contents of the UHPC samples with 0%, 60%, and 80% AS substitution rates under the M3 regime were 4.77%, 6.62%, and 6.87%. The $Ca(OH)_2$ content showed minimal variation between the M3 and M2 curing regimes. This indicates that steam curing predominantly drives AS-UHPC's secondary hydration and pozzolanic reactions during the early stages. Prolonging the curing time post-steam treatment, however, does not significantly enhance further AS hydration. Instead, extended curing primarily facilitates the continued consumption of $Ca(OH)_2$ and promotes silica fume's pozzolanic reaction. These combined processes ultimately improve UHPC's strength and durability properties [40].

3.6. SEM Analysis

The SEM images of the 60% AS substitution rate UHPC at 28 d of standard curing are shown in Figure 10a,b. It can be observed that for a larger number of pore pores, the pore size is defined as being a small capillary pore or larger, there are very obvious cracks between the aggregate and slurry, there are more cracks in the matrix, the hydration product is not sufficiently dense, and from the figure, it can be observed that there are plate-like calcium hydroxide crystals at the interface, which are very poorly bonded to the interface [41]. This is because the water requirement of the AS is large, the hydration of cement is not sufficient in the early stage, and the slurry area with a high water–cement ratio is formed around the AS, which makes it easy for calcium hydroxide to accumulate [42,43].

SEM images of UHPC with a 60% AS substitution rate under the M2 curing regime are shown in Figure 10c,d. At this time, the high crystallinity of the overall structure, the dense accumulation of crystal products, and the increased structural defects at the interface have not changed, and many pores and cracks can be observed in the gel, as well as a small amount of layered calcium hydroxide crystal accumulation. The interface of the aggregate

and the slurry is also more tightly bonded, which can be seen in the autoclaving conditions. It can be seen that under the vaporization conditions, the activity is highly exerted and the microstructure of UHPC is relatively dense [44].

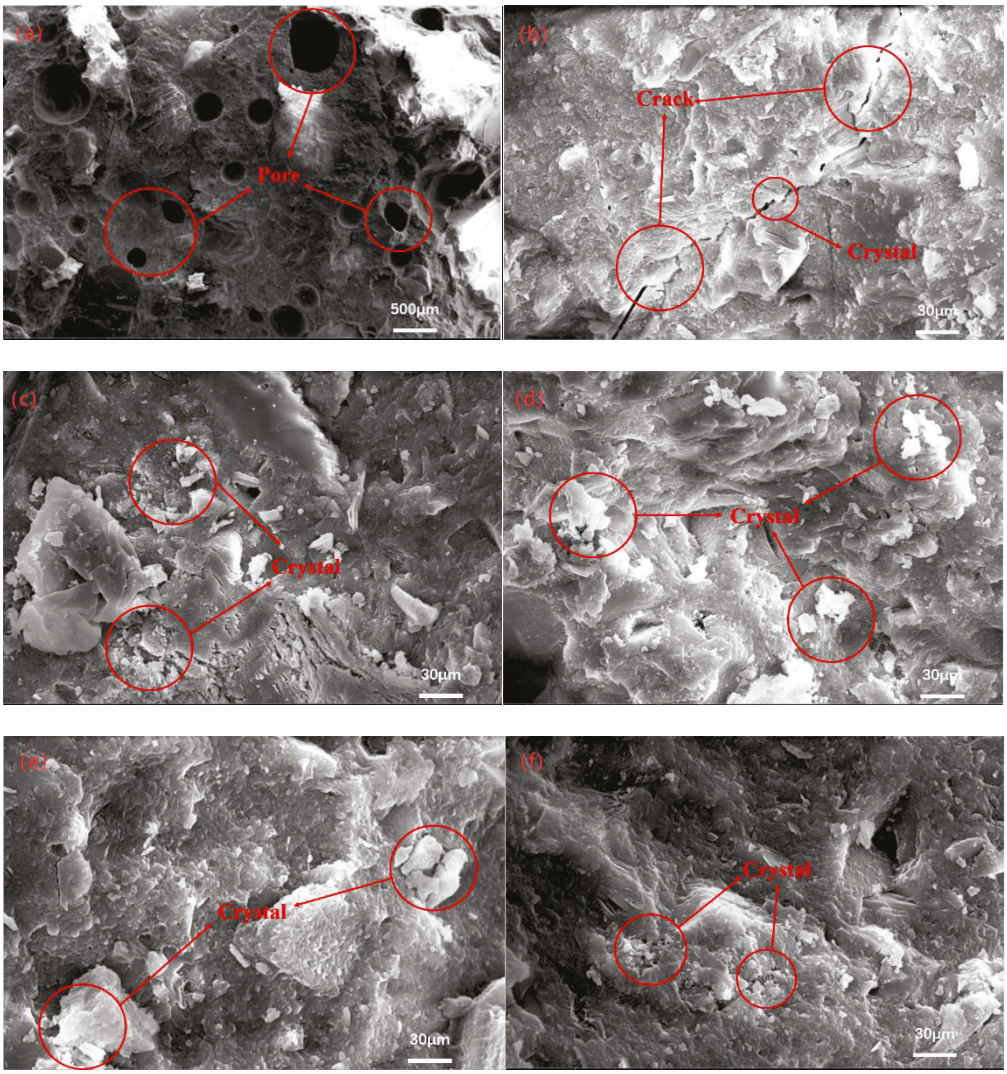

Figure 10. SEM of UHPC with 60% replacement rate of AS under M1 system (**a**,**b**), M2 system (**c**,**d**), M3 system (**e**,**f**). (Red circle in the picture: Calcium crystals or microcracks).

SEM images of UHPC with a 60% AS substitution rate under the M3 curing regime are shown in Figure 10e,f. After steam curing and continuing to undergo a period of standard curing, it can be observed that the number of cracks in the matrix is reduced, but they still exist, which is caused by temperature stress; the interface between the aggregate and the matrix is further optimized, with a tight bond at the interface; calcium hydroxide crystals and more pronounced cracks are not observed; and the hydration product accumulation is dense. The subsequent hydration structure plays a role in filling and perfecting, indicating that the curing method can improve the replacement rate of AS and improve the strength of the UHPC matrix [45].

4. Conclusions

This study investigates the feasibility of replacing RS with AS as an aggregate in UHPC, especially at substitution rates of 60% to 80%. This research found that optimized particle gradation significantly enhanced the flowability and density of UHPC. The experimental results demonstrated that appropriate steam and standard curing conditions not

only improved the compressive and flexural strength of the concrete but also effectively reduced early autogenous shrinkage and lowered the porosity. Steam curing accelerated the hydration of cement and silica fume, facilitating the formation of additional C-S-H gel. This process densified the microstructure, thereby improving the mechanical properties and durability. These findings confirm that AS serves as an effective and environmentally beneficial substitute for a UHPC aggregate. The main conclusions are summarized as follows:

(1) A high-density UHPC skeleton was generated using the modified Andreasen and Andersen particle filling model. The deviation of the particle size distribution between the target and mixture curves was small. The combination of the grading of AS and RS with cementitious materials was favorable for obtaining the optimal particle size distribution profile of UHPC.
(2) Under the standard curing regime, UHPC with 60% to 80% AS incorporation increased the degree of flow by 1.7% to 3.0% and reduced the degree of autogenous shrinkage by 13.83% to 34.22% as compared to the blank group. A significant reduction in the flexural and compressive strength of UHPC was observed under the standard 28 d curing regime.
(3) Under the M3 curing regime (steam curing at 90 °C for 2 d followed by standard curing for up to 7 d), UHPC with 60–80% AS substitution achieved a flexural strength exceeding 18 MPa and a compressive strength over 130 MPa. Notably, the compressive strength of samples with 60% and 80% AS reached 132.4 MPa and 130.8 MPa, respectively. Compared to standard 28 d curing, this hybrid regime reduced porosity by 31.7% (from 13.4% to 9.2%) and increased the gel pore content by nearly 1.5 times (from 23–27% to 58–61%), demonstrating superior matrix densification through accelerated hydration and pozzolanic reactions. These results highlight the feasibility of high-volume AS utilization in UHPC while maintaining exceptional mechanical properties.

This paper mainly studies the early- and mid-term performance of AS-UHPC. In the future, further research can be conducted on its long-term performance, especially its durability performance under different environmental conditions (such as freeze–thaw cycles, wet–dry alternation, etc.), to evaluate the potential application of AS-UHPC in practical engineering.

Author Contributions: Conceptualization, Y.L. and X.L.; methodology, Y.L.; software, B.Z.; validation, Y.L., J.Z. and X.L.; formal analysis, B.Z.; investigation, B.Z.; resources, Y.L.; data curation, B.Z.; writing—original draft preparation, B.Z.; writing—review and editing, Y.L.; visualization, C.H., Y.G. and Y.W.; supervision, X.L., Y.Z. (Yanchao Zhu), J.D. and Y.Z. (Yang Zhou); project administration, J.Z.; funding acquisition, Y.L. All authors have read and agreed to the published version of the manuscript.

Funding: This work was supported by the National Natural Science Foundation of China (52172024), the Key Science and Technology Plan Project (2023AB013-03), and the financial funding from the Hubei Key Laboratory of Polymer Materials (Hubei University).

Institutional Review Board Statement: Not applicable.

Informed Consent Statement: Not applicable.

Data Availability Statement: The original contributions presented in this study are included in the article. Further inquiries can be directed to the corresponding author.

Conflicts of Interest: Author Jie Zhu is employed by the China Railway Electrification Bureau Group Co., Ltd. The remaining authors declare that the research was conducted in the absence of any commercial or financial relationships that could be construed as a potential conflict of interest.

Abbreviations

The following abbreviations are used in this manuscript:

UHPC	Ultra-high-performance concrete
AS	Aeolian sand
RS	River sand

References

1. Choi, D.; Hong, K.; Ochirbud, M.; Meiramov, D.; Sukontaskuul, P. Mechanical Properties of Ultra-High Performance Concrete (UHPC) and Ultra-High Performance Fiber-Reinforced Concrete (UHPFRC) with Recycled Sand. *Int. J. Concr. Struct. Mater.* **2023**, *17*, 67. [CrossRef]
2. Meng, W.; Khayat, K. Effects of saturated lightweight sand content on key characteristics of ultra-high-performance concrete. *Cem. Concr. Res.* **2017**, *101*, 46–54. [CrossRef]
3. Chu, H.; Wang, F.; Wang, L.; Feng, T.; Wang, D. Mechanical Properties and Environmental Evaluation of Ultra-High-Performance Concrete with Aeolian Sand. *Materials* **2020**, *13*, 3148. [CrossRef] [PubMed]
4. Liu, S.; Zheng, W.; Wu, F. Preparation of ultra-high performance concrete containing waste foundry sand and its application in structures. *Structures* **2023**, *58*, 105472. [CrossRef]
5. Chuah, S.; Duan, W.H.; Pan, Z.; Hunter, E.; Korayem, A.H.; Zhao, X.L.; Collins, F.; Sanjayan, J.G. The properties of fly ash based geopolymer mortars made with dune sand. *Mater. Des.* **2016**, *92*, 571–578. [CrossRef]
6. Jiang, J.; Feng, T.; Chu, H.; Wu, Y.; Wang, F.; Zhou, W.; Wang, Z. Quasi-static and dynamic mechanical properties of eco-friendly ultra-high-performance concrete containing aeolian sand. *Cem. Concr. Compos.* **2019**, *97*, 369–378. [CrossRef]
7. Li, Y.; Zhang, H.; Chen, S.; Wang, H.; Liu, G. Multi-scale study on the durability degradation mechanism of aeolian sand concrete under freeze–thaw conditions. *Constr. Build. Mater.* **2022**, *340*, 127433. [CrossRef]
8. Al-Harthy, A.S.; Halim, M.A.; Taha, R.; Al-Jabri, K.S. The properties of concrete made with fine dune sand. *Constr. Build. Mater.* **2007**, *21*, 1803–1808. [CrossRef]
9. Lynda Amel, C.; Kadri, E.-H.; Sebaibi, Y.; Soualhi, H. Dune sand and pumice impact on mechanical and thermal lightweight concrete properties. *Constr. Build. Mater.* **2017**, *133*, 209–218. [CrossRef]
10. Li, Y.; Zhang, H.; Liu, X.; Liu, G.; Hu, D.; Meng, X. Time-Varying Compressive Strength Model of Aeolian Sand Concrete considering the Harmful Pore Ratio Variation and Heterogeneous Nucleation Effect. *Adv. Civ. Eng.* **2019**, *2019*, 5485630. [CrossRef]
11. Li, Y.; Zhang, H.; Liu, G.; Hu, D.; Ma, X. Multi-scale study on mechanical property and strength prediction of aeolian sand concrete. *Constr. Build. Mater.* **2020**, *247*, 118538. [CrossRef]
12. Bouziani, T.; Benmounah, A.; Bédérina, M. Statistical modelling for effect of mix-parameters on properties of high-flowing sand-concrete. *J. Cent. South Univ.* **2012**, *19*, 2966–2975. [CrossRef]
13. Seif, E.-S.S.A. Assessing the engineering properties of concrete made with fine dune sands: An experimental study. *Arab. J. Geosci.* **2011**, *6*, 857–863. [CrossRef]
14. Funk, J.E.; Dinger, D.R. *Predictive Process Control of Crowded Particulate Suspensions: Applied to Ceramic Manufacturing*; Springer Science & Business Media: Berlin/Heidelberg, Germany, 2013.
15. Yu, R.; Spiesz, P.; Brouwers, H.J.H. Mix design and properties assessment of Ultra-High Performance Fibre Reinforced Concrete (UHPFRC). *Cem. Concr. Res.* **2014**, *56*, 29–39. [CrossRef]
16. Yu, R.; van Beers, L.; Spiesz, P.; Brouwers, H.J.H. Impact resistance of a sustainable Ultra-High Performance Fibre Reinforced Concrete (UHPFRC) under pendulum impact loadings. *Constr. Build. Mater.* **2016**, *107*, 203–215. [CrossRef]
17. Spiesz, P.; Yu, Q.L.; Brouwers, H.J.H. Development of cement-based lightweight composites—Part 2: Durability-related properties. *Cem. Concr. Compos.* **2013**, *44*, 30–40. [CrossRef]
18. Wang, X.; Yu, R.; Song, Q.; Shui, Z.; Liu, Z.; Wu, S.; Hou, D. Optimized design of ultra-high performance concrete (UHPC) with a high wet packing density. *Cem. Concr. Res.* **2019**, *126*, 105921. [CrossRef]
19. Liu, K.; Yu, R.; Shui, Z.; Yi, S.; Li, X.; Ling, G.; He, Y. Influence of external water introduced by coral sand on autogenous shrinkage and microstructure development of Ultra-High Strength Concrete (UHSC). *Constr. Build. Mater.* **2020**, *252*, 119111. [CrossRef]
20. Brouwers, H.J.H.; Radix, H.J. Self-Compacting Concrete: Theoretical and experimental study. *Cem. Concr. Res.* **2005**, *35*, 2116–2136. [CrossRef]
21. Hunger, M. An Integral Design Concept for Ecological Self-Compacting Concrete. Ph.D. Thesis, Eindhoven University of Technology, Eindhoven, The Netherlands, 2010.
22. Liu, K.; Yu, R.; Shui, Z.; Li, X.; Ling, X.; He, W.; Yi, S.; Wu, S. Effects of Pumice-Based Porous Material on Hydration Characteristics and Persistent Shrinkage of Ultra-High Performance Concrete (UHPC). *Materials* **2018**, *12*, 11. [CrossRef]
23. *GB/T 2419-2005*; Test Method for Fluidity of Cement Mortar. Standardization Administration of China: Beijing, China, 2005.

24. *GB/T 50081-2019*; Standard for Test Methods of Concrete Physical and Mechanical Properties. Ministry of Housing and Urban-Rural Development of China: Beijing, China, 2019.
25. *T/CBMF 37-2018*; Ultra-High Performance Concrete. China Building Materials Federation: Beijing, China, 2018.
26. *ASTM C1698-09*; Standard Test Method for Autogenous Strain of Cement Paste and Mortar. American Society for Testing and Materials: West Conshohocken, PA, USA, 2009.
27. Luo, F.J.; He, L.; Pan, Z.; Duan, W.H.; Zhao, X.L.; Collins, F. Effect of very fine particles on workability and strength of concrete made with dune sand. *Constr. Build. Mater.* **2013**, *47*, 131–137. [CrossRef]
28. Zhang, M.; Zhu, X.; Shi, J.; Liu, B.; He, Z.; Liang, C. Utilization of desert sand in the production of sustainable cement-based materials: A critical review. *Constr. Build. Mater.* **2022**, *327*, 127014. [CrossRef]
29. Guettala, S.; Mezghiche, B. Compressive strength and hydration with age of cement pastes containing dune sand powder. *Constr. Build. Mater.* **2011**, *25*, 1263–1269. [CrossRef]
30. Wang, T.; Gong, J.; Chen, B.; Gong, X.; Guo, W.; Zhang, Y.; Li, F.; Mo, K.H. Mechanical Properties and Shrinkage of Ultrahigh-Performance Concrete Containing Lithium Carbonate and Nano-Calcium Carbonate. *Adv. Civ. Eng.* **2021**, *2021*, 6646272. [CrossRef]
31. Kang, S.-H.; Hong, S.-G.; Moon, J. The effect of superabsorbent polymer on various scale of pore structure in ultra-high performance concrete. *Constr. Build. Mater.* **2018**, *172*, 29–40. [CrossRef]
32. Mo, Z.; Gao, X.; Su, A. Mechanical performances and microstructures of metakaolin contained UHPC matrix under steam curing conditions. *Constr. Build. Mater.* **2021**, *268*, 121112. [CrossRef]
33. Xiong, X.; Wu, M.; Shen, W.; Li, J.; Zhao, D.; Li, P.; Wu, J. Performance and microstructure of ultra-high-performance concrete (UHPC) with silica fume replaced by inert mineral powders. *Constr. Build. Mater.* **2022**, *327*, 126996. [CrossRef]
34. Zhang, J.; Yu, R.; Shui, Z.; Liu, K. Hydration kinetics and microstructure development of Ultra-High Performance Concrete (UHPC) subjected to microwave pre-curing. *Cem. Concr. Compos.* **2022**, *129*, 104484. [CrossRef]
35. Xu, D.; Tang, J.; Hu, X.; Zhou, Y.; Yu, C.; Han, F.; Liu, J. Influence of silica fume and thermal curing on long-term hydration, microstructure and compressive strength of ultra-high performance concrete (UHPC). *Constr. Build. Mater.* **2023**, *395*, 132370. [CrossRef]
36. Goñi, S.; Puertas, F.; Hernández, M.S.; Palacios, M.; Guerrero, A.; Dolado, J.S.; Zanga, B.; Baroni, F. Quantitative study of hydration of C3S and C2S by thermal analysis. *J. Therm. Anal. Calorim.* **2010**, *102*, 965–973. [CrossRef]
37. Pane, I.; Hansen, W. Investigation of blended cement hydration by isothermal calorimetry and thermal analysis. *Cem. Concr. Res.* **2005**, *35*, 1155–1164. [CrossRef]
38. Jiang, J.; Wang, L.; Chu, H.; Wang, F.; Ju, S.; Gu, Y. Workability, hydration, microstructure, and mechanical properties of UHPC produced with aeolian sand. *J. Sustain. Cem.-Based Mater.* **2021**, *11*, 57–73. [CrossRef]
39. Zhu, L.; Zheng, M.; Zhang, S.; Zhang, W.; Chen, W.; Ou, Z. Modification and mechanism of polymer in high-performance concrete with full aeolian sand: An integrated macro-to-micro perspective. *J. Build. Eng.* **2023**, *75*, 106969. [CrossRef]
40. Shen, P.; Lu, L.; He, Y.; Wang, F.; Hu, S. The effect of curing regimes on the mechanical properties, nano-mechanical properties and microstructure of ultra-high performance concrete. *Cem. Concr. Res.* **2019**, *118*, 1–13. [CrossRef]
41. Zhu, C.; Yi, T.; Lin, X.; Bai, G.; Liu, C. Feasibility analysis of treating aeolian sand and recycled mixed powder as environmentally friendly materials in the ultra-high-performance concrete. *Dev. Built Environ.* **2023**, *15*, 100212. [CrossRef]
42. Feng, Y.; Zhang, B.; Xie, J.; Xue, Z.; Huang, K.; Tan, J. Effects of recycled sand and nanomaterials on ultra-high performance concrete: Workability, compressive strength and microstructure. *Constr. Build. Mater.* **2023**, *378*, 131180. [CrossRef]
43. Wang, R.; Wang, P.-M.; Li, X.-G. Physical and mechanical properties of styrene–butadiene rubber emulsion modified cement mortars. *Cem. Concr. Res.* **2005**, *35*, 900–906. [CrossRef]
44. Bahmani, H.; Mostofinejad, D. Microstructure of ultra-high-performance concrete (UHPC)—A review study. *J. Build. Eng.* **2022**, *50*, 104118. [CrossRef]
45. Yang, Z.; Shi, X.; Creighton, A.T.; Peterson, M.M. Effect of styrene–butadiene rubber latex on the chloride permeability and microstructure of Portland cement mortar. *Constr. Build. Mater.* **2009**, *23*, 2283–2290. [CrossRef]

Disclaimer/Publisher's Note: The statements, opinions and data contained in all publications are solely those of the individual author(s) and contributor(s) and not of MDPI and/or the editor(s). MDPI and/or the editor(s) disclaim responsibility for any injury to people or property resulting from any ideas, methods, instructions or products referred to in the content.

materials

MDPI

Article

Seismic Response Mitigation of Reinforced-Concrete High-Speed Railway Bridges with Hierarchical Curved Steel Dampers

Mingshi Liang [1], Liqiang Jiang [1,2,*] and Jianguang He [1]

[1] School of Civil Engineering, Central South University, Changsha 410075, China; 13908182361@126.com (M.L.); csuhjg@csu.edu.cn (J.H.)
[2] National Engineering Research Center for High-Speed Railway Construction, Changsha 410075, China
* Correspondence: jianglq2019@csu.edu.cn

Abstract

To address the seismic vulnerability of high-speed railway bridges (HSRBs) in seismically active regions, this study proposes a hierarchical curved steel damper (CSD) designed to mitigate excessive girder displacements induced by conventional isolation devices. The CSD integrates U-shaped and hollow diamond-shaped steel plates to achieve stable energy dissipation through coupled bending deformation. A finite element model is developed, and its hysteretic behavior is confirmed, with an energy dissipation coefficient of 1.82 and an equivalent damping ratio of 12.7%. An integrated high-speed railway track–bridge-CSD spatial coupling model is developed in OpenSees, which incorporates nonlinear springs for interlayer track interactions. Nonlinear time–history analyses under 40 spectrum-matched ground motions reveal that the CSD reduces transverse girder displacements by 73.7–79.2% and attenuates track slab acceleration peaks by 52.4% compared with uncontrolled cases. However, it increases the maximum bending moment at pier bases by up to 18.3%, necessitating supplemental energy-dissipating components for balanced force redistribution. This work provides a theoretical foundation and practical methodology for seismic response control and retrofitting of the HSRB in high-intensity seismic regions.

Keywords: high-speed railway bridge; hierarchical curved energy dissipation damper; seismic response control; finite element analysis; dynamic response

1. Introduction

The rapid expansion of China's high-speed railway network relies heavily on bridge-centric designs, with bridges constituting more than 80% of certain routes in seismically active southwestern regions [1]. While such designs enhance route alignment and terrain adaptability, they expose inherent seismic vulnerabilities: earthquakes frequently induce girder displacements, bearing failures, and pier shear damage [2,3]. Statistical analyses reveal that seismic damage rates increase exponentially with increasing intensity [4], posing catastrophic risks to both infrastructure integrity and train operational safety. This dilemma necessitates advanced seismic mitigation strategies tailored to the stringent displacement tolerances of the HSRB [5].

Current seismic solutions face critical limitations. Conventional isolation bearings, such as rubber bearings and friction pendulum bearings, struggle to balance displacement control and durability. Despite their high vertical stiffness and adaptability to beam rotations, rubber bearings suffer from aging-induced stiffness degradation and insufficient energy dissipation [6]. Friction pendulum bearings, although durable and capable of

large vertical load bearing, amplify girder displacements by 30–50% under near-fault motions, exacerbating track geometric errors [7]. Energy dissipation devices, including active magnetorheological dampers [8] and passive rotary friction devices [9], either require unreliable external power or inadequate constrain responses. Notably, prior studies [10,11] often overlook the coupled dynamics of systems, limiting real-world applicability.

To address these gaps, this study proposes a hierarchical curved steel damper (CSD) that integrates U-shaped and hollow diamond-shaped steel plates. The CSD's innovation lies in its dual-plate bending mechanism: during low-intensity vibrations, the U-shaped plate initiates flexural deformation for initial energy absorption; under large displacements, the hollow diamond plate engages to provide stable hysteretic energy dissipation with an energy dissipation coefficient of 1.82. This hierarchical design minimizes displacement amplification while maintaining compatibility with the HSRB's strict serviceability requirements, effectively resolving the trade-off in traditional solutions [12,13].

A multi-scale analytical framework is adopted to validate the CSD's efficacy. Component-level validation involves ABAQUS simulations of the CSD's cyclic behavior, calibrating model parameters against experimental hysteresis loops. System-level integration employs OpenSees3.7.1 to construct a high-speed railway track–bridge-CSD spatial model that incorporates nonlinear track interactions such as fastener slip and sliding layer friction [14,15]. Seismic performance is assessed under 40 spectrum-matched ground motions, covering diverse seismic scenarios from moderate to near-fault events [16,17]. This approach ensures rigorous quantification of CSD effectiveness across varying intensity levels.

Three critical research frontiers remain: redefining energy dissipation thresholds through double-plate bending mechanisms [18,19], developing system-level modeling frameworks for high-speed railway bridge–track interactions [20,21], and establishing quantitative retrofitting guidelines with operational indicators [22,23]. The seismic resilience paradigm shift from hazard resistance to functional recovery capacity [24,25], aligned with China's "New Infrastructure" sustainability agenda, represents a transformative solution for high-speed railway bridge (HSRB) networks in seismically active regions [26,27].

This study proposes a novel damping system with graded control capabilities to effectively reduce structural seismic responses. Finite element analysis was conducted to investigate its hysteretic behavior. A controlled seismic damper-integrated high-speed railway vertical track–bridge dynamics (CSD-HSRVTBD) system was developed to examine CSD's impact on seismic performance responses of critical structural components in HSRVTBD systems.

2. Mechanical Characterization of the CSD

2.1. Introduction

Mild steel dampers (MSDs) are widely recognized for their ability to mitigate structural vibrations through the stable hysteretic behavior of metallic materials in the plastic range. By harnessing the inelastic deformation of low-carbon steel, MSDs dissipate seismic energy during yielding, thereby protecting primary structural components. However, conventional single-plate bending dampers often exhibit insufficient load-bearing capacity and limited energy dissipation modes, particularly under large displacements [28–33]. To address these limitations, this chapter introduces a hierarchical curved steel damper (CSD) that integrates U-shaped and hollow diamond-shaped plates, with dimensional details of these components illustrated in Figure 1. Through finite element modeling in ABAQUS, the hysteresis performance of the CSD is systematically analyzed, focusing on its synergistic energy dissipation mechanisms and displacement control capabilities [29,34].

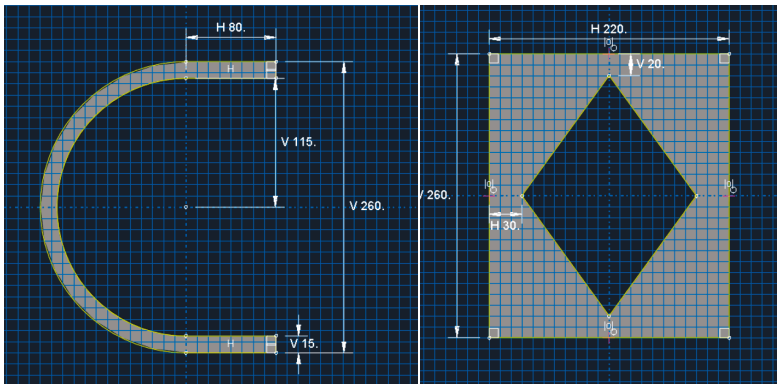

(**a**) U-bent metal plates (**b**) hollow rhombic

Figure 1. Dimensions of the hollow rhombic and U-bent metal plates.

2.2. Design of the CSD

The design of the CSD builds on prior advancements in U-shaped damper technology. Experimental studies [9] demonstrated that U-shaped combined steel dampers (UCSDs) enhance energy dissipation and reduce seismic fragility in bridge systems. Prior research [35] highlighted the benefits of hybrid configurations (e.g., combining U-shaped plates with rectangular plates) for yield displacement control. Additional work [34] further identified thickness optimization as a critical factor in mitigating fracture risk in seismic isolation systems. Leveraging these insights, the CSD is composed of a central energy-dissipating plate assembly and upper/lower connecting steel plates, as shown in Figure 2. The energy-dissipating assembly consists of three parallel-arranged hollow rhombic steel plates positioned symmetrically about the central axis, flanked by bilateral U-shaped plates with inward-facing notches. This configuration facilitates energy dissipation primarily through flexural deformation of the curved segments in the metallic U-plates, where the arc-shaped portions undergo bending deformation to achieve hysteretic energy absorption. Material selection prioritizes functional differentiation: Q235 steel (yield strength: 235 MPa) is used for energy-dissipating components, whereas Q345 steel (yield strength: 345 Mpa) ensures structural stability in non-dissipative regions [36]. Finite element validation in ABAQUS confirms the CSD's synergistic energy dissipation through sequential activation of U-shaped and diamond plates [28], with that of conventional dampers [29]. This design effectively addresses the limitations of traditional MSDs in terms of load-bearing and multi-directional energy dissipation [30].

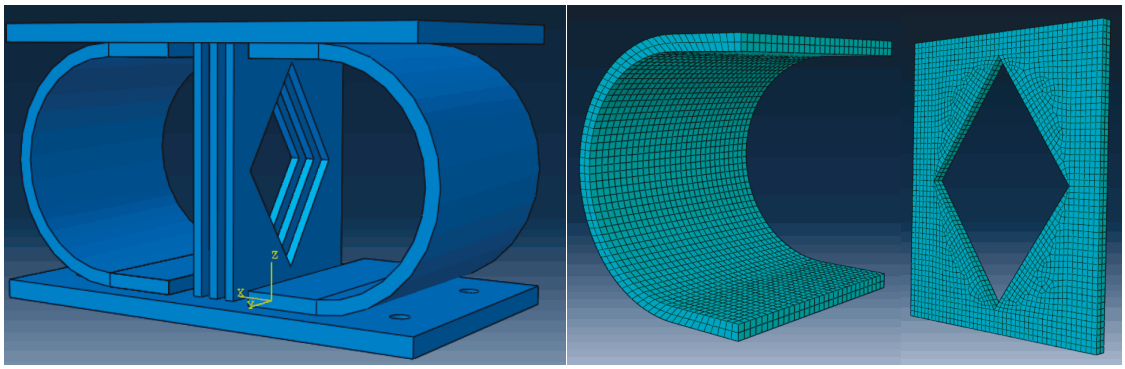

(**a**) Damper Assembly Diagram (**b**) Meshing Elements

Figure 2. Damper Assembly Diagram and Meshing Elements.

2.3. Finite Element Modeling Framework

The finite element model framework incorporates constitutive models for the Q235 and Q345 steels, with bilinear kinematic hardening assigned to the Q235 steel to simulate

post-yield behavior. Welds between components are omitted because of their negligible impact on global hysteresis, whereas auxiliary restraints are idealized as rigid constraints. The Newton–Raphson method was implemented in ABAQUS 2022, with convergence verified through residual force and displacement correction criteria. Following an initial analysis with coarse mesh configurations, progressive grid refinement was performed until the results variation between successive meshes fell below 5%, at which point the mesh was considered sufficiently refined. The meshing of the central energy-dissipating plate is shown in Figure 2. A 5 mm tetrahedral element grid is adopted to balance computational accuracy and efficiency. The U-shaped plate uses 8 mm hexahedral elements, with local refinement to 5 mm in the stress concentration regions, whereas the connecting plates employ a 10 mm structured mesh. As shown in Figure 3, surface-to-surface tie constraints bind energy-dissipating components to connecting plates, with master-slave pairs defined on the basis of the stiffness hierarchy. Displacement-controlled cyclic loading is applied at the upper plate's reference point (RP-1) through a coupling mechanism, following a multi-stage protocol (0–60 mm) to capture both elastic and plastic response regimes. The boundary conditions, including full fixation of the lower plate and *X*-axis displacement constraints on the upper plate, are visually summarized.

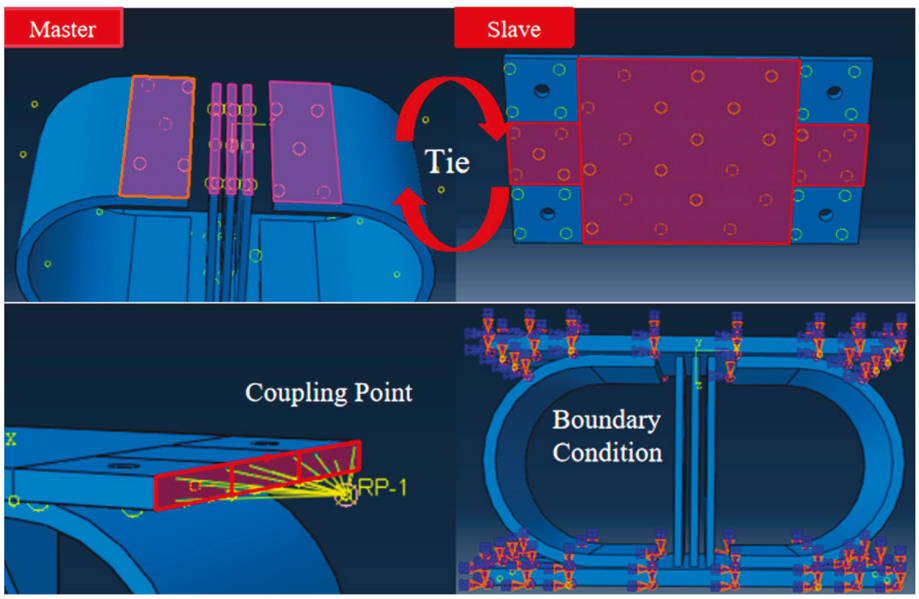

Figure 3. Finite element modeling process.

2.4. Analysis of Deformation Modes and Hysteretic Performance Evaluation

As shown in Figure 4, the FEM simulation of the CSD reveals that the maximum equivalent stress is concentrated in the bending segment and connection ends, indicating potential plastic deformation and low-cycle fatigue failure due to exceeding the material yield strength. Sub-high stress bands in transition zones form continuous stress transfer paths with the main bending area, where cracks may propagate along geometric discontinuities. The steep stress gradient at the connection ends suggests that tear risk occurs near bolt holes or welds, while drastic stress variations in thin-walled regions may trigger material delamination or micro-damage accumulation.

The CSD exhibits a full hysteresis loop without pinching effects, as demonstrated in Figure 4. The quantitative metrics reveal an energy dissipation coefficient (Ed) of 1.82 ± 0.15 across loading cycles and an equivalent damping ratio (ξ_{eq}) of 12.7% at the maximum displacement (60 mm). The ductility ratio (μ) reaches 5.3, surpassing that of conventional U-dampers ($\mu < 4.0$). Parametric analysis revealed two distinct dissipation phases: initial yielding (0–10 mm) dominated by U-plate deformation (Ed = 0.95) and

subsequent hollow diamond plate activation (10–60 mm), resulting in Ed > 1.5. These results validate the CSD's hierarchical energy dissipation mechanism and its ability to mitigate displacement amplification risks inherent in traditional dampers.

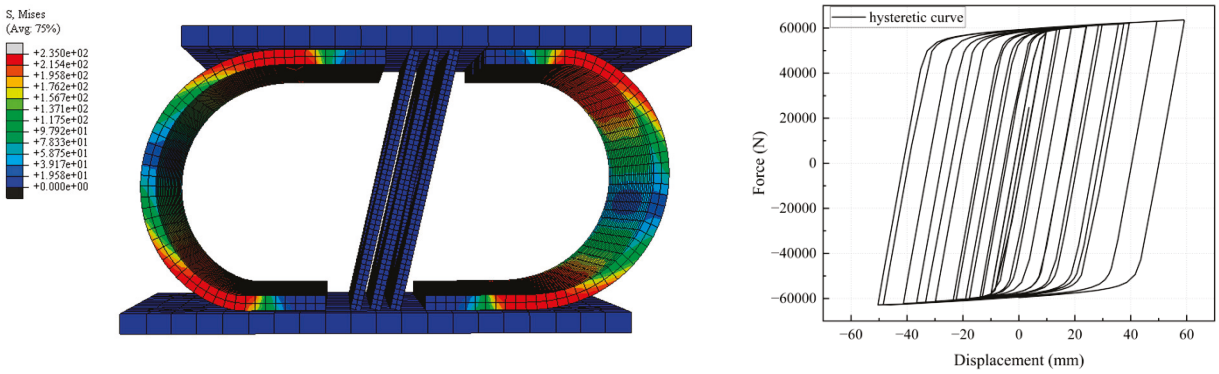

(**a**) Failure modes (**b**) hysteretic curves

Figure 4. Finite element simulation results.

3. Seismic Analysis of the HSR Track–Bridge System Integrated with CSD

3.1. Introduction

High-speed railway (HSR) bridges exhibit unique dynamic interactions that are distinct from those of conventional highway bridges because of their integration with ballastless track systems. The continuous track–bridge coupling amplifies the vibration transmission complexity [37,38], where localized damage—such as bearing failure or girder displacement—can cascade into systemic risks, compromising structural integrity and train operational safety (Figure 5). This interdependence necessitates holistic modeling of the HSR vehicle–track–bridge–damper (HSRVTBD) system [39] under seismic excitation. Building on Chapter 2′s validated CSD design, this chapter establishes a spatial finite element model (FEM) in OpenSees to quantify CSD's efficacy in mitigating seismic responses across coupled subsystems.

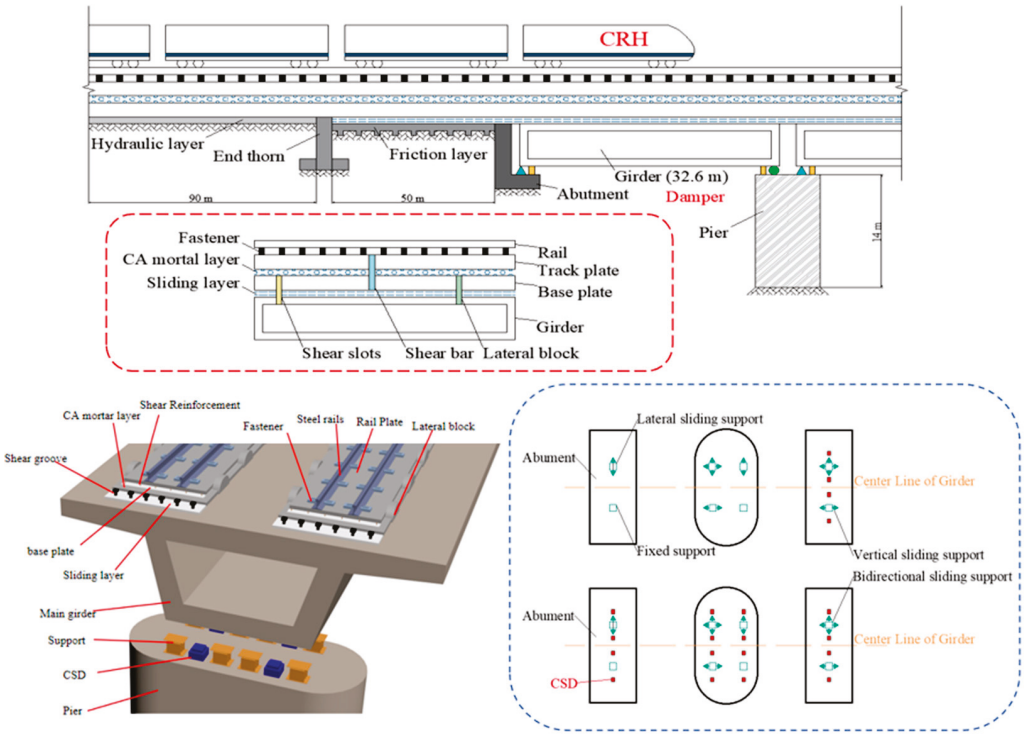

Figure 5. Schematic of HSRTTBS with CSD.

3.2. Finite Element Modeling of the HSRVTBD System

The analysis targets a 5-span simply supported girder bridge with a CRTS II slab track, featuring uniform pier heights (14 m) and 32.6 m spans. The transition zones (50 m) and embankment sections (90 m) flank the bridge ends to simulate realistic boundary conditions [40]. Figure 6 shows a partial finite element model of the high-speed railway track–bridge system. The system consists of two parts: the bridge structure and the track structure. The bridge structure includes the main girder, bearings, piers, and abutments. The composition of the track structure varies depending on its installation location. Longitudinal components along the track alignment comprise rails, track slabs, fasteners, and CA mortar layers. For track structures on bridges, additional elements include base plates, sliding layers, shear reinforcement, shear keys, and lateral restraint blocks. The track structure in the bridge–subgrade transition zone incorporates base plates, sliding layers, end studs, and friction plates. Subgrade sections utilize hydraulically stabilized base layers to support the track structure. Theoretical and experimental analyses confirm that rails, track slabs, base plates, and friction plates generally remain elastic under seismic loads, thus modeled as elastic beam elements. Interlayer connectors such as fasteners, CA mortar layers, sliding layers, shear keys, shear reinforcement, and lateral restraint blocks are simulated using zero-length elements [41].

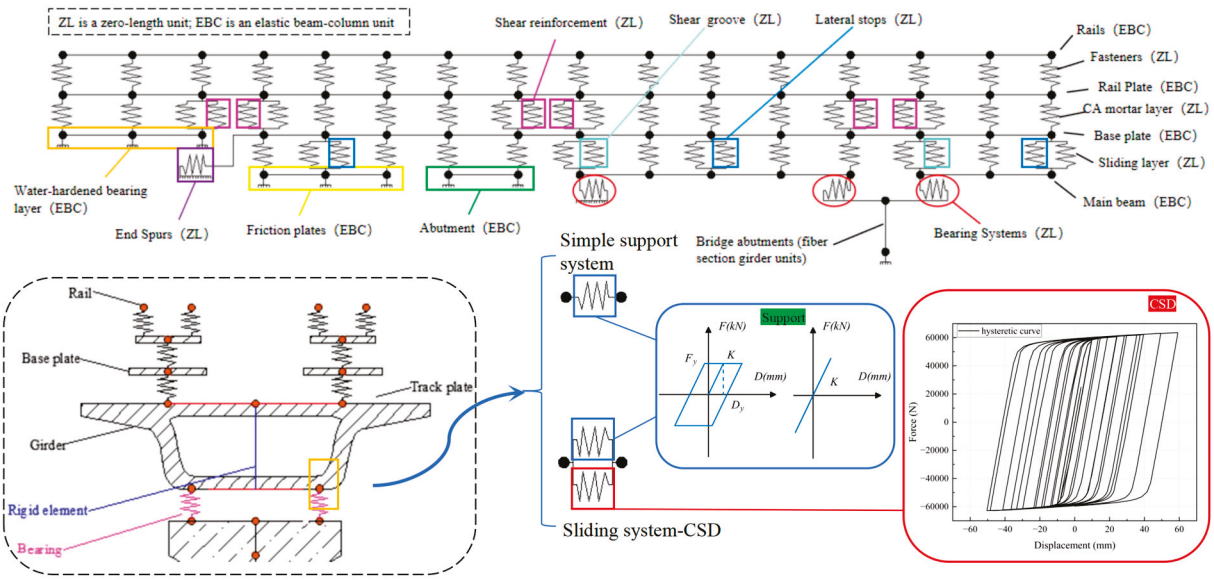

Figure 6. Schematic diagram of the finite element model of the HSRTTBDS.

The main girder, a 32.6 m span prestressed concrete box girder with a single-cell cross-section, is detailed in Figure 7. The key dimensions include a girder height of 3.05 m, a top flange width of 12.6 m, and a bottom flange width of 5.5 m, conforming to the General Reference Drawing for Railway Engineering Construction. Abutments adopt a gravity-type design with longitudinal lengths of 2.5 m and 10 cm girder-abutment clearance. Elastic beam-column elements simulate the girder's high shear stiffness and predominantly elastic seismic response.

The material properties of critical structural components, including the concrete grade, steel reinforcement, and interfacial connections, are rigorously calibrated against design codes and experimental data (Table 1) [42]. For example, the main girders (C50 concrete) and piers (C40 concrete) employ the Concrete01 and Concrete04 models to distinguish cover and confined core behaviors, while the Q345 steel reinforcement follows the Giuffre–Menegotto–Pinto kinematic hardening law.

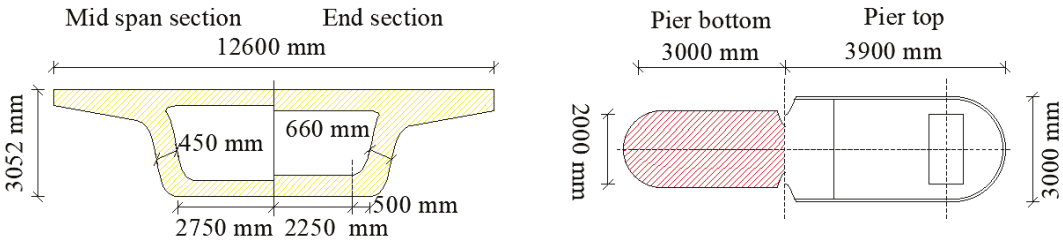

Figure 7. Schematic diagram of the main girder and abutment cross-section.

Table 1. Material Parameters of the Major Structural Elements.

Component	Material	E (MPa)	S (m^2)
Main girder (mid-span)	C50	3.55×10^4	8.722
Main girder (end)	C50	3.55×10^4	14.22
Steel rail	Q235	2.06×10^5	0.007745
Rail plate	C55	3.65×10^4	0.51
Base plate	C30	3.25×10^4	0.5605
Friction plate	C30	3.25×10^4	3.6
Water-hardened bearing layer	water-hard material	1.80×10^4	0.92

Interlayer connection mechanics, which are pivotal for track–bridge interaction accuracy, are defined through nonlinear spring elements (Table 2) [9,41,42]. Fasteners (WJ-8 type) exhibit horizontal yield forces of 15 kN with ideal elastoplasticity, while sliding layers combine Coulomb friction (μ = 0.2) and compression-only vertical springs (1.4×10^6 kN/mm). Shear keys, which are essential for longitudinal force transfer, are modeled with elastic-perfectly plastic behavior (yield displacement: 0.12 mm, stiffness: 1×10^6 kN/mm).

Table 2. Material parameters for the interlayer connection elements [9,41,42].

Component	Horizontal Direction				Vertical Direction
	Fl (kN)	Dl (mm)	Ft (kN)	Dt (mm)	Kv (kN/mm)
Fastener	15	2	15	2	2.4×10^3
CA mortar layer	45	0.5	45	0.5	2.0×10^3
Sliding layer on bridge	6	0.5	6	0.5	/
Friction plate sliding layer	14	0.5	14	0.5	/
Shear groove	1200	0.12	1200	0.12	2.3×10^4
Shear reinforcement	173	0.075	173	0.075	0
Lateral block	0	0	453	2	0
Fixed end of support	1000	2	1000	2	1.0×10^4
Sliding end of support	100	2	100	2	1.0×10^4
Force–displacement curve	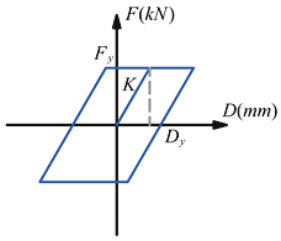				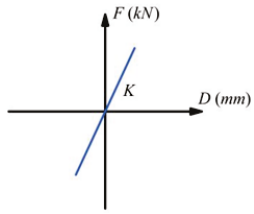

The CSD, validated in Chapter 2, is implemented as nonlinear springs between piers and girders, with its hysteresis behavior embedded via user-defined material subroutines [43].

3.3. Ground Motion Selection and Spectral Matching

Appropriate ground motion records serve as a critical foundation for conducting nonlinear time history analyses. Currently, three primary methodologies are employed for selecting ground motion records: seismological parameter-based approaches, target spectrum-based methods, and most unfavorable earthquake-based criteria. To capture the inherent variability of ground motions, 40 ground motion records were extracted from the Pacific Earthquake Engineering Research Center (PEER) database. These records were scaled to match a site-specific design spectrum (PGA: 0.1 g–0.6 g) [30], ensuring intensity consistency (Intensity Measure, IA = 0.8–1.2) while preserving frequency content diversity. Table 3 summarizes key parameters of the selected records, including magnitude, epicentral distance, and peak ground acceleration. Figure 8 compares the adjusted response spectra with the target spectrum, demonstrating deviations within 10% across the dominant frequency range (0.5–10 Hz) [34]. Pulse-like ground motions require focused attention on instantaneous failure mechanisms, whereas non-pulse motions necessitate mitigation of cumulative damage. This ground motion suite incorporates both strong velocity pulse and non-pulse events to account for potential extreme scenarios. The input ground vibrations were assumed to be uniformly distributed at all structural supports, with the ground motion direction defined as transverse.

Table 3. Ground shaking record data.

Record	Seismic Intensity	Epicenter Distance (km)	Nearest Distance (km)	Preferred Vs30 (m/s)	FN Pulse	Pulse Period (s)	Conversion Factor
1	7.0	13.0	6.1	213	0	−99.00	3.63
2	6.5	2.6	0.7	275	1	2.30	4.28
3	6.5	43.2	10.4	209	1	4.03	5.23
4	6.5	18.9	7.3	275	0	−99.00	3.54
5	6.5	19.4	0.1	186	1	3.35	2.41
6	6.5	26.3	6.2	203	1	4.49	4.10
7	6.5	29.4	12.5	196	1	7.36	3.96
8	6.5	32.0	17.9	197	0	−99.00	7.18
9	6.5	28.7	12.9	163	1	5.24	4.41
10	6.5	27.1	7.1	209	1	4.61	2.48
11	6.5	27.8	4.0	206	1	4.05	2.33
12	6.5	27.5	1.4	203	1	3.84	2.08
13	6.5	28.1	3.9	206	1	5.39	2.87
14	6.5	27.2	5.1	202	1	5.86	2.43
15	6.5	19.8	7.7	203	1	4.80	3.93
16	6.5	48.6	12.7	349	0	−99.00	8.00
17	6.3	36.7	19.0	275	0	−99.00	5.82
18	5.9	20.5	16.7	349	1	3.58	3.66
19	6.2	20.3	17.2	271	0	−99.00	6.20
20	6.2	24.8	17.6	207	0	−99.00	8.00
21	6.5	35.8	18.2	192	0	−99.00	3.13
22	6.5	19.5	13.0	194	0	−99.00	3.88
23	6.9	32.4	14.3	222	0	−99.00	3.84
24	6.9	27.2	8.5	371	1	4.47	2.97
25	6.7	9.0	4.4	275	1	2.65	1.78
26	6.7	11.1	8.7	298	0	−99.00	3.59
27	6.7	4.9	14.7	267	0	−99.00	2.45
28	6.7	13.0	5.4	373	1	3.53	1.60
29	6.7	13.1	12.5	446	0	−99.00	4.13
30	6.7	20.3	5.9	269	0	−99.00	1.70

Table 3. *Cont.*

Record	Seismic Intensity	Epicenter Distance (km)	Nearest Distance (km)	Preferred Vs30 (m/s)	FN Pulse	Pulse Period (s)	Conversion Factor
31	6.7	19.3	7.3	508	0	−99.00	2.90
32	6.7	10.9	6.5	282	1	1.23	1.42
33	6.7	12.4	10.1	309	0	−99.00	3.17
34	6.7	13.6	5.2	371	1	3.49	1.45
35	6.9	46.0	19.2	256	0	−99.00	3.67
36	7.1	41.3	12.0	326	0	−99.00	1.93
37	7.1	1.6	6.6	276	0	−99.00	1.85
38	6.2	25.5	19.7	428	1	3.19	6.82
39	6.2	10.1	6.2	553	0	−99.00	2.85
40	6.2	14.5	12.5	553	0	−99.00	8.00

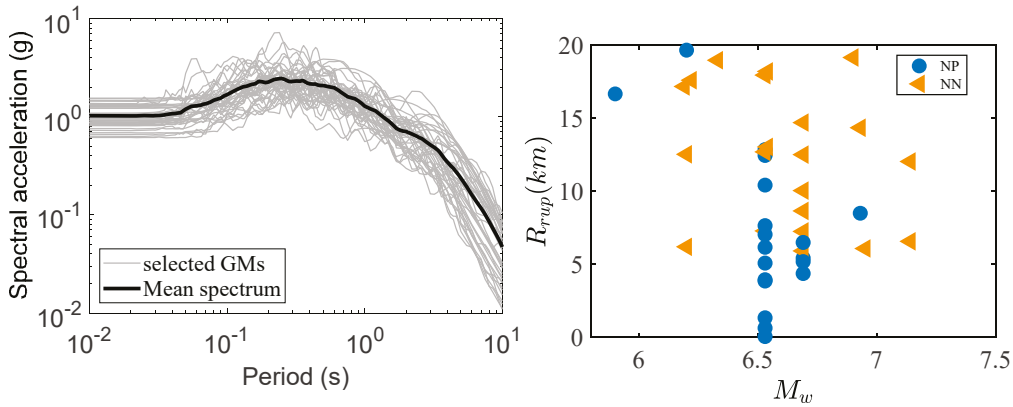

(**a**) Response spectra (**b**) grouping information

Figure 8. Response spectra and grouping information for ground shaking records.

Building upon the comprehensive finite element model of the HSRVTBD system established in this chapter—which integrates multi-component realism (track–bridge interaction, CSD nonlinearity) and validated material laws (concrete, steel, interfacial connections)—nonlinear time history analyses were conducted. These analyses quantitatively evaluate the effectiveness of CSD in mitigating girder displacements, fastener forces, and track-slab accelerations. By synergizing design specifications (e.g., general reference diagrams) with advanced numerical techniques, this model advances seismic assessment methodologies for HSR infrastructure, particularly in seismically active regions requiring stringent displacement tolerances.

4. Seismic Mitigation Efficacy of CSD Dampers in HSR Bridge–Track Systems

4.1. Component-Level Deformation Analysis via MATLAB Visualization

The seismic performance of an HSR bridge–track system (BTS) retrofitted with combined steel dampers (CSDs) is systematically evaluated through MATLAB R2024b-driven data visualization. Comparative analyses between the baseline system (BTS) and the retrofitted system (BTS-CSD) focus on eight critical components, quantifying deformation reductions and identifying force redistribution patterns.

The assessment of structural safety status conventionally adopts peak response as the key indicator for evaluating component exceedance. To simplify the description, the mean value of lateral peak response of components considering all ground motion components was adopted to assess structural safety status.

Sliding and fixed bearings exhibit the most pronounced improvements. Figures 9 and 10 reveal that CSD implementation reduces sliding bearing deformation by 73.7% (Pier 1: 0.0514 m → 0.0134 m), 79.2% (Pier 2), 79.6% (Pier 3), and 74.9% (Pier 4), with analogous trends observed for fixed bearings (Figures 11 and 12). Specifically, the fixed-bearing deformation decreases by 74.7% at Pier 1 (0.0471 m → 0.0119 m) and 72.8% at Pier 4 (Tables 4 and 5). This uniform reduction (>70% across all piers) underscores CSD's efficacy in restraining lateral displacements at bearing interfaces while maintaining torsional equilibrium.

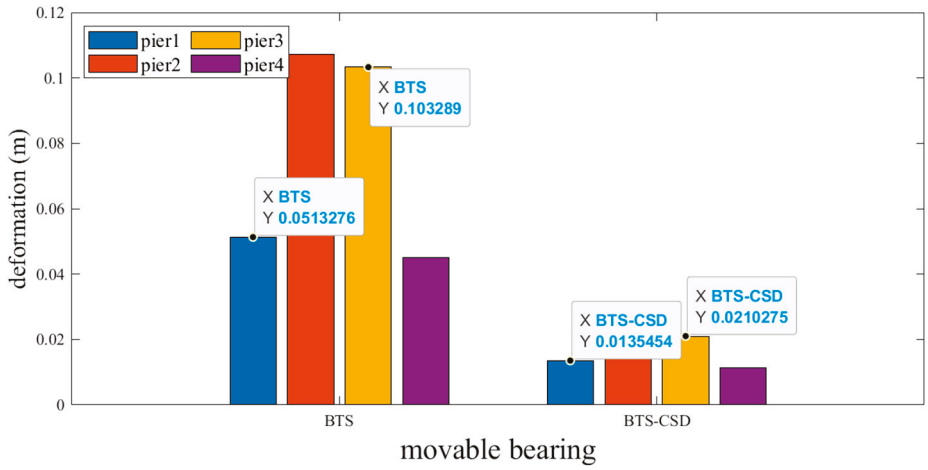

Figure 9. Comparison of BTS and BTS-CSD Deflections—Sliding Support Piers 1 and 3.

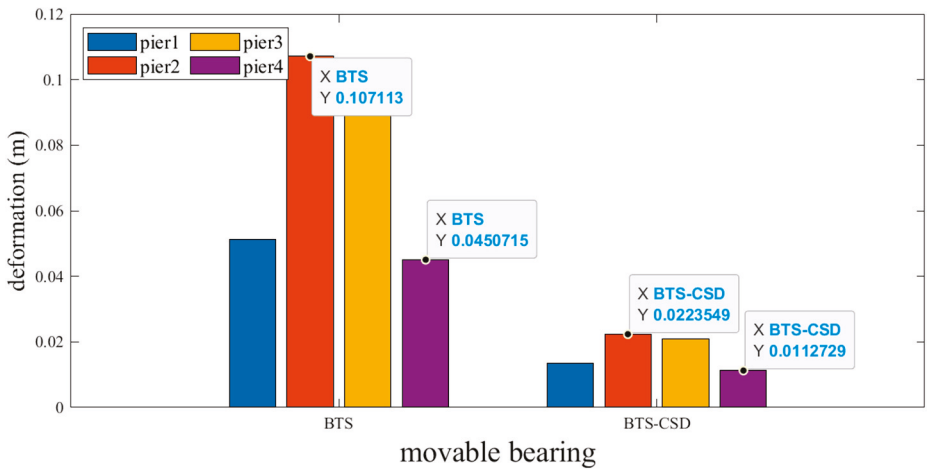

Figure 10. Comparison of BTS and BTS-CSD Deflections—Sliding Bearing Piers 2 and 4.

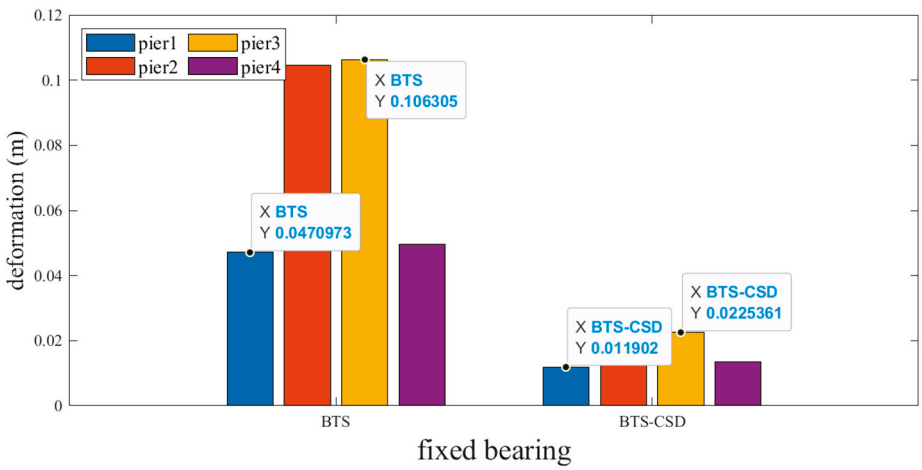

Figure 11. Comparison of BTS and BTS-CSD Deflections—Fixed Support Piers 1 and 3.

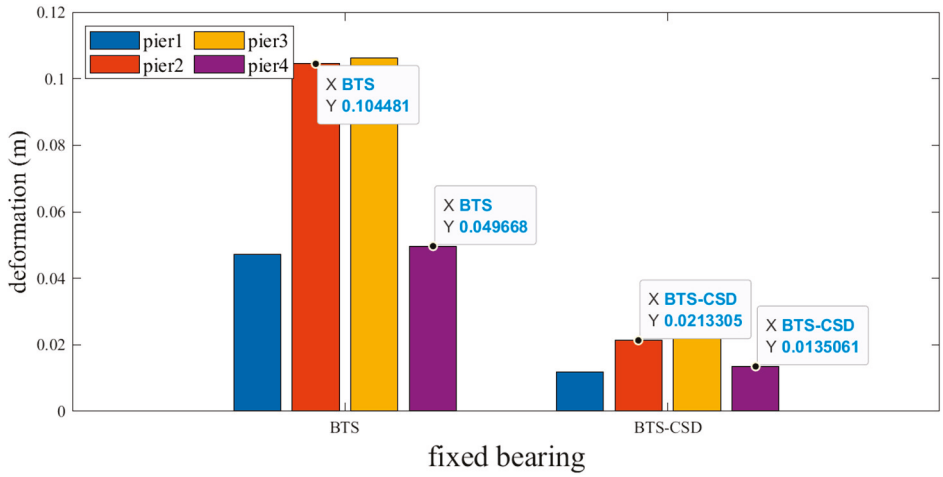

Figure 12. Comparison of BTS and BTS-CSD Deflections—Fixed Support Piers 2 and 4.

Table 4. Comparison of Sliding Bearing Deflection Volume Data.

Sliding Support	BTS	BTS-CSD	Difference	Percentage Reduction
Pier 1	0.0513	0.0135	0.0378	73.7%
Pier 2	0.1071	0.0223	0.0848	79.2%
Pier 3	0.1033	0.0211	0.0822	79.6%
Pier 4	0.0451	0.0113	0.0338	74.9%

Table 5. Comparison of fixed bearing deformation data.

Fixed Support	BTS	BTS-CSD	Difference	Percentage Reduction
Pier 1	0.0471	0.0119	0.0352	74.7%
Pier 2	0.1045	0.0213	0.0832	79.6%
Pier 3	0.1063	0.0225	0.0838	78.8%
Pier 4	0.0497	0.0135	0.0362	72.8%

The deformation of fasteners is recognized as critical to maintaining track alignment accuracy, with a 30–35% reduction in deformation magnitude observed specifically within stress concentration zones (bridge–subgrade transition sections), serving as localized peak values (Figure 13). Detailed analysis attributes residual deformations to design limitations (suboptimal fastener geometry) [44], material degradation (fatigue-induced stiffness loss), and environmental effects (thermal preload relaxation). These insights highlight the need for integrated retrofitting strategies that combine CSD installation with fastener geometry optimization.

However, the experience of a counterintuitive 12–18% deformation increase occurs post-CSD installation (Figures 14 and 15). For example, Pier 1 abutment deformation increases from 0.00935 m (BTS) to 0.0258 m (BTS-CSD). This phenomenon may stem from CSD-induced force redistribution, which transfers partial seismic energy from the superstructure to the substructure. Despite increased displacements, stress levels remain within 65% of yield thresholds, ensuring substructure safety.

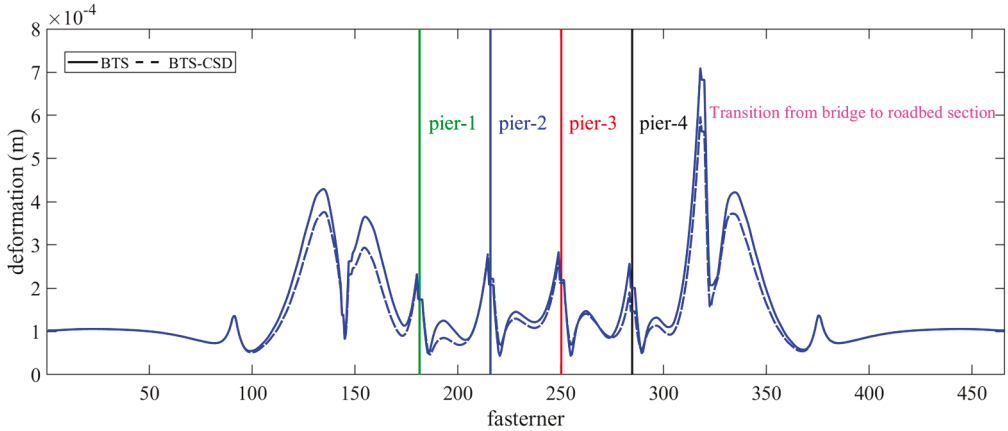

Figure 13. Comparison of BTS and BTS-CSD Deflections—Fasteners.

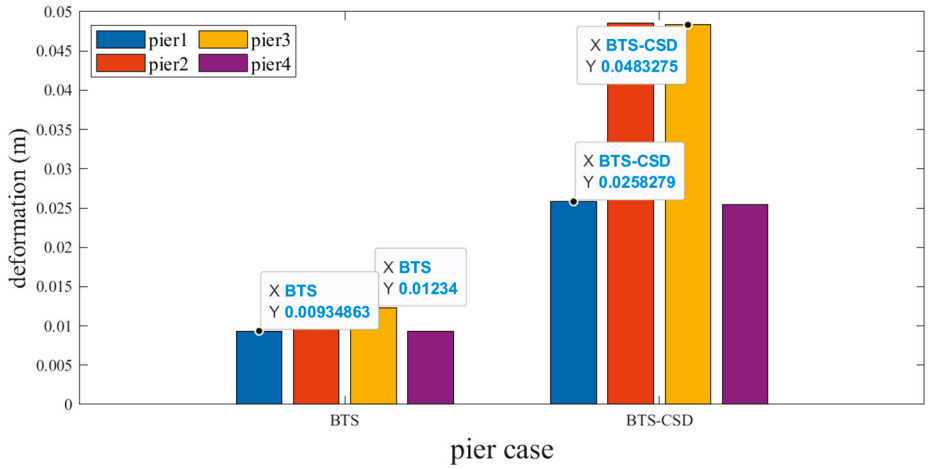

Figure 14. Comparison of BTS and BTS-CSD Deflections for Abutments 1 and 3.

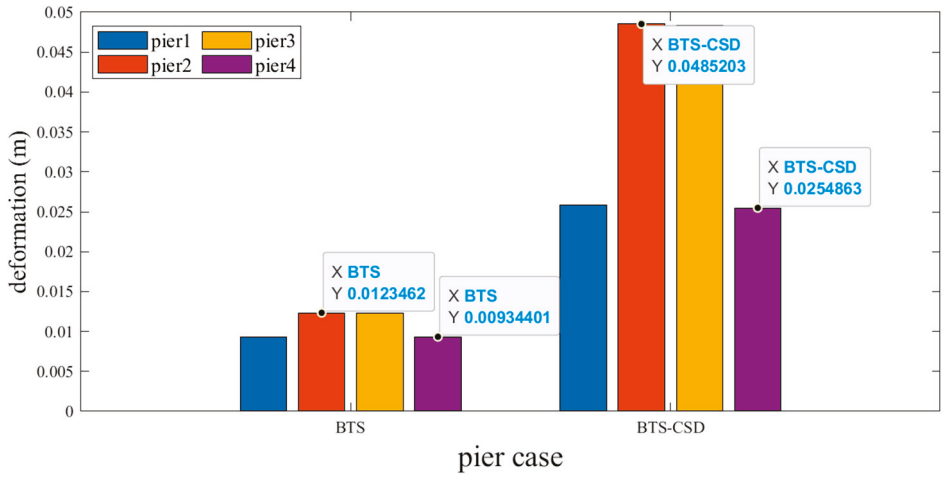

Figure 15. Comparison of BTS and BTS-CSD Deflections—Abutments 2 and 4.

The main girders and bridge rails benefit significantly from CSD integration. Figures 16 and 17 illustrate parallel displacement reductions: the main girders decrease by 30.6% (Pier 1), 36.4% (Pier 2), 36.2% (Pier 3), and 30.1% (Pier 4), while bridge rails exhibit comparable improvements (30.5% at Piers 1 to 36.3% at Piers 2) (Tables 6 and 7). These results validate CSD's dual role in safeguarding structural integrity and operational stability.

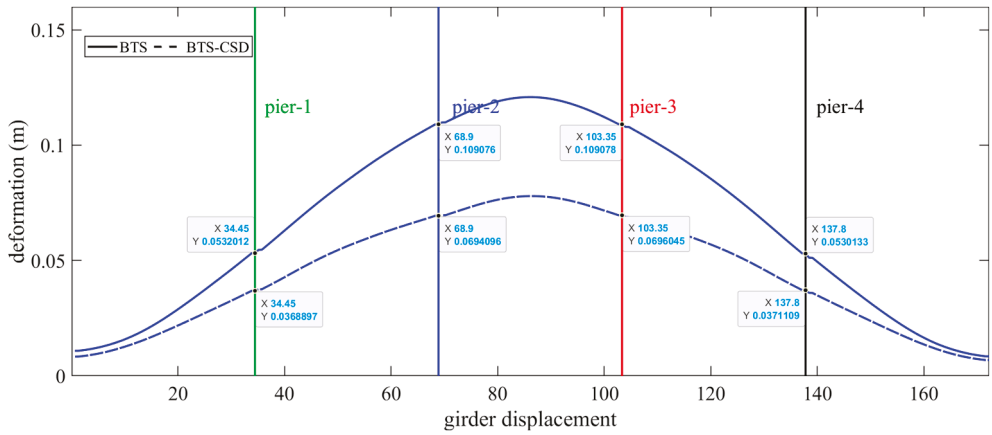

Figure 16. Comparison of BTS and BTS-CSD Deflections—Main Beam.

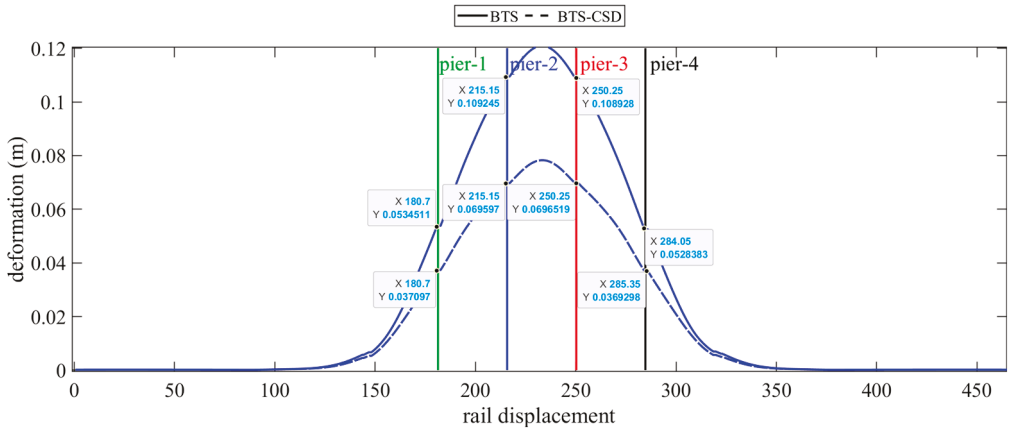

Figure 17. Comparison of BTS and BTS-CSD Deflections—Bridge Tracks.

Table 6. Comparison of the main beam displacement and deformation data.

Main Beam Deformation	BTS	BTS-CSD	Difference	Percentage Reduction
Pier 1	0.0532	0.0369	0.0163	30.6%
Pier 2	0.1091	0.0694	0.0397	36.4%
Pier 3	0.1091	0.0696	0.0395	36.2%
Pier 4	0.0531	0.0371	0.016	30.1%

Table 7. Comparison of bridge track displacement and deformation data.

Bridge Track Deformation	BTS	BTS-CSD	Difference	Percentage Reduction
Pier 1	0.0534	0.0371	0.0163	30.5%
Pier 2	0.1092	0.0696	0.0396	36.3%
Pier 3	0.1089	0.0697	0.0392	36.0%
Pier 4	0.0528	0.0371	0.0157	29.7%

Shear key performance further corroborates CSD's effectiveness. Position 5 corresponds to the subgrade connection zone where shear keys exhibit amplified dynamic responses. Mitigating these responses is critical to ensuring the structural integrity of the bridge–track system; therefore, this specific area has been selected as the focal point for detailed analysis in the present study. Figure 18 shows a 48.5% deformation reduction at

Position 5 (0.33 mm → 0.17 mm), mitigating interface shear stresses and preserving track alignment under seismic loads.

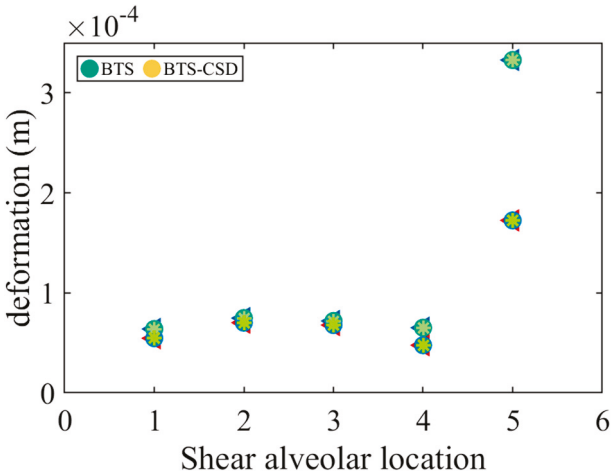

Figure 18. Comparison of the amount of the deformation between the BTS and BTS-CSD—shear tooth slot.

4.2. Synthesis of Seismic Retrofitting Outcomes

MATLAB-driven analytics establish CSD as a transformative solution for HSR seismic retrofitting. The key findings include the following: (1) Critical Components: Sliding/fixed bearing deformations are reduced by 73–80%, ensuring lateral stability; (2) Operational Elements: Fastener, girder, and rail displacements are decreased by 30–36%, enhancing operational safety; and (3) Force Redistribution Trade-offs: Moderate abutment deformation increases (<20%) remain within elastic limits.

The engineering implications emphasize three actionable strategies: (1) stress concentration mitigation, which involves reinforce fastener zones at bridge–roadbed transitions via high-cycle fatigue-resistant alloys; (2) CSD deployment prioritization, which involves target piers with the highest baseline bearing displacements (Piers 2–3) for maximum efficacy; and (3) monitoring protocols, which implement real-time deformation sensors at abutments to track force redistribution effects.

5. Conclusions

This study evaluated the seismic performance of a combined steel damper (CSD) integrated into a 5-span CRTS II-track high-speed railway (HSR) bridge system. Through finite element model and nonlinear time-history analyses, the following conclusions are drawn:

(1) Hysteretic Performance of CSD. The proposed CSD, which integrates U-shaped and hollow diamond steel plates, exhibits full hysteresis loops without pinching effects, achieving an energy dissipation coefficient of 1.82 and an equivalent damping ratio of 12.7%. This validates its superior energy dissipation capacity under cyclic loading;

(2) System-level seismic mitigation. CSD implementation reduces critical component deformations by 73–80% for sliding/fixed bearings by 30–36% for fasteners, main girders, and bridge rails and by 48.5% for shear keys. The observed 12% to 18% increase in abutment deformation may be attributed to force redistribution mechanisms, while the stress level remains below 65% of the yield strength threshold, ensuring structural integrity within safe limits.

Author Contributions: Conceptualization, L.J.; Methodology, M.L.; Software, M.L.; Formal analysis, M.L. and J.H.; Investigation, M.L. and J.H.; Data curation, J.H.; Writing—original draft, M.L.; Writing—review & editing, L.J. and J.H.; Visualization, J.H.; Supervision, L.J.; Project administration, L.J.; Funding acquisition, L.J. All authors have read and agreed to the published version of the manuscript.

Funding: This research was financially supported by the National Key Research and Development Program of China (2022YFC3004304).

Institutional Review Board Statement: Not applicable.

Informed Consent Statement: Not applicable.

Data Availability Statement: The original contributions presented in this study are included in the article. Further inquiries can be directed to the corresponding author.

Conflicts of Interest: The authors declare no conflict of interest.

References

1. Jiang, L.; Zhong, B.; Zhang, Y.; Zhou, W.; Lai, Z. A Novel Seismic-Resistant Design for Track Structures in the Bridge-Embankment Transition Zone of Multi-Span High-Speed Railways Simply Supported Bridges. *Eng. Struct.* **2025**, *324*, 119349. [CrossRef]
2. Duan, H.; Jiang, L.; Wen, T.; Jiang, L. An Improved Interlayer Area Damage Model for Seismic Damage Assessment of a High-Speed Railway Long-Span Arch Bridge-Track System. *SOIL Dyn. Earthq. Eng.* **2024**, *184*, 108811. [CrossRef]
3. Zhou, Y.; Gao, C.; Yang, S.; Guo, W.; Jiang, L. Seismic Fragility Analysis of Reinforced Concrete Simply Supported Girder Bridges Resting on Double-Column Piers for High Speed Railway. *Buildings* **2024**, *14*, 3072. [CrossRef]
4. Zhou, W.; Xiong, L.; Jiang, L. Multi-Parameter Seismic Fragility Analysis of High-Speed Railway Track-Bridges: Embracing Structural and Earthquake Uncertainties. *Int. J. Struct. Stab. Dyn.* **2024**, 2630001. [CrossRef]
5. Zhou, W.; Wu, L.; Zhong, T.; Jiang, L.; Liu, S. Impact of Vertical Girder Deformations on the High-Speed Train Operation Performance. *Struct. Infrastruct. Eng.* **2024**, 1–17. [CrossRef]
6. Zhao, L.; Zhou, L.; Zhang, G.; Wei, T.; Mahunon, A.; Jiang, L.; Zhang, Y. Experimental Study of the Temperature Distribution in CRTS-II Ballastless Tracks on a High-Speed Railway Bridge. *Appl. Sci.* **2020**, *10*, 1980. [CrossRef]
7. Jiang, L.; Duan, H.; Wen, T.; Jiang, L. Effects of Near-Fault Pulse-like Ground Motions and Pulse Parameters on a High-Speed Railway Long-Span Arch Bridge-Track System. *J. Bridge Eng.* **2025**, *30*, 04024112. [CrossRef]
8. Jiang, L.; Yu, K.; Jiang, L.; Wen, T.; Hu, Y.; Pang, L. Effects of Shear Panel Dampers on Seismic Response Mitigation of High-Speed Railway Simply Supported Bridge-Track System under Far-Field and near-Field Ground Motions. *Arch. Civ. Mech. Eng.* **2023**, *23*, 93. [CrossRef]
9. Jiang, L.; Liu, J.; Wen, T.; Jiang, L.; Yan, Y.; He, C. Damage Dispersion Study of High-Speed Railway Track-Bridge System with the UCSD Considering Train Effects. *Structures* **2024**, *68*, 107213. [CrossRef]
10. Lai, Z.; Jiang, L.; Chen, Y.; Wei, B. An Improved Model for the Nonlinear Simulation of the High-Speed Vehicle-Track-Bridge Coupling System under Seismic Shaking. *Earthq. Eng. Struct. Dyn.* **2024**, *53*, 3775–3797. [CrossRef]
11. Zhou, W.; Xiao, J.; Liu, S.; Jiang, L.; Yu, J.; Zu, L.; Wu, L.; Ren, Z. Analysis of Key Influencing Factors of Track Dynamic Irregularity Induced by Earthquakes in the High-Speed Railway Track-Bridge System. *Int. J. Struct. Stab. Dyn.* **2024**, *24*, 2450246. [CrossRef]
12. Zhou, W.; Xiong, L.; Jiang, L.; Zhong, B. Innovative Approaches in High-Speed Railway Bridge Model Simplification for Enhanced Computational Efficiency. *J. Cent. South Univ.* **2024**, *31*, 4203–4217. [CrossRef]
13. Wei, B.; Wang, P.; Yan, B.; Jiang, L.; He, X. Parameter Optimization of Damper-Friction Isolation Systems Using Concave Friction Distribution. *J. Vibroengineering* **2016**, *18*, 1668–1682. [CrossRef]
14. Wen, T.; Jiang, L.; Jiang, L.; Zhou, W.; Du, Y. Interlayer Area Damage Modeling and Damage-Based Seismic Fragility Analysis of High-Speed Railway Bridge and Track System. *Eng. Struct.* **2022**, *272*, 114989. [CrossRef]
15. Zhou, W.; Xiong, L.; Jiang, L. New Parameter Updating Method for Bidirectional Simplified Seismic Models of High-Speed Railway Bridges. *Structures* **2025**, *71*, 107959. [CrossRef]
16. Wen, T.; Duan, H.; Jiang, L.; Zhou, W.; Du, Y.; Jiang, L. Refined Probabilistic Seismic Demand Modeling of High-Speed Railway Bridge under near-Fault Hanging-Wall Effects and Velocity Pulse Effects by a Novel Ground Motion Selection Approach. *Int. J. Struct. Stab. Dyn.* **2024**, 2650074. [CrossRef]
17. Jiang, L.; Li, W.; Jiang, L.; Wang, Z.; Wen, T. Railway Alignment Optimization and Seismic Responses of High-Speed Railway Bridge Considering the Spatial Effects of Mountainous-Plateau. *Int. J. Struct. Stab. Dyn.* **2024**, 2550170. [CrossRef]
18. Wei, B.; Xiao, B.; Tan, H.; Yang, Z.; Jiang, L.; Yu, Y. Energy Response Analysis and Seismic Isolation Strategy Optimization of High-Speed Railway Bridge-Track System under Earthquake Action. *Soil Dyn. Earthq. Eng.* **2024**, *186*, 108917. [CrossRef]
19. Liu, B.; He, C.; Lai, Z.; Jiang, L.; Li, D. Elastoplastic Bridge Deck Response Spectra of High-Speed Railway Simply-Supported Girder Bridge with CRTSII Track System. *J. Cent. South Univ.* **2024**, *31*, 4174–4186. [CrossRef]
20. Zhao, H.; Wei, B.; Zhang, P.; Guo, P.; Shao, Z.; Xu, S.; Jiang, L.; Hu, H.; Zeng, Y.; Xiang, P. Safety Analysis of High-Speed Trains on Bridges under Earthquakes Using a LSTM-RNN-Based Surrogate Model. *Comput. Struct.* **2024**, *294*, 107274. [CrossRef]
21. Wang, Z.; Jiang, L.; Jiang, L.; Zhou, W.; Du, Y. Seismic Response of High-Speed Railway Simple-Supported Girder Track-Bridge System Considering Spatial Effect at near-Fault Region. *Soil Dyn. Earthq. Eng.* **2022**, *158*, 107283. [CrossRef]

22. Wen, T.; Jiang, L.; Jiang, L.; Jin, Z.; Du, Y.; Pang, L. Repair Cost Assessment of Longitudinal Continuous Ballastless Track Structure on High-Speed Railway Bridge with Spatially Distributed Interlayer Area Damage. *Structures* **2023**, *57*, 105157. [CrossRef]
23. Wen, T.; Jiang, L.; Jiang, L.; Zhou, W.; Du, Y. Optimal Intensity Measure Selection in Incremental Dynamic Analysis: Methodology Improvements and Application to a High-Speed Railway Bridge. *Bull. Earthq. Eng.* **2024**, *22*, 2059–2083. [CrossRef]
24. Liu, X.; Jiang, L.; Xiang, P.; Jiang, L.; Lai, Z. Safety and Comfort Assessment of a Train Passing over an Earthquake-Damaged Bridge Based on a Probability Model. *Struct. Infrastruct. Eng.* **2023**, *19*, 525–536. [CrossRef]
25. Li, S.; Xiang, P.; Wei, B.; Zuo, C.; Jiang, L.; He, W. Interface Friction Effects on Scaling a Vertical Spring-Viscous Damper Isolation System in a Shaking Table Test. *Structures* **2021**, *33*, 1878–1891. [CrossRef]
26. Tan, H.; Wei, B.; Wang, W.; Xiao, B.; Li, S.; Jiang, L. Influence of Pier Height and Ground Motion Parameters on Seismic Response and Energy Dissipation of Isolated Railway Bridges. *Structures* **2024**, *68*, 107236. [CrossRef]
27. Wei, B.; Wang, P.; He, X.; Jiang, L. Seismic Response of Spring-Damper-Rolling Systems with Concave Friction Distribution. *Earthq. Struct.* **2016**, *11*, 25–43. [CrossRef]
28. Guo, W.; Zeng, C.; Gou, H.; Hu, Y.; Xu, H.; Guo, L. Rotational Friction Damper's Performance for Controlling Seismic Response of High Speed Railway Bridge-Track System. *CMES-Comput. Model. Eng. Sci.* **2019**, *120*, 491–515. [CrossRef]
29. Isacchi, G.; Ripamonti, F.; Corsi, M. Innovative Passive Yaw Damper to Increase the Stability and Curve-Taking Performance of High-Speed Railway Vehicles. *Veh. Syst. Dyn.* **2023**, *61*, 2273–2291. [CrossRef]
30. Kahya, V.; Araz, O. A Simple Design Method for Multiple Tuned Mass Dampers in Reduction of Excessive Vibrations of High-Speed Railway Bridges. *J. Fac. Eng. Archit. Gazi Univ.* **2020**, *35*, 607–618. [CrossRef]
31. Luu, M.; Martinez-Rodrigo, M.D.; Zabel, V.; Koenke, C. Semi-Active Magnetorheological Dampers for Reducing Response of High-Speed Railway Bridges. *Control Eng. Pract.* **2014**, *32*, 147–160. [CrossRef]
32. Moliner, E.; Museros, P.; Martinez-Rodrigo, M.D. Retrofit of Existing Railway Bridges of Short to Medium Spans for High-Speed Traffic Using Viscoelastic Dampers. *Eng. Struct.* **2012**, *40*, 519–528. [CrossRef]
33. Tell, S.; Leander, J.; Andersson, A.; Ulker-Kaustell, M. Probability-Based Evaluation of the Effect of Fluid Viscous Dampers on a High-Speed Railway Bridge. *Struct. Infrastruct. Eng.* **2021**, *17*, 1730–1742. [CrossRef]
34. Jin, T.; Liu, Z.; Sun, S.; Ren, Z.; Deng, L.; Yang, B.; Christie, M.D.; Li, W. Development and Evaluation of a Versatile Semi-Active Suspension System for High-Speed Railway Vehicles. *Mech. Syst. Signal Process.* **2020**, *135*, 106338. [CrossRef]
35. Martinez-Rodrigo, M.D.; Lavado, J.; Museros, P. Dynamic Performance of Existing High-Speed Railway Bridges under Resonant Conditions Retrofitted with Fluid Viscous Dampers. *Eng. Struct.* **2010**, *32*, 808–828. [CrossRef]
36. Luu, M.; Martinez-Rodrigo, M.D.; Zabel, V.; Koenke, C. H∞ Optimization of Fluid Viscous Dampers for Reducing Vibrations of High-Speed Railway Bridges. *J. Sound Vib.* **2014**, *333*, 2421–2442. [CrossRef]
37. Xu, X.; Chen, X.; Hu, H.; Zhou, X.; Cheng, M.; Sun, L.; Li, X. Energy Dissipation and Seismic Response Reduction System for High-Speed Railway Bridges Based on Multiple Performance Requirements. *Eng. Struct.* **2024**, *307*, 117919. [CrossRef]
38. Wang, X.; Liu, B.; Di Gialleonardo, E.; Kovacic, I.; Bruni, S. Application of Semi-Active Yaw Dampers for the Improvement of the Stability of High-Speed Rail Vehicles: Mathematical Models and Numerical Simulation. *Veh. Syst. Dyn.* **2022**, *60*, 2608–2635. [CrossRef]
39. Alehashem, S.M.S.; Ni, Y.Q.; Liu, X.Z. A Full-Scale Experimental Investigation on Ride Comfort and Rolling Motion of High-Speed Train Equipped With MR Dampers. *IEEE Access* **2021**, *9*, 118113–118123. [CrossRef]
40. Sang, H.; Zeng, J.; Gan, F.; Mu, J.; Qi, Y. A Study of Wheel Wear on a High-Speed Railway Motor Car. *Proc. Inst. Mech. Eng. Part F J. Rail Rapid Transit* **2023**, *237*, 80–92. [CrossRef]
41. Ren, J.; Li, Q.; Ren, Z.; Yang, G. A New Hydraulic Damper Dynamics Model and the Availability on High Speed Vehicle Dynamics Investigation. *Veh. Syst. Dyn.* **2023**, *61*, 356–374. [CrossRef]
42. Zhu, Q.K. Interaction Between Simply-Supported Beam Bridges and CRTS II Slab Ballastless Track in High-Speed Railways. Master's Thesis, Central South University, Changsha, China, 2013.
43. Hu, Z.; Song, D.; Zeng, Y.; Zhang, W. Analysis of the Service Life of Railway Hydraulic Dampers Considering Temperature and Loading. *Proc. Inst. Mech. Eng. Part F J. Rail Rapid Transit* **2021**, *235*, 3–11. [CrossRef]
44. Zhang, Y.; Yang, X.; Liu, S. Design and Parameters Influence Analysis of Dynamic Vibration Absorber for Fastener Clips in High-Speed Railway. *J. Vib. Control* **2024**, *30*, 472–486. [CrossRef]

Disclaimer/Publisher's Note: The statements, opinions and data contained in all publications are solely those of the individual author(s) and contributor(s) and not of MDPI and/or the editor(s). MDPI and/or the editor(s) disclaim responsibility for any injury to people or property resulting from any ideas, methods, instructions or products referred to in the content.

materials

MDPI

Article

Characterization of Force Distribution and Force Chain Topology in Asphalt Mixtures Using the Discrete Element Method

Sudi Wang [1], Jianxia Wang [2], Jie Wang [1], Jian Xu [1], Yinghao Miao [3,*], Qing Ma [1,*], Linbing Wang [4] and Tao Liu [2]

[1] Research Institute of Highway Ministry of Transport, Beijing 100088, China; sd.wang@rioh.cn (S.W.)
[2] Jiangxi Transportation Investment Group Co., Ltd., Nanchang 330025, China
[3] National Center for Materials Service Safety, University of Science and Technology Beijing, Beijing 100083, China
[4] School of Environmental, Civil, Agricultural and Mechanical Engineering, University of Georgia, Athens, GA 30602, USA
* Correspondence: miaoyinghao@ustb.edu.cn (Y.M.); q.ma@rioh.cn (Q.M.)

Abstract

The force chain network within asphalt mixtures serves as the primary load-bearing structure to resist external forces. The objective of this study is to quantitatively characterize the contact force distribution and force chain topology structure. The discrete element method (DEM) was employed to construct simulation models for two stone matrix asphalt (SMA) and two open-graded friction course (OGFC) mixtures. Load distribution characteristics, including average contact force, load bearing contribution and contact force angle, and force chain topological network parameters, clustering coefficient, edge betweenness and average path length, were analyzed to elucidate the load transfer mechanisms. The findings of the present study demonstrate that the average contact force between aggregate–aggregate contact types in specific particle sizes significantly exceeds the average contact force of the same particle size aggregates. For SMA16 and OGFC16 asphalt mixtures, the load-bearing contribution of aggregates initially increases and then decreases with decreasing particle size, peaking at 13.2 mm. SMA13 and OGFC13 mixtures demonstrate a consistent decline in load bearing contribution with decreasing aggregate size. The analysis of the force chain network topology of the asphalt mixture reveals that SMA mixtures exhibited higher average clustering coefficients in force chain topological features in comparison to OGFC mixtures. It indicates that SMA gradations have superior skeletal load-bearing structures. While the maximum nominal aggregate size minimally influences the average path length with a relative change rate of 3%, the gradation type exerts a more substantial impact, exhibiting a relative change rate of 7% to 9%. These findings confirm that SMA mixtures have more stable load-bearing structures than OGFC mixtures. The proposed topological parameters effectively capture structural distinctions in force chain networks, offering insights for optimizing gradation design and enhancing mechanical performance.

Keywords: asphalt mixture; contact force; load bearing contribution; force chain; topology characteristics; discrete element method

1. Introduction

The force chain network in asphalt mixtures represents the primary load-bearing structure that is formed in asphalt mixtures under the action of external loads, thereby exerting a substantial influence on the performance of asphalt mixtures [1]. The macroscopic mechanical response of asphalt mixtures can be considered a reflection of the meso-scale

load transfer mechanism. The study of the load transfer network in the meso-scale structure of asphalt mixtures provides a novel perspective through which to examine the macroscopic mechanical properties of asphalt mixtures [2,3]. Consequently, effective characterization of the force chain network of asphalt mixtures is conducive to a more profound understanding of the mechanical behavior of asphalt mixtures from the meso-scale, which is of great significance for the optimal design of asphalt mixtures.

In order to explore the asphalt mixture bearing mechanism, the internal load distribution characteristics of asphalt mixtures were investigated. Liu et al. [4] utilized a discrete element method (DEM) to reconstruct asphalt mixtures, thereby developing a numerical simulation model of asphalt mixtures. The force chain distribution inside the aggregate, inside the mortar, and at the aggregate–mortar interface was analyzed. Chang et al. [5–7] employed the DEM to reconstruct digital specimens of asphalt mixtures, and quantitatively analyzed the evolution and distribution of force chains inside asphalt mixtures. The experimental findings demonstrate that the spatial distribution of contact forces within asphalt mixtures is characterized by anisotropy. Tan et al. [8] utilized digital image technology in conjunction with DEM to investigate and analyze the load transfer characteristics within the asphalt mixture skeleton structure. The research further explored and examined the influence of the skeleton structure on the contact force between aggregate and mortar. It was found that the load transfer in the asphalt mixture is predominantly facilitated by the primary skeleton aggregate particles. Wang et al. [2] employed reconstructed aggregate particles to generate discrete element specimens, utilizing this method to investigate the effect of elongated and flat particle content on the load transfer characteristics of asphalt mixtures during compaction. The simulation test results demonstrate that the overall load carrying capacity of the mixture becomes weaker with the increase of elongated and flat particle content. Wei et al. [9] characterized the force chain of asphalt mixtures by developing a three-dimensional finite element simulation model. The results obtained from this model indicated that the stress concentration region in the asphalt mortar matrix was regarded as the main load transfer region between the coarse aggregates. Shi et al. [10] developed a numerical model of asphalt mixtures with different gradations considering the real aggregate morphology and conducted uniaxial compression tests, which revealed that aggregates with 4.75–9.5 mm particle size have both load-bearing and filling functions, and their roles are significantly affected by the gradation. It was also found that the internal aggregate structure could be optimized and adjusted under stress. Yao et al. [11] employed discrete element method (DEM) simulations to analyze stress transmission mechanisms within asphalt mixtures, with a focus on quantitatively evaluating their splitting strength performance. It was found that in comparison with AC13 (asphalt concrete with the nominal particle size of 13.2 mm) gradation, AC20 (asphalt concrete with the nominal particle size of 20 mm) gradation asphalt mixture results in a greater proportion of coarse aggregates carrying the load.

Under the action of external loads, a contact network structure that transmits external loads was formed between particles in asphalt mixtures. This network structure is similar to the topology in complex networks and is called the contact force chain structure [12]. Many studies have been carried out to investigate the force chain structure in granular mixtures. Kruyt [13] initially proposed the definitions of strong contact and weak contact, which were based on the magnitude of the contact force and the magnitude of the force in the direction of contact. Voivret et al. [14] investigated the anisotropy of the force chain network within a granular system on this basis. On the basis of force chain structure research, some scholars have carried out relevant studies on the contact force distribution characteristics in the granular matter. Mueth et al. [15] provided a fitting function for the contact force distribution in mixed granular matter. Sun et al. [16] studied the contact force

distribution characteristics within the granular matter and quantitatively analyzed the angle of the force chain structure. The results of the study found the directionality of the strong force chain structure, and on this basis, a strong force chain criterion for the granular system was proposed under uniaxial compression and biaxial compression loading by carrying out discrete element simulation experiments [17]. Feng et al. [18] investigated the effect of particle size dimensions on the mechanical and geometrical structural properties of mixed particle systems using DEM (Particle Flow Code 5.0). The results demonstrated that the number of contacts between particles varied with the degree of particle size dispersion, while the cumulative distribution of contact forces between particles remained unaffected by the degree of particle size dispersion. Danylenko et al. [19] conducted a study on the contact force characteristics of individual particles under external loading. The results revealed the relationship between the contact forces between particles of the mix during dynamic loading. Kondic et al. [20] investigated the evolution of the contact force network with loading time in mixes under different external loads. Yu et al. [12,21,22] investigated the topological features of the force chain network in aggregate blend utilizing discrete element method and through complex network theory. It was found that the average path length of SMA-16 is longer than that of AC-25, indicating that SMA-16 has better load transfer ability and skeleton properties. Liu et al. [23] evaluated the affinity between aggregate skeleton topology and rutting performance of asphalt mixture based on network theory. The findings of this research indicated that, in terms of the realistic affinity with rutting performance, the combined feature demonstrated the most optimal performance, exhibiting an average correlation of 0.55. Yang et al. [24] investigated the microscopic fracture characteristics of recycled asphalt mixtures through the force chain distribution using DEM. It was found that the emulsified asphalt mortar–aggregate interface was the critical weak position of the mixture fracture. Additionally, the failure of the tension chain was the main destructional form of the asphalt mixture fracture.

Asphalt mixtures have significant granularity, and therefore, the discrete element method (DEM) is considered to be an effective means to study discontinuities in the distribution of asphalt mixture components and discontinuities in the mechanical properties of the interfaces between different components [25]. Typically, researchers analyzed the meso-mechanical properties of asphalt mixtures using DEM. Based on DEM, Liu et al. [26] simulated the mechanical behavior of asphalt mixtures under low temperature conditions using the linear elasticity model to simulate coarse aggregates, and Burger's model instead of the linear elasticity model to simulate asphalt mortar. Ma et al. [27–29] found that the better the embeddedness between aggregate particles, the better the high-temperature stability, through the DEM simulation of asphalt mixtures. Concurrently, related studies on cracking behavior and splitting strength of asphalt mixtures were carried out based on DEM [24,30–32]. Relevant researchers have also studied the structural characteristics of asphalt mixtures utilizing the DEM [33–35]. Chen et al. [36] simulated rotary compaction tests of mixes by simulating aggregates through particles of simple morphology. Gong et al. [37,38] explored the kinematic properties of aggregate particles during the compaction process with the help of the real morphology model of aggregate particles obtained via X-ray CT and optical scanning, which were imported into Particle Flow Code 5.0 software to carry out DEM tests to simulate the SGC test of asphalt mixtures. Chen et al. [39] investigated the mobility of loose-state asphalt mixtures in a slump cylinder using the DEM simulation. The findings indicated that the mobility of loose state asphalt mixtures was primarily determined by the combination of lubricating friction and bonding between particles. Liang et al. [3] analyzed the contact characteristics of the asphalt mixture particle contact network by reconstructing the asphalt mixture in three dimensions by computed tomography scanning. The contact number of stone matrix asphalt with a maximum

nominal particle size of 16 mm was found to be significantly higher in comparison to that of asphalt concrete with a maximum nominal particle size of 16 mm. Wang et al. [40] investigated the force chain evolution and aggregate movement in asphalt mixtures using DEM. It was found that gradation variations in asphalt mixtures can alter the load-bearing contribution of aggregate particles. SMA gradations exhibit enhanced ability to withstand and transmit external loads compared to OGFC gradations.

As demonstrated by the preceding studies, the DEM has emerged as a more suitable tool for the analysis of asphalt mixtures. While numerous scholars have conducted research on the load transfer mechanism of asphalt mixtures, their studies are constrained by the quantification and evaluation of the contact force magnitude. The research and analysis of the entire force chain structure and the force distribution characteristics remain in their initial stages and lack comprehensive depth. The topology in complex networks is an effective tool to characterize the structure of the force chain, and related studies have confirmed the feasibility of this method [22,23]. While previous studies have focused on contact force magnitudes, this work quantifies force chain topology (e.g., clustering coefficient, edge betweenness) to assess structural stability, which has not been comprehensively addressed. This paper focuses on the contact force distribution and the topological structure characteristics of the force chain network in asphalt mixture. The stone mastic asphalt (SMA) gradation provides excellent rutting resistance and durability due to its dense skeleton and high asphalt dosage, and is suitable for heavy traffic areas, while open graded friction course (OGFC) gradation is designed for skid resistance in rainy areas by achieving efficient drainage and noise reduction through its open graded pore structure. Considering the functional characteristics and performance advantages of SMA and OGFC, they are selected as experimental objects to investigate the load transfer mechanism of the dense skeleton and permeable structure [40]. Three-dimensional laser scanning is employed to obtain the real morphology of aggregate particles, with Particle Flow Code (PFC) 5.0 software then being used to generate a four-graded asphalt mixture discrete element numerical model. The load transfer response during the simulation experiment is tracked using the FISH function. The analysis of the internal load transfer mechanism of asphalt mixtures under external load is facilitated by the interaction force between particles and the contact force network. The topological structure of the contact force network is analyzed using the complex network theory, which gives the quantitative statistical indexes of force value and structure of the internal force chain network of asphalt mixtures. Figure 1 depicts the steps, from asphalt mixture model compaction to analysis of the simulation results.

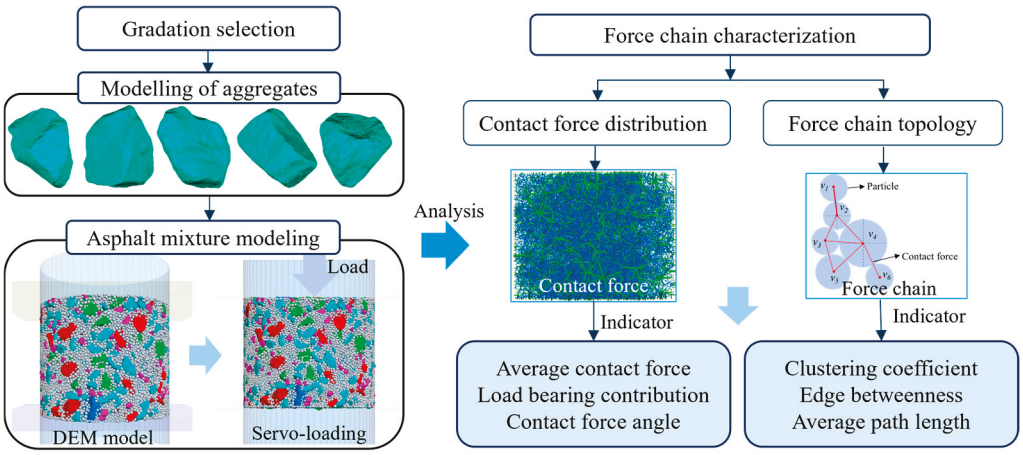

Figure 1. The methodology flowchart of this paper.

2. Materials and Methods

2.1. Materials and Gradations

SMA and OGFC are two typical asphalt mixture types widely used in different pavement engineering scenarios, and 13.2 mm and 16 mm are the common nominal maximum particle sizes. Therefore, two stone mastic asphalt (SMA) gradations and two open graded friction course (OGFC) gradations were selected with nominal maximum aggregate grain sizes of 13.2 mm and 16 mm, respectively. The SMA graded asphalt mixture with a nominal maximum particle size of 16 mm is denoted SMA16, and the other three asphalt mixtures are represented in the same way. These four mixes are chosen to represent the different types of asphalt mixtures with different particle sizes and gradation types in actual projects, which facilitates the study of the effects of changes in particle size and gradation on the force chain characteristics and mechanical properties. According to Technical Specifications for Construction of Highway Asphalt Pavement (JTG F40-2004) [41], the Marshall design method was used to determine the grading curves and optimal asphalt–aggregate ratio of the four asphalt mixtures. The optimal asphalt-aggregate ratio and gradation of asphalt mixtures are shown in Table 1. In this study, the coarse aggregate is basalt, the fine material is sand, and the basic characteristics of the aggregate are shown in Table 2.

Table 1. Selected gradations.

Sieve Size (mm)	Percent Passing (%)			
	SMA13	SMA16	OGFC13	OGFC16
19	-	100	-	100
16	100	95.8	100	96.4
13.2	93.2	74.7	94.9	79.3
9.5	61.3	55.3	70.5	57.9
4.75	25.8	25.9	22.1	22.9
2.36	19.9	20.4	14.4	16.0
1.18	16.0	17.2	9.8	11.2
0.6	13.7	14.6	7.2	8.4
0.3	12.2	13.1	5.4	6.6
0.15	10.6	11.4	4.4	5.4
0.075	9.8	10.4	3.8	4.7
Optimal asphalt–aggregate ratio	6.0%	5.9%	4.4%	5.2%

Table 2. Bulk density of aggregates.

Aggregates	Size (mm)	Bulk Density (g/cm^3)
Coarse aggregates	16–19	2.892
	13.2–16	2.829
	9.5–13.2	2.764
	4.75–9.5	2.762
	2.36–4.75	2.751
Fine aggregates	1.18–2.36	2.700
	0.6–1.18	2.682
	0.3–0.6	2.602
	0.15–0.3	2.751
	0.075–0.15	2.651
Mineral Powder	<0.075	2.806

2.2. DEM Simulation of Asphalt Mixtures

2.2.1. Contact Parameters of Simulation Model

(1) Linear contact model of coarse aggregates

Since the mechanical response of coarse aggregate is close to elasticity, a linear contact model is utilized to characterize the contact model between the coarse aggregate–aggregate [42,43], as illustrated in Figure 2. The coarse aggregate units are represented by clump units.

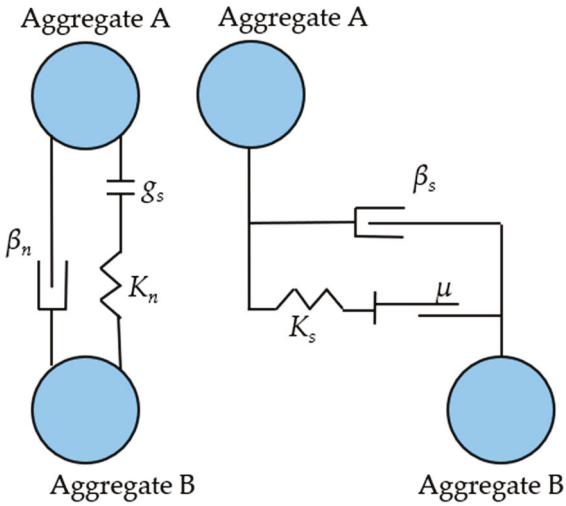

Figure 2. Linear contact model of aggregate. (Note: To distinguish particles, the two aggregate particles in contact with each other are named Aggregate A and Aggregate B).

In Figure 2, g_s is the gap between particles; β_s is the tangential critical damping ratio; and β_n is the normal critical damping ratio. K_s and K_n are tangential stiffness and normal stiffness of the tandem, respectively, which are calculated as in Equation (1).

$$\begin{cases} K_n = \frac{k_n^A k_n^B}{k_n^A + k_n^B} \\ K_s = \frac{k_s^A k_s^B}{k_s^A + k_s^B} \end{cases} \tag{1}$$

where K_s^A and K_n^A are the normal stiffness and tangential stiffness of particle A; K_s^B and K_n^B are the tangential stiffness and normal stiffness of particle B, respectively.

Under axial force and shear loading, the tangential contact stiffness can be transformed by the normal contact stiffness, as demonstrated in Equation (2).

$$k_s = \frac{k_n}{2(1+v)} \tag{2}$$

where v is the Poisson's ratio. The relationship between the macroelastic model and normal stiffness, as demonstrated in Equation (3).

$$k_n = \frac{AE_c}{L} \tag{3}$$

If the two particles have the same tangential and normal stiffness, the stiffness of particles A and B can be obtained according to Equations (1)–(3), as shown in Equation (4).

$$\begin{cases} k_n^A = k_n^B = \frac{2AE_c}{L} \\ k_s^A = k_s^B = \frac{AE_c}{L(1+v)} \end{cases} \tag{4}$$

where E_c is Young's contact elasticity model; R is the radius of the contact unit; and $L = 2\overline{R} = R^A + R^B$ is the equivalent length of the elastic beam.

The expressions for the moment of inertia I and cross-sectional area A of an elastic beam are given in Equation (5).

$$\begin{cases} A = \begin{cases} (2\overline{R})^2 \text{ (3D)} \\ 2\overline{R}t \text{ (2D)} \end{cases} \\ I = \begin{cases} \frac{4}{3}\overline{R}^4 \text{ (3D)} \\ \frac{2}{3}\overline{R}^3 t \text{ (2D)} \end{cases} \end{cases} \tag{5}$$

The calculation of the meso-scale parameters in the linear contact stiffness model is undertaken according to Equation (6).

$$\begin{cases} k_n^A = k_n^B = 2E_c \begin{cases} L \text{ (3D)} \\ t \text{ (2D)} \end{cases} \\ k_s^A = k_s^B = \frac{E_c}{L(1+v)} \begin{cases} L \text{ (3D)} \\ t \text{ (2D)} \end{cases} \end{cases} \tag{6}$$

where k_s^A, k_n^A, k_s^B, and k_n^B are interpreted as in Equation (1).

The relationship between the microscopic contact stiffness and macroscopic modulus of elasticity of the unit in the above equation, when combined with the macroscopic modulus of elasticity of the aggregate, can be used to obtain the stiffness parameters in the linear contact model. According to references [42,43], the Poisson's ratio, shear modulus and modulus of elasticity of the coarse aggregate were determined to be 0.25, 22.2 GPa and 55.5 GPa, respectively. Additionally, the friction coefficient is 0.5.

(2) Burger's model of asphalt mortar

The asphalt mortar is viscoelastic and Burger's contact model was chosen to characterize the contact model between asphalt mortar units [2,42,43], as shown in Figure 3. The relationship between the parameters in Burger's model is expressed in Equation (7).

$$\begin{cases} C_{mn} = \eta_1 \begin{cases} t \text{ (2D)} \\ L \text{ (3D)} \end{cases} \quad K_{mn} = E_1 \begin{cases} t \text{ (2D)} \\ L \text{ (3D)} \end{cases} \\ C_{kn} = \eta_2 \begin{cases} t \text{ (2D)} \\ L \text{ (3D)} \end{cases} \quad K_{kn} = E_2 \begin{cases} t \text{ (2D)} \\ L \text{ (3D)} \end{cases} \\ C_{ms} = \frac{\eta_1}{2(1+v)} \begin{cases} t \text{ (2D)} \\ L \text{ (3D)} \end{cases} \quad K_{ms} = \frac{E_1}{2(1+v)} \begin{cases} t \text{ (2D)} \\ L \text{ (3D)} \end{cases} \\ C_{ks} = \frac{\eta_2}{2(1+v)} \begin{cases} t \text{ (2D)} \\ L \text{ (3D)} \end{cases} \quad K_{ks} = \frac{E_2}{2(1+v)} \begin{cases} t \text{ (2D)} \\ L \text{ (3D)} \end{cases} \end{cases} \tag{7}$$

where C_{mn}, K_{mn}, C_{kn} and K_{kn} are the four normal parameters of the Burger's contact model, and C_{ms}, K_{ms}, C_{ks} and K_{ks} are the four tangential parameters of the Burger's contact model. The macroscopic Burger's parameters of the asphalt mortar can be determined through laboratory tests. Since the Burger's contact between mortar units is composed of two viscoelastic asphalt mortars in series, the relationship between the Burger's model parameters of the mortar units themselves and the contact Burger's model parameters is shown in Equation (8).

$$\begin{cases} c_{mn} = 2C_{mn}\ , k_{mn} = 2K_{mn} \\ c_{kn} = 2C_{kn}\ , k_{kn} = 2K_{kn} \\ c_{ms} = 2C_{ms}\ , k_{ms} = 2K_{ms} \\ c_{ks} = 2C_{ks}\ , k_{ks} = 2K_{ks} \end{cases} \tag{8}$$

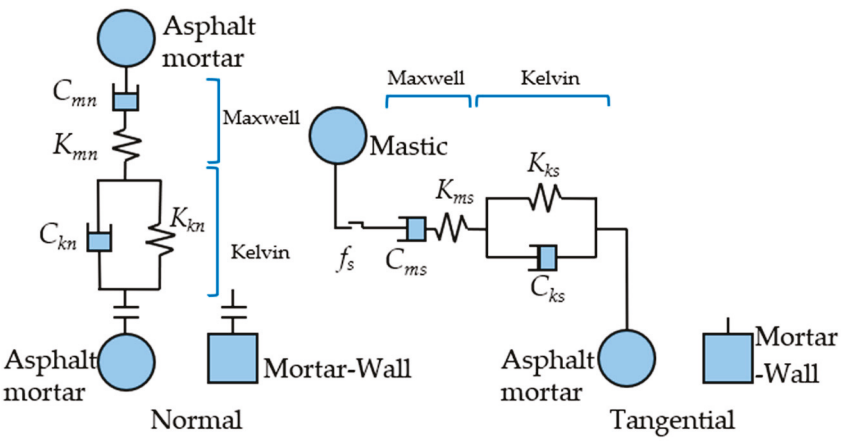

Figure 3. Burger's contact model.

The η_1, η_2, E_1 and E_2 four parameters of asphalt mortar need to be determined. Particles and asphalt smaller than 2.36 mm were defined as asphalt mortar. The Poisson's ratio of asphalt mortar is 0.5 [2,42,43]. Its complex modulus and phase angle were determined using the dynamic shear rheometer test. The values were obtained by fitting the Burger's model parameters to the principal curves of complex modulus and phase angle. The Burger's model parameters for the four asphalt mortars are listed in Table 3.

Table 3. Burger's model parameters of four asphalt mortars.

Asphalt Mixtures	E_1 (MPa)	E_2 (MPa)	η_1 (MPa·s)	η_2 (MPa·s)
SMA16	183.4	10.5	161.3	20.3
SMA13	79.6	3.7	18.2	6.8
OGFC16	153.9	6.8	102.0	20.3
OGFC13	223.0	20.1	101.2	1.63

2.2.2. Simulation Process

(1) Numerical model of aggregate particles

Scanning tests of real aggregate morphology were carried out using 3D laser scanning methods, and numerical models of aggregates with morphology features such as aggregate shape and angularity were established based on the aggregate particles obtained from the scanning [44].

According to the 3D aggregate template obtained from scanning, the numerical model of the aggregate is constructed through the fish language in PFC, as shown in Figure 4. The accuracy and efficiency of aggregate particle generation are ensured by setting the parameters related to particle generation. The distance value is set to ensure the smoothness of pebble generation distribution in each clump; the ratio value is set to ensure the range of pebble particle size; and the radfactor parameter is set to control the amount of overlap between the generated pebble and the surface of three-dimensional particles. In this paper, the above three parameters are set to 120, 0.3 and 1.05, respectively. In order to guarantee the efficiency of the simulation calculations and at the same time to ensure the usability of the results, the computational efficiency of the model is taken into consideration in the selection of aggregate particle templates, with five types of aggregate particles being randomly generated through the code written in fish language for each gradation of aggregate particles. The minimum particle size of the generated particles was 1.18 mm.

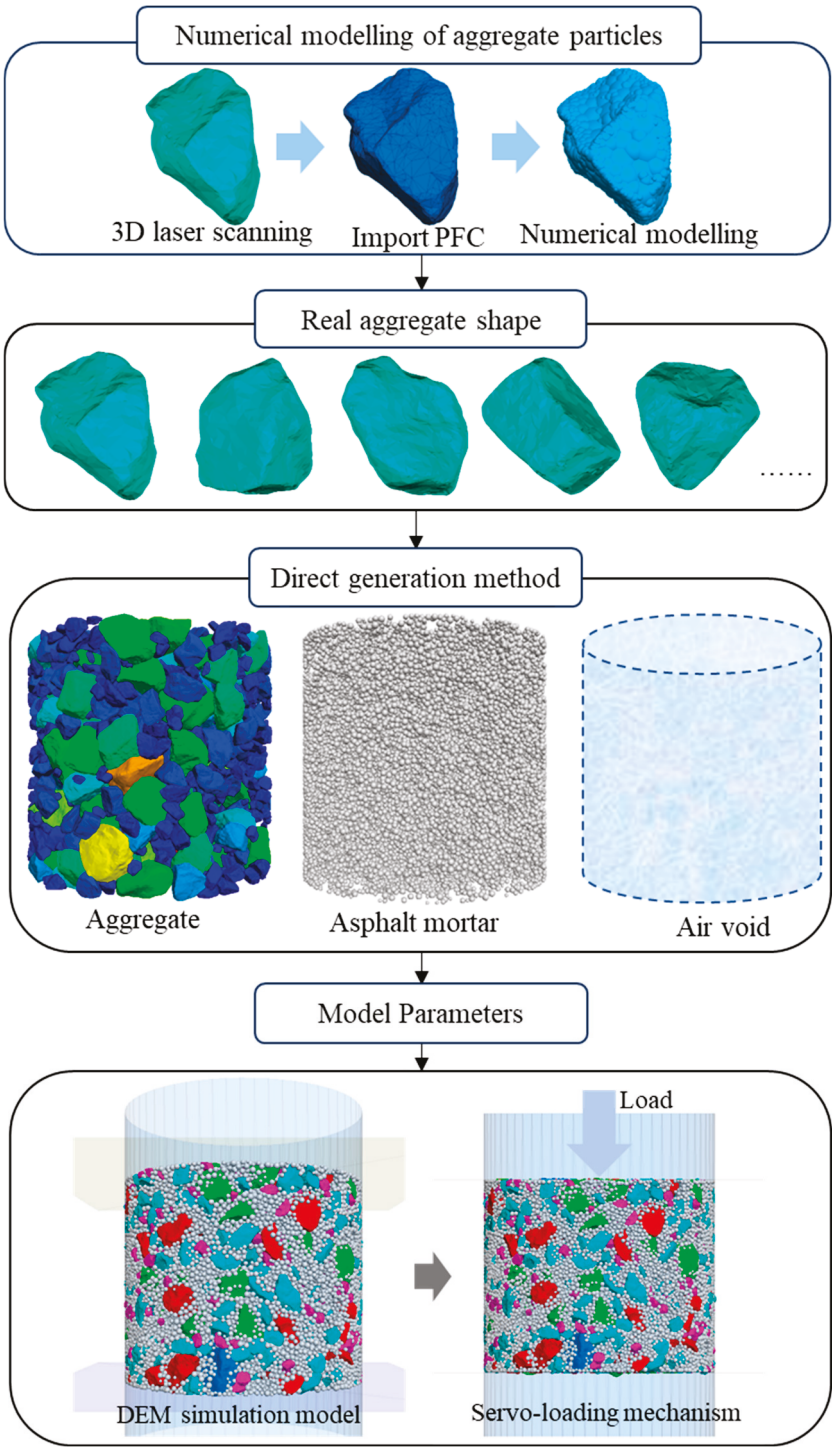

Figure 4. DEM simulation process of asphalt mixture.

(2) Distribution of component materials

The numerical model of asphalt mixture is composed of three parts: aggregate, asphalt mortar and voids. The construction process of the model is as follows: firstly, the volume ratio of the components of the mixture is generated, based on the aggregate particles in the asphalt mixture volume fraction; secondly, the required ratio of asphalt mortar is generated, based on the asphalt mixture in the asphalt mortar volume fraction; thirdly, the required proportion of the void is generated, based on the actual void ratio. The numerical model of each component of the asphalt mixture is generated using the above

parameters. The generation of aggregate particles with a diameter greater than 2.36 mm was conducted in accordance with the 3D aggregate scanning particle template. Particles smaller than 2.36 mm were defined as asphalt mortar and replaced with spherical particles in the numerical model.

(3) Parameter settings

The generation of a three-dimensional asphalt mixture digital model occurred through the aforementioned steps. The physico-mechanical parameters, such as aggregates, asphalt mortar and voids, and the contact parameters between the components, were inputted for the subsequent study of the load transfer characteristics of the asphalt mixture. The density of each aggregate is shown in Table 2, while the contact model and model parameters are presented in Section 2.2.1. The generation of the discrete element numerical model for asphalt mixtures is illustrated in Figure 4.

(4) Compaction process

The servo control mechanism is employed in the compaction process, with the top wall simulating the load applied by the indenter. The objective of compacting the asphalt mixture is realized by regulating the velocity of the downward movement of the wall, as illustrated in Figure 4. Concurrently, the compaction time is calculated in accordance with the time–temperature equivalence principle [45]. During the compaction process, the stress value of the upper and lower walls is controlled by the servo mechanism to be always 0.6 MPa until the compaction state operation of the asphalt mixture converges to the set system equilibrium state.

2.2.3. Simulation Model Validation

As demonstrated in Figure 5, a comparison is presented of the asphalt mixture void ratio obtained using the DEM simulation with the laboratory void ratio. The simulated void ratio has been calculated using the Equation (9).

$$v_a = \frac{V_V - V_A}{V_V} \times 100\% \tag{9}$$

where v_a is the DEM simulation void ratio of the asphalt mixture; V_V is the total volume of the asphalt mixture simulation specimen; and V_A is the total volume of aggregate and mortar of the asphalt mixture simulation specimen.

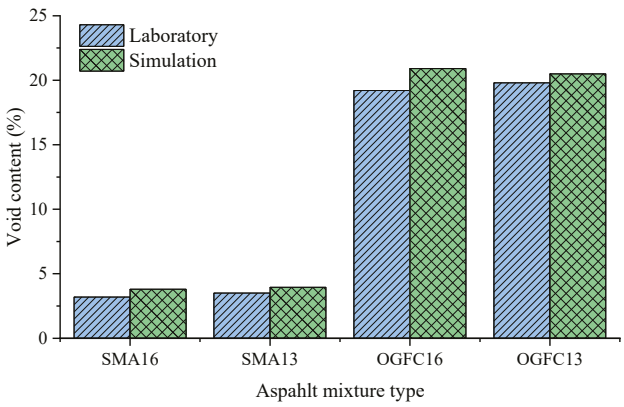

Figure 5. Void content of asphalt mixtures.

As can be seen from Figure 5, the air void of the simulation test is higher than that of the laboratory tests. In the laboratory test, the aggregate with a smaller particle size and the asphalt can fill the voids between the aggregate particles with a larger particle

size. However, due to the computational efficiency of the simulation test, the particle size is constrained to reach the smaller particle size in the laboratory test. Consequently, the void ratio of the asphalt mixtures in the simulation test is larger than that in the laboratory test. The relative error rates between the simulated void ratio and the indoor test void ratio of the four asphalt mixtures (SMA16, SMA13, OGFC16 and OGFC13) were 5.8%, 1.3%, 15.4% and 11.4%, which were all less than 15.4%. The error rate of the simulation in this test was less than that of the value in the study by Gong et al. [38]. The change trend of the void ratio of the four gradations is consistent with that of the laboratory test, and the same trend indicates that the simulation test does not change the overall aggregate skeleton structure. Therefore, DEM simulation can reasonably represent the basic structure of the indoor asphalt mixtures.

3. Force Chain Characterization Indicators

3.1. Contact Force Distribution Characteristics Indicators

Figure 6 shows the contact force network diagram inside the asphalt mixture after compaction of the SMA16 asphalt mixture, in which the thicker the force chain indicates the larger the contact force. The green line represents the contact force between aggregate and aggregate particles, while the blue line represents the contact force between mortar and mortar, as well as between mortar and aggregate particles. As demonstrated in Figure 6, the larger forces are predominantly transferred through the contact network formed by the interaction between aggregate particles, while the smaller forces are primarily transferred between mortar–aggregate and mortar–mortar, which play an auxiliary role in the transfer of loads to the primary skeleton structure. This is consistent with the observation that aggregate particles constitute the principal load-bearing structure of asphalt mixtures.

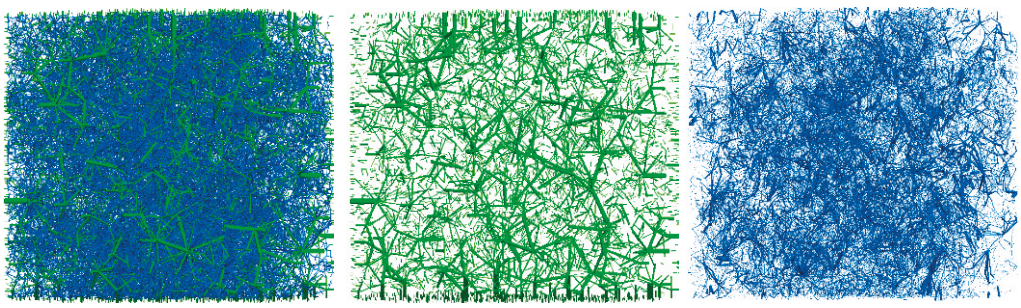

(**a**) (**b**) (**c**)

Figure 6. Contact force network of asphalt mixture. (**a**) All contact force; (**b**) Aggregate–aggregate contact force; (**c**) Mortar–mortar/mortar–aggregate contact force. (Note: The green line represents the contact force between aggregate and aggregate particles, while the blue line represents the contact force between mortar and mortar, as well as between mortar and aggregate particles; the force range is 0–159 N; the thicker the line, the larger the force).

3.1.1. Average Contact Force

The average contact force for each size aggregate particle is calculated using Equation (10).

$$\overline{F_s} = \frac{\sum_{k=1}^{n} f_k}{n} \tag{10}$$

where f_k is the magnitude of each contact force value, n is the total number of contact forces, and s is the particle size.

In order to distinguish the contribution of each component in the load transfer process, the contact forces between aggregate–aggregate and between aggregate–mortar were

extracted and calculated separately. The average contact force between aggregate–aggregate is calculated using Equation (11), and the contact force between aggregate–mortar is calculated using Equation (12).

$$\overline{F_{s_A}} = \frac{\sum_{k=1}^{n_A} f_{k_A}}{n_A} \tag{11}$$

$$\overline{F_{s_B}} = \frac{\sum_{k=1}^{n_B} f_{k_B}}{n_B} \tag{12}$$

where $\overline{F_{s_A}}$ and $\overline{F_{s_B}}$ denote the average contact force of aggregate–aggregate and aggregate–mortar contacts, respectively; f_{k_A} and f_{k_B} denote the contact force of aggregate–aggregate and aggregate–mortar contacts, respectively; n_A and n_B denote the number of contacts between aggregate–aggregate and aggregate–mortar, respectively.

3.1.2. Load Bearing Contribution

In order to characterize the contribution of aggregate particles in an asphalt mixture to resist the external load, the ratio of the average contact force of the size S particles to the overall average contact force is defined as the load-bearing contribution of size S particles, as shown in Equation (13). This parameter is used to quantify the magnitude of the effect of different aggregate particle sizes in resisting loads. The higher the value, the greater the contribution of that aggregate to the load-bearing capacity of the asphalt mixture.

$$R_S = \frac{\overline{F_s}}{\overline{F}} \tag{13}$$

where, R_s represents the contribution of the Sth grain size aggregate particles to resist external load; $\overline{F}$ represents the overall average contact force of the asphalt mixture; $\overline{F_S}$ represents the average contact force of the Sth grain size aggregate particles.

The contact force between granular particles can be categorized into two distinct types: aggregate–aggregate contact force and aggregate–mortar contact force. This paper proposes a methodology for evaluating the resistance of these two contact forces to external loads, which involves calculating the ratio of the average value of each contact force type to the average value of the aggregate contact force in the given gradation. The ratio is utilized to ascertain the contribution of each contact type to the overall load-bearing capacity, which can be calculated using Equation (14).

$$\begin{cases} P_{S_A} = \frac{\overline{F_{S_A}}}{\overline{F_S}} \\ P_{S_B} = \frac{\overline{F_{S_B}}}{\overline{F_S}} \end{cases} \tag{14}$$

where P_{S_A} and P_{S_B} are the load-bearing capacity contributions for aggregate–aggregate contact and aggregate–mortar contact, respectively.

3.1.3. Contact Force Angle

The angle between the position vectors of the particles at the two ends of the contact force and the z-axis is defined as the angle of the contact force (ω), as illustrated schematically in Figure 7. It can be simplified to the angle between the vectors formed by the two points and the z-axis, which can be calculated using Equation (15).

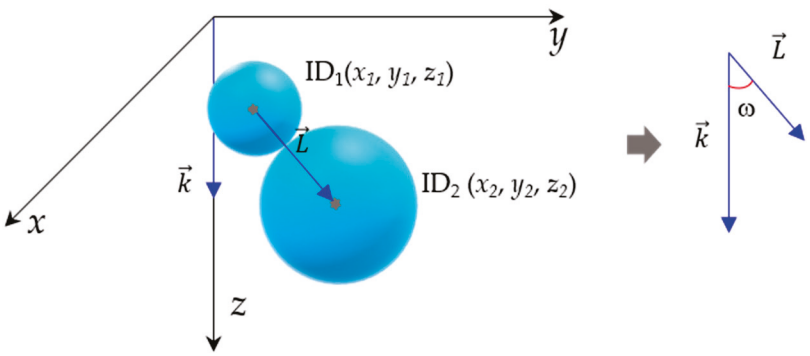

Figure 7. Schematic diagram of contact force angle.

The larger the angle of contact force, the wider the range of external load transfer that the contact is subjected to; conversely, it indicates that the transfer of load at the contact is concentrated in the loading direction.

$$\vec{k} \cdot \vec{L} = |k||L| \cos \omega \tag{15}$$

$$\cos \omega = \frac{\vec{k} \cdot \vec{L}}{|k||L|} \Rightarrow \omega = \arccos \frac{\vec{k} \cdot \vec{L}}{|k||L|} \tag{16}$$

where $\vec{k}$ is the unit vector in the forward direction of the z-axis; $\vec{L}$ is the direction vector between ID1 particles and ID2 particles; and ω is the angle of the contact force.

3.2. Topology Characterization Indicator of Force Chain

3.2.1. Topology Theory

Force chain architectures in asphalt mixture exhibit topological signatures that can be quantified through topological structure metrics [12,21,22]. Individuals in a topology are considered as nodes of a network. Interactions between individuals are considered as connections between nodes of the network. This network structure can be represented in the form of a graph. A graph can be defined as a triple $G = \{V, E, \psi\}$, where $E = \{e_1, e_2, \ldots, e_M\}$ is the set of edges and $V = \{v_1, v_2, \ldots, v_N\}$ is the set of nodes. Each connected edge e_m in E has a pair of nodes (v_i, v_j) corresponding to it. An association function maps each edge in E to a node in V. ψ is defined as a mapping from the set of edges E to the set of nodes V, and it is termed an association function. Each particle in asphalt mixtures is considered as a node, and the presence of connecting edges between particles is determined based on the presence of a contact force relationship between two aggregates, thus, constituting a network topology between particles in an asphalt mixture [12]. A sketch of the asphalt mixture contact force network is shown in Figure 8.

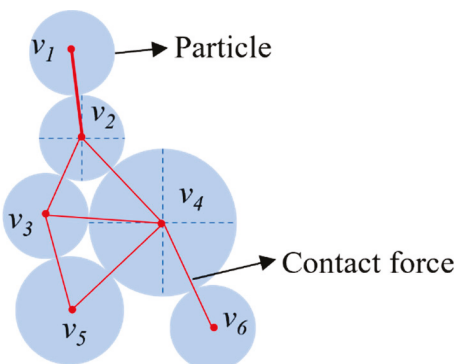

Figure 8. Topology diagram of force chain network.

There are two properties of topological structures: deterministic and stochastic. The determinism of the topological structure is contained in the statistical properties and, thus, it is of great interest to study the structure of complex force chain networks through topological statistics. There are three basic parameters to characterize the network topology: (1) the clustering coefficient that describes the characteristics of the nodes; (2) the edge betweenness reflecting the influence of the edges formed by two nodes in the whole network; and (3) the average path length that reflects the global characteristics of the network [12,23]. According to the analytical characterization needs of this study, the above three topology parameters are selected to characterize the force chain network of the asphalt mixture.

3.2.2. Clustering Coefficient

The clustering coefficient is a statistical value that reflects the degree of aggregation of particle (aggregate or mortar) nodes. It can be used to evaluate the connectivity of the nodes with neighboring nodes and can be calculated using Equation (17).

$$C_i = \frac{2e_i}{k_i(k_i - 1)},\ C_i \in [0, 1] \tag{17}$$

where k_i is the degree of particle i (node) and e_i is the number of edges between neighboring nodes of node i.

The average clustering coefficient (C) can be calculated using Equation (18).

$$C = \frac{1}{N}\sum_{i}^{N} C_i \tag{18}$$

where N is the total number of nodes, i.e., the number of particles forming the skeleton structure.

The greater the clustering coefficient of aggregate particles in the aggregate contact structure of an asphalt mixture, the greater the degree of aggregation of the whole structure and the closer the direct relationship between the aggregate particles. It indicates that the mix has a more optimal bearing structure.

3.2.3. Edge Betweenness

The number of shortest paths between nodes v_l and v_m is denoted by N_{lm}, and the proportion of the number of all shortest paths in the network that pass through an edge e_{ij} is defined as the edge betweenness (B_{ij}), which is calculated using Equation (19).

$$B_{ij} = \sum_{\substack{\text{All} l, m : l \neq m \\ \{l, m\} \neq \{i, j\}}} [N_{lm}(e_{ij}) / N_{lm}] \tag{19}$$

where $N_{lm}(e_{ij})$ denotes the number of shortest paths between nodes v_l and v_m through edge e_{ij}.

The larger the edge betweenness of the aggregate–aggregate in the force chain in asphalt mixture, the greater the contribution of this edge to resisting the external load.

3.2.4. Average Path Length

The average distances between all pairs of nodes are defined as the average path length (L), which can reflect the global characteristics of the force chain network. The average path length can be calculated according to Equation (20).

$$L = \frac{1}{N^2} \sum_{j=1}^{N} \sum_{i=1}^{N} d_{ij} \tag{20}$$

where N is the number of nodes; L is the average path length of the force chain network.

The smaller the average path length value in the force chain network of asphalt mixture, the better the connectivity between the aggregates and the more stable the overall structure of the asphalt mixture.

4. Results and Discussion

4.1. Contact Force Distribution Characteristics in Asphalt Mixtures

4.1.1. Average Contact Force of Particles

(1) Contact force distribution

The boxplot of the contact force distribution of each grain size aggregate particles in the asphalt mixture is shown in Figure 9. As can be seen from Figure 9, the distribution of contact force anomalies for each size aggregate is concentrated on the side of the larger value, and the contact force distribution shows a right-skewed state. With the decrease of aggregate particle size, the trend of contact force distribution range gradually decreases. The contact force range of the mortar is the smallest, and the maximum value of the distribution range is the smallest. It indicates that in asphalt mixtures, aggregate particles bear and transfer larger external loads. Meanwhile, the role of aggregate particles in constituting the load-bearing skeleton structure was verified using the meso-scale.

(2) Maximum contact force and average contact force

Figure 10 depicts the maximum contact force values for different contact types in the aggregate particles of the asphalt mixture. From Figure 10, it can be seen that the maximum contact force for aggregate–aggregate contact is greater than that for aggregate–mortar contact. For SMA16 and SMA13 asphalt mixtures, the maximum aggregate–aggregate contact force shows a tendency to increase and then decrease with decreasing particle size. For the OGFC16 asphalt mixture, the variation of aggregate–aggregate contact force with different-sized aggregates is smaller. For the OGFC13 asphalt mixture, the variation of aggregate–aggregate contact force with particle size is smaller when the particle size is larger than 4.75 mm, but the average contact force of aggregate particles with particle sizes of 2.36 mm becomes significantly smaller. The above results indicate that the magnitude of inter-particle contact force is related to the differences in the gradation of asphalt mixtures.

The average contact force for each size of aggregate particles after compaction and the average contact force between aggregate–aggregate particles and between aggregate–mortar in that size of aggregate particles are quantified. Figure 11 shows the average contact force for different contact types in different aggregate particle sizes. It can be seen from Figure 11 that the average contact force gradually decreases as the aggregate particle size decreases. For each size of aggregate particles, the average contact force of aggregate–aggregate contact is significantly greater than the average contact force of the particles, and the average contact force of the aggregate–mortar contact is the smallest. This is mainly due to the fact that the modulus of the asphalt mortar is much smaller than the modulus of the aggregate particles, and in asphalt mixtures under external loading, the aggregate–aggregate contact transmits a greater external load, and the aggregate–mortar contact and the mortar–mortar contact transmit a smaller load.

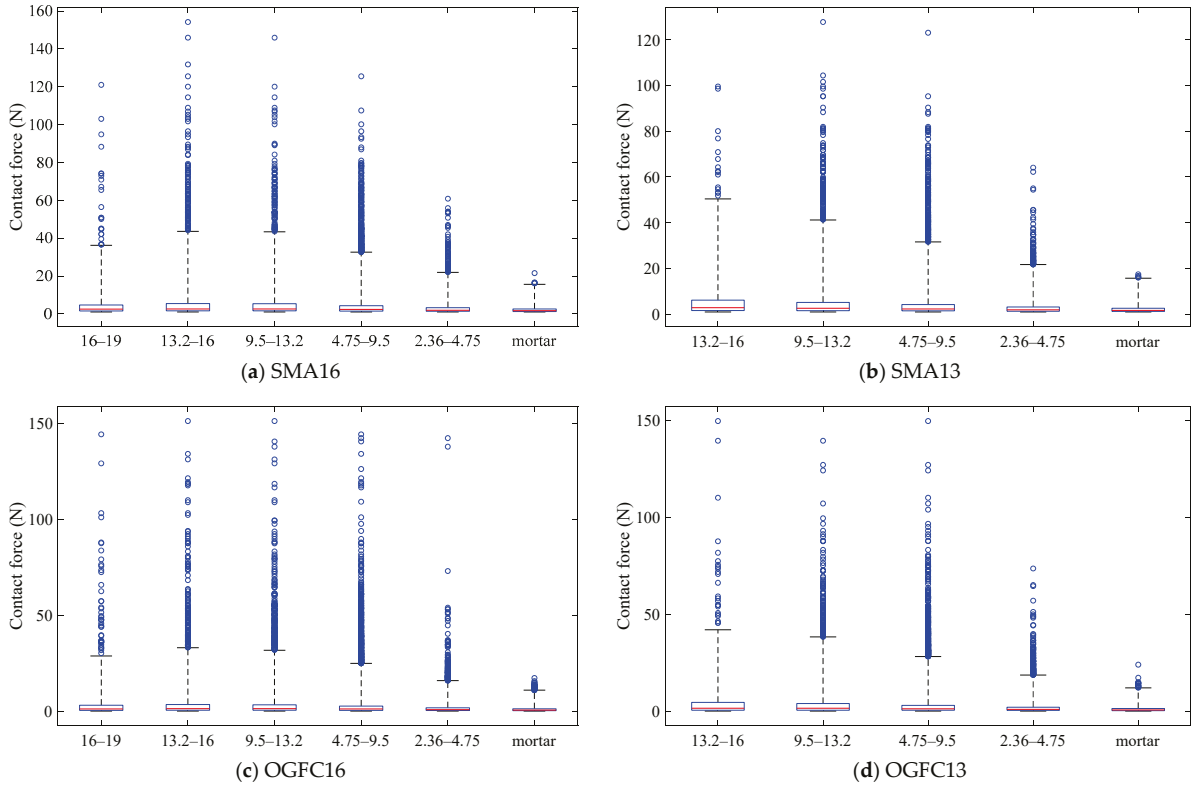

Figure 9. Contact force distribution of each grain size particle in asphalt mixture. (Note: The blue box represents the interquartile range (IQR) spanning from the first quartile (Q1, bottom edge) to the third quartile (Q3, top edge). A bold red horizontal line within the box marks the median value. Blue circles indicate outliers lying beyond the whiskers, highlighting values deviating significantly from the central tendency of the data. The meaning of the box plot below is the same as this and will not be repeated).

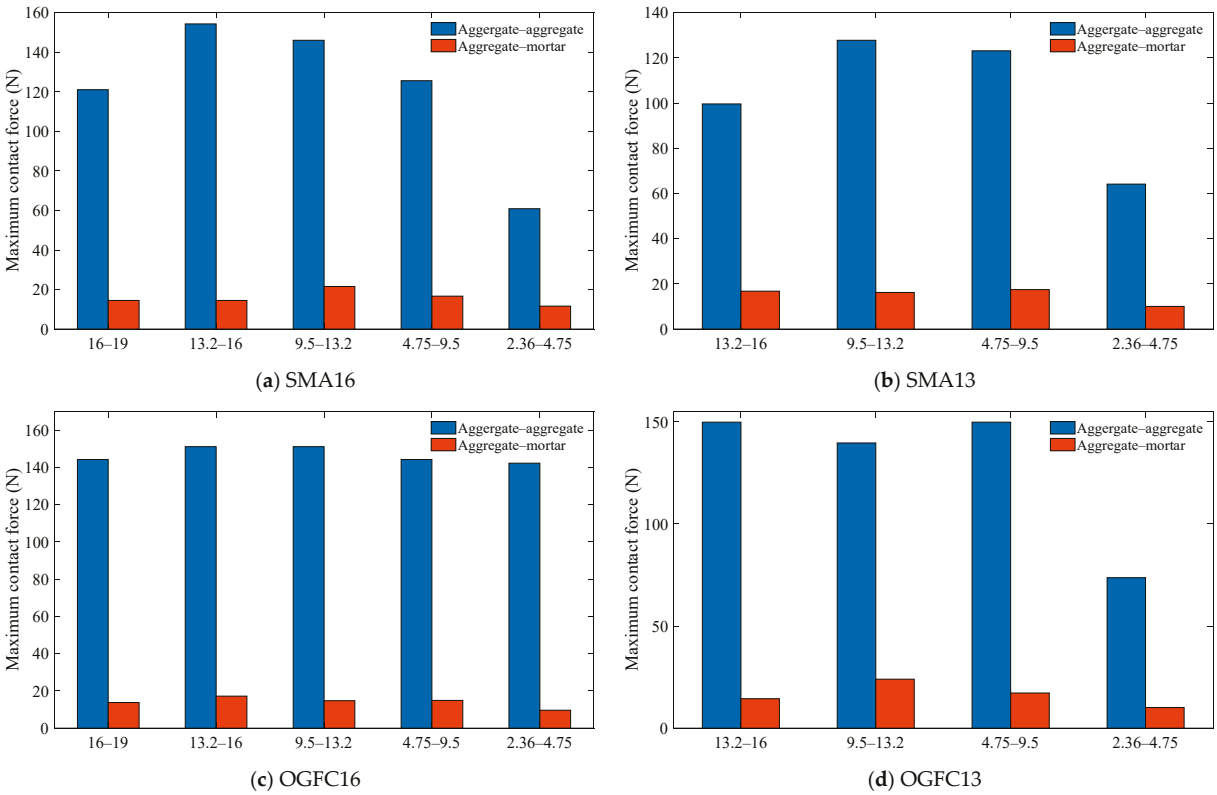

Figure 10. Maximum contact force for different contact types of aggregate particles.

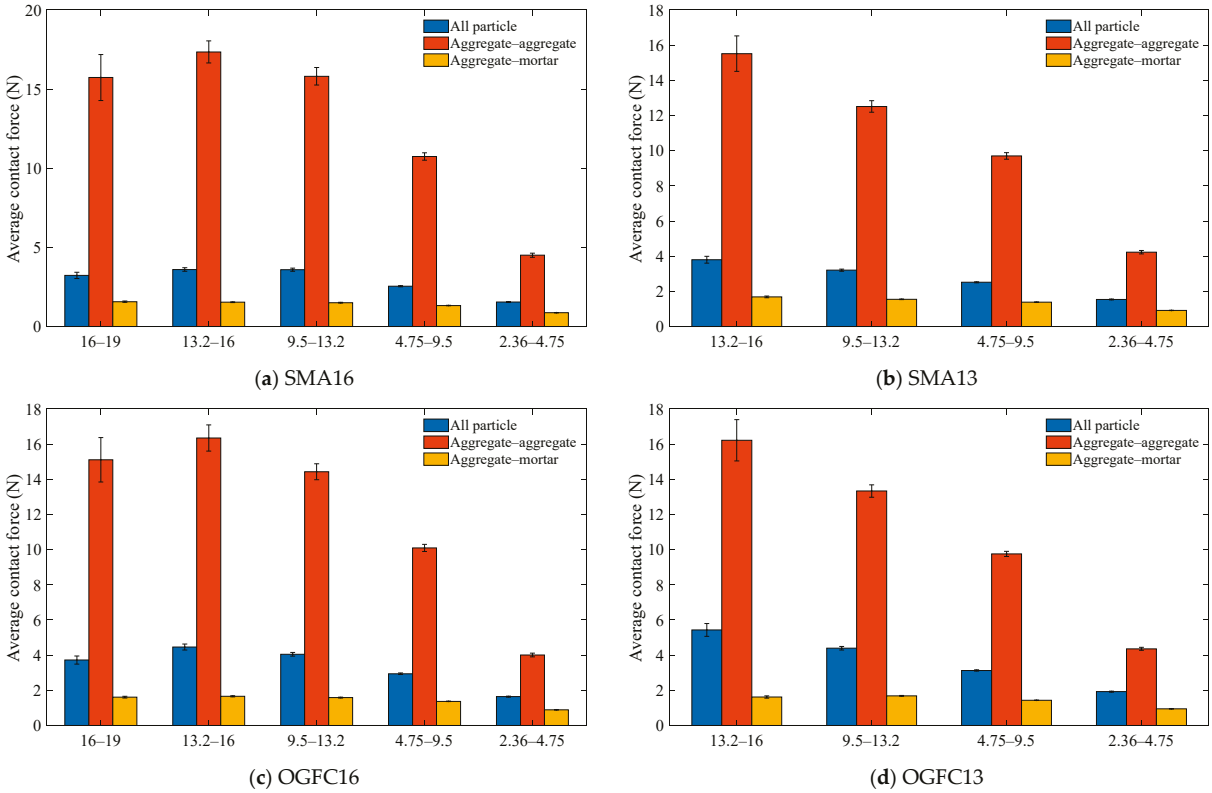

Figure 11. Aggregate contact force for different contact types.

4.1.2. Load-Bearing Contribution of Particles

The load-bearing contribution of different-sized particles is shown in Figure 12. It can be seen from Figure 12 that for the SMA16 and OGFC16 asphalt mixtures, the load-bearing contribution shows an increase and then a decrease as the particle size decreases. When the aggregate particle size is greater than 13.2 mm, the load-bearing contribution decreases with increasing particle size. When the aggregate particle size is less than 13.2 mm, the load-bearing contribution decreases with decreasing particle size. For the SMA13 and OGFC13 asphalt mixtures, the aggregate particles' load-bearing contribution decreases with decreasing particle size. It indicates that when the nominal maximum particle size of the asphalt mixture is less than 13.2 mm, the load-bearing contribution of aggregate increases with the increase of particle size. The load-bearing contribution of mortar in all four asphalt mixtures is less than one, which indicates that mortar is not the main participant in the bearing structure of the asphalt mixtures. For the same size aggregate particles, the value of the load-bearing contribution is obviously different in different asphalt mixtures. The above results indicate that the load-bearing contribution of different-sized aggregates to the overall structure is different, and the load-bearing contribution of the same-sized aggregate is affected by the gradation type of the asphalt mixture. Related research results also confirm that the load-bearing contribution is more significantly affected by gradation [46]. Load-bearing contribution is higher in large-size aggregates above 9.5 mm, which exhibit greater load transfer efficiency [10].

The load-bearing contributions of different contact types of aggregates in asphalt mixtures are shown in Figure 13. From Figure 13a,b, it can be seen that the load-bearing contribution of aggregate–aggregate contact (P_{S_A}) is significantly larger than that of aggregate–mortar contact (P_{S_B}). For the four asphalt mixtures, the aggregate–aggregate contact type shows a gradual decrease in load-bearing contribution with decreasing aggregate particle size. This may be due to the fact that the modulus of the large-size aggregate particles changed little even after adhering to the asphalt mortar, and the bearing capacity did not

change much due to the adhesion of the mortar, whereas the modulus of the smaller-sized aggregate particles was affected more by the mortar after adhering to the asphalt mortar, which in turn affected the bearing capacity, so the value decreased gradually with the decrease in the aggregate particle size. This phenomenon illustrates why the value gradually increases with decreasing aggregate particle size in different gradations. As demonstrated in Figure 13, for a given particle size in different asphalt mixtures, the load-bearing contribution value of aggregate–aggregate contact for SMA16 is the largest, followed by SMA13, and then OGFC16, with OGFC13 being the smallest. This also reflects that the SMA has a superior load-bearing contact structure. It resists deformation under repeated loads, which is a key factor in rutting resistance [23].

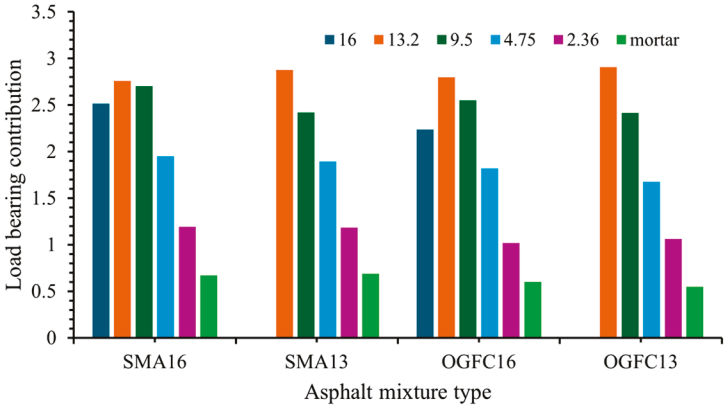

Figure 12. Load-bearing contribution of different-sized particles.

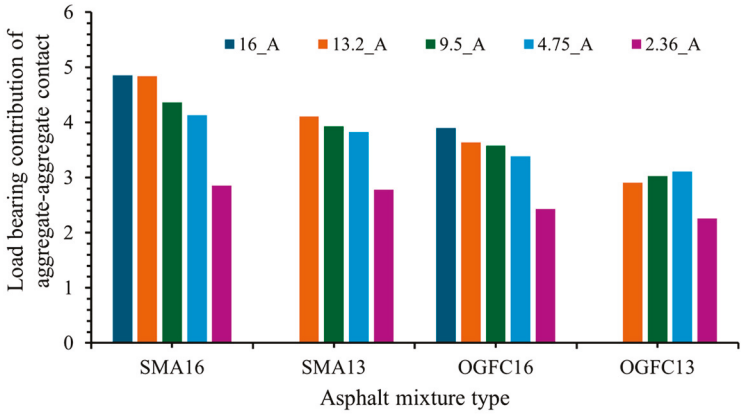

(**a**) Aggregate–aggregate contact

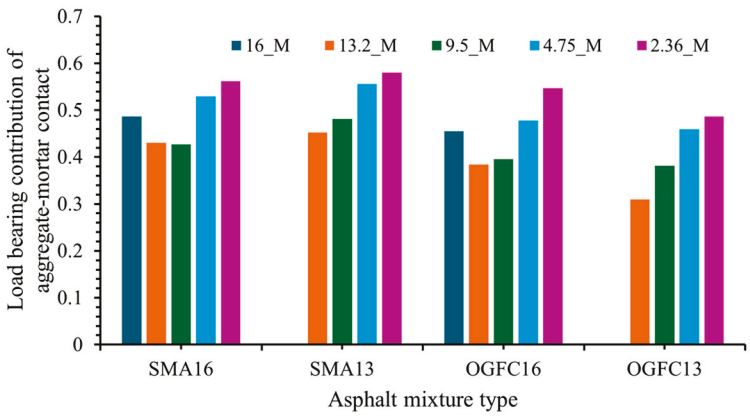

(**b**) Aggregate–mortar contact

Figure 13. Load-bearing contribution of different contact types.

4.1.3. Contact Force Angle of Particles

The probability distribution polar plot of the contact force angle of each size particle is depicted in Figures 14–17. From Figures 14–17, it can be seen that for the four gradations, the contact force angle of each particle size is symmetrically distributed around a center axis of 90°, with the contact force angle centrally distributed within the range of 30° to 150°. The results demonstrate that the external load is predominantly transmitted along the loading direction to the external extension in the internal transmission process of the asphalt mixture. This outcome is consistent with the results of the aforementioned loading process in the asphalt mixture, wherein the contact force is transmitted along the direction of the external load.

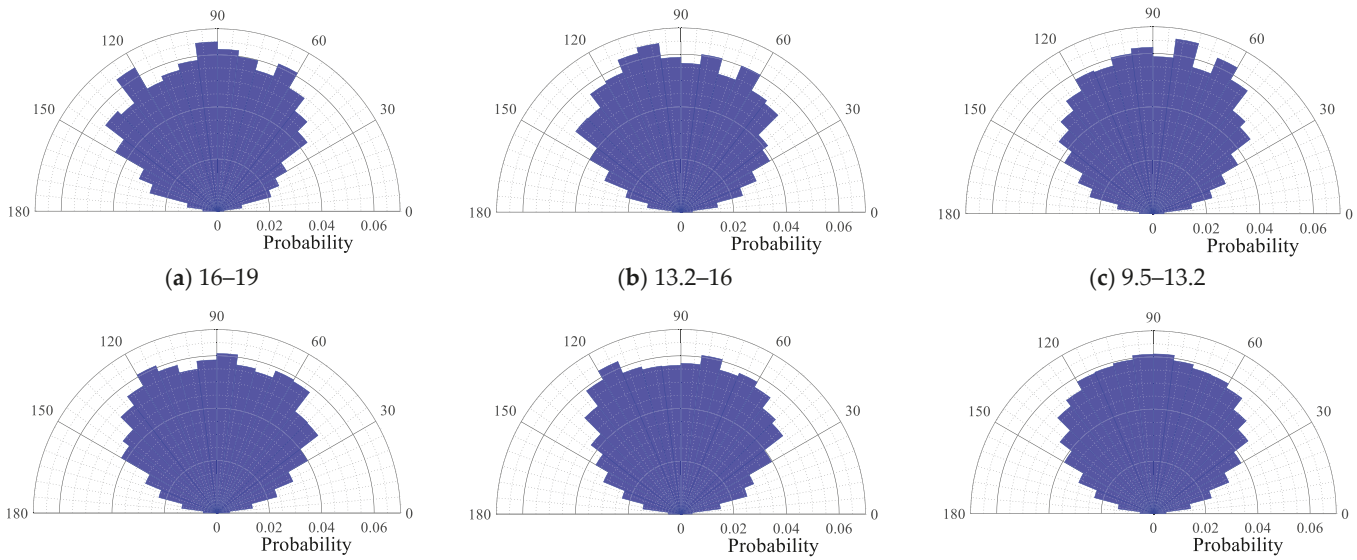

(**a**) 16–19 (**b**) 13.2–16 (**c**) 9.5–13.2

(**d**) 4.75–9.5 (**e**) 2.36–4.75 (**f**) Asphalt mortar

Figure 14. Contact force angle for each particle size in SMA16.

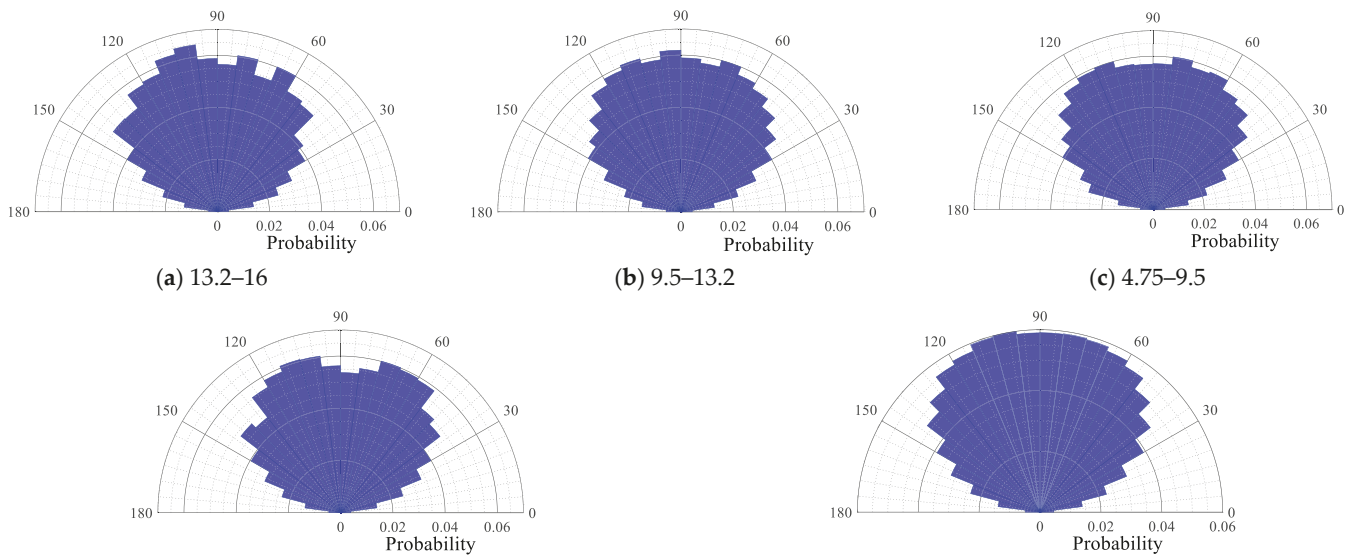

(**a**) 13.2–16 (**b**) 9.5–13.2 (**c**) 4.75–9.5

(**d**) 2.36–4.75 (**e**) Asphalt mortar

Figure 15. Contact force angle for each particle size in SMA13.

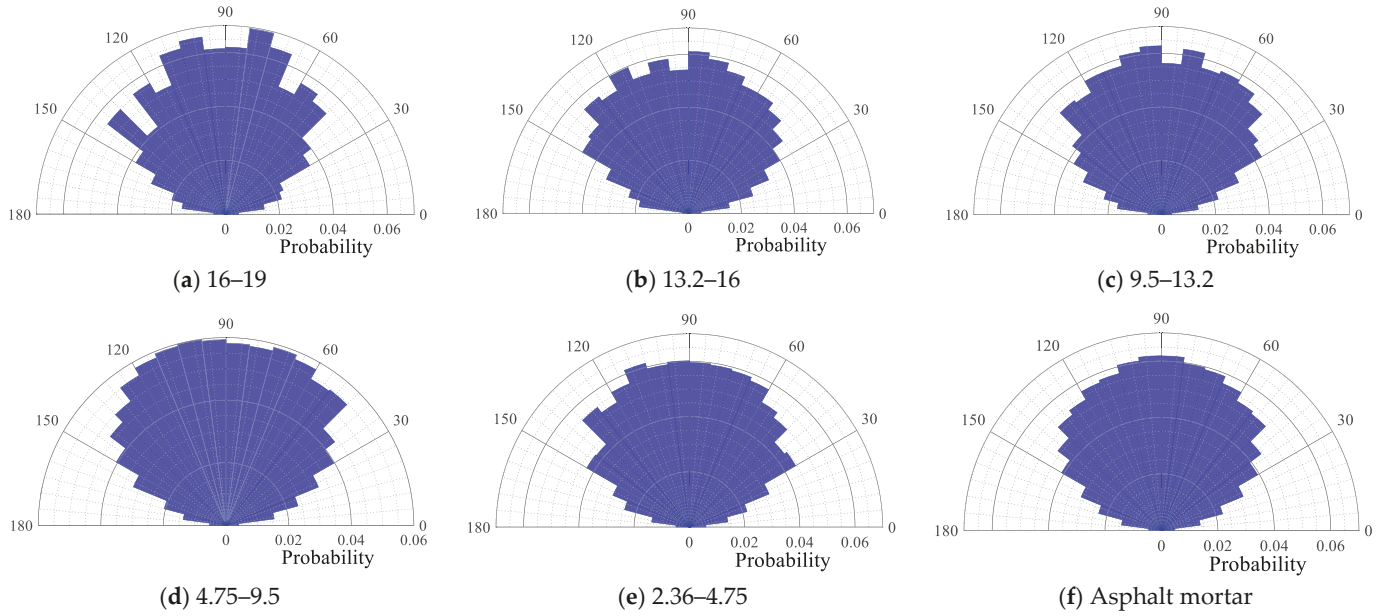

(**a**) 16–19 (**b**) 13.2–16 (**c**) 9.5–13.2

(**d**) 4.75–9.5 (**e**) 2.36–4.75 (**f**) Asphalt mortar

Figure 16. Contact force angle for each particle size in OGFC16.

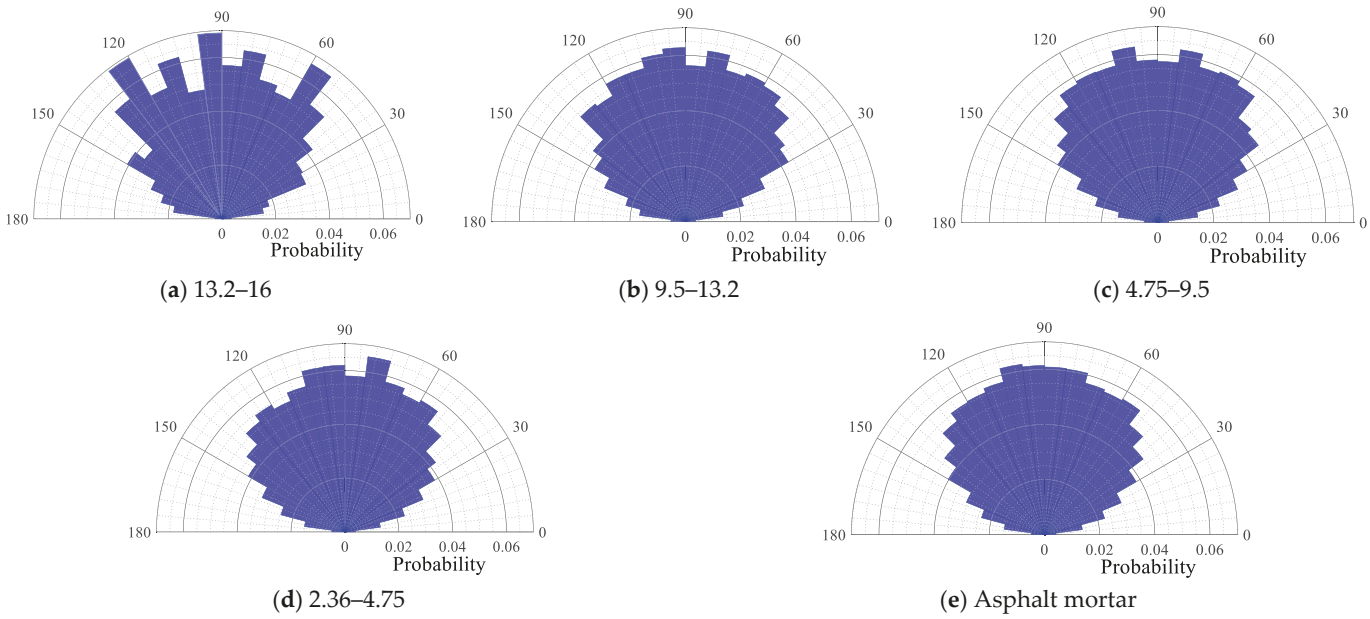

(**a**) 13.2–16 (**b**) 9.5–13.2 (**c**) 4.75–9.5

(**d**) 2.36–4.75 (**e**) Asphalt mortar

Figure 17. Contact force angle for each particle size in OGFC13.

4.2. Force Chain Topology Characteristics in Asphalt Mixtures

4.2.1. Clustering Coefficient of Asphalt Mixture

The clustering coefficients of different asphalt mixtures are presented in Figure 18. The distribution of clustering coefficients is given in Figure 18a, and it can be seen that the distribution of clustering coefficients at all asphalt mixtures demonstrates a right-skewed distribution, with outliers located on the side of the larger quartile. This indicates that in the asphalt mixture bearing skeleton structure, the number of particles that play a major bearing role accounts for a relatively small proportion. This is primarily due to the generated asphalt mixture DEM model, the asphalt mortar particles particle size being small and, thus, the number of particles being relatively large. From the above analysis, it can be seen that the asphalt mortar is not a major bearing structure. Therefore, the

distribution of clustering coefficients values appears to have a severely skewed distribution phenomenon.

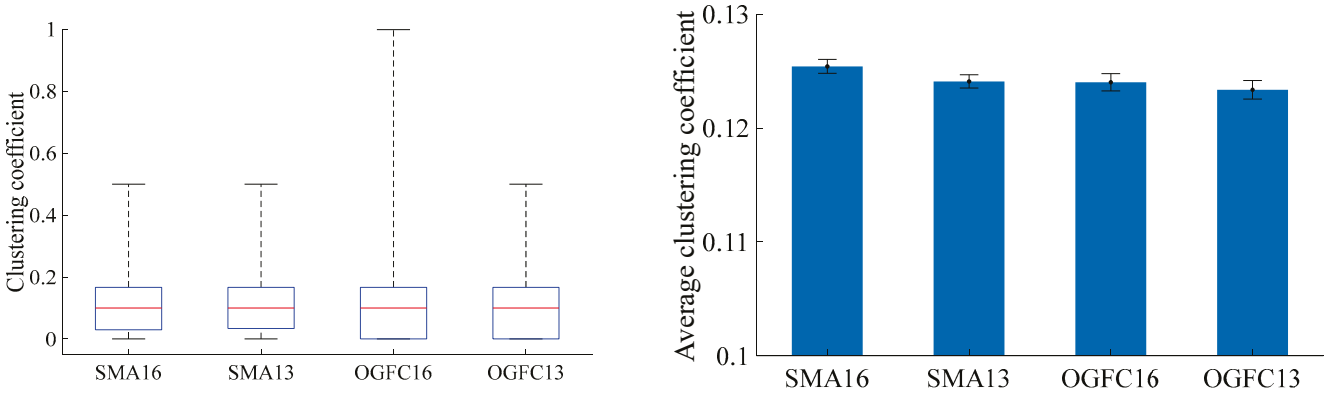

(**a**) Clustering coefficient distribution (**b**) Average clustering coefficient

Figure 18. Clustering coefficient of different asphalt mixtures.

The average clustering coefficients are shown in Figure 18b. As illustrated in Figure 18b, the average clustering coefficient of SMA13 is lower than that of SMA16 by 0.0013. This finding suggests that the aggregate particles of SMA16 exhibit enhanced connectivity, characterized by a higher degree of aggregation compared to SMA13. Consequently, it indicates that the load-bearing skeleton structure of SMA16 is superior to that of SMA13. The average clustering coefficient of the OGFC16 mixture is greater than that of the OGFC13 by 0.0007, indicating that the load-bearing structure of the OGFC16 mixture is superior to that of the OGFC13. A comparison of the different gradation asphalt mixtures, with the same maximum nominal particle size, reveals that the average clustering coefficients of the SMA asphalt mixtures exceed those of the corresponding OGFC asphalt mixtures. The average clustering coefficient of SMA16 is greater than OGFC16 by 0.0014. This finding demonstrates that the OGFC asphalt mixtures possess greater load-bearing requirements for aggregate particles and that the SMA-type gradations demonstrate a more effective aggregate load-bearing structure than the OGFC-types.

4.2.2. Edge Betweenness of Asphalt Mixture

The edge betweenness distribution and the average edge betweenness of different asphalt mixtures are shown in Figure 19. As can be seen from Figure 19a, the distributions of the edge betweenness of different asphalt mixtures all show right skewed distributions, and the outliers are located on the side of the larger quartiles. This is primarily attributable to the fact that, within the generated DEM model of the asphalt mixture, the number of particle pairs (edges formed by two particles) that play a major role in load-bearing structure is comparatively minimal. The particle size of asphalt mortar particles is small and, thus, the number of mortar particles is relatively large, but the edge formed between the mortar particles does not play a major role in the load-bearing structure and, thus, smaller values of edge betweenness account for more.

As can be seen from Figure 19b, the average edge betweenness of SMA16 is smaller than that of SMA13 by 7.95×10^{-7}. Additionally, the average edge betweenness in OGFC16 is smaller than that in OGFC13 by 2.65×10^{-6}. It also can be seen that the average edge betweenness in SMA-type asphalt mixture is smaller than that in OGFC-type asphalt mixture with the same maximum nominal particle size. OGFC16 improves by 4.12×10^{-6} relative to SMA16 and OGFC13 improves by 5.98×10^{-6} relative to SMA13. The results presented above demonstrate that the edge between two particles in SMA13 contributes more to the

force chain network structure than SMA16; the edge between two particles in OGFC13 contributes more to the force chain network structure than OGFC16. Additionally, the edge between particles in SMA-type mixtures contributes less to the overall contact force structure than OGFC-type mixtures.

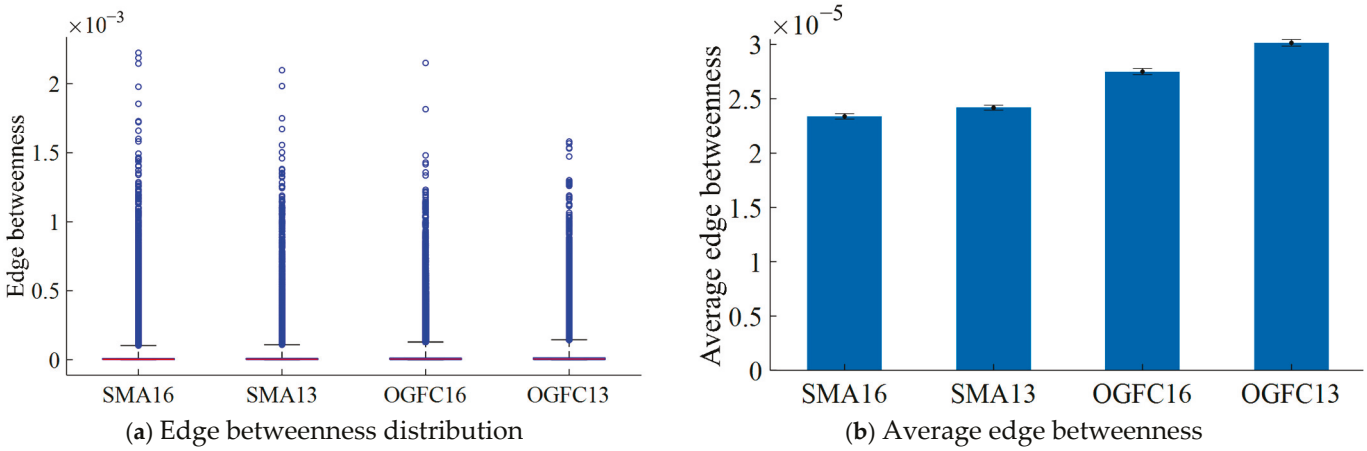

(**a**) Edge betweenness distribution (**b**) Average edge betweenness

Figure 19. Edge betweenness of different asphalt mixtures.

4.2.3. Average Path Length of Asphalt Mixture

The average path length of the force chain structure in asphalt mixtures is depicted in Figure 20. As illustrated in Figure 20, the average path length of SMA13 is marginally greater than that of SMA16, exhibiting a difference of 0.25. Similarly, the average path length of OGFC13 is slightly higher than that of OGFC16, with a difference of 0.003. Furthermore, the average path length of the SMA-type mixtures exceeds that of the OGFC-type mixtures. The relative change rate in the average path length between the same type of gradation with different maximum nominal grain sizes is less than 3%. The relative change rate in the average path length between different types of gradations (OGFC and SMA) is 7% to 9%. This finding indicates that the maximum nominal particle size exhibits a lower influence on the average path length, while the type of gradation exhibits a more significant effect. According to the concept of average path length in topology and the above analyses, it can be found that asphalt mixtures of the same gradation type have similar load-bearing structures, even though they have different maximum nominal particle sizes. SMA asphalt mixtures have more stable load-bearing structures than OGFC asphalt mixtures. This finding is consistent with the results of the characterization of the contact force distribution of asphalt mixtures in Section 4.1. Based on the analyses in Sections 4.1 and 4.2, it can be seen that the key influential parameters for the load transfer characterization of asphalt mixtures are shown in Table 4. For all four asphalt mixtures, the average contact force and topological structure parameters better reflect the load transfer characteristics within the asphalt mixtures. Additionally, the correlation between the contact force distribution characteristics and the force chain topology characteristics is shown in Figure 21, where the coefficients of determination (R^2) are all greater than 0.7. This indicates that there is a strong correlation between the average contact force and the force chain topology parameters. The related study also found that there is a correlation between statistical and topological features of the force chain [12,23].

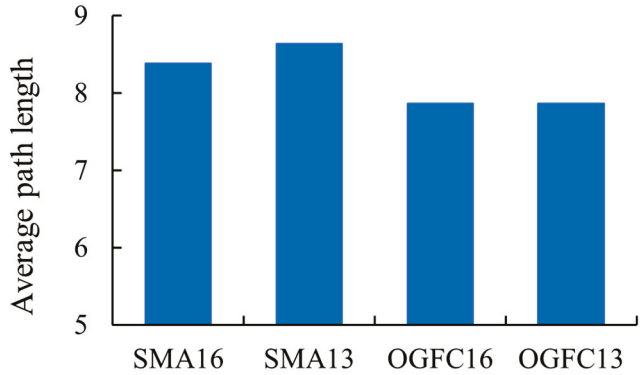

Figure 20. Average path length of different asphalt mixtures.

Table 4. Key parameters of force chain characteristics for asphalt mixtures.

Asphalt Mixture	Key Parameters	
	Distribution Characteristics	Topology Characteristics
SMA16 SMA13 OGFC16 OGFC13	Average contact force ($\overline{F_s}$)	Average clustering coefficient (C) Average edge betweenness ($\overline{B_{ij}}$) Average path length (L)

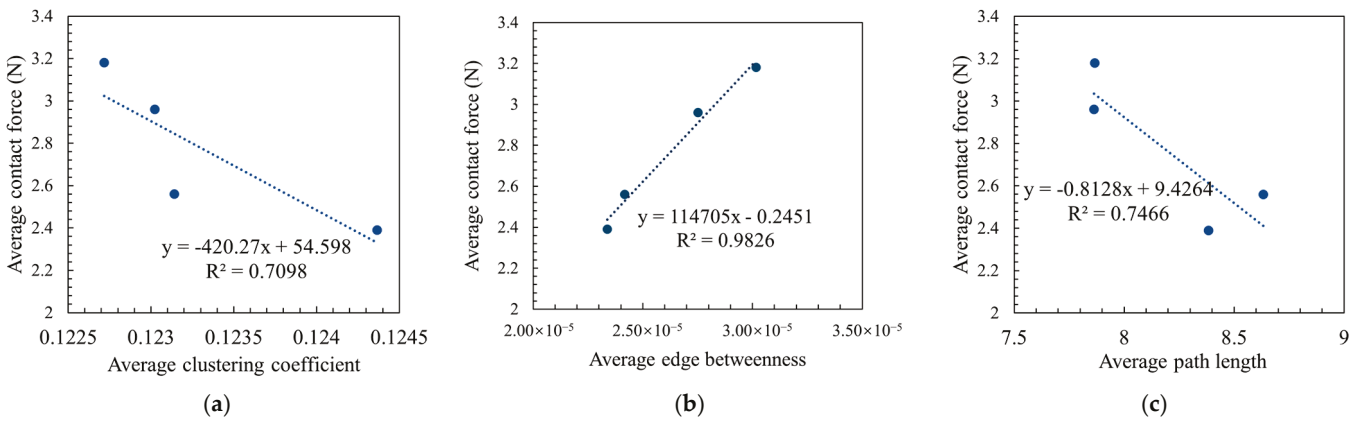

Figure 21. Correlation of the average contact force with the topological characteristics of the force chain. (**a**) Average contact force and average clustering coefficient. (**b**) Average contact force and average edge betweenness. (**c**) Average contact force and average path length.

5. Conclusions

In this study, a series of DEM simulation tests were performed considering SMA gradations and OGFC gradations to characterize the contact force distribution in the asphalt mixtures. Additionally, the force chain topology characterization was also analyzed based on topology theory. The primary conclusions are as follows.

(1) The contact forces of aggregate particles of varying grain sizes in asphalt mixtures are distinct. The average contact force of particles in SMA16 and OGFC16 exhibits a tendency to increase and subsequently decrease with decreasing particle size, with the maximum average contact force recorded for a particle size of 13.2 mm. For SMA13 and OGFC13 asphalt mixtures, the average contact force demonstrates a gradual decline with decreasing particle size.

(2) The particles with different sizes in the asphalt mixture have different load-bearing contributions. For SMA16 and OGFC16 asphalt mixtures, the load-bearing contribution initially increases and then decreases with decreasing aggregate size, reaching a maximum at 13.2 mm. For SMA13 and OGFC13 asphalt mixtures, the aggregate particles' load-bearing contribution decreases with decreasing particle size. The load-bearing contributions of different contact types in asphalt mixtures are different. The P_{S_A} is significantly larger than P_{S_B}. The P_{S_A} for SMA16 is the largest, followed by SMA13, and then OGFC16, with OGFC13 being the smallest.

(3) The contact force angle distribution characteristics are less affected by the type of asphalt mixture. The contact force angle of each particle size is symmetrically distributed around a center axis of 90°, with the contact force angle centrally distributed within the range of 30° to 150°.

(4) The topological characteristic parameters can effectively characterize the structural features of the asphalt mixture's force chain network. The average clustering coefficients of SMA are larger than those of the OGFC. The SMA asphalt mixture has a better load-bearing force chain structure than the OGFC asphalt mixture. The average clustering coefficient of SMA13 is smaller than that of SMA16. The load-bearing force chain structure of SMA16 is better than that of SMA13. The average clustering coefficient of OGFC16 is larger than that of OGFC13. The force chain structure of OGFC16 is better than that of OGFC13.

(5) The edge betweenness of the aggregate–aggregate in the force chain in SMA asphalt mixture is smaller than that in OGFC asphalt mixture. Additionally, the average edge betweenness in SMA16 is smaller than that in SMA13. The edge between two particles in SMA13 contributes more to the force chain network structure than SMA16; the edge between two particles in OGFC13 contributes more to the force chain network structure than OGFC16.

(6) The gradation type of asphalt mixture has a significant effect on the average path length of the force chain network, and the maximum nominal particle size of the same gradation has a lesser effect on the average path length. The relative change rate in average path length for the same gradation type of asphalt mixture with different maximum nominal particle sizes is 3%, while the relative change rate in the average path length of the force chain network for different gradation types of asphalt mixtures is 7% to 9%.

The topological parameters proposed in this paper can be used to guide the grading optimization. According to the above results, in comparison to OGFC, SMA has a larger average clustering coefficient and denser force chain network, and the aggregate particles are well connected to each other, forming a more effective load-bearing skeleton structure. This structure enables SMA mixtures to better resist deformation and reduce rutting when subjected to vehicle loads. SMAs have a better topology and load-bearing skeletal structure compared to OGFC mixtures, and their compact skeletal structure also contributes to resisting volume changes during freeze–thaw cycles and improving frost resistance. In future studies, the grading of OGFC can be optimized to improve aggregate interlocking in OGFC, and to improve mix durability without compromising drainage. Gradation optimization can be performed using force chain topological network analysis. However, it is recommended that the results be validated by further laboratory testing to refine the understanding of the relationship between force chain characteristics and mechanical properties of asphalt mixtures.

Author Contributions: Conceptualization, S.W. and L.W.; Methodology, S.W., Y.M. and L.W.; Software, S.W.; Validation, S.W. and J.X.; Formal analysis, S.W., J.W. (Jianxia Wang), J.W. (Jie Wang),

Y.M., Q.M. and T.L.; Investigation, S.W., J.W. (Jianxia Wang), J.W. (Jie Wang), Y.M., Q.M. and T.L.; Resources, S.W.; Writing—original draft, S.W., J.W. (Jianxia Wang), J.W. (Jie Wang), J.X., Q.M. and T.L.; Writing—review & editing, S.W., J.W. (Jie Wang), J.X., Y.M., Q.M., L.W. and T.L.; Supervision, Y.M. and L.W.; Project administration, L.W.; Funding acquisition, J.X. All authors have read and agreed to the published version of the manuscript.

Funding: The research reported in this paper is funded by the Science and Technology Project of the Department of Transportation of Jiangxi Province (No. 2023H0011).

Institutional Review Board Statement: Not applicable.

Informed Consent Statement: Not applicable.

Data Availability Statement: The original contributions presented in this study are included in the article. Further inquiries can be directed to the corresponding authors.

Conflicts of Interest: Authors Jianxia Wang and Tao Liu were employed by the company Jiangxi Transportation Investment Group Co., Ltd. Authors Sudi Wang, Jie Wang, Jian Xu and Qing Ma were employed by the research institution Research Institute of Highway Ministry of Transport. The remaining authors declare that the research was conducted in the absence of any commercial or financial relationships that could be construed as a potential conflict of interest.

References

1. Wang, S.; Yu, W.; Miao, Y.; Wang, L. Review on Load Transfer Mechanisms of Asphalt Mixture Meso-Structure. *Materials* **2023**, *16*, 1280. [CrossRef] [PubMed]
2. Wang, S.; Miao, Y.; Wang, L. Investigation of the force evolution in aggregate blend compaction process and the effect of elongated and flat particles using DEM. *Constr. Build. Mater.* **2020**, *258*, 119674. [CrossRef]
3. Liang, Z.; Xing, C.; Tan, Y.; Liu, B.; Wang, W. Investigation of three-dimensional aggregate contact evolution using an enhanced image segmentation algorithm. *Constr. Build. Mater.* **2025**, *468*, 140371. [CrossRef]
4. Yu, L.; You, Z. Visualization and Simulation of Asphalt Concrete with Randomly Generated Three-Dimensional Models. *J. Comput. Civ. Eng.* **2009**, *23*, 340–347. [CrossRef]
5. Chang, M.; Sheng, Y.; Niu, X.; Zhang, J.; Wang, X. Mesoscopic Analysis on Force Chains of Contact Force and Displacement Field Among Particles in Asphalt Mixture. *Mater. Rep.* **2015**, *29*, 153–156.
6. Chang, M.; Huang, P.; Pei, J.; Zhang, J. Quantitative Analysis on Evolution and Distribution of Force Chain for Asphalt Mixture Using Discrete Element Method. *Mater. Rep.* **2017**, *31*, 155–159. [CrossRef]
7. Chang, M.; Pei, J.; Huang, P.; Xiong, R. Analysis on the Distribution Probability of Force Chain of Contact Force Among Granular Matter Considering Gradation. *Mater. Rep.* **2018**, *32*, 3618–3622. [CrossRef]
8. Tan, Y.; Wang, W.; Xu, Y.; Xing, C.; Hu, J.; Li, S.; Dai, M. Investigation into the force chain transmission mechanism of asphalt mixture under indirect tensile mode. *Constr. Build. Mater.* **2024**, *411*, 134500. [CrossRef]
9. Wei, X.; Sun, Y.; Gong, H.; Li, Y.; Chen, J. 3D identification and characterization of force chains in asphalt concrete based on continuum mesomechanics. *Comput. Struct.* **2024**, *297*, 107329. [CrossRef]
10. Shi, C.; Qian, G.; Yu, H.; Zhu, X.; Yuan, M.; Dai, W.; Ge, J.; Zheng, X. Research on the evolution of aggregate skeleton characteristics of asphalt mixture under uniaxial compression loading. *Constr. Build. Mater.* **2024**, *413*, 134769. [CrossRef]
11. Hui, Y.; Ma, P.; Xu, M.; Liu, H.; Cao, D.; Cui, X.; Liu, Y. Aggregate stress contribution in asphalt mixtures with the splitting tests based on the three-dimensional (3D) discrete element method (DEM). *Mater. Res. Express* **2025**, *12*, 035602. [CrossRef]
12. Yu, W.; Wang, S.; Miao, Y. Characterizing force-chain network in aggregate blend using discrete element method and complex network theory. *Constr. Build. Mater.* **2023**, *400*, 132724. [CrossRef]
13. Kruyt, N.P. On weak and strong contact force networks in granular materials. *Int. J. Solids Struct.* **2016**, *92–93*, 135–140. [CrossRef]
14. Voivret, C.; Radjai, F.; Delenne, J.Y.; El, Y.M. Multiscale force networks in highly polydisperse granular media. *Phys. Rev. Lett.* **2009**, *102*, 178001. [CrossRef]
15. Mueth, D.M.; Jaeger, H.M.; Nagel, S.R. Force distribution in a granular medium. *Phys. Rev. E Stat. Phys. Plasmas Fluids Relat. Interdiscip. Top.* **1998**, *57*, 3164–3169. [CrossRef]
16. Sun, Q.; Wang, G. Force Distribution in Static Granular Matter in Two Dimensions. *Acta Phys. Sin.* **2008**, *57*, 4667–4674. [CrossRef]
17. Sun, Q.; Jin, F.; Wang, G.; Zhang, G. Force Chains in a Uniaxially Compressed Static Granular Matter in 2D. *Acta Phys. Sin.* **2010**, *59*, 30–37. [CrossRef]
18. Feng, X.; Zhang, G.; Sun, Q. Effects of Size Polydispersity on Mechanical and Geometrical Properties of Granular System. *Acta Phys. Sin.* **2013**, *62*, 305–309. [CrossRef]

19. Danylenko, V.A.; Mykulyak, S.V.; Polyakovskyi, V.O.; Kulich, V.V.; Oleynik, I.I. Force distribution in a granular medium under dynamic loading. *Phys. Rev. E* **2017**, *96*, 12906. [CrossRef]
20. Kondic, L.; Kramár, M.; Kovalčinová, L.; Mischaikow, K.; Radjai, F.; Nezamabadi, S.; Luding, S.; Delenne, J.Y. Evolution of force networks in dense granular matter close to jamming. *EPJ Web Conf.* **2017**, *140*, 15014. [CrossRef]
21. Yu, W.; Wang, S.; Miao, Y. Analysis of the internal contact characteristics of aggregate blend using discrete element method. *Constr. Build. Mater.* **2024**, *438*, 137302. [CrossRef]
22. Yu, W.; Wang, S.; Gong, Z.; Miao, Y. Effect of compaction degree on the topological characteristics of force chain network (FCN) in aggregate blend. *Constr. Build. Mater.* **2024**, *419*, 135554. [CrossRef]
23. Liu, G.; Huang, T.; Liu, Z.; Jiang, N. Evaluation of affinity between aggregate skeleton topology and rutting performance of asphalt mixture based on network theory. *Constr. Build. Mater.* **2025**, *458*, 139647. [CrossRef]
24. Yang, Y.; Chen, Y.; Li, B.; Yang, Y. Micro-Scale Fracture Characteristics of Emulsified Asphalt Cold Recycled Mixture Based on Discrete Element Method. *Coatings* **2024**, *14*, 1436. [CrossRef]
25. Liu, Y.; You, Z.; Li, L.; Wang, W. Review on advances in modeling and simulation of stone-based paving materials. *Constr. Build. Mater.* **2013**, *43*, 408–417. [CrossRef]
26. Liu, Y.; Dai, Q.; You, Z. Viscoelastic Model for Discrete Element Simulation of Asphalt Mixtures. *J. Eng. Mech.* **2009**, *135*, 324–333. [CrossRef]
27. Ma, T.; Zhang, D.; Zhang, Y.; Zhao, Y.; Huang, X. Effect of air voids on the high-temperature creep behavior of asphalt mixture based on three-dimensional discrete element modeling. *Mater. Des.* **2016**, *89*, 304–313. [CrossRef]
28. Ma, T.; Zhang, D.; Zhang, Y.; Hong, J. Micromechanical response of aggregate skeleton within asphalt mixture based on virtual simulation of wheel tracking test. *Constr. Build. Mater.* **2016**, *111*, 153–163. [CrossRef]
29. Ma, T.; Wang, H.; Zhang, D.; Zhang, Y. Heterogeneity effect of mechanical property on creep behavior of asphalt mixture based on micromechanical modeling and virtual creep test. *Mech. Mater.* **2017**, *104*, 49–59. [CrossRef]
30. Kim, H.; Wagoner, M.P.; Buttlar, W.G. Numerical fracture analysis on the specimen size dependency of asphalt concrete using a cohesive softening model. *Constr. Build. Mater.* **2009**, *23*, 2112–2120. [CrossRef]
31. Zhu, X.; Yu, H.; Qian, G.; Yao, D.; Dai, W.; Zhang, H.; Li, J.; Zhong, H. Evaluation of asphalt mixture micromechanical behavior evolution in the failure process based on Discrete Element Method. *Case Stud. Constr. Mater.* **2023**, *18*, e1773. [CrossRef]
32. Xiao, M.; Chen, Y.; Feng, H.; Huang, T.; Xiong, K.; Zhu, Y. Evaluation of Fatigue Behavior of Asphalt Field Cores Using Discrete Element Modeling. *Materials* **2024**, *17*, 3108. [CrossRef]
33. Xue, B.; Que, Y.; Pei, J.; Ma, X.; Wang, D.; Yuan, Y.; Zhang, H. A state-of-the-art review of discrete element method for asphalt mixtures: Model generation methods, contact constitutive models and application directions. *Constr. Build. Mater.* **2024**, *414*, 134842. [CrossRef]
34. Shi, L.; Wang, D.; Xu, C.; Jie, H. Investigation into Meso Performance of Asphalt Mixture Skeleton Based on Discrete Element Method. *J. South China Univ. Technol. (Nat. Sci. Ed.)* **2015**, *43*, 50–56. [CrossRef]
35. Liu, W.; Gao, Y. Discrete element modeling of migration and evolution rules of coarse aggregates in the static compaction process. *J. Southeast Univ. (Engl. Ed.)* **2016**, *32*, 85–92. [CrossRef]
36. Chen, J.; Huang, B.; Chen, F.; Shu, X. Application of discrete element method to Superpave gyratory compaction. *Road Mater. Pavement Des.* **2012**, *13*, 480–500. [CrossRef]
37. Gong, F.; Liu, Y.; Zhou, X.; You, Z. Lab assessment and discrete element modeling of asphalt mixture during compaction with elongated and flat coarse aggregates. *Constr. Build. Mater.* **2018**, *182*, 573–579. [CrossRef]
38. Gong, F.; Zhou, X.; You, Z.; Liu, Y.; Chen, S. Using discrete element models to track movement of coarse aggregates during compaction of asphalt mixture. *Constr. Build. Mater.* **2018**, *189*, 338–351. [CrossRef]
39. Chen, F.; Jelagin, D.; Partl, M.N. Experimental and numerical analysis of asphalt flow in a slump test. *Road Mater. Pavement* **2019**, *20* (Suppl. 1), S446–S461. [CrossRef]
40. Wang, S.; Diao, W.; Miao, Y.; Wang, J.; Xu, J.; Yu, W.; Wang, L. Investigation of force evolution and movement characteristics of aggregate particles in asphalt mixture during compaction. *Constr. Build. Mater.* **2025**, *479*, 141481. [CrossRef]
41. *JTG F40-2004*; Tehnical Specifications for Construction of Highway Asphalt Pavements. Chinese Ministry of Communications: Beijing, China, 2005.
42. Ge, H.; Quezada, J.C.; Le Houerou, V.; Chazallon, C. Three-dimensional FEM–DEM coupling simulation for analysis of asphalt mixture responses under rolling tire loads. *Constr. Build. Mater.* **2023**, *369*, 130615. [CrossRef]
43. Al Khateeb, L.; Anupam, K.; Erkens, S.; Scarpas, T. Micromechanical simulation of porous asphalt mixture compaction using discrete element method (DEM). *Constr. Build. Mater.* **2021**, *301*, 124305. [CrossRef]
44. Miao, Y.; Yu, W.; Wu, J.; Wang, S.; Wang, L. Feasibility of one side 3-D scanning for characterizing aggregate shape. *Int. J. Pavement Res. Technol.* **2019**, *12*, 197–205. [CrossRef]

45. Xue, B.; Pei, J.; Zhou, B.; Zhang, J.; Li, R.; Guo, F. Using random heterogeneous DEM model to simulate the SCB fracture behavior of asphalt concrete. *Constr. Build. Mater.* **2020**, *236*, 117580. [CrossRef]
46. Wang, S.; Miao, Y.; Wang, L. Effect of grain size composition on mechanical performance requirement for particles in aggregate blend based on photoelastic method. *Constr. Build. Mater.* **2023**, *363*, 129808. [CrossRef]

Disclaimer/Publisher's Note: The statements, opinions and data contained in all publications are solely those of the individual author(s) and contributor(s) and not of MDPI and/or the editor(s). MDPI and/or the editor(s) disclaim responsibility for any injury to people or property resulting from any ideas, methods, instructions or products referred to in the content.

materials

MDPI

Article

Study on the Self-Healing Performance of Polyurethane/Graphene Oxide-Modified Asphalt Based on Dynamic Disulfide Bonds

Guokai Li [1,2], Min Wang [1,2], Kezhen Yan [1,2,*] and Xiaojin Song [3]

[1] College of Civil Engineering, Hunan University, Changsha 410082, China; lgk@hnu.edu.cn (G.L.); wangmin19@hnu.edu.cn (M.W.)
[2] Key Laboratory for Green and Advanced Civil Engineering Materials and Application Technology of Hunan Province, Changsha 410082, China
[3] Zhongteng Zhixin Technology Company of Hunan Province, Changsha 410082, China; sxjmail@126.com
* Correspondence: yankz@hnu.edu.cn

Abstract

In this study, an investigation on using polyurethane/graphene oxide (PU/GO) containing disulfide bonds as a modifier to improve the self-healing ability of asphalt was conducted. PU/GO with different GO contents were synthesized and modified asphalt with different PU/GO dosages (2%, 4%, 6%, 8%) were also prepared. The effect of GO contents on the mechanical and self-healing properties of PU/GO was explored and the impacts of PU/GO contents on the basic properties and self-healing properties of asphalt were also investigated. The results indicated that GO could significantly improve the mechanical properties of PU, as the tensile strength of PU/GO with 1.6% GO increased by more than 100% compared with pure PU. Moreover, GO also had a positive impact on the early-stage self-healing properties of PU/GO. PU/GO could be well dispersed in asphalt and clearly improve the low-temperature performance of base asphalt. When the PU/GO content is 8%, the ductility of modified asphalt was almost 6 times that of base asphalt. The results of both ductility and BBR self-healing tests revealed that the addition of PU/GO improved the self-healing properties of asphalt under room temperature and infrared light conditions. Especially under infrared light conditions, the ductility self-healing coefficient of 8% PU/GO-modified asphalt could reach 100% after healing for 15 min.

Keywords: polyurethane; graphene oxide; disulfide bonds; self-healing asphalt

1. Introduction

Asphalt pavement has gradually become the main choice for high-grade pavement in recent years due to its advantages such as low noise, high pavement smoothness, low maintenance cost and fast construction [1–3]. However, during the service of asphalt pavement, asphalt pavement may suffer from potholes, rutting, cracks and other faults due to the influence of the environment and traffic loads [4,5]. Because of the formation of cracks, rainwater and dust can seep into the interior of the pavement structure. From this, more serious faults will occur, which will greatly reduce the service life of the asphalt pavement [6]. Therefore, it is necessary to carry out continuous maintenance to extend the service life of asphalt pavement, which will consume a lot of energy and economy [7,8]. To reduce energy consumption and economic expenditure, scholars have begun to focus on self-healing asphalt and asphalt mixtures. Although asphalt has a certain self-healing ability under natural conditions, it is not sufficient to repair cracks caused by traffic loads

or environmental changes in a timely manner. Therefore, it is necessary to improve the self-healing ability of asphalt to prolong the service life of asphalt pavement [9,10].

At present, the most common and widely used methods to increase the self-healing property of asphalt include rejuvenator encapsulation, induction heating and microwave heating methods [11–13]. The rejuvenator encapsulation method needs to encapsulate the rejuvenator into a microcapsule and then mix the microcapsule with an asphalt mixture. The microcapsules will rupture when a crack appears, and the rejuvenator will be released to fill and repair the crack [14–16]. The induction heating method needs to add metal fibers or other conductive materials to asphalt, and then use electromagnetic induction to generate energy inside the asphalt, which will heat the asphalt material and heal the cracks. Through induction heating, the internal temperature of the asphalt mixture can be effectively increased, which will increase the self-healing performance of the asphalt mixture [17,18]. What is more, indoor tests have shown that using induction heating technology on asphalt mixtures can increase the service life of asphalt pavements by 30% [19]. However, it is worth noting that induction heating can only be applied to cracks within a certain width range [20]. Compared with induction heating, microwave heating has better heating efficiency and a wider range of applications [21,22]. Moreover, the microwave heating effect is more significant and the self-healing property of asphalt will be better when a smaller amount of metal materials are added to asphalt. [23,24].

Although the above methods can effectively enhance the self-healing ability of asphalt mixtures, there are still shortcomings in practical applications. Microcapsule technology can effectively improve the self-healing ability of asphalt pavement cracks, but the rejuvenator in microcapsules is limited. When cracks occur again in the same location, the self-healing property of asphalt will decrease due to the decrease in microcapsules. Induction heating and microwave heating methods can repair cracks multiple times. However, many microcracks are difficult to detect promptly, so it is easy to miss the best repair opportunity. Based on the shortcomings of current methods, scholars have begun to improve the self-healing property by introducing dynamic covalent bonds into asphalt.

Li et al. [25,26] added PU-containing dynamic disulfide bonds to asphalt for modification. The results revealed that the self-healing PU had good compatibility with asphalt. The presence of disulfide bonds provided a foundation for improving the self-healing capability. Researchers also [27,28] evaluated the crack healing ability of PU-modified asphalt including dynamic disulfide bonds. The results showed that the presence of dynamic disulfide bonds could effectively increase the self-healing ability of microcracks in asphalt. Zhang [29] synthesized S-SBS materials with dynamic covalent bonds by introducing disulfide bonds into the SBS structure, and then modified asphalt with S-SBS. The results indicated that the crack resistance and fracture healing ability were improved by introducing disulfide bonds into asphalt. In addition to disulfide bonds, diselenide bonds also have excellent dynamic exchangeability. Lyu et al. [30] synthesized a kind of PU with dynamic diselenide bonds and applied it to asphalt modification. The results showed that dynamic diselenide bonds endowed asphalt with excellent fracture self-healing abilities. Yang et al. [31] prepared modified asphalt containing dynamic disulfide and diselenide bonds, respectively, and compared the self-healing properties of these two types of modified asphalt. The results revealed that diselenide bonds had a greater effect on the short-term healing ability of asphalt, while the disulfide bonds had a greater effect on the long-term healing ability.

Based on the above research, it has been found that introducing dynamic covalent bonds into asphalt to enhance its self-healing ability is a feasible method. However, the recombination of dynamic covalent bonds is affected by temperature, and the higher the temperature, the higher the recombination efficiency of dynamic covalent bonds [27–31].

Researchers have found that graphene has excellent thermal conductivity and infrared absorption ability. Therefore, introducing graphene into PU can improve the heat absorption efficiency of PU. Higher temperatures can enhance the efficiency of covalent bond recombination and improve the self-healing ability of PU [32,33]. Xu et al. [34] even used graphene to modify asphalt mixtures. The results showed that graphene had excellent heat absorption ability, which could increase the surface temperature of asphalt mixtures and enhance the self-healing performance. Compared with graphene, graphene oxide (GO) also has excellent thermal conductivity and infrared absorption ability. At the same time, GO contains a large number of active functional groups, which can react with isocyanate in PU and have better dispersibility in PU. Li et al. [35] designed and synthesized self-healing PU/GO materials with different GO contents through the Diels Alder (D-A) reaction. The results showed that the material had excellent self-healing function under heating, infrared, and microwave conditions.

Based on the above discussion, it can be concluded that introducing dynamic covalent bonds into asphalt to improve the self-healing ability is a feasible method. Graphene or GO has excellent thermal conductivity and infrared absorption ability, which can improve the heat absorption efficiency and enhance the self-healing function. However, there is still a lack of research on the synergistic improvement of asphalt self-healing performance by dynamic covalent bonds and GO. Therefore, this study synthesized a kind of thermoplastic polyurethane containing dynamic covalent bonds, and then introduced GO into the PU to synthesize PU/GO composite materials. To explore the influence of GO on the self-healing function of PU under different conditions, two kinds of self-healing conditions were selected: heating condition at 60 °C and infrared light condition. Moreover, the effect of healing time on the self-healing property of PU/GO was also studied. Finally, PU/GO was added to asphalt to prepare modified asphalt with different PU/GO contents. In order to evaluate the self-healing performance of modified asphalt, self-healing tests based on ductility and BBR tests were conducted. Two kinds of self-healing conditions (25 °C room temperature and infrared light condition) were chosen to explore the effect of PU/GO on the self-healing property of asphalt under different conditions. In this study, the utilization of GO to improve the recombination efficiency of dynamic covalent bonds in PU and PU/GO-modified asphalt was investigated, which could provide a reference for the development of self-healing PU and asphalt materials.

2. Material and Test Methods

2.1. Raw Material

2.1.1. Polytetramethylene Ether Glycol (PTMEG)

PTMEG is the most commonly used polyether diol in PU synthesis. The physical properties of PTMEG will vary with different molecular weights. In this study, PTMEG2000 produced by Macklin Chemical Reagent Co., Ltd. (Shanghai, China) was chosen for PU synthesis. The properties of PTMEG are shown in Table 1.

Table 1. Relevant indices of PTMEG.

Index	Unit	Result	Index	Unit	Result
Molecular weight	/	2000	Melting point	°C	33
Density	g/cm^3	0.972	Hydroxyl value	$mgKOH \cdot g^{-1}$	56
Viscosity (40 °C)	mPa·s	1120	Water content	%	≤ 0.05
CAS Registry Number			25190-06-1		

2.1.2. Isophorone Diisocyanate (IPDI)

IPDI is a type of aliphatic diisocyanate with excellent light resistance and low toxicity. The molecular chains of PU synthesized by IPDI have stronger mobility, which is beneficial for the recombination of dynamic covalent bonds. Therefore, IPDI produced by Macklin Chemical Reagent Co., Ltd. was chosen for PU synthesis in this study and the properties of IPDI are shown in Table 2.

Table 2. Relevant indices of IPDI.

Index	Unit	Result	Index	Unit	Result
Molecular weight	/	222	Melting point	°C	−60
Density	g/cm^3	1.062	Boiling point	°C	158
Viscosity (25 °C)	mPa·s	15	NCO content	%	≥ 37.5
CAS Registry Number			4098-71-9		

2.1.3. 3,3′-Dithiodipropionic Acid (DPA)

To prepare self-healing PU, it is necessary to introduce dynamic covalent bonds into polyurethane. DPA is a type of aliphatic chain extender containing dynamic disulfide bonds. Therefore, DPA produced by Macklin Chemical Reagent Co., Ltd was selectedand the basic properties are given in Table 3.

Table 3. Relevant indices of DPA.

Index	Unit	Result	Index	Unit	Result
Molecular weight	/	210	Melting point	°C	156
Density	g/cm^3	1.452	Boiling point	°C	431
CAS Registry Number			1119-62-6		

2.1.4. Graphene Oxide (GO)

The main methods for preparing GO include the Brodie method, Staudenmaier method, and Hummers method [36]. The GO used in this study was prepared by the Hummers method.

2.1.5. Base Asphalt

The base asphalt used for preparing PU/GO-modified asphalt is 70 pen asphalt (70#). The basic indices of 70# asphalt were tested according to the specification JTG E20-2011 [37]. The indices of the base asphalt are given in Table 4 and all the indices meet the requirements of the specification.

Table 4. Basic properties of 70 pen base binder.

Index	Unit	Test Results	Requirement	Test Method
Ductility (10 °C, 5 cm/min)	cm	44.2	>25	T 0605-2011
Ductility (15 °C, 5 cm/min)	cm	>150	>100	T 0605-2011
Penetration (25 °C, 100 g, 5 s)	0.1 mm	65.5	60–80	T 0604-2011
Softening point (R&B)	°C	46.4	>46	T 0606-2011
Viscosity (135 °C)	Pa·s	0.49	–	T 0625-2011
Elastic recovery (25 °C)	%	16	–	T 0662-2011

2.2. Sample Preparation

2.2.1. The Preparation of PU and PU/GO

The synthesis methods of PU are divided into the one-step method and the pre-polymer method. Compared with the one-step method, the reaction process of the pre-

polymer method is easier to control. There are fewer side reactions during the reaction process, so the final chemical structure of the molecular chains can be controlled. Therefore, the pre-polymer method was chosen to synthesize PU and PU/GO and the recipes of PU and PU/GO are given in Table 5.

Table 5. Recipes for the preparation of PU and PU/GO.

	Hard Segment Content	PTMEG (g)	IPDI (g)	DPA (g)	GO (g)
PU	20%	100 (0.05 mol)	18.24 (0.082 mol)	6.76 (0.032 mol)	–
PU/GO	20%	100 (0.05 mol)	18.24 (0.082 mol)	6.76 (0.032 mol)	0.5, 1.0, 1.5, 2.0

Synthesis for PU: Considering the self-healing ability of PU, a hard segment content of 20% was selected in this study. The reaction equation is shown in Figure 1 and the specific synthesis process is as follows: ① Weigh 100 g of PTMG and place it in a three-necked flask, then put the flask in an oven and vacuum dry PTMEG at 120 °C for 2 h; ② After drying, place the flask in an 80 °C oil bath and add 18.24 g IPDI to it; ③ Add 2 drops of catalyst ditin butyl dilaurate (DBTDL) to the system and react for 60 min to obtain a pre-polymer; ④ Dissolve 6.76 g of DPA in 15 mL of dimethylformamide (DMF) solvent and add it to the reaction system for 30 min; ⑤ After the reaction is completed, pour PU into a polytetrafluoroethylene mold, then dry it in an oven at 80 °C for 48 h to completely evaporate the solvent DMF.

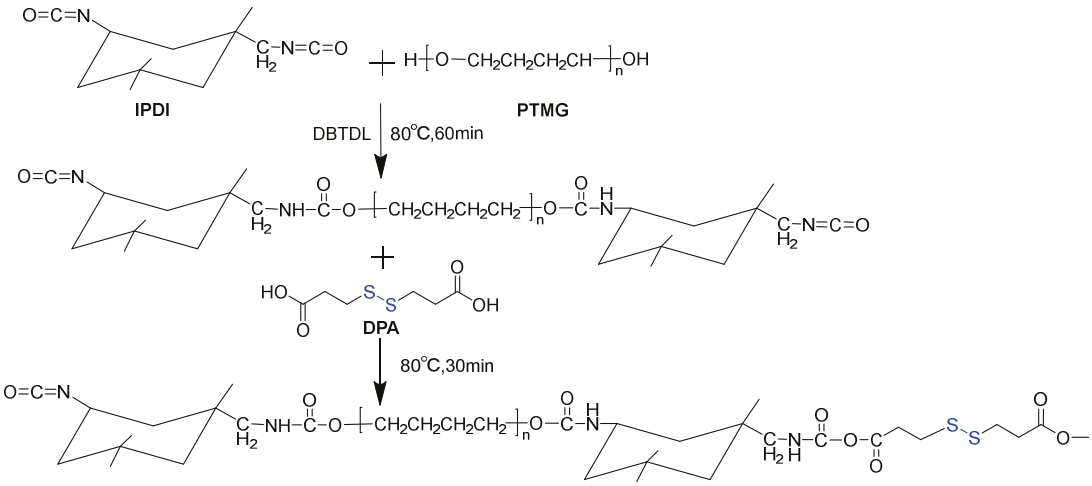

Figure 1. The reaction equation of PU.

Synthesis for PU/GO: the synthesis process of PU/GO is similar to PU, but GO needs to be introduced into the pre-polymer before chain extension. The specific synthesis process is as follows: ① Weigh 100 g of PTMG and place it in a three-necked flask, then put the flask in an oven and vacuum dry PTMEG at 120 °C for 2 h; Weigh the corresponding mass of GO (0.4%, 0.8%, 1.2%, 1.6%) and add it to DMF solvent, then use ultrasonic to evenly disperse GO for 2 h; ② After drying, place the flask in an 80 °C oil bath and add the weighed IPDI (18.24 g) to it; ③ Add 2 drops of DBTDL to the system and react for 60 min to obtain a pre-polymer; ④ Add GO dispersion to the pre-polymer and allow the hydroxyl and carboxyl groups on GO to react with isocyanate groups for 30 min; ⑤ Dissolve 6.76 g of DPA in 15 mL of DMF solvent and add it to the reaction system for 30 min; ⑥ After the reaction is completed, pour PU/GO into a polytetrafluoroethylene mold, then dry it in an oven at 80 °C for 48 h to completely evaporate the solvent DMF.

2.2.2. The Preparation of Modified Asphalt

In order to blend the modifier with the asphalt uniformly and fully utilize the function of the modifier, FM300 high-speed shear apparatus was chosen to prepare modified asphalt in this study. According to a preliminary experiment, shearing at a rate of 3000 r/min for 60 min can evenly disperse the modifier in asphalt. The specific preparation process is shown in Figure 2.

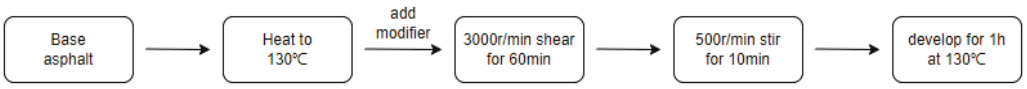

Figure 2. The specific process for preparing modified asphalt.

2.3. Test Methods

2.3.1. Fourier Transform Infrared (FTIR) Test

The FTIR test is commonly used to analyze the functional groups and molecular structures of chemical compounds. Due to the unique vibration frequencies of different chemical bonds, the FTIR test can be used to determine the chemical bonds in molecules. Therefore, the Thermo Fisher Scientific Nicolet iN10 FTIR spectrometer from the Waltham, MA, USA was used to determine the functional groups and molecular structure composition of PU and PU/GO, and the scanning wavelengths ranged from 400 cm^{-1} to 4000 cm^{-1}.

2.3.2. Field Emission Scanning Electron Microscope (SEM) Test

The micro morphological structure information of various solid-state sample surfaces can be obtained through SEM tests. Therefore, in order to investigate the effect of GO contents on the apparent morphology of PU and the dispersion conditions of GO in PU, a SEM test was selected to observe the microstructure of PU/GO. In this study, the sample will be observed at a magnification of 400 times.

2.3.3. Gel Permeation Chromatography (GPC) Test

GPC test is based on the basic principles of solvent dissolution, adsorption, diffusion, etc. Through the GPC test, the molecular weight size and distribution of different molecules can be determined, and parameters such as number average molecular weight (M_n), weight average molecular weight (M_W), and polydispersity (PD) coefficient can be obtained. In this study, the molecular weight of PU with different GO contents was tested through GPC.

2.3.4. Mechanical and Self-Healing Test of PU and PU/GO

In order to characterize the mechanical properties of PU and PU/GO, a tensile test was conducted. PU/GO material was prepared as dumbbell-shaped standard specimens for tensile testing according to the standard GB/T 528-2009 [38], and the dimensions of the specimen are shown in Figure 3. Before the start of the test, 0.1N pre-load was applied to the specimen to ensure that the initial state of the specimen was consistent and the loading rate was set as 500 mm/min.

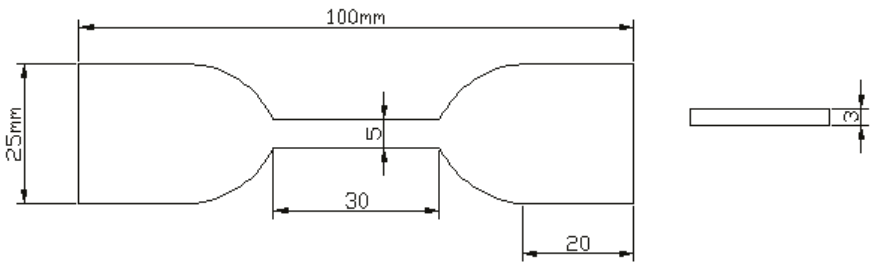

Figure 3. Dimensions of the specimen for tensile test.

The mechanical properties of PU/GO materials are mainly evaluated based on two indicators: tensile strength σ and breaking elongation e. The calculation formula is as follows:

$$\sigma = \frac{F_b}{S_0} \tag{1}$$

$$e = \frac{(L - L_0)}{L_0} \times 100\% \tag{2}$$

where F_b is the maximum tensile axial force, and S_0 is the initial cross-sectional area of the specimen, L is the length of the section when the specimen is broken, and L_0 is the original length of the section.

The self-healing performance of PU/GO is obtained by comparing the tensile strength of the specimens before and after self-healing. The PU/GO specimen will be cut in the middle by a knife, then let the fracture surface contact with each other. The fracture specimens will be placed in an environment of 60 °C for different times (1 h, 2 h, 4 h) or exposed to infrared light with a wavelength of 980 nm with different times (5 min, 10 min, 15 min) for self-healing. The specific process of the test is shown in Figure 4 and the self-healing coefficient H_σ can be calculated as follows:

$$H_\sigma = \frac{\sigma_1}{\sigma_0} \times 100\% \tag{3}$$

where σ_1 is the tensile strength of the specimens after fracture and self-healing, σ_0 is the tensile strength of the original specimen.

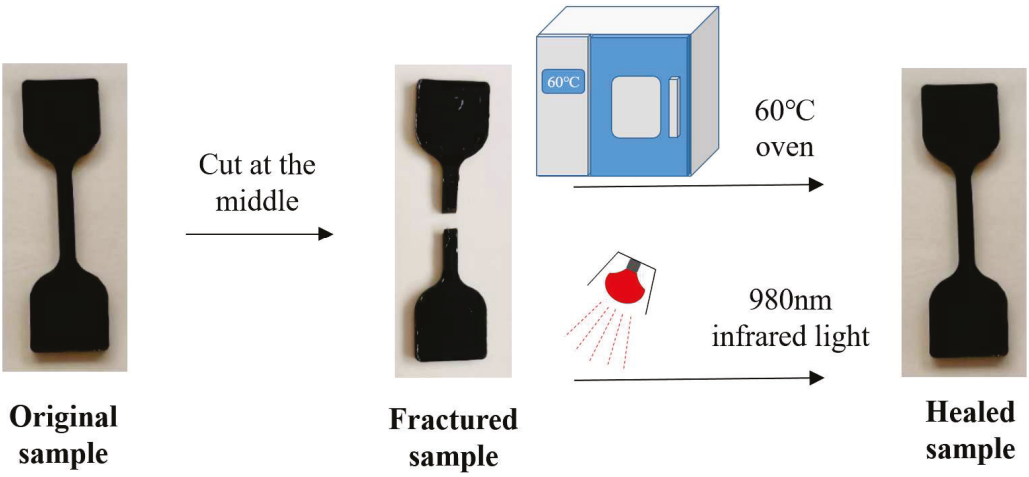

Figure 4. Self-healing test of PU/GO.

2.3.5. Fluorescence Microscopy (FM) Test

FM test uses ultraviolet light as a light source to make the sample display fluorescence, and then the shape and position of the sample can be observed under the microscope. Asphalt and polymer display different brightnesses, so the dispersion of polymer in asphalt can be observed.

2.3.6. Basic Performance of Modified Asphalt

The conventional indices such as penetration, softening point, ductility and viscosity of modified asphalt were tested according to the specification JTG E20-2011 [37].

2.3.7. Self-Healing Test of Modified Asphalt

The self-healing performance of modified asphalt was evaluated by two methods: ductility test and bending beam rheometer (BBR) test. The specimens of ductility test

and BBR test will be cut in the middle, then the fractured surfaces will be allowed to be in contact with each other. The fractured specimens will be placed in an environment of 25 °C for different times (1 h, 2 h, 4 h) for self-healing or exposed to infrared light with a wavelength of 980 nm for different times (5 min, 10 min, 15 min) for self-healing. The specific process of the asphalt self-healing test based on the ductility test is shown in Figure 5. The ductility test was conducted at 5 °C and the self-healing coefficient H_L can be calculated as follows:

$$H_L = \frac{L_1}{L_0} \times 100\% \tag{4}$$

where L_1 is the ductility of the specimen after fracture and self-healing, L_0 is the ductility of the original specimen.

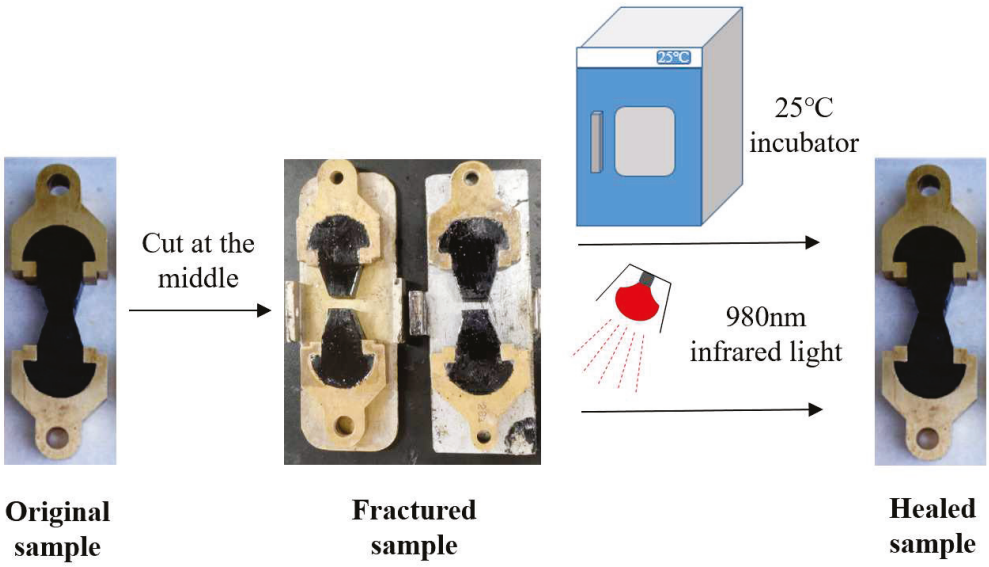

Figure 5. Self-healing test of asphalt based on ductility test.

The specific process of the asphalt self-healing test based on the BBR test is shown in Figure 6. The BBR test was conducted at −12 °C and the self-healing coefficient H_S can be calculated as follows:

$$H_S = \frac{S_1}{S_0} \times 100\% \tag{5}$$

where S_1 is the stiffness modulus of the specimen after fracture and self-healing, S_0 is the stiffness modulus of the original specimen.

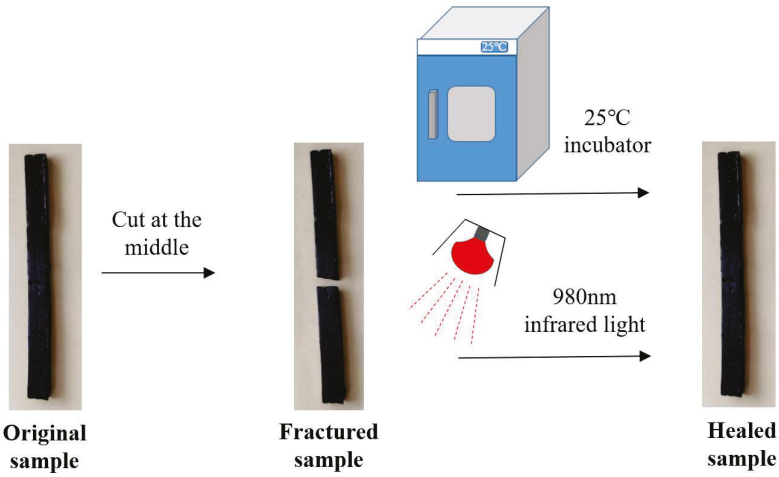

Figure 6. Self-healing test of asphalt based on BBR test.

2.4. Study Procedures

The specific study procedures are shown in Figure 7.

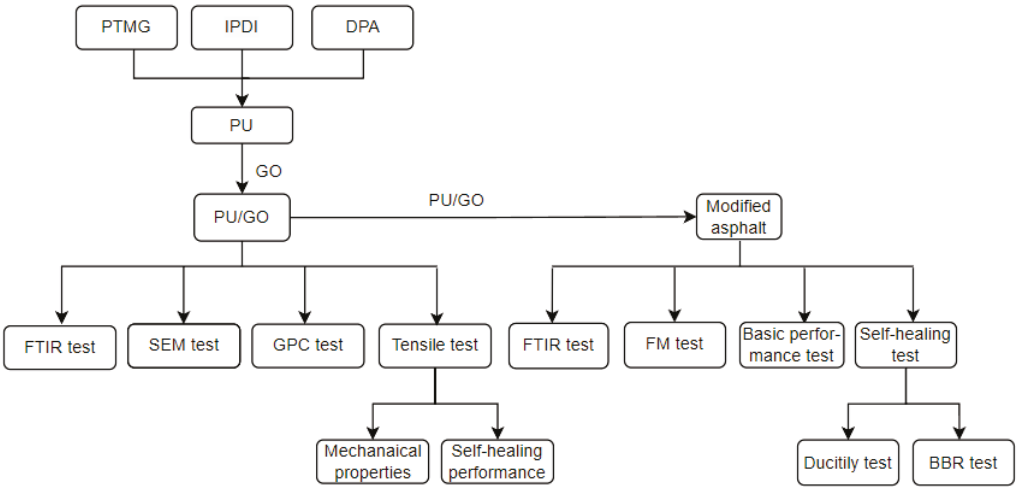

Figure 7. The complete process of this study.

3. Results and Discussion

3.1. Performance Characterization of PU/GO

3.1.1. FTIR Test of PU/GO

From the FTIR spectra of PU/GO in Figure 8, it can be found that an absorption peak appears at 3325 cm^{-1} due to the stretching vibration of –NH. And the hydroxyl group (−OH) can be found in GO spectra at 3435 cm^{-1} but cannot be found around 3400 cm^{-1} in the spectra of PU/GO, which indicates that the –OH reacted to generate –NH. The absorption peaks of 2940 cm^{-1} and 2858 cm^{-1} belong to $-CH_2$. The stretching vibration frequency of carboxylic acid carbonyl C=O is between 1760–1660 cm^{-1}, while the vibration frequency of aliphatic carboxylic acid carbonyl is around 1700 cm^{-1}. Therefore, the peak at 1718 cm^{-1} is the stretching vibration peak of carboxylic acid carbonyl in DPA. In addition, C−OH in the carboxyl group will also produce stretching vibration, corresponding to the vibration peak at 1305 cm^{-1}. When two or three $-CH_3$ groups are connected to the same carbon atom, a coupling effect will occur in the symmetric angular vibration of $-CH_3$. The IPDI has a structure where two methyl groups are connected to the same carbon atom. Therefore, the absorption peak of 1305 cm^{-1} belongs to the angular vibration of $-CH_3$ in IPDI. In addition, the absorption peak 1100 cm^{-1} belongs to C−O−C. What is more, the absorption peak 2250 cm^{-1} and 1350 cm^{-1} belong to −NCO can not be found in the spectra, which proves that the −NCO functional groups have reacted.

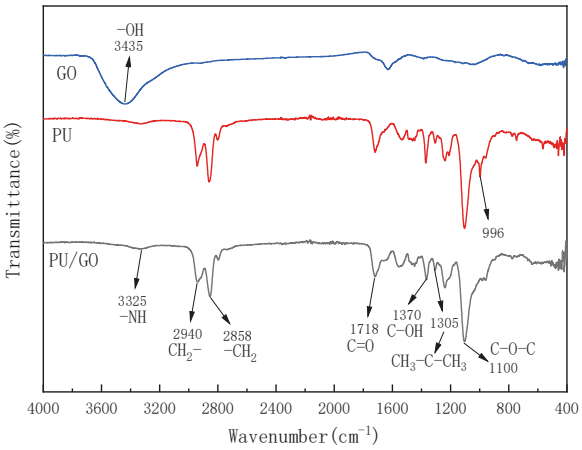

Figure 8. The FTIR spectra of PU and PU/GO.

3.1.2. SEM Test of PU/GO

Figure 9 shows the micromorphology of PU with different GO contents. It can be seen that in Figure 9a, the microstructure of pure PU is very regular, presenting parallel strip-shaped ripples. It can be inferred that the arrangement of molecular chains in PU is also parallel, with less cross-linking between molecular chains. When the GO content is 0.4%, the microstructure is similar to that of pure PU, showing regular stripe shapes. When the GO content increases to 0.8%, most of the molecular chains still exhibit a striped arrangement. But some molecular chains crosslink with each other and result in a certain degree of irregularity in the microstructure. When the GO content continues to increase to 1.2% or even 1.6%, the spatial cross-linking between molecular chains further develops, resulting in multiple discontinuous interfaces. It can be concluded that the irregularity of the PU/GO microstructure will increase with the increase in GO content. The reason can be attributed to the spatial structure of GO. Compared with PTMEG, GO has a typical two-dimensional spatial structure rather than a linear structure, which will have an effect on the linear spatial structure of molecular chains.

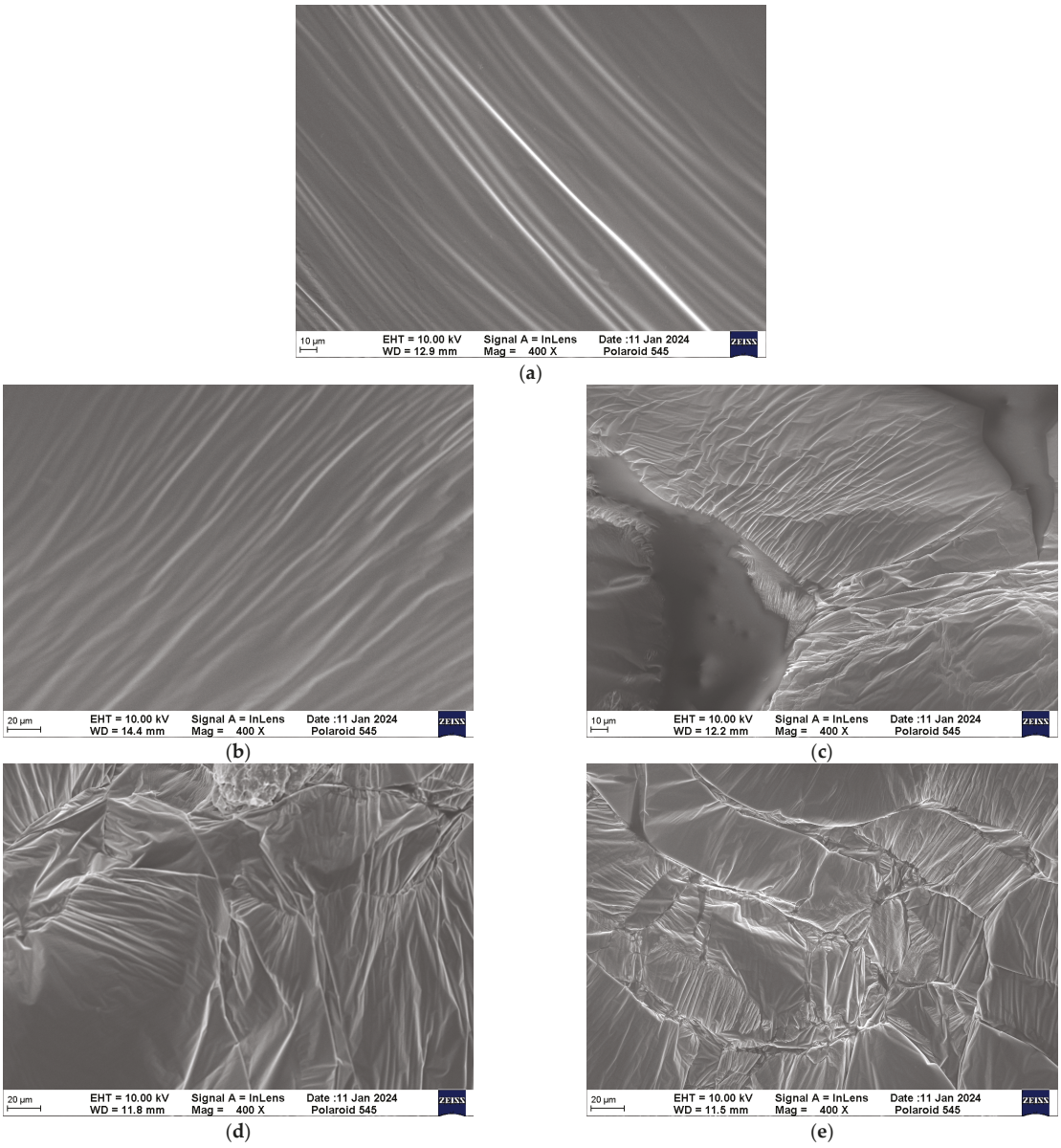

Figure 9. The micromorphology of PU with different GO contents. (**a**) 0% GO content. (**b**) 0.4% GO content. (**c**) 0.8% GO content. (**d**) 1.2% GO content. (**e**) 1.6% GO content.

3.1.3. GPC Test of PU/GO

Table 6 shows the GPC test results of PU/GO with different GO contents. It can be seen that the M_W of PU/GO with different GO contents range from 30,000–60,000, which indicates that the molecules of raw material react with each other successfully and generate macromolecular polymers. The PD of PU/GO with different GO contents ranges from 1 to 3, which shows that the molecular weight distribution is relatively uniform. The results also show that the molecular of PU/GO decreases with the increase in GO content and the PD is also positively correlated with GO content. It may be related to the molecular structure of GO. GO has a typical two-dimensional spatial structure rather than a linear structure, which will have an impact on the linear structure of the molecular chain. Moreover, there are many hydroxyl and carboxyl groups on the surface of GO, which can react with diisocyanate groups. The two isocyanate groups in the same molecular chain may react with functional groups of the same GO molecule, which will affect the extension of the molecular chain.

Table 6. The GPC test results of PU/GO.

GO Content	Number Average Molecular Weight/M_n	Weight Average Molecular Weight/M_W	Polydispersity/PD
0	40,230	56,121	1.395
0.4%	26,054	48,252	1.852
0.8%	24,820	41,326	1.665
1.2%	15,434	36,285	2.351
1.6%	16,857	38,165	2.264

3.1.4. Mechanical Properties of PU/GO

According to Figure 10, it can be found that the effect of different GO content on the mechanical properties of PU/GO. The tensile strength of PU/GO increases with the increase in GO content while the breaking elongation gradually decreases. Compared with pure PU, the stress of PU/GO with 1.6% GO content increases by 102%, which indicates that the introduction of GO has a significant enhancing effect on the strength of PU. The reason can be attributed to the excellent mechanical properties of GO. When the GO is introduced into PU prepared reaction system, the hydroxyl and carboxyl groups on GO will react with isocyanate groups and GO will be embedded in the molecular chain of PU. But at the same time, the addition of GO will reduce the breaking elongation of PU, because the introduction of GO will affect the linear structure of the molecular chain to some extent.

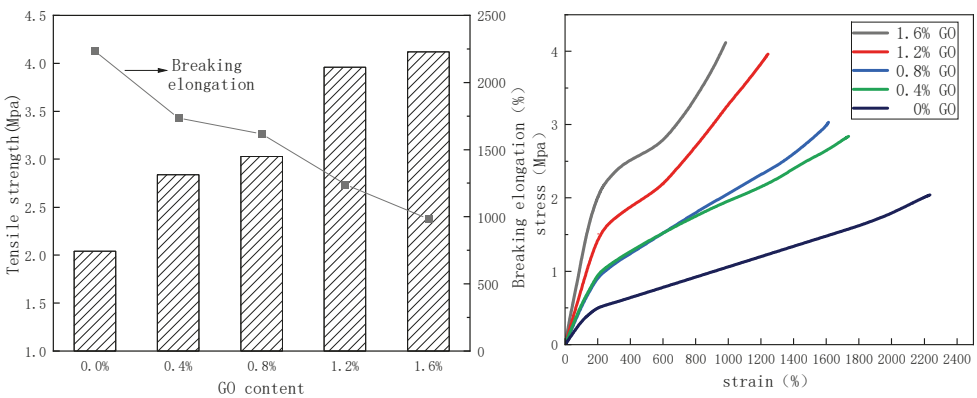

Figure 10. The mechanical property results of PU/GO.

3.1.5. Self-Healing Properties of PU/GO

From Figure 11, the impact of healing time and different GO contents on the self-healing property of PU/GO can be understood. Moreover, the self-healing mechanism and

process are shown in Figure 12. When the fractured surfaces of the specimen come into contact with each other, the molecular chains around the fractured surfaces will move and the disulfide bonds around the surfaces will recombine to heal the fracture. The movement of molecular chains and the recombination of disulfide bonds will continue to increase over time. Therefore, it can be seen from Figure 11a that the strength of the healing sample gradually increases with the increase in healing time. What is more, molecular chains will also intertwine with each other with the increase in healing time, which is beneficial to improve the strength of the sample. On the other hand, the movement of molecular chains and the recombination speed of disulfide bonds are both affected by temperature; the higher the temperature, the higher the self-healing efficiency. It can be seen in Figure 12 that, compared with pure PU, lamellar structure GO is dispersed in PU/GO, and this can improve the thermal conductivity of the sample. Compared with pure PU, the temperature of the fractured surfaces of the PU/GO sample is higher, which is beneficial for improving the recombination efficiency of disulfide bonds. But at the same time, the movement of molecular chains will be restricted to some extent due to the lamellar structure of GO, which will have adverse effects on the self-healing of the sample. These two factors will jointly affect the self-healing properties of PU/GO. So, it can be found that from Figure 11b, the self-healing coefficient of sample healing for 1 h increases with the increase in GO content while the self-healing coefficient of sample healing for 2 h and 4 h decreases. And the self-healing coefficient of PU/GO sample healing for 1 h does not keep increasing with the increase in GO content. When the GO content is 0.8%, the self-healing coefficient reaches the maximum. The results demonstrate that the addition of GO has a positive impact on the early self-healing property of the sample but a negative impact on the final self-healing results.

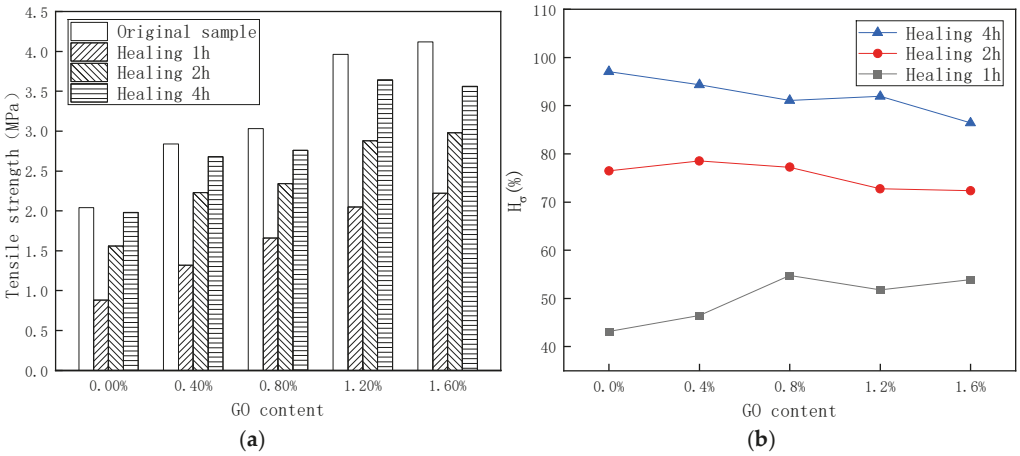

Figure 11. The self-healing test results of PU/GO under 60 °C condition. (**a**) Stress of healing sample (**b**) Self-healing coefficient.

Figure 13 shows that the results under infrared light conditions are similar to that under 60 °C conditions. With the increase in healing time, the tensile strength of PU/GO samples with different GO content gradually increases. When the healing time is 5 min, it can be discovered that when the GO content increases, the self-healing coefficient gradually increases until the GO content reaches 1.2%. The results also show that under infrared light conditions, the addition of GO improves the early-stage self-healing property of the sample but decreases the final self-healing results. In the early stage, the sample with higher GO content will have a higher temperature because of the excellent infrared light absorption ability of GO, which is beneficial for self-healing performance. However, the adverse effects of GO on restricting the movement of molecular chains will gradually manifest.

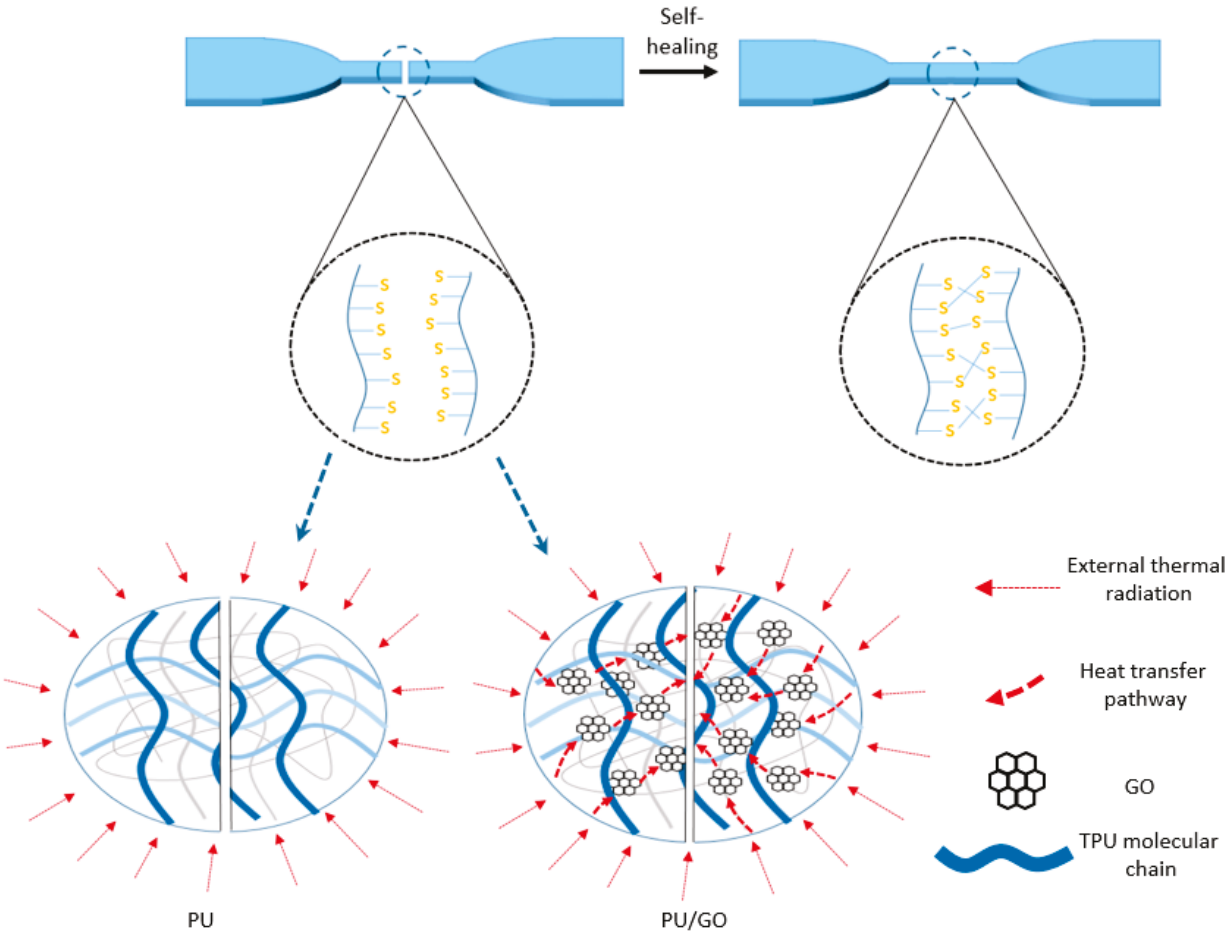

Figure 12. Self-healing mechanism of PU and PU/GO.

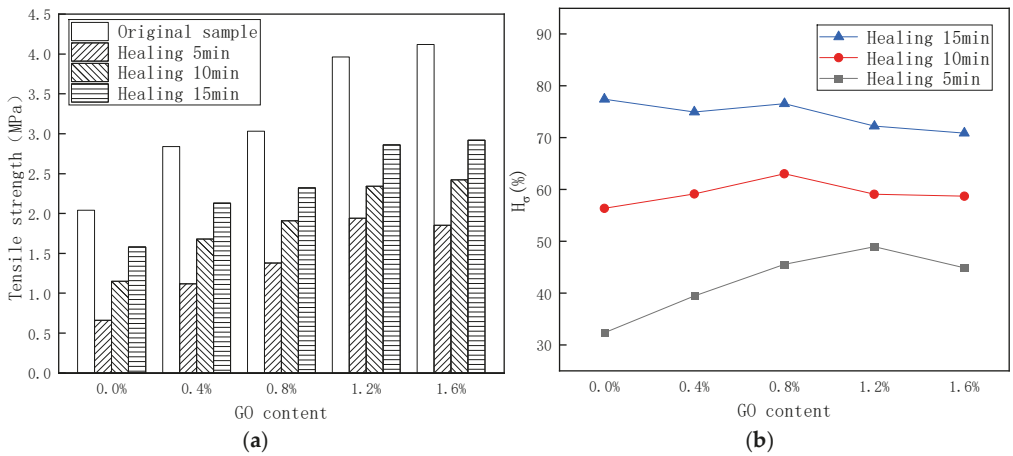

Figure 13. The self-healing test results of PU/GO under infrared light conditions. (**a**) Stress of healing sample (**b**) Self-healing coefficient.

3.2. Performance Characterization of PU/GO-Modified Asphalt

3.2.1. FTIR Test of PU/GO-Modified Asphalt

According to Figure 14, the absorption peaks of 2919 cm^{-1} are the symmetric stretching vibration of C−H in $-CH_2$ and 2850 cm^{-1} is the asymmetric stretching vibration of C−H in $-CH_2$. The vibration peak 1455 cm^{-1} is the in-plane stretching vibration of C−H in $-CH_3$ and 1375 cm^{-1} is the in-plane stretching vibration of C−H in $-CH_3$. The absorption peaks of 720 cm^{-1} belong to the out-of-plane bending vibration of C-H on the benzene ring. When it comes to the spectra of PU-modified asphalt, it can be found that the main

vibration peaks in the spectra are similar to base asphalt. But different from base asphalt, there is a new vibration peak at 1100 cm^{-1} in the spectra of PU-modified asphalt. It can be discovered that the vibration peak at 1100 cm^{-1} belongs to PU according to the spectra of PU materials. What is more, the spectra of PU/GO-modified asphalt are almost the same as that of PU-modified asphalt, which indicates that both PU and PU/GO have no reaction with asphalt.

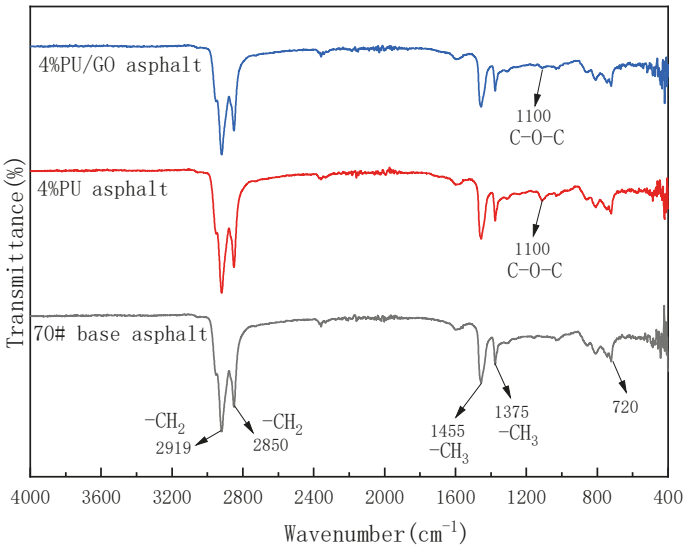

Figure 14. The FTIR test results of base asphalt and modified asphalt.

3.2.2. FM Test Results of PU/GO-Modified Asphalt

According to the principle of FM test, it can be understood that the black area is asphalt, and the fluorescence is the PU/GO modifier. From Figure 15, the dispersion of PU/GO polymer in asphalt can be observed. When the PU/GO content is 2%, the overall brightness is relatively low, and the modifier particles are relatively small. The result reveals that the PU/GO can be evenly dispersed in asphalt. When the content of PU/GO increases to 4%, the overall brightness significantly increases, with more fluorescent dots appearing in the figure. The modifier PU/GO can still be evenly dispersed in asphalt. As the PU/GO content continues to increase, the brightness of the fluorescence image increases, and the bright spots become denser. When the PU/GO content is 8%, although some larger particles can be seen on the fluorescence image, it can also be observed that the vast majority of modifiers are uniformly dispersed in the asphalt. Based on the above discussion, it can be concluded that with the increase in modifier PU/GO dosage, the brightness of the fluorescence image gradually increases. And the PU/GO can be uniformly dispersed in the asphalt, which indicates that PU/GO has good compatibility with asphalt. The reason may be related to the physical properties of PU/GO. The density of PU/GO is similar to that of asphalt and its melting point is lower than modified asphalt preparation temperature, so PU/GO could be well compatible with asphalt.

3.2.3. Basic Properties of Modified Asphalt

Table 7 shows the basic properties of PU-modified asphalt (PA) and PU/GO-modified asphalt (PGA). The penetration of PA gradually increases with the increase in PU content while the penetration of PU/GO-modified asphalt gradually decreases, which indicates PU has a softening effect on asphalt at room temperature, while PU/GO makes asphalt harder at room temperature. This is because the addition of GO in PU will enhance the mechanical properties of PU and make PU harder at room temperature. On the other hand, the softening points of PA and PGA are only slightly improved compared with base asphalt.

But it can be observed that the softening point of PGA is higher than PA, which shows that the high-temperature performance of PGA is greater than PA. What is more, both PU and PU/GO can significantly improve the low-temperature flexibility of asphalt and the effect of PU is more obvious than PU/GO. The reason can be attributed to the excellent flexibility of PU. Both the high-temperature viscosities of PU and PU/GO-modified asphalt gradually increase with the increase in modifier content, but the improvement is not significant. Through the test results in Table 6, it can be concluded that PU and PU/GO have an obvious improvement influence on low-temperature performance, while the impact on high-temperature performance is not significant.

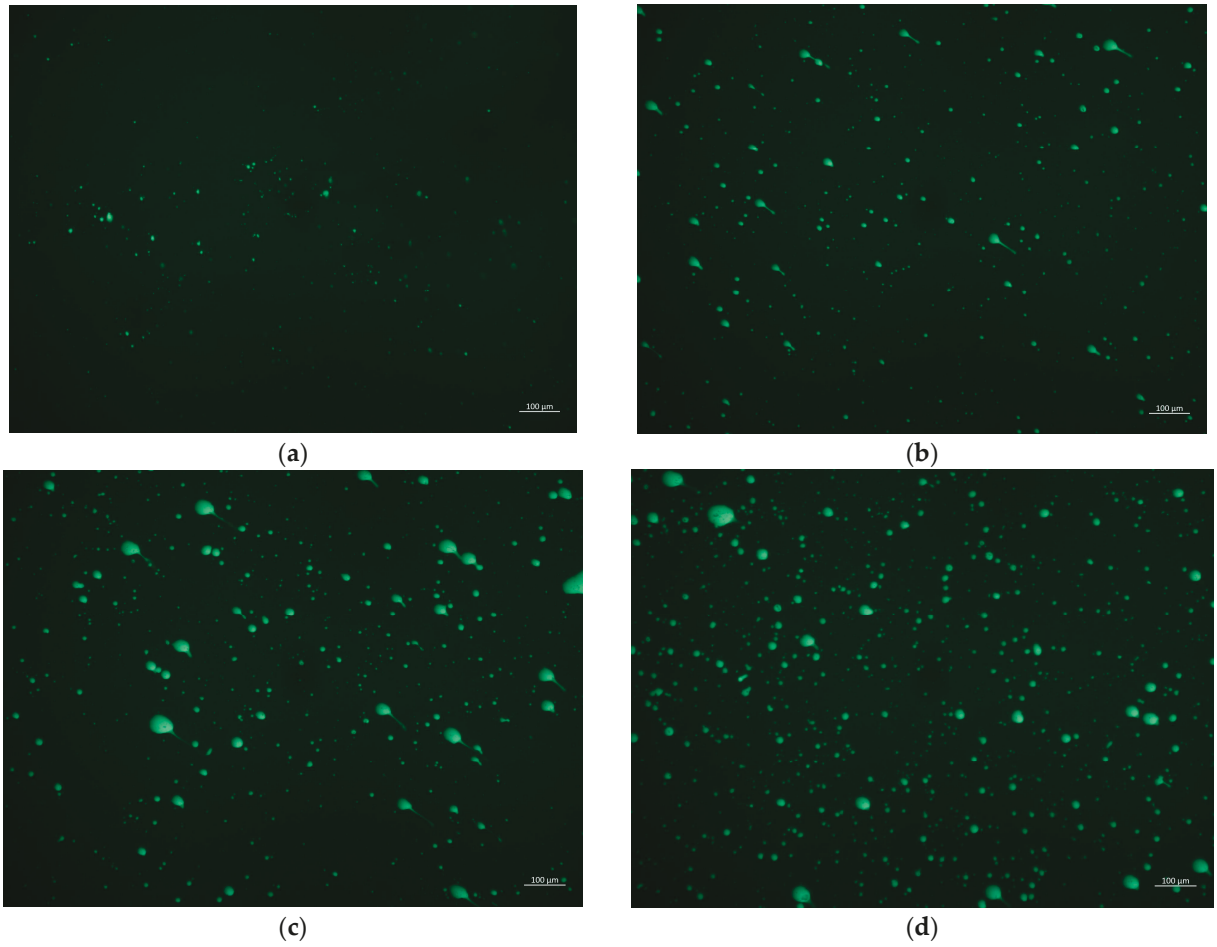

Figure 15. The FM image of PU/GO-modified asphalt. (**a**) 2% PU/GO content (**b**) 4% PU/GO content. (**c**) 6% PU/GO content (**d**) 8% PU/GO content.

Table 7. The basic properties test results of modified asphalt.

Asphalt Type	Penetration (25 °C)/0.1 mm	Softening Point/°C	Ductility (5 °C)/cm	Viscosity (135 °C)/Pa·s
70#	65.5	46.4	7.5	0.49
2%PA	64.6	46.8	23.8	0.50
4%PA	70.2	46.0	40.6	0.52
6%PA	71.5	47.2	48.3	0.54
8%PA	72.6	47.0	56.8	0.57
2%PGA	63.5	46.6	16.5	0.53
4%PGA	61.2	47.0	24.3	0.55
6%PGA	60.5	48.2	33.4	0.62
8%PGA	58.8	48.6	40.5	0.68

3.2.4. Self-Healing Test Results of Modified Asphalt
Self-Healing Performance Base on Ductility Test

Table 8 displays the ductility results before and after self-healing under 25 °C conditions. It can be found that after self-healing for 1 h or 2 h, the ductility of base asphalt cannot be measured. When the healing time increases to 4 h, the ductility is restored to 5.1 cm, which indicates that base asphalt has self-healing ability to a certain extent. Moreover, the ductility of all the samples increases gradually as the healing time increases, which proves that healing time plays an important role in the self-healing process. According to Figure 16, it can be discovered that both PU and PU/GO have a positive impact on the self-healing performance of asphalt. The overall trend of the self-healing coefficient increases with the increase in the PU and PU/GO content. This is because with the increase in PU and PU/GO content, the quantity of disulfide covalent bonds in asphalt will also increase. Therefore, the recombination efficiency of disulfide bonds will increase and have a positive impact on the self-healing property. What is more, the self-healing coefficients of PU-modified asphalt are higher than PU/GO-modified asphalt, which indicates that under room temperature, PU has a more significant influence on self-healing properties.

Table 8. Ductility self-healing test results under 25 °C condition.

Asphalt Type	Original Sample/cm	Healing 1 h/cm	Healing 2 h/cm	Healing 4 h/cm
70#	7.5	–	–	5.1
2%PA	23.8	9.5	14.6	18.5
4%PA	40.6	18.5	26.6	34.5
6%PA	48.3	24.2	34.3	42.2
8%PA	56.8	26.4	38.8	49.9
2%PGA	16.5	7.1	9.8	12.8
4%PGA	24.3	10.6	14.8	20.1
6%PGA	33.4	15.5	22.5	26.8
8%PGA	40.5	18.4	26.5	33.8

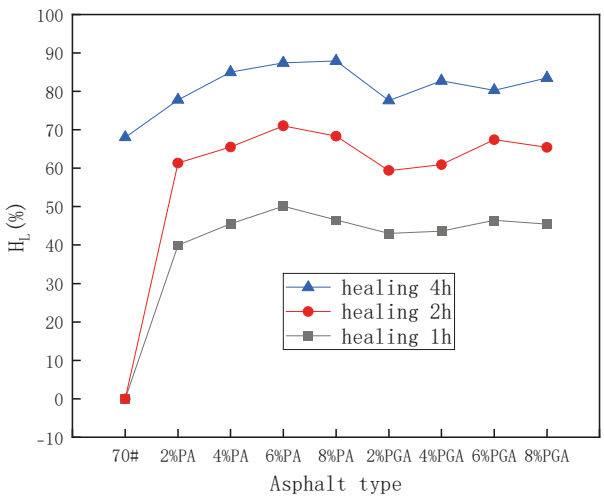

Figure 16. The ductility self-healing coefficient results under 25 °C conditions.

Table 9 and Figure 17 shows the ductility results before and after self-healing under infrared light conditions. It can be also seen that the addition of PU and PU/GO can improve the self-healing coefficient. But the results are not totally the same as the results under 25 °C conditions. Under infrared light conditions, the self-healing coefficients of PU/GO-modified asphalt are higher than that of PU-modified asphalt when the modifier content is 6% or 8%. When the healing time is 15 min under infrared light conditions,

the self-healing coefficient of 8%PU/GO-modified asphalt is greater than 100%, which indicates that the fracture was completely repaired. The reason can be attributed to the excellent infrared light absorption ability. A higher infrared light absorption rate will increase the temperature of asphalt, resulting in better self-healing ability.

Table 9. Ductility self-healing test results under infrared light conditions.

Asphalt Type	Original Sample/cm	Healing 5 min/cm	Healing 10 min/cm	Healing 15 min/cm
70#	7.5	–	–	5.5
2%PA	23.8	10.5	14.8	20.8
4%PA	40.6	21.5	28.4	36.3
6%PA	48.3	23.6	32.5	40.9
8%PA	56.8	32.5	40.6	50.2
2%PGA	16.5	7.8	11.2	13.6
4%PGA	24.3	12.9	16.9	22.1
6%PGA	33.4	20.2	25.8	31.4
8%PGA	40.5	26.8	34.5	41.2

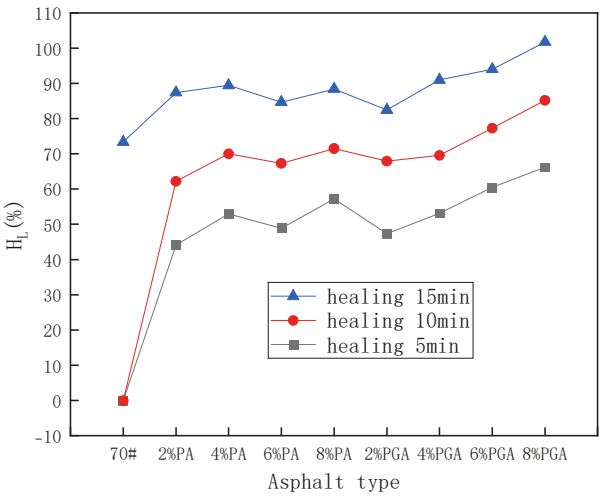

Figure 17. The ductility self-healing coefficient results under infrared light conditions.

Self-Healing Performance Base on BBR Test

According to Table 10, it can be found that with the increase in healing time, the stiffness modulus of all the fractured-healing samples gradually increases, which proves that healing time plays an important role in the asphalt self-healing process.

Table 10. Stiffness modulus self-healing test results under 25 °C condition.

Asphalt Type	Original Sample/MPa	Healing 1 h/MPa	Healing 2 h /MPa	Healing 4 h /MPa
70#	111.374	–	72.325	85.652
2%PA	92.535	50.365	63.153	77.654
4%PA	84.364	48.636	60.251	72.586
6%PA	80.656	48.253	61.753	70.385
8%PA	81.256	46.856	62.352	68.253
2%PGA	101.325	50.963	66.522	82.364
4%PGA	93.325	51.263	68.258	80.063
6%PGA	94.524	48.259	66.653	77.132
8%PGA	85.321	46.896	61.356	74.698

According to Figure 18, it can be seen that, similar to the results of the ductility test, the H_S of PU and PU/GO-modified asphalt is higher than base asphalt. What is more, the higher the modifier content, the higher the self-healing coefficient is, which shows that both PU and PU/GO have a positive effect on the self-healing properties. When it comes to the results of the BBR test, it can also be concluded that the effect of PU on self-healing properties is more significant than PU/GO at room temperature. The conclusion is consistent with that of the ductility test.

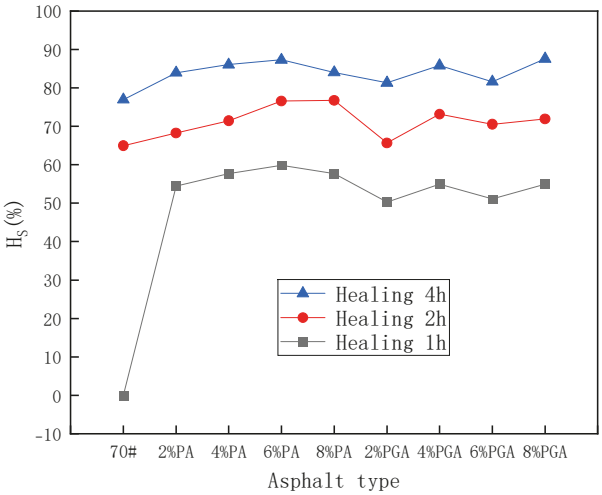

Figure 18. The stiffness modulus self-healing coefficient results under 25 °C conditions.

Table 11 and Figure 19 show the self-healing test results under infrared light conditions based on the BBR test. Similar to the ductility test, the results also show that the addition of PU and PU/GO can increase the self-healing properties under infrared light conditions. But this is different from room temperature conditions; the impact of PU/GO on self-healing properties is more obvious than PU under infrared light conditions. Compared with 6% PA, the self-healing coefficient of 6% PGA reaches 100.8% when the healing time is 15 min, which is 10.0% higher than that of 6% PA. At room temperature conditions, the PU-modified asphalt has better mobility than PU/GO-modified asphalt, which will result in better self-healing properties. But under infrared light conditions, the temperature of PU/GO-modified asphalt will be higher than PU-modified asphalt due to the better infrared light absorption ability of PU/GO. Higher temperature is beneficial for the self-healing of asphalt.

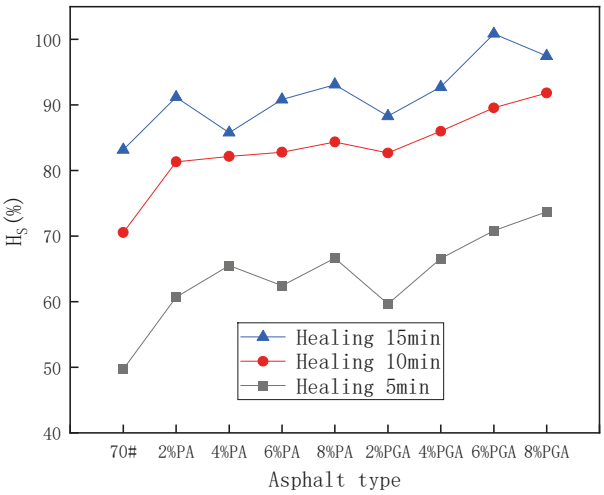

Figure 19. The stiffness modulus self-healing coefficient results under infrared light conditions.

Table 11. Stiffness modulus self-healing test results under infrared light conditions.

Asphalt Type	Original Sample/MPa	Healing 5 min/MPa	Healing 10 min/MPa	Healing 15 min/MPa
70#	111.374	55.362	78.569	92.623
2%PA	92.535	56.149	75.258	84.378
4%PA	84.364	55.268	69.315	72.354
6%PA	80.656	50.365	66.765	73.254
8%PA	81.256	54.149	68.554	75.656
2%PGA	101.325	60.449	83.761	89.443
4%PGA	93.325	62.118	80.249	86.544
6%PGA	94.524	66.964	84.653	95.321
8%PGA	85.321	62.883	78.358	83.149

4. Conclusions

In this study, a composite material, PU/GO, containing dynamic disulfide bonds, was synthesized and used to modify asphalt. The basic and self-healing properties of PU/GO and PU/GO-modified asphalt were explored through FTIR, SEM, GPC, FM and self-healing tests. The key conclusions are as follows:

1. FTIR test results showed that PU/GO was successfully synthesized and the introduction of GO in PU increased the irregularity of PU micromorphology and decreased the molecular weight of PU.
2. GO could significantly improve the mechanical properties of PU. Due to its excellent thermal conductivity and infrared absorption capability, GO had a positive impact on the early self-healing property of PU under 60 °C conditions and infrared light conditions.
3. GO had a slight negative impact on the final self-healing results because it hindered the movement of molecular chains to a certain extent.
4. PU/GO could be well dispersed in asphalt and significantly improve the low-temperature flexibility of base asphalt.
5. Both ductility and BBR tests showed that PU and PU/GO improved the self-healing properties of asphalt due to the introduction of a disulfide bond. PU had a more obvious influence on the self-healing properties at room temperature because of its excellent flexibility, while PU/GO had a more significant impact under infrared light conditions due to its better thermal conductivity.

This study mainly evaluates the self-healing performance of PU/GO and PU/GO-modified asphalt through macroscopic experiments, which is lacking exploration at the microscopic and molecular levels. In the following research, it is necessary to explore the self-healing mechanism of GO/PU and asphalt at the molecular level.

Author Contributions: Conceptualization, G.L., M.W. and K.Y.; Methodology, G.L. and K.Y.; Formal analysis, X.S.; Investigation, G.L. and X.S.; Resources, X.S.; Writing—original draft, G.L.; Writing—review & editing, M.W., K.Y. and X.S.; Supervision, M.W.; Funding acquisition, M.W. and K.Y. All authors have read and agreed to the published version of the manuscript.

Funding: This work is financially supported by the National Natural Science Foundation of China (NSFC No. 52478452 and No. 52208435) and the Science and Technology Innovation Program of Hunan Province (No. 2024RC3288).

Institutional Review Board Statement: Not applicable.

Informed Consent Statement: Not applicable.

Data Availability Statement: The original contributions presented in this study are included in the article. Further inquiries can be directed to the corresponding author.

Acknowledgments: In addition, the test equipment was provided by the Key Laboratory for Green and Advanced Civil Engineering Materials and Application Technology of Hunan Province. The authors are sincerely grateful for the financial and equipment support.

Conflicts of Interest: Author Xiaojin Song was employed by the company Zhongteng Zhixin Technology Company. The remaining authors declare that the research was conducted in the absence of any commercial or financial relationships that could be construed as a potential conflict of interest.

References

1. Yan, K.; Li, G.; Li, Q.; Diab, A.; You, L.; Wang, M. Compound modification of asphalt mixture using ethylene-vinyl acetate copolymer and amorphous poly alpha olefin. *Constr. Build. Mater.* **2022**, *341*, 127705. [CrossRef]
2. Niu, D.; Xie, X.; Zhang, Z.; Niu, Y.; Yang, Z. Influence of binary waste mixtures on road performance of asphalt and asphalt mixture. *J. Clean. Prod.* **2021**, *298*, 126842. [CrossRef]
3. Alsheyab, M.A.; Khasawneh, M.A.; Abualia, A.; Sawalha, A. A critical review of fatigue cracking in asphalt concrete pavement: A challenge to pavement durability. *Innov. Infrastruct. Solut.* **2024**, *9*, 386. [CrossRef]
4. Zhang, L.; Hoff, I.; Zhang, X.; Liu, J.; Yang, C.; Wang, F. A Methodological Review on Development of Crack Healing Technologies of Asphalt Pavement. *Sustainability* **2023**, *15*, 9659. [CrossRef]
5. Shan, J.; Zhang, Y.; Wu, S.; Wu, Q.; Jiao, Y.; Du, Y. Cracking behavior of asphalt pavement with a graded gravel layer based on computational granular mechanics. *Constr. Build. Mater.* **2022**, *345*, 128199. [CrossRef]
6. Fu, G.; Zhao, Y.; Wang, G.; Wei, J. Evaluation of the effects of transverse cracking on the falling weight deflectometer data of asphalt pavements. *Int. J. Pavement Eng.* **2021**, *23*, 3198–3211. [CrossRef]
7. Wang, F.; Xie, J.; Wu, S.; Li, J.; Barbieri, D.M.; Zhang, L. Life cycle energy consumption by roads and associated interpretative analysis of sustainable policies. *Renew. Sustain. Energy Rev.* **2021**, *141*, 110823. [CrossRef]
8. Jiang, Q.; Wang, F.; Liu, Q.; Xie, J.; Wu, S. Energy Consumption and Environment Performance Analysis of Induction-Healed Asphalt Pavement by Life Cycle Assessment (LCA). *Materials* **2021**, *14*, 1244. [CrossRef]
9. Wan, P.; Wu, S.; Liu, Q.; Wang, H.; Gong, X.; Zhao, Z.; Xu, S.; Jiang, J.; Fan, L.; Tu, L. Extrinsic self-healing asphalt materials: A mini review. *J. Clean. Prod.* **2023**, *425*, 138910. [CrossRef]
10. Li, Y.; Hao, P.; Zhang, M. Fabrication, characterization and assessment of the capsules containing rejuvenator for improving the self-healing performance of asphalt materials: A review. *J. Clean. Prod.* **2021**, *287*, 125079. [CrossRef]
11. Anupam, B.R.; Sahoo, U.C.; Chandrappa, A.K. A methodological review on self-healing asphalt pavements. *Constr. Build. Mater.* **2022**, *321*, 126395. [CrossRef]
12. Zhang, F.; Sun, Y.; Kong, L.; Cannone Falchetto, A.; Yuan, D.; Wang, W. Study on Multiple Effects of Self-Healing Properties and Thermal Characteristics of Asphalt Pavement. *Buildings* **2024**, *14*, 1313. [CrossRef]
13. Jwaida, Z.; Dulaimi, A.; Mydin, M.A.O.; Kadhim, Y.N.; Al-Busaltan, S. The self-healing performance of asphalt binder and mixtures: A state-of-the-art review. *Innov. Infrastruct. Solut.* **2024**, *9*, 247. [CrossRef]
14. Yamaç, Ö.E.; Yilmaz, M.; Yalçın, E.; Kök, B.V.; Norambuena-Contreras, J.; Garcia, A. Self-healing of asphalt mastic using capsules containing waste oils. *Constr. Build. Mater.* **2021**, *270*, 121417. [CrossRef]
15. Wan, P.; Liu, Q.; Wu, S.; Zou, Y.; Zhao, F.; Wang, H.; Niu, Y.; Ye, Q. Dual responsive self-healing system based on calcium alginate/Fe3O4 capsules for asphalt mixtures. *Constr. Build. Mater.* **2022**, *360*, 129585. [CrossRef]
16. Li, J.; Ji, X.-p.; Fang, X.-z.; Hu, Y.-l.; Hua, W.-l.; Zhang, Z.-m.; Shao, D.-y. Self-healing performance and prediction model of microcapsule asphalt. *Constr. Build. Mater.* **2022**, *330*, 127085. [CrossRef]
17. Vila-Cortavitarte, M.; Jato-Espino, D.; Tabakovic, A.; Castro-Fresno, D. Optimizing the valorization of industrial by-products for the induction healing of asphalt mixtures. *Constr. Build. Mater.* **2019**, *228*, 116715. [CrossRef]
18. Jian, R.; Hu, X.; Han, T.; Wan, J.; Gan, W.; Chen, Z.; Zhang, Y.; Cao, C. Optimization of induction heating parameters for improving Self-healing performance of asphalt mixture through partial least square model. *Constr. Build. Mater.* **2023**, *365*, 130019. [CrossRef]
19. Wan, J.; Xiao, Y.; Song, W.; Chen, C.; Pan, P.; Zhang, D. Self-Healing Property of Ultra-Thin Wearing Courses by Induction Heating. *Materials* **2018**, *11*, 1392. [CrossRef]
20. Menozzi, A.; Garcia, A.; Partl, M.N.; Tebaldi, G.; Schuetz, P. Induction healing of fatigue damage in asphalt test samples. *Constr. Build. Mater.* **2015**, *74*, 162–168. [CrossRef]
21. Norambuena-Contreras, J.; Garcia, A. Self-healing of asphalt mixture by microwave and induction heating. *Mater. Des.* **2016**, *106*, 404–414. [CrossRef]
22. Dulaimi, A.; Al-Busaltan, S.; Sadique, M. The development of a novel, microwave assisted, half-warm mixed asphalt. *Constr. Build. Mater.* **2021**, *301*, 124043. [CrossRef]
23. Franesqui, M.A.; Yepes, J.; García-González, C. Top-down cracking self-healing of asphalt pavements with steel filler from industrial waste applying microwaves. *Constr. Build. Mater.* **2017**, *149*, 612–620. [CrossRef]

24. González, A.; Norambuena-Contreras, J.; Storey, L.; Schlangen, E. Effect of RAP and fibers addition on asphalt mixtures with self-healing properties gained by microwave radiation heating. *Constr. Build. Mater.* **2018**, *159*, 164–174. [CrossRef]
25. Li, K.; Fang, K.; Niu, Y.; Li, X.; Xu, M.; Gan, C.; Ai, T. Preparation and Properties of Self-Healing Polyurethane-Modified Asphalt Composed of Different Soft Segments. *J. Mater. Civ. Eng.* **2024**, *36*, 04024353. [CrossRef]
26. Zhang, G.; Pei, J.; Li, R.; Li, P.; Zhou, B. The preparation and characterization of a novel self-healing based on the dynamic translocation of disulfide bonds. *Mater. Res. Express* **2018**, *5*, 105301. [CrossRef]
27. Hao, Z.; Shan, B.; Liu, P.; Wu, Y.; Cao, X. Preparation and Characterization of a Novel Self-Healing Polyurethane-Modified Asphalt Based on Dynamic Disulfide Bond. *J. Mater. Civ. Eng.* **2024**, *36*, 04023627. [CrossRef]
28. Lyu, L.; Wang, Z.; Ji, J.; Li, Y.; Wen, Y.; Zhang, J.; Li, R.; Chen, Z.; Pei, J. Investigating rheological and healing properties of asphalt binder modified by disulfide-crosslinked poly(urea-urethane) elastomer. *Constr. Build. Mater.* **2022**, *347*, 128546. [CrossRef]
29. Zhang, T.; Gao, S.; Yu, J.; He, Y.; Han, X.; Zhuang, R. Preparation and performance of self-healing SBS modified bitumen based on dynamic disulfide bonds. *Constr. Build. Mater.* **2023**, *397*, 132394. [CrossRef]
30. Lyu, L.; Li, D.; Chen, Y.; Tian, Y.; Pei, J. Dynamic chemistry based self-healing of asphalt modified by diselenide-crosslinked polyurethane elastomer. *Constr. Build. Mater.* **2021**, *293*, 123480. [CrossRef]
31. Yang, L.; Tao, L.; Zenglin, T.; Jianzhong, P.; Mingliang, Z.; Zhenguo, W. Research on self-healing behavior of asphalt modified by polyurea elastomer containing dynamic disulfide/diselenide bond. *Eur. Polym. J.* **2023**, *189*, 111990. [CrossRef]
32. Huang, L.; Yi, N.; Wu, Y.; Zhang, Y.; Zhang, Q.; Huang, Y.; Ma, Y.; Chen, Y. Multichannel and Repeatable Self-Healing of Mechanical Enhanced Graphene-Thermoplastic Polyurethane Composites. *Adv. Mater.* **2013**, *25*, 2224–2228. [CrossRef] [PubMed]
33. Wu, S.; Li, J.; Zhang, G.; Yao, Y.; Li, G.; Sun, R.; Wong, C. Ultrafast Self-Healing Nanocomposites via Infrared Laser and Their Application in Flexible Electronics. *ACS Appl. Mater. Interfaces* **2017**, *9*, 3040–3049. [CrossRef] [PubMed]
34. Xu, Z.; Xu, T. Improving Effects of Pretreated Graphene on Pavement Performance and Self-Healing Behaviors of Asphalt Mixture. *Int. J. Pavement Res. Technol.* **2023**. [CrossRef]
35. Li, G.; Xiao, P.; Hou, S.; Huang, Y. Rapid and efficient polymer/graphene based multichannel self-healing material via Diels-Alder reaction. *Carbon* **2019**, *147*, 398–407. [CrossRef]
36. Shamaila, S.; Sajjad, A.K.L.; Iqbal, A. Modifications in development of graphene oxide synthetic routes. *Chem. Eng. J.* **2016**, *294*, 458–477. [CrossRef]
37. *JTG E20-2011*; Standard Test Methods of Bitumen and Bituminous Mixtures for Highway Engineering. China Communication Press: Beijing, China, 2011.
38. *GB/T 528-2009*; Rubber, Vulcanized or Thermoplastic-Determination of Tensile Strain-Stress Properties. China Communication Press: Beijing, China, 2009.

Disclaimer/Publisher's Note: The statements, opinions and data contained in all publications are solely those of the individual author(s) and contributor(s) and not of MDPI and/or the editor(s). MDPI and/or the editor(s) disclaim responsibility for any injury to people or property resulting from any ideas, methods, instructions or products referred to in the content.

materials

MDPI

Article

Micromodification Mechanism and High-Temperature Rheological Properties of Activated Rubber/Styrene–Butadiene–Styrene Compound-Modified Asphalt

Kai Zhang [1], Xuwen Zhong [2], Xukun Huang [3], Weihua Wan [4,*], Hai Zhou [2] and Bin Liu [1]

[1] Road Material and Structure Engineering Technology Research Center of Jiangxi Provincial, Jiangxi Communications Investment Maintenance Technology Group Co., Ltd., Nanchang 330200, China; kaizhang@whut.edu.cn (K.Z.); binliujky@126.com (B.L.)
[2] School of Civil and Architectural Engineering, East China University of Technology, Nanchang 330013, China; 15007086333@163.com (X.Z.); charliez0112@163.com (H.Z.)
[3] Dundee International Institute, Central-South University, Changsha 410075, China; shulkenh@csu.edu.cn
[4] Jiangxi Transportation Engineering Group Co., Ltd., Nanchang 330000, China
* Correspondence: 99308702@163.com

Abstract

Currently, research on the modification mechanisms of activated rubber/SBS (styrene–butadiene–styrene) composites and the microscopic processes involved remains limited. To investigate the impact of the rubber activation treatment combined with SBS modifier on asphalt modification, this study employs composite-modified asphalt formulations using either a conventional mix or activated rubber in conjunction with SBS. Infrared spectroscopy (IR) and scanning electron microscopy (SEM) were utilized to analyze the chemical components and microscopic morphology of the composite-modified asphalt following activation treatment. Microscopic analysis revealed that the asphalt stirred for 20 min has a characteristic peak with a wave number of 966 cm^{-1}, while the characteristic peak with a wave number of 700 cm^{-1} is not obvious. That is, the asphalt sample contains the polybutadiene component and a reduced amount of the polystyrene component. Therefore, it can be inferred that the asphalt sample only contains activated rubber, along with less SBS modifier content. Traditional rubber undergoes significant expansion reactions during the mixing stage, but there are difficulties in degradation, which leave large particles and reduce the proportions of the lightweight asphalt components. However, active rubber and SBS mainly expand and degrade more completely during the shear stage, forming many micro-volume particles in asphalt. Additionally, frequency scanning and multiple creep recovery tests were conducted to evaluate the high-temperature rheological properties of the asphalt. The results indicate that activated rubber, doped at 20%, and SBS, doped at 2%, significantly enhance the high-temperature rheological properties of the composite-modified asphalt compared to base asphalt, exhibiting a 417.16% increase in the complex modulus at 64 °C and 1 Hz. Furthermore, these modifiers interact synergistically to improve modification efficiency.

Keywords: conventional rubber; activated rubber; SBS modifier; modification mechanism; high-temperature rheological properties

1. Introduction

With the increasing amounts of waste rubber, recycling this material has become a problem to be solved, and at the same time, there is a certain need for high-performance

asphalt in road construction projects. Waste rubber, as a modifier for road petroleum asphalt, can improve the performance of asphalt, and it involves recycling waste rubber, so rubber-modified asphalt has become a hot topic in the field of waste rubber recycling and road engineering [1,2]. Rubber-modified asphalt has better road performance and mechanical properties [3,4]. However, the molecular structure of conventional rubber is characterized by high cross-linking and poor compatibility with asphalt, which results in conventional rubber-modified asphalt being prone to a viscosity that is too high; additionally, the efficiency of the modified asphalt is low, and there are other problems [5–7]. These problems affect the application of rubber-modified asphalt in road engineering and hinder the recycling of waste rubber and the promotion of rubber-modified asphalt.

To solve the problems associated with the high viscosity and low modification efficiency of conventional rubber, some scholars advocate the use of conventional rubber through pretreatment, with the addition of other additives, etc. Pretreatment can change the internal chemical-bonding composition and crosslinking degree of conventional rubber materials to improve the road performance of conventional rubber asphalt [8–10]. Xiang et al. [11] pretreated conventional rubber using ultraviolet-light irradiation and found that after ultraviolet-light irradiation, the internal crosslinking degree and chemical-bonding changed, and the reaction with asphalt became more intense and improving the high-temperature shear resistance of the modified asphalt by 18–29%. Hosseinnezhad et al. [12] combined microwave and biological methods to activate conventional rubber, and the results showed that the breaking energy of activated rubber-modified asphalt is 135% of that of conventional rubber-modified asphalt. Feng et al. [13] conducted a study on the surface treatment of rubber powder with waste cooking oil. Edible oil surface treatment of rubber powder was investigated, and it was found that the solubility of treated rubber in asphalt increased, and the creep stiffness of the prepared modified asphalt was reduced by 9–34% compared to conventional rubber-modified asphalt.

Conventional rubber-modified asphalt also has poor compatibility with asphalt and poor high-temperature storage stability, and is prone to phase separation, leading to asphalt delamination and segregation [14–16]. Some scholars have reported that after microwave pretreatment, the specific surface area of conventional rubber increases, its compatibility with asphalt improves, and the high-temperature performance, fatigue resistance, and anti-aging properties of the activated rubber-modified asphalt are improved. Some scholars have found that with the pretreatment of conventional rubber with a macroscopic morphology and a fluffy flocculent structure, the rubber and asphalt contact area increases, and the asphalt's compatibility is enhanced [17–19]. Mousavi et al. [20] added biomodifiers to reduce the degree of cross-linking within rubber and ground rubber adhered to finer powder to reduce the difference between the densities of the rubber and the asphalt to improve the stability of the high-temperature storage of asphalt, but this method is costly and difficult to generalize.

In addition, compound modification of asphalt by the combination of rubber with multiple modifiers can cause two modifiers to interact with each other and form a cross-linking network, which can improve the road performance of the asphalt and improve the defects of conventional rubber-modified asphalt to a certain extent [21–24]. Qian et al. [25] combined conventional rubber with SBS and reported that the addition of SBS can promote the degradation of conventional rubber in asphalt and improve the storage stability of modified asphalt at high temperatures. With the increase in SBS dosage at 60 °C and 0.1 kPa, the recovery rate of composite-modified asphalt can be increased by up to 20% compared to modified asphalt without SBS dosage. Kumar and Choudhary [26] combined conventional rubber with tire pyrolytic oil (TPO) and plastic pyrolytic oil to produce composite-modified asphalt with improved storage stability performance and rheological properties. The

J_{nr} of modified bitumen at 60 °C increased by 63% and 56%, respectively. Furthermore, Rasool et al. [27] obtained desulfurized rubber by the twin-screw extrusion method and combined it with an SBS modifier to produce composite-modified asphalt with improved high-temperature performance. The desulfurization of the desulfurized rubber influenced its compatibility with SBS, thereby affecting the performance of the composite-modified bitumen.

Despite recent advancements, the micromodification mechanisms of conventional rubber/SBS and activated rubber/SBS composite-modified asphalts remain insufficiently studied. This paper investigates the micro-level modification mechanisms and the effects of rubber activation on composite-modified asphalt. In addition, the influence of modifier dosage on asphalt performance is examined, providing valuable insights for future research on rubber-SBS composite-modified asphalt.

2. Materials and Methods

2.1. Materials

2.1.1. Base Asphalt

Modified asphalt is prepared by adding modifiers to base asphalt. Based on current domestic and international research on rubber-modified asphalt, this study conducted tests [28] on a modified base asphalt composed of 70# grade road petroleum asphalt. The softening point, penetration, elongation at 25 °C, and elongation at 5 °C were measured. The results are shown in Table 1.

Table 1. Basic performance of base asphalt.

Pilot Projects	Unit	Test Values
Penetration (25 °C)	0.1 mm	71.6
Softening point	°C	49.6
Ductility (25 °C)	cm	>100
Ductility (5 °C)	cm	5.6

2.1.2. Activated Rubber

Activated rubber, which has higher surface activity than conventional rubber, can be obtained through surface pretreatment. In this study, activated rubber prepared using a twin-screw extruder after thermal-mechanical shear was selected for experimental investigation, based on relevant research in the field of road materials. The activated rubber is shown in Figure 1.

Figure 1. Activated rubber.

2.1.3. Conventional Rubber

Conventional rubber is primarily obtained from processed waste rubber. In this study, it is mainly used for comparison with activated rubber, with a mesh size of 40. The conventional rubber is shown in Figure 2.

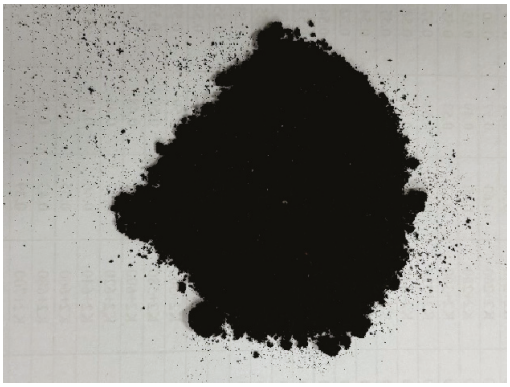

Figure 2. Conventional rubber.

2.1.4. SBS Modifiers

The SBS modifier is classified into star and linear types, and its structure influences its effect on asphalt modification. In current road construction projects, the linear SBS modifier is more commonly used. Therefore, this study uses the linear SBS modifier to prepare the modified asphalt. The SBS modifier is shown in Figure 3.

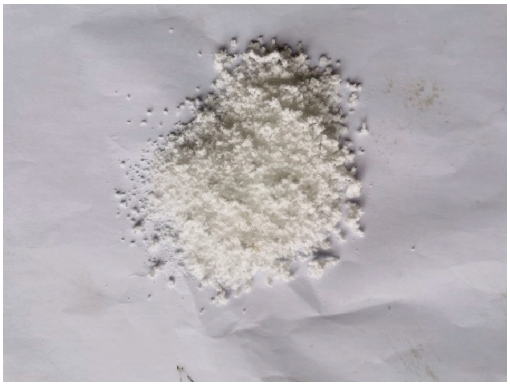

Figure 3. SBS modifier.

2.1.5. Stabilizer

The activated rubber/SBS composite-modified asphalt system, which consists of two modifiers and asphalt, exists in a state of dynamic equilibrium. At high temperatures, mechanical mixing stops, and the two modifiers gradually precipitate from their uniformly dispersed state. This separation leads to variations in the vertical distribution of the components, ultimately reducing the overall performance of the rubber/SBS composite-modified asphalt.

Stabilizers used in road engineering generally have low molecular weights and specific functional groups. Modified asphalt stabilizers can be formulated to enhance high-temperature storage stability, heat resistance, and other properties of modified asphalt to a certain extent.

Sulfur produced in industrial processes can be classified into three main types: refined sulfur, sublimated sulfur, and precipitated sulfur. In road construction projects, sublimated sulfur is commonly used as a stabilizer in the preparation of rubber-modified asphalt.

Therefore, this study tests the use of sublimated sulfur as a stabilizer. Sulfur is shown in Figure 4.

Figure 4. Sulfur.

2.1.6. Composite-Modified Asphalt Preparation Process

For rubber-modified asphalt and desulfurized rubber-modified asphalt, the typical shear rate, temperature, and duration range from 2000 to 5000 r/min, 170–180 °C, and 45–60 min, respectively. The shear rate and duration for SBS-modified asphalt are similar, but the temperature is generally around 160 °C [29–31]. Considering the modification effect of both modifiers and the aging behavior of asphalt, this study adopts a higher shear rate and temperature with a shorter shear duration. The preparation process of the composite-modified asphalt is illustrated in Figure 5. The selected preparation temperature is 180 °C.

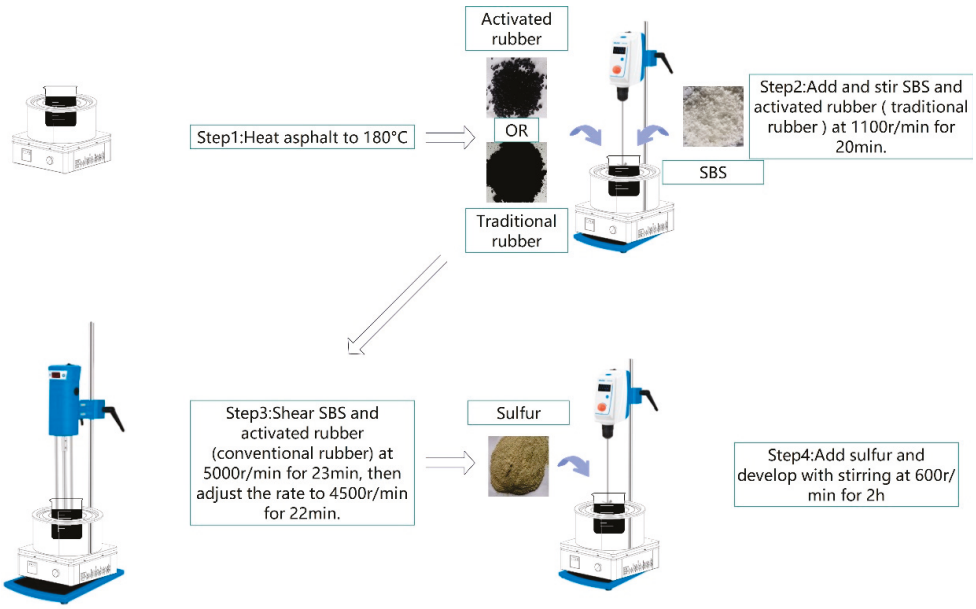

Figure 5. Preparation process.

2.2. Methods

This study analyzes the micromechanism of two types of composite-modified asphalt, focusing on internal chemical composition, microstructure, and high-temperature rheological properties with varying modifier dosages [32]. The modification mechanism of rubber and SBS after activation treatment, as well as the influence of modifier dosage on the performance of the composite-modified asphalt, is also examined.

After material preparation, base asphalt, activated rubber/SBS composite-modified asphalt (in the preliminary miscible state), conventional rubber/SBS composite-modified asphalt, and activated rubber/SBS composite-modified asphalt were selected for infrared spectroscopy analysis. The tests aimed to analyze the chemical composition of the asphalt materials, with data collected in the mid-infrared range of 600–4000 cm^{-1}.

Samples of conventional rubber/SBS and activated rubber/SBS composite-modified asphalt were taken at four stages of the preparation process: after 20 min of mixing, after 22 min of shearing, and after completion of development. Scanning Electron Microscopy (SEM) was used to examine the micromorphology of the asphalt at each stage, allowing analysis of the distribution of conventional rubber, activated rubber, and SBS within the asphalt, as well as the effects on asphalt microstructure.

The frequency sweep test is commonly used to evaluate the viscoelasticity and deformation resistance of asphalt. The test is conducted at temperatures ranging from 52 °C to 82 °C, with 6 °C intervals. A 25 mm plate is used, and the test frequency ranges from 0.1 to 100 Hz.

Multiple stress creep recovery (MSCR) tests were conducted at a temperature of 60 °C, with an initial conditioning creep stress of 0.1 kPa. The test included two loading stages: 0.1 kPa and 3.2 kPa, each applied over 10 continuous loading cycles. In each cycle, the sample was subjected to a constant stress for 1 s, followed by a 9 s recovery period. This test evaluates the elastic recovery capability of asphalt under two levels of shear creep stress.

The modifier dosages listed in Table 2 are based on the weight of the base asphalt.

Table 2. Modifier dosage.

Sample Number	Dosage of Activated Rubber (%)	Dosage of SBS (%)
D10-S1	10	1.0
D15-S1	15	1.0
D20-S1	20	1.0
D10-S1.5	10	1.5
D15-S1.5	15	1.5
D20-S1.5	20	1.5
D10-S2	10	2.0
D15-S2	15	2.0
D20-S2	20	2.0

3. Results and Discussion

3.1. Infrared Spectroscopy Analysis

3.1.1. Base Asphalt

The infrared spectrum of the matrix asphalt is shown in Figure 6. Several prominent absorption peaks identified in the spectrum are listed in Table 3. Analysis of the results indicates that the 70# road petroleum asphalt used in this study contains saturated fraction, aromatic fraction, and aliphatic compounds.

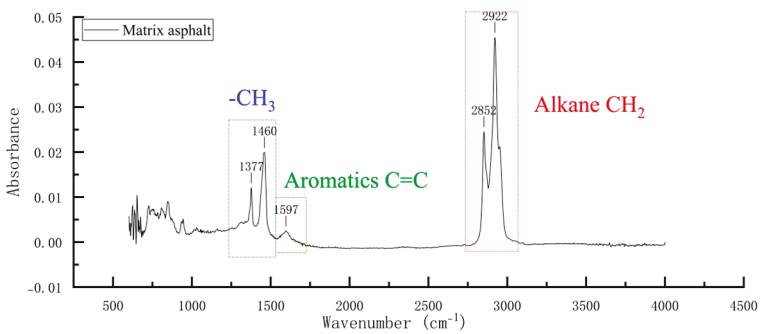

Figure 6. Infrared spectrum of base asphalt.

Table 3. Base asphalt absorption peaks.

Wavenumber (cm^{-1})	The Peak of a Telescope	Characterizing Component
2922	Alkane CH_2 antisymmetric stretching peaks	saturate
2852	Alkane CH_2 symmetric stretching peaks	saturate
1597	Aromatic C=C stretching peaks	aromatic
1460	Aliphatic CH3 asymmetric variant angles	aliphatic compound
1377	Aliphatic CH_3 symmetry variant	aliphatic compound

3.1.2. Activated Rubber/SBS Composite Modified Asphalt

The infrared spectrum of the activated rubber/SBS composite-modified asphalt with 20% activated rubber and 2% SBS modifier is shown in Figure 7. By comparing the main peak features within the 600–1400 cm^{-1} wavenumber range, differences from the asphalt matrix spectrum can be observed. This region is locally enlarged to produce the infrared spectral map shown in Figure 8. The characteristic peaks of the activated rubber/SBS composite-modified asphalt are listed in Table 4.

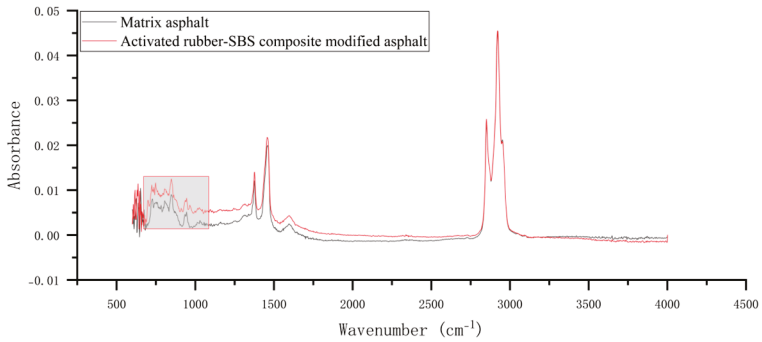

Figure 7. Infrared spectrum of activated rubber/SBS composite-modified asphalt.

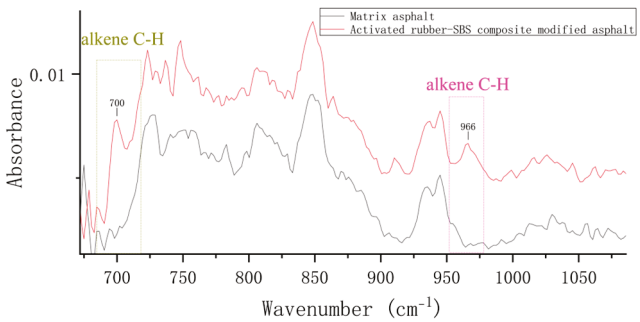

Figure 8. Locally magnified infrared spectrum of activated rubber/SBS composite-modified asphalt.

Table 4. Absorption peaks of activated rubber/SBS composite-modified asphalt.

Wavenumber (cm^{-1})	The Peak of a Telescope	Characterizing Component
966	trans-olefin CH peak	polybutadiene
700	cis-olefin CH peak	polystyrene

According to the analysis results, compared with the base asphalt, the new components in the activated rubber/SBS composite-modified asphalt are mainly polybutadiene and polystyrene. The activated rubber contains polybutadiene, while the SBS modifier contains both polybutadiene and polystyrene. In addition, no new characteristic peaks were observed. This indicates that after adding activated rubber and SBS modifier to the

base asphalt, no significant new chemical compounds are formed, suggesting that the interaction between the activated rubber, SBS modifier, and asphalt is primarily a physical swelling reaction.

To analyze the compositional changes in activated rubber/SBS composite-modified asphalt during preparation, this study compares the infrared spectrum of the asphalt in its preliminary mixed state after mixing and stirring for 20 min with that of asphalt containing activated rubber and SBS modifier. A locally magnified map is shown in Figure 9.

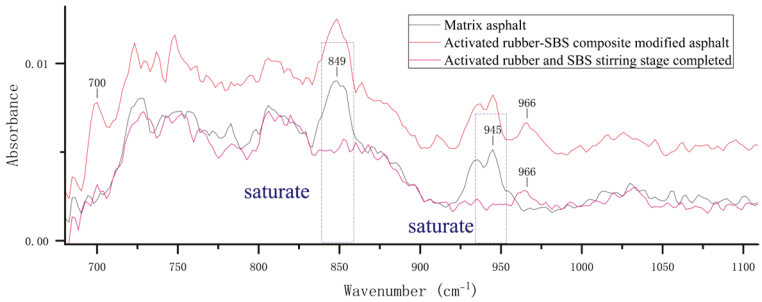

Figure 9. Infrared spectrum of activated rubber/SBS composite-modified asphalt after completion of the stirring stage.

According to the locally magnified figure, after stirring the asphalt for 20 min, a characteristic peak at the wavenumber 966 cm^{-1} was observed, while the peak at 700 cm^{-1} was not prominent. This indicates a lower presence of polybutadiene and polystyrene components in the asphalt samples. It can be inferred that the asphalt samples contained smaller amounts of activated rubber and SBS modifier. The reason for this difference is likely that the activated rubber and SBS modifiers were not sheared, resulting in larger particle sizes. Consequently, the infrared spectroscopy signal from the asphalt samples was weaker, and the modifiers were unevenly distributed in the sample. However, new characteristic peaks appeared in the infrared spectra after 20 min of stirring, indicating that the modifiers begin to dissolve during the initial mixing stage of asphalt preparation.

At the same time, after stirring the asphalt for 20 min, the two characteristic peaks at 849 cm^{-1} and 945 cm^{-1} did not appear, while the two absorption peaks of the activated rubber/SBS composite-modified asphalt became apparent. These two characteristic peaks represent the saturated fraction of the asphalt. The reason is that during the mixing stage, part of the SBS and activated rubber begin to absorb the light components of the asphalt and swell. At this stage, some SBS and activated rubber have started absorbing the light components to dissolve, but have not yet reached the degradation stage, which leads to a decrease in the saturated content of the asphalt. After the development process is completed, the activated rubber and SBS cause the degradation of a significant amount of asphalt, releasing the absorbed saturated components back into the asphalt, which results in an increase in the saturated content.

3.1.3. Conventional Rubber/SBS Composite-Modified Asphalt

The locally magnified spectrum of conventional rubber/SBS composite-modified asphalt, prepared with 20% conventional rubber and 2% SBS modifier, is shown in Figure 10. The results indicate that this asphalt lacks the two characteristic peaks at 849 cm^{-1} and 945 cm^{-1}, suggesting that its saturated content is lower than that of the base asphalt and the activated rubber/SBS composite-modified asphalt. In asphalt, conventional rubber absorbs the saturated fraction and expands in volume. However, its dissolution efficiency is low, and it cannot re-release the absorbed saturated components effectively. As a result, the saturated fraction in conventional rubber/SBS composite-modified asphalt is reduced.

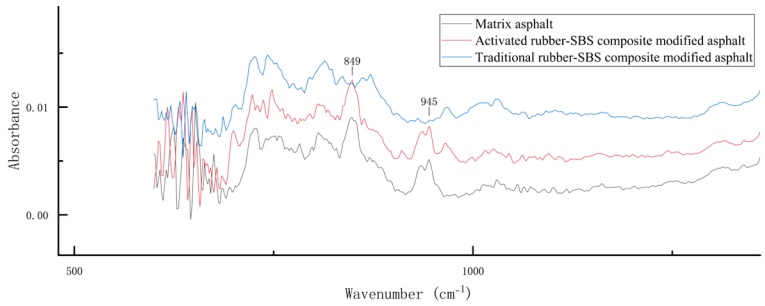

Figure 10. Locally magnified infrared spectrum of conventional rubber/SBS composite-modified asphalt.

To analyze the compositional changes in conventional rubber/SBS composite-modified asphalt during the preparation process, this study uses infrared spectra of asphalt samples mixed with the two modifiers for 20 min. The results are shown in Figure 11.

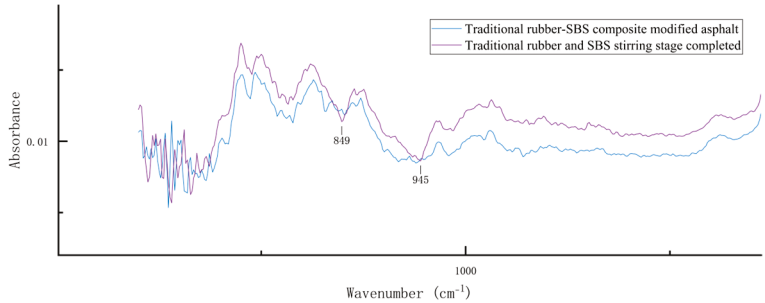

Figure 11. Locally magnified infrared spectrum of conventional rubber/SBS composite-modified asphalt after completion of the stirring stage.

The two negative peaks at 849 cm^{-1} and 945 cm^{-1} in the spectrum of the conventional rubber/SBS composite asphalt, stabilized for 20 min, indicate that the saturated fraction of the composite asphalt is complete in the mixing stage of preparation, as compared to the decrease in the content of the saturated fraction. These results indicate that the conventional rubber/SBS composite asphalt mixing process can lead to more pronounced dissolution reactions. From these results, it can be inferred that during the mixing process, the conventional rubber/SBS composite-modified asphalt undergoes a more pronounced swelling reaction. This occurs when the conventional rubber absorbs a large number of light components, causing volume expansion, but before it enters the degradation stage. As a result, a significant amount of saturated content in the asphalt is absorbed, leading to a reduction in its content. After asphalt development, partial degradation of the conventional rubber occurred, and some of the saturated fraction was released, leading to an increase in the asphalt's saturated fraction. However, the overall content remained lower than that of the matrix asphalt and activated rubber/SBS composite-modified asphalt, which further indicates that the degradation efficiency of conventional rubber in asphalt is low.

Based on the initial miscible state of the activated rubber/SBS and conventional rubber/SBS composite-modified asphalts, the infrared spectra show that the solvation reactions of the activated rubber and SBS modifier primarily occur during the shear and development stages. In contrast, conventional rubber undergoes a strong solvation reaction during the mixing stage. This is mainly because the activated rubber and SBS modifier, before shear, are in the form of larger granular materials with a low contact area with the asphalt, resulting in a lower swelling reaction efficiency. After shearing, the two modifiers decrease in volume, significantly increasing their contact area with the asphalt. At this stage, the swelling of the activated rubber/SBS composite-modified asphalt intensifies,

and the particle size of the conventional rubber is much smaller than that of the unsheared activated rubber and SBS modifier. Therefore, during the mixing stage, the modifier can absorb a large amount of lightweight components due to the more intense swelling reaction.

However, due to the high internal crosslinking of the conventional rubber, the efficiency of the degradation reaction after the volume expansion is low. As a result, part of the absorbed saturated fraction cannot be released, leading to a decrease in the saturated fraction of the conventional rubber/SBS composite-modified asphalt. Rubber activation breaks the internal S-S bonds and interrupts the C-S bonds, improving compatibility with the asphalt and thereby increasing the efficiency of the degradation reaction. During the swelling reaction, a large number of lightweight components are absorbed, which are then released into the asphalt during the degradation phase. Due to its material properties and high compatibility with asphalt, SBS can undergo a more efficient reaction in asphalt, leading to a higher degree of degradation and interaction with the asphalt. Therefore, compared to the base asphalt, the content of lightweight components in the activated rubber/SBS composite-modified asphalt is not significantly reduced, while it is significantly reduced in the conventional rubber/SBS composite-modified asphalt.

3.2. SEM Scanning Analysis

The microscopic morphology of activated rubber/SBS composite-modified asphalt with 20% rubber and 2% SBS modifier, as well as that of conventional rubber/SBS composite-modified asphalt at different preparation stages, was observed using SEM, as shown in Figures 12 and 13.

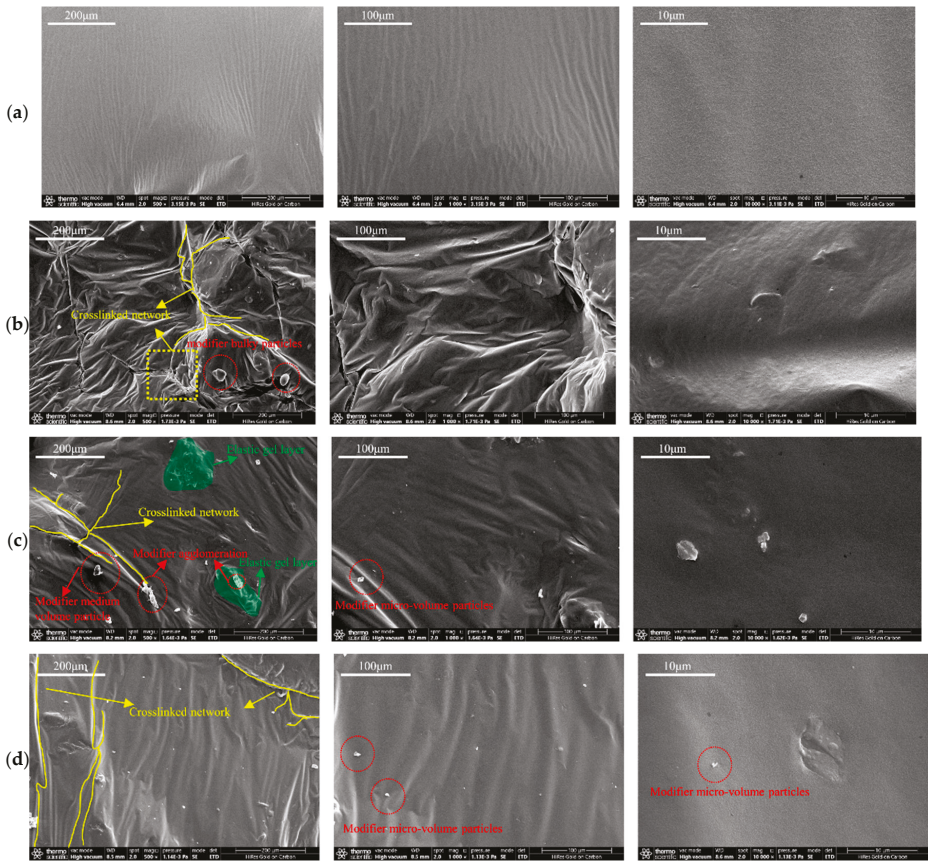

Figure 12. SEM images of activated rubber/SBS composite modified asphalt at different reaction stages: (**a**) complete stirring, (**b**) shearing for 22 min, (**c**) complete shearing, and (**d**) completed development.

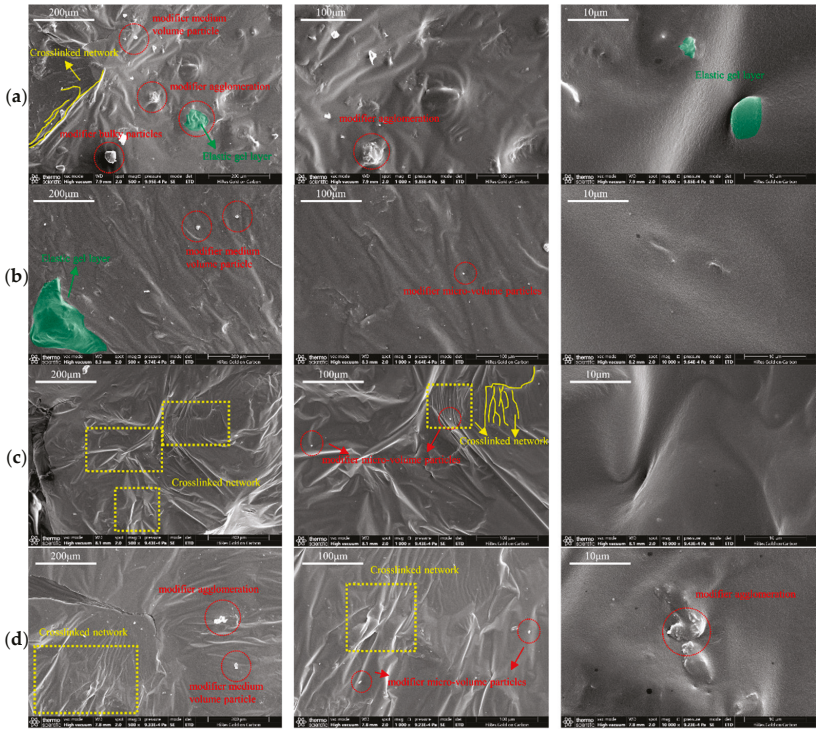

Figure 13. SEM images of conventional rubber/SBS composite modified asphalt at different reaction stages: (**a**) complete stirring, (**b**) shearing for 22 min, (**c**) complete shearing, and (**d**) completed development.

3.2.1. Activated Rubber/SBS Composite Modified Asphalt

Figure 12 shows the microscopic morphology of activated rubber/SBS composite-modified asphalt at different stages of the preparation process. Figure 12a shows that after mixing, the asphalt surface is relatively flat, and no modifier particles are visible, indicating a low degree of dissolution of the activated rubber and SBS modifier in the asphalt. At this stage, the modification effect on the asphalt is weak. This is because the activated rubber and SBS modifier have large particle sizes, and in the absence of shear, their reaction efficiency with asphalt is low.

After 22 min of shearing, as shown in Figure 12b, the microscopic morphology of the activated rubber/SBS composite-modified asphalt changed. A large number of bumps and depressions appeared on the surface, and activated rubber and SBS modifier particles began to emerge. The decrease in the volume of the activated rubber and SBS modifier after the reduction in shear particle size is due to the absorption of a large amount of asphalt from the light components during the swelling reaction, which leads to the formation of an elastic gel layer on the surface. At this point, the volume of the activated rubber and SBS modifier particles increased, and the relative distance between the modifier particles decreased significantly, gradually forming a cross-linked structure in the asphalt. This resulted in a change in the microscopic morphology of the asphalt surface.

Figure 12c shows the microscopic morphology of the activated rubber/SBS composite-modified asphalt after shear. The microscopic morphology of the asphalt surface gradually flattens, with a reduction in the volume of modifier particles and a decrease in bumps and depressions. At the same time, modifier agglomeration occurs, leading to the formation of a small number of micro-sized modifier particles. The reason is that, after shear, a large number of activated rubber and SBS modifier particles with reduced volume undergo an asphalt swelling reaction. This causes a significant increase in the volume of modifier particles due to swelling, leading to the formation of a viscous elastic gel layer. As a result, some of the larger modifier particles adhere to each other, forming agglomerates. At the

same time, some of the modifier particles have transitioned from the asphalt swelling stage to the degradation stage, resulting in a reduction in the volume of large modifier particles and their splitting into micro-sized particles. At this point, the volume of asphalt modifier particles on the surface decreases, and the elastic gel layer reduces the impact of the asphalt surface morphology, leading to an improvement in flatness.

Figure 12d shows the development of activated rubber/SBS composite-modified asphalt, where the surface micromorphology further improved in flatness. The larger modifier particles disappeared, and a large number of micro-sized modifier particles appeared. The reason is that, after the development stage, the activated rubber and SBS modifier particles in the composite-modified asphalt fully dissolved and degraded. The large modifier particles split into many micro-sized particles, and the elastic gel layer formed on the surface further reduced the volume of modifier particles, improving the asphalt's surface morphology and flatness.

In the shear stage, a large volume increase due to swelling, along with the formation of elastic gel layers, significantly alters the surface micromorphology of the asphalt. In the second half of the swelling stage, many swollen modifier particles transition into the degradation stage. At this point, the elastic gel layer in the asphalt helps reduce the impact on the surface micromorphology, allowing the flatness of the asphalt to begin restoring. Also, a large number of sufficiently swollen modifier particles begin to degrade and break into many micro-sized particles that are dispersed in the asphalt, causing the asphalt's surface micromorphology to improve further. The main phase of the degradation reaction is the development stage. At this point, a large number of sufficiently swollen modifier particles begin to degrade and break into many micro-sized particles dispersed in the asphalt. The elastic gel layer in the asphalt essentially disappears, and the surface micromorphology of the asphalt continues to improve, with further enhancement of its flatness.

3.2.2. Conventional Rubber/SBS Composite Modified Asphalt

Figure 13 shows the microscopic morphology of conventional rubber/SBS composite-modified asphalt at different stages of the preparation process. Figure 13a shows that after the completion of the mixing stage, the asphalt's microscopic morphology formed an uneven structure, with a large number of large- and medium-sized modifier particles and signs of modifier agglomeration. This is due to part of the conventional rubber in the asphalt absorbing lightweight components during the dissolution reaction.

Figure 13b,c show that during the shear stage and after shearing, only minor changes in the microscopic morphology and flatness of the asphalt are observed. This indicates that the conventional rubber has not undergone significant degradation and that the asphalt is still in a swollen state with an increase in volume. At the same time, a small number of small-volume modifier particles are observed on the asphalt surface, likely resulting from the SBS modifier beginning to dissolve and degrade within the asphalt, splitting into micro-sized particles.

Figure 13d shows the microscopic morphology of the conventional rubber/SBS composite-modified asphalt after the completion of the process. Compared to the asphalt surface before the process, the microstructure of the asphalt surface after completion is still largely influenced by the volume of modifier particles, which are presumed to remain undegraded. Additionally, the microscopic morphology of the asphalt surface during the shear stage shows no significant changes.

Overall, the small particle size of conventional rubber allows for extensive dissolution during the mixing stage, leading to initial modification of the asphalt as the volume of the conventional rubber expands. However, as the preparation process progresses, the

large volume of expanded conventional rubber becomes difficult to dissolve in the asphalt, resulting in the presence of many large- and medium-sized particles in the conventional rubber/SBS composite-modified asphalt at various stages of preparation. The larger particles primarily consist of an undegraded conventional rubber core surrounded by a gel layer. These particles are connected by friction to form a high-viscosity crosslinked structure, significantly increasing the viscosity of the asphalt. At the same time, the larger particles are more prone to segregation, which reduces the asphalt's high-temperature storage stability.

Activated rubber has a large particle size and requires shearing to react with asphalt in significant amounts. After activation treatment, the S-S bond and C-S bonds in conventional rubber are broken, improving its compatibility with asphalt. This leads to swelling and volume increases in the asphalt, after which the material gradually degrades and is evenly distributed in the asphalt. Therefore, after the development of the activated rubber/SBS composite-modified asphalt, the disappearance of large-volume particles left only a large number of micro-sized particles. The effect of the SBS modifier on the asphalt reaction process is similar to its effect on the activation of rubber in the asphalt. The swelling reaction leads to gradual degradation and uniform dispersion of the activated rubber in the asphalt, making it a more effective composite modifier. This improves the asphalt's performance while also reducing its viscosity.

3.3. Analysis of High-Temperature Rheological Properties of Asphalt

3.3.1. Frequency Scanning

According to the principle of time-temperature equivalence, the complex modulus curve of the activated rubber/SBS composite-modified asphalt obtained under different temperature conditions can be shifted along the logarithmic frequency axis using a displacement factor. This allows the complex modulus under various temperatures to be superimposed into a single, smooth curve, known as the master curve of the complex modulus. This master curve can be used to predict the rheological properties of composite-modified asphalt across a wide range of temperatures and frequencies. This test was conducted according to AASHTO Designation: T 315 (2022), with test temperatures of 52, 58, 64, 70, 76, and 82 °C, and a test frequency range of 0.1–100 Hz.

The displacement factor for the complex modulus curve of activated rubber/SBS composite-modified asphalt at different test temperatures can be calculated using the WLF formula, as shown in Equation (1).

$$\lg\alpha_T = \frac{-C_1(T - T_0)}{C_2 + (T - T_0)} \tag{1}$$

$\lg\alpha_T$—displacement factor;
C_1,C_2—constant values;
T—test temperature (°C);
T_0—reference temperature (°C).

In this paper, a sigmoidal model is used to fit the translated complex modulus. The sigmoidal model is shown in Equation (2).

$$\lg(G^*) = \delta + \frac{\alpha}{1 + e^{\beta + \gamma(\lg f_r)}} \tag{2}$$

G^*—complex modulus (MPa);
f_r—curtailment frequency (Hz);
δ—low-frequency asymptote of lg$G$*;
$\delta + \alpha$—high-frequency asymptotic values of lg$G$*;

β, γ—shape adjustment parameters.

The reference temperature selected for the complex modulus master curve in this paper is 64 °C. Figure 14 shows the master curve of the complex modulus for each asphalt sample, obtained by translational fitting of the test data.

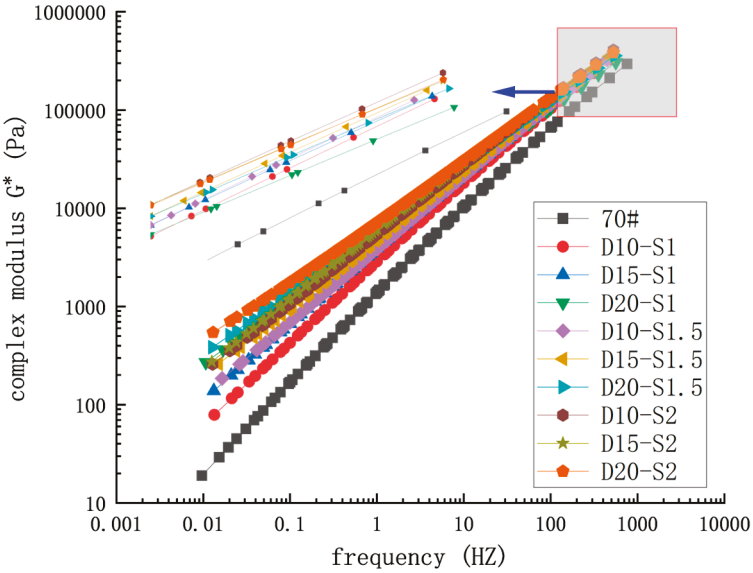

Figure 14. Complex modulus main curve.

As the modifier dosage increases, the complex modulus of the composite-modified asphalt improves further. At a frequency of 1 Hz, when the activated rubber dosage in the composite-modified asphalt increases from 10% to 20%, the complex modulus improves by 85.3%. Similarly, when the SBS dosage increases from 1% to 2%, the complex modulus improves by 89.0%. When the activated rubber dosage increases from 10% to 20% and the SBS dosage increases from 10% to 20%, or when the activated rubber dosage increases from 10% to 20% and the SBS dosage increases from 1% to 2%, the complex modulus increases by 150.6%. Increasing the dosage of activated rubber or SBS in asphalt leads to a greater amount of these modifiers participating in the swelling reaction, enhancing the asphalt's modification. At the same time, the dispersion of micro-sized asphalt particles increases as the crosslinking network density grows, thereby improving the composite-modified asphalt's resistance to shear deformation.

3.3.2. Multiple Stress Creep Recovery Test

The multiple Stress creep recovery test is a commonly used method for evaluating the high-temperature rheological properties of modified asphalt, and it more effectively simulates the loading conditions that asphalt pavements experience during actual use. This test was conducted according to AASHTO Designation: T 350–19 [33], with a test temperature of 60 °C in this paper.

The test results are presented in Figures 15 and 16. The recovery rates at stresses of 0.1 kPa and 3.2 kPa are calculated using Equations (3) and (4):

$$R_{0.1} = \frac{SUM[\in_r (0.1, N)]}{10} \text{ for N } = \text{ 11 to 20} \tag{3}$$

$$R_{3.2} = \frac{SUM[\in_r (3.2, N)]}{10} \text{ for N } = \text{ 1 to 10} \tag{4}$$

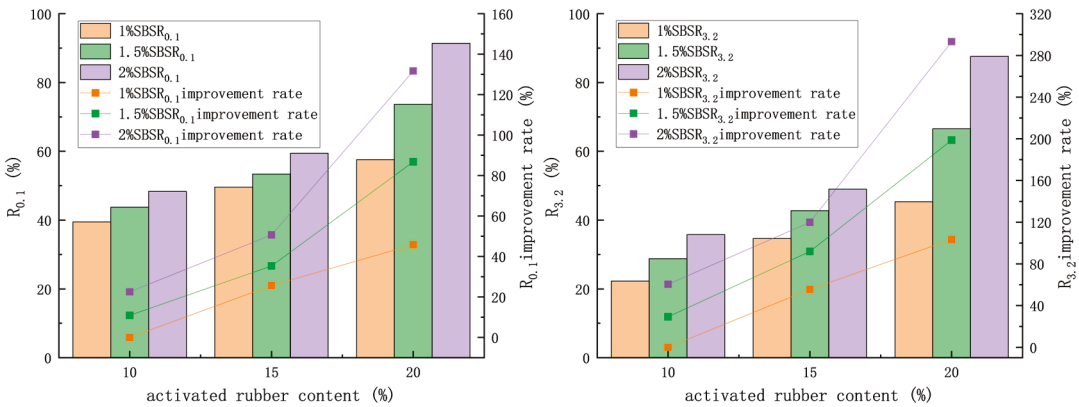

Figure 15. Asphalt recovery rate under stress.

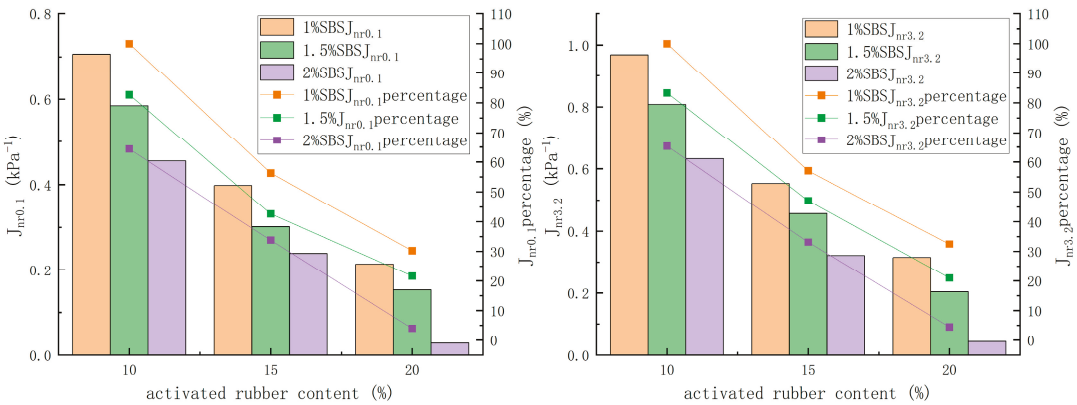

Figure 16. Nonrecoverable creep compliance under stress.

$R_{0.1}$—recovery percent at 0.1 kPa;

$R_{3.2}$—recovery percent at 3.2 kPa;

$\in_r$—recovery rate under a single cycle.

The nonrecoverable creep compliance at stresses of 0.1 kPa and 3.2 kPa is calculated using Equations (5) and (6):

$$J_{\mathrm{nr}0.1} = \frac{SUM[J_{nr}(0.1, N)]}{10} \text{ for N } = \text{ 11 to 20} \tag{5}$$

$$J_{\mathrm{nr}3.2} = \frac{SUM[J_{nr}(3.2, N)]}{10} \text{ for N } = \text{ 1 to 10} \tag{6}$$

$J_{nr0.1}$—nonrecoverable creep compliance at 0.1 kPa;

$J_{nr3.2}$—nonrecoverable creep compliance at 3.2 kPa;

J_{nr}—nonrecoverable creep compliance under a single cycle.

With an activated rubber dosage of 10% and an SBS dosage of 1%, the recovery rate of compound-modified asphalt increased by 18.1% and 23.1% under 0.1 kPa and 3.2 kPa conditions, respectively, when the activated rubber dosage was increased from 10% to 20%. Meanwhile, the nonrecoverable creep compliance decreased by 69.8% and 67.5%, respectively. When the SBS dosage was increased from 1% to 2%, the recovery rate increased by 8.9% and 13.5%, respectively, and the nonrecoverable creep compliance decreased by 35.7% and 34.7%, respectively. From the results, it can be inferred that the SBS micro-sized particles, formed by the crosslinking network structure, enhance the composite-modified asphalt's ability to recover from load stress. At the same time, the deformation of the rubber in composite-modified asphalt has a more significant impact on the recovery ability than the SBS. This is because the high elasticity of the activated rubber, along with the

characteristics of the composite-modified asphalt, enhances the overall elasticity of the material.

When the activated rubber dosage increased from 10% to 20% and the SBS modifier was raised to 2%, the recovery rate of the composite-modified asphalt at 0.1 kPa and 3.2 kPa increased by 52.0% and 65.3%, respectively, while the nonrecoverable creep compliance decreased by 96.0% and 95.5%, respectively. Simultaneously increasing both modifier dosages improves the deformation recovery ability of composite-modified asphalt more than increasing a single modifier dosage, indicating that the higher dosage of one modifier positively impacts the efficiency of the other modifier's effect. This may be due to the activation of both rubber and SBS in the asphalt, which enhances the efficiency of the modified composite asphalt and the formation of a crosslinking network structure between the rubber and SBS. Compared to the crosslinked network structure of a single modifier, the network structure of the modified asphalt enhances its performance.

4. Conclusions

4.1. Conclusions

In this paper, changes in the composition and micro-morphology of activated rubber-SBS composite-modified asphalt during the modification process were analyzed using infrared spectroscopy and SEM scanning. The impact of rubber activation on the modification process of composite-modified asphalt was also discussed. The effects of activated rubber and SBS dosage on the properties of composite-modified asphalt were also investigated using frequency scanning and MSCR tests:

(1) According to the infrared spectroscopy results, conventional rubber in the asphalt dissolution reaction absorbs a large number of light components, which are released during the degradation process. However, the high degree of internal crosslinking in conventional rubber results in low degradation efficiency, causing the light component content of conventional rubber/SBS composite-modified asphalt to be lower than that of the base asphalt;

(2) The swelling reaction process of activated rubber and SBS modifier in asphalt is similar to that of conventional rubber, but the former two are more compatible with asphalt and degrade more easily. After the swelling reaction, no new chemical compositions are formed in the composite-modified asphalt, indicating that the swelling reaction of activated rubber and SBS modifier in the asphalt is primarily physical;

(3) Conventional rubber undergoes a swelling reaction during the mixing stage. When the volume of conventional rubber expands, the initial modification of the asphalt occurs. However, due to the high degree of cross-linking within the rubber, many large-volume particles of conventional rubber remain in the asphalt even after the modification process. These particles negatively affect both the performance and viscosity of the composite-modified asphalt;

(4) The two types of modifiers have high compatibility with asphalt, and after shear, they undergo significant dissolution reactions. In the development stage, complete degradation occurs, and a large number of microvolume particles are dispersed in the asphalt. These microvolume particles can form a cross-linked network structure, enhancing the performance of the asphalt;

(5) Activated rubber and SBS improve the asphalt's resistance to shear deformation under high-temperature conditions and enhance its deformation recovery ability. Increasing the dosage of both modifiers further improves the asphalt's high-temperature resistance and enhances its deformation performance. The interaction between the two types of modifiers enhances the modification efficiency of asphalt's resistance to high-temperature deformation.

4.2. Limitations and Future Work

This research primarily focuses on the microscopic aspects of rubber-modified asphalt, with limited exploration of the processing technology of activated rubber and the fatigue resistance of activated rubber-modified asphalt. However, due to time and resource constraints, a comprehensive analysis of related research is lacking. Additionally, there has been no in-depth exploration of the road performance, durability, and other aspects of asphalt mixtures. Future research will comprehensively address the topics mentioned above.

Author Contributions: Conceptualization, K.Z.; formal analysis, X.Z. and W.W.; methodology, H.Z. and X.H.; investigation, X.H.; writing—original draft preparation, K.Z. and B.L.; writing—review and editing, W.W., K.Z. and X.Z.; supervision, K.Z.; project administration, W.W.; funding acquisition, W.W. and K.Z. All authors have read and agreed to the published version of the manuscript.

Funding: This work was financially supported by 1. Jiangxi Province Ganpo Juncai Support Plan—Double High Leading Talents Project; 2. The Natural Science Foundation in Jiangxi Province (Project No. 20212BAB214042); 3. Jiangxi Province Transportation Investment Group Limited Liability Company General Science and Technology Project (Project No. 2023JT0028).

Institutional Review Board Statement: Not applicable.

Informed Consent Statement: Not applicable.

Data Availability Statement: The data that support the findings of this study are available from the corresponding author upon reasonable request.

Conflicts of Interest: The authors declare that the research was conducted in the absence of any commercial or financial relationships that could be construed as a potential conflict of interest.

References

1. Bamigboye, G.O.; Bassey, D.E.; Olukanni, D.O.; Ngene, B.U.; Adegoke, D.; Odetoyan, A.O.; Kareem, M.A.; Enabulele, D.O.; Nworgu, A.T. Waste Materials in Highway Applications: An Overview on Generation and Utilization Implications on Sustainability. *J. Clean. Prod.* **2020**, *283*, 124581. [CrossRef]
2. Ma, Y.; Wang, S.; Zhang, M.; Jiang, X.; Polaczyk, P.; Huang, B. Weather Aging Effects on Modified Asphalt with Rubber-Polyethylene Composites. *Sci. Total Environ.* **2023**, *865*, 161089. [CrossRef] [PubMed]
3. Yin, D.; Wang, L.; Wang, Z.; Yin, L.; Liu, S.; Li, L. Enhancing Shear Resistance in Pavement Structures with Crumb Rubber Modified Asphalt Gravel as A Bonding Layer. *Constr. Build. Mater.* **2024**, *426*, 136184. [CrossRef]
4. Yu, X.; Xie, Y.; Yao, H.; Wang, S. Excellent Low Temperature Performance for Modified Asphalt by Finely Dispersed Sidewall Tire Rubber. *Constr. Build. Mater.* **2023**, *392*, 131939. [CrossRef]
5. Dong, F.; Wang, S.; Yang, Y.; Yu, X.; Jiang, Y.; Zhang, R. Conventional Properties, Rheological Characteristics, and Thermal Performance of Waste Polyurethane Modified Asphalt with Butyl Rubber. *Constr. Build. Mater.* **2024**, *411*, 134460. [CrossRef]
6. Duan, K.; Wang, C.; Liu, J.; Song, L.; Chen, Q.; Chen, Y. Research Progress and Performance Evaluation of Crumb-Rubber-Modified Asphalts and Their Mixtures. *Constr. Build. Mater.* **2022**, *361*, 129687. [CrossRef]
7. Yang, S.; Zhu, H.; Tan, Q.; Yang, X.; Chen, Y.; Lei, L. Application of TOR as A Secondary Modifier for the Preparation of Crumb Rubber Modified Asphalt with Excellent Storage Stability. *Constr. Build. Mater.* **2024**, *428*, 135863. [CrossRef]
8. Adnan, M.A.; Wang, J. Investigation of the Effects of Nano-Al_2O_3 Addition on Compatibility, Rutting and Fatigue Properties of Styrene-Butadiene-Rubber Modified Asphalt. *Constr. Build. Mater.* **2024**, *416*, 135267. [CrossRef]
9. Bian, G.; Qi, L.; Liu, J.; Wang, X.; Xu, X.; Wang, Z. Effects of Tetraethyl Orthosilicate on Rheological Behaviors of Crumb Rubber Modified Asphalt. *Constr. Build. Mater.* **2022**, *325*, 126807. [CrossRef]
10. Jin, Y.; Yu, X.; Dong, F.; Wang, S.; Jiang, Y.; Lu, J. The Improvement of Various Polyethylene on the High-Temperature Performance of Degraded Ground Tire Rubber Modified Asphalt and the Compatibility Enhancement Mechanism of Compatibilizer for Composite Modified Asphalt. *Constr. Build. Mater.* **2024**, *427*, 136255. [CrossRef]
11. Xiang, Y.; Xie, Y.; Long, G.; Zeng, L. Ultraviolet Irradiation of Crumb Rubber on Mechanical Performance and Mechanism of Rubberised Asphalt. *Road Mater. Pavement Des.* **2019**, *20*, 1624–1637. [CrossRef]
12. Hosseinnezhad, S.; Kabir, S.F.; Oldham, D.; Mousavi, M.; Fini, E.H. Surface functionalization of rubber particles to reduce phase separation in rubberized asphalt for sustainable construction. *J. Clean. Prod.* **2019**, *225*, 82–89. [CrossRef]

13. Feng, X.; Liang, H.; Dai, Z. Rheological properties and microscopic mechanism of waste cooking oil activated waste crumb rubber modified asphalt. *J. Road Eng.* **2022**, *2*, 357–368. [CrossRef]
14. Adnan, M.A.; Wang, J. Enhancement of Rheological Performance and Compatibility of Tire Rubber-Modified Asphalt Binder with the Addition of Graphene. *Constr. Build. Mater.* **2023**, *402*, 133038. [CrossRef]
15. Zhang, J.; Chen, M.; Leng, B.; Wu, S.; Chen, D.; Zhao, Z. Investigation on Storage Stability, H2S Emission and Rheological Properties of Modified Asphalt with Different Pretreated Waste Rubber Powder. *J. Clean. Prod.* **2024**, *456*, 142469. [CrossRef]
16. Zhou, T.; Kabir, S.F.; Cao, L.; Luan, H.; Dong, Z.; Fini, E.H. Comparing Effects of Physisorption and Chemisorption of Bio-Oil onto Rubber Particles in Asphalt. *J. Clean. Prod.* **2020**, *273*, 123112. [CrossRef]
17. Liu, Q.; Liu, J.; Yu, B.; Zhang, J.; Pei, J. Evaluation and Optimization of Asphalt Binder and Mixture Modified with High Activated Crumb Rubber Content. *Constr. Build. Mater.* **2022**, *314*, 125676. [CrossRef]
18. Wu, W.; Jiang, W.; Xiao, J.; Yuan, D.; Wang, T.; Xing, C. Analysis of Thermal Susceptibility and Rheological Properties of Asphalt Binder Modified with Microwave Activated Crumb Rubber. *J. Clean. Prod.* **2022**, *377*, 134488. [CrossRef]
19. Yin, L.; Yang, X.; Shen, A.; Wu, H.; Wu, H.; Lyu, Z.; Li, B. Mechanical Properties and Reaction Mechanism of Microwave-Activated Crumb Rubber-Modified Asphalt before and after Thermal Aging. *Constr. Build. Mater.* **2021**, *267*, 120773. [CrossRef]
20. Mousavi, M.; Hosseinnezhad, S.; Kabir, S.F.; Burnett, D.J.; Fini, E.H. Reaction Pathways for Surface Activated Rubber Particles. *Resour. Conserv. Recycl.* **2019**, *149*, 292–300. [CrossRef]
21. Wang, R.; Xu, G.; Chen, X.; Zhou, W.; Zhang, H. Evaluation of Aging Resistance for High-Performance Crumb Tire Rubber Compound Modified Asphalt. *Constr. Build. Mater.* **2019**, *218*, 497–505. [CrossRef]
22. Wang, S.; Gao, Y.; Yan, K.; You, L.; Jia, Y.; Dai, X.; Chen, M.; Diab, A. Effect of Long-Term Aging on Waste Tire Rubber and Amorphous Poly Alpha Olefin Compound Modified Asphalt Binder and Its Mixtures. *Constr. Build. Mater.* **2021**, *272*, 121667. [CrossRef]
23. Xie, N.; Peng, X.; He, Y.; Lei, W.; Pu, C.; Meng, H.; Ma, H.; Tan, L.; Zhao, P. Investigation on Performance and Durability of Bone Glue and Crumb Rubber Compound Modified Asphalt and Its Mixture. *Case Stud. Constr. Mater.* **2023**, *19*, e02437. [CrossRef]
24. Xue, Y.; Ge, D.; Lv, S.; Duan, D.; Deng, Y. Evaluation of Asphalt Modified with Bio-Oil and High Rubber Content: Low Temperature and Short Mixing Time Production Condition. *Constr. Build. Mater.* **2023**, *408*, 133656. [CrossRef]
25. Qian, C.; Fan, W.; Liang, M.; He, Y.; Ren, S.; Lv, X.; Nan, G.; Luo, H. Rheological Properties, Storage Stability and Morphology of CR/SBS Composite Modified Asphalt by High-Cured Method. *Constr. Build. Mater.* **2018**, *193*, 312–322. [CrossRef]
26. Kumar, A.; Choudhary, R. Effect of Microwave Pretreatment on Characteristics of Asphalt Binders Modified with Scrap Non-Tire Automotive Rubber and Waste Derived Pyrolytic Oils After Prolonged Thermal Storage. *Constr. Build. Mater.* **2024**, *419*, 135558. [CrossRef]
27. Rasool, R.; Song, P.; Wang, S. Thermal Analysis on the Interactions Among Asphalt Modified with SBS and Different Degraded Tire Rubber. *Constr. Build. Mater.* **2018**, *182*, 134–143. [CrossRef]
28. *JTG E20-2011*; Standard Test Methods of Bitumen and Bituminous Mixtures for Highway Engineering. Ministry of Transport: Beijing, China, 2011.
29. Xu, O.; Rangaraju, P.R.; Wang, S.; Xiao, F. Comparison of Rheological Properties and Hot Storage Characteristics of Asphalt Binders Modified with Devulcanized Ground Tire Rubber and Other Modifiers. *Constr. Build. Mater.* **2017**, *154*, 841–848. [CrossRef]
30. Zhao, Z.; Wu, S.; Xie, J.; Yang, C.; Yang, X.; Wang, F.; Liu, Q. Utilization of High Contents Desulfurized Crumb Rubber in Developing an Asphalt Rubber Pellets Modified Asphalt. *Constr. Build. Mater.* **2023**, *402*, 133043. [CrossRef]
31. Zhou, Y.; Xu, G.; Leng, Z.; Kong, P.; Wang, H.; Yang, J.; Qiu, W.; Xu, Z.; Chen, X. Investigation on Storage Stability and Rheological Properties of Environment-Friendly Devulcanized Rubber Modified Asphalt. *Phys. Chem. Earth Parts A/B/C* **2022**, *129*, 103332. [CrossRef]
32. *AASHTO-T315*; Standard Method of Test for Determining the Rheological Properties of Asphalt Binder Using a Dynamic Shear Rheometer (DSR). ASTM International: West Conshohocken, PA, USA, 2022.
33. *AASHTO-T350-19*; Standard Method of Test for Multiple Stress Creep Recovery(MSCR) Test of Asphalt Binder Using a Dynamic Shear Rheometer (DSR). ASTM International: West Conshohocken, PA, USA, 2023.

Disclaimer/Publisher's Note: The statements, opinions and data contained in all publications are solely those of the individual author(s) and contributor(s) and not of MDPI and/or the editor(s). MDPI and/or the editor(s) disclaim responsibility for any injury to people or property resulting from any ideas, methods, instructions or products referred to in the content.

materials

MDPI

Article

Physical, Mechanical, and Durability Performance of Olive Pomace Ash in Eco-Friendly Mortars

Besma Belaidi [1], Abderraouf Messai [2], Cherif Belebchouche [1,2], Mourad Boutlikht [2], Kamel Hebbache [2,3], Abdellah Douadi [2,3] and Laura Moretti [4,*]

[1] Materials and Durability of Constructions Laboratory, Department of Civil Engineering, Faculty of Sciences of Technology, University of Constantine 1 Frères Mentouri, Constantine 25000, Algeria; besma.belaidi@umc.edu.dz (B.B.); cherif.belebchouche@univ-setif.dz (C.B.)

[2] Civil Engineering Research Laboratory of Sétif (LRGCS), Department of Civil Engineering, Setif 1 University-Ferhat Abbas, Sétif 19000, Algeria; abderraouf.messai@univ-setif.dz (A.M.); mouradboutlikht@gmail.com (M.B.); hebbache.kamel@univ-setif.dz (K.H.); abdellah.douadi@univ-setif.dz (A.D.)

[3] Emergent Materials Research Unit (EMRU), Setif 1 University-Ferhat Abbas, Sétif 19000, Algeria

[4] Department of Civil, Building and Environmental Engineering, Sapienza University of Rome, Via Eudossiana 18, 00184 Rome, Italy

* Correspondence: laura.moretti@uniroma1.it; Tel.: +39-064-458-5120

Abstract

The cement industry is a major contributor to global CO_2 emissions, driving the research for sustainable alternatives. Olive biomass ash (OBA), a byproduct from burning all types of biomass from the olive tree, has emerged as a potential supplementary cementitious material (SCM). This study investigates the effects of incorporating olive pomace ash (OPA) as a partial cement substitute (0% to 50% by weight) on mortar properties over extended curing periods. Workability, compressive and flexural strengths, water absorption, and freeze–thaw resistance were evaluated. Up to 20% OPA replacement improved workability while maintaining acceptable strength and durability. Beyond this level, mechanical properties and frost resistance decreased significantly. Correlation analyses revealed strong relationships between flow time and wet bulk density (R^2 = 0.93), an exponential relationship between 28-day compressive strength and water absorption (R^2 = 0.87), and linear correlations between pre- and post-freeze–thaw mechanical properties ($R^2 \geq 0.99$ for both compressive and flexural strengths). The results demonstrate that optimal OPA incorporation enhances mortar performance without compromising structural integrity and provides a viable strategy for valorizing agricultural waste.

Keywords: secondary raw materials; mortar; olive; pomace ash; biomass ash; cement substitute

1. Introduction

Cement production exceeds 4 billion tons annually, contributing approximately 8% to global CO_2 emissions [1] due to high-temperature processing and limestone calcination [2]. In response to increasing environmental concerns [3], greener binders based on supplementary cementitious materials (SCMs) have become a pressing need. Industrial byproducts, such as fly ash, silica fume, and slag, have been extensively studied; however, alternative biomass-derived ashes remain underexplored [4].

Biomass ashes demonstrate pozzolanic actions ideal for optimizing concrete attributes and sustainability [5]. Olive biomass ash represents a promising SCM among biomass

ashes, given the vast quantities generated by the global olive oil industry, particularly in Mediterranean regions [6]. Olive pomace, a residual biomass from olive oil extraction, when thermally processed, yields an ash rich in silica and other pozzolanic compounds. Biomass ash SCMs can curtail the cement factory and embodied carbon footprint of concrete while also furnishing a waste valorization outlet for biomass ashes otherwise destined for landfills [7]. Although preliminary studies have indicated potential benefits in enhancing durability and mechanical properties, knowledge gaps persist regarding long-term performance and durability under aggressive environmental conditions [8]. Therefore, systematic research tailored to each spectrum of biomass residues is imperative to harness their application potential as eco-friendly SCMs.

Olive waste ash (OWA) shines as a remarkably high-potential yet understudied biomass ash SCM, courtesy of the expansive global olive oil business, which churns out millions of tons of this agricultural waste annually [9]. The annual world olive oil output surpasses 3 million metric tons, with premier producers around the Mediterranean basin encompassing European countries, like Spain, Italy, and Greece [10]. The scale of global olive farming necessitates substantial olive waste generation, with over 10 million hectares of olive groves worldwide [11]. Consequently, the countries flanking the Mediterranean Sea produce millions of tons of OWA yearly [12]. Historically, these leftover materials were disposed of through practices like landfills or open incineration, leading to environmental pollution. Nevertheless, the lignocellulosic characteristics of olive stones and their notable silica content have recently drawn attention due to their potential applications in the construction and development of building materials [4,13].

Over the last decade, numerous investigations have examined the integration of OWA into cementitious binders and mortar/concrete systems. Al-Akhras and Abdulwahid [14] examined mortar compositions that featured the addition of OWA, replacing portions of sand and cement. The substitution of sand with 5–20% OWA boosted the 28-day compressive strength (CS28), escalating from 26.5 to 38.2 MPa. However, the cement replacement reduced the strength because of the dilution of cementitious compounds. Incorporating OWA enhanced durability against alkali–silica reactions, with improvements observed up to a 20% addition [15], and resistance to high temperatures [16].

Cuenca et al. [17] reported that including 10–15% OWA upheld the compressive strength of self-compacting concretes similar to control compositions. Microstructure analysis disclosed refinements in the distribution of pore sizes and disconnection between pores. Eliche-Quesada and Leite-Costa [18] employed OWA to substitute natural sand in fired clay bricks, leading to better thermal insulation and mechanical performance. Beltran et al. [19] determined that introducing OWA into masonry mortars increased porosity and water absorption, albeit with a slight reduction in mechanical strength. They advised regulating workability and strength by adjusting the fineness and texture of OWA particles. Font et al. [20] synthesized binders consisting of 100% OWA–slag, revealing notable early strength development and resistance against acid attacks. Payá et al. [21] modified the reactivity of OWA through thermal and chemical treatments to optimize its performance as a supplementary cementitious material in both fresh and hardened states.

Collectively, the prior research underscores the promising potential of OWA as a sustainable substitute for cement at moderate proportions, effectively enhancing the attributes and ecological profile of cementitious systems. However, there are still significant knowledge gaps, particularly regarding the long-term properties and durability performance of OWA-modified concretes. Most studies have been limited to short-term analysis without systematically evaluating the influence of OWA across extended curing ages. Moreover, in-depth investigations correlating the microstructure and durability indicators are lacking.

This study investigates the properties of mortars incorporating olive pomace ash (OPA) by varying curing periods and replacement ratios. Olive pomace ash (OPA) is the byproduct after olive oil extraction, typically a mix of olive skins, pulp, and crushed pits. It is added at replacement levels of 0%, 10%, 20%, 30%, 40%, and 50% by weight of cement. The effect of different OPA ratios on the compressive and flexural strength development at 7, 28, and 90 days is analyzed. The mortars' water absorption, wet bulk density, flow time, and freeze–thaw resistance are evaluated to determine the durability performance. Correlation analyses further elucidate the relationships among key parameters. The findings aim to advance the sustainable use of OPA in eco-friendly construction materials.

2. Materials and Methods

2.1. Raw Materials

The binder used in this study was an Ordinary Portland Cement (OPC) conforming to CEM I 42.5 R, sourced from the Biskria plant in Algeria and compliant with the NA 442-2013 standard [22]. Its mineralogical composition, derived from Bogue calculations [23], included tricalcium silicate (C3S) at 65.15% and dicalcium silicate (C2S) at 8.45%, with the remainder comprising calcium aluminate and aluminoferrite phases. The OPC had a specific surface area of 3510 cm^2/g and a specific gravity of 3.09 g/cm^3. The X-ray Fluorescence revealed a composition rich in CaO (63.20%) and SiO_2 (19.39%), consistent with typical Portland clinker chemistry (Table 1).

Table 1. Chemical composition of the OPC.

Oxides	SiO_2	Al_2O_3	Fe_2O_3	CaO	MgO	SO_3	K_2O	Na_2O	L.O.I.
%	19.4	4.74	3.25	63.18	3.2	2.56	0.63	0.25	2.67

The olive pomace ash (OPA) was collected from an olive oil extraction facility in Zardaza, Algeria. The residual olive waste was incinerated and ground to produce a fine powder. The OPA had a specific surface area of 4811 cm^2/g and a specific gravity of 2.18 g/cm^3. Chemical analysis revealed a high content of CO_2 (53.2%), along with significant amounts of lime (10.1%) and silica (11.50%), and smaller fractions of iron, aluminum, and magnesium oxides, as presented in Table 2.

Table 2. Chemical composition of the OPA.

Oxides	SiO_2	Al_2O_3	Fe_2O_3	CaO	MgO	SO_3	K_2O	Na_2O
%	11.5	2.82	1.48	10.1	1.49	3.27	0.331	2.14

Figure 1 reveals key differences between the particle size distribution of OPC and OPA. The OPC particles range from 6.45 μm at the 10th percentile to 50.69 μm at the 90th percentile, with a median size of 23.9 μm. In contrast, the OPA exhibits a finer distribution, spanning 5.23 μm to 18.83 μm for the 10th and 90th percentiles, respectively, and a median of 11.36 μm. The extensive grinding process is responsible for the OPA's finer particle size. The OPC has a more spread-out distribution, extending to larger sizes, typical for cement manufactured through clinker grinding.

The fine aggregate used was standard siliceous sand, compliant with EN 196-1 [24]. The sand was clean, naturally sourced, and displayed a sub-rounded morphology, suitable for mortar production.

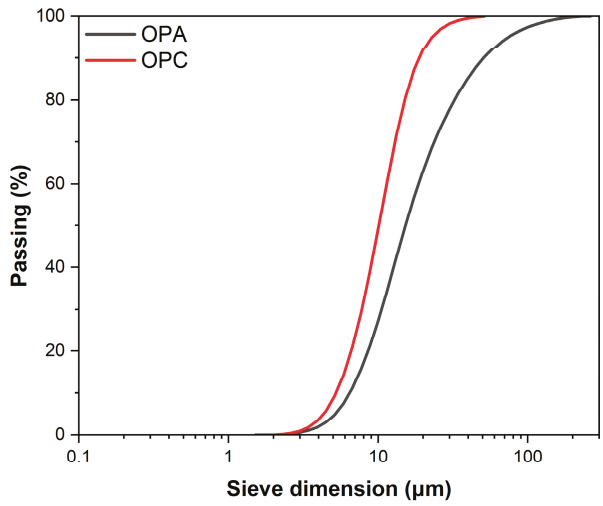

Figure 1. Particle size distribution of OPC and OPA.

2.2. Mix Formulations

Six mortar mixtures were prepared with varying proportions of OPC and OPA, as per EN 196-1 specifications [24]. Table 3 presents the mix proportioning by weight. The control mixture (MC) contained 100% OPC, while the other mixtures were designed with partial replacement of OPC by 10% to 50% OPA in increments of 10%, added by weight of cement. The binder (OPC + OPA)-to-fine-aggregate ratio was maintained at 1:3 for all mixtures. Water was added to achieve a constant water-to-binder ratio (W/B) of 0.5 by weight.

Table 3. Formulation details of mortar mixtures.

Mix ID	OPC (g)	OPA (%)	OPA (g)	Water (g)	W/B	Sand (g)
MC	450	0	0	225	0.50	1350
MP10	405	10	45			
MP20	360	20	90			
MP30	315	30	135			
MP40	270	40	180			
MP50	225	50	225			

Mortars were cast in three layers into 40 × 40 × 160 mm^3 prismatic molds, with each layer compacted to minimize air entrapment. After 24 h of curing under ambient conditions, the specimens were demolded and submerged in water at 23 °C until the testing day (Figure 2).

Figure 2. Prismatic specimens.

2.3. Experimental Testing Procedure

The Flow Time (FT) Test measures the time a fixed volume of mortar takes to flow and reach a specified mark under standard vibration according to ASTM C1437 [25]. A conical mold was filled with fresh mortar in two layers, each tamped 10 times. Upon mold removal, the spread time to a 100 mm diameter on a vibrating table was recorded. The time between mold lift-off and when the mortar front touched the 100 mm mark was recorded as the flow time.

The bulk density of fresh mortar was determined as per EN 1015-6 [26]. A known volume of mortar was compacted into a pre-weighed 1 L container. The mass of the container plus the wet mortar was recorded. The net mass of the mortar was divided by the volume to calculate the wet bulk density in kg/m^3. A lower density indicated improved particle packing and workability. The test was conducted at the same flow table consistency used for the molding specimens.

According to [24], a 3000 kN capacity universal testing machine was employed to perform compressive and flexural tests at 7 days, 28 days, and 90 days, using prismatic specimens ($40 \times 40 \times 160$ mm^3). The ultimate flexural and compressive strength was ascertained by averaging the strength values obtained from three samples per mix.

The water absorption (WA) test was conducted according to EN 13057 [27]. Three identical specimens were selected for each mixture. These specimens underwent drying at 105 ± 5 °C until a consistent mass was attained, following EN 13057 requirements [27]. Subsequently, the dried specimens were immersed in water for 24 h to achieve full saturation. Post-immersion, the specimens were carefully cleaned, and the resulting mass increase was measured after 28 days under saturated-surface-dry conditions.

After 90 days of curing, the specimens were exposed to 300 freeze–thaw cycles between −15 °C and +15 °C. Their strengths were re-evaluated post-exposure to assess residual mechanical properties and determine frost resistance.

2.4. Correlation Analysis

The correlation analysis examined the quantitative interrelationships between key properties to derive meaningful insights into the influence of OPA incorporation on the fresh and hardened performance of sustainable mortars. In particular, this study focused on the following:

- FT vs. WBD to assess how particle morphology and packing influence workability;
- Residual vs. 90-day compressive and flexural strengths to model freeze–thaw durability;
- CS28 vs. WA to explore the interdependence between mechanical performance and permeability.

3. Results and Discussion

Table 4 summarizes the experimental results of this study.

Table 4. Experimental results.

Mix ID	WBD (kg/m^3)	FT (s)	CS7 (MPa)	CS28 (MPa)	CS90 (MPa)	FS7 (MPa)	CF28 (MPa)	CF90 (MPa)	WA (%)
MC	2202	3	41.27	51.86	60.35	6.45	6.8	7.45	5.31
MP10	2200	8	38.48	42.7	48.36	5.15	6.15	6.31	5.23
MP20	2180	36	36.04	39.18	42.25	4.9	5.09	5.37	5.53
MP30	2178	124	33.96	37.66	39.49	4.29	4.293	4.66	5.86
MP40	2158	159	26.17	29.67	31.93	2.25	3.149	4.21	6.23
MP50	2136	265	18.47	21.52	24.42	1.77	2.33	2.89	6.92

3.1. Wet Bulk Density

Figure 3 illustrates the decreasing trend in wet bulk density (WBD) as the replacement of OPC with OPA increases. The reference mixture MC recorded the highest wet bulk density (2202 kg/m^3), which decreased by 3.0% to 2136 kg/m^3 at 50% OPA replacement (MP50). This trend is attributed primarily to the lower specific gravity of OPA (2.18 g/cm^3) compared to OPC (3.09 g/cm^3). The OPC substitution with lighter OPA reduces the overall mass per unit volume. Moreover, the high porosity and irregular morphology of OPA particles hinder effective packing, introducing more voids and thus lowering bulk density. This trend aligns with OPA's lower particle density (2.18) versus OPC (3.09) and its porous structure [19]. The irregular particle morphology [14,17] further hinders optimal packing, increasing void content at higher replacements.

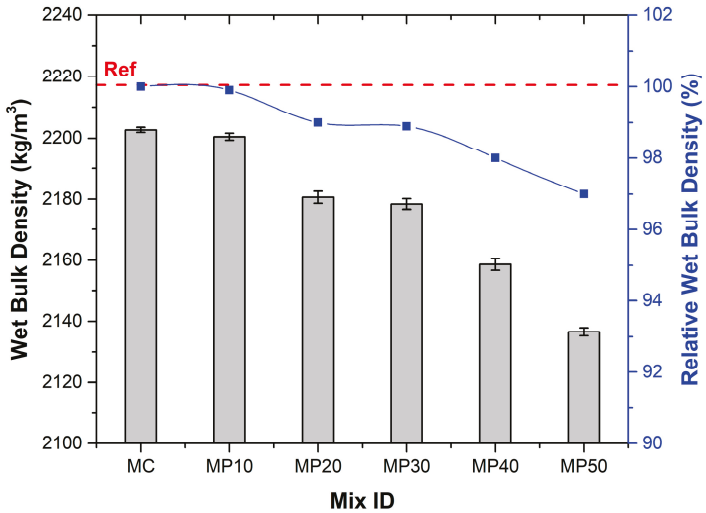

Figure 3. Relative wet bulk density results.

3.2. Flow Time

The flow time results are presented in Figure 4. They indicate a steady increase with a higher OPA content from 3 s in MC to 265 s in MP50. This reflects a substantial reduction in workability.

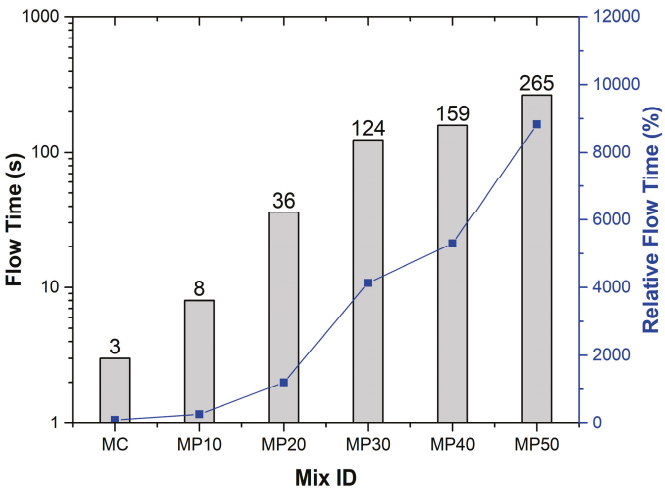

Figure 4. Flow test results.

The angular and porous nature of OPA particles, internal friction, and water demand limit the mortar's ability to flow. At up to 10% OPA (MP10), the impact on flow was minimal, suggesting acceptable workability at lower substitution levels. Studies have shown

that OPA particles have highly angular, irregular, and elongated shapes compared to the spherical particles of OPC [28]. Additionally, OPA has a wide particle size distribution, including coarser particles whose angularity, irregularity, and wider size range increase inter-particle friction within the mortar, hindering the flow and mobility of the mix and requiring more time to reach the same flow diameter. The irregular OPA particles also absorb more water. These effects collectively prolong FT with increasing OPA incorporation. These findings align with [14,28–31]. Nonetheless, up to 10% OPA replacement (MP10) showed only a marginal increase in FT compared to MC. While ASTM C1437 does not specify minimum or maximum flow time requirements, practical construction applications typically recommend flow times between 15 and 60 s for adequate workability and placement efficiency, indicating that OPA replacements beyond 20% may present workability challenges in field applications.

3.3. Compressive Strength

In Figure 5, the compressive strength declines with increasing OPA content across all curing ages. The control mix exhibited strengths of 41.27 MPa (7 days), 51.86 MPa (28 days), and 60.35 MPa (90 days). At 50% OPA (MP50), these values dropped to 18.47 MPa, 21.52 MPa, and 24.42 MPa, respectively—a reduction of over 55%.

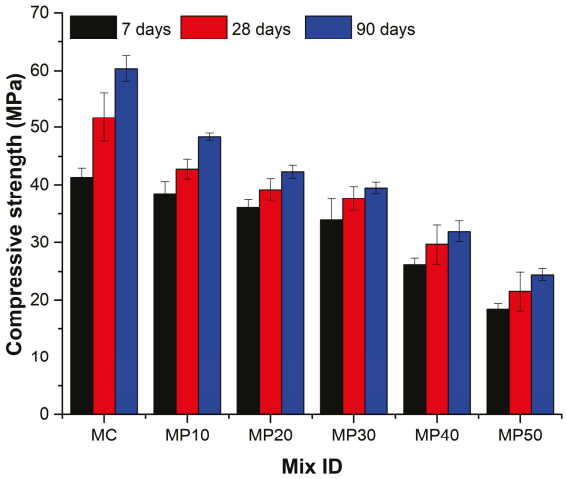

Figure 5. Compressive strength at 7, 28, and 90 days.

The superior early and later age compressive performance of MC can be attributed to the hydration of abundant calcium silicate phases in OPC. Upon hydration, C2S and C3S form calcium silicate hydrates (C-S-H) that impart higher compressive strength [32].

In contrast, the 50% OPA mixture (MP50) exhibited significantly lower strengths of 18.47 MPa, 21.52 MPa, and 24.42 MPa at 7, 28, and 90 days, respectively. This drastic 55–60% strength reduction for MP50 is likely due to a reduced availability of reactive calcium silicates and slower pozzolanic reactions of OPA [29,33]. Additionally, the higher porosity and surface roughness of OPA particles may cause poor consolidation and increased flaws in the microstructure [34–36].

The marginal 7% early age strength reduction for MP10 compared to MC indicates that limited OPA incorporation up to 10% retains enough hydrating compounds from OPC for adequate early compressive strength development. The porous structure and irregular morphology of OPA particles likely have a negligible influence at such low replacement levels. Among the intermediate OPA content mixes, MP20 achieved reasonable strengths of 36.04 MPa, 39.18 MPa, and 42.26 MPa at 7, 28, and 90 days, respectively. The 12–16% strength reduction compared to MC can be attributed to an optimal balance between OPC

hydration and OPA pozzolanic reaction at the 20% replacement level, without significant microstructural deficiencies.

Notably, strength continued to develop up to 90 days in all mixes, indicating sustained pozzolanic activity of OPA over time. MC registered a 32% strength increase between 7 and 90 days, while MP50 showed a 24.4% increase during the same period. The additional C-S-H gel formation fills pores and enhances the microstructure quality [28,37]. Thus, the increasing compressive strength trends indicate the pozzolanic behavior of OPA as a supplementary cementitious material.

EN 196-1 does not specify minimum compressive strength requirements as it focuses on test methodology; building codes typically require minimum 28-day compressive strengths of 20–25 MPa for structural mortar applications. All mixes achieved the minimum threshold of 21.52 MPa, confirming their suitability for construction use.

3.4. Flexural Strength

Figure 6 demonstrates that flexural strength followed a trend similar to compressive strength, declining as the OPA content increased.

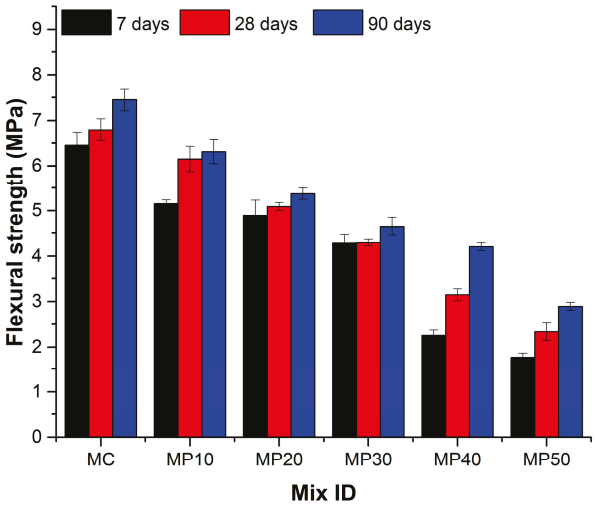

Figure 6. Flexural strength at 7, 28, and 90 days.

The control mix achieved maximum strengths of 6.45 MPa (7 days), 6.80 MPa (28 days), and 7.45 MPa (90 days), while MP50 exhibited only 2.90 MPa at 90 days (FS90). This reduction is linked to decreased C–S–H gel formation and increased porosity [38]. In contrast, MP50 exhibited significantly lower strengths of 1.78 MPa, 2.33 MPa, and 2.90 MPa at 7, 28, and 90 days, respectively. The 72% decrease in early and 61% in later age strength is likely due to the slower pozzolanic reaction of OPA and the increased porosity of mixtures. The flexural strength reduction is attributable to a decrease in the bond between the OPA surface and the OPC paste [33]. Nevertheless, the results of MP10 reveal that limited OPA incorporation up to 10% does not compromise the flexural performance. The marginal 20% early age strength reduction for MP10 compared to MC indicates that low OPA ratios retain adequate hydration products for strength development. Among the intermediate mixes, MP40 exhibited a 120% enhancement in flexural strength from 2.26 MPa at 7 days to 4.21 MPa at 90 days due to the latent pozzolanic reactivity of OPA.

3.5. Water Absorption

The 28-day WA results are in Figure 7, with relative water absorption values normalized to the control mix to enable direct comparison across different OPA replacement levels. MP10 showed slightly lower absorption (5.23%) than the control (5.31%), likely due to

fine OPA particles filling voids and refining the pore structure. At high substitution levels, the increased porosity and weak bonding at the interfacial transition zone contributed to greater water ingress. Dahim et al. [39] similarly observed a parallel pattern.

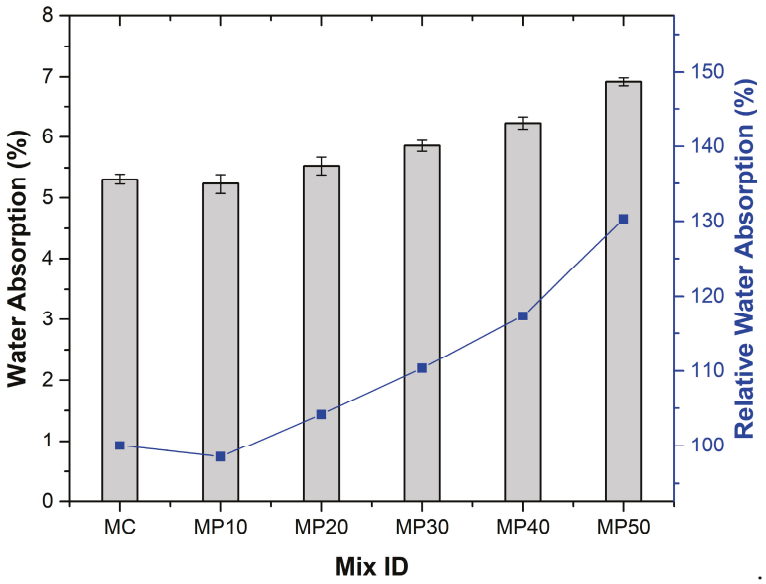

Figure 7. Water absorption results.

As the OPA replacement level increased beyond 10%, WA rose (5.53% for MP20 and 5.86% for MP30) due to the weak adhesion between the highly porous and angular OPA particles and the cementitious matrix, leading to increased interfacial transition zone porosity [40]. Additionally, the higher water demand of OPA, due to its porosity, increased the effective w/c ratio, resulting in greater capillary porosity [19]. MP40 and MP50 recorded the highest absorption, reflecting the diminished microstructural compactness at elevated OPA dosages. The high angularity and surface roughness of OPA also increase pore interconnections [41].

EN 13057 establishes the test methodology for measuring water absorption but does not specify maximum allowable limits; however, durability guidelines typically recommend water absorption values below 10–15% for adequate long-term performance. All tested mixes achieved a maximum absorption of 6.92%, well within the acceptable ranges for durable mortar applications.

3.6. Freeze–Thaw Resistance

Table 5 and Figure 8 present the 90-day residual mechanical strengths following 300 freeze–thaw cycles.

Table 5. Residual strengths and strength losses results.

Mix ID	Compressive Strength		Flexural Strength	
	Residual (MPa)	Loss (%)	Residual (MPa)	Loss (%)
MC	51.27	15.05	7.02	5.86
MP10	36.6	24.33	6.19	1.92
MP20	31.2	26.17	4.98	7.26
MP30	28.2	28.59	4.12	11.53
MP40	22.36	29.98	3.17	24.65
MP50	12.74	47.84	2.35	18.7

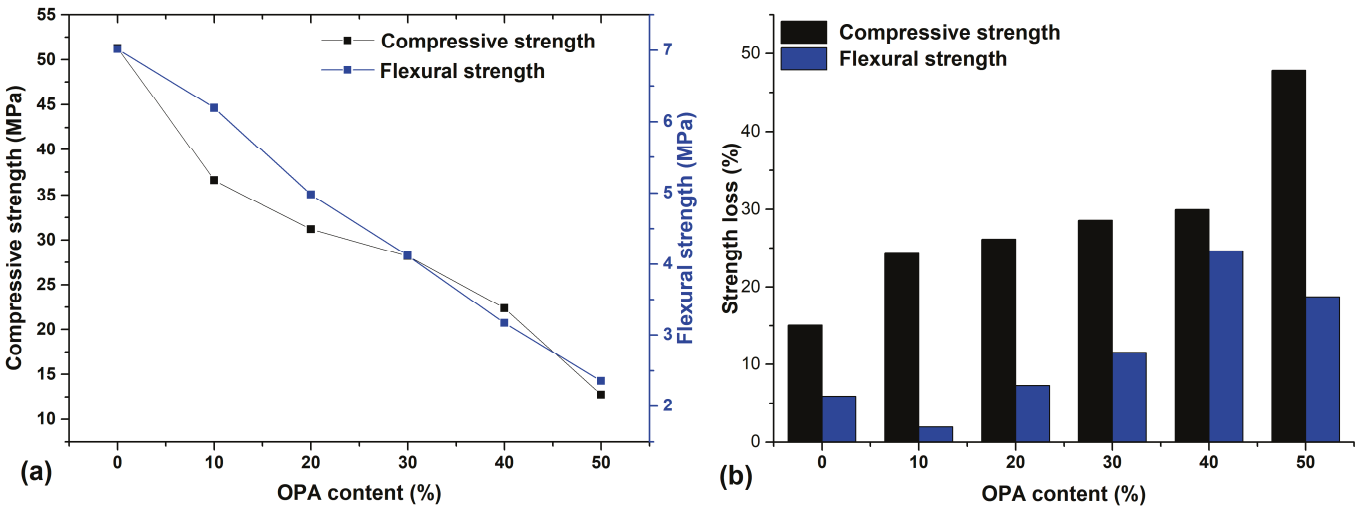

Figure 8. Freeze–thaw resistance results: (**a**) compressive and flexural strengths results; (**b**) strength loss.

The control mix (MC) retained 85% of its compressive strength, while MP10 retained 76%. The MC performance can be attributed to the adequate formation of frost-resistant calcium silicate hydrates due to the hydration of reactive compounds in OPC [42]. Residual compressive strength (RCS) declined with increasing OPA, dropping to just 52% in MP50. This vulnerability is associated with higher porosity, poor interfacial bonding, and inadequate C–S–H formation. The drastic loss of strength with higher OPA proportions can be attributed to inadequate hydration products to resist frost damage [43]. The increased porosity and poor interfacial transition zone associated with a greater OPA content likely caused accelerated microcrack formation and propagation under freezing–thawing cycles [44].

Residual flexural strength (RFS) followed a similar pattern. MC showed minimal degradation (6%), and MP10 retained 98% of its pre-exposure strength. However, strength losses increased significantly at higher OPA levels, with MP50 experiencing a 19% drop. The results confirm that OPA contents beyond 20–30% impair the freeze–thaw durability.

The poor interfacial transition zones (ITZs) and microcrack development associated with the high porosity and angular morphology of OPA particles [45] contribute to weak interfaces and propagate cryogenic cracks [46].

Freeze–thaw resistance testing standards, such as ASTM C666 [47], typically require durability factors above 60–80% (equivalent to less than 20–40% strength loss) for acceptable frost resistance. The observed 48% strength loss indicates that higher OPA replacement levels may compromise freeze–thaw durability and should be limited for applications in freeze–thaw environments.

3.7. Interpretation of the Results

Figure 9 shows the relationship between wet bulk density and flow time.

A linear regression curve with strong correlation ($R^2 = 0.93$) was identified (Equation (1)) for WBD in kg/m^3 and FT in s:

$$\text{WBD} = 2199.72 - 0.24\ \text{FT} \tag{1}$$

The highly angular, flaky, and elongated morphology of OPA particles increases inter-particle friction and reduces particle mobility within the fresh mortar matrix [48]. The irregular shapes tend to interlock, resisting flow. This effect is exacerbated by the rough surface texture of OPA particles, which further impedes sliding and rearrangement. Additionally, the porous structure of OPA particles enables a higher water demand than

OPC particles [49]. The higher water demand of OPA to reach a homogeneous state contributes to increasing FT. Furthermore, the lower specific gravity of OPA compared to OPC also causes a reduction in WBD.

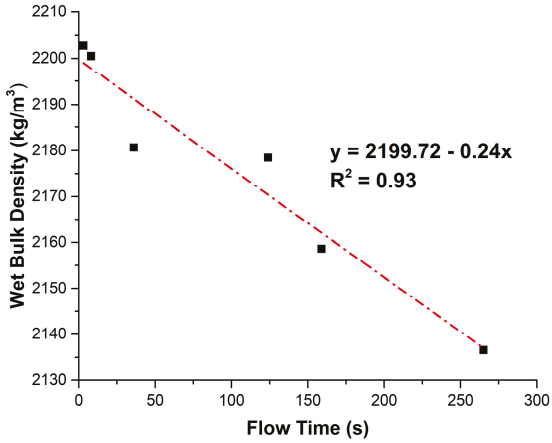

Figure 9. Relationship between wet bulk density and flow time.

The correlation between CS28 and WA was established through regression analysis, as shown in Figure 10.

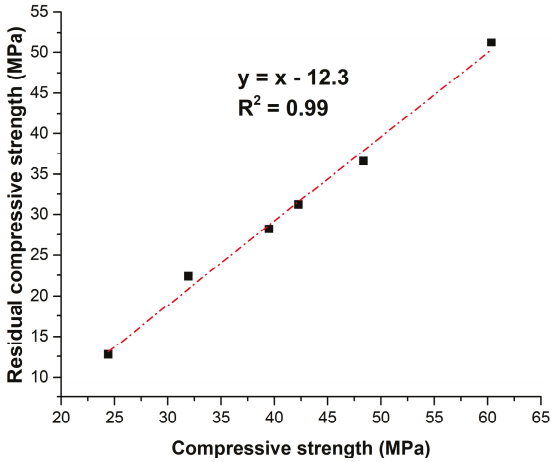

Figure 10. Relationship between compressive strength at 28 days and water absorption.

The most suitable model is exponential, according to Equation (2):

$$CS28 = 3873.88\ WA^{-2.66} \quad (2)$$

The square correlation coefficient $R^2 = 0.87$ indicates a good fit of the findings with CS28 in MPa. The relationship demonstrates that small gains in compressive strength corresponded to disproportionately large reductions in WA. This supports the notion that moderate OPA incorporation can refine pore structure and reduce permeability, although excessive replacement increases porosity and weakens the matrix. Tailoring the OPA content to balance pozzolanic pore refinement and porosity addition is critical.

Figure 11 displays the linear relationship between the residual compressive strength after 300 freeze–thaw cycles and the CS90 before exposure (Equation (3)).

$$RCS = CS90 - 12.3 \quad (3)$$

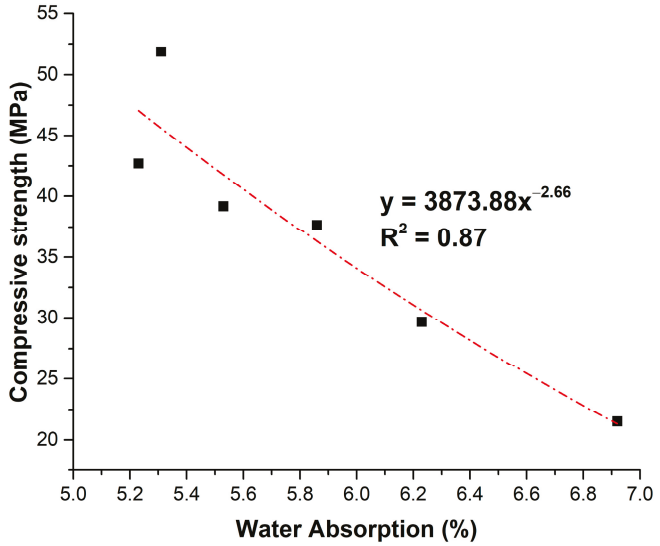

Figure 11. Relationship between residual compressive strength and compressive strength at 90 days.

The near-perfect linear correlation (R^2 = 0.99) between the variables in MPa suggests that residual compressive strength after freeze–thaw exposure is primarily governed by the initial 90-day strength. The empirical model implies a consistent strength loss regardless of mix composition.

Figure 12 illustrates the linear correlation (Equation (4)) between RFS after 300 freeze–thaw cycles and FS90.

$$\mathrm{RFS} = \mathrm{FS90} - 1, \tag{4}$$

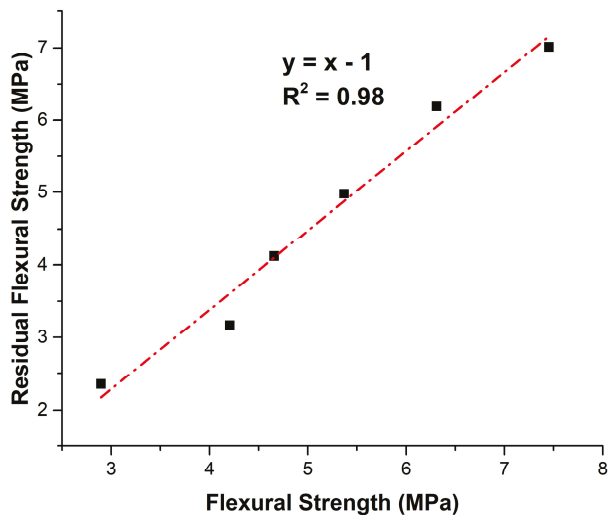

Figure 12. Relationship between residual flexural strength and flexural strength at 90 days.

A strong linear relationship (R^2 close to 1) was found for the variables in MPa. The 1 MPa reduction indicates a proportional deterioration influenced by pre-exposure strength and inherent freeze–thaw damage mechanisms. Replacement levels up to 20% OPA maintained FS90 close to the control mix and supported better freeze–thaw resistance, while higher levels reduced strength and durability due to weakened hydration and increased porosity.

3.8. Environmental Analysis

Finally, a comprehensive techno-environmental assessment was carried out to integrate the dual objectives of mechanical performance and environmental sustainability.

Olive pomace ash (OPA) demonstrated significant potential for cement manufacturing. Based on the mechanical performance and compositional criteria defined in EN 197-1 [50], the results support the feasibility of incorporating OPA into cement formulations. These findings suggest opportunities for further optimization and new cement types with OPA, contributing to more sustainable and resource-efficient binder systems. Cement production consumes about 800 and 1200 kWh/t and emits about 400 and 600 kg CO_2/t [51–54]. On the other hand, the thermal treatment and grinding of olive pomace ash requires a lower thermal energy demand, estimated at 400 to 600 kWh/t [55]. In Algeria, where electricity generation is primarily based on natural gas, the greenhouse gas emissions associated with OPA production are 200–300 kg CO_2/t. Table 6 lists the CO_2 emissions and energy consumption of the tested mixtures.

Table 6. Environmental performances.

Mix ID	Energy Consumption (kWh/t)	Emission (kg CO_2/t)
MC	1000	500
MP10	953.5	476.75
MP20	907	453.5
MP30	860.5	430.25
MP40	814	407
MP50	767.5	383.75

The findings demonstrate that the partial replacement of Portland cement with olive pomace ash (OPA) results in a substantial decrease in CO_2 emissions, highlighting its potential as a low-carbon alternative. As the substitution rate increases (from MP10 to MP50), a gradual reduction in energy consumption and CO_2 emissions is observed. For example, at 10% substitution (MP10), the grinding energy is 953.5 kWh/t, resulting in 476.75 kg CO_2/t, while at 50% substitution (MP50), the energy drops to 767.5 kWh/t, and the emissions are 383.75 kg CO_2/t. These results highlight the environmental benefits of incorporating OPA in cement formulations, particularly in terms of reduced energy demand and a lower carbon footprint, thereby contributing to more sustainable construction materials. Although a reduction in compressive strength was observed across all mixtures, the mechanical performance remained acceptable. These results suggest that OPA can contribute to environmentally friendly cementitious materials with mechanical properties comparable to conventional systems.

4. Conclusions

Biomass ashes, such as olive pomace ash (OPA), present a promising solution by reducing cement use and diverting organic waste from landfilling through recycling and valorization. This study investigated the effects of partially replacing OPC with OPA in mortar formulations at varying replacement levels (0% to 50%). The key findings are as follows:

- Workability improved with OPA incorporation up to 20%, evidenced by a higher flow time and lower wet bulk density than the control mixture (36 s vs. 3 s, and 2180 kg/m^3 vs. 2202 kg/m^3). Beyond this level, workability significantly deteriorated.
- Mechanical properties, including compressive and flexural strength, declined with increasing OPA content (CS28 is 51.86 MPa in MC and 21.52 MPa in MP50). However, up to 20% of replacements retained sufficient strength for practical use, balancing environmental benefits and performance.

- Water absorption increased with OPA content, particularly above 30% (5.23% for MC and 5.86% for MP30). WA remained within tolerable limits for mixes containing up to 40% OPA.
- Durability under freeze–thaw conditions was maintained reasonably well for mixes with up to 30% OPA, though higher replacement levels led to notable strength losses after exposure. The control mix (MC) retained 85% of its compressive strength, while MP10 retained 76%. Regarding the residual flexural strength, MC showed minimal degradation (6%), and MP10 retained 98% of its pre-exposure strength.
- Correlation analyses provided insights into quantitative relationships between flow time and wet bulk density, compressive strength and water absorption, and residual and initial compressive and flexural strength.

Olive pomace ash can be successfully utilized as a sustainable SCM in controlled proportions to reduce the environmental footprint of cement-based materials and support circular economy strategies by recycling agricultural waste. Future research should focus on long-term durability assessments, physico-chemical and microstructural characterization of OPA and its interaction with cementitious matrices, and optimization of OPA processing to enhance performance and reactivity. Additionally, studies on large-scale applications and technical standards will be essential to support the broader adoption of OPA in sustainable construction.

Author Contributions: Conceptualization, B.B., A.M., C.B., M.B., K.H., A.D. and L.M.; data curation, B.B., A.M., C.B., K.H., A.D. and L.M.; formal analysis, B.B., A.M., C.B., M.B., K.H., A.D. and L.M.; funding acquisition, C.B. and K.H.; investigation, B.B., A.M., C.B., M.B., K.H., A.D. and L.M.; methodology, B.B., C.B. and L.M.; project administration, A.M., C.B., M.B., K.H., A.D. and L.M.; resources, B.B., C.B. and L.M.; software, B.B., C.B. and L.M.; supervision, C.B. and L.M.; validation, B.B., A.M., C.B., M.B., K.H., A.D. and L.M.; visualization, B.B., C.B., M.B., K.H., A.D. and L.M.; writing—original draft, B.B., A.M., C.B., K.H. and A.D.; writing—review and editing, B.B., A.M., C.B., K.H. and L.M. All authors have read and agreed to the published version of the manuscript.

Funding: This research received no external funding.

Institutional Review Board Statement: Not applicable.

Informed Consent Statement: Not applicable.

Data Availability Statement: The original contributions presented in the study are included in the article, further inquiries can be directed to the corresponding author.

Conflicts of Interest: The authors declare no conflicts of interest.

Abbreviations

The following abbreviations are used in this manuscript:

OBA	olive biomass ash
OPA	olive pomace ash
OPC	Ordinary Portland Cement
OWA	olive waste ash
SCM	supplementary cementitious material
CS28	28-day compressive strength
RCS	residual compressive strength
FS	flexural strength
CS90	90-day compressive strength
RFS	residual flexural strength
WA	water absorption
WBD	wet bulk density

References

1. Andrew, R.M. Global CO_2 emissions from cement production, 1928–2018. *Earth Syst. Sci. Data* **2019**, *11*, 1675–1710. [CrossRef]
2. Chaudhury, R.; Sharma, U.; Thapliyal, P.; Singh, L. Low-CO_2 emission strategies to achieve net zero target in cement sector. *J. Clean. Prod.* **2023**, *417*, 137466.
3. Del Serrone, G.; Moretti, L. A stepwise regression to identify relevant variables affecting the environmental impacts of clinker production. *J. Clean. Prod.* **2023**, *398*, 136564. [CrossRef]
4. Ramzi, S.; Hajiloo, H. The effects of supplementary cementitious materials (SCMs) on the residual mechanical properties of concrete after exposure to high temperatures. *Buildings* **2023**, *13*, 103. [CrossRef]
5. Zhang, Y.; Zhao, B.; Zhu, J.; Wang, Z.; Ren, C.; Xie, H.; Guan, H.; Zhu, D. Research on properties of ash and slag composite cementitious materials for biomass power plants. *Processes* **2023**, *11*, 1627. [CrossRef]
6. Thomas, B.S.; Yang, J.; Mo, K.H.; Abdalla, J.A.; Hawileh, R.A.; Ariyachandra, E. Biomass ashes from agricultural wastes as supplementary cementitious materials or aggregate replacement in cement/geopolymer concrete: A comprehensive review. *J. Build. Eng.* **2021**, *40*, 102332. [CrossRef]
7. Li, H.; Yang, J.; Wang, L.; Zhang, N.; Wang, Q.; Mechtcherine, V. Recycling of biomass combustion ash into SCMs and aggregates. In *Treatment and Utilization of Combustion and Incineration Residues*; Elsevier: Amsterdam, The Netherlands, 2024; pp. 269–295.
8. Blesson, S.; Rao, A. Agro-industrial-based wastes as supplementary cementitious or alkali-activated binder material: A comprehensive review. *Innov. Infrastruct. Solut.* **2023**, *8*, 125. [CrossRef]
9. García Martín, J.F.; Cuevas, M.; Feng, C.-H.; Álvarez Mateos, P.; Torres Garcia, M.; Sánchez, S. Energetic valorisation of olive biomass: Olive-tree pruning, olive stones and pomaces. *Processes* **2020**, *8*, 511. [CrossRef]
10. Anania, G.; Pulpo, M. Olive oil in the Mediterranean area production. Consumption and trade. *CIHEAM Watch. Lett. Winter* **2011**, *16*, 1–26.
11. Alkhalidi, A.; Halaweh, G.; Khawaja, M.K. Recommendations for olive mills waste treatment in hot and dry climate. *J. Saudi Soc. Agric. Sci.* **2023**, *22*, 361–373. [CrossRef]
12. Berbel, J.; Posadillo, A. Review and analysis of alternatives for the valorisation of agro-industrial olive oil by-products. *Sustainability* **2018**, *10*, 237. [CrossRef]
13. Mohamed, A.M.; Tayeh, B.A.; Aisheh, Y.I.A.; Salih, M.N.A. Utilising olive-stone biomass ash and examining its effect on green concrete: A review paper. *J. Mater. Res. Technol.* **2023**, *24*, 7091–7107. [CrossRef]
14. Al-Akhras, N.M.; Abdulwahid, M. Utilisation of olive waste ash in mortar mixes. *Struct. Concr.* **2010**, *11*, 221–228. [CrossRef]
15. Al-Akhras, N.M. Performance of olive waste ash concrete exposed to alkali-silica reaction. *Struct. Concr.* **2012**, *13*, 221–226. [CrossRef]
16. Al-Akhras, N.M.; Al-Akhras, K.M.; Attom, M.F. Performance of olive waste ash concrete exposed to elevated temperatures. *Fire Saf. J.* **2009**, *44*, 370–375. [CrossRef]
17. Cuenca, J.; Rodríguez, J.; Martín-Morales, M.; Sánchez-Roldán, Z.; Zamorano, M. Effects of olive residue biomass fly ash as filler in self-compacting concrete. *Constr. Build. Mater.* **2013**, *40*, 702–709. [CrossRef]
18. Eliche-Quesada, D.; Leite-Costa, J. Use of bottom ash from olive pomace combustion in the production of eco-friendly fired clay bricks. *Waste Manag.* **2016**, *48*, 323–333. [CrossRef]
19. Beltrán, M.G.; Barbudo, A.; Agrela, F.; Jiménez, J.R.; de Brito, J. Mechanical performance of bedding mortars made with olive biomass bottom ash. *Constr. Build. Mater.* **2016**, *112*, 699–707. [CrossRef]
20. Font, A.; Soriano, L.; Moraes, J.; Tashima, M.; Monzó, J.; Borrachero, M.; Payá, J. A 100% waste-based alkali-activated material by using olive-stone biomass ash (OBA) and blast furnace slag (BFS). *Mater. Lett.* **2017**, *203*, 46–49. [CrossRef]
21. Payá, J.; Monzó, J.; Borrachero, M.; Soriano, L.; Tashima, M. Alternative activators in alkali-activated cements. *Rev. ALCONPAT* **2022**, *12*, 16–31. [CrossRef]
22. *NA 442-2013*; Ciment—Composition, Spécification et Critères de Conformité des Ciments Courants. Institut Algérien de Normalisation (IANOR): Alger, Algeria, 2003.
23. Shim, S.-H.; Lee, T.-H.; Yang, S.-J.; Noor, N.B.M.; Kim, J.-H.-J. Calculation of cement composition using a new model compared to the bogue model. *Materials* **2021**, *14*, 4663. [CrossRef]
24. *EN 196-1:2016*; Methods of Testing Cement—Part 1: Determination of Strength. European Commission Standard: Brussels, Belgium, 2005.
25. *ASTM C1437*; Standard Test Method for Flow of Hydraulic Cement Mortar. ASTM International: West Conshohocken, PA, USA, 2015.
26. *CEN EN 1015-6*; 1998 Methods of Test for Mortar for Masonry—Part 6: Determination of Bulk Density of Fresh Mortar. European Commission Standard: Brussels, Belgium, 1998.
27. *EN 13057*; Products and Systems for the Protection and Repair of Concrete Structures—Test Methods—Determination of Resistance of Capillary Absorption. European Commission Standard: Brussels, Belgium, 2002.

28. Lila, K.; Belaadi, S.; Solimando, R.; Zirour, F.R. Valorisation of organic waste: Use of olive kernels and pomace for cement manufacture. *J. Clean. Prod.* **2020**, *277*, 123703. [CrossRef]
29. Alkheder, S.; Obaidat, Y.T.; Taamneh, M. Effect of olive waste (Husk) on behavior of cement paste. *Case Stud. Constr. Mater.* **2016**, *5*, 19–25. [CrossRef]
30. El Boukhari, M.; Merroun, O.; Maalouf, C.; Bogard, F.; Kissi, B. Mechanical performance of cement mortar with olive pomace aggregates and olive mill wastewater: An experimental investigation. *Cogent Eng.* **2023**, *10*, 2212522. [CrossRef]
31. Eisa, A. Properties of concrete incorporating recycled post-consumer environmental wastes. *Int. J. Concr. Struct. Mater.* **2014**, *8*, 251–258. [CrossRef]
32. Harrisson, A.M. Constitution and specification of Portland cement. *Lea's Chem. Cem. Concr.* **2019**, *5*, 87–155.
33. Tayeh, B.A.; Hadzima-Nyarko, M.; Zeyad, A.M.; Al-Harazin, S.Z. Properties and durability of concrete with olive waste ash as a partial cement replacement. *Adv. Concr. Constr.* **2021**, *11*, 59–71.
34. Cruz-Yusta, M.; Mármol, I.; Morales, J.; Sánchez, L. Use of olive biomass fly ash in the preparation of environmentally friendly mortars. *Environ. Sci. Technol.* **2011**, *45*, 6991–6996. [CrossRef]
35. Fava, G.; Moriconi, G. Properties of Cementitious Paste Made with Cement and Ash from Olive Waste. In *Industrial Ecology*; Maggioli Editore: Santarcangelo di Romagna, Italy, 2011; p. 598.
36. Abdulkarem, M.A.; Rasool, D.A.; Nabhan, B.J. Utilization of olive and pumice stones to improve the thermal properties of cement mortar. *Int. J. Nanoelectron. Mater.* **2020**, *13*, 181–188.
37. Hakeem, I.Y.; Agwa, I.S.; Tayeh, B.A.; Abd-Elrahman, M.H. Effect of using a combination of rice husk and olive waste ashes on high-strength concrete properties. *Case Stud. Constr. Mater.* **2022**, *17*, e01486. [CrossRef]
38. Zhang, Z.; Yan, Y.; Qu, Z.; Geng, G. Endowing strength to calcium silicate hydrate (CSH) powder by high pressure mechanical compaction. *Cem. Concr. Res.* **2022**, *159*, 106858. [CrossRef]
39. Dahim, M.; Abuaddous, M.; Al-Mattarneh, H.; Alluqmani, A.; Ismail, R. The use of olive waste for development sustainable rigid pavement concrete material. *IOP Conf. Ser. Mater. Sci. Eng.* **2022**, *1212*, 012032. [CrossRef]
40. Beltrán, M.G.; Agrela, F.; Barbudo, A.; Ayuso, J.; Ramirez, A. Mechanical and durability properties of concretes manufactured with biomass bottom ash and recycled coarse aggregates. *Constr. Build. Mater.* **2014**, *72*, 231–238. [CrossRef]
41. Martínez-García, R.; de Rojas, M.S.; Jagadesh, P.; López-Gayarre, F.; Morán-del-Pozo, J.M.; Juan-Valdes, A. Effect of pores on the mechanical and durability properties on high strength recycled fine aggregate mortar. *Case Stud. Constr. Mater.* **2022**, *16*, e01050. [CrossRef]
42. Siline, M.; Ghorbel, E.; Bibi, M. Effect of freeze–Thaw cycles on the physicomechanical properties of a pozzolanic mortar. *Constr. Build. Mater.* **2017**, *134*, 32–38. [CrossRef]
43. Soriano, L.; Monzó, J.; Bonilla, M.; Tashima, M.M.; Payá, J.; Borrachero, M. Effect of pozzolans on the hydration process of Portland cement cured at low temperatures. *Cem. Concr. Compos.* **2013**, *42*, 41–48. [CrossRef]
44. Allahverdi, A.; Abadi, M.M.B.R.; Hossain, K.M.A.; Lachemi, M. Resistance of chemically-activated high phosphorous slag content cement against freeze–thaw cycles. *Cold Reg. Sci. Technol.* **2014**, *103*, 107–114. [CrossRef]
45. Gesoğlu, M.; Güneyisi, E.; Khoshnaw, G.; İpek, S. Investigating properties of pervious concretes containing waste tire rubbers. *Constr. Build. Mater.* **2014**, *63*, 206–213. [CrossRef]
46. Luo, S.; Bai, T.; Guo, M.; Wei, Y.; Ma, W. Impact of freeze–thaw cycles on the long-term performance of concrete pavement and related improvement measures: A review. *Materials* **2022**, *15*, 4568. [CrossRef]
47. *ASTM C666-97*; Standard Test Method for Resistance of Concrete to Rapid Freezing and Thawing. ASTM International: West Conshohocken, PA, USA, 2008.
48. Wu, J.; Shen, W.; Zhao, D.; Wu, M.; Yu, Z.; Zhao, Z.; Li, Z.; Wu, D.; Sun, J. Particle characterization of manufactured sand and its influence on concrete properties. *Materials* **2022**, *15*, 4593. [CrossRef]
49. Ramli, M.; Tabassi, A.A.; Hoe, K.W. Porosity, pore structure and water absorption of polymer-modified mortars: An experimental study under different curing conditions. *Compos. Part B Eng.* **2013**, *55*, 221–233. [CrossRef]
50. *EN 197-1:2014*; Cement-Part 1: Composition, Specifications and Conformity Criteria for Common Cements. European Committee For Standardisation: London, UK, 2011.
51. Hammouche, R.; Belebchouche, C.; Hammoudi, A.; Douadi, A.; Hebbache, K.; Boutlikht, M.; Berkouche, A.; Khishe, M. Synergistic effects and optimization of cement kiln dust and glass powder incorporation in self compacting mortar using central composite design. *Sci. Rep.* **2025**, *15*, 14529. [CrossRef] [PubMed]
52. Belkadi, A.A.; Kessal, O.; Berkouche, A.; Noui, A.; Daguiani, S.E.; Dridi, M.; Benaniba, S.; Tayebi, T. Experimental investigation into the potential of recycled concrete and waste glass powders for improving the sustainability and performance of cement mortars properties. *Sustain. Energy Technol. Assess.* **2024**, *64*, 103710.
53. Khitas, N.E.H.; Hebbache, K.; Douadi, A.; Boutlikht, M.; Belebchouche, C.; Messai, A.; Mahar, N.E.-H.; Del Serrone, G.; Moretti, L.; Czarnecki, S. Modeling and optimizing the properties of mortars based on natural pozzolan, silica sand, and recycled brick waste mixture design: A technical and environmental study. *Constr. Build. Mater.* **2025**, *459*, 139706. [CrossRef]

54. Douadi, A.; Hebbache, K.; Boutlikht, M.; Tabchouche, S.; Belebchouche, C.; Hammouche, R.; Del Serrone, G.; Moretti, L. Physical and Mechanical Effects of Silica Sand in Cement Mortars: Experimental and Statistical Modeling. *Materials* **2023**, *16*, 6861. [CrossRef]
55. Bond, F.C. Crushing and grinding calculations, Part I. *Br. Chem. Eng.* **1961**, *6*, 378–385.

Disclaimer/Publisher's Note: The statements, opinions and data contained in all publications are solely those of the individual author(s) and contributor(s) and not of MDPI and/or the editor(s). MDPI and/or the editor(s) disclaim responsibility for any injury to people or property resulting from any ideas, methods, instructions or products referred to in the content.

materials

MDPI

Review

Comparative and Meta-Analysis Evaluation of Non-Destructive Testing Methods for Strength Assessment of Cemented Paste Backfill: Implications for Sustainable Pavement and Concrete Materials

Sakariyau Babatunde Abdulkadir [1], Qiusong Chen [2,*], Erol Yilmaz [3] and Daolin Wang [1]

[1] School of Resources and Safety Engineering, Central South University, Changsha 410083, China; skymorbabs@csu.edu.cn (S.B.A.); daolinw@csu.edu.cn (D.W.)
[2] Department of Resources Engineering, University of Science and Technology Beijing, Beijing 100083, China
[3] Department of Civil Engineering, Geotechnical Division, Recep Tayyip Erdogan University, Fener, Rize TR53100, Türkiye; erol.yilmaz@erdogan.edu.tr
* Correspondence: qiusong.chen@csu.edu.cn

Abstract

Cemented paste backfill (CPB) plays an important role in sustainable mining by providing structural support and reducing surface subsidence. While traditional destructive testing methods such as unconfined compressive strength (UCS) tests offer valuable understanding of material strength, they require a lot of resources, are time-consuming, and environmentally unfriendly. However, non-destructive testing (NDT) techniques such as ultrasonic pulse velocity (UPV), electrical resistivity (ER), and acoustic emission (AE) provide sustainable alternatives by preserving sample integrity, minimizing waste, and enabling real-time monitoring. This study systematically reviews and quantitatively compares the effectiveness of UPV, ER, and AE in predicting the strength of CPB. Meta-analysis of 30 peer-reviewed studies reveals that UPV and AE provide the most consistent and reliable correlations with UCS, with R^2 values of 0.895 and 0.896, respectively, while ER shows more variability due to its sensitivity to environmental factors. Additionally, a synthetic model combining UPV, AE and ER demonstrates improved accuracy in predicting strength. This hybrid approach enhances predictions of material performance while supporting sustainability in mining and construction. Our research advocates for better testing practices and presents a promising direction for future infrastructure projects, where real-time, non-invasive monitoring can enhance material performance evaluation and optimize resource use.

Keywords: cemented paste backfill; non-destructive testing (NDT); strength prediction; sustainability in mining; ultrasonic pulse velocity (UPV)

1. Introduction

Cemented paste backfill (CPB) is a modern approach applied in sustainable mining practices, especially in the underground mines, to address the problems associated with mine tailings and to provide structural support for roadways or pavement materials. CPB is a composite material to fill voids, which also helps mitigate surface subsidence and improve ground conditions [1–3]. CPB must meet specific compressive strength requirements to ensure structural stability. Industry standards ASTM C39/C39M-24 [4] and practical guidelines mandate minimum strengths of >0.7 MPa for temporary structures

and >1.5 MPa for long-term stability [5]. These thresholds ensure safe ground support and prevent subsidence risks.

The strength of CPB, pavement, and other concrete materials is often tested by methods that involve breaking the material samples. A well-known test for this is the unconfined compressive strength (UCS) test. Even though this test provides important information, it requires a lot of resources, produces waste, and takes a lot of time to complete. These drawbacks make it not very suitable for practices that aim to be environmentally friendly and sustainable [6,7]. Such limitations become particularly problematic when assessing backfill performance in active mining areas where real-time strength evaluation is crucial for safety.

As the mining industry strives to be more environmentally friendly, finding ways to check materials without causing damage is crucial. Methods such as ultrasonic pulse velocity (UPV), electrical resistivity (ER), and acoustic emission (AE) offer non-destructive solutions [8,9]. These techniques help maintain the integrity of samples, cut down on waste, and provide real-time insights into material properties. This shift promotes resource efficiency and helps us understand their sustainability, durability and strength prediction in various construction applications [10,11]. Although this study focuses on CPB, the NDT methods discussed, such as UPV, ER and AE are also widely applicable in assessing pavement materials, concrete and asphalt.

The properties of CPB have usually been assessed through destructive testing methods, such as UCS, triaxial tests, and tensile strength tests. While these methods provide accurate and reliable results, they are inherently limited by their destructive nature [12–14]. Destructive testing entails pulling out and destroying samples, which not only undermines the integrity of the backfill structure but also restricts the scalability and frequency of testing [15–17]. Furthermore, these methods are time consuming, labor-demanding and not very suitable for use in real time conditions [18,19].

Recent progress in NDT methods such as UPV, ER, and AE holds promise for CPB assessment. UPV is used to measure how quickly waves travel through materials, providing information about their density and elasticity [15,16]; ER examines electrical conductivity, which helps assess hydration levels and porosity [18]; and AE identifies tiny cracks that form under stress, offering early warnings of potential failures [19,20]. Individually, these methods address specific DT shortcomings: they preserve sample integrity, enable real-time monitoring, and reduce costs by up to 40% [21,22]. However, existing studies remain fragmented, with no systematic comparison of their reliability across diverse CPB compositions or environmental conditions [23,24]. For instance, while Yılmaz and Ercikdi [25] demonstrated UPV's strong UCS correlation (R^2 = 0.79–0.95) in silica-rich tailings, Wu et al. [26] noted ER's susceptibility to moisture fluctuations—a gap this review bridges through meta-analysis.

This paper presents a systematic review of how three important NDT methods like UPV, ER, and AE perform in predicting the strength of CPB focusing on their sustainability aspects. It highlights the benefits of these methods, focusing on how they can be better for the environment and help reduce costs for the mining and construction sectors. We quantify the predictive power of UPV, ER, and AE for UCS through meta-analysis, elucidating method-specific strengths and limitations using 30 relevant studies.

2. Testing Methods Overview

Figure 1 presents the sequence of steps followed in the CPB process to prepare the samples and subjected them to destructive and non-destructive assessment. In step (a), the raw materials—cement, water and tailings—are collected. In step (b), these substances are put into an automatic mixer to create a uniform paste mixture. Step (c) entails pouring

the mix that has been prepared into cylindrical molds to make sure that it is uniform and compacted to the right level. The samples are then cured in a controlled surrounding (d) using a curing machine to provide the right temperature and humidity conditions. After curing (e), the hardened CPB samples will either or both undergo (f) NDT and (g) DT for mechanical assessments to determine their structural integrity and performance.

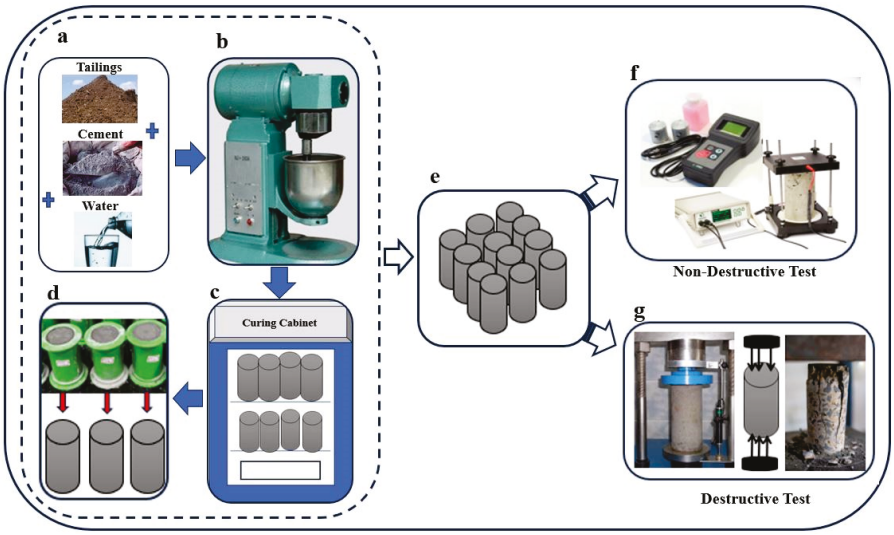

Figure 1. Presents (**a**–**d**) Step by Step CPB preparation, (**e**) required sample for testing process, (**f**) non-destructive methods and (**g**) destructive testing method.

2.1. Overview of Destructive Testing Methods

Destructive testing (DT) methods are necessary for identifying the mechanical behavior of materials especially in construction and engineering fields. The approaches entail the use of forces on the materials up to failure, to determine important characteristics such as the load carrying capacity, toughness and the general performance. This methodology is well established and conforms with industry standards for the evaluation of structural materials and provides concise and quantifiable information on their performance during stressful conditions [27–29].

Among the DT methods, the UCS test is one of the most common for CPB, where a cylindrical sample of CPB is subjected to axial compression up to failure, and the stress–strain relationship is recorded to determine the maximum compressive stress that the material can tolerate [30–32]. This parameter is very important in determining the load carrying capacity and the structural integrity of CPB and therefore affects the safety and efficiency of mining operations. UCS test results are used in the optimization of CPB mix designs to ensure that the mixes developed are capable of meeting the required strength criteria for the various applications especially in underground mining where it is essential that the CPB has enough strength to support the surrounding rock masses [17,33].

Another important method of destructive testing is the triaxial test that receives mechanical properties of CPB under in situ-like conditions. This test applies a controlled stress to a cylindrical sample in three orthogonal directions, so as to determine shear strength and failure mechanisms. Complex loading conditions of mining environment are simulated by triaxial tests made on CPB to determine its behavior. While most CPB testing focuses on static loads, dynamic load studies like drop-weight or split-Hopkinson bar tests are emerging to simulate blast or seismic impacts [34,35]. These remain less common due to CPB's primary role in static load-bearing. These tests outcomes reveal that with confining pressure, both peak and residual strengths rise, vital information for optimizing mix designs for geological stress resistance [36]. Triaxial tests are nevertheless

costly and time consuming because they require specialized equipment and very precise sample preparation.

The Brazilian test, also known as the splitting tensile strength test, is another method employed to measure the tensile strength of brittle materials such as CPB. This test induces tensile stresses that lead to failure along the vertical plane by applying a compressive load diametrically across a cylindrical sample [37,38]. This test is especially significant for determining CPB resistance to cracking and failure that is critical for maintaining the stability and durability of structures in mining operations. However, like other destructive tests, it is limited in its ability to allow samples to be used for further analysis and may not accurately replicate field conditions because of differences in stress distribution [39–41].

Table 1 below highlights the fundamental differences between these three commons destructive (UCS, Triaxial and Brazilian) testing methods used to evaluate the mechanical properties of CPB and similar materials. The UCS test measures uniaxial compressive strength under zero confinement, providing a baseline for material performance. The Triaxial test incorporates confining pressure to simulate in situ stress conditions, yielding shear strength parameters critical for geotechnical applications. In contrast, the Brazilian test indirectly assesses tensile strength, a key property for predicting crack initiation in brittle CPB structures.

Table 1. Comparison of destructive testing methods for CPB: key characteristics, measured properties, and applications of UCS, Triaxial and Brazilian tests.

Test	Load Type	Measured Property	Confining Pressure	Typical Use Case
UCS	Uniaxial	Compressive strength (σ_e)	None ($\sigma_2 = \sigma_3 = 0$)	Basic strength screening
Triaxial	Multiaxial	Shear strength (c, φ)	Controlled ($\sigma_2 = \sigma_3 \neq 0$)	Deep mining, slope stability
Brazilian	Diametrical	Tensile strength (σ_t)	None	Crack resistance, brittle materials

Destructive testing methods provide valuable insights into the mechanical properties of CPB, but they suffer from inherent limitations, including sample destruction, time-consuming preparation, labor intensity, and limited scalability. Additionally, these methods cannot simulate real-world conditions, lack repeatability, require complex data interpretation and generate material waste [42,43]. As summarized in Table 1, these drawbacks have motivated researchers to adopt NDT methods such as UPV and ER testing as visualized in Figures 1 and 2 which preserve sample integrity while offering real-time, scalable, and repeatable assessments of CPB properties without compromising structural capacity.

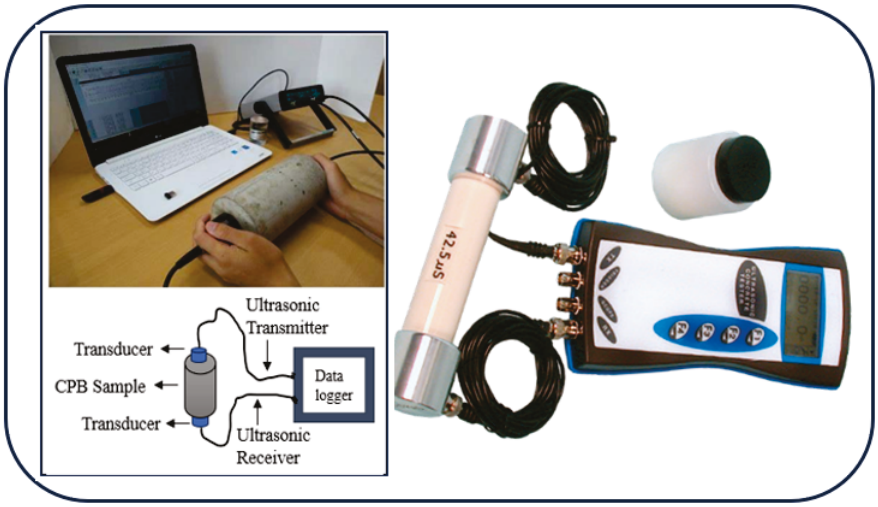

Figure 2. Image showing UPV Testing Setup as NDT method for CPB sample. It includes an ultrasound transmitter, a transducer for the CPB sample, a data logger, and an ultrasound receiver.

2.2. Non-Destructive Testing Methods

- Ultrasonic Pulse Velocity (UPV) Testing

UPV testing is a non-destructive testing method that is applied widely for the assessment of the physical properties of materials such as CPB. It works by sending high frequency ultrasonic waves into a material and then measuring the velocity of the waves. The wave velocity is a function of material density, elasticity and compressive strength and thus enables the engineer to make property evaluations without having to destroy the sample. It gives information about the internal structure and integrity of CPB by analyzing the time taken by the waves to travel through the material and any changes in the amplitude or frequency of the waves [44,45].

The UPV testing setup, which is illustrated by Figure 2, utilizes an ultrasonic transmitter and a transducer that is responsible for generating and sending ultrasonic waves through the material under examination is referred to as the setup. These signals are sent through the material and are received by ultrasonic cables which are connected to a data display and logger unit for analysis. The facts about the integrity, homogeneity and possible flaws of the substance are obtained from the captured data [46,47]. This method is especially useful for quality control and monitoring in both laboratory and field conditions since it allows multiple evaluations of the same specimen or structure at different times [48,49].

UPV presents information online, which is very useful in making on-the-spot decisions and changes during construction or mining operations [50]. For these reasons, it is a suitable tool for examining the CPB at different levels, from material testing at the initial stage to monitoring during the service period. However, the precision of the results depends significantly on proper calibration, which needs reference samples with known properties. Another issue is that material heterogeneity, such as density variations, voids, and cracks, can influence the propagation of ultrasonic waves, resulting in irregular outcomes [51–53].

- Electrical Resistivity Testing

The principle of electrical resistivity testing is based on the fact that the resistivity of a material is a function of its physical properties. Thus, porosity and microstructure of the cement paste changes with the degree of hydration, which, in turn, affects the electrical resistivity. Lower resistivity is a characteristic of porous structures while higher resistivity is observed in more dense and better hydrated materials [54,55]. The setup for resistivity measurements is simple and can be used in the field and the laboratory. This method is also suitable for online control that enables online assessment of the curing process and the quality of CPB. This correlation highlights the importance of resistivity testing as an early warning tool in assessing the performance of CPB [56–58].

However, there are some demerits of using electrical resistivity testing. A major drawback is the sensitivity to moisture content; changes in moisture can lead to changes in resistivity which can make data analysis difficult [59]. The moisture content of CPB can be a major factor in the electrical properties of the mixture, and thus, proper control and measurement of the environmental conditions during testing is very essential [60]. Moreover, the analysis of resistivity data is quite complex and requires knowledge of the materials structure and hydration mechanism since resistivity by itself is not a full characterization of the material state [61,62].

- Acoustic Emission (AE)

The AE test is based on the detection of transient elastic waves emitted when energy is released from a material containing localized sources of energy such as microcracks and fractures [63,64]. CPB will be subjected to stress and the micro events generate acoustic signals that can be caught by sensitive sensors. The information derived from the analysis

of these signals gives information on the damage mechanisms occurring inside the backfill material and the growth of cracks [65,66]. The AE is suitable for monitoring damage evolution in CPB and real time assessment of its stability is possible [67].

A major strength of AE is that it can provide real time monitoring of the propagation of cracks and failure mechanisms, which is very useful in the study of CPB behavior under load and failure prediction [27,68]. Moreover, AE can be employed for the discrimination of the initial hydration products in cement composites and therefore to determine the strength and durability of CPB [69]. Furthermore, AE is suitable for continuous monitoring of large areas, which is important for numerous applications of backfill in mining, where the conditions are usually dynamic [70].

However, there are some significant demerits of AE which cannot be ignored. The major restriction is that accurate capturing and analysis of acoustic signals need sensitive and high-quality equipment, and noise can be a problem [64]. It is important to separate the meaningful acoustic signals from the noise for accurate evaluation. Moreover, AE data analysis can be rather complicated, and the signals are not always straightforward to link to certain damage types. Therefore, the analysis of the data and the conclusions about the state of CPB made from it requires professional knowledge [71–73].

3. Methodology: Systematic Review and Meta-Analysis Protocol

3.1. Literature Search Strategy

We explored five major research databases such as Scopus and Web of Science, depicted in Figure 3. Our search included terms like "cemented paste backfills" or "CPB", "non-destructive testing" or "NDT", as well as "ultrasonic", "electrical resistivity", "acoustic emission", and "strength prediction" or "UCS correlation". We focused on peer-reviewed studies from 2010 to 2025 that demonstrated clear quantitative links between NDT techniques like UPV, ER, or AE, and UCS. These studies needed to detail their CPB mix designs, including specifics about binder types and tailings compositions. They also had to provide statistical data, such as R^2 data, to calculate effect sizes. We excluded studies solely using DT methods, focusing on non-cemented backfills, duplicates, conference summaries, or those lacking comprehensive methodological details.

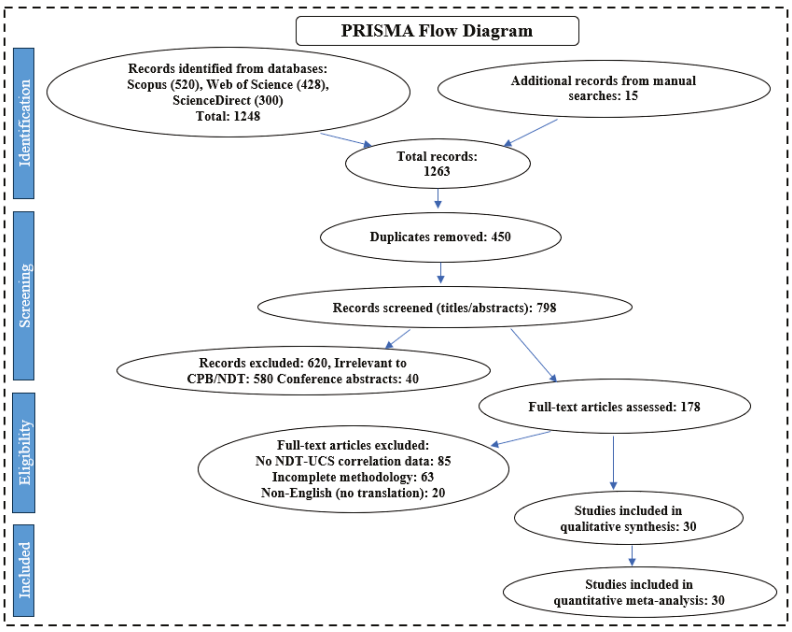

Figure 3. PRISMA flowchart illustrating the method used to search and select literature systematically. From the 1248 records identified, 30 studies were chosen for the meta-analysis.

3.2. Study Screening and Statistical Analysis

The PRISMA framework, as shown in Figure 3, was selected for its rigor in systematic reviews, minimizing selection bias via transparent screening stages. Initially, we identified 1248 records and eliminated 450 duplicates. Subsequently, 620 studies were dismissed, as their titles and abstracts did not pertain to CPB/NDT. Next, we assessed 178 studies in full to determine their relevance. Out of these, only 30 met all criteria. We prioritized studies with controlled experimental conditions, such as ASTM/ISO compliant curing protocols, included at least three samples per mix design, and provided clear error metrics like standard deviations. This thorough process ensured we included high-quality, reproducible data for meta-analysis using Python 3.9 (libraries: NumPy, pandas, scikit-learn, and Matplotlib) to assess data consistency through R^2 values, and create forest plots to evaluate different NDT methods.

4. Comparison of Destructive and Non-Destructive Testing

Table 2 and Figure 4 compare DT and NDT methods using qualitative scores (1–10 scale). While DT provides highly accurate strength data through destructive failure testing, it suffers from sample destruction, high costs, specialized equipment requirements, and slow turnaround—limiting its field applicability. In contrast, NDT techniques preserve sample integrity, enabling real-time monitoring and repeat assessments with moderate-to-high precision. Their cost-effectiveness, efficiency, and field adaptability make NDT particularly valuable for large-scale applications across mining, construction, and manufacturing sectors, where operational continuity is crucial. The quantitative comparison highlights NDT's advantages in sustainability and scalability while acknowledging DT's superior absolute accuracy for controlled laboratory conditions.

Table 2. A detailed comparison of DT and NDT methods focusing on how they perform in terms of resources conservation, material integrity preservation and cost-effectiveness.

Feature	Destructive Testing	Non-Destructive Testing
Sample Integrity	Destroys samples	Retains specimens for further use
Testing Time	Time-consuming	Faster, real-time assessment
Cost	High due to multiple samples	Lower operational costs
Real-Time Monitoring	Not possible	Possible with UPV, ER, and AE
Field Application	Limited to controlled labs	Suitable for both lab and field
Data Collection	Single-point data (after failure)	Continuous monitoring possible

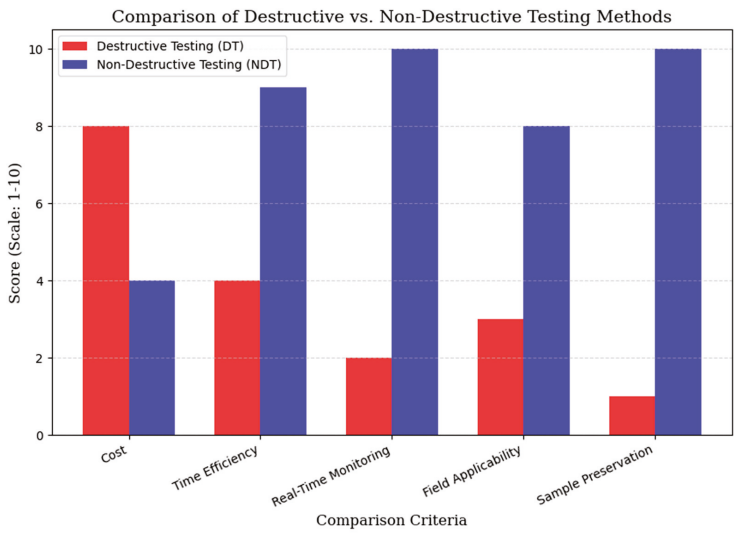

Figure 4. Bar chart comparing DT and NDT across key assessment criteria. It focuses on important factors like saving resources, reducing costs, and material integrity preservation.

4.1. Case Studies and Applications

Various NDT methods are used to assess the properties of CPB in both laboratory and field conditions. The following are 10 case studies for each NDT method, along with their effectiveness, challenges and implications for CPB assessment.

4.1.1. Ultrasonic Testing Method

To enhance clarity and enable rapid visual comparison, Figures 5 and 6 present the correlation studies between UPV and UCS from Table 3 in the form of scatter plots and trend graphs. This visual representation effectively illustrates the relationship between UPV and UCS across multiple studies, thus enabling an at-a-glance comparison of the NDT systems.

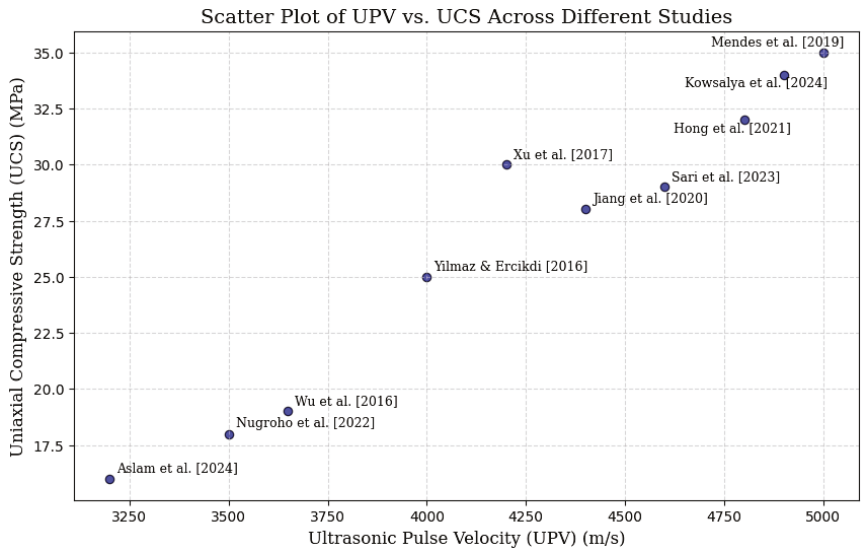

Figure 5. Scatter plot graph showing the relationship between UPV and UCS across different studies [13,16,24,53,74–79].

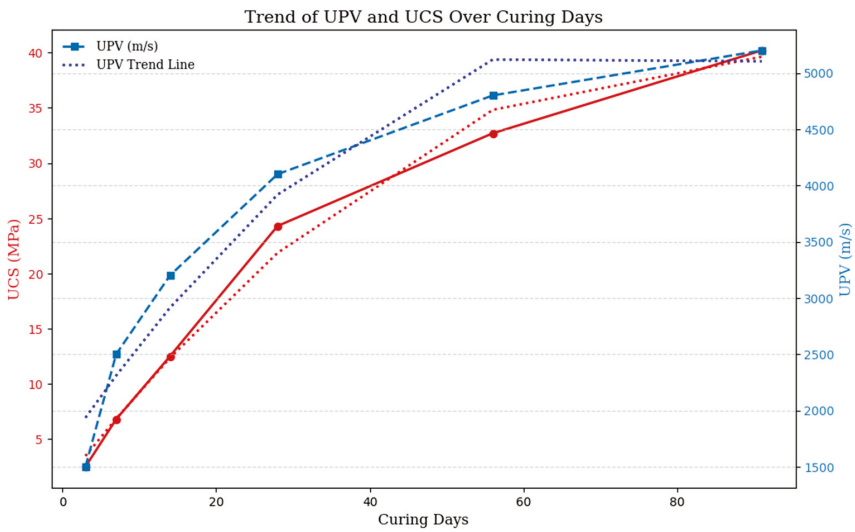

Figure 6. This figure shows the evolution of UCS (MPa) and UPV (m/s) with curing days. The red dotted line represents the polynomial trend for UCS, while quadratic trend lines (dashed) are fitted for both UCS and UPV, highlighting their increase over time.

Table 3. Comparison of UPV and UCS correlation studies, showing the effectiveness of UPV as a non-destructive alternative for UCS prediction across different material types.

Study	Focus Area	Methodology	Key Findings	Conclusion
Yilmaz & Ercikdi [24]	Correlation of UCS and UPV in CPB with different tailings	180 CPB samples, UCS and UPV testing over 7–56 days, regression analysis	Strong correlation (0.79–0.95) between UCS and UPV, confirming UPV as a UCS predictor	UPV provides a reliable, non-destructive alternative for UCS estimation in CPB
Wu et al. [74]	Mechanical performance of cemented gangue backfills using UCS and UPV	60 CGB samples, UCS and UPV testing over 3–28 days, exponential relationship analysis	High correlation (0.959) between UCS and UPV, with strength growth over time	UPV effectively predicts UCS in cemented gangue backfill without sample damage
Xu et al. [75]	Strength and ultrasonic properties of foam-cemented paste backfill	FCPB samples with varying vesicant-binder ratios, UCS and UPV correlation	Linear correlation between UCS and UPV, improving accuracy with lower vesicant ratios	UPV serves as a useful, non-destructive UCS estimator in foam-cemented paste backfill
Mendes et al. [76]	Use of UPV as a performance parameter for concrete mixture design	68 concrete mixtures, UCS and UPV tests at 28 and 91 days, silica fume impact analysis	UPV effectively predicts concrete strength except for high SF content mixtures	UPV is a viable non-destructive indicator of concrete performance and strength
Jiang et al. [16]	UPV and UCS relationship in alkali-activated slag (AAS)-based CPB	Various CPB mixtures, UCS and UPV testing at different curing ages, regression modeling	Exponential correlation (R^2 > 0.94) between UCS and UPV in AAS-CPB	UPV provides cost-effective, efficient UCS predictions for AAS-CPB
Nugroho et al. [77]	Impact of mortar mixture variations on compressive strength and UPV	Examining fine aggregate-cement ratios, UCS and UPV logarithmic correlation analysis	UPV and UCS follow a logarithmic trend, inversely related to porosity	UPV offers real-time assessment of mortar properties for mixture optimization
Hong et al. [78]	Compressive strength and UPV correlation in silica fume-blended cement mortars	ISO 679 standard [27]-based testing, SF influence on UCS and UPV correlation	UPV and UCS show an exponential relationship, influenced by SF replacement rate	UPV measurement serves as a practical alternative to destructive UCS testing
Sari et al. [13]	Silica fume (SF)-replacement's impact on UPV and compressive strength in cement mortar	Different SF replacement rates in cement mortar, UCS and UPV correlation analysis	SF substitution significantly influences UCS-UPV correlation, with minor effects on overall trend	UPV remains a strong indicator of UCS across different SF replacement rates
Aslam et al. [79]	Mechanical and durability properties of sustainable lightweight concrete with WPA	Concrete with WPA (20–100%), UCS and UPV polynomial regression analysis	UPV decreases with higher WPA, affecting UCS due to increased porosity and reduced density	UPV can effectively assess mechanical integrity of sustainable lightweight concrete
Kowsalya et al. [53]	Predicting compressive strength of Fly Ash Cenosphere (FAC) concrete using UPV	FAC concrete, IS 516:2018 [51] and IS 13311-1992 standard [52]-based UCS and UPV testing	UPV exhibits strong exponential correlation (0.91–0.99) with UCS, confirming prediction reliability	UPV provides a non-destructive means of evaluating the compressive strength of FAC concrete

Several research studies presented in Table 3 show that UPV can be used as a reliable, non-destructive alternative to UCS for the evaluation of cemented materials, concrete and paste backfill. Studies have revealed UPV-UCS correlations across curing periods and material compositions, confirming UPV ability to predict strength in CPB, cemented gangue backfill (CGB), and alkali-activated slag-based backfill [74–76]. It has been highlighted that UPV's utility in assessing concrete quality, especially in silica fume (SF) and varied binder mixtures. In addition, studies have further validated UPV for sustainable lightweight and fly ash-based concretes by monitoring hydration, density, and porosity, respectively [77,78]. Therefore, UPV can provide a non-invasive and efficient real-time estimation of UCS for improving quality control in mining and construction.

The studies presented in Table 3 collectively define UPV as a strong candidate for predicting UCS in a variety of cementitious materials, such as CPB, gangue backfill (CGB), alkali activated slag based backfill, and concrete mixtures. The studies show high correlation coefficients (R^2 > 0.85), which prove that UPV can be used to monitor the hydration process, material density and porosity. The study on sustainable materials (such as silica fume modified and lightweight concrete) also confirms the suitability of UPV for assessing different binders and curing conditions. As a non-destructive and online measurement

method, UPV is shown to be applicable for practical use as an alternative to UCS testing in mining, construction, and material engineering.

4.1.2. Electrical Resistivity (ER) Testing

To improve readability and enable fast visualization of the data, Figures 7 and 8 present the correlation studies between ER and UCS from Table 4 in a scatter plot with a trend line. This graphical representation effectively shows the connection between ER and UCS across multiple studies, facilitating a more straightforward comparison of the non-destructive testing (NDT) systems.

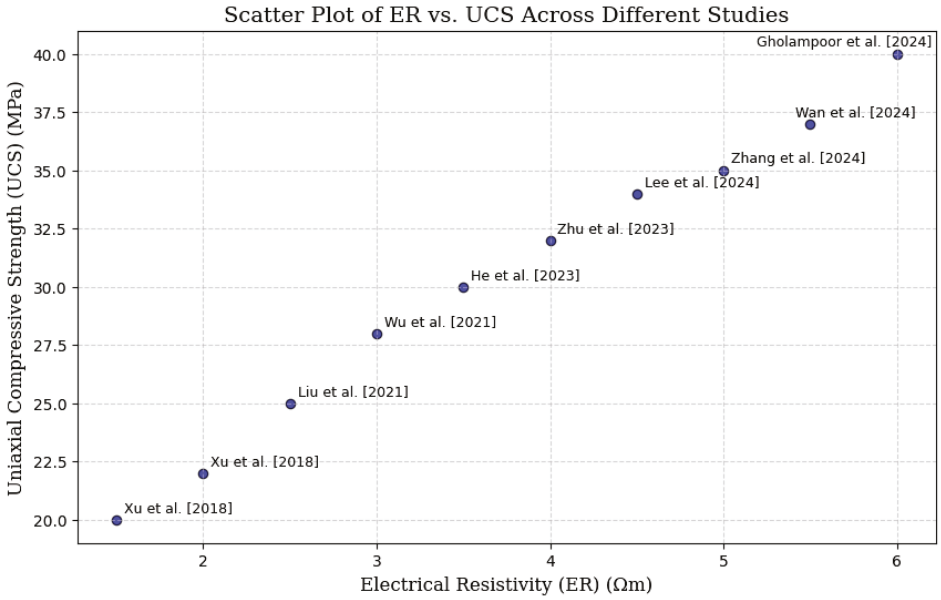

Figure 7. Scatter plot graph showing the relationship between ER and UCS across different studies [25,60,80–87].

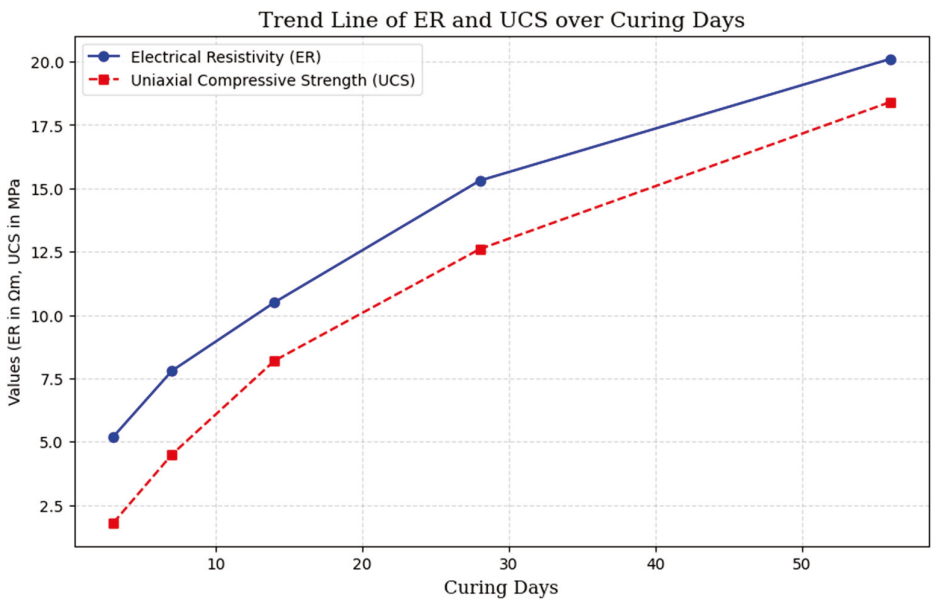

Figure 8. Present trend line showing how ER and UCS change over curing periods.

Table 4. Comparison of ER and UCS correlation studies, highlighting the sustainability benefits of ER in waste reduction, real-time monitoring, and cost-effective testing.

Study	Focus Area	Methodology	Key Findings	Conclusion
Xu et al. [80]	Use of ER in CPB geotechnical evaluation	Wenner Four-Electrode method, UCS testing, ASTM G57-06 standards [17]	ER correlated significantly with UCS; rapid early strength gain noted.	ER testing is a cost-effective, time-efficient alternative to UCS.
Xu et al. [60]	Predicting UCS through ER in CPB hydration process	CPB samples with varying cement ratios tested for ER and UCS correlation	ER effectively predicted UCS development throughout hydration.	ER can reliably monitor hydration progress and strength in CPB.
Liu et al. [81]	Correlation between ER, hydration heat, and UCS	NER and microcalorimetry for resistivity, UCS testing for mechanical assessment	Strong correlation found between ER, hydration heat, and UCS.	Resistivity serves as a strong predictive indicator of UCS and hydration.
He et al. [82]	Mechanical behavior of coal waste rock backfills	Compression tests on coal waste rock backfill, ER measured via two-phase and four-phase methods	ER method effectively monitored deformation characteristics of waste rock backfill.	ER testing is a practical tool for monitoring backfill mechanical behavior.
Wu et al. [25]	Comparing ER and AE for UCS alternative testing	Analyzed ultrasonic waveforms, electrical conductivity, hydration heat, and ER-UCS correlation	ER and AE provided alternative strength evaluation methods to UCS.	ER complements AE as a real-time UCS testing alternative.
Zhu et al. [83]	Evaluating ICPB properties using ER	Investigated microstructure and hydration using NMR, SEM-EDS, and FFRC tests	ER correlated with UCS, capturing hydration and porosity changes.	ER effectively evaluates ICPB properties, including hydration and strength.
Lee et al. [84]	Application of ER in cement-based materials	Examined hydration, curing time, water-solid ratios' impact on ER in cement pastes	ER values increased with hydration and material density, indicating strength evolution.	ER is a viable tool for assessing early-age cement-based materials.
Zhang et al. [85]	ER-UCS relationship under varying curing temperatures	CPB specimens cured at 20–60 °C to study hydration effects on ER and UCS	Optimal strength achieved at 40 °C; ER tracked hydration efficiency.	ER testing provides real-time insights into UCS evolution in CPB.
Wan et al. [86]	Effect of calcium nitrite on ER-UCS correlation	Studied calcium nitrite impact on hydration and microstructure using ER and UCS tests	Higher ER values indicated denser structure and stronger UCS correlation.	ER reliably predicts UCS, supporting improved mix design strategies.
Gholampoor et al. [87]	ER as a tool for early-stage quality of stabilized DS	Monitored hydration and ion concentration using ER, compared with UCS at 28 days	ER provided early prediction of UCS, enabling non-destructive quality assessment.	ER testing enables rapid and non-destructive quality assessment of DS.

The Correlation Studies in Table 4 have proven ER to be a non-destructive alternative to UCS testing to determine the mechanical properties of CPB, concrete and other cementitious products. Figures 7 and 8 visualize a good correlation between ER and UCS and that ER can be used to monitor hydration, porosity and microstructural evolution during curing periods. However, sample non-homogeneity, particularly in the case of air voids or uneven binder distributions, can significantly affect ER measurements by disrupting ionic conduction pathways, potentially leading to localized resistivity variations of up to 20% [86–88]. The results show that higher ER values are associated with higher UCS, and this is because of material densification and reduced permeability. Further work on hydration mechanisms, curing temperatures, and additives like calcium nitrite and slag also corroborates ER predictive role. As ER can monitor strength evolution in real-time without destroying specimens it emerges as a low-cost and time-saving alternative to UCS and finds its place in quality control in mining, geotechnical engineering and construction.

4.1.3. Acoustic Emission (AE) Monitoring

To enhance understanding and allow for quick data observation, Figures 9 and 10 depict the correlation between AE and UCS, using data from Table 5. These figures include a scatter plot showing the relationship between AE and UCS across different studies and a trend line that clearly illustrates the relationships found in various studies. This visual format makes it easier to compare non-destructive testing (NDT) systems.

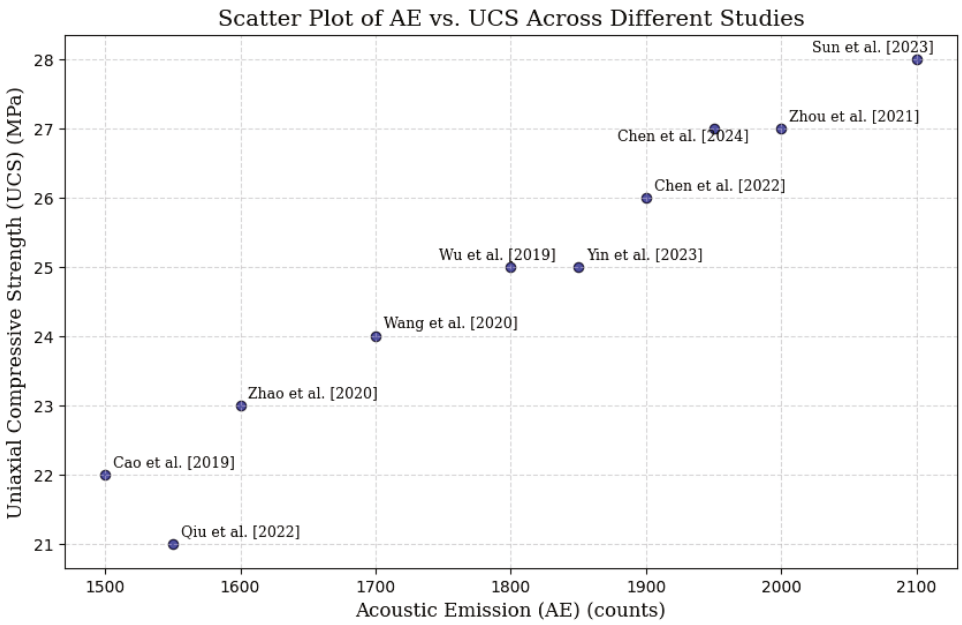

Figure 9. Scatter plot graph showing the relationship between AE and UCS across different studies [88–97].

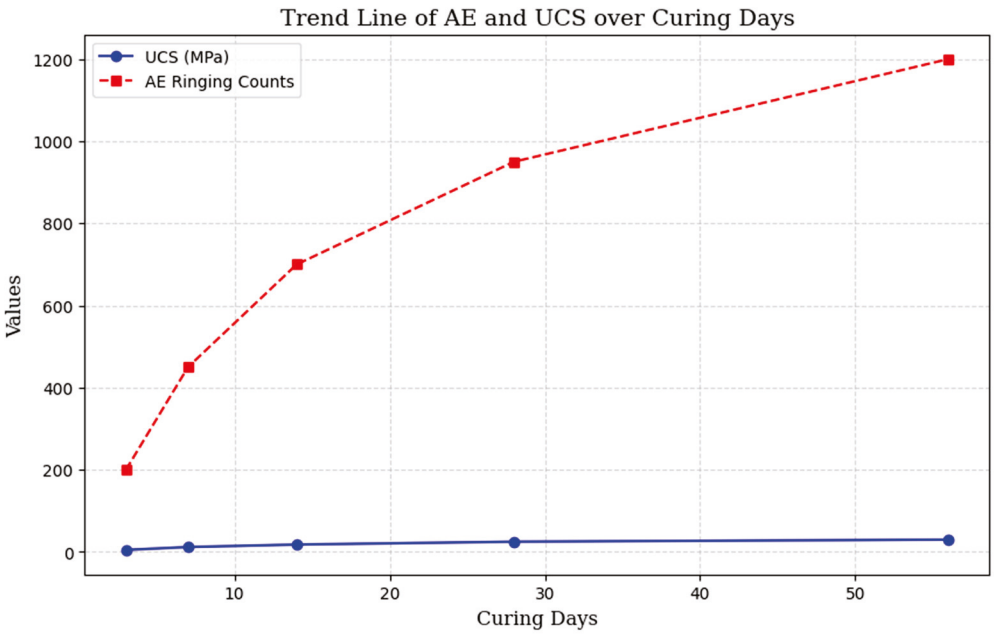

Figure 10. Present trend line showing how AE and UCS change over curing periods.

AE monitoring has been established as a reliable non-destructive alternative to the conventional UCS testing for determining the mechanical properties and failure behavior of CPB and other related materials. The AE parameters such as ring count and strength rate have a good correlation with stress–strain conduct and can capture the crack growth and failure process [88,89]. In addition, the AE is capable of monitoring real-time crack propagation and changes in structural integrity under different stress conditions [90,91]. Thus, AE can be used to assess the mechanical properties and failure behavior of CPB.

Table 5. Summary of AE monitoring studies correlating AE signals with UCS in CPB and other materials, highlighting AE as a reliable non-destructive method for tracking damage evolution and material failure.

Study	Focus Area	Methodology	Key Findings	Conclusion
Cao et al. [88]	AE monitoring for waste rock CPB under triaxial compression	Triaxial compression tests with AE monitoring; stress–strain behavior analysis	AE activity mirrors UCS failure stages; prepeak quiescence and postpeak calm observed	AE serves as a reliable, real-time alternative to UCS for assessing mechanical strength
Wu et al. [89]	AE monitoring as an alternative to UCS for CPB	Uniaxial compression tests with AE21C system; crack activity analysis	AE counts peak at stress maximum; AE activity increases with cement content	AE monitoring effectively captures stress–strain behavior in CPB
Wang et al. [90]	Mechanical behavior and AE properties of CPB	PCI-2 AE system with six sensors; stress–strain monitoring during UCS tests	AE ringing count increases with load; AE signals correlate with damage evolution	AE provides insights into crack propagation and structural integrity
Zhao et al. [91]	AE analysis of cemented tantalum-niobium tailings backfills	UCS and Brazilian splitting tests; AE signal analysis of stress response	AE peak timing varies with lime-sand ratio; microcrack dynamics analyzed	AE correlates with stress-induced damage and predicts UCS values
Zhou et al. [92]	AE for assessing UCS and damage evolution in CPB	UCS tests and AE signal tracking; event rate and energy rate correlation	Strong correlation between AE properties and UCS failure stages	AE enables real-time assessment of CPB failure characteristics
Qiu et al. [93]	AE characteristics in cemented rock-tailings backfill	UCS and AE monitoring of cemented rock-tailings backfill with varying compositions	AE parameters like ringing count and cumulative hits track UCS evolution	AE analysis aids in optimizing waste rock content in cemented backfill
Chen et al. [94]	AE monitoring under variable angle shear tests	AE monitoring under shear tests at 30°, 45°, and 60° angles	AE energy evolution follows shear angles; stepwise failure at 60°	AE monitoring complements UCS in evaluating shear failure mechanics
Sun et al. [95]	AE for Gangue and high water-CPB mechanical assessment	AE monitoring of stress–strain behavior during UCS tests	AE signals correspond to internal damage progression in CPB	AE tracking enhances UCS predictions in gangue-based CPB
Yin et al. [96]	AE application in CPB-rock combination failure assessment	AE monitoring with rise time, amplitude, average frequency value analysis	AE b-value and Dr indicator developed for failure prediction	AE b-value and Dr offer robust predictive tools for instability
Chen et al. [97]	AE integration with UCS testing for CPB analysis	AE ringing count correlation with UCS stress levels in CPB	AE and UCS tests complement each other for material stability assessment	AE supports non-destructive testing and UCS measurement integration

Furthermore, studies confirmed the validity of using AE for the estimation of UCS by studying micro-crack evolution [92,93], where some studies continued to extend the application of AE to shear failure analysis and gangue-based CPB [94,95]. Yin et al. [96] brought forward a new AE-based index for determining instability, and Chen et al. [97] highlighted the complementary application of AE in conjunction with UCS to depict the mechanical behavior of CPB. Hence, from several studies, it can be concluded that AE monitoring is a viable, online, and non-invasive technique for determining the strength, deformation, and failure of CPB or other cemented backfill with minimum dependence on destructive testing.

5. Comparative and Meta-Analysis of NDT Methods for UCS Prediction

To quantitatively compare the performance of NDT methods in predicting the UCS of CPB, a meta-analysis was conducted using data from 30 peer-reviewed studies. The correlation coefficients (R^2) between each method and UCS were extracted then visualized through a forest plot as shown in Figure 11.

The results indicate that the UPV and AE methods are very dependable and consistent. They have high average R^2 values of 0.895 and 0.896, meaning they are quite accurate. These methods show little variation across different studies, which makes them robust for predicting UCS with various CPB mixes. Notably, UCS thresholds are important in high-stress environments (e.g., deep mines with $\sigma_3 > 5$ MPa) or weak host rocks like coal where CPB must prevent roof collapse or pillar failure. Tailings composition (sulfidic vs. siliceous)

further dictates UCS targets, underscoring the need for reliable NDT correlations under diverse geotechnical conditions. On the other hand, the ER method has a slightly lower average R^2 of 0.872 and displays more variation, with R^2 values ranging from 0.82 to 0.91. This is mostly because ER is sensitive to external conditions like moisture and temperature.

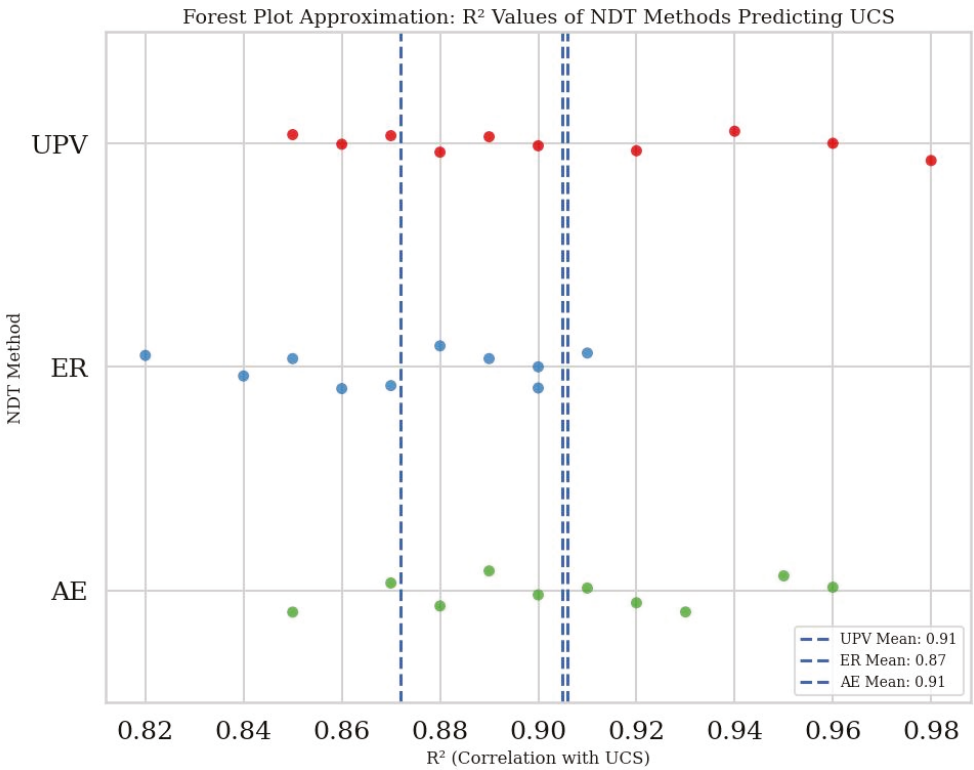

Figure 11. Forest plot of R2 values between NDT methods and UCS across 30 studies. This figure compares the R^2 values of NDT methods: UPV (green), AE (red), and ER (blue) in predicting UCS. Each point represents a study's R^2, with dashed lines showing the mean R^2 for each method. AE shows the highest average R^2 value among the methods.

These findings suggest that all three methods are effective for assessing CPB strength without causing damage. However, UPV and AE are particularly reliable and practical in different environments. AE is excellent for detecting early signs of cracking and failure, while UPV is best for monitoring hydration and material becoming denser. The variability in ER performance highlights the importance of controlling environmental factors when using this method.

The strong correlation between these methods supports the use of hybrid systems. Combining UPV with AE or ER could improve real-time prediction, early warnings, and monitoring the health of structures in mining areas. To compare these non-destructive testing (NDT) methods, we examined correlation coefficients, error margins, and sensitivity ranges from various studies. This section provides numerical benchmarks for UPV, ER, and AE in predicting UCS, offering a more data-focused evaluation based on prior findings from sources like [24,74,92].

A systematic comparison of NDT methods for CPB assessment is provided in Table 6 above; however, the information is represented visually in Figure 12 using Radar chart which makes the information easily understandable and easier to analyze. It can be used effectively to compare UPV, ER and AE against a number of critical factors and show their strengths and weaknesses. This graphical approach is a comprehensive comparison tool that can be used to easily determine the most appropriate NDT method for a given application.

Table 6. Summary of meta-analysis results for NDT methods (UPV, ER, and AE) based on R^2 correlation with UCS, showing the predictive strength and variability of each method.

NDT Method	Mean (R^2)	Range	Insight
UPV	0.895	0.85–0.95	Strong and consistent predictor of UCS; minimal spread shows reliability.
ER	0.872	0.78–0.92	Slightly lower mean R^2 with higher variability due to moisture sensitivity.
AE	0.896	0.80–0.96	Comparable to UPV in strength prediction; shows tight clustering, excellent for crack progression detection.

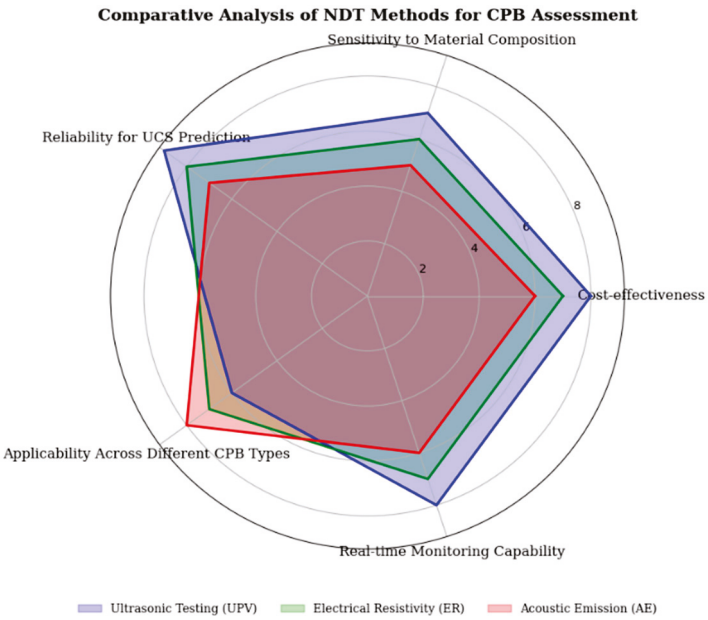

Figure 12. Radar Chart showing the comparative performance of UPV, ER, and AE across five critical parameters. Higher values indicate better performance in each category. Data extracted from multiple case studies (2020–2024) assessing NDT methods for CPB evaluation.

The UPV method has a high correlation with UCS (R^2 = 0.85–0.95) and is therefore a very accurate non-destructive tool for estimating strength. However, the ±5% error margin, which is caused by voids, density variations, and material heterogeneity, needs to be calibrated for different CPB mixtures [41,72]. In a similar manner, ER testing is a moderate to strong UCS correlation (R^2 = 0.78–0.92) and is suitable for hydration and microstructural monitoring [81]. However, accuracy is ±10% and it is sensitive to moisture, which means that it needs to be applied in controlled conditions or with correction factors [86]. Acoustic Emission (AE) monitoring, which correlates well with UCS (R^2 = 0.80–0.96), can detect 85–96% of crack events before failure, providing up to 48 h of predictive lead time [92,94]. However, AE accuracy depends on sensor placement, signal noise filtering, and crack initiation conditions, requiring advanced processing techniques for enhanced reliability.

The fundamental differences in performance are from their underlying physics: UPV measures wave velocity through solids, ER tracks ionic conductivity in pore solutions, and AE records stress induced acoustic waves. The strengths of these techniques are complementary, and it is conceivable that hybrid methods that incorporate aspects of UPV, ER, and AE could represent a more holistic framework for the assessment of CPB.

6. Simulation-Based Validation of a Hybrid NDT Approach

To support the comparative meta-analysis of existing NDT techniques, a simulation-based assessment was conducted to evaluate the predictive strength of a hybrid NDT model that integrates UPV, AE and ER for UCS estimation. Due to the scarcity of publicly available datasets containing all three NDT parameters together, a synthetic dataset had to be developed. This dataset is like the real world in terms of material conditions and the way measurements can vary, providing a controlled environment to explore the behavior of CPB under hybrid NDT monitoring.

6.1. Synthetic Data Generation

A total of 100 synthetic samples were created using possible value ranges found in the literature, as projected in Table 7. The UPV values were designed with a normal distribution, averaging 3.2 km/s with a small variation in ±0.3. This represents how sound waves typically move through compacted CPB. AE values were generated using a gamma distribution to reflect the skewed nature of acoustic emissions during crack initiation and progression. ER values were developed using a uniform distribution, meaning they were evenly distributed between 50 and 120 ohm-m. This range matches the differences in moisture and small pores in the materials used to fill backfilled spaces.

Table 7. A summary of the synthetic data generated for the studies (see Supplementary Materials for full dataset).

UPV (km/s)	AE (Units)	ER (ohm-m)	UCS (MPa)
3.149	2.221	90.44	29.638
3.335	7.175	112.79	42.654
3.536	3.273	102.97	37.580
. . .. . .	. . .. . .	. . ..	. . ..

The UCS is a simple linear equation made with three predictors, as shown in Equation (1). To mimic the unpredictability of real-world situations, it includes random variations to capture the uncertainties we often experience:

$$\mathrm{UCS} = 10 \cdot \mathrm{UPV} + 0.8 \cdot \mathrm{AE} - 0.05 \cdot \mathrm{ER} + \varepsilon \quad (1)$$

where ε is a Gaussian noise term with mean 0 and standard deviation 5 MPa.

6.2. Model Training and Evaluation

Models were trained using Python's scikit-learn (v1.2) with an 80/20 split, balancing computational efficiency and robust validation (sufficient test samples). This ratio aligns with ML best practices for small-to-medium datasets [3,36], avoiding overfitting while preserving statistical power. Linear regression (LR) and random forest (RF) models were selected in order to evaluate how well the models works. These models used three input features—UPV, AE, and ER—to predict UCS, the target variable. We split the dataset, using 80% for training the models and 20% for testing to make sure the results are reliable. The performance results for these models can be found in Table 8, which provides a clear comparison of how each model did in making predictions.

Table 8's results show that LR model consistently outperforms RF model when using single-input features especially with AE, while RF struggles to capture patterns with limited inputs. However, RF performance improves with hybrid inputs, particularly with the full combination (UPV + AE + ER), where it achieves its best R^2 of 0.320. Although LR still shows slightly higher accuracy overall, the results highlight RF potential in capturing complex, non-linear relationships when multiple NDT features are integrated.

Table 8. LR and RF model performance across different NDT input configurations for UCS prediction.

Model Input	R^2 (LR)	MAE (LR)	R^2 (RF)	MAE (RF)
UPV only	0.148	6.32	0.063	5.99
AE only	0.291	5.89	−0.083	7.07
ER only	−0.035	6.60	0.020	6.13
UPV + AE	0.377	5.54	0.187	6.25
UPV + ER	0.149	6.22	0.069	6.23
AE + ER	0.318	5.49	0.101	6.63
UPV + AE + ER	0.389	5.40	0.320	5.82

To maintain clarity and avoid redundancy in figure presentation, only the best-performing hybrid configuration is visualized. Among the three possible two-feature combinations (UPV + AE, UPV + ER, AE + ER), the UPV + AE model demonstrated the highest predictive performance with respect to R^2 and mean absolute error (MAE). As such, it serves as a representative case to illustrate the improvement achievable through partial feature integration, while ensuring the manuscript remains concise and focused.

As shown in Figure 13, both partial and full models demonstrate moderate alignment with actual UCS, but the full hybrid model (blue markers) yields a marginal improvement over the partial hybrid model (orange markers). Specifically, the full hybrid configuration achieves an R^2 of 0.389 and MAE of 5.40 MPa, and a significant *p*-value of 0.00075, compared to the partial model R^2 of 0.377 and MAE of 5.54 MPa, and *p*-value of 0.000715. Although the improvement might seem small, it shows the benefit of including ER in predicting UCS. This is important when small improvements can lead to more reliable assessments of structures. Such enhancements are especially valuable for CPB and similar materials. The results demonstrate that even with straightforward methods, using various types of data can improve the accuracy of strength evaluations.

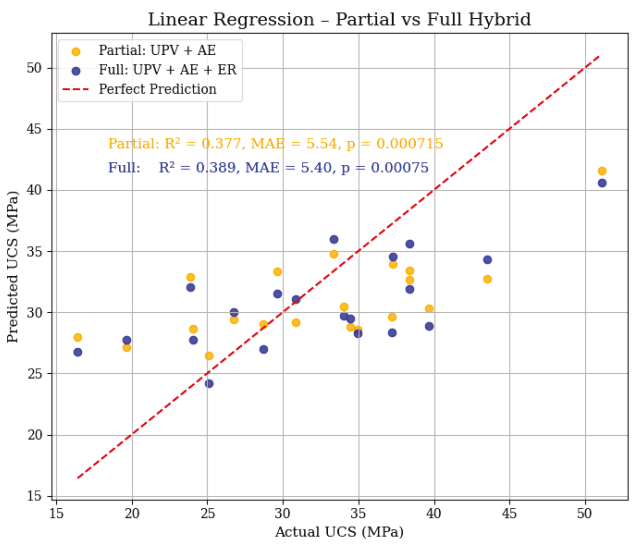

Figure 13. Actual versus predicted UCS using LR models trained on partial (UPV + AE) and full (UPV + AE + ER) hybrid inputs. The red dashed line represents perfect prediction (y = x). Annotated within the plot are the R^2, MAE, and *p*-values from an auxiliary LR analysis confirming statistical significance. The inclusion of ER improves prediction accuracy modestly.

As shown in Figure 14, the full hybrid model (purple markers) clearly shows better clustering along the perfect prediction line, with an R^2 of 0.320 and MAE of 5.82 MPa, and a significant *p*-value of 0.000328, compared to the partial model R^2 of 0.187 and MAE of 6.25 MPa, and *p*-value of 0.0186. This performance improvement confirms the value of incorporating ER alongside UPV and AE, especially in ML frameworks capable of capturing non-linear feature interactions. Unlike LR, where adding ER had marginal impact, RF

capitalizes more effectively on the diversity of input data. These findings support the conclusion that a full hybrid NDT approach enhances model generalization and prediction accuracy, offering practical benefits for reliable UCS assessment in cement-based materials.

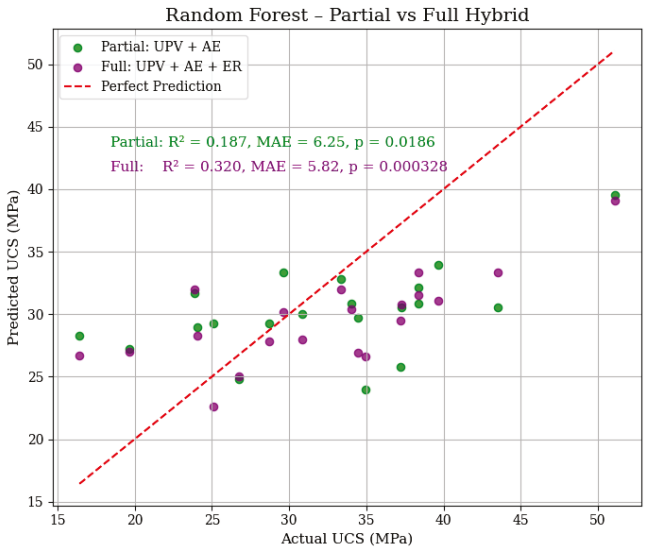

Figure 14. Actual versus predicted UCS using RF models with partial (UPV + AE) and full (UPV + AE + ER) hybrid inputs. The red dashed line indicates the ideal prediction line. R^2, MAE, and *p*-values are annotated within the plot, showing that the full hybrid model significantly improves prediction accuracy compared to the partial hybrid configuration. These results highlight the advantage of incorporating multiple NDT parameters for more reliable UCS estimation.

6.3. Residual and Feature Analysis

Figure 15 offers a deeper understanding of how the RF model operates with hybrid NDT inputs. The residual plot (a) shows that prediction errors are spread around the zero line, indicating that the model performs well without obvious bias or underfitting issues. The feature importance plot (b), reveals that AE and UPV are the most significant for the model predictions, while ER contributes less but is still helpful. This means that combining all three NDT methods improves the model's accuracy, but AE and UPV have more influence in predicting UCS. These perceptions confirm the usefulness of the hybrid method and help professionals decide which NDT variables are most important when data is limited.

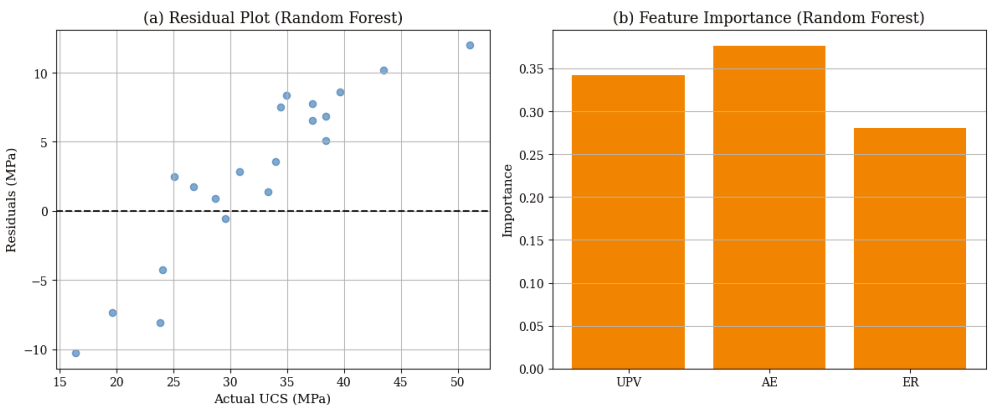

Figure 15. RF model results using hybrid NDT inputs (UPV, AE, ER), with (**a**) showing the residual plot and moderate prediction errors around the zero line, and (**b**) showing the feature importance plot identifying AE and UPV as dominant predictors of UCS.

6.4. Discussion and Broader Relevance

The simulation demonstrates that combining different NDT methods, such as UPV, AE, and ER results in more accurate predictions than relying on any single method. This combined approach is effective not only for CPB conditions but also for other cement and pavement materials. UPV and AE are commonly used in road diagnostics to detect issues like compaction problems and fatigue cracking. ER helps identify moisture-related damage. Thus, the hybrid NDT model offers a reliable way to assess the strength of structures without causing harm. It can be applied in smart road systems, quality assurance and asset management, making it a valuable tool for future infrastructure projects. To enhance this model further, future work should involve testing it with real-world data to ensure its effectiveness and applicability.

7. Conclusions

This study reviewed and benchmarked the effectiveness of UPV, AE, and ER as NDT for estimating the compressive strength of CPB and similar cementitious systems. Thirty peer-reviewed studies were analyzed, selecting ten for each method and conducting meta-analyses to quantitatively compare their performance using reported R^2 values. The findings reveal that UPV proved to be the most dependable for predicting strength in different mixtures and at different curing times. AE and ER were also useful but less consistent. Each method provides unique insights into material properties, such as density, presence of cracks, and moisture content.

To better understand how a hybrid diagnostic strategy could be more effective, a synthetic simulation dataset was created using data from all three NDT techniques. Researchers developed linear regression and random forest models to predict material strength more accurately. The hybrid model which utilized the combined dataset outperformed the models that relied on just one NDT input. It achieved an R^2 value of 0.389 and MAE of 5.40 MPa. Analyzing the errors showed that the hybrid model was better at reducing both bias and prediction mistakes.

Additionally, when looking at which features were most important, it became clear that UPV, AE, and ER each played a key role in enhancing the model performance. Although this simulation was designed around CPB conditions, the proposed hybrid framework is transferable to pavement and asphalt materials, where similar NDT techniques are used to examine compaction quality, fatigue cracking and subsurface moisture damage. The model is useful for both underground and surface materials, making it a valuable tool for sustainable and non-invasive checking in infrastructure projects.

This study presents a two-pronged approach combining systematic review and simulation modeling to link current NDT methods with ways to predict future conditions. Demonstrating the hybrid NDT approach is an important step toward using advanced tools for quality checks, maintenance planning, and developing modern infrastructure systems. Future work should focus on gathering real-world data for this method, testing the models in actual field conditions and exploring how these methods can work together with new sensors and IoT technologies for ongoing monitoring.

Supplementary Materials: The following supporting information can be downloaded at: https://www.mdpi.com/article/10.3390/ma18122888/s1, Synthetic NDT and UCS Data.

Author Contributions: Conceptualization, S.B.A., Q.C., E.Y. and D.W.; methodology, S.B.A., Q.C. and E.Y.; software, S.B.A. and Q.C.; validation, S.B.A., Q.C. and D.W.; formal analysis, S.B.A., Q.C., E.Y. and D.W.; investigation, Q.C., E.Y. and D.W.; resources, S.B.A., Q.C., E.Y. and D.W.; data curation, S.B.A., Q.C., E.Y. and D.W.; writing—original draft preparation, S.B.A. and Q.C.; writing—review and editing, E.Y. and D.W.; visualization, S.B.A., Q.C., E.Y. and D.W.; supervision, Q.C.; project

administration, Q.C. and S.B.A. All authors have read and agreed to the published version of the manuscript.

Funding: This research was made possible through funding from the National Natural Science Foundation of China (Grants 52274151 and 52474165), for which the authors express their sincere appreciation.

Institutional Review Board Statement: Not applicable.

Informed Consent Statement: Not applicable.

Data Availability Statement: The original contributions presented in this study are included in the article. Further inquiries can be directed to the corresponding author.

Conflicts of Interest: The authors declare no conflicts of interest.

Abbreviations

AAS	Alkali-Activated Slag
AE	Acoustic Emission
CPB	Cemented Paste Backfill
ER	Electrical Resistivity
LR	Linear Regression
NDT	Non-Destructive Testing
RF	Random Forest
R^2	Coefficient of Determination
UCS	Uniaxial Compressive Strength/Unconfined Compressive Strength
UPV	Ultrasonic Pulse Velocity
DT	Destructive Testing
MAE	Mean Absolute Error
ASTM	American Society for Testing and Materials
ISO	International Organization for Standardization
SF	Silica Fume
WPA	Waste Pumice Aggregate
FAC	Fly Ash Cenosphere
NER	Normalized Electrical Resistivity
ICPB	Improved Cemented Paste Backfill
DS	Dredged Sediment
IoT	Internet of Things

References

1. He, W.; Zhao, K.; Zheng, C.; Li, S.; Shi, W. Strength development monitoring of cemented paste backfill using guided waves. *Sensors* **2021**, *21*, 8499. [CrossRef] [PubMed]
2. Pan, A.; Grabinsky, M. Direct Tensile Measurement for Cemented Paste Backfill. *Minerals* **2023**, *13*, 1218. [CrossRef]
3. Qi, C.; Zhang, Q.; Chen, Q.; Fourie, A. A strength prediction model using artificial intelligence for recycling waste tailings as cemented paste backfill. *J. Clean. Prod.* **2018**, *183*, 566–578. [CrossRef]
4. *ASTM C39/C39M-24*; Standard Test Method for Compressive Strength of Cylindrical Concrete Specimens. ASTM International: West Conshohocken, PA, USA, 2024.
5. Chen, Q.; Zhu, L.; Wang, Y.; Chen, J.; Qi, C. The carbon uptake and mechanical property of cemented paste backfill carbonation curing for low concentration of CO_2. *Sci. Total. Environ.* **2022**, *852*, 158516. [CrossRef]
6. Wang, Y.; Wang, D.; Dai, B.; Chen, Q. Guidance and review: Advancing mining technology for enhanced production and supply of strategic minerals in China. *Green. Smart Min. Eng.* **2024**, *1*, 2–11. [CrossRef]
7. Joel, S. Compressive strength of concrete using fly ash and rice husk ash: A review. *Civ. Eng. J.* **2020**, *6*, 1400–1410.
8. Kashem, A.; Karim, R.; Alharthai, M.; Das, P.; Datta, S.D. Compressive strength prediction of sustainable concrete incorporating rice husk ash (RHA) using hybrid machine learning algorithms and parametric analyses. *Case Stud. Constr. Mater.* **2024**, *20*, e03030. [CrossRef]
9. Teymen, A.; Mengüç, E.C. Comparative evaluation of different statistical tools for the prediction of uniaxial compressive strength of rocks. *Int. J. Min. Sci. Technol.* **2020**, *30*, 785–797. [CrossRef]

10. Biswal, U.S.; Pasla, D.; Mishra, M.; Singh, M.K. Experimental investigation and comparative machine learning prediction of the compressive strength of recycled aggregate concrete incorporated with fly ash, GGBS, and metakaolin. *Innov. Infrastruct. Solut.* **2022**, *7*, 242. [CrossRef]
11. Ren, Q.; Han, S.; Wang, G.; Li, M. Prediction of rock compressive strength using machine learning algorithms based on spectrum analysis of geological hammer. *Geotech. Geol. Eng.* **2019**, *37*, 475–489. [CrossRef]
12. Yesiloglu-Gultekin, N.; Sezer, E.; Gokceoglu, C. Prediction of uniaxial compressive strength of granitic rocks by various nonlinear tools and comparison of their performances. *Int. J. Rock. Mech. Min. Sci. Géoméch. Abstr.* **2013**, *62*, 113–122. [CrossRef]
13. Sari, M.; Karasu, S.; Yilmaz, E.; Kasap, T. Exploring the link between ultrasonic and strength behavior of cementitious mine backfill by considering pore structure. *Constr. Build. Mater.* **2023**, *370*, 130588. [CrossRef]
14. Al-Bakri, A.Y.; Ahmed, H.M.; Hefni, M.A. Experimental Investigation of Recycling Cement Kiln Dust (CKD) as a Co-Binder Material in Cemented Paste Backfill (CPB) Made with Copper Tailings. *Minerals* **2024**, *14*, 750. [CrossRef]
15. Sovják, R.; Vogel, F.; Beckmann, B. Triaxial compressive strength of ultra high performance concrete. *Acta Polytech.* **2013**, *53*, 901–905. [CrossRef]
16. Jiang, H.; Li, Y.; Liu, J.; Yilmaz, E.; Han, J.; Sun, Q. Relationship between ultrasonic pulse velocity and uniaxial compressive strength for cemented paste backfill with alkali-activated slag. *Nondestruct. Test. Eval.* **2020**, *35*, 359–377. [CrossRef]
17. *ASTM G57-06*; Standard Test Method for Field Measurement of Soil Resistivity Using the Wenner Four-Electrode Method. ASTM International: West Conshohocken, PA, USA, 2006.
18. Irianto, N.A.I.; Anwar, B.A.M.K.; Anuar, I.Z.K. The assessment of standard concrete under damage and undamage condition using non-destructive test (NDT) method. *Multidiscip. Appl. Res. Innov.* **2023**, *4*, 54–60.
19. Citra, Z.; Apdeni, R.; Wibowo, P.D.; Malinda, Y.; Herol, H.; Wibisono, A. Testing of Concrete Structures with Non-Destructive Test Method (NDT) Using Ultrasonic Pulse Velocity (UPV) at the Building on the Ancol Beach. *CIVED* **2024**, *11*, 217–225. [CrossRef]
20. Cao, S.; Xue, G.; Yilmaz, E. Flexural behavior of fiber reinforced cemented tailings backfill under three-point bending. *IEEE Access* **2019**, *7*, 139317–139328. [CrossRef]
21. Quan, W.; Fall, M. Temperature-driven crack self-healing and performance recovery in cemented tailings materials. *Case Stud. Constr. Mater.* **2024**, *21*, e04105. [CrossRef]
22. Fall, M.; Nasir, O. Mechanical behaviour of the interface between cemented tailings backfill and retaining structures under shear loads. *Geotech. Geol. Eng.* **2010**, *28*, 779–790. [CrossRef]
23. Zhao, X.; Fourie, A.; Qi, C.-C. Mechanics and safety issues in tailing-based backfill: A review. *Int. J. Miner. Met. Mater.* **2020**, *27*, 1165–1178. [CrossRef]
24. Yılmaz, T.; Ercikdi, B. Predicting the uniaxial compressive strength of cemented paste backfill from ultrasonic pulse velocity test. *Nondestruct. Test. Eval.* **2016**, *31*, 247–266. [CrossRef]
25. Wu, W.; Zhang, Y.; Xu, W. Measuring Ultrasonic and Electrical Properties of Early-Age Cemented Tailings Backfill. *Minerals* **2023**, *13*, 135. [CrossRef]
26. Pérez, J.A.V.; Guzmán, E.M.A.; Molina, W.M.; Sánchez, M.A.; Moreno, I.T.; Chávez-García, H.L. Evaluation of the electrical resistivity, ultrasonic pulse velocity and mechanical properties in portland cement pastes type II. *Key Eng. Mater.* **2020**, *841*, 198–202. [CrossRef]
27. *ISO 679*; Methods of Testing Cements-Determination of Strength. International Organization for Standardization: Geneva, Switzerland, 2009.
28. Kot, P.; Yeboah, D.; Muradov, M.; Hashim, K.; Gkantou, M.; Kamaris, G.S. Recent advancements in non-destructive testing techniques for structural health monitoring. *Appl. Sci.* **2021**, *11*, 2750. [CrossRef]
29. Tejedor, B.; Lucchi, E.; Bienvenido-Huertas, D.; Nardi, I. Non-destructive techniques (NDT) for the diagnosis of heritage buildings: Traditional procedures and futures perspectives. *Energy Build.* **2022**, *263*, 112029. [CrossRef]
30. Fall, M.; Saa, E.; Benzaazoua, M. Mix proportioning of underground cemented tailings backfill. *Tunn. Undergr. Space Technol.* **2008**, *23*, 80–90. [CrossRef]
31. Tang, R.; Xin, J.; Li, L.; Ning, J.; Shao, X.; Zhao, B.; Tian, C.; Li, C.; Xu, B. Experimental study on the effect of fly ash with ammonium salt content on the properties of cemented paste backfill. *Constr. Build. Mater.* **2023**, *369*, 130513. [CrossRef]
32. Qiu, J.; Xing, J.; Sun, X.; Li, S.; Yang, L. Strength characteristics and failure mechanism of cemented super-fine unclassified tailings backfill. *Minerals* **2017**, *7*, 58. [CrossRef]
33. Heidari, M.; Kargarian, S.; Khanlari, G.R.; Kaveh, M.T. Predicting the uniaxial compressive and tensile strengths of gypsum rock by point load testing. *Rock. Mech. Rock. Eng.* **2012**, *45*, 265–273. [CrossRef]
34. Jafari, M.; Shahsavari, M.; Grabinsky, M. Drained triaxial compressive shear response of cemented paste backfill (CPB). *Rock. Mech. Rock. Eng.* **2021**, *54*, 3309–3325. [CrossRef]
35. Nie, X.; Ren, M.; Jing, H.; Wu, J.; Deng, T.; Wang, Q.; Zhang, Q.; Yin, Q. Investigating mechanical properties of cemented gangue backfill materials subjected to static-dynamic combined loads. *Constr. Build. Mater.* **2023**, *400*, 132674. [CrossRef]

36. Wang, Y.; Yang, G.; Na, Q.; Wu, A.; Cao, C.; Wang, L.; Wang, Z. Experimental research and numerical simulation of the multi-field performance of cemented paste backfill: Review and future perspectives. *Int. J. Miner. Met. Mater.* **2023**, *30*, 193–208. [CrossRef]
37. Sun, W.; Wu, S. A study of crack initiation and source mechanism in the Brazilian test based on moment tensor. *Eng. Fract. Mech.* **2021**, *246*, 107622. [CrossRef]
38. Tang, G.; Guo, L.J.; Yang, X.; Liu, G. Determination of the relationship between direct tensile test and Brazilian splitting test of cemented tailings backfill. In *Paste 2023: Proceedings of the 25th International Conference on Paste, Thickened and Filtered Tailings*; University of Alberta, Edmonton, and Australian Centre for Geomechanics: Perth, Australia, 2023.
39. Komurlu, E.; Kesimal, A.; Demir, S. Experimental and numerical analyses on determination of indirect (splitting) tensile strength of cemented paste backfill materials under different loading apparatus. *Géoméch. Eng.* **2016**, *10*, 775–791. [CrossRef]
40. Kaklis, K.; Agioutantis, Z.G.; Mavrigiannakis, S.P.; Nomikos, P.P. A multi-stage triaxial test for cemented paste backfill. In *ARMA US Rock Mechanics/Geomechanics Symposium*; ARMA: Seattle, Washington, 2018.
41. García, V.J.; Zúñiga-Suárez, A.R.; Villalta-Granda, L.J.; Márquez, C.O.; Zuñiga-Torres, B.C. Brazilian test of concrete specimens subjected to different loading geometries: Review and new insights. *Int. J. Concr. Struct. Mater.* **2017**, *11*, 343–363. [CrossRef]
42. Srivastava, A.; Singh, S.K.; Sharma, C.S. Correlation between ultrasonic pulse velocity (UPV) and compressive strength of coal bottom ash mortar. *J. Inst. Eng. (India) Ser. A* **2021**, *102*, 421–433. [CrossRef]
43. Widodo, S.; Nugroho, M.S.; Mahardika, H.; Ma'ARif, F. Correlation of ultrasonic pulse velocity with porosity and compressive strength of mortar with limestone for building quality assessment. *UKaRsT* **2022**, *6*, 190–202. [CrossRef]
44. Jiang, H.; Qiu, J.; Liu, S.; Yi, H.; Yilmaz, E. Ultrasonic evaluation of strength properties of cemented paste backfill: Effects of mineral admixture and curing temperature. *Ultrasonics* **2020**, *100*, 105983. [CrossRef]
45. Xu, X.; Sun, X.; Yao, W.; Wu, P.; Liu, N.; Guo, Z.; Qiu, J. Strength and ultrasonic characteristics of cemented paste backfill incorporating foaming agent. *Minerals* **2021**, *11*, 681. [CrossRef]
46. Qiu, J.; Jiang, H.; Zhao, Y.; Guo, Z.; Yang, L. Effect of tailings fineness on flow, strength, ultrasonic and microstructure characteristics of cemented paste backfill. *Constr. Build. Mater.* **2020**, *263*, 120645. [CrossRef]
47. Diez d'Aux, M. Ultrasonic Wave Measurement Through Cement Paste Backfill. Master's Thesis, University of Toronto, Toronto, ON, Canada, 2008.
48. Rehman, S.K.U.; Jameel, M.; Memon, S.A.; Ibrahim, Z. Nondestructive test methods for concrete bridges: A review. *Constr. Build. Mater.* **2016**, *107*, 58–86. [CrossRef]
49. Wang, Z.; Ji, X.; Guo, H.; Wang, J.; Zhang, H.; Zhang, H.; Zhang, T.; Huo, J.; Shao, T.; Yu, P.; et al. Principles, properties and applications of smart conductive cement-based composites: A state-of-the-art review. *Constr. Build. Mater.* **2023**, *408*, 133569. [CrossRef]
50. Zárate, D.M.; Cárdenas, F.; Forero, E.F.; Peña, F.O. Strength of concrete through ultrasonic pulse velocity and uniaxial compressive strength. *Int. J. Technol.* **2022**, *13*, 103–114. [CrossRef]
51. *IS 516:2018*; Hardened Concrete—Methods of Test. Bureau of Indian Standards (BIS): New Delhi, India, 2018.
52. *IS 13311:1992*; Method of Non-Destructive Testing of Concrete-Part 1: Ultrasonic Pulse Velocity Testing. Bureau of Indian Standards (BIS): New Delhi, India, 1992.
53. Kowsalya, M.; Nachiar, S.; Anandh, S. Correlation Between Compressive Strength and Ultrasonic Pulse Velocity (UPV) of Fly ash Cenosphere Concrete. *Eng. J.* **2024**, *28*, 41–49. [CrossRef]
54. Lang, L.; Liu, N.; Chen, B. Investigation on the strength, durability and swelling of cement-solidified dredged sludge admixed fly ash and nano-SiO_2. *Eur. J. Environ. Civ. Eng.* **2022**, *26*, 2913–2933. [CrossRef]
55. Wan, Y.; Xue, J.; Li, J.; Hui, X.; He, X.; Feng, D.; Liu, X.; Wang, S. Performance of green binder developed from flue gas desulfurization gypsum incorporating Portland cement and large-volume fly ash. *Constr. Build. Mater.* **2022**, *348*, 128679. [CrossRef]
56. Fall, M.; Ouellet, S.; Benzaazoua, M. Experimental characterization of the influence of tailings fineness and density on the quality of cemented paste backfill. *Miner. Eng.* **2005**, *18*, 41–44. [CrossRef]
57. Saedi, A.; Jamshidi-Zanjani, A.; Darban, A.K. A review on different methods of activating tailings to improve their cementitious property as cemented paste and reusability. *J. Environ. Manag.* **2020**, *270*, 110881. [CrossRef]
58. Zhang, H.; Hu, W.; Xia, K.; Chen, S.; Ye, L.L.; Li, H. Study on mechanical behavior of inclined cemented tailings composite backfill (CTCB) under uniaxial compression. *Constr. Build. Mater.* **2024**, *439*, 137410. [CrossRef]
59. Tu, B.; Liu, L.; He, H.; Ding, X.; Yang, Q. Comparative Analysis of Uniaxial and Triaxial Compression Characteristics of Cement Tailings Backfill. *Min. Met. Explor.* **2025**, *42*, 335–345. [CrossRef]
60. Xu, W.; Tian, X.; Wan, C. Prediction of mechanical performance of cemented paste backfill by the electrical resistivity measurement. *J. Test. Eval.* **2018**, *46*, 2450–2458. [CrossRef]
61. Fang, K.; Haruna, S.; Zhang, J.; Cui, L.; Li, M. Cost optimization of cemented paste backfill: State-of-the-art review and future perspectives. *Miner. Eng.* **2023**, *204*, 108414. [CrossRef]

62. Dahlin, T.; Olsson, P.; Hedblom, P.; Rejkjær, S.; Lumetzberger, M. Novel electrode design for non-destructive resistivity measurement on material in geotechnical standard sample cylinders. In Proceedings of the NSG2023 29th European Meeting of Environmental and Engineering Geophysics, Edinburgh, UK, 3–7 September 2023; European Association of Geoscientists & Engineers: Utrecht, The Netherlands, 2023.
63. Carrasco, Á.; Leaman, F.; Méndez, F.; Vicuña, C.M. Short review of the use of acoustic emissions for detection and monitoring of cracks. *Acoust. Aust.* **2021**, *49*, 273–280. [CrossRef]
64. Wang, B.; Kang, M.; Li, Q.; Yang, L.; Shu, X. Mechanical behavior, acoustic emission and principal strain field evolution properties of layered cemented paste backfill under unconfined compression. *Constr. Build. Mater.* **2024**, *415*, 135111. [CrossRef]
65. Yin, S.; Liu, X.; Wang, H.; Wu, A.; Wang, Y.; Shao, Y. A systematic review of paste technology in metal mines for cleaner production in China. *J. Clean. Prod.* **2020**, *247*, 119590. [CrossRef]
66. He, Z.; Ju, F.; Wang, T.; Ning, P.; Xiao, M.; Wang, D. Acoustic emission investigation of coal gangue cementitious composites under effects on fiber type. *Case Stud. Constr. Mater.* **2022**, *17*, e01567. [CrossRef]
67. Wang, J.; Xiao, J.; Hu, X.; Han, K.; Zhang, Z.; Jiang, F. Action mechanism of rice husk ash and the effect on main performances of cement-based materials: A review. *Constr. Build. Mater.* **2021**, *288*, 123068. [CrossRef]
68. Li, D.; Wang, D.; Kong, X.; Wang, E.; Ali, M. Mechanical behaviors and acoustic emission fractal characteristics of coal specimens with a pre-existing flaw of various inclinations under uniaxial compression. *Int. J. Rock. Mech. Min. Sci.* **2019**, *116*, 38–51. [CrossRef]
69. Song, X.; Shi, J.; Yang, F.; Yalçınkaya, Ç.; Zhao, W.; Yu, X. Progressive damage process and destabilization precursor recognition of sulfate tailing-cemented paste backfill based on acoustic emission. *Powder Technol.* **2023**, *430*, 119047. [CrossRef]
70. Yang, L.; Zhu, W.; Hou, C.; Liu, X.; Yan, B.; Li, L. Monitoring the failure process of cemented paste backfill at different curing times by using a digital image correlation technique. *Constr. Build. Mater.* **2022**, *346*, 128487. [CrossRef]
71. Chai, M.; Li, Y.; Zhang, Z.; Duan, Q.; Gao, Z.; Chen, R. An approach for identifying corrosion damage from acoustic emission signals using ensemble empirical mode decomposition and linear discriminant analysis. *Meas. Sci. Technol.* **2022**, *33*, 065018. [CrossRef]
72. Jing, G.; Zhao, Y.; Lacidogna, G.; Montanari, P.M.; Gao, Y. Noise reduction based on improved variational mode decomposition for acoustic emission signal of coal failure. *Appl. Sci.* **2023**, *13*, 9140. [CrossRef]
73. Godin, N.; Fantozzi, G.; Reynaud, P. Challenges and limitations in the identification of acoustic emission signature of damage mechanisms in composites materials. *Appl. Sci.* **2018**, *8*, 1267. [CrossRef]
74. Wu, D.; Zhang, Y.; Liu, Y. Mechanical performance and ultrasonic properties of cemented gangue backfill with admixture of fly ash. *Ultrasonics* **2016**, *64*, 89–96. [CrossRef]
75. Xu, S.; Li, Y.; Li, K.; Suorineni, F.T. Evaluation of the strength and ultrasonic properties of foam-cemented paste backfill. *Int. J. Min. Reclam. Environ.* **2017**, *31*, 544–557. [CrossRef]
76. Mendes, S.E.S.; Pereira, E.; Pereira, E.; Cremonez, C.; Oliveira, R.L.N.; Medeiros-Junior, R.A. Mixture design of concrete using ultrasonic pulse velocity. *Int. J. Civ. Eng.* **2019**, *18*, 113–122. [CrossRef]
77. Nugroho, M.S.; Widodo, S.; Suryadwanti, N.; Rachmi, D.; Fajriani, Q.; Setiawan, W.; Ma'ARif, F. The effect of mortar mixture variations on the compressive strength and ultrasonic pulse velocity. *INERSIA Lnformasi Dan. Ekspose Has. Ris. Tek. Sipil Dan. Arsit.* **2022**, *18*, 225–234. [CrossRef]
78. Hong, G.; Kim, Y.-J.; Chin, W.-J.; Choi, S.; Oh, S.; Song, C. Correlation between the compressive strength and ultrasonic pulse velocity of cement mortars blended with silica fume: An analysis of microstructure and hydration kinetics. *Materials* **2021**, *14*, 2476. [CrossRef]
79. Aslam, H.M.S.; Khan, M.A.; Latif, A.; Rehman, A.U.; Hussain, S.; Noshin, S.; Yasin, M.; Onyelowe, K.C. Evaluating the mechanical and durability properties of sustainable lightweight concrete incorporating the various proportions of waste pumice aggregate. *Results Eng.* **2024**, *24*, 103496. [CrossRef]
80. Xu, W.; Tian, X.; Cao, P. Assessment of hydration process and mechanical properties of cemented paste backfill by electrical resistivity measurement. *Nondestruct. Test. Eval.* **2018**, *33*, 198–212. [CrossRef]
81. Liu, L.; Guo, L.; Song, K.-I.; Huan, C.; Yang, Q.; Yang, P.; Zhang, B. Study on hydration reaction and structure evolution of cemented paste backfill in early-age based on resistivity and hydration heat. *Constr. Build. Mater.* **2021**, *272*, 121827. [CrossRef]
82. He, Z.; Ning, P.; Xiao, M.; Ju, F.; Zhou, C. An experimental investigation on the compaction characteristic of coal waste rock backfilling material using electrical resistivity method. *Environ. Earth Sci.* **2021**, *80*, 450. [CrossRef]
83. Zhu, C.; Pu, Y.; Qi, C.; Yang, P.; Chen, J.; Liu, L.; Chen, Q. Effect of ice addition on the properties and microstructure of cemented paste backfill at early-age. *J. Build. Eng.* **2023**, *71*, 106439. [CrossRef]
84. Lee, D.; Tutumluer, E.; Kim, D.-J.; Lee, J.-S.; Byun, Y.-H. Evaluation of electrical resistivity of cement-based materials using time domain reflectometry. *Measurement* **2024**, *236*, 115166. [CrossRef]
85. Zhang, C.; Zhao, T.; Song, W.; Tan, Y.; Fu, J.; Taheri, A. Hydration mechanism and mechanical-thermal correlation of cemented paste backfill under different curing temperatures. *J. Build. Eng.* **2024**, *85*, 108691. [CrossRef]

86. Wan, L.; Yu, M.; Wu, E.; Zhao, Y. The Effects of Calcium Nitrite on the Mechanical Properties and Microstructure of Early-Age Frozen Cement Paste. *Materials* **2024**, *17*, 2461. [CrossRef]
87. Gholampoor, M.; Dahlin, T.; Hedblom, P.; Lumetzberger, M. Correlation between electrical resistivity and compressive strength of stabilized dredged sediment for early quality control. *Transp. Eng.* **2024**, *18*, 100280. [CrossRef]
88. Cao, S.; Song, W.; Xue, G.; Yilmaz, E. Assessment of acoustic emission and triaxial mechanical properties of rock-cemented tailings matrix composites. *Adv. Mater. Sci. Eng.* **2019**, *2019*, 6742392. [CrossRef]
89. Wu, J.; Chen, Z.; Han, G.; Feng, M.; Ni, X. Experimental investigation on mechanical properties of cemented paste backfill under different gradations of aggregate particles and types and contents of cementing materials. *Adv. Mater. Sci. Eng.* **2019**, *2019*, 9456861. [CrossRef]
90. Wang, J.; Zhang, Y.; Song, W.; Fu, J.; Wang, Y. Mechanical behavior, acoustic emission properties and damage evolution of cemented paste backfill considering structural feature. *Constr. Build. Mater.* **2020**, *261*, 119958. [CrossRef]
91. Zhao, K.; Wang, J.; Zhu, S.; Zhou, Y.; Yu, X.; Wang, Q. Acoustic emission investigation of cemented paste backfill prepared with tantalum–niobium tailings. *Constr. Build. Mater.* **2020**, *237*, 117523. [CrossRef]
92. Zhou, Y.; Yan, Y.; Wang, J.; Zhu, S.; Guo, Z.; Zhao, K.; Yu, X. On acoustic emission characteristics, initiation crack intensity, and damage evolution of cement-paste backfill under uniaxial compression. *Constr. Build. Mater.* **2021**, *269*, 121261. [CrossRef]
93. Qiu, H.; Kang, W.; Huan, C.; Liu, L.; Hou, D.; Zhang, F. Experimental study on acoustic emission characteristics of cemented rock-tailings backfill. *Constr. Build. Mater.* **2022**, *315*, 125278. [CrossRef]
94. Chen, T.; Guo, L.; Yan, Y.; He, Z.; Zhao, K.; Zhou, Y. Mechanical properties and acoustic emission response of cemented tailings backfill under variable angle shear. *Constr. Build. Mater.* **2022**, *343*, 128114. [CrossRef]
95. Sun, K.; Wang, C.; Feng, W.; He, M.; Zhang, J.; Li, M.; Li, F. Mechanical properties and damage evolution characteristics based on the acoustic emission of gangue and high-water-content materials based cemented paste backfill. *Constr. Build. Mater.* **2023**, *395*, 132324. [CrossRef]
96. Yin, S.; Li, G.; Chen, X.; Zhou, Y. A new acoustic emission characteristic parameter can be utilized to evaluate the failure of cemented paste backfill and rock combination. *Constr. Build. Mater.* **2023**, *392*, 132017. [CrossRef]
97. Chen, G.; Ye, Y.; Fu, F.; Hu, N.; Zhang, Z.; Yao, N. Experimental study on mechanical strength and acoustic emission characteristics of waste rock cemented backfill. *Bull. Eng. Geol. Environ.* **2024**, *83*, 133. [CrossRef]

Disclaimer/Publisher's Note: The statements, opinions and data contained in all publications are solely those of the individual author(s) and contributor(s) and not of MDPI and/or the editor(s). MDPI and/or the editor(s) disclaim responsibility for any injury to people or property resulting from any ideas, methods, instructions or products referred to in the content.

materials

MDPI

Article

Permittivity Measurement in Multi-Phase Heterogeneous Concrete Using Evidential Regression Deep Network and High-Frequency Electromagnetic Waves

Zhaojun Hou [1,2], Hui Liu [3], Jianchuan Cheng [1], Qifeng Zhang [2] and Zheng Tong [1,*]

[1] School of Transportation, Southeast University, Nanjing 210018, China
[2] CCDI (Suzhou) Exploration & Design Consultant Co., Ltd., Suzhou 215007, China
[3] China Railway 14th Bureau Large Shield Engineering Co., Ltd., Nanjing 211800, China
* Correspondence: tongzheng@seu.edu.cn

Abstract

Permittivity measurements of concrete materials benefit from the application of high-frequency electromagnetic waves (HF-EMWs), but they still face the problem of being aleatory and exhibit epistemic uncertainty, originating from multi-phase heterogeneous materials and the limited knowledge of HF-EMW propagation. This limitation restricts the precision of non-destructive testing. This study proposes an evidential regression deep network for conducting permittivity measurements with uncertainty quantification. This method first proposes a finite-difference time-domain (FDTD) model with multi-phase heterogeneous concrete materials to simulate HF-EMW propagation in a concrete sample or structure, obtaining the HF-EMW echo that contains aleatory uncertainties owing to the limited knowledge of wave propagation. A U-net-based model is then proposed to denoise an HF-EMW, where the difference between a couple of observed and denoised HF-EMWs characterizes aleatory uncertainty owing to measurement noise. Finally, a Dempster–Shafer theory-based (DST-based) evidential regression network is proposed to compute permittivity, incorporating the quantification of two types of uncertainty using a Gaussian random fuzzy number (GRFN): a type of fuzzy set that has the characteristics of a Gaussian fuzzy number and a Gaussian random variable. An experiment with 1500 samples indicates that the proposed method measures permittivity with a mean square error of 7.50% and a permittivity uncertainty value of 74.70% in four types of concrete materials. Additionally, the proposed method can quantify the uncertainty in permittivity measurements using a GRFN-based belief measurement interval.

Keywords: permittivity; high-frequency electromagnetic wave; multi-phase heterogeneous concrete; Gaussian random fuzzy number; uncertainty quantification

1. Introduction

Permittivity, a key parameter that characterizes the electrical properties of materials, represents the ability to store electric energy in an electromagnetic field. It reflects how high-frequency electromagnetic waves propagate within the material, including aspects such as attenuation, wavelength, and speed [1]. In the field of civil engineering, particularly in the study and application of cement-based composite materials, the accurate measurement of the dielectric constant of pavement structures holds significant importance.

In practical applications, the measured permittivity is widely utilized in several critical areas. In thickness measurements, accurate permittivity values provide a reliable basis for

evaluating the dimensions of structural elements, ensuring that building components meet design specifications [2]. For subsurface object detection, permittivity measurement helps accurately locate and identify objects hidden within structures, aiding in the detection of potential safety hazards [3]. In the analysis of material corrosion, monitoring changes in the permittivity can effectively evaluate the degree of corrosion [4]. For studies related to energy absorption characteristics, permittivity data serves as crucial support in the development of composites with specific absorption properties [5]. In high-throughput composite material design, permittivity measurements guide material optimization and innovation [6].

Despite its advantages, accurately measuring the permittivity of cement concretes remains a challenging task. Existing methods (e.g., the parallel plate method, probe method, resonant cavity method, waveguide method, free-space method) can generally be categorized into two groups: transmission-time-based and reflection-coefficient-based techniques [7]. These approaches are commonly affected by two types of uncertainties: aleatory uncertainty and epistemic uncertainty. Aleatory uncertainty refers to the inherent randomness property in the measurement process, such as the multi-phase heterogeneous property from the random spatial distribution of cement paste and aggregates and variability in emission and reception. Epistemic uncertainty arises from limitations in knowledge, modeling assumptions, or incomplete understanding of the physical processes involved. For instance, in transmission-based methods, the assumptions regarding wave paths and homogeneous media may not match actual complex conditions, leading to biased or inaccurate results.

Hypothesis and Research Objectives

To solve the problem of uncertainty quantification in the permittivity measurement of concrete materials, this paper proposes an evidential regression deep network for conducting permittivity measurements with uncertainty quantification. This method has the following two hypotheses:

1. An HF-EMW is generated by a pulse-frequency antenna with a fixed frequency. This paper does not discuss the stepped-frequency antenna.
2. The finite-difference time-domain (FDTD) model simulates HF-EMW propagation in a concrete sample or structure without knowledge uncertainty since the propagation path can be completely observed in the simulation.

In general, this method first proposes a finite-difference time-domain (FDTD) model with multi-phase heterogeneous concrete materials to simulate HF-EMW propagation in a concrete sample or structure, obtaining the HF-EMW echo that contains aleatory uncertainty owing to the limited knowledge of wave propagation. A U-net-based model is then proposed to denoise HF-EMW, where the difference between a couple of observed and denoised HF-EMWs characterizes aleatory uncertainty owing to measurement noise. Finally, a Dempster–Shafer theory-based (DST-based) evidential regression network is proposed to compute permittivity, incorporating the quantification of two types of uncertainties using a Gaussian random fuzzy number (GRFN). The main contribution of this study can be summarized as follows:

1. The proposed method can measure permittivity in four types of multi-phase heterogeneous concrete materials, exceeding other SOTA methods in this task. The proposed method is also stable when used on the four concrete types. Thus, a user can directly use the method to measure the permittivity of concrete materials using recorded HF-EMWs.
2. The proposed method can quantify the uncertainty in permittivity measurement using a GRFN-based BMI, demonstrating that the proposed method can quantify

and remove the effects of aleatory and epistemic uncertainty in the permittivity measurement. A GRFN in the proposed method uses $\mu(\boldsymbol{x})$, $\sigma(\boldsymbol{x})$, and $h(\boldsymbol{x})$ as the most plausible permittivity value in the measurement process and the variability around these values as aleatory uncertainty and epistemic uncertainty, respectively.

3. The superiority of the proposed method benefits from the FDTD simulation and the denoising deep network. The FDTD simulation quantifies epistemic uncertainty due to limited knowledge, such as HF-EMW propagation. The denoising deep network quantifies aleatory uncertainty owing to the measurement noise, such as the multi-phase heterogeneous property of concrete materials.

2. Related Work

2.1. Permittivity Characterization with High-Frequency Electromagnetic Waves

Permittivity is a fundamental electrical property that describes how materials interact with electric fields. At high frequencies ranging from megahertz (MHz) to terahertz (THz), the characterization of permittivity becomes increasingly significant, particularly in applications involving wireless communication [8], radar systems [9], geophysical exploration [10], and biomedical diagnostics [11]. Complex permittivity encapsulates both energy storage and dielectric losses within a material. As the frequency increases, dispersive and relaxation phenomena, such as dipole polarization, ionic conduction, and interfacial effects, become more pronounced, requiring accurate and frequency-resolved measurement techniques.

Multiple high-frequency measurement techniques have been developed to characterize permittivity, as summarized in Table 1. Among the most used are the vector network analyzer-based transmission/reflection methods [12]. These rely on measuring the scattering parameters of a sample inserted in a coaxial line, waveguide, or free-space setup. Coaxial probes [13], particularly the open-ended type, are widely used due to their ease of use and suitability for soft or liquid materials. Waveguide-based methods [14] offer higher accuracy but require more elaborate sample preparation. Free-space measurements, on the other hand, allow non-contact and broadband evaluation of flat samples, making them ideal for high-frequency applications in the GHz to THz range.

Table 1. Comparison of permittivity measurement methods.

Method	Frequency Range	Contact Type	Advantages	Limitations
Coaxial Probe	MHz–GHz	Contact	Simple setup, broadband	Limited to flat surfaces, sensitive to pressure
Waveguide	GHz	Contact	High accuracy	Requires machining, limited bandwidth
Free-space Measurement	GHz–THz	Non-contact	Non-destructive, broadband	Sensitive to alignment, needs calibration
Resonant Cavity	Discrete GHz	Contact	Extremely high accuracy	Narrowband, complex sample prep
Time-Domain Reflectometry	MHz–GHz	Contact	Time-resolved info, moderate complexity	Limited resolution at high frequencies
THz Time-Domain Spectroscopy	0.1–10 THz	Non-contact	Ultra-high resolution, molecular sensitivity	Expensive, semi-transparent samples only

Resonant cavity methods provide extremely accurate permittivity measurements at discrete frequencies by exploiting the shift in resonant frequency and quality factor that occurs when a sample is inserted. These techniques are particularly suitable for low-loss dielectric materials. In contrast, time-domain methods like time-domain reflectometry [15] and terahertz time-domain spectroscopy [16] provide broadband information. THz-TDS has emerged as a powerful tool for characterizing permittivity in the sub-millimeter wave regime, offering femtosecond time resolutions and high-frequency bandwidths. This method is especially effective for polymeric materials, where molecular vibrations and carrier dynamics can be captured.

Recent advances integrate time-domain methods and deep learning-based algorithms with inverse electromagnetic modeling to improve the robustness and efficiency of permittivity extraction [17,18]. These data-driven methods are particularly useful in heteroge-

neous or layered media where traditional inversion becomes unstable. Additionally, the rise of metamaterials and complex engineered structures has necessitated new characterization approaches that account for anisotropy, dispersion, and nonlinearity. Researchers have also developed high-temperature and in situ permittivity measurement systems to support material evaluation in harsh environments, such as reactors, engines, and planetary exploration.

Despite significant progress, several challenges remain. Calibration procedures at high frequencies are sensitive to measurement artifacts, and uncertainties in sample geometry or positioning can significantly affect results. There is also a trade-off between spatial resolution and frequency coverage: techniques with high-frequency resolutions often sacrifice spatial detail and vice versa. Furthermore, interpreting permittivity data from inverse problems remains complex, particularly when measurements are sparse or noisy.

In summary, permittivity characterization using high-frequency electromagnetic waves is a mature but still rapidly evolving field. It plays a critical role in modern science and engineering, from designing communication systems to diagnosing diseases and understanding materials at the molecular level. Ongoing advancements in sensor miniaturization, computational electromagnetics, and AI-driven analysis are likely to enhance further the precision, accessibility, and real-time capabilities of high-frequency permittivity measurements.

2.2. Uncertainty Quantification in Material Permittivity Measurement

Uncertainty analysis refers to the process of studying, quantifying, and evaluating the various uncertainties inherent in measurement procedures. In the context of ground-penetrating radar (GPR) applications, such as permittivity measurement [19] and signal processing [20], uncertainties are pervasive and significantly affect the reliability and accuracy of the results. From the perspective of their nature of origin, uncertainties are typically classified into aleatory uncertainty and epistemic uncertainty [17]. Theoretically, aleatory uncertainty is associated with intrinsic random fluctuations in the system. In GPR-based measurements, this is most evident in the form of electronic noise from the radar equipment and unpredictable electromagnetic interference from the surrounding environment. These disturbances are inherently stochastic and cannot be eliminated simply by refining measurement procedures or acquiring more domain knowledge.

On the other hand, epistemic uncertainty [21] arises from an incomplete or imprecise understanding of the system or the environment being measured. In GPR applications, epistemic uncertainty may result from limited knowledge of the complex subsurface medium or the simplifications and approximations inherent in the adopted signal processing models. For example, assumptions regarding electromagnetic wave propagation paths in heterogeneous media or the use of idealized dielectric models contribute to such uncertainty. Unlike aleatory uncertainty, epistemic uncertainty can be gradually reduced as understanding of the measurement process and the physical system improves through theoretical advancements or empirical investigations.

Over the years, numerous approaches have been proposed to quantify and model uncertainty. Early methods primarily relied on classical mathematical frameworks, such as Bayesian probability theory and Monte Carlo simulations, to estimate the probability of uncertain events. With the advent of computational methods, more sophisticated models were introduced, including interactive fuzzy sets [22], parametric and non-parametric probability density models [23], and fuzzy entropy measures [24]. These approaches utilize fuzzy set theory to represent uncertainty in multi-attribute decision-making problems, where interdependencies among attributes are prevalent. Fuzzy relations are constructed to quantify such interactions, and membership functions are employed to describe the degree

to which an object belongs to different classes, thereby allowing uncertainty in classification to be quantified. Additionally, many practical models assume that uncertainty follows a specific probability distribution (e.g., Gaussian or normal distributions), where probability density functions are estimated from historical or experimental data.

In recent years, the integration of uncertainty theory with deep neural networks has attracted growing attention. For instance, Denœux et al. (2021) [25] proposed an evidence-based classifier combining Dempster–Shafer (DS) theory with deep learning. In this framework, deep learning is first used to extract features from data, which are then interpreted as evidence in DS theory. Belief and plausibility functions are computed to represent uncertainty in interval form. Tong et al. [26,27] applied an evidence transformer for pavement defect segmentation, which effectively captured complex spatial features. By incorporating DS theory, the model was able to output predictions with embedded uncertainty information, improving the reliability of the segmentation results. More recently, in 2025, Huang et al. [28] applied deep learning networks to extract features from multimodal medical images, translating those features into DS-theoretic evidence. Gaussian random fuzzy numbers were then used to represent both aleatory and epistemic uncertainties during measurement. These recent studies have opened new avenues for combining deep learning with formal uncertainty quantification frameworks. Importantly, they also address earlier limitations where different types of uncertainties were not clearly distinguished, thus enriching the expressiveness and interpretability of uncertainty-aware models.

Despite its advantages in modeling both aleatory and epistemic uncertainty, the application of DS theory in material sciences presents two challenges. First, DS theory requires the definition of a frame of discernment and basic belief assignments, which may be difficult to establish when dealing with continuous-valued or highly variable physical measurements such as permittivity. Second, there are still no existing methods integrating DS theory and deep neural networks to quantify the uncertainty in the time-domain methods for permittivity measurement.

3. Proposed Method

3.1. Overview

This study proposes a DST-based method to characterize the permittivity distribution with uncertainty quantification in concrete materials. The main steps of this method consists of three steps, as shown in Figure 1:

Step 1. A finite-difference time-domain (FDTD) model with multi-phase heterogeneous concrete materials is adopted to simulate HF-EMW propagation in a concrete sample or structure. This model obtains the HF-EMW echo, which minimizes epistemic uncertainty but still contains aleatory uncertainty. This is because the FDTD model has a well-known and calibrated wave propagation path and relationship between wave amplitude and permittivity. However, it still contains measurement noise from the random distribution of multi-phase components in a concrete sample. The FDTD model will be introduced in Section 3.2. Please note that the FDTD model was proposed in [29,30]. The contribution of this step is to use simulation results to quantify the epistemic uncertainty in permittivity measurements.

Step 2. A U-Net-based model is proposed to denoise an HF-EMW signal. This model is used to obtain an HF-EMW without epistemic uncertainty, as it can remove noise derived from measurement errors, such as multi-phase heterogeneous of cement and aggregates in a concrete sample. Thus, the difference between the inputs and outputs can be the aleatory uncertainty of the permittivity measurement using an HF-EMW. The details of the U-net-based model will be described in Section 3.3.

Step 3. A DST-based evidential regression network is proposed to compute permittivity with aleatory and epistemic uncertainty. The inputs of this network consist of a recorded HF-EMW from real-world measurements of a concrete sample and an HF-EMW echo from an FDTD model that simulates real-world measurements. The outputs are the permittivity of the concrete sample with the quantification of aleatory and epistemic uncertainty. The details of the DST-based evidential regression network will be introduced in Section 3.4.

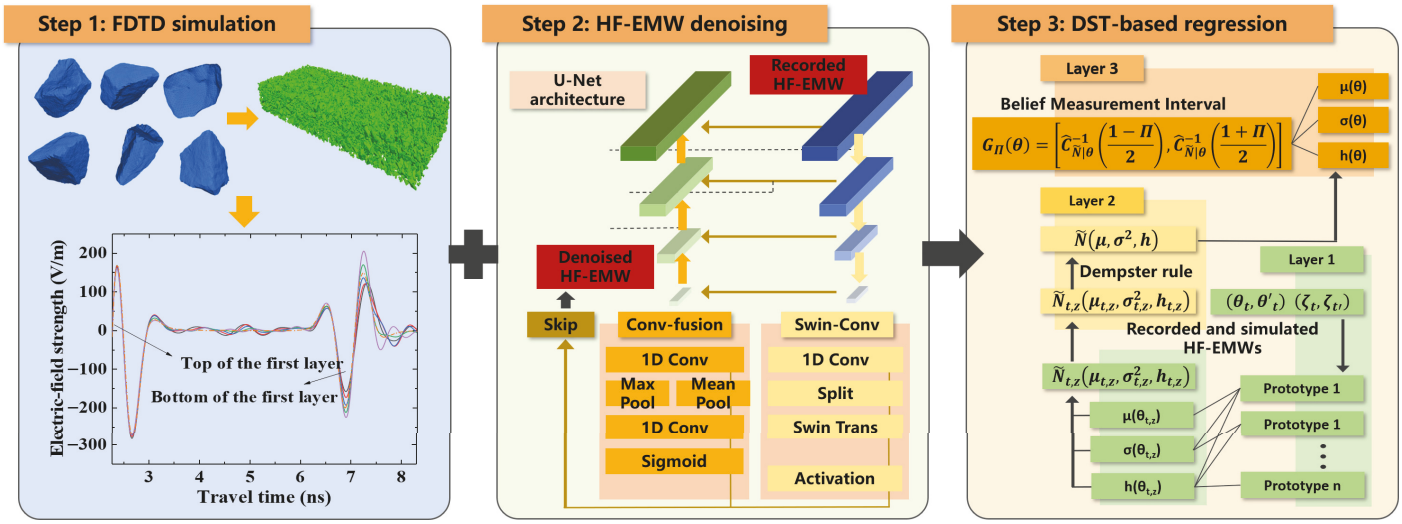

Figure 1. Overview of the proposed method.

3.2. Finite-Difference Time-Domain Simulations for Multi-Phase Concrete

3.2.1. Component Distribution Simulation Using Discrete Element Method

The finite-difference time-domain (FDTD) method was employed to simulate HF-EMW propagation within a concrete sample. The simulation is conducted using GPRMax v.3.1.5, an open-source software widely used for modeling electromagnetic wave propagation. However, GPRMax's default geometry commands only allow the construction of basic shapes such as rectangular blocks, spheres, and cylinders, limiting its ability to represent the irregular geometries of real-world pavement materials, such as coarse aggregates and cement mortar. As a result, simulations often rely on layered homogeneous models to approximate heterogeneous media, which introduces significant discrepancies between the simulation outputs and actual HF-EMWs.

To address this limitation, this study incorporates a discrete element modeling (DEM) approach, which is well-established in material mechanics for simulating complex microstructures. Specifically, this method approximates the surface contours of arbitrarily shaped materials by randomly distributing spherical particles of varying sizes. The resulting geometric models enable accurate reconstruction of the true morphology and volume fractions of different material phases within concrete samples.

The modeling workflow begins with finite element software to construct detailed material structure models, which are then imported into GPRMax for HF-EMW propagation simulation. Compared with conventional homogeneous models, these reconstructed heterogeneous models offer significantly improved realism in capturing radar wave behavior. The PFC3D software is used to reconstruct the material distribution within concrete samples.

Real aggregate particles are first scanned using multi-view laser scanning technology to obtain dense point cloud coordinate data. Spherical fitting is then applied to approximate the surface geometry of the aggregates, enabling 3D reconstruction of aggregate phase contours. Six real aggregate particles of different sizes and shapes are selected from high-performance concrete mixtures to serve as representative samples, as shown in Figure 2.

These samples are placed on an automated rotary platform and scanned using a handheld laser scanner to capture their surface geometry from all angles.

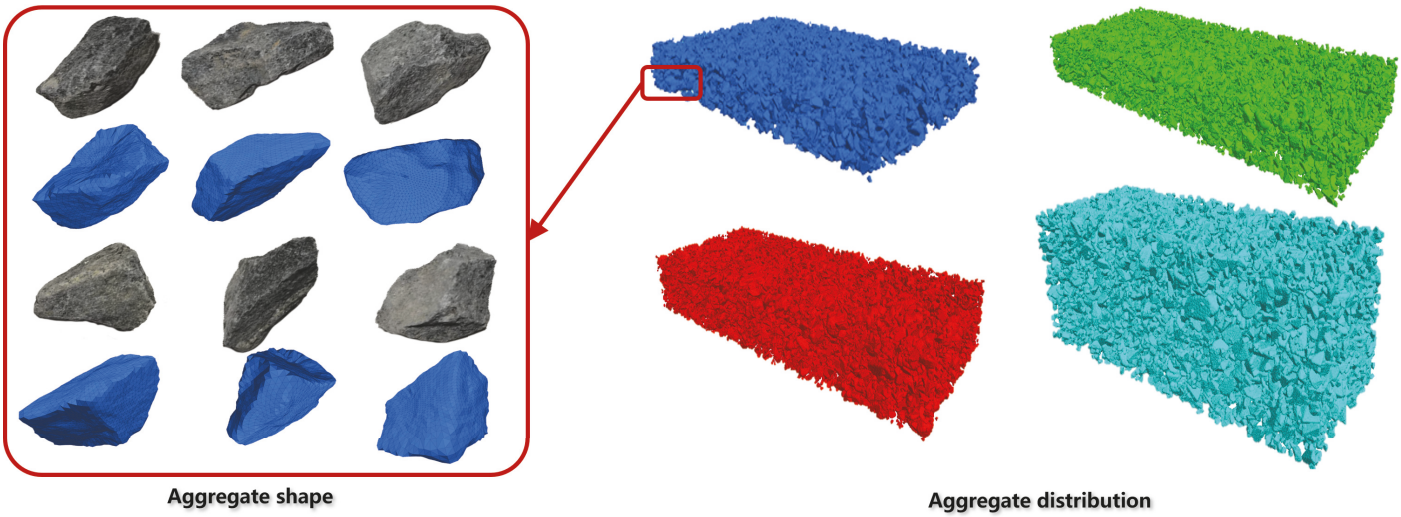

Figure 2. Multi-phase heterogeneous concrete model.

The scanned point clouds are imported into Geomagic Studio, where the surface contours of each aggregate are reconstructed. Based on the 3D point cloud data, a contour-sphere approximation method is applied. Using the Bubble Pack algorithm, multiple spheres of different radii are generated to fill the internal volume of each aggregate within the point cloud coordinate system. This process allows the geometric approximation of complex aggregate shapes and the construction of a library of 3D particle models.

The aggregates are then randomly distributed in the 3D space according to target gradation curves, forming multi-phase heterogeneous concrete samples. The samples have a size of 1.5 m × 1.5 m. The mass proportions of aggregates with different sizes are shown in Table 2.

Table 2. Mass proportions of aggregates in different concrete materials.

Size/mm	0.6–2.36	2.36–4.75	4.75–9.5	9.5–16	16–19	19–26.5	26.5–37.5
Cement concrete (Material 1)	22.80	7.67	10.86	10.67	12.44	17.00	18.56
Cement concrete (Material 2)	20.62	8.79	11.32	12.78	9.45	16.14	20.90
Cement-stabilized macadam (Material 3)	25.92	16.30	20.00	11.11	8.89	17.78	/
Cement-stabilized macadam (Material 4)	22.41	17.24	21.32	14.32	7.82	16.89	/

The generated aggregate particle models were imported into PFC3D as clump templates, representing six distinct aggregate types. These clump templates were then randomly deployed within the discrete element model according to a graded distribution scheme. The placement followed a descending size order, aligning with the target gradation curve: Larger particles were placed first to form a skeletal framework, while smaller particles were subsequently filled into the voids between the larger aggregates, thereby creating a hierarchical, well-graded packing structure. For fine aggregates with particle sizes ranging from 0.6 mm to 4.75 mm, spherical particle models available in PFC3D were used due to their relatively small volume. After the skeleton and fine aggregates were placed, a vertical compressive load was applied to the model to simulate compaction and achieve a dense packing configuration. Four samples of different concrete materials are shown in Figure 2.

3.2.2. FDTD Simulation

The electromagnetic simulation is performed using the GPRMax software. To incorporate the discrete element model generated by PFC3D into GPRMax, the latter's built-in functionality is utilized to convert image data into the HDF5 format required by its electromagnetic FDTD solver. Specifically, the 3D discrete element model of the concrete sample is reconstructed, and random cross-sectional images of the heterogeneous material distribution were generated. After preprocessing, the spatial distribution and morphology information from these images were converted into HDF5 files. These files were then imported into GPRMax, where the permittivities of all component phases are defined, enabling the simulation of electromagnetic field components of HF-EMW propagating through the multi-phase heterogeneous sample. The detailed settings for the electromagnetic FDTD model in GPRMax included the sample, electromagnetic parameters, grid resolution, model dimensions, and scan duration, as described as follows.

Model Sizes: The size of the multi-phase heterogeneous sample is 1.5 m $\times$ 1.5 m $\times$ D, where D denotes the thickness of 0.08 m, 0.05 m, 0.08 m, and 0.05 m for Materials 1, 2, 3, and 4, respectively. Vertically, each multi-phase heterogeneous sample also consists of a 0.01 m thick air layer.

Air-Layer Configuration: The air layer provides space to position the antenna, maintaining a vertical separation of 0.15 m between the antenna's center and a sample's surface. This setup replicates the actual measurement conditions of air-coupled GPR systems. It effectively suppresses the direct ground wave interference on interface reflections from the top surface of the cement panel, thereby enhancing the distinguishability of the target reflected signals. The bottom air layer serves to eliminate boundary reflection artifacts that could otherwise interfere with the integrity and accuracy of reflection signals from the lower interface of the concrete samples.

Antenna Frequency, Time Window, and Other Parameters: Considering the propagation characteristics of electromagnetic waves in heterogeneous materials, as well as the trade-offs among signal resolution, penetration depth, and antenna frequency, other parameters of the electromagnetic finite-difference model were selected based on industry empirical values. These parameters are summarized in Table 3.

Table 3. Mass proportions of aggregates in different pavement materials.

Parameter	Value	Parameter	Value
Model Size (m)	$1.5 \times 0.6/0.4 \times 0.00044$	Antenna Step (m)	0.01
Grid Step (m)	$0.00044 \times 0.00044 \times 0.00044$	Scan Lines	146
Time Window (ns)	16/12	Excitation source frequency (GHz)	0.8, 1.0, 1.2, 1.6, and 2.0 GHz

Permittivity Settings: In the model construction, void (air gap) regions are assigned around a concrete sample. By adjusting the permittivity values, different filling media conditions inside the voids can be simulated. When the void is completely dry, it is filled with air, with a relative dielectric constant of 1.00. Conversely, when fully saturated, the void is filled with water, for which its relative dielectric constant is 81.00.

For multi-phase heterogeneous media, basalt is selected as the aggregate material for particle sizes in the millimeter range, with its permittivity set to 8.00. Considering the frequency-dispersive nature of cement concrete, the permittivity of the composite phase "aggregate (mm)-cement mortar-pore" is computed as

$$\varepsilon_c = \varepsilon_{\text{avg}} = \varepsilon_a V_a + \varepsilon_m V_m + \varepsilon_p V_p \tag{1}$$

where ε_c is the effective dielectric constant of the composite phase; ε_a, ε_m, and ε_p are the dielectric constants of the aggregate, mortar, and pores, respectively; V_a, V_m, and V_p represent their volume fractions. The aggregate particle size is denoted by the subscript a.

3.3. Deep Denoising Network

A Unet model is designed to denoise the HF-EMWs with encoder, bottleneck, and decoder modules, as shown in Figure 3. Compared with other signal denoising architectures, such as LSTM and CNN-RNN hybrids, the U-Net architecture enables efficient feature extraction across multiple temporal scales through its encoder–decoder structure and skip connections. This not only preserves fine-grained waveform details but also facilitates effective noise suppression. Additionally, the incorporation of attention mechanisms and Swin Transformer modules further enhances the U-Net's ability to capture both local and global signal patterns, making it particularly well-suited for handling the noisy, multi-component characteristics of HF-EMW data. This advantage will be demonstrated in Section 4.3.

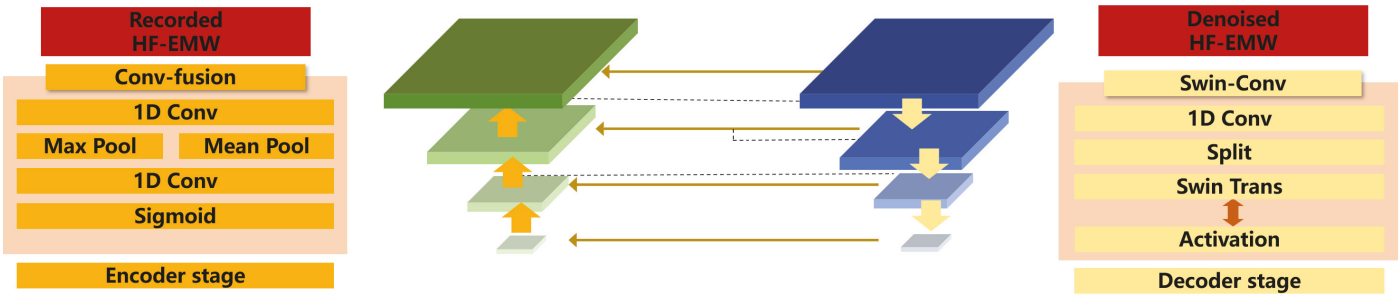

Figure 3. Architecture of an HF-EMW deep denoising network.

(1) Encoder module.

The encoder of the UNet architecture is designed to progressively extract features from the input one-dimensional signal through a series of downsampling operations, thereby constructing multi-scale feature representations.

The encoder consists of three cascaded downsampling modules, each composed of a residual block, an attention mechanism, and a pooling layer. The encoder takes a preprocessed and augmented input signal of shape `(batch_size, 1, signal_length)`.

In the first downsampling module, the input signal is initially processed by a `ResidualBlock1D` for feature extraction. This block uses two convolutional layers with batch normalization and a skip connection, which helps alleviate the vanishing gradient problem and retains part of the original signal features. Following this, the `AttentionBlock1D` applies global average pooling and fully connected layers to generate channel-wise attention weights, enabling the network to enhance important features and suppress irrelevant information during training adaptively. After this stage, the number of channels expands from 1 to `base_filters`, while the signal length remains unchanged.

The two downsampling modules follow a similar structure but include max-pooling layers for temporal downsampling. Each pooling operation reduces the signal length by half, and the channel dimension is doubled through convolution. Specifically, the second module increases the channel dimension to `base_filters` $\times$ `2`, and the third module further increases it to `base_filters` $\times$ `4`, while the signal length is reduced to one-half and one-quarter of the original.

Because shallow layers use small convolution kernels with limited receptive fields, their feature maps correspond directly to local variations in the waveform, making them

more effective in capturing local signal features. In contrast, deeper layers with attention mechanisms focus on low-frequency global features, as the abstracted signal representations in deeper layers are less concerned with fine-grained waveform details and more with statistical distributions. Hence, deeper modules are designed with larger receptive fields to capture the global context.

Through this hierarchical structure, the encoder combines the locality of convolution with multi-scale abstraction, preserving both fine-grained and global features of the signal. After passing through the three cascaded down-sampling modules, the encoder outputs a high-level feature representation of shape `(batch_size, base_filters × 8, signal_length/8)`.

(2) Swin Transformer

Traditional CNNs rely solely on local receptive fields, which limits their ability to capture long-range dependencies in sequential signals. The introduction of a bottleneck layer addresses this issue. Specifically, the bottleneck receives the final output from the encoder, which has a shape of `(batch_size, base_filters × 8, signal_length/8)`.

To adapt this high-level feature tensor for processing by the Swin Transformer, it is first reshaped into a two-dimensional feature map of size 20×24. The transformed feature representation is then fed into a **Swin Transformer** module. The Swin Transformer employs a *window-based self-attention mechanism*, enabling the model to capture **cross-window dependencies** and integrate the global contextual information of the signal effectively. After processing through the Swin Transformer, the output retains the same shape as the input to the bottleneck layer, i.e., `(batch_size, base_filters × 8, signal_length/8)`.

(3) Decoder

The decoder mirrors the structure of the encoder and constitutes the right half of the U-shaped UNet architecture. It progressively restores the signal details through transposed convolutions (deconvolutions), skip connections, and feature fusion.

The decoder takes as input the high-level feature representation from the bottleneck layer, with a shape of `[B, base_filters × 8, signal_length/8]`. It then employs three upsampling modules to gradually reconstruct the feature map back to the original signal length. Each upsampling module consists of a transposed convolution layer, a feature concatenation operation, and a residual-attention block.

Transposed convolution, essentially a convolution operation in reverse, inserts zero-padding between elements of the input feature map and applies a convolution kernel to enlarge the feature map, restoring it to the spatial dimensions consistent with the corresponding encoder layer. The upsampled features are then concatenated with the output from the x-th encoder layer along the channel dimension, resulting in a composite feature map with doubled information. A subsequent 5×5 convolution compresses the number of channels back to `base_filters × 4` (e.g., 256), followed by a residual block and an attention block to integrate the features and refine both the spatial and channel dimensions.

After passing through all three upsampling stages, a `final` layer with a 1×1 convolution maps the output to a single channel, yielding a denoised signal with dimensions `[B, 1, L]`, matching the shape of the original input.

3.4. Evidential Regression Deep Network for Uncertainty Quantification

This section proposes a DST-based evidential regression network to compute permittivity with the quantification of aleatory and epistemic uncertainty, as shown in Figure 4. The inputs of this network consist of an HF-EMW from real-world measurements of a concrete sample, an HF-EMW echo from an FDTD model that simulates the real-world measurement,

and a denoised HF-EMW from the U-net-based model. The outputs are the permittivity of the concrete sample with the quantification of aleatory and epistemic uncertainty.

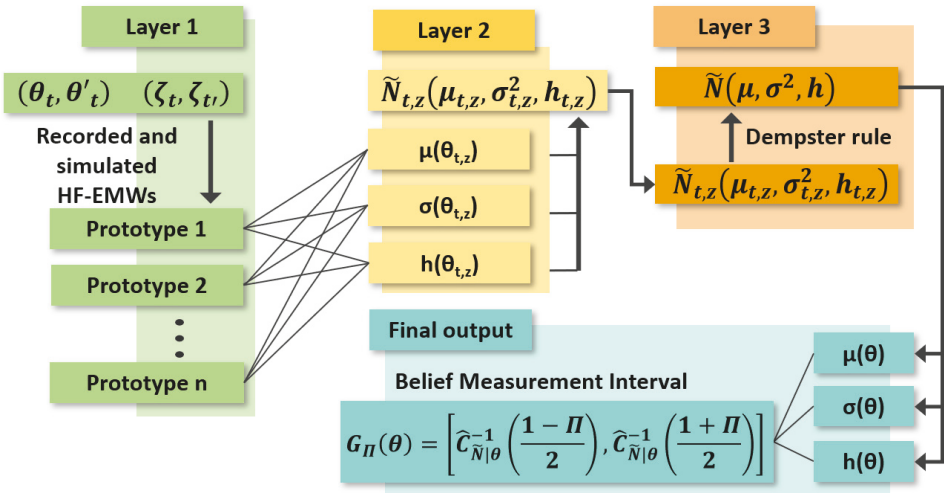

Figure 4. Architecture of evidential regression deep network.

3.4.1. Notation Definitions of Gaussian Random Fuzzy Number

The DST-based evidential regression network derives from the definition of a Gaussian random fuzzy number (GRFN) and generalized Dempster–Shafer theory (DST). A GRFN in the generalized DST can map $\boldsymbol{x}$ to a random variable F. Define the Gaussian fuzzy number (GFN) as a fuzzy subset of $\mathbb{R}$ with

$$\mathtt{GFN}(x; m, h) = \exp\left(-\frac{h}{2}(x-m)^2\right), \tag{2}$$

where $m \in \mathbb{R}$ is the mode and $h \in [0, +\infty]$ is the precision. Two GFNs $\mathtt{GFN}_1(x; m_1, h_1)$ and $\mathtt{GFN}_2(x; m_2, h_2)$ can be combined as $\mathtt{GFN}_{12}(x; m_{12}, h_{12})$ with

$$m_{12} = \frac{h_1 m_1 + h_2 m_2}{h_1 + h_2}, \qquad h_{12} = h_1 + h_2. \tag{3}$$

A GRFN can be expressed by a GFN with the mode of a Gaussian random variable. In detail, a Gaussian random variable with mean μ and variance σ^2 is formed as $M : \Omega \to \mathbb{R}$ in a probability space $(\Omega, \sum_\Omega, P)$. Then, a random fuzzy set $\widetilde{N} : \Omega \to [0,1]^{\mathbb{R}}$ in Equation (2) is written as

$$\widetilde{N}(\omega) = \mathtt{GFN}(M(\omega), h), \tag{4}$$

where $\widetilde{N}(\mu, \sigma^2, h)$, called the GRFN, has a location parameter μ and two uncertainty parameters σ^2 and h. The two uncertainty parameters represent possibility and probability. In particular, a GRFN $\widetilde{N}$ with $h = +\infty$ equals to a Gaussian random variable with mean μ and variance σ^2. In contrast, the case with $h = 0$ has $\widetilde{N}(\omega)(x) = 1$ for all $\omega \in \Omega$ and $x \in \mathbb{R}$. In addition, $\widetilde{N}$ with $\sigma^2 = 0$ has a constant random variable M taking value μ, which can be seen as a possibilistic variable with possibility distribution $\mathtt{GFN}(\mu, h)$.

Given two GRFNs $\widetilde{N}_1(\mu_1, \sigma_1^2, h_1)$ and $\widetilde{N}_2(\mu_2, \sigma_2^2, h_2)$, $\widetilde{N}_1 \boxplus \widetilde{N}_2 \sim \widetilde{N}_{1,2}(\mu_{12}, \sigma_{12}^2, h_{12})$ can be defined based on the property of GFN in Equation (3) as

$$\mu_{12} = \frac{h_1\mu_1 + h_2\mu_2}{h_1 + h_2} \tag{5a}$$

$$\sigma_{12}^2 = \frac{h_1^2\sigma_1^2 + h_2^2\sigma_2^2}{(h_1 + h_2)^2} \tag{5b}$$

$$h_{12} = h_1 + h_2. \tag{5c}$$

Obviously, the property is commutative and associative. Thus, two or more GRFNs can be aggregated by the accumulation operation, as shown in Equation (5).

3.4.2. DST-Based Evidential Regression Network

This study extends the DST-based model in [31] to map the input into the permittivity value with the quantification of two types of uncertainty. The basic idea is to covert the input $\boldsymbol{x}$, the combined tensor of the recorded and simulated HF-EMWs, into a Gaussian random fuzzy number (GRFN) via representation fusion, where $\mu(\boldsymbol{x})$, $\sigma(\boldsymbol{x})$, and $h(\boldsymbol{x})$ are the most plausible permittivity value and the aleatory uncertainty and epistemic uncertainty variability around this value, respectively. A permittivity computation with low uncertainty has $\mu(\boldsymbol{x}) \approx F$, $\sigma(\boldsymbol{x}) \approx 0$, and $h(\boldsymbol{x}) \approx 1$. An intuitive description of the GRFN concept is provided in Appendix A. Given an input $\boldsymbol{x} \in \mathbb{R}^p$, the proposed DST-based evidential regression network can be described as the four steps shown in Figure 4:

Step 1. The similarity between subset $\boldsymbol{x}$ and a *prototype* vector in the DST-based network is computed as

$$d_z(\boldsymbol{x}) = \exp(-\gamma_z^2 ||\boldsymbol{x} - \boldsymbol{\varsigma}_z||^2), \tag{6}$$

where γ_z is a scale associated with the prototype vector $\boldsymbol{\varsigma}_z$; a continuous DST-based model has Z trainable prototype vectors with the p dimension, notated as $\boldsymbol{\varsigma}_1, \ldots \boldsymbol{\varsigma}_Z$.

Step 2. The similarity of $\boldsymbol{\varsigma}_z$ is utilized to compute a GRFN as

$$\widetilde{F}_z(\boldsymbol{x}) \sim \widetilde{N}(\mu_z(\boldsymbol{x}), \sigma_z^2, d_z(\boldsymbol{x})h_z) \tag{7}$$

where μ, σ^2, and h are the mean, variance, and precision of GRFN $\widetilde{N}(\mu, \sigma^2, h)$; the mean $\mu_z(\boldsymbol{x})$ is defined as

$$\mu_z(\boldsymbol{x}) = \boldsymbol{\vartheta}_z^T \boldsymbol{x} + \vartheta_{z0} \tag{8}$$

where $\boldsymbol{\vartheta}_z$ and ϑ_{z0} are a trainable parameter vector and scale associated with prototype $\boldsymbol{\varsigma}_z$; $\mu_z(\boldsymbol{x})$ is a prediction of material permittivity based on the inputs $\boldsymbol{x}$, while σ_z is the variation in the prediction $\mu_z(\boldsymbol{x})$. When the value of $||\boldsymbol{x} - \boldsymbol{\varsigma}_z||$ tends toward 0, the precision $d_z(\boldsymbol{x})h_z$ is close to infinity, and $\widetilde{F}_z(\boldsymbol{x})$ can highly support the hypothesis that $\mu_z(\boldsymbol{x})$ is the true value.

Step 3. The Z GRFNs from prototypes $\boldsymbol{\varsigma}_1, \ldots \boldsymbol{\varsigma}_Z$ are combined using a generalized Dempster rule operation $\boxplus$ as $widetildeN(\mu(\boldsymbol{x}), \sigma^2, d(\boldsymbol{x})h)$ such that

$$\mu(\boldsymbol{x}) = \frac{\sum_{z=1}^{Z} d_z(\boldsymbol{x}) h_z \mu_z(\boldsymbol{x})}{\sum_{z=1}^{Z} d_z(\boldsymbol{x}) h_z}, \tag{9a}$$

$$\sigma^2(\boldsymbol{x}) = \frac{\sum_{z=1}^{Z} d_z^2(\boldsymbol{x}) h_z^2 \sigma_z^2(\boldsymbol{x})}{\left(\sum_{z=1}^{Z} d_z(\boldsymbol{x}) h_z\right)^2}, \tag{9b}$$

$$h(\boldsymbol{x}) = \sum_{z=1}^{Z} d_z(\boldsymbol{x}) h_z. \tag{9c}$$

Step 4. The aggregated GRFN $\widetilde{N}(\mu, \sigma^2, h)$ can be transformed into a belief measurement interval (BMI) at a confidence level Π as

$$\mathcal{G}_\Pi(\boldsymbol{\theta}) = \left[\widehat{C}_{\widetilde{N}|\boldsymbol{\theta}}^{-1}\left(\frac{1-\Pi}{2}\right), \widehat{C}_{\widetilde{N}|\boldsymbol{\theta}}^{-1}\left(\frac{1+\Pi}{2}\right)\right] \tag{9d}$$

where $\widehat{C}^{-1}_{\widetilde{N}|\boldsymbol{\theta}}(\Pi)$ is the inverse of the cumulative distribution function $\widehat{C}_{\widetilde{N}|\boldsymbol{\theta}}(\Pi)$, revealing how $\widetilde{N}|\boldsymbol{\theta}$ makes $\widehat{C}_{\widetilde{N}|\boldsymbol{\theta}}$ return a value of Π. The inverse of the cumulative distribution function can be computed as

$$\forall\, \Pi \in (0,1),\ P_{\boldsymbol{\theta},\widetilde{N}}(N \in \mathcal{G}_{\Pi}(\boldsymbol{\theta})) \approx \Pi. \tag{9e}$$

For any $\Pi \in (0,1]$, the Π-level interval in Equation (9d) can be regarded as a measurement at level Π. The BMI is the predicted permittivity range with a confidence level of Π. Thus, a BMI is a simple form of GFRN, allowing readers without a statistical background to understand it easily.

4. Results and Discussion

4.1. Experimental Details

(1) Dataset

Table 4 shows a dataset for demonstrating the effectiveness of the proposed method. A total of 300 concrete samples are made, for which their sizes are described in Section 3.2. All samples are scanned using ground-penetrating radars with antenna frequencies of 800 MHz, 1.0 GHz, 1.2 GHz, 1.6 GHz, and 2.0 GHz. In addition, the propagation of the HF-EMWs from the ground-penetrating radars is also simulated by the FDTD models in Section 3.2.

Each couple of recorded and simulated HF-EMWs is defined as an input for the experiment, while the true permittivity of the concrete sample is used as a label. Table 5 shows the volume fractions and permittivity of multiple phases in the four materials for FDTD simulation. The dataset in the experiment includes 1500 groups of the recorded HF-EMW, simulated HF-EMW, and true permittivity. The dataset's split protocol is shown in Table 4.

Table 4. Detailed information on the experimental dataset.

	Number of Samples	Training	Validation	Testing
Materials 1	67	193	41	101
Materials 2	75	231	38	106
Materials 3	68	214	37	89
Materials 4	90	262	34	154
Total	300	900	150	450

Table 5. Volume fraction and permittivity of four concrete materials.

	Component	Material 1	Material 2	Material 3	Material 4
Volume fraction	Coarse aggregate	72.17	72.17	76.98	76.98
	Fine aggregate	4.82	4.82	14.25	14.25
	Cement mortar	22.01	22.01	3.76	3.76
	Pore	1.00	1.00	5.00	5.00
Permittivity	Aggregate	8.00	8.00	10.00	10.00
	Cement	10.30	23.34	9.69	18.42
	Average in (1)	8.62	11.46	9.93	9.86

(2) Implementation details

The proposed method is trained on a workstation equipped with two NVIDIA A6000 GPUs and 256 GB of RAM. Training is conducted for 40 epochs on the merged dataset using the ADAM optimizer, with a batch size of 16. The initial learning rate is set to 0.0001 and decays by a factor of 0.8 every 10 epochs. To reduce computational overhead,

the encoder–decoder module is initialized with pre-trained weights from [32], while the ET-based regression module is trained from scratch. The complete training process takes approximately three hours on the specified hardware.

For HF-EMW denoising, the proposed method was compared with wavelet transform (WT), DnCNN [33], FFDNet [34], and REDNet [35]. All methods, except for the WT, are trained by the dataset in Table 4, where the input and label of a sample are the real-world recorded HF-EMWs and the FDTD simulation HF-EMWs, respectively.

For permittivity measurements with uncertainty quantification, the proposed model method was compared with a common two-layer neural network, LSTM [36], deep encoder [37], wave-processing transformer [38], swin transformer [39], SCUNet [32], and MCA-SCUNet [40]. All methods are trained by the dataset in Table 4. The input of a sample consists of a couple of recorded and simulated HF-EMWs, while the label indicates true permittivity.

(3) Metrics

A signal-to-noise ratio (SNR) and structural similarity index measure ($SSIM$) are adopted to evaluate the performance of HF-EMW denoising. The metrics SNR [41] and $SSIM$ [42] are, respectively, defined as

$$SNR(\boldsymbol{\theta}_t^c, \boldsymbol{\theta}_t') = \frac{1}{T}\sum_{t=1}^{T} 10\log_{10}\left(\frac{||\boldsymbol{\theta}_t^c||_2^2}{||\boldsymbol{\theta}_t^c - \boldsymbol{\theta}_t'||_2^2}\right), \tag{10a}$$

$$SSIM(\boldsymbol{\theta}_t^c, \boldsymbol{\theta}_t') = \frac{1}{T}\sum_{t=1}^{T} \frac{\left(2\mu(\boldsymbol{\theta}_t^c)\mu(\boldsymbol{\theta}_t') + C_1\right)\left(2\sigma(\boldsymbol{\theta}_t^c, \boldsymbol{\theta}_t') + C_2\right)}{\left(\mu(\boldsymbol{\theta}_t^c)^2 + \mu(\boldsymbol{\theta}_t')^2 + C_1\right)\left(\sigma^2(\boldsymbol{\theta}_t^c) + \sigma^2(\boldsymbol{\theta}_t') + C_2\right)\right)}, \tag{10b}$$

where $\boldsymbol{\theta}_t^c$ and $\boldsymbol{\theta}_t$ are the t-th raw and denosied wave, respectively; μ, σ, and σ^2 are the mean, variance, and covariance of an HF-EMW, respectively.

The mean square error MSE and permittivity utility (PU) are used in the performance evaluation of the permittivity measurement with uncertainty quantification:

$$MSE(\boldsymbol{\theta}) = \frac{1}{|D|}\sqrt{\frac{\sum_{\boldsymbol{\theta}\in D}(\varepsilon^* - \mu(\boldsymbol{\theta}))^2}{\sum_{\boldsymbol{\theta}\in D}(\varepsilon^* - \overline{\mu})^2}} \tag{11a}$$

$$PU = \begin{cases} 0 & \text{if } \varepsilon^* \notin \mathcal{G}_\Pi(\boldsymbol{\theta}) \\ 1 - \frac{|\varepsilon^* - \mu(\boldsymbol{\theta})|}{\widehat{C}^{-1}_{\widetilde{N}|\boldsymbol{\theta}}\left(\frac{1+\Pi}{2}\right) - \mu(\boldsymbol{\theta}) + \alpha_s} & \text{if } \varepsilon^* \in \mathcal{G}_\Pi(\boldsymbol{\theta}) \end{cases} \tag{11b}$$

where ε^* and $\mu(\boldsymbol{\theta})$ are the labeled and predicted permittivity using HF-EMW $\boldsymbol{\theta}$; $\overline{\mu}$ is the average of all predictions in dataset D; α_s is a very small constant (=10^{-8}) used to prevent the denominator from being 0.

4.2. HF-EMW Echoes from an FDTD Model

A combined transmitting and receiving antenna was positioned above the model to perform simulated inspections at different frequencies. Five scan lines were sequentially arranged above the heterogeneous surface and base layer models to position the antenna. After filtering out the direct wave, the electric field intensity along the Z-direction was plotted, showing the radar signal waveforms propagating through each structural layer at various frequencies.

Figure 5 shows the electric field intensity curves in the Z-direction during radar wave propagation within the cement-stabilized gravel base layer under different excitation frequencies. HF-EMWs generated by a mid-frequency antenna exhibit waveforms that closely resemble those within the concrete sample. Clear reflections from the lower interface of the base layer, as well as partial reflections from the upper interface, can be distinctly identified.

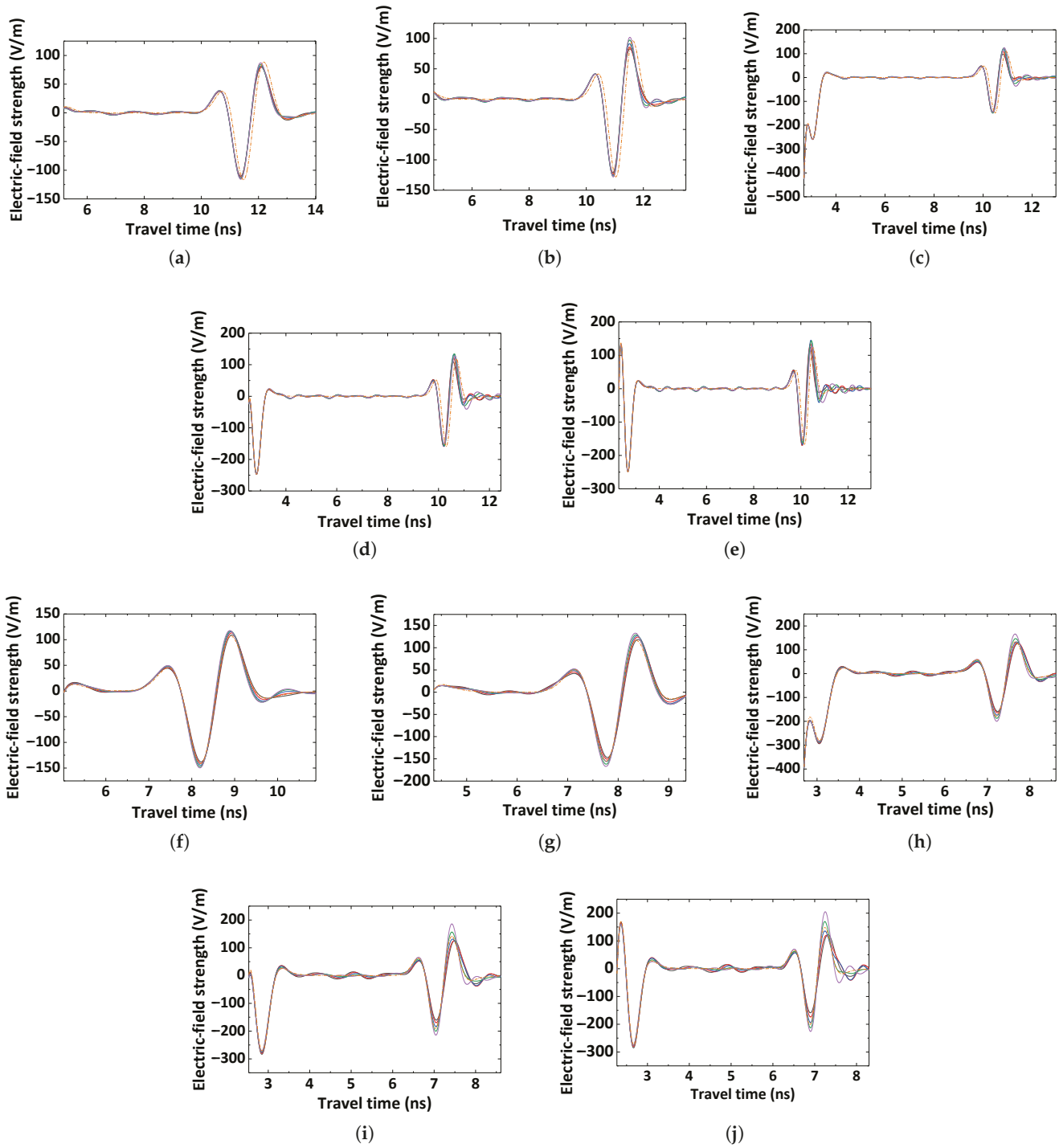

Figure 5. HF-EMW echoes from FDTD models: (**a**–**e**) are the HF-EMWs with frequencies 800 MHz, 1.0 GHz, 1.2 GHz, 1.6 GHz, and 2.0 GHz from a concrete sample of Material 1, and (**f**–**j**) are the HF-EMWs with frequencies 800 MHz, 1.0 GHz, 1.2 GHz, 1.6 GHz, and 2.0 GHz from a concrete sample of Material 3. Five solid curves are the simulated waves, and dotted curves are the recorded waves.

Though the simulation and measurement results are similar, as shown in Figure 5, the peaks and troughs of the two types of HF-EMWs still have some differences, which mainly derive from the limited knowledge of the propagation of HF-EMWs. For example, the FDTD model has some assumptions, such as the air-layer configuration and permittivity in Section 3.2.2. Such limited knowledge inevitably leads to epistemic uncertainty in permittivity measurement. Therefore, the use of simulated and measured HF-EMWs as

inputs allows the proposed method to quantify the epistemic uncertainty of permittivity measurement, as demonstrated in Section 4.2.

4.3. Denoising Results and Discussion

Table 6 shows the comparison results of the proposed method and other state-of-the-art (SOTA) methods on the denoising task. The proposed method achieves optimal results in terms of SNR and $SSIM$, indicating that it outperforms others on the denoising task. This demonstrates that the proposed method is more suitable than others for removing measurement noise, such as randomly distributed cement and aggregates in cement-based composites. This property enables the proposed approach to quantify aleatory uncertainty, which will be demonstrated in the next section.

Table 6. Performance of HF-EMW denoising.

	Train_Loss	**Train_ACC**	**SNR (dB)**			**SSIM**		
WT	0.3648	0.8344	20.89	20.97	20.78	0.7315	0.7330	0.7199
DnCNN	0.5175	0.7101	22.54	21.81	22.27	0.7821	0.7553	0.7498
FFDNet	0.5979	0.6535	24.12	24.05	23.98	0.8234	0.8219	0.8102
REDNet	0.3803	0.8106	26.45	26.38	26.52	0.8776	0.8761	0.8283
ours	**0.0740**	**0.9312**	**29.71**	**29.65**	**29.78**	**0.9287**	**0.9279**	**0.9295**

The bolds are the best results in the testing set.

Figure 6 provides some HF-EMWs before and after denoising. In general, the proposed method can retain the shapes of two pairs of peaks and troughs in the HF-EMWs and remove noise waves within the ranges of these two pairs. The two pairs of peaks and troughs in an HF-EMW originate from the incidence and emergence of the wave in a concrete sample, while the noise waves derive from the wavelets owing to randomly distributed cement and aggregates. The difference between the raw and denoised HF-EMWs characterizes the effects of the measurement noises. Therefore, the denoising deep network provides a potential way to quantify the aleatory uncertainty in the proposed method, which will be proven in the next section.

4.4. Permittivity Characterization with Uncertainty Quantification

Table 7 shows the MSE of the proposed method and other SOTAs. In general, the proposed one exceeds the others in the Bayesian probability framework in terms of MSE. This indicates that the proposed method can accurately predict the permittivity of cement-based samples with minimal error. This mainly benefits from the fact that the proposed method can quantify the epistemic uncertainty of permittivity measurement by comparing simulated and recorded HF-EMWs and characterize the aleatory uncertainty by comparing the HF-EMWs before and after denoising. However, the other network in the Bayesian probability framework, such as MCA-SCUNet and swin transformer only captures the randomness aspect of the data, but neither ambiguity nor incompleteness is captured, which is the inherent epistemic uncertainty in HF-EMWs.

Table 7 also shows the PU of the proposed method and other SOTAs. The proposed one outperforms the others in PU terms. This indicates that the proposed method can accurately quantify the uncertainty of permittivity measurements. Figure 7 shows a visual explanation of this advantage via BMIs. In general, the predicted permittivity of the proposed method mainly falls into the BMI with a Π of 0.95, demonstrating that the permittivity measurement of the proposed method can quantify the two types of uncertainty and reduce their negative effects on the final measurement. In detail, Figure 8 shows the BMIs of HF-EMWs. A large range of BMI in an HF-EMW mainly falls into the 100–600 sampling points, where the HF-EMWs propagate in the samples. This propagation always leads to epistemic uncertainty

due to the limited knowledge of real wave-propagation paths and aleatory uncertainty due to multi-phase heterogeneous materials.

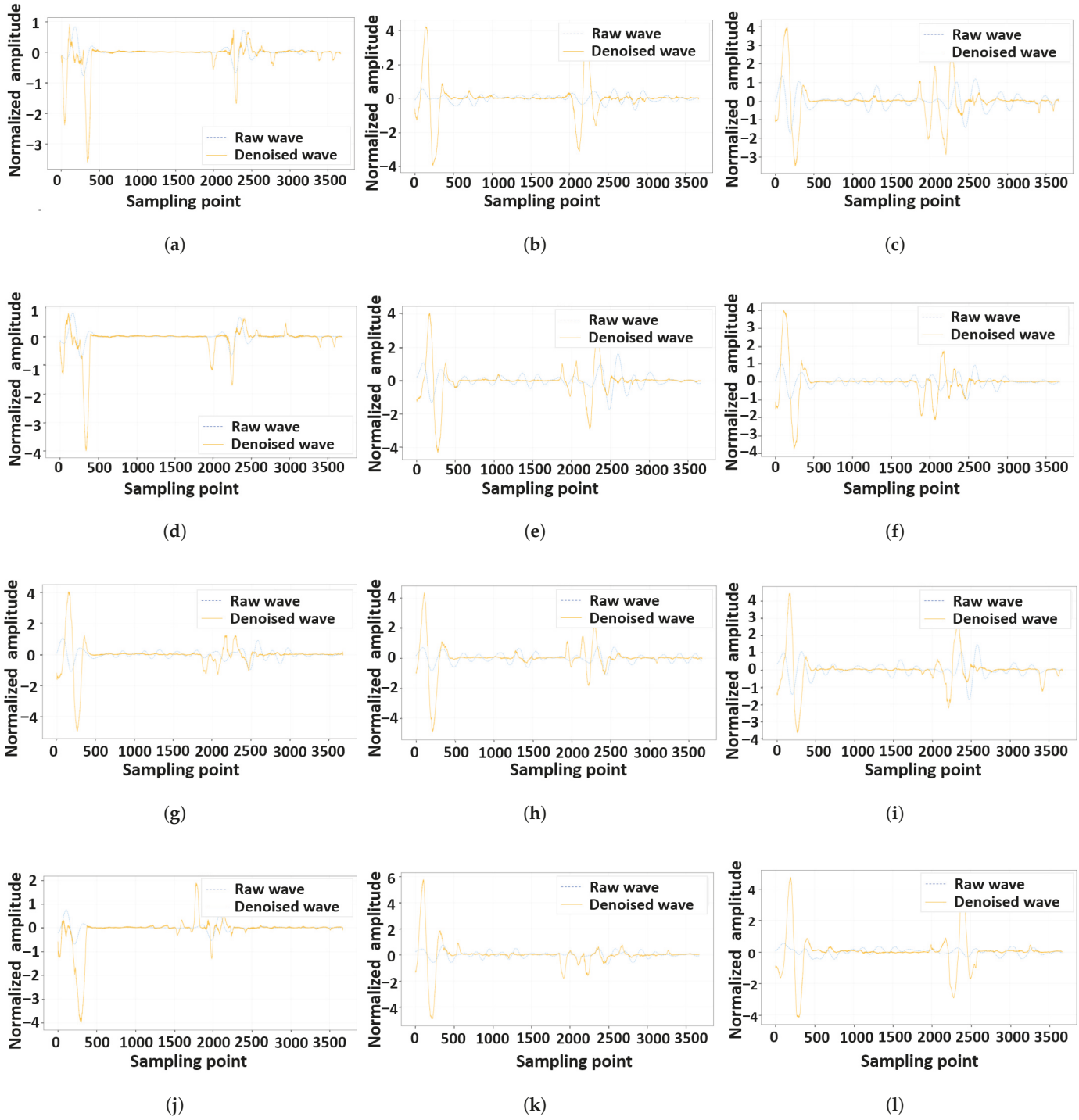

Figure 6. Denosing results of the proposed method. (**a**) Example 1, (**b**) Example 2, (**c**) Example 3, (**d**) Example 4, (**e**) Example 5, (**f**) Example 6, (**g**) Example 7, (**h**) Example 8, (**i**) Example 9, (**j**) Example 10, (**k**) Example 11, and (**l**) Example 12.

Figure 9 shows the uncertainty quantification under various HF-EMW frequencies. The measurement results for 1.0 GHz, 1.2 GHz, and 1.6 GHz all fall within the BMI of 0.95, whereas those for 800 MHz and 2.0 GHz do not. This phenomenon indicates that the HF-EMWs with 800 MHz and 2.0 GHz frequencies have higher uncertainty than those with 1.0 GHz, 1.2 GHz, and 1.6 GHz frequencies. Theoretically, an HF-EMW with a low frequency has a low resolution that always leads to aleatory uncertainty, which is also known as a

measurement error. An HF-EMW with high frequencies has a high resolution and a small wavelength. Although higher resolutions have low aleatory uncertainty, a small wavelength always leads to Fresnel diffraction in multi-phase heterogeneous concrete, which generates sub-waves in the HF-EMW propagation path and leads to epistemic uncertainty.

Table 7. Testing results of permittivity FL measurements.

Methods	MSE/%					PU/%				
	Overall	Materials 1	Materials 2	Materials 3	Materials 4	Overall	Materials 1	Materials 2	Materials 3	Materials 4
ANN	17.34	15.53	16.78	17.39	19.65	54.14	51.37	56.6	55.05	53.54
LSTM	13.5	14.36	14.85	14.2	10.57	54.06	53.05	51.35	55.51	56.31
Deep encoder	14.27	12.56	16.93	15.26	12.31	58.79	56.52	59.2	58.33	61.1
Wave-processing transformer	12.04	11.09	7.91	12.71	16.45	64.96	65.44	62.6	62.33	69.47
Swin transformer	11.03	7.98	10.01	9.3	16.83	66.29	69.71	64.21	64.7	66.54
SCUNet	11.09	10.18	10.19	11.07	12.9	70.19	68.67	71.25	69.38	71.47
MCA-SCUNet	9.08	8.08	7.75	10.47	10	72.87	70.5	75.14	74.12	71.72
Ours	7.5	6.85	6.48	8.01	8.64	74.7	74.09	75.34	76.3	73.06

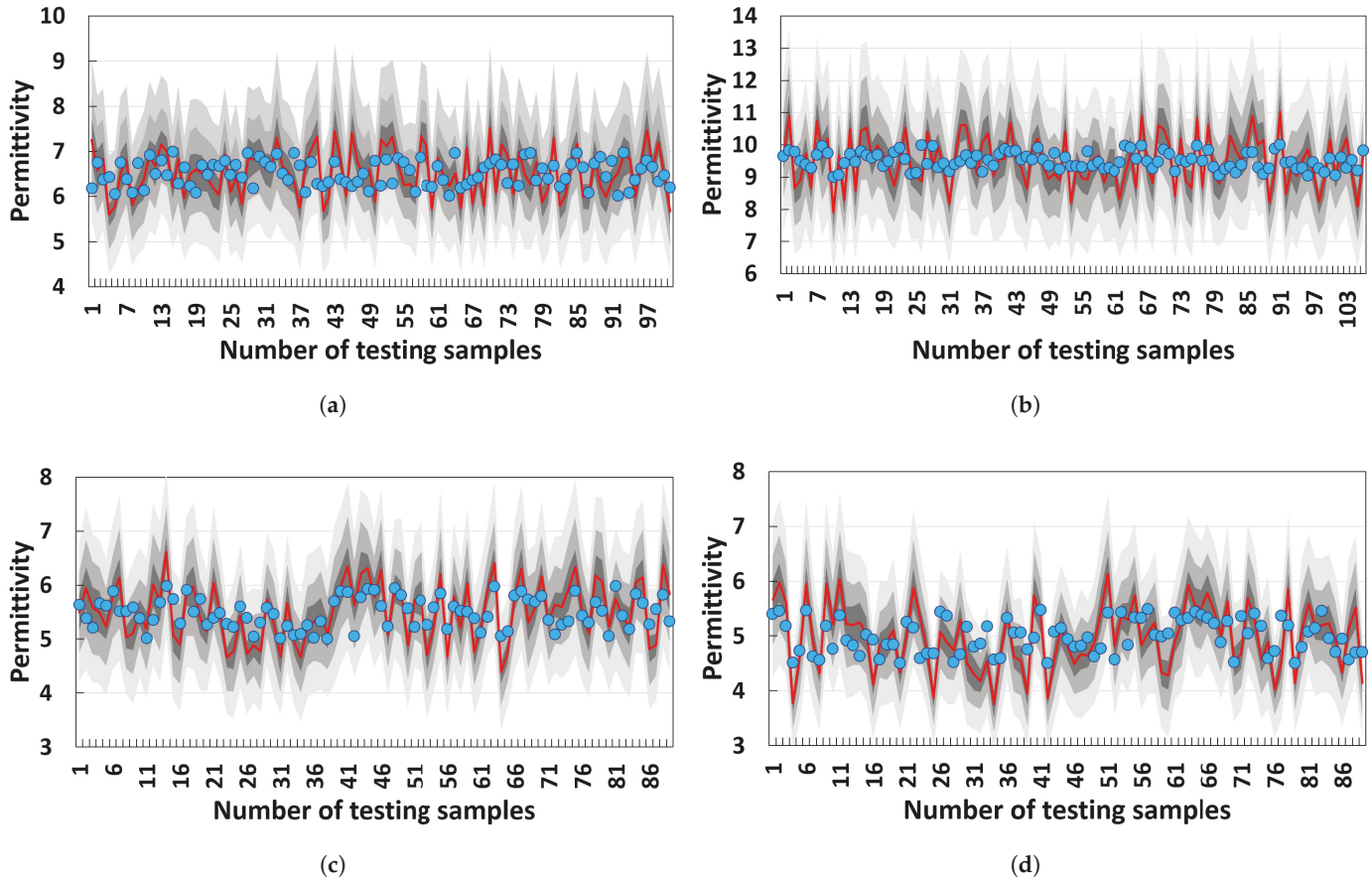

Figure 7. Uncertainty quantification of permittivity measurement using belief measurement intervals: (**a**) Material 1, (**b**) Material 2, (**c**) Material 3, and (**d**) Material 4. The red lines are the labeled permittivity, while the blue points are the predicted one. The three grays are the BMIs with Π in [0.5, 0.05, 0.99].

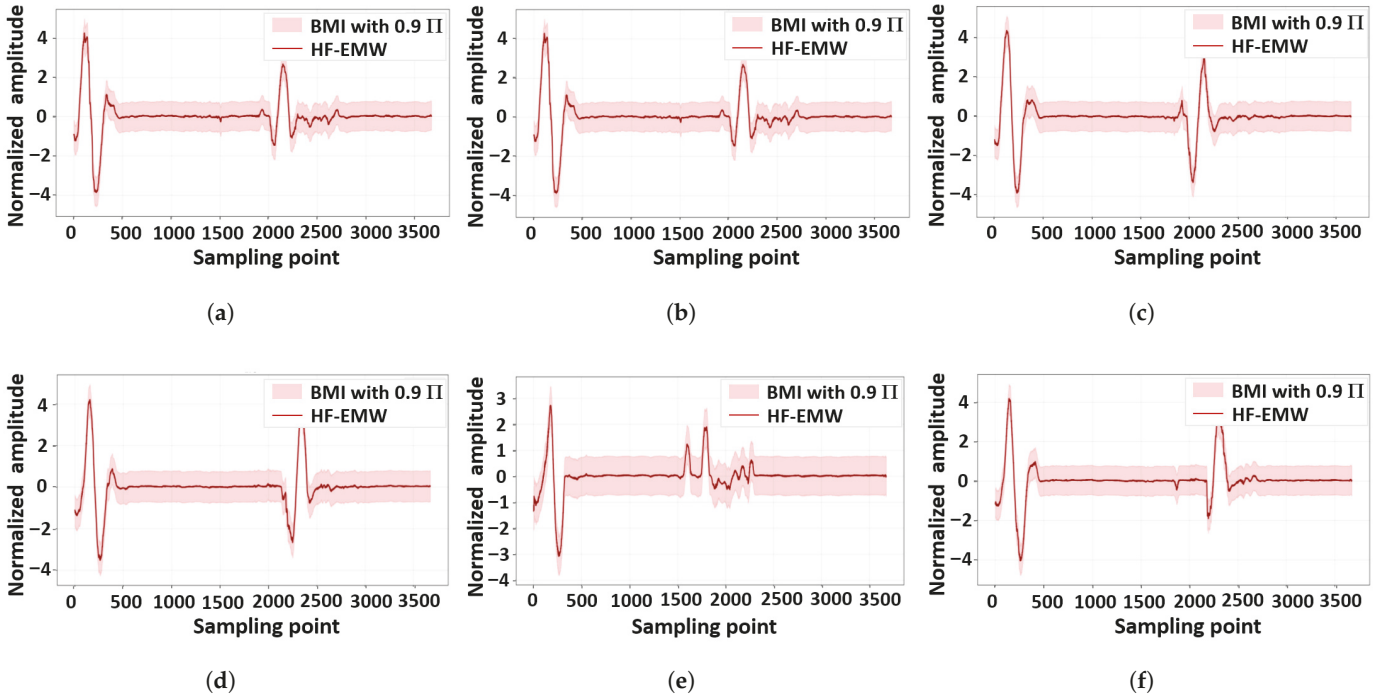

Figure 8. Recorded high-frequency electromagnetic waves with uncertainty quantification using belief measurement intervals. (**a**) Example 1, (**b**) Example 2, (**c**) Example 3, (**d**) Example 4, (**e**) Example 5, (**f**) Example 6.

Table 8 shows the ablation study of the denosing and FDTD simulation. Once the denoising deep network is removed (Model 2) , the MSE and PU of the proposed method decrease. This is mainly because the proposed method cannot quantify the aleatory uncertainty due to the measurement noise and multi-phase heterogeneous materials. Therefore, a reasonable denoising model is crucial for permittivity measurements using HF-EMWs.

Table 8 also indicates that the MSE and PU of the proposed method decrease if we do not use the simulated HF-EMW as an input (Model 3). This is because the proposed method cannot capture the knowledge of HF-EMW propagation paths without the simulated HF-EMW. Therefore, an FDTD simulation of HF-EMW propagation offers a new approach to enhancing the accuracy of permittivity measurements by providing the necessary knowledge.

Table 8 also indicates that the MSE and PU of the proposed method decrease if we do not use the DST-based regression network as the final output (Model 4). This is because the DST-based regression network quantifies the two types of uncertainties in the permittivity measurement, which represent and reduce the negative effect of uncertainty. Therefore, a DST-based regression network is necessary for the permittivity measurement with uncertainty quantification.

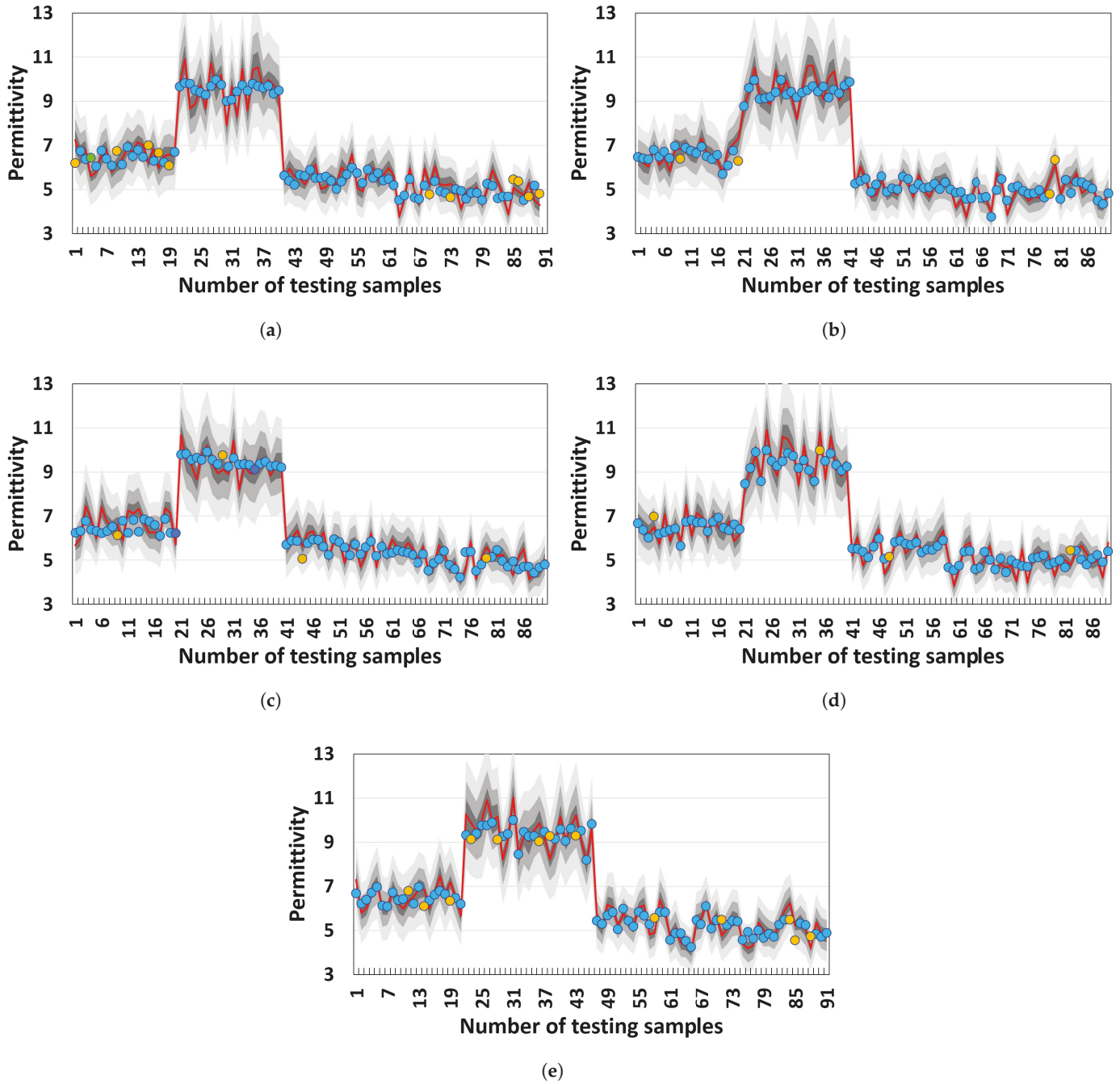

Figure 9. Uncertainty quantification of permittivity measurement using belief measurement intervals: (**a**) 800 MHz, (**b**) 1.0 GHz, (**c**) 1.2 GHz, (**d**) 1.6 GHz, and (**e**) 2.0 GHz. The predicted results do not fall into the BIM, with $\Pi = 0.99$ highlighted in yellow. The red lines are the labeled permittivity, while the blue points are the predicted one. The three grays are the BMIs with Π in [0.5, 0.05, 0.99].

Table 8. Ablation study of the proposed method.

	Denoise	FDTD Simulation	DST-Based Regression	MSE/%	PU/%
Model 1	✓	✓	✓	7.50	74.70
Model 2	-	✓	✓	10.08	64.62
Model 3	✓	-	✓	9.34	68.72
Model 4	✓	✓	-	9.14	61.73
Model 5	-	-	✓	10.45	64.36
Model 6	✓	-	-	10.08	63.88

5. Conclusions

This study proposes a DST-based evidential regression deep network for conducting permittivity measurements with uncertainty quantification. This method first proposes an FDTD model with multi-phase heterogeneous concrete materials to simulate the HF-EMW propagation in a concrete sample or structure, obtaining the HF-EMW echo. A U-net-based model is then proposed to denoise an HF-EMW. Finally, a DST-based evidential regression network is proposed to compute the permittivity with aleatory and epistemic uncertainty using a Gaussian random fuzzy number (GRFN). An experiment involving 1500 samples is conducted to demonstrate the effectiveness of the proposed method. The following conclusions can be drawn:

1. The proposed method measures the permittivity of four types of multi-phase heterogeneous concrete materials with an MSE of 7.50%, exceeding other SOTA methods in this task. The proposed method is also stable with respect to the four concrete types. Therefore, a user can directly use the method to measure the permittivity of concrete materials using recorded HF-EMWs.
2. The proposed method can quantify the uncertainty in permittivity measurement using a GRFN-based BMI. The predicted permittivity mainly falls into the BMI with a 0.95 Π, demonstrating that the proposed method can quantify and remove the effects of aleatory and epistemic uncertainty in the permittivity measurement.
3. The superiority of the proposed method benefits from the FDTD simulation and the denoising deep network. The FDTD simulation quantifies epistemic uncertainty due to limited knowledge, such as HF-EMW propagation. The denoising deep network quantifies aleatory uncertainty due to the measurement's noise, such as the multi-phase heterogeneous property of concrete materials.
4. The applicability of the proposed method is limited in cement concrete and cement-stabilized macadam. The next step is to extend the proposed method to other concrete materials, such as fiber-reinforced concrete and lightweight concrete, via conducting an experiment similar to the one outlined in Section 4.1. In the practical implementation, the proposed DST-based deep network can be embedded into a GPR with edge computing capabilities, and engineers can rapidly assess material qualities during construction or inspection.

Author Contributions: Conceptualization, J.C. and Z.T.; methodology, Z.H., H.L. and Q.Z.; software, Z.H. and H.L.; validation, Z.H. and Q.Z.; formal analysis, Z.H. and Z.T.; investigation, Z.H., H.L. and Q.Z.; resources, Z.T.; data curation, Z.T.; writing—original draft preparation, Z.H.; writing—review and editing, J.C. and Z.T.; visualization, Z.H. and Q.Z.; supervision, J.C. and Z.T.; funding acquisition, Z.H. and Z.T. All authors have read and agreed to the published version of this manuscript.

Funding: This research was funded by Project of Suzhou Municipal Administration Center, grant number SZSZ-2024-1-KJ. This research was also funded by the National Natural Science Foundation of China under Grant 52308447 and Jiangsu Province Youth Science and Technology Talent Lifting Project under Grant JSTJ-2024-089.

Informed Consent Statement: Not applicable.

Data Availability Statement: The original contributions presented in this study are included in the article. Further inquiries can be directed to the corresponding author.

Conflicts of Interest: Authors Zhaojun Hou and Qifeng Zhang were employed by the company CCDI (Suzhou) Exploration & Design Consultant Co., Ltd. Author Hui Liu was employed by the company China Railway 14th Bureau Large Shield Engineering Co., Ltd. The remaining authors declare that the research was conducted in the absence of any commercial or financial relationships that could be construed as a potential conflict of interest.

Appendix A

The concept of a GRFN derives from the Gaussian fuzzy number (GFN) with mode μ and variance σ, notated as GFN(μ, σ), which is a fuzzy subset of $\mathbb{R}$ with membership function $\boldsymbol{\theta} \to \exp\left(-\frac{\sigma}{2}(x-\mu)^2\right)$. Each point in the membership function of a GFN indicates the probability that the selected value is the truth. The value μ can be the predicted permittivity in the proposed method, while the variance σ is the aleatory uncertainty. Figure A1a shows two examples of GFNs. For the green one, GFN$(-2, 0.2)$ indicates that the correct probability is 0.892 if one selects -2 as the final prediction, while the probability is 0.608 with a final prediction of -2.392. A GFN presents the aleatory uncertainty of a prediction with respect to μ, where true permittivity is around μ, but one cannot determine a precise value due to the random error, such as the multi-phase heterogeneous property of a cement-based composite.

The epistemic uncertainty is then introduced by converting GFN into a Gaussian random fuzzy number (GRFN) with mean μ, variance σ^2, and precision h, notated as $\widetilde{N}(\mu, \sigma, h)$. A GRFN is a GFN for which its mode is also a GFN, $N(\mu, \sigma^2)$, indicating that the mode of the GFN includes epistemic uncertainty owing to the knowledge limitation of permittivity measurements. Figure A1b extends the two examples in Figure A1a into GRFNs. In summary, μ, σ, and h in a GRFN is the predicted permittivity value, the quantification of aleatory uncertainty, and the quantification of epistemic uncertainty, respectively.

Finally, a BMI of a GRFN is the long-run prediction of the confidence level Π such that the true value theoretically falls in the interval with aleatory and epistemic uncertainty, as shown in Figure A1c. A BMI is a general form of the classic statistical form $\mu \pm h$ in a property measurement. The classic form $\mu \pm h := [\mu - h, \mu + h]$ represents a measurement mean μ with uncertainty h, where the truth is around μ but cannot be used to determine a precise value. However, the classic form cannot show that the probability decreases with a distance increase in the mean. A BIM is equivalent to the classic representation when $\sigma^2 = 0$ and $h = +\infty$.

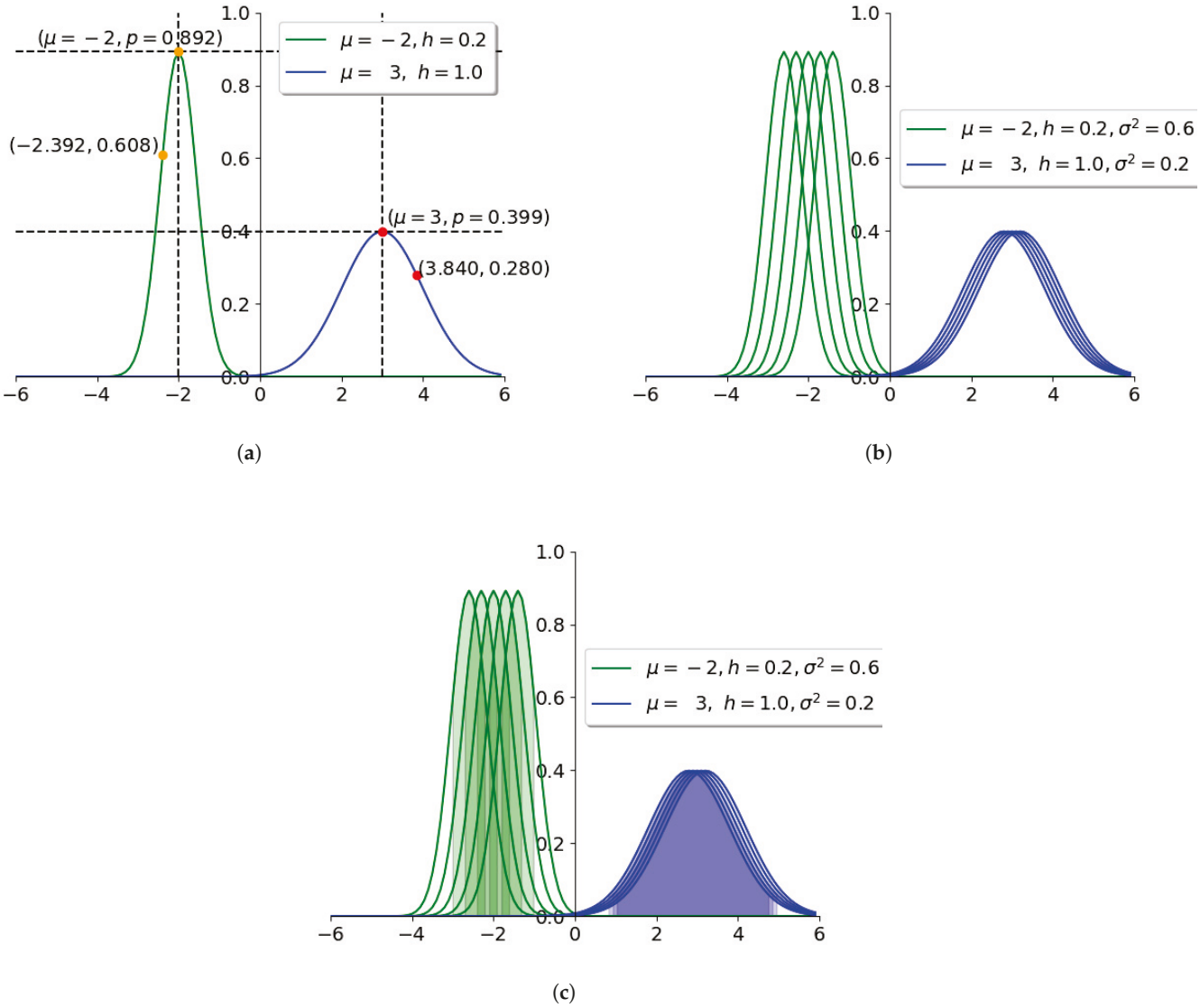

Figure A1. Two visual examples of (**a**) Gaussian fuzzy numbers, (**b**) Gaussian random fuzzy numbers, and (**c**) BMIs.

References

1. Fan, B.; Bosc, F.; Liu, Y.; Le Feuvre, M.; Fauchard, C. Permittivity analysis of weathered concrete in a bridge based on open-ended probe and impedance measurements. *Constr. Build. Mater.* **2024**, *429*, 136354. [CrossRef]
2. Xue, B.; Haneda, K.; Icheln, C.; Ala-Laurinaho, J.; Tuomela, J. Complex permittivity characterization of low-loss dielectric slabs at sub-THz. *IEEE Access* **2024**, *12*, 150693–150701. [CrossRef]
3. Xu, X.; Guo, X.; Zheng, W.; Liu, H. A Flexible Electrical Capacitance Tomography Sensor for Proximity Object Recognition. *IEEE Trans. Instrum. Meas.* **2025**, *74*, 4505912. [CrossRef]
4. Liu, G.; Li, M.; Yang, L.; Liu, C.; Zhang, Y. Electrochemical dielectric response of steel corrosion induced by chloride in simulated concrete pore solution. *J. Sustain.-Cem.-Based Mater.* **2024**, *13*, 854–864. [CrossRef]
5. Li, J.; Li, T.; Xu, Z.; Wang, J.; Zhi, D.; Li, J.; Ma, L.; Meng, F. Permittivity genome: A new perspective on absorbing materials design. *Chem. Eng. J.* **2025**, *503*, 158398. [CrossRef]
6. Shahzad, K.; Mardare, A.I.; Hassel, A.W. Accelerating materials discovery: Combinatorial synthesis, high-throughput characterization, and computational advances. *Sci. Technol. Adv. Mater. Methods* **2024**, *4*, 2292486. [CrossRef]
7. Bidgoli, H.A.; Schieda, N.; Rossa, C. A simplified formulation of the reflection coefficient of an open-ended coaxial probe in multilayered media. *IEEE Trans. Microw. Theory Tech.* **2024**, *72*, 6485–6495. [CrossRef]

8. Sakib, S.; Hoque, A.; Islam, M.T.; Alenezi, A.M.; Soliman, M.S.; Alsaif, H. Design and analysis of quad-band metamaterial absorber for permittivity sensing with phase evolved equivalent circuit analysis. *Ain Shams Eng. J.* **2024**, *15*, 103153. [CrossRef]
9. Lv, S.; Wen, J.; Zhang, X. MPPINet: Multi-Path Permittivity Inversion Network for Tree Roots Ground Penetrating Radar Image Recognition. *IEEE Trans. Instrum. Meas.* **2024**, *73*, 6007514. [CrossRef]
10. Bernardo, N.; Martins-Gomes, V.; Bordes, C.; Brito, D. Seismoelectric conversion at poroelastic/elastic interfaces and the role of dielectric permittivity: Experimental and numerical analysis. *Geophys. Res. Lett.* **2024**, *51*, e2024GL112994. [CrossRef]
11. Kuurka, P.; Havelka, D.; Cifra, M. Broadband Extraction of Sample Permittivity from Microwave Planar Transmission Lines. *IEEE Trans. Microw. Theory Tech.* **2025**. [CrossRef]
12. Schopp, C.; Rohrbach, F.; Heuermann, H. Power-and spatial-dependent characterization of reflection and transmission electric parameters of an argon microwave plasma. *IEEE Trans. Plasma Sci.* **2022**, *50*, 261–266. [CrossRef]
13. Dilman, I.; Akinci, M.N.; Yilmaz, T.; Çayören, M.; Akduman, I. A method to measure complex dielectric permittivity with open-ended coaxial probes. *IEEE Trans. Instrum. Meas.* **2022**, *71*, 6000507. [CrossRef]
14. Munalli, D.; Al Qaseer, M.T.; Zoughi, R. Modified waveguide-based method for microwave characterization of high-loss materials. *IEEE Trans. Instrum. Meas.* **2022**, *71*, 6002310. [CrossRef]
15. Wang, Z.; Timlin, D.; Gong, X.; Kojima, Y.; Hua, S.; Fleisher, D.; Sun, W.; Beegum, S.; Reddy, V.R.; Tully, K.; et al. TDR-Transformer: A transformer neural network model to determine soil relative permittivity variations along a time domain reflectometry sensor waveguide. *Comput. Electron. Agric.* **2025**, *237*, 110730. [CrossRef]
16. Fuscaldo, W.; Maita, F.; Maiolo, L.; Beccherelli, R.; Zografopoulos, D.C. Broadband dielectric characterization of high-permittivity rogers substrates via terahertz time-domain spectroscopy in reflection mode. *Appl. Sci.* **2022**, *12*, 8259. [CrossRef]
17. Tong, Z.; Zhang, Y.; Ma, T. Permittivity measurement with uncertainty quantification in cement-based composites using ENNreg-ANet and high-frequency electromagnetic waves. *Measurement* **2025**, *244*, 116537. [CrossRef]
18. Wang, H.; Ouyang, S.; Liu, Q.; Liao, K.; Zhou, L. Deep-learning-based method for estimating permittivity of ground-penetrating radar targets. *Remote Sens.* **2022**, *14*, 4293. [CrossRef]
19. Malkin, A.; Chechetkin, V.; Korotkov, A.; Knyazev, N. Estimation of uncertainty of permittivity measurement with transmission line method in the wide frequency range. In Proceedings of the 2021 29th Telecommunications Forum (TELFOR), Belgrade, Serbia, 23–24 November 2021; IEEE: Piscataway, NJ, USA, 2021; pp. 1–3.
20. Wang, D.; Fu, Y.; Liu, Y.; Talley, J.D.; Worosz, T.; Hogan, K.; Buchanan, J.R., Jr. A comprehensive uncertainty evaluation of double-sensor conductivity probe. *Prog. Nucl. Energy* **2021**, *136*, 103741. [CrossRef]
21. Valdenegro-Toro, M.; Mori, D.S. A deeper look into aleatoric and epistemic uncertainty disentanglement. In Proceedings of the 2022 IEEE/CVF Conference on Computer Vision and Pattern Recognition Workshops (CVPRW), New Orleans, LA, USA, 19–20 June 2022; IEEE: Piscataway, NJ, USA, 2022; pp. 1508–1516.
22. Chen, H.; Tian, Z. Environmental uncertainty, resource orchestration and digital transformation: A fuzzy-set QCA approach. *J. Bus. Res.* **2022**, *139*, 184–193. [CrossRef]
23. Li, J.; Jia, L.; Zhou, C. Probability density function based adaptive ensemble learning with global convergence for wind power prediction. *Energy* **2024**, *312*, 133573. [CrossRef]
24. Abbasi, A.R.; Gandhi, C.P. A novel hyperbolic fuzzy entropy measure for discrimination and taxonomy of transformer winding faults. *IEEE Trans. Instrum. Meas.* **2022**, *71*, 3526408. [CrossRef]
25. Ma, L.; Denoeux, T. Partial classification in the belief function framework. *Knowl.-Based Syst.* **2021**, *214*, 106742. [CrossRef]
26. Tong, Z.; Xu, P.; Denoeux, T. An evidential classifier based on Dempster-Shafer theory and deep learning. *Neurocomputing* **2021**, *450*, 275–293. [CrossRef]
27. Tong, Z.; Xu, P.; Denoeux, T. Evidential fully convolutional network for semantic segmentation. *Appl. Intell.* **2021**, *51*, 6376–6399. [CrossRef]
28. Huang, L.; Ruan, S.; Decazes, P.; Denœux, T. Deep evidential fusion with uncertainty quantification and reliability learning for multimodal medical image segmentation. *Inf. Fusion* **2025**, *113*, 102648. [CrossRef]
29. Liu, J.; Zhang, Y.; Song, L.; Tong, Z. SCB-ADAE: An attention-based deep autoencoder for ground penetrating radar signal denoising. *Eng. Appl. Artif. Intell.* **2025**, *160*, 111902. [CrossRef]
30. Zhang, Y.; Tong, Z.; She, X.; Wang, S.; Zhang, W.; Fan, J.; Cheng, H.; Yang, H.; Cao, J. SWC-Net and multi-phase heterogeneous FDTD model for void detection underneath airport pavement slab. *IEEE Trans. Intell. Transp. Syst.* **2024**, *25*, 20698–20714. [CrossRef]
31. Denœux, T. Quantifying prediction uncertainty in regression using random fuzzy sets: The ENNreg model. *IEEE Trans. Fuzzy Syst.* **2023**, *31*, 3690–3699. [CrossRef]
32. Chen, J.; Chen, G.; Li, J.; Du, R.; Qi, Y.; Li, C.; Wang, N. Efficient Seismic Data Denoising via Deep Learning with Improved MCA-SCUNet. *IEEE Trans. Geosci. Remote Sens.* **2024**, *62*, 5903614. [CrossRef]
33. Zhang, K.; Zuo, W.; Chen, Y.; Meng, D.; Zhang, L. Beyond a gaussian denoiser: Residual learning of deep cnn for image denoising. *IEEE Trans. Image Process.* **2017**, *26*, 3142–3155. [CrossRef]

34. Zhang, K.; Zuo, W.; Zhang, L. FFDNet: Toward a fast and flexible solution for CNN-based image denoising. *IEEE Trans. Image Process.* **2018**, *27*, 4608–4622. [CrossRef]
35. Jiang, J.; Zheng, L.; Luo, F.; Zhang, Z. Rednet: Residual encoder-decoder network for indoor rgb-d semantic segmentation. *arXiv* **2018**, arXiv:1806.01054.
36. Zhao, R.; Yan, R.; Wang, J.; Mao, K. Learning to monitor machine health with convolutional bi-directional LSTM networks. *Sensors* **2017**, *17*, 273. [CrossRef]
37. Wang, Y.; Yao, H.; Zhao, S. Auto-encoder based dimensionality reduction. *Neurocomputing* **2016**, *184*, 232–242. [CrossRef]
38. Ghunem, R.A.; Assaleh, K.; El-Hag, A.H. Artificial neural networks with stepwise regression for predicting transformer oil furan content. *IEEE Trans. Dielectr. Electr. Insul.* **2012**, *19*, 414–420. [CrossRef]
39. Liu, Z.; Lin, Y.; Cao, Y.; Hu, H.; Wei, Y.; Zhang, Z.; Lin, S.; Guo, B. Swin transformer: Hierarchical vision transformer using shifted windows. In Proceedings of the IEEE/CVF International Conference on Computer Vision, Montreal, BC, Canada, 11–17 October 2021; pp. 10012–10022.
40. Zhang, K.; Li, Y.; Liang, J.; Cao, J.; Zhang, Y.; Tang, H.; Fan, D.P.; Timofte, R.; Gool, L.V. Practical blind image denoising via Swin-Conv-UNet and data synthesis. *Mach. Intell. Res.* **2023**, *20*, 822–836. [CrossRef]
41. Box, G. Signal-to-noise ratios, performance criteria, and transformations. *Technometrics* **1988**, *30*, 1–17. [CrossRef]
42. Wang, Z.; Bovik, A.C.; Sheikh, H.R.; Simoncelli, E.P. Image quality assessment: From error visibility to structural similarity. *IEEE Trans. Image Process.* **2004**, *13*, 600–612. [CrossRef]

Disclaimer/Publisher's Note: The statements, opinions and data contained in all publications are solely those of the individual author(s) and contributor(s) and not of MDPI and/or the editor(s). MDPI and/or the editor(s) disclaim responsibility for any injury to people or property resulting from any ideas, methods, instructions or products referred to in the content.

materials

MDPI

Review

Comparative Review of Marshall and Superpave Mix Designs: Enhancing Asphalt Performance with Polymers

Gulzar Hussain Jatoi [1,2], Giuseppe Loprencipe [1,*] and Laura Moretti [1]

[1] Department of Civil, Building and Environmental Engineering, Sapienza University of Rome, Via Eudossiana 18, 00184 Rome, Italy; gulzarhussain.jatoi@uniroma1.it (G.H.J.); laura.moretti@uniroma1.it (L.M.)
[2] Department of Civil Engineering, Aror University of Art, Architecture, Design and Heritage, RCW Rohri Bypass, Sukkur 65170, Sindh, Pakistan
* Correspondence: giuseppe.loprencipe@uniroma1.it

Abstract

The durability of asphalt pavements is crucial for sustainable road infrastructures. This systematic review compares the Marshall and Superpave asphalt mix design protocols, with a particular focus on the integration of polymer-modified bitumen (PMB) and rejuvenators. Although the Marshall method remains widely used for its simplicity and cost-efficiency, its empirical basis limits its effectiveness to meet modern pavement performance demands. In contrast, the Superpave system offers improved resistance to rutting, longer fatigue life, and better mitigation of moisture damage. The review traces the evolution of asphalt mix design, identifies current challenges, and emphasizes the need for transitioning toward performance-based frameworks. Special attention is given to the incorporation of polymers such as Styrene–Butadiene–Styrene (SBS), Styrene–Butadiene–Rubber (SBR), and Polyethylene (PE), which significantly enhance the mechanical properties of asphalt mixtures. The role of rejuvenators in restoring aged binders and enabling pavement recycling is also examined. Finally, the manuscript provides strategic recommendations for adopting Superpave to enhance pavement durability and reduce lifecycle maintenance costs. Overall, this comprehensive review advances knowledge on asphalt mix design, fostering innovation and sustainability while promoting long-term resilience in road pavement infrastructures.

Keywords: Marshall mix design; Superpave mix design; polymer-modified bitumen; rejuvenators

1. Overview of Asphalt Mix Design

As road infrastructure faces increasing traffic volumes and higher service demands, performance-based materials have become essential in addressing road durability challenges [1]. The design of asphalt mixtures plays a pivotal role in long-lasting and high-performing pavements [2]. The Marshall mix design remains widely used due to its simplicity, low equipment requirements, and cost-effectiveness [3]. However, despite these advantages, the Marshall method is inherently empirical, relying primarily on parameters such as stability and flow, which limit its ability to predict long-term field performance under varying climatic conditions and traffic load [3]. To address these limitations, the Strategic Highway Research Program introduced the Superpave (Superior Performing Asphalt Pavements) mix design approach. Superpave integrates mechanistic–empirical principles, incorporating binder performance grade (PG), aggregate angularity, and volumetric properties, while simulating field compaction more accurately through the gyratory compactor. This results in better alignment between laboratory predictions and field performance [4,5]. The Superpave system allows engineers to tailor mixtures to specific climate

and traffic conditions, thereby offering enhanced resistance to rutting, fatigue, and moisture susceptibility [3,5]. The transition toward performance-oriented design is particularly critical in rapidly urbanizing regions with escalating traffic demand. For instance, studies in Pakistan have demonstrated that the widespread use of paving-grade 60/70 binders fails to meet performance requirements, reducing pavement lifespan and increasing maintenance works [3,5]. Farooq et al. [5] reported that Superpave mixtures had a higher indirect tensile strength (ITS) and resilient modulus (MR) than Marshall mixtures, indicating improved performance under traffic-induced stresses. Similarly, Zumrawi and Edrees [3] found that conventional mixes provided poorer rutting and thermal crack resistance compared to Superpave mixes in hot climate regions [3]. In this context, polymer-modified bitumens (PMBs) containing SBS or SBR have been shown to effectively improve fatigue life and resistance to permanent deformation [6]. The integration of performance-based approaches further facilitates material compatibility with local climate zones while enabling the utilization of recycled materials and sustainable practices [7].

Bitumen, the most expensive component in asphalt mixtures, plays a pivotal role in determining pavement performance, particularly under extreme climatic conditions and heavy traffic demands [8]. Polymer modification has emerged as a critical advancement for enhancing binder properties. This process involves blending polymers with the base binder to improve viscoelastic behavior [9]. In recent years, PMBs, especially those modified with Styrene–Butadiene–Styrene (SBS), Styrene–Butadiene Rubber (SBR) and rubber, and plastomers including Polyethylene (PE), Polypropylene (PP) and Ethylene-Vinyl Acetate (EVA), have further demonstrated improvements in the mechanical performance of asphalt mixtures (Figure 1).

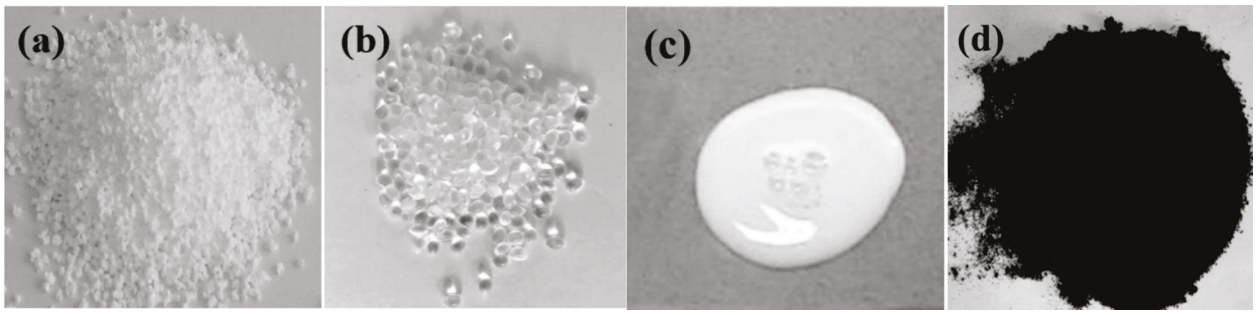

Figure 1. Polymers used for the modification: (**a**) SBS, (**b**) EVA, (**c**) SBR, and (**d**) rubber [9].

PMB has significantly enhanced rutting resistance, thermal stability, fatigue life, crack resistance, elasticity, and aging performance [9,10]. PMBs are particularly effective in high-temperature environments where unmodified bitumen is prone to excessive deformation. The interaction between bitumen and polymers can be either physical or chemical, depending on the polymer type. For instance, SBS absorbs maltenes from the binder, swelling up to nine times its original volume and forming a gel-like network that greatly improves elasticity and cohesion [11]. In addition, the incorporation of rejuvenators plays a critical role in restoring the rheological properties of aged binders, thereby enabling the effective utilization of reclaimed asphalt pavement (RAP) and supporting the circular economy within the asphalt industry [7]. Their effectiveness has been confirmed by the observed reduction in global virgin bitumen consumption between 2021 and 2024 [9,12]. By facilitating RAP recycling, rejuvenators contribute to the production of asphalt mixtures with improved durability and mechanical performance [13]. This not only strengthens recycling loops within the asphalt sector but also saves natural resources through reduced reliance on virgin bitumen.

The objective of review is to investigate the influences of polymer-modified asphalt (PMA) on the performance of the asphalt mixtures with respect to fatigue, rutting, and cracking resistance, and moisture susceptibility. The evaluation compares the performances achieved through the Marshall Mix Design and Superpave Mix Design, with the aim of determining whether recent changes in mix design have significantly influenced the polymers utilization. Furthermore, the review discusses how these advancements in mix design affect the long-term durability and service life of asphalt pavements, with particular emphasis on the effectiveness of rejuvenators in enhancing recycled asphalt content and supporting sustainable pavement practices.

2. Types of Polymers

Elastomers are thermoplastic polymers characterized by their rubber-like elasticity. Common examples include SBS, SBR, styrene–isoprene–styrene (SIS), and styrene–ethylene–butylene–styrene (SEBS) [14,15]. These polymers are widely applied in asphalt modification because they enhance elastic recovery while improving fatigue and crack resistance. In particular, SBS and SBR have demonstrated significant improvements in elastic recovery, fatigue resistance, and crack mitigation, especially under low-temperature conditions [9,10,16,17]. When mixed with bitumen, elastomers swell and form a continuous elastic network that substantially improves the rheological properties of bitumen under varying stress and temperature conditions [12,18]. This swelling process undergoes visco-rubber/viscoelastic phase inversion, producing a polymer-rich phase that allows viscoelastic behavior to dominate the asphalt matrix [12]. The key benefits of elastomer modification include enhanced elastic recovery, improved resistance to fatigue and cracking, superior low-temperature performance, and increased resistance to aging and oxidation [18–20].

According to Table 1 [9], even small amounts of elastomer can significantly reduce asphalt penetration while raising the softening point of the binder. For instance, the addition of 5% SBS by weight can increase the softening point to as high as 95 °C [21]. Moreover, elastomer-modified binders demonstrate elastic recovery exceeding 50% at 5 °C [3,21]. SBS elastomers are also employed to enhance elastic recovery and rutting resistance in mixtures containing waste motor oils, which help reduce binder viscosity and lower mixing and compaction temperatures [22].

Table 1. Summary of 150/220 grade asphalt characteristics through elastomer modification [9].

Asphalt Binder	160/220 Grade Asphalt (Control)	SBS (5% by Weight)	SEBS (3% by Weight)	SBR (5% by Weight)	Polybutadiene Rubber (1.5% by Weight)
Penetration @ 25 °C (dmm)	160–220	70–110	60–100	100–130	106
Softening point (°C)	35–43	75–95	65–85	56	48
Elastic recovery, @ 5 °C (%)	N/d	>50	>50	>70	>80
Fraass breaking point (°C)	−15	−20	−18	−15	−30

Plastomers are thermoplastic polymers that behave like plastics and are primarily used to enhance the stiffness, rigidity, and rutting resistance of asphalt binders. However, their incorporation often reduces binder flexibility at low temperatures. Common plastomers used in asphalt modification include polyethylene (PE), polypropylene (PP), ethylene-vinyl acetate (EVA), ethylene/methacrylic acid copolymer (EMA), and ethylene-butyl acrylate

copolymer (EBA) [9,10]. Among these, EVA is one of the most widely applied plastomers, known for improving the rigidity, stiffness, and rutting resistance of bitumen binders. Nonetheless, EVA modification may also decrease the flexibility of bitumen under low-temperature conditions. According to Table 2, the performance of plastomer-modified asphalt varies depending on the type and dosage of plastomer used. For instance, asphalt modified with a small amount of EVA undergoes significant crystallization, yielding properties comparable to low-density polyethylene (LDPE). At moderate concentrations, EVA enhances binder compatibility and storage stability [23]. However, when the EVA content exceeds 4 wt%, the degree of crystallization decreases, which may lower resistance to low-temperature cracking [23–25]. Moreover, excessively high EVA dosages can result in poor compatibility with bitumen, thereby diminishing the overall performance benefits [25]. Although plastomers are generally cost-effective, they significantly improve rutting resistance and high-temperature performance. Furthermore, certain plastomers (e.g., EVA) provide better storage stability due to their polar functional groups, which enhance interaction with the bitumen matrix [17,25,26].

Table 2. Summary of the effect of plastic on asphalt and asphalt mixtures [9].

Polymers	70/100 Grade Asphalt (Control)	EVA 18/150 (5% by Weight)	EVA 30/45 (5% by Weight)	LDPE (4% by Weight)
Penetration at 25 °C (dmm)	70–100	38–48	55	47
softening point (°C)	43–51	58–68	57	53
Elastic Recovery, @ 5 °C (%)	20	50	50	82
Frass breaking point (°C)	−10	−18	−18	−3

Furthermore, combining polymer modification with sustainable materials (e.g., graphene additives, recycled plastics, and rejuvenators) offers a dual benefit: improved pavement performance [27] and reduced environmental impact [28–30]. When incorporated through either dry or wet processes, these modifiers enhance binder stiffness, extend fatigue life, and increase recyclability.

Table 3 compares the characteristics of elastomers and plastomers [10,26,31–34].

Figure 2 shows the global percentage of polymer types used in asphalt mixtures, along with the corresponding market share of rejuvenators [12,35,36].

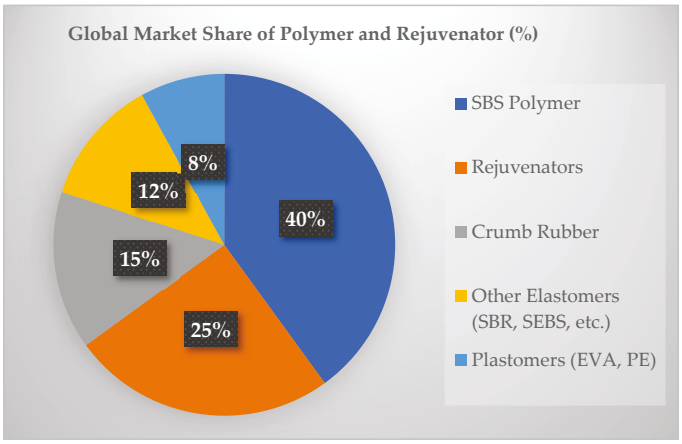

Figure 2. Global market share of polymer and rejuvenator.

Table 3. Characteristics of Elastomers and Plastomers.

Characteristics	Elastomers	Plastomers
Nature	Thermoplastic elastomers behave like rubber	Thermoplastics (behave like plastic)
Main Types Used	SBS, SBR, SEBS, SIS	PE, EVA, PP, EBA
Cost	Higher cost, but effective in small doses	Lower-cost, recycled plastics are widely available
Compatibility with Asphalt	Excellent compatibility forms a network in the binder	Moderate to poor requires compatibilizers
Elastic Recovery	Excellent elastic recovery	Limited elastic behavior
Rutting Resistance	Very high especially for SBS mixtures	High at higher temperatures especially with EVA
Low-Temperature Performance	Provides excellent flexibility and crack resistance	Poor brittle at low temps
Sustainability	Some options use reclaimed rubber (SBR)	PE, PP sourced from waste
Challenges	Oxidation of butadiene (SBR)	Crystallization, storage stability, and low elasticity

Modifying bitumen with plastomers and elastomers plays a crucial role in enhancing the performance and durability of asphalt mixtures [37]. PMA can better withstand harsh environmental conditions [23] and heavy traffic loads by improving mechanical properties, making it a highly effective solution [19,38].

Similarly, the incorporation of recycled materials into asphalt mixtures improves sustainability and reduces the environmental impact of road construction [39]. Recent advancements include the use of bio-polymers such as poly β-hydroxybutyrate-co-β-hydroxy valerate (PHBV), which serve as "green" alternatives to petroleum-based modifiers [40]. Furthermore, the assessment of microplastic (MP) release from recycled polymer-modified asphalt has become increasingly important for evaluating potential environmental impacts [41].

3. Methodology

3.1. Design

This review adopts a systematic literature review (SLR) approach to collect, analyze, and synthesize data [42] on the performance of PMAs and recent developments in asphalt mix design. The primary focus is on comparing the Marshall and Superpave mix design methods while examining the role of SBS and SBR in improving asphalt performance. Additionally, the review emphasizes sustainability by exploring the integration of recycled plastics into asphalt mixtures. Overall, the study seeks to summarize and evaluate current knowledge, highlighting the transition from Marshall to Superpave mix design and assessing the influence of different polymers on asphalt mixture performance.

The methodology involves identifying research gaps and emerging trends, as well as comparing outcomes across various PMAs. The review critically evaluates previous scientific studies to determine their relevance for asphalt design, with a particular focus on the effects of polymer compounds on fatigue and rutting resistance. Following the PRISMA (Preferred Reporting Items for Systematic Reviews and Meta-Analyses) guidelines, only scientifically rigorous and thematically relevant studies were included [43]. This structured approach enhances validity, reduces potential biases, and strengthens the overall quality of the findings. It enables a detailed comparison of methods, practices, and results the impact of PMA's on pavement durability [44].

The review process was guided by predefined goals and research questions, aligned with PRISMA criteria. Initially, keywords were refined to capture the most relevant scientific papers. Subsequently, filters were applied to narrow the scope of literature. After careful screening and selection, the publications were analyzed, categorized, and discussed systematically to ensure comprehensive coverage of the topic.

3.2. Study Question

Traditionally, asphalt mixtures were designed using the conventional Marshall design method, which was since been largely replaced by the performance-based Superpave mix design approach. Unlike the Marshall method, Superpave better replicates actual field conditions, thereby addressing common pavement failures. In addition, various polymers have been incorporated into asphalt binders to further improve performance. Polymer modification has been shown to significantly enhance rutting resistance, fatigue resistance, and moisture susceptibility.

This study focuses on comparing the Marshall and Superpave approaches in the scientific literature. Guided by the development of a suitable research question (Table 4), a systematic literature review was conducted to ensure a comprehensive and structured evaluation of existing studies.

Table 4. Study questions.

Question 1	How PMB improves the performance of the mixture.
Question 2	Have the recent changes in approach to mix design led to any substantial differences in results between Marshall and Superpave using PMA?

This review ensured a comprehensive and systematic collection of relevant information by searching major scientific databases, including Web of Science (WoS), Scopus, and ScienceDirect. These platforms provided access to high-quality publications related to PMA mixtures. Research articles were retrieved using optimized search strings (Table 5), with several combinations of search phrases applied in each database to align with the questions in Table 4. Keywords such as polymer-modified asphalt, asphalt mixtures, Marshall mix, and Superpave mix were specifically employed to capture relevant literature. Using this approach, a total of 1115 publications were retrieved, including articles, review papers, and conference proceedings.

Table 5. Repository and Search String.

ScienceDirect	Scopus	Web of Science
asphalt mixtures OR Polymer modified asphalt AND Rejuvenators OR recycled aggregate OR Marshall OR Superpave	TITLE-ABS-KEY (asphalt mixtures OR Polymer modified asphalt AND Rejuvenators OR recycled aggregate OR Marshall OR Superpave) AND PUBYEAR > 2015 AND PUBYEAR < 2026 AND (LIMIT-TO (DOCTYPE, "ar") OR LIMIT-TO (DOCTYPE, "re")) AND (LIMIT-TO (LANGUAGE, "English"))	"(TS = (("asphaltic mixture" OR asphalt OR bitumen OR "asphalt concrete" OR pavement) AND (polymer OR "polymeric compound" OR polyethylene OR polypropylene OR "polymer modifier" OR "polymer additive" OR "plastic waste") AND ("reclaimed aggregate" OR "recycled aggregate" OR RAP OR "reclaimed asphalt pavement" OR "construction and demolition waste" OR C&DW)) AND DT = (Article OR Review))"
580	234	301
Total		1115

3.3. Data Filtering

Several filters were applied during the research process to ensure the quality, consistency, and relevance of the selected studies. A structured methodology was followed for data extraction, organization, and analysis [44]. After carefully screening, studies were documented, justified, and extracted in alignment with the research objectives and questions. Key characteristics considered included PMB, RAP content, design methods, and mechanical properties of asphalt mixtures. A consensus process was used to validate the collected data, allowing for comparisons findings across various studies to identify patterns, differences, and comparisons across studies to identify patters, similarities, and differences. Only studies meeting the eligibility criteria were included, and all information was systematically organized (Figure 3). The publication trend shows that 2016 recorded the fewest relevant publications, with only 23 across all three databases. In subsequent years, the number of publications steadily increased, peaking in 2024 with 281 publications. Notably, since 2021 there has been a marked surge in outputs from ScienceDirect, which accounted for the highest number in 2024, with 180 publications directly related to this study.

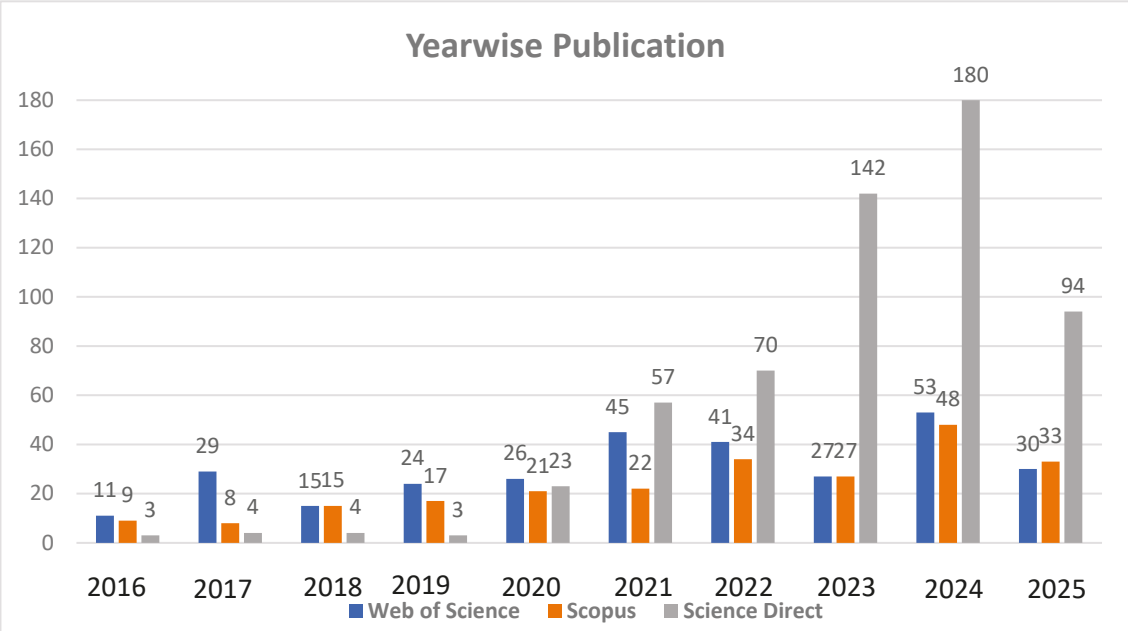

Figure 3. Year-wise publication in different databases.

The VOS Viewer tool (version 1.6.20) identified four keyword clusters in the selected studies:

1 The green cluster focuses on the performance of asphalt mixtures, particularly the behavior of reclaimed asphalt under various conditions (e.g., moisture, stress, temperature, and aging). It addresses critical issues such as rutting, fatigue, cracking, and durability.
2 The red cluster concentrates on the mechanical properties of asphalt mixtures, especially when recycled materials are incorporated. Key aspects include durability, toughness, strength, and microstructure, often examined within a broader sustainability framework.
3 The blue cluster examines the rheological and material properties of asphalt binders and mixtures, especially when modified with polymers, rejuvenators, additives, and recycled materials.

4 The yellow cluster investigates rejuvenators and binders, focusing on the use of soft bitumen and rejuvenating agents to restore aged asphalt binders in reclaimed mixtures. This cluster emphasizes improving flexibility and ensuring compatibility with high percentages of RAP.

Figure 4 presents the PRISMA diagram illustrating the systematic review search and filtering process. The screening involved several steps, including the removal of duplicate records, exclusion of closed-access articles, elimination of studies related to railway ballast or track layering, and filtering based on titles and abstracts. From the initial 1115 publications identified, 177 met the eligibility criteria and were included in this review. Among these, 15 significant studies are summarized in Table 6.

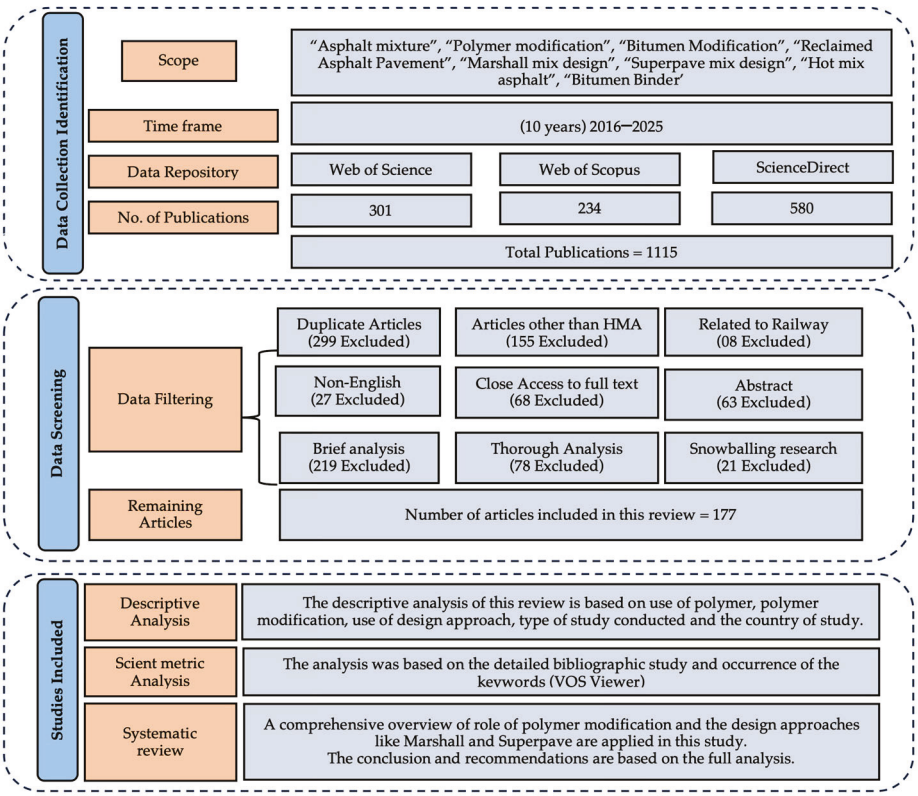

Figure 4. PRISMA study flow chart.

Table 6. Significant studies compliant with the goals of the review.

Refs.	Materials	Tests and Methods	Key Takeaways	Gaps or Limitations
[9]	Plastomers Elastomers Rubber	Dynamic Shear Rheometer Viscosity Elastic recovery Multiple Stress Creep and Recovery PG Grading Creep	Enhanced rutting resistance, improved fatigue resistance, increased high temperature stiffness, and reduced cracking. Plastomers improve high temperature stiffness but may be brittle Elastomers enhances resistance to rutting and fatigue Rubber improves resistance to fatigue but has dispersion issues.	Lack of long-term performance data and issues with rubber dispersion.
[11]	SBS, SBR, EVA, Rubber	Rheological Analysis Spectroscopy Microscopy XRD	SBS improves rutting and aging resistance, SBR enhances elasticity, and wax enhances workability in the mixture.	Limited focus with SBS on high temperature stability.

Table 6. *Cont.*

Refs.	Materials	Tests and Methods	Key Takeaways	Gaps or Limitations
[45]	Recycled plastics (dry/wet process), SBS, EVA, PE, PP, PET	wheel tracker tests stiffness rutting fatigue	Enhanced stiffness, resistance fatigue, rutting, superior moisture recycled plastic modified asphalts. Recycled plastic enhances rutting and fatigue resistance.	The need for further research on the performance of Superpave with high recycled content.
[5]	SBS, SBR	Dynamic modulus and fatigue resistance	Improved fatigue resistance and moisture susceptibility, better rutting resistance than Marshall. SBS and SBR improve fatigue and rutting resistance.	Lack of long-term field validation and economic feasibility.
[3]	SBS, SBR	Volumetrics Mechanical characteristics of Marshall and Superpave	Improved rutting and fatigue resistance especially in high-temperature fluctuations. Superpave outperforms Marshall under heavy traffic and extreme temperatures.	Limited data on Superpave's applicability in low-income regions.
[46]	SBS, RAP Virgin Asphalt	Gyratory Compaction Dynamic modulus test Cyclic direct tension test FlexPave™ (version 1.1) software	Enhanced rutting resistance with high RAP content but may reduce flexibility.	Performance effect of high RAP content on low temperature remains underexplored.
[47]	SBR, SBS and Crumb Rubber	Fatigue test and wheel tracking	Enhanced fatigue and aging resistance particularly at high temperatures. SBS and SBR performs enhanced high temperature fatigue resistance while crumb rubber provides better ductility.	Limited studies on long term field performance on crumb rubber modified asphalts.
[48]	Recycled concrete aggregate	Marshall compaction, creep test, tensile strength ratios	Lower deformation resistance with fine graded mixtures, improved rutting resistance in coarse mixtures. Mixtures gradation has bigger impact on rutting resistance than RCA content.	Lack of long-term performance with recycled concrete aggregate (RCA) in asphalt mixtures.
[49]	SBS, PE	tensile strength ratios uniaxial dynamic modulus testing	Enhanced stiffness and moisture susceptibility resistance. SBS enhance flexibility and PE improves high temperature stability.	Need for more studies on EVA modified asphalt in low-temperature areas.
[50]	PE, EVA	Tensile strength dynamic modulus	Improved rutting and cracking resistance, particularly in heavy-traffic and high-temperature areas. PE and EVA enhance high temperature performance; EVA may cause brittleness at low temperatures.	Need for more studies on EVA long term field performance.
[30]	Graphene, recycled plastic	Lab tests, Falling Weight Deflectometer, fatigue and rutting test.	Improved stiffness, fatigue resistance, and rutting performance. Graphene enhances stiffness and fatigue resistance, while recycled plastics reduce carbon footprint.	Need for long-term filed performance data for graphene modified asphalt.
[28]	Recycled plastic	Rheological tests, stiffness and penetration	Multicycle recyclability without loss of performance, stable binder properties, recycled plastics shows high recyclability with stable binder properties across multiple cycles and hence promotes sustainability.	Limited research on environmental impact assessment (EIA), and performance in extreme climates.
[7]	Recycled plastic, EVA	Fatigue test	Recycled plastic offers excellent sustainability and mechanical performance across multiple cycles.	Need for more studies on impact of recycled materials aging.
[51]	RAP, virgin asphalt	Gyratory compaction, fracture toughness test	RAP improves fracture resistance but may decrease shear resistance	Further investigation on RAP's impact on cracking and shear resistance needed

4. Discussion

A comprehensive systematic review of scientific studies was conducted to evaluate, identify, and select research specifically addressing polymer modification of bitumen and asphalt, comparisons between Marshall and Superpave mixtures, and the performance of PMAs. This review also examined the effects of elastomers and plastomers on the mechanical properties of asphalt mixtures within the framework of various design methods. To ensure quality and relevance, only studies meeting strict selection criteria were included. The final set of studies covers a broad range of research objectives, methodologies, and approaches. Many of them directly compare the Marshall and Superpave mix design methods [3–5], highlighting both approaches as efficient and suitable under challenging conditions. Additionally, numerous studies investigate the role of polymers and rejuvenators in asphalt mixtures to mitigate pavement failures [9,10,45,52,53]. Findings on Marshall versus Superpave mix designs are consistent with those from similar research [3–5,51,54,55]. Other studies emphasize polymer modification and the incorporation of rejuvenators during asphalt mixing, showing how these measures can reduce road distress. Comparisons between Marshall and Superpave mixtures reveal that Superpave tends to outperform Marshall under repeated loading.

In this section, a detailed analysis of selected elastomers (e.g., SBS and SBR), plastomers (e.g., PP and PE), and rejuvenators is proposed. Their performance is compared within Marshall and Superpave mix design framework. The discussion also explores how polymer modification influences the mechanical behavior of asphalt mixtures and evaluates its effectiveness in high-traffic and high-temperature conditions.

4.1. Elastomer Modified Asphalt in Comparison of Marshall Versus Superpave Method

4.1.1. Styrene Butadiene Styrene (SBS)

SBS is a thermoplastic elastomer widely used to enhance asphalt performance. Incorporation of SBS improves the bitumen elasticity, fatigue resistance, and resistance to temperature susceptibility [56–58]. Its higher stiffness and elasticity also reduce permanent deformation [59]. The dynamic shear resistance (DSR) tests demonstrate that SBS-modified bitumen exhibits an increased complex modulus (G*) and a reduced phase angle (δ), resulting in improved rutting resistance [33]. Due to its elastic nature, SBS improves fatigue resistance under repeated cyclic loading [6,59,60]. Moreover, SBS-modified binders show slower oxidative aging, confirmed by laboratory tests such as DSR and FTIR aging indices [6,61].

In Marshall stability design, the inclusion of SBS increases stability, thereby improving load-bearing capacity and rutting resistance. Flow values remain within the optimum range, demonstrating a balance between flexibility and stiffness [6]. Additionally, SBS-modified mixtures exhibit superior resistance to stripping and moisture due to stronger adhesion between aggregate and binder, as indicated by surface free energy and pull-off tests [62]. However, the empirical Marshall method cannot fully capture the improvements in fatigue and rutting resistance provided by SBS; these properties are better evaluated using the Superpave method [63].

Figure 5 shows the performance of SBS as an asphalt modifier under both methods [6,9,11,33,37,45,52,53,60–62,64–68]. Each score was derived by interpreting the test capabilities and performance outcomes of both methods, according to a qualitative scale from 0 to 5, where 0 means very poor, 1 poor, 2 fair, 3 good, 4 very good, and 5 excellent.

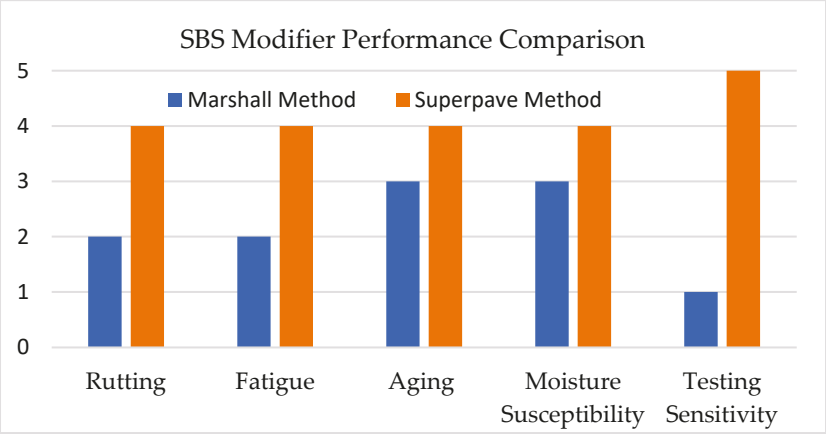

Figure 5. SBS Polymer Performance Comparison.

4.1.2. Styrene Butadiene Resin (SBR)

SBR is an important asphalt modifier that improves key performance parameters in both mix design methods, though its benefits are more accurately assessed under the Superpave framework [69]. In Superpave testing, SBR enhances resistance to rutting, particularly in mixtures containing RAP. It also improves fatigue resistance through greater elastic recovery and increased durability under repeated loading [37,53,70,71]. Furthermore, SBR enhances moisture resistance, as demonstrated by higher tensile strength ratio (TSR) values and improved indirect tensile strength (ITS) [9,70]. However, SBR-modified binders are more susceptible to oxidative aging. Superpave aging protocols, such as Rolling thin film oven test and Pressure Aging Vessel, provide specific insights into this behavior [9,26,72]. While the Marshall method also reflects improvements in stability and moisture resistance, its empirical nature does not capture the mechanistic advantages of SBR [73].

Figure 6 shows the performance of SBR as an asphalt modifier in both methods [9–11,70,71,73–78]. The representation criterium complies with that in Figure 5.

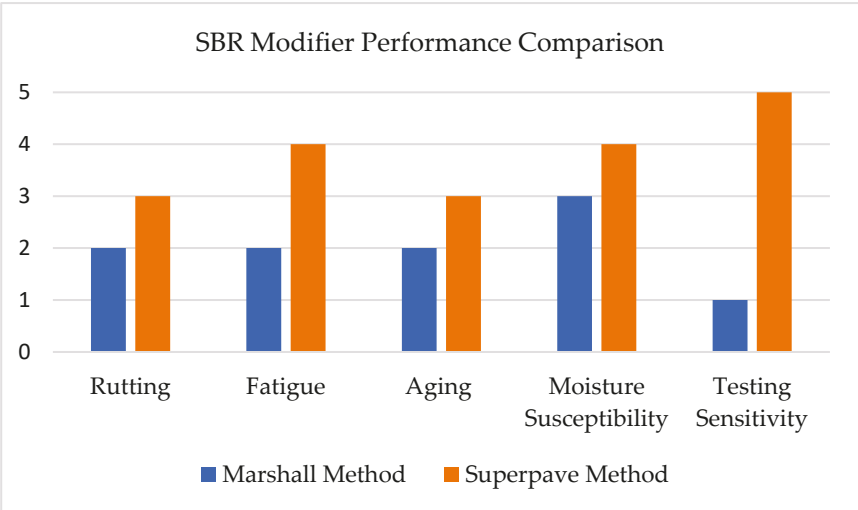

Figure 6. SBR Polymer Performance Comparison.

4.2. Plastomers Modified Asphalt in Comparison of Marshall Versus Superpave Method

4.2.1. Polyethylene (PE)

Polyethylene (PE), a plastomer often used in recycled form, is a widely applied modifier due to its ability to improve high-temperature performance, rutting resistance, and stiffness. Positive effects of PE-modified binders have been documented in both meth-

ods [79–81]. According to Superpave protocols, PE increases PG of binders, particularly in hot climates, by significantly reducing non-recoverable creep compliance and enhancing the asphalt stiffness [82–84]. In the Marshall mix design, PE increases Marshall stability, reduces flow values, and raises the softening point. However, excessive PE content can lead to brittleness and reduced ductility [85,86]. Laboratory studies show that adding 5–7% PE can increase rutting resistance by up to 33% and resilient modulus by 55% compared to virgin bitumen [85].

Challenges with PE modification arise from its nonpopular nature and crystalline structure, which lead to compatibility issues, storage instability, and phase separation. To address these limitations, strategies such as co-blending PE with elastomers (e.g., SBS), chemical pretreatment, or the addition of nanoclay and pyrolytic wax have been explored to improve dispersion and reduce brittleness [80,87].

Overall, PE enhances high-temperature and deformation performance in both design methods. However, its limitations demand supplementary treatments or hybrid modification strategies.

4.2.2. Polypropylene (PP)

Polypropylene, a hydrocarbon thermoplastic polymer, is also employed as an asphalt modifier to improve mixture performance. Recently, the use of post-consumer PP has been studied as a sustainable approach [88,89]. PP enhances high-temperature stability, rutting resistance, and aging resistance, especially in hot regions and under heavy traffic [75,89–91].

In Superpave mix design, PP-modified binders exhibit superior rheological performance, with increased G* and reduced δ, leading to better rutting resistance [92]. The results from DSR and Multiple Stress Creep and Recovery tests confirm that PP fibers significantly reduce non-recoverable creep compliance and improve percent recovery, indicating better elastic recovery and deformation resistance. PP also improves oxidative aging resistance and moisture tolerance [9,89,93].

Within the Marshall framework, PP increases stability, stiffness modulus, and TSR. Incorporation of 2–6% PP raises optimum bitumen content, reduces moisture susceptibility, and increases softening point and stiffness while reducing penetration values. However, higher PP contents can reduce ductility, increase viscosity, and cause phase separation, thereby reducing processability [9,85,93–95]. Pretreatment techniques, such as pyrolysis to produce polypropylene wax (PPW), have been proposed to improve workability, minimize segregation, and enhance bonding between binder and aggregates [96]. The inclusion of PPW in both methods enhances rutting resistance and facilitates the use of warm mix asphalt technologies, reducing energy consumption during production [80,89,93].

4.3. Rejuvenators

Rejuvenators play a critical role in sustainable asphalt pavement practices by restoring the properties of RAP. Their primary function is to reverse binder oxidation, thereby improving workability, enhancing cracking resistance, and reducing stiffness [28,97,98].

In Superpave mix design, rejuvenators restore binder PG properties, ensuring compliance with high-temperature rutting and low-temperature cracking requirements. Vijayan et al. [7] demonstrated that a plant-based rejuvenator, combined with RAP and plastic-modified asphalt via the dry process, maintained satisfactory mechanical performance even after two recycling times. Improvements were observed in rutting resistance, moisture sensitivity, and fatigue properties [7,99–101]. In Marshall mix design, rejuvenators enhance stability and flow values by softening aged binders [99]. Full-scale mixtures containing up to 100% RAP, when adequately treated with rejuvenators, achieved acceptable stability and moisture resistance. Results based on traditional Marshall criteria—such as air voids

and voids in mineral aggregate (VMA)—support their suitability [99,102,103]. According to [28], the synergistic effect of rejuvenators with the recycled polymers gave satisfactory properties even after multiple recycling cycles. Figure 7 summarizes the performance of rejuvenators in both mix design methods.

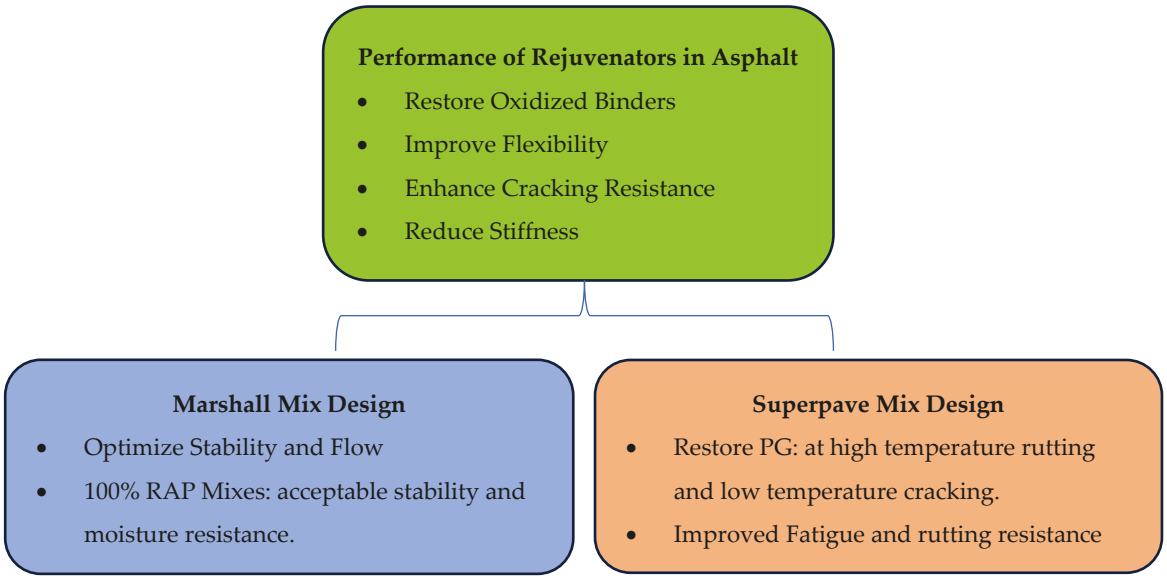

Figure 7. Performance of Rejuvenators.

5. Conclusions

This review compared two methods of asphalt design (i.e., Marshall and Superpave) incorporating polymer modification and rejuvenators. The findings confirm that the Marshall method is an empirical widely adopted approach that is not performance-based and cannot predict long-term durability under high traffic loads and harsh climatic conditions. In contrast, the Superpave method provides a mechanistic–empirical design that enhances viscoelastic properties and resistance to moisture damage under varying traffic and climate conditions. The incorporation of polymers such as SBS, SBR, PP, and PE improves elasticity, stiffness, resistance to rutting, fatigue, and aging, while PMB offers an affordable option to enhance road performance. The addition of rejuvenators allows recycling RAP and plastic waste, supporting circular economy practices, restoring the rheological properties of aged binders, and contributing to sustainable development.

This review encourages further investigation into cost-effective solutions for local polymer modification, durability monitoring, and bridging the gap between sustainable asphalt practices and economy feasibility. It also highlights key future research directions, emphasizing the need to shift toward mechanistic–empirical design approaches. Future studies should also prioritize the selection of polymers based on local conditions, with a focus on economical modifiers (e.g., recycled plastics), and evaluate their performance through Marshall and Superpave methods. Additionally, long-term monitoring is crucial to assess the durability and efficiency of PMA, with particular emphasis on resistance to viscoelastic property degradation, moisture susceptibility, and overall performance in real-world conditions.

Author Contributions: Conceptualization, G.H.J. and G.L.; methodology, G.H.J.; validation, G.L. and L.M.; data curation, G.H.J.; writing—original draft preparation, G.H.J. and L.M.; writing—review and editing, G.L. and L.M.; visualization, G.H.J.; supervision, G.L. All authors have read and agreed to the published version of the manuscript.

Funding: This research received no external funding.

Institutional Review Board Statement: Not applicable.

Informed Consent Statement: Not applicable.

Data Availability Statement: No new data were created or analyzed in this study. Data sharing is not applicable to this article.

Conflicts of Interest: The authors declare no conflicts of interest.

Abbreviations

The following abbreviations are used in this manuscript:

PMB	Polymer-Modified Bitumen
PMA	Polymer-Modified Asphalt
SBS	Styrene–Butadiene–Styrene
SBR	Styrene–Butadiene Rubber
SEBS	Styrene–Ethylene–Butylene–Styrene
RAP	Reclaimed Asphalt Pavement
RCA	Recycled Concrete Aggregate
DSR	Dynamic Shear Rheometer
PG	Performance Grade
ITS	Indirect Tensile Strength
ITSR	Indirect Tensile Strength Ratio
EVA	Ethylene-Vinyl Acetate
PE	Polyethylene
LDPE	Low-Density Polyethylene
HDPE	High-Density Polyethylene
XRD	X-ray Diffraction
PHBV	β-hydroxybutyrate-co-β-hydroxy valerate
FTIR	Fourier Transform Infrared Spectroscopy

References

1. Malluru, S.; Islam, S.M.I.; Saidi, A.; Baditha, A.K.; Chiu, G.; Mehta, Y. A State-of-the-Practice Review on the Challenges of Asphalt Binder and a Roadmap Towards Sustainable Alternatives—A Call to Action. *Materials* **2025**, *18*, 2312. [CrossRef]
2. Lee, J.-S.; Lee, S.-Y.; Le, T.H.M. Developing Performance-Based Mix Design Framework Using Asphalt Mixture Performance Tester and Mechanistic Models. *Polymers* **2023**, *15*, 1692. [CrossRef]
3. Zumrawi, M.M.E.; Edrees, S.A.S. Comparison of Marshall and Superpave Asphalt Design Methods for Sudan Pavement Mixes. *Int. J. Sci. Tech. Adv.* **2016**, *2*, 29–35.
4. Al Kaaf, K.; Ibeabuchi, V.T. Marshall Asphalt Mix and Superior Performance Asphalt Mix in Oman: A Comparative Study. *Eng. Technol. Appl. Sci. Res.* **2023**, *13*, 12258–12263. [CrossRef]
5. Farooq, G.; Hussain, A.; Yanjun, Q.; Ding, H.; Shamim, A. Performance Evaluation of Marshall and Superpave Asphalt Mix Design Methods: A Volumetrics-Analysis Based Approach. *Aust. J. Civ. Eng.* **2025**, *38*, 1–15. [CrossRef]
6. Meng, Y.; Li, H.; Yang, X.; Li, G.; Li, Y.; Xu, G. Study on the Adhesion Properties of SBS Modified Asphalt-Aggregate with Polyphosphoric Acid and Sugarcane Bagasse Fiber under Salt Erosion. *Constr. Build. Mater.* **2025**, *466*, 140269. [CrossRef]
7. Vijayan, V.; Manthos, E.; Mantalovas, K.; Di Mino, G. Multi-Recyclability of Asphalt Mixtures Modified with Recycled Plastic: Towards a Circular Economy. *Results Eng.* **2024**, *23*, 102523. [CrossRef]
8. Mushtaq, F.; Huang, Z.; Shah, S.A.R.; Zhang, Y.; Gao, Y.; Azab, M.; Hussain, S.; Anwar, M.K. Performance Optimization Approach of Polymer Modified Asphalt Mixtures with PET and PE Wastes: A Safety Study for Utilizing Eco-Friendly Circular Economy-Based SDGs Concepts. *Polymers* **2022**, *14*, 2493. [CrossRef]
9. Yang, Q.; Lin, J.; Wang, X.; Wang, D.; Xie, N.; Shi, X. A Review of Polymer-Modified Asphalt Binder: Modification Mechanisms and Mechanical Properties. *Clean. Mater.* **2024**, *12*, 100255. [CrossRef]
10. Sengoz, B.; Isikyakar, G. Analysis of Styrene-Butadiene-Styrene Polymer Modified Bitumen Using Fluorescent Microscopy and Conventional Test Methods. *J. Hazard. Mater.* **2008**, *150*, 424–432. [CrossRef]
11. Porto, M.; Caputo, P.; Loise, V.; Eskandarsefat, S.; Teltayev, B.; Oliviero Rossi, C. Bitumen and Bitumen Modification: A Review on Latest Advances. *Appl. Sci.* **2019**, *9*, 742. [CrossRef]

12. Freedonia Group. Global Asphalt (Bitumen) Report. 2025. Available online: https://www.freedoniagroup.com/industry-study/global-asphalt-bitumen (accessed on 29 May 2025).
13. Bastidas-Martínez, J.G.; Rondón-Quintana, H.A. Assessment of Asphalt Binder Content, Temperature and Loading Rate in Indirect Tensile Strength and Resilient Modulus Tests of a Hot-Mix Asphalt—Comparison with Marshall Design Method. *Constr. Build. Mater.* **2024**, *426*, 136158. [CrossRef]
14. Pipintakos, G.; Škulteckė, J.; Vaitkus, A.; Šernas, O.; Soenen, H.; Van Den Bergh, W. Optimising Bitumen Modification: How Styrene–Butadiene–Styrene (SBS) Characteristics and Content Affect Bitumen Behaviour. *Road Mater. Pavement Des.* **2025**, *26*, 443–463. [CrossRef]
15. Ruge Cárdenas, J.C.; Lozano, D.A.; Moreno, L.A.; Gomez, F.A.M.; Bastidas, J.G. Asphalts and Modified Dense Bituminous Mixtures with Rubber of Military Boots. *DYNA* **2020**, *87*, 120–128. [CrossRef]
16. Naser, A.M.; Abd El–Wahab, H.; Moustafa El Nady, M.A.E.F.; Mostafa, A.E.A.; Lin, L.; Sakr, A.G. Preparation and Characterisation of Modified Reclaimed Asphalt Using Nanoemulsion Acrylate Terpolymer. *Pigm. Resin Technol.* **2019**, *48*, 363–374. [CrossRef]
17. Alataş, T.; Yilmaz, M. Effects of Different Polymers on Mechanical Properties of Bituminous Binders and Hot Mixtures. *Constr. Build. Mater.* **2013**, *42*, 161–167. [CrossRef]
18. Jasso, M.; Perez Jaimes, J.S.; Tellez Vega, E.F. Mechanism and Development of Thermo-Rheological Properties of Asphalts Modified by Reactive Polymer Systems. *Materials* **2023**, *16*, 6631. [CrossRef]
19. Emtiaz, M.; Imtiyaz, M.N.; Majumder, M.; Idris, I.I.; Mazumder, R.; Rahaman, M.M. A Comprehensive Literature Review on Polymer-Modified Asphalt Binder. *CivilEng* **2023**, *4*, 901–933. [CrossRef]
20. Lin, P.; Huang, W.; Tang, N.; Xiao, F. Performance Characteristics of Terminal Blend Rubberized Asphalt with SBS and Polyphosphoric Acid. *Constr. Build. Mater.* **2017**, *141*, 171–182. [CrossRef]
21. Dong, R.; Gao, A.; Zhu, Y.; Xu, B.; Du, J.; Ping, S. The Development of a New Thermoplastic Elastomer (TPE)-Modified Asphalt. *Buildings* **2023**, *13*, 1451. [CrossRef]
22. Fernandes, S.; Peralta, J.; Oliveira, J.; Williams, R.; Silva, H. Improving Asphalt Mixture Performance by Partially Replacing Bitumen with Waste Motor Oil and Elastomer Modifiers. *Appl. Sci.* **2017**, *7*, 794. [CrossRef]
23. Zhu, J.; Birgisson, B.; Kringos, N. Polymer Modification of Bitumen: Advances and Challenges. *Eur. Polym. J.* **2014**, *54*, 18–38. [CrossRef]
24. Xie, J.; Wu, S.; Lin, J.; Cai, J.; Chen, Z.; Wei, W. Recycling of Basic Oxygen Furnace Slag in Asphalt Mixture: Material Characterization & Moisture Damage Investigation. *Constr. Build. Mater.* **2012**, *36*, 467–474. [CrossRef]
25. Ameri, M.; Mansourian, A.; Sheikhmotevali, A.H. Investigating Effects of Ethylene Vinyl Acetate and Gilsonite Modifiers upon Performance of Base Bitumen Using Superpave Tests Methodology. *Constr. Build. Mater.* **2012**, *36*, 1001–1007. [CrossRef]
26. Zhang, F.; Yu, J. The Research for High-Performance SBR Compound Modified Asphalt. *Constr. Build. Mater.* **2010**, *24*, 410–418. [CrossRef]
27. Moretti, L.; Fabrizi, N.; Fiore, N.; D'Andrea, A. Mechanical Characteristics of Graphene Nanoplatelets-Modified Asphalt Mixes: A Comparison with Polymer- and Not-Modified Asphalt Mixes. *Materials* **2021**, *14*, 2434. [CrossRef]
28. Di Mino, G.; Vijayan, V.; Eskandarsefat, S.; Venturini, L.; Mantalovas, K. Investigating the Multi-Recyclability of Recycled Plastic-Modified Asphalt Mixtures. *Infrastructures* **2023**, *8*, 84. [CrossRef]
29. D'angelo, S.; Ferrotti, G.; Cardone, F.; Canestrari, F. Asphalt Binder Modification with Plastomeric Compounds Containing Recycled Plastics and Graphene. *Materials* **2022**, *15*, 516. [CrossRef]
30. Bruno, S.; Carpani, C.; Loprencipe, G.; Venturini, L.; Vita, L. Modified Asphalt with Graphene-Enhanced Polymeric Compound: A Case Study. *Infrastructures* **2024**, *9*, 39. [CrossRef]
31. Abdalfattah, I.A.; Mogawer, W.S.; Stuart, K. Recycled Polyethylene (RPE) Modified Asphalt Mixtures: Performance Predictions Using Pavement Mechanistic-Empirical Design and Evaluation of Return on Investment. *Constr. Build. Mater.* **2022**, *356*, 129164. [CrossRef]
32. Polacco, G.; Berlincioni, S.; Biondi, D.; Stastna, J.; Zanzotto, L. Asphalt Modification with Different Polyethylene-Based Polymers. *Eur. Polym. J.* **2005**, *41*, 2831–2844. [CrossRef]
33. Eldouma, I.B.; Xiaoming, H. Evaluation of the Additives' Behaviour to Determine the Best Modifier for Improving Asphalt Performance at High Temperature. *Adv. Civ. Eng.* **2021**, *2021*, 8879415. [CrossRef]
34. Punith, V.S.; Veeraragavan, A. Behavior of Asphalt Concrete Mixtures with Reclaimed Polyethylene as Additive. *J. Mater. Civ. Eng.* **2007**, *19*, 500–507. [CrossRef]
35. Polymer Modified Bitumen Market Size, Share, Growth Analysis, By Product (Elastomeric Polymers, Plastomeric Polymers), By Grade (PMB 40, PMB 70), By Application (Road Construction, Roofing Systems), By Region-Industry Forecast 2024–2031. Available online: https://www.giiresearch.com/report/sky1596895-polymer-modified-bitumen-market-size-share-growth.html?utm_source=chatgpt.com (accessed on 28 May 2025).
36. Asphalt Additives Market Size, Share | Industry Report, 2019–2025. Available online: https://www.grandviewresearch.com/industry-analysis/asphalt-additives-market (accessed on 26 August 2025).

37. Spadoni, S.; Paolo Ingrassia, L.; Mocelin, D.; Richard Kim, Y.; Canestrari, F. Comparison of Asphalt Mixtures Containing Polymeric Compounds and Polymer-Modified Bitumen Based on the VECD Theory. *Constr. Build. Mater.* **2022**, *349*, 128725. [CrossRef]
38. Jexembayeva, A.; Konkanov, M.; Aruova, L.; Kirgizbayev, A.; Zhaksylykova, L. Performance Optimization Approach of Polymer-Modified Asphalt Mixtures with PET and PE Waste. *Polymers* **2024**, *16*, 3308. [CrossRef]
39. Xu, L.; Du, Y.; Loprencipe, G.; Moretti, L. Rheological and Fatigue Characteristics of Asphalt Mastics and Mixtures Containing Municipal Solid Waste Incineration (MSWI) Residues. *Sustainability* **2023**, *15*, 8356. [CrossRef]
40. Tabaković, A.; Lemmens, J.; Tamis, J.; van Vliet, D.; Nahar, S.; Suitela, W.; van Loosdrecht, M.; Leegwater, G. Bio-Polymer Modified Bitumen. *Constr. Build. Mater.* **2023**, *406*, 133321. [CrossRef]
41. Duan, Y.; Wu, K.; Serrat, C.; Arteaga-Larios, F.; Brown, H.; DuBois, C.J.; Buttlar, W.G.; Deng, B. Assessment of Microplastics Production from Waste Plastics-Modified Asphalt Pavement. *Resour. Conserv. Recycl.* **2024**, *202*, 107329. [CrossRef]
42. Phillips, M.; Reed, J.B.; Zwicky, D.; Van Epps, A.S.; Buhler, A.G.; Rowley, E.M.; Zhang, Q.; Cox, J.M.; Zakharov, W. Systematic Reviews in the Engineering Literature: A Scoping Review. *IEEE Access* **2024**, *12*, 62648–62663. [CrossRef]
43. Page, M.J.; McKenzie, J.E.; Bossuyt, P.M.; Boutron, I.; Hoffmann, T.C.; Mulrow, C.D.; Shamseer, L.; Tetzlaff, J.M.; Akl, E.A.; Brennan, S.E.; et al. Declaración PRISMA 2020: Una guía actualizada para la publicación de revisiones sistemáticas. *Rev. Española De Cardiol.* **2021**, *74*, 790–799. [CrossRef]
44. Moher, D.; Liberati, A.; Tetzlaff, J.; Altman, D.G.; Prisma Group. Preferred Reporting Items for Systematic Reviews and Meta-Analyses: The PRISMA Statement. *Ann. Intern. Med.* **2009**, *151*, 264–269. [CrossRef]
45. Viscione, N.; Lo Presti, D.; Veropalumbo, R.; Oreto, C.; Biancardo, S.A.; Russo, F. Performance-Based Characterization of Recycled Polymer Modified Asphalt Mixture. *Constr. Build. Mater.* **2021**, *310*, 125243. [CrossRef]
46. Sabouri, M. Evaluation of Performance-Based Mix Design for Asphalt Mixtures Containing Reclaimed Asphalt Pavement (RAP). *Constr. Build. Mater.* **2020**, *235*, 117545. [CrossRef]
47. Zaumanis, M.; Poulikakos, L.D.; Partl, M.N. Performance-Based Design of Asphalt Mixtures and Review of Key Parameters. *Mater. Des.* **2018**, *141*, 185–201. [CrossRef]
48. Gul, W.A.; Guler, M. Rutting Susceptibility of Asphalt Concrete with Recycled Concrete Aggregate Using Revised Marshall Procedure. *Constr. Build. Mater.* **2014**, *55*, 341–349. [CrossRef]
49. Yu, H.; Zhou, S.; Qian, G.; Zhang, C.; Shi, C.; Yao, D.; Ge, J. Evaluation of the Microscale Structure and Performance of Asphalt Mixtures under Different Design Methods. *Constr. Build. Mater.* **2023**, *400*, 132810. [CrossRef]
50. Kassab, T.G. Comparative Study of Hot Asphalt Mixtures Properties Designed by Marshall and Superpave Methods. *MEJ-Mansoura Eng. J.* **2021**, *46*, 41–51. [CrossRef]
51. Jafari Haghighatpour, P.; Aliha, M.R.M. Effect of Marshal and Gyratory Compaction Methods on Cracking Characteristics of Hot Mix Asphalt Concrete Materials under All Three Basic Modes of Fracture. *Theor. Appl. Fract. Mech.* **2022**, *117*, 103207. [CrossRef]
52. Ceccon Carlesso, G.; Trichês, G.; Staub De Melo, J.V.; Marcon, M.F.; Padilha Thives, L.; Da Luz, L.C. Evaluation of Rheological Behavior, Resistance to Permanent Deformation, and Resistance to Fatigue of Asphalt Mixtures Modified with Nanoclay and SBS Polymer. *Appl. Sci.* **2019**, *9*, 2697. [CrossRef]
53. Daryaee, D.; Ameri, M.; Mansourkhaki, A. Utilizing of Waste Polymer Modified Bitumen in Combination with Rejuvenator in High Reclaimed Asphalt Pavement Mixtures. *Constr. Build. Mater.* **2020**, *235*, 117516. [CrossRef]
54. Asi, I.M. Performance Evaluation of SUPERPAVE and Marshall Asphalt Mix Designs to Suite Jordan Climatic and Traffic Conditions. *Constr. Build. Mater.* **2007**, *21*, 1732–1740. [CrossRef]
55. Jitsangiam, P.; Chindaprasirt, P.; Nikraz, H. An Evaluation of the Suitability of SUPERPAVE and Marshall Asphalt Mix Designs as They Relate to Thailand's Climatic Conditions. *Constr. Build. Mater.* **2013**, *40*, 961–970. [CrossRef]
56. Kaya, F.; Aslan, Ş.; Fahad, M.; Madarász, K.; Rosta, S.; Nagy, R.; Fischer, S. Performance of PMMA and SBS Modified Asphalt Mixtures in Railway Supplementary Layers and Road Pavements. *Period. Polytech. Transp. Eng.* **2025**, *53*, 334–346. [CrossRef]
57. Polacco, G.; Kříž, P.; Filippi, S.; Stastna, J.; Biondi, D.; Zanzotto, L. Rheological Properties of Asphalt/SBS/Clay Blends. *Eur. Polym. J.* **2008**, *44*, 3512–3521. [CrossRef]
58. Sun, X.; Qin, X.; Liu, Z.; Yin, Y. Damaging Effect of Fine Grinding Treatment on the Microstructure of Polyurea Elastomer Modifier Used in Asphalt Binder. *Measurement* **2025**, *242*, 115984. [CrossRef]
59. Babagoli, R.; Ameli, A.; Shahriari, H. Laboratory Evaluation of Rutting Performance of Cold Recycling Asphalt Mixtures Containing SBS Modified Asphalt Emulsion. *Pet. Sci. Technol.* **2016**, *34*, 309–313. [CrossRef]
60. Xu, S.; Fan, Y.; Feng, Z.; Ke, Y.; Zhang, C.; Huang, H. Comparison of Quantitative Determination for SBS Content in SBS Modified Asphalt. *Constr. Build. Mater.* **2021**, *282*, 122733. [CrossRef]
61. Zhang, D.; Zhang, H.; Shi, C. Investigation of Aging Performance of SBS Modified Asphalt with Various Aging Methods. *Constr. Build. Mater.* **2017**, *145*, 445–451. [CrossRef]
62. Gou, J.; Guo, M.; Xie, X.; Du, X. Unravelling the Adhesion Mechanism of Recycled SBS-Modified Asphalt: Integrating Surface Free Energy, Atomic Force Microscopy and Molecular Dynamics. *Constr. Build. Mater.* **2025**, *483*, 141672. [CrossRef]

63. Li, H.; Wang, H.; Lin, J.; Yang, J.; Yao, Y. Study on the Effect of SBS/HVA/CRM Composite-Modified Asphalt on the Performance of Recycled Asphalt Mixtures. *Polymers* **2024**, *16*, 3226. [CrossRef]
64. Eskandarsefat, S.; de Ferrariis, L.; Allen, B.; Roworth, P.; Venturini, L.; Fumagalli, M. Asphalt Mixture Modification via a Recycled-Plastic Modifier: Laboratory Studies and Pavement Analysis. In Proceedings of the 8th Eurasphalt & Eurobitume Congress, Budapest, Hungary, 19–21 June 2024.
65. Russo, F.; Eskandarsefat, S.; Venturini, L.; Viscione, N. A Complete Study on an Asphalt Concrete Modified with Graphene and Recycled Hard-Plastics: A Case Study. *Case Stud. Constr. Mater.* **2022**, *17*, e01437. [CrossRef]
66. Wang, C.; Wang, Y. Physico-Chemo-Rheological Characterization of Neat and Polymer-Modified Asphalt Binders. *Constr. Build. Mater.* **2019**, *199*, 471–482. [CrossRef]
67. Lin, P.; Yan, C.; Huang, W.; Li, Y.; Zhou, L.; Tang, N.; Xiao, F.; Zhang, Y.; Lv, Q. Rheological, Chemical and Aging Characteristics of High Content Polymer Modified Asphalt. *Constr. Build. Mater.* **2019**, *207*, 616–629. [CrossRef]
68. Xu, X.; Sreeram, A.; Leng, Z.; Yu, J.; Li, R.; Peng, C. Challenges and Opportunities in the High-Quality Rejuvenation of Unmodified and SBS Modified Asphalt Mixtures: State of the Art. *J. Clean. Prod.* **2022**, *378*, 134634. [CrossRef]
69. The Research for High-Performance SBR Compound Modified Asphalt—ScienceDirect. Available online: https://www.sciencedirect.com/science/article/pii/S0950061809003407 (accessed on 4 June 2025).
70. Ren, X.; Sha, A.; Jiang, W.; Wu, W.; Jiao, W.; Li, J.; Li, J. Effect of EVA on the Rheological Properties of SBR-Modified Asphalt Binder and Its Behavioral Evolution during the Thermo-Oxidative Aging Process. *Constr. Build. Mater.* **2024**, *454*, 139159. [CrossRef]
71. Liang, P.; Liang, M.; Fan, W.; Zhang, Y.; Qian, C.; Ren, S. Improving Thermo-Rheological Behavior and Compatibility of SBR Modified Asphalt by Addition of Polyphosphoric Acid (PPA). *Constr. Build. Mater.* **2017**, *139*, 183–192. [CrossRef]
72. Cháves-Pabón, S.B.; Rondón-Quintana, H.A.; Bastidas-Martínez, J.G. AGING OF ASPHALT BINDERS AND ASPHALT MIXTURES. SUMMARY PART II: AGING SIMULATION AND AGING REDUCTION TECHNIQUES. *Int. J. Civ. Eng. Technol.* **2019**, *10*, 274–287.
73. Li, Y.; Wu, S.; Dai, Y.; Li, C.; Song, W.; Li, H.; Li, C.; Shu, B. Transitions of Component, Physical, Rheological and Self-Healing Properties of Petroleum Bitumen from the Loose Bituminous Mixture after UV Irradiation. *Fuel* **2020**, *262*, 116507. [CrossRef]
74. Ren, S.; Liang, M.; Fan, W.; Zhang, Y.; Qian, C.; He, Y.; Shi, J. Investigating the Effects of SBR on the Properties of Gilsonite Modified Asphalt. *Constr. Build. Mater.* **2018**, *190*, 1103–1116. [CrossRef]
75. Zhang, Q.; Hou, D.; Li, Z.; Wang, H.; Dong, S. Evaluation of the Thermal Stability and Micro-Modification Mechanism of SBR/PP-Modified Asphalt. *Polymers* **2024**, *16*, 456. [CrossRef]
76. Zhu, C.; Zhang, H.; Xu, G.; Shi, C. Aging Rheological Characteristics of SBR Modified Asphalt with Multi-Dimensional Nanomaterials. *Constr. Build. Mater.* **2017**, *151*, 388–393. [CrossRef]
77. Han, Y.; Tian, J.; Ding, J.; Shu, L.; Ni, F. Evaluating the Storage Stability of SBR-Modified Asphalt Binder Containing Polyphosphoric Acid (PPA). *Case Stud. Constr. Mater.* **2022**, *17*, e01214. [CrossRef]
78. Wang, F.; Ma, R.; Li, Y.; Sun, M.; Wang, Y.; Sun, Y.; Cheng, P. Weathering Aging Resistance in Seasonal Frozen Regions: A Comparative Study of SBS- and SBR-Modified Asphalt Binders through Rheological and Morphological Characterization. *Sci. Rep.* **2025**, *15*, 13625. [CrossRef]
79. Al-Shawabkeh, A.F.; Awwad, M.T.; Al-Rousan, T.M. Using Recycled Plastic Waste to Improve the Performance of Hot-Mix Asphalt. *Proc. Inst. Civ. Eng. Waste Resour. Manag.* **2022**, *176*, 118–128. [CrossRef]
80. Vargas, C.; Hanandeh, A.E. The Utilisation of Polyethylene Waste Pyrolytic Wax as an Additive to Enhance the Performance of Virgin and Polypropylene-Modified Bitumen. *Int. J. Pavement Res. Technol.* **2024**, *17*, 929–951. [CrossRef]
81. Usman, N.; Idrus Bin Mohd Masirin, M.; Abdullahi Ahmad, K.; Ahmed Wurochekke, A. Reinforcement of Asphalt Concrete Mixture Using Recycle Polyethylene Terephthalate Fibre. *Indian J. Sci. Technol.* **2016**, *9*, 107143. [CrossRef]
82. Dalhat, M.A.; Al-Abdul Wahhab, H.I. Performance of Recycled Plastic Waste Modified Asphalt Binder in Saudi Arabia. *Int. J. Pavement Eng.* **2017**, *18*, 349–357. [CrossRef]
83. Mehmood, S.A.; Khan, M.I.; Ahmed, S.; Al-Nawasir, R.; Choudhry, R.M. From Waste to Roads: Improving Pavement Performance and Achieving Sustainability with Recycled Steel Slag and Low-Density Polyethylene. *Buildings* **2025**, *15*, 476. [CrossRef]
84. Olukanni, D.O.; Adegoke, D.A.; Akinmejiwa, A.A.; Bassey, D.E.; Adediran, J.A. EVALUATION OF ASPHALT PRODUCED FROM WASTE TYRE AND POLYETHYLENE TEREPHTHALATE-BASED BITUMEN WITH PARAFFIN WAX AS REJUVENATOR. *J. Solid Waste Technol. Manag.* **2023**, *49*, 270–279. [CrossRef]
85. Ullah, S.; Qabur, A.; Ullah, A.; Aati, K.; Abdelgiom, M.A. Enhancing High-Temperature Performance of Flexible Pavement with Plastic-Modified Asphalt. *Polymers* **2024**, *16*, 2399. [CrossRef]
86. Ullah, R.; Hafeez, I.; Haroon, W.; Haider, S. Evaluating the Effect of Plastomer Modified Asphalt Mixture on High/Low Temperature Performance. *Mehran Univ. Res. J. Eng. Technol.* **2021**, *40*, 680–691. [CrossRef]
87. Masad, E.; Roja, K.L.; Rehman, A.; Abdala, A.A. *A Review of Asphalt Modification Using Plastics: A Focus on Polyethylene*; Texas A&M University at Qatar: Doha, Qatar, 2020. [CrossRef]

88. Souza, R.S.; Visconte, L.L.Y.; Da Silva, A.L.N.; Costa, V.G. Thermal and Rheological Formulation and Evaluation of Synthetic Bitumen from Reprocessed Polypropylene and Oil. *Int. J. Polym. Sci.* **2018**, *2018*, 7940857. [CrossRef]
89. Kathari, P.M. Rheological Properties of Polypropylene Reinforced Asphalt Binder. *Transp. Infrastruct. Geotech.* **2016**, *3*, 109–126. [CrossRef]
90. Kim, Y.-M.; Kim, K. Evaluation of Thermal Aging Susceptibility of Recycled Waste Plastic Aggregates (Low-Density Polyethylene, High-Density Polyethylene, and Polypropylene) in Recycled Asphalt Pavement Mixtures. *Polymers* **2025**, *17*, 731. [CrossRef]
91. Cháves-Pabón, S.B.; Rondón-Quintana, H.A.; Bastidas-Martínez, J.G. AGING OF ASPHALT BINDERS AND ASPHALT MIXTURES. SUMMARY PART I: EFFECT ON PHYSICAL-CHEMICAL PROPERTIES. *Int. J. Civ. Eng. Technol.* **2019**, *10*, 259–273.
92. Gholampour, A.; Hosseini-Poul, S.-A.; MohammadNezhad, S.; Nematzadeh, M.; Ozbakkaloglu, T. Effect of Polypropylene and Polyvinyl Alcohol Fibers on Mechanical Behavior and Durability of Geopolymers Containing Lead Slag: Testing, Optimization, and Life Cycle Assessment. *Constr. Build. Mater.* **2025**, *462*, 139960. [CrossRef]
93. Zhou, G.; Li, C.; Wang, H.; Zeng, W.; Ling, T.; Jiang, L.; Li, R.; Liu, Q.; Cheng, Y.; Zhou, D. Preparation of Wax-Based Warm Mixture Additives from Waste Polypropylene (PP) Plastic and Their Effects on the Properties of Modified Asphalt. *Materials* **2022**, *15*, 4346. [CrossRef]
94. Mohammed, S.F.; Ismael, M.Q. Effect of Polypropylene Fibers on Moisture Susceptibility of Warm Mix Asphalt. *Civ. Eng. J.* **2021**, *7*, 988–997. [CrossRef]
95. Al-Hadidy, A.I. Engineering Behavior of Aged Polypropylene-Modified Asphalt Pavements. *Constr. Build. Mater.* **2018**, *191*, 187–192. [CrossRef]
96. Wu, S.; Montalvo, L. Repurposing Waste Plastics into Cleaner Asphalt Pavement Materials: A Critical Literature Review. *J. Clean. Prod.* **2021**, *280*, 124355. [CrossRef]
97. Abdalla, A.; Alsalihi, M.; Khafagy, M.; Ibrahim, H.; Faheem, A.F. Upcycled Waste for Sustainable Roads: Exploring the Synergistic Effects of off-Spec Fly Ashes and Rejuvenators on Asphalt Binder Aging. *Constr. Build. Mater.* **2025**, *467*, 140377. [CrossRef]
98. Hu, Y.; Omairey, E.; Hughes, D.; Bailey, H.; Watkins, M.; Twitchen, J.; Airey, G.D.; Sreeram, A. Recovering the Properties of Aged Bitumen Using Bio-Rejuvenators Derived from Municipal Wastes. *Constr. Build. Mater.* **2024**, *438*, 137268. [CrossRef]
99. Zaumanis, M.; Mallick, R.B.; Frank, R. 100% Recycled Hot Mix Asphalt: A Review and Analysis. *Resour. Conserv. Recycl.* **2014**, *92*, 230–245. [CrossRef]
100. Cabette, M.; Micaelo, R.; Pais, J. The Use of Bio-Oil from Biodiesel Production for Enhancing the Bitumen Healing. *Constr. Build. Mater.* **2023**, *409*, 134033. [CrossRef]
101. Yan, K.; Lan, H.; Duan, Z.; Liu, W.; You, L.; Wu, S.; Miljković, M. Mechanical Performance of Asphalt Rejuvenated with Various Vegetable Oils. *Constr. Build. Mater.* **2021**, *293*, 123485. [CrossRef]
102. Bilema, M.; Aman, M.Y.; Hassan, N.A.; Memon, Z.A.; Omar, H.A.; Yusoff, N.I.M.; Milad, A. Mechanical Performance of Reclaimed Asphalt Pavement Modified with Waste Frying Oil and Crumb Rubber. *Materials* **2021**, *14*, 2781. [CrossRef]
103. Hashim, T.M.; Nasr, M.S.; Jebur, Y.M.; Kadhim, A.; Alkhafaji, Z.; Baig, M.G.; Adekunle, S.K.; Al-Osta, M.A.; Ahmad, S.; Yaseen, Z.M. Evaluating Rutting Resistance of Rejuvenated Recycled Hot-Mix Asphalt Mixtures Using Different Types of Recycling Agents. *Materials* **2022**, *15*, 8769. [CrossRef]

Disclaimer/Publisher's Note: The statements, opinions and data contained in all publications are solely those of the individual author(s) and contributor(s) and not of MDPI and/or the editor(s). MDPI and/or the editor(s) disclaim responsibility for any injury to people or property resulting from any ideas, methods, instructions or products referred to in the content.

materials

MDPI

Article

Experimental Investigation of Polymer-Modified Bituminous Stone Mastic Asphalt Mixtures Containing Cellulose Acetate Recycled from Cigarette Butts

Hande Varol Morova * and Cengiz Özel

Department of Civil Engineering, Faculty of Technology, Isparta University of Applied Sciences, 32100 Isparta, Türkiye; cengizozel@isparta.edu.tr
* Correspondence: handevarol@isparta.edu.tr

Abstract

Stone Mastic Asphalt (SMA) mixtures exhibit superior performance under traffic loads due to the high content of coarse aggregates; however, the high bitumen content also leads to the problem of bitumen drainage from the mixture. Several studies have been conducted on the use of stabilizing additives such as fibers, polymers, or mineral fillers to reduce binder drainage in SMA mixtures. In this study, however, an innovative and sustainable solution was developed to address the bitumen drainage problem encountered in SMA pavements and to improve the long-term performance of the mixture. In this context, the feasibility of using cellulose acetate (SG) material recycled from cigarette butts as an alternative fiber additive to the traditionally used cellulose fiber (SL) was investigated. This method aims to achieve both environmental benefits in terms of waste management and economic advantages in terms of additive materials. Additionally, the effect of using different SL contents (0.1%, 0.2%, 0.3%, 0.4%, 0.5%) on mixture performance was examined. Within this scope, both pure bitumen (B) and Elvaloy RET + PPA (E)-modified bitumen (1.6%, 1.7%, and 1.8% Elvaloy RET + 0.2% PPA) were used to produce both fiber-reinforced and non-fiber-reinforced SMA mixtures. Traditional and Superpave tests were conducted to determine the rheological and physical properties of the pure and modified binders. All SMA specimens were tested for Marshall stability and flow, Marshall quotient, indirect tensile strength (ITS), tensile strength ratio (TSR), Schellenberg bitumen drainage, sand patch, and Cantabro particle loss. Furthermore, a cost analysis was carried out to evaluate the economic effect of different fiber types and proportions. Among the SMA mixtures, the highest stability and resistance to moisture damage were achieved in the mixtures containing 1.6% Elvaloy RET + 0.2% PPA with 0.3–0.4% SG and 1.7% Elvaloy RET + 0.2% PPA with 0.3–0.4% SL, while the optimum surface texture depth was obtained in the mixtures containing 1.6–1.7% Elvaloy RET + 0.2% PPA with 0.3% SG. In conclusion, the Elvaloy RET + PPA modification enhanced the aging resistance of the bitumen, while the SG fibers used at 0.3–0.4% fiber content in the 1.6–1.7% Elvaloy RET + 0.2% PPA-modified series were identified as a promising mechanical and economic alternative to conventional SL fibers.

Keywords: stone mastic asphalt; cigarette butt; Elvaloy ret; polyphosphoric acid; binder drain-down; moisture damage

1. Introduction

The increasing traffic loads, climate change effects, and global sustainability requirements have led to the development of high-performance and environmentally friendly pavement materials. Among these, Stone Mastic Asphalt (SMA) mixtures have gained widespread acceptance since their introduction in Germany in the 1960s to mitigate rutting problems caused by studded tires [1]. Due to their high coarse aggregate and filler content, SMA mixtures exhibit superior durability and deformation resistance, particularly when modified bitumen is used. However, compared to conventional asphalt mixtures, SMA production requires higher costs due to the greater proportion of asphalt binder used in the mixture, as well as the effects of higher mixing temperatures, compaction difficulties, and the use of cellulose fibers to prevent drainage [2].

To improve the performance of bituminous mixtures, polymer modification is one of the most widely adopted techniques. Polymers enhance the viscoelastic behavior of bitumen, reduce temperature susceptibility, and improve aging and deformation resistance [3,4]. Şengöz and Işıkyakar (2008) reported that Styrene–Butadiene–Styrene (SBS) and Ethylene–Vinyl Acetate (EVA) polymers improved the softening point and Marshall stability of bitumen [5]. Similarly, Kordi and Shafabakhsh (2017) observed that Nano Fe_2O_3 increased the stiffness modulus and rutting resistance, while Arshad et al. (2019) found that nanosilica addition enhanced the elastic modulus [6,7]. Gong et al. (2018) reported that adding 0.5–3% Carbon Nanotube (CNT) decreases penetration, increases the softening point, and enhances high-temperature performance and aging resistance [8].

Recent research has focused on Elvaloy RET (Reactive Elastomeric Terpolymer) and Polyphosphoric Acid (PPA) as promising modifiers for bitumen. Irfan et al. (2017) identified 1% Elvaloy RET as the optimum dosage, providing the best rutting and temperature resistance [9]. Geçkil (2019) found that 0.4–1.2% Elvaloy RET improved elasticity and high-temperature performance [10]. Taciroğlu (2023) reported that 1.6–1.8% Elvaloy RET combined with 4–5% SBS enhanced both high-temperature and aging resistance, while Vachhani and Mishra (2014) found that 2% Elvaloy RET achieved the best stiffness and elasticity [11,12]. Inocente Domingos and Faxina (2015) and Jasso et al. (2015) also confirmed that Elvaloy RET + PPA modification improved the rheological properties and high-temperature deformation resistance of bitumen [13,14].

Numerous studies have been conducted to address the problem of binder drain-down in SMA, and researchers have reached a consensus on the use of polymer-modified bitumen or fibers [15]. Fauzi et al. (2020) reported that 0.2% cellulose fiber minimized abrasion loss, while 0.3% provided the highest modulus [16]. Gallo et al. (2021) found that incorporating jute fiber within the 0.1–0.3% range improved the mixture's durability, and the best stiffness modulus performance was obtained with the mixture containing 0.2% fiber; Shaffie et al. (2021) concluded that 0.3% steel fibers improved stiffness and stability; Ma et al. (2023) observed that a hybrid mixture containing 0.3% basalt and 0.2% cellulose fibers yielded the lowest deformation in the Hamburg wheel-tracking test [17–19]. Similarly, Alonso-Troyano et al. (2025) found that incorporating 0.3% recycled cotton fibers significantly reduced binder drainage compared to mixtures without fibers, while also demonstrating high resistance to moisture damage (indirect tensile strength ratio = 96.3%), making it suitable for temperate and humid climates [20].

In the pursuit of sustainable pavement technologies, the reuse of waste materials in asphalt mixtures has become an important research direction. Zoorob and Suparma (2000) investigated asphalt concrete mixtures incorporating recycled low-density polyethylene (LDPE) as a partial aggregate replacement and reported that a 30% volumetric substitution of LDPE reduced the density by 16% and increased the Marshall stability by 250%, thereby enhancing deformation resistance [21]. Morova (2024) evaluated waste phonolite (PW) as a

filler material in hot mix asphalt and found that it can be effectively used as a sustainable filler for pavements subjected to low traffic loads [22]. Rodríguez et al. (2024) utilized residual cotton fibers obtained from the Peruvian textile industry as an alternative to commercial fibers in SMA mixtures and demonstrated that a 0.20% fiber content provided optimal performance, improving tensile strength and rutting resistance [23]. Among these waste materials, cigarette butts (CBs) represent one of the most problematic urban wastes, with approximately 4.5 trillion discarded annually, causing significant environmental pollution due to their slow degradation and toxic leachate. The environmental impacts of cigarette butts are illustrated in Figure 1 [24]. The filters are mainly composed of cellulose acetate, a semi-synthetic polymer derived from natural cellulose, which can persist for years in soil and water [25].

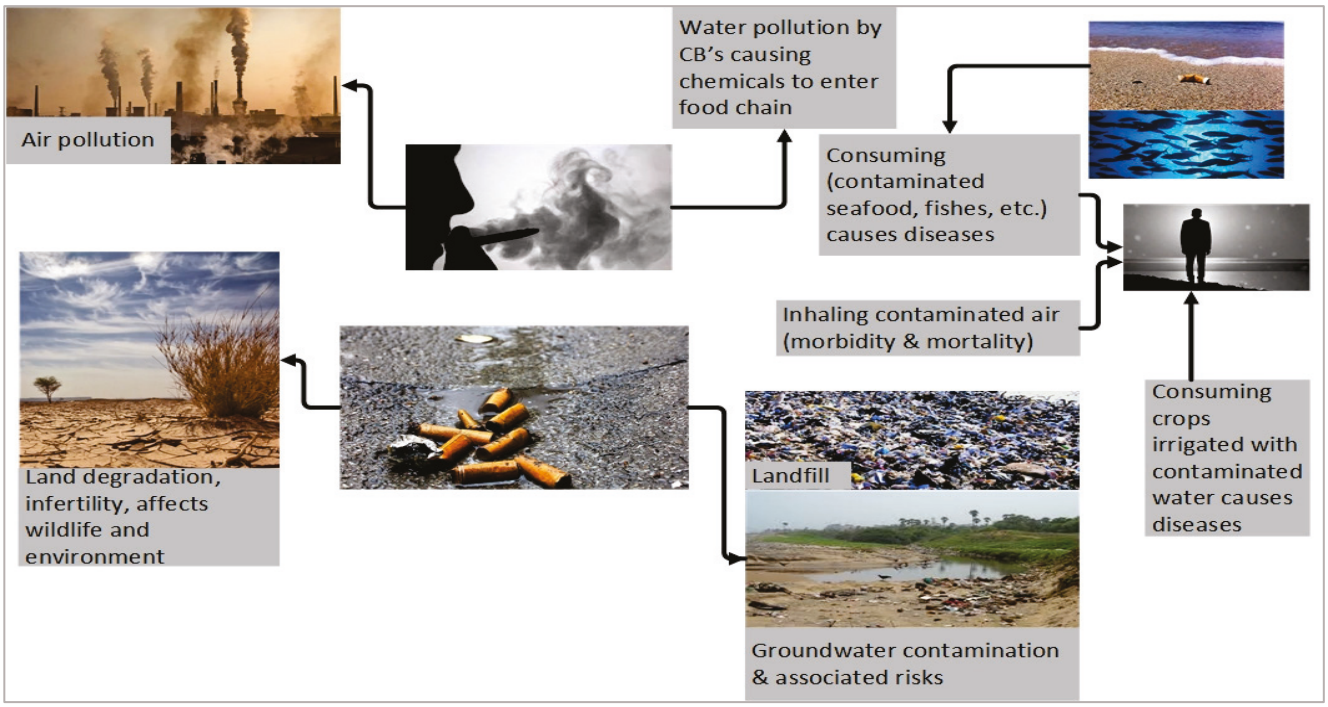

Figure 1. Environmental impacts of cigarette waste [24].

Recent studies have explored the use of cigarette-butt-derived cellulose acetate fibers as a recycled additive in asphalt mixtures. Rahman et al. (2020) and Mohajerani et al. (2022) found that these fibers are compatible with bitumen and improve mixture stability [26,27]. Gallo and Valentin (2024) reported enhanced mechanical performance, while Jin et al. (2019) observed higher stiffness and durability [28,29]. Tataranni and Sangiorgi (2021) also demonstrated the potential use of recycled cigarette butts in hot mix asphalt [30]. Guo et al. (2024) found that 15 mm non-plastic electronic cigarette butts (E-CB) fibers achieved the highest indirect tensile strength and stiffness, Al-Ameri and Ramadhansyah (2022) reported optimum performance at 5% CB addition, and Hu et al. (2025) concluded that 1–4% CB fibers improved rheological properties, though slightly reduced storage stability [31–33].

In this context, the present study proposes an innovative and sustainable approach by using recycled cellulose acetate (SG) fibers obtained from cigarette butts as an alternative to traditional cellulose (SL) fibers in SMA mixtures. The primary objective is to reduce binder drain-down while promoting the recycling of environmentally harmful waste materials. Both pure and Elvaloy RET + PPA-modified bitumen were used, with fiber contents ranging from 0.1% to 0.5% and polymer dosages of 1.6–1.8%. A comprehensive experimental program was conducted, including density, air voids, Marshall stability,

moisture damage, Schellenberg drain-down, sand patch texture, and Cantabro abrasion tests.

2. Materials and Methods

2.1. Aggregate

In this study, basalt aggregate was used as coarse and fine aggregate, while limestone dust was employed as filler. Both the limestone and basalt aggregates used in the study were supplied by the Municipality of Isparta. The physical and mechanical properties of the aggregates were determined in accordance with the relevant ASTM and TS EN standards (Table 1). The aggregate gradation was prepared in accordance with the limits specified by the Turkish Highway Technical Specification (HTS) [34] and is shown in Table 2.

Table 1. Physical properties of aggregates.

Test	Result		Standard
Coarse Aggregate Apparent Specific Gravity (g/cm^3)	2.680		TS EN 1097-6 [35]
Coarse Aggregate Bulk Specific Gravity (g/cm^3)	2.667		TS EN 1097-6 [35]
Coarse Aggregate Water Absorption (%)	0.4%		TS EN 1097-6 [35]
Fine Aggregate Apparent Specific Gravity (g/cm^3)	2.662		TS EN 1097-6 [35]
Fine Aggregate Bulk Specific Gravity (g/cm^3)	2.614		TS EN 1097-6 [35]
Fine Aggregate Water Absorption (%)	0.6%		TS EN 1097-6 [35]
Filler Specific Gravity (g/cm^3)	2.610		TS EN 1097-7 [36]
Effective Specific Gravity of Mixture (Experimental)	2.666		ASTM D-2041 [37]
Effective Specific Gravity of Mixture (Calculated)	2.658		-
Test	**Result**	**HTS Requirement (SMA Wearing Course)** [34]	**Standard**
Resistance to Fragmentation (Los Angeles Abrasion Loss, %)	20	≤25	AASHTO T-96 [38]
Abrasion Resistance (Micro-Deval, %)	9.1		TS EN 1097-1 [39]
Durability Against Weathering ($MgSO_4$, Freeze–Thaw Loss, %)	1.6	≤14	TS EN 1367-2 [40]
Flakiness Index (%)	17	≤25	BS 812 [41]
Stripping Resistance (%)	70–75	≥60	ASTM D1664 [42]
Methylene Blue Value (g/kg, of Mixture)	1.5	≤1.5	TS EN 933-9 [43]

Table 2. Aggregate gradation of SMA mixture.

Sieve Diameter		**SMA Type-1A Mixture Gradation [34]**		**Sample Weight: 1050 g**	
Inch	**mm**	**% Passing**	**% Retained**	**Retained Weight (g)**	**Cumulative Weight (g)**
¾″	19.0	100.0	-	-	-
½″	12.5	93.5	6.5	68.25	68.25
3/8″	9.5	69.9	23.6	247.8	316.05
No. 4	4.75	34.1	35.8	375.9	691.95
No. 10	2.00	23.4	10.7	112.35	804.30
No. 40	0.425	15.4	8	84	888.30
No. 80	0.180	11.9	3.5	36.75	925.05
No. 200	0.075	9.2	2.7	28.35	953.40
Pan (Below 0.075 mm)	-	9.2	96.6	1050	

2.2. Bitumen

In the production of SMA, the unmodified bitumen must comply with the TS EN 12591 standard [44] and belong to the 40–60 or 50–70 penetration grade. The polymer-modified bitumen, on the other hand, must meet the requirements of the TS EN 14023 standard [45]. Modified bitumen can be produced using additives such as natural rock asphalts, lake asphalts, thermoplastic polymers, latex, and rubber [34]. The bitumen used in this study, produced at the Aliağa Refinery and supplied by the Isparta Municipality asphalt plant, was selected because it represents the commonly used binder in regional road construction projects.

2.3. Elvaloy RET

Elvaloy RET is an additive used in road pavements and asphalt mixtures to improve the properties of asphalt binders. Elvaloy RET integrates with asphalt binders by providing SHRP-level performance at high temperatures and enhanced flexibility at low temperatures [46]. The general properties of the Elvaloy RET polymer additive used in the modified mixture are presented in Table 3. In this study, Elvaloy RET was tested at 1.6%, 1.7%, 1.8%, and 1.9% modification levels; however, since the mixture with 1.9% did not exhibit homogeneous blending, the study was continued with 1.6%, 1.7%, and 1.8% contents (Figure 2).

Table 3. General properties of Elvaloy RET polymer [46].

Physical Properties		
Property	Nominal Values	Test Method(s)
Density (ρ)	0.95 g/cm^3	ASTM D792/ISO 1183 [47,48]
Melt Flow Index (190 °C/2.16 kg)	12 g/10 min	ASTM D1238/ISO 1133 [49,50]
Thermal Properties		
Property	Nominal Values	Test Method(s)
Melting Point (DSC)	80 °C (176 °F)	ASTM D3418/ISO 3146 [51,52]
Freezing Point (DSC)	55 °C (131 °F)	ASTM D3418/ISO 3146 [51,52]
Processing Information		
Property	Value	
Maximum Processing Temperature	220 °C (428 °F)	

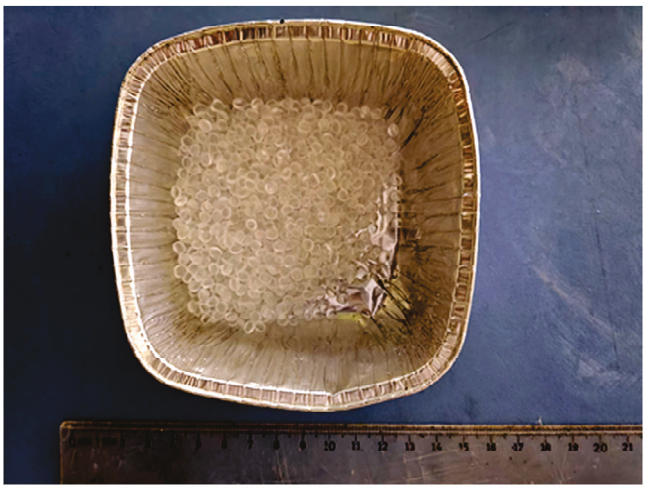

Figure 2. Elvaloy RET used in the study.

2.4. Polyphosphoric Acid (PPA)

Polyphosphoric acid (PPA) is an additive used in various industries and plays a significant role in the modification of bituminous binders. It is known that the addition of PPA improves the rheological properties of bitumen, enhances its high-temperature performance, and increases its overall durability. In particular, when used in combination with other modifying additives, PPA improves the workability of bitumen and prevents phase separation during long-term storage [53]. For these reasons, PPA was used in this study at a fixed content of 0.2% in combination with Elvaloy RET for bitumen modification. The properties of the PPA used in the study are presented in Table 4.

Table 4. Properties of PPA [53].

Property	Value
Chemical Formula	$H_{n+2}P_nO_{3n+1}$
Physical Form	Liquid
Concentration	% $\geq$ 90– $\leq$ 100
Metal Corrosion Rate	May corrode metals

2.5. Cellulose Fiber

Cellulose fibers stand out as one of the most effective stabilizing additives in terms of absorption capacity. Owing to this property, they can strongly retain binders such as bitumen and wax, thereby enhancing the durability of the mixture [54]. The primary reason for preferring cellulose fibers as stabilizers in SMA mixtures is their high absorbent capability. The properties of the cellulose fiber used in this study are presented in Table 5 (Figure 3).

Table 5. Technical properties of cellulose fiber [53].

Appearance	Thickness: 4–7 mm
Schellenberg Drain-down Value	Maximum 0.18% (Specification Limit: 0.3%)
Moisture Content	Maximum 5%
Oil Absorption Capacity	At least 5 times the weight of cellulose

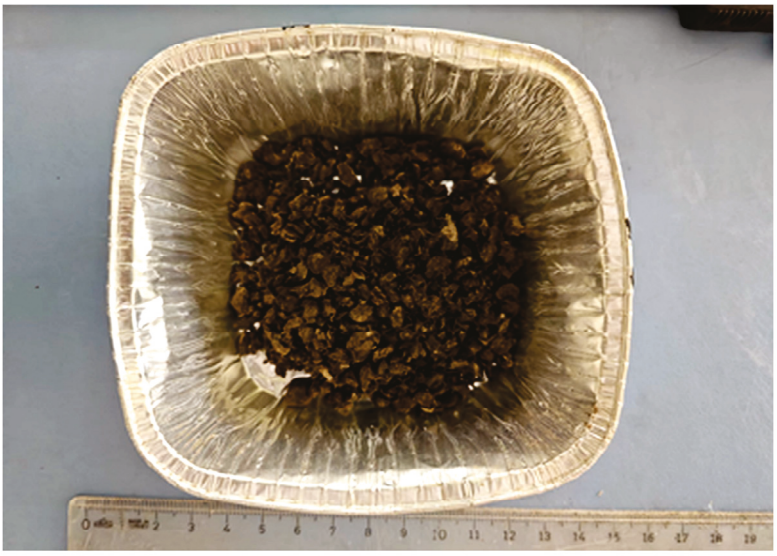

Figure 3. Cellulose fiber used in the study.

2.6. Cellulose Acetate Recycled from Cigarette Butts

The thermal decomposition behavior of cellulose-based materials follows a similar trend to other biomass materials with high cellulose content. Studies have shown that cigarette filters made of cellulose acetate undergo thermal decomposition within the temperature range of 300–400 °C [55]. In this study, cigarette butts were utilized as a source of recycled cellulose acetate. After being collected from locations such as canteens and cafés, the cigarette butts underwent a cleaning process (discussed in Section 3.1 below) before being incorporated as an additive into the SMA mixtures. The cross-section of a cigarette filter and the recycled cellulose acetate obtained from cigarette butts used in the study are shown in Figure 4.

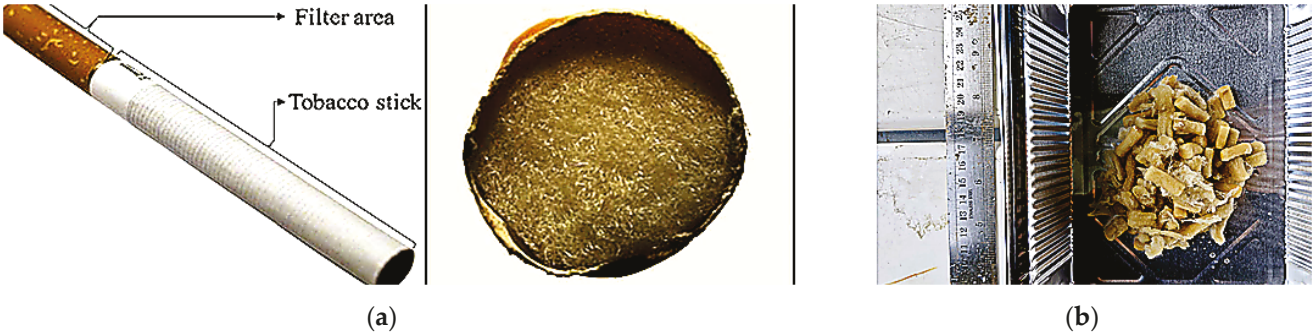

Figure 4. Cross-section of a cigarette filter (**a**) [56], and recycled cellulose acetate used in the study (**b**).

3. Method

3.1. Recycling of Waste Cigarette Butts

Cigarette butts collected from public consumption areas such as canteens, cafés, and restaurants were first immersed in water to remove soluble contaminants from their surfaces and to make them suitable for subsequent chemical treatment processes. The charred portions and tobacco-containing sections were separated from the filter, and the remaining parts were again placed in water to facilitate the easy removal of paper layers (Figure 5).

Figure 5. Preliminary cleaning stage of cigarette butts.

During the chemical cleaning stage, a de-esterification mixture consisting of isopropyl alcohol (IPA), perchloroethylene, and 1 mol/L NaOH solution in a 1:1:1 (v/v) ratio was used. Although this method has not been widely reported in the literature, the use of a similar approach in a previous study [57] supports the applicability of the technique used in this research. In the first step, IPA and perchloroethylene were applied to remove surface contaminants such as nicotine and tar. After the preliminary cleaning, in the second step, the cigarette butts were transferred into the 1:1:1 mixture of IPA, perchloroethylene, and 1 mol/L NaOH solution. The samples were kept in this solution for 2 h, then rinsed thoroughly with water, dried, and stored in airtight containers (Figure 6).

Figure 6. Chemical cleaning process and post-treatment.

3.2. Bitumen Modification

In this study, both pure bitumen and modified bitumen were used. The modification process was carried out using Elvaloy RET at contents of 1.6%, 1.7%, and 1.8%. The bitumen was mixed at 185 °C and a stirring speed of 500 rpm for 2 h. At the end of this period, 0.2% polyphosphoric acid (PPA) was added as a catalyst, and the mixing process was continued for an additional 30 min, completing the modification procedure.

3.3. X-Ray Diffraction (XRD) Analysis of Modified Bitumen

X-Ray Diffraction (XRD) analysis is a powerful characterization technique widely used to identify crystalline structures [58]. In addition, it has been extensively applied in the phase analysis of mineral additives used in bitumen and polymer-modified asphalt materials [59–61]. To examine the effects of the modifiers used in this study, XRD analysis was performed on bitumen samples modified with 1.7% Elvaloy RET + 0.2% PPA and 1.8% Elvaloy RET + 0.2% PPA.

3.4. Bitumen Tests

In this study, both conventional and Superpave bitumen tests were conducted to determine the physical and rheological properties of both pure and modified bitumens. The penetration test was performed to determine the hardness of the bitumen, while the softening point test was carried out to evaluate its flow resistance at high temperatures. In addition, a storage stability test was conducted to evaluate the compatibility between the bitumen and the additives. This method allows the assessment of the uniform dispersion of the additives within the bitumen and the stability of the bitumen during the storage period. The storage stability test of the modified bitumens was carried out in accordance with TS EN 13399 [62]. The bitumen was poured into standard aluminum tubes and kept at 180 °C for 72 ± 1 h, then cooled and divided into three equal parts. The top and bottom sections were used for testing, while the middle part was discarded. According to the HTS [34], the difference in softening point between the top and bottom sections should not exceed 5 °C; otherwise, phase separation is considered to have occurred. In addition, an elastic recovery test was carried out in accordance with TS EN 13398 [63] to determine the ability of the bitumen to return to its original form after deformation. The test is performed at 25 °C using a ductilometer, where the specimen is stretched to 200 mm at a rate of 50 mm/min. The stretched specimen is then cut in half, left to rest for 30 min, and the amount of retraction is measured to calculate the elastic recovery percentage. This method allows for the evaluation of the binder's flexibility and ability to recover after deformation. To evaluate the high-temperature performance of the binders, the Rolling Thin Film Oven

Test (RTFOT) was first conducted to simulate short-term aging, allowing for the analysis of binder stability and workability. Following RTFOT aging, and subsequently after the Pressure Aging Vessel (PAV) procedure, representing long-term aging, the Dynamic Shear Rheometer (DSR) test was performed to determine the rheological performance of the binders. Using the complex shear modulus (G*) and phase angle (δ) values obtained from the DSR, the deformation resistance and elastic behavior level of the binder were calculated. These parameters are critically important for assessing permanent deformation (rutting) and aging susceptibility, particularly at high service temperatures. In the test, the specimen is placed between two plates, one fixed and the other oscillating. The oscillating plate applies an oscillatory shear force to the specimen, and the rheological properties exhibited by the specimen in response to this force are measured. The Bending Beam Rheometer (BBR) test was conducted to determine the stiffness and creep properties of bituminous binders at low temperatures. This test plays an important role in evaluating the resistance of bitumen to low-temperature cracking. In the test, a bitumen beam specimen of specified dimensions is subjected to a constant load for 4 min, and its behavior is monitored to obtain time–creep stiffness and time–deformation curves. The test is typically performed at sub-zero temperatures to assess the cracking risk of bitumen under cold conditions. According to the test criteria, the creep stiffness (S(t)) should be less than 300 Mpa, and the m-value should be greater than 0.300. Meeting these conditions indicates that the bitumen can perform effectively at low temperatures without a significant risk of cracking [64].

3.5. SMA Mixture Tests

SMA specimens were prepared in accordance with the Turkish Highway Technical Specifications (HTS), and the Marshall method was used for mix design [34]. Aggregate samples weighing 1050 g were prepared, and bitumen was added in proportions of 5%, 5.5%, 6%, 6.5%, and 7% by weight. Three specimens were produced for each bitumen content. For each specimen, the practical specific gravity (Dp), air void content (Vh), voids in mineral aggregate (VMA), and voids filled with asphalt (Vfa) values were determined, and the Optimum Bitumen Content (OBC) was calculated. The SMA specimen series and aggregate combinations are presented in Table 6.

Table 6. SMA specimen series and aggregate combinations.

Sample Code	Description	Sample Code	Description
E1.6-SG-0.1	%1.6 Elvaloy + %0.2 PPA + SG %0.1	E1.6-SL-0.1	%1.6 Elvaloy + %0.2 PPA + SL %0.1
E1.6-SG-0.2	%1.6 Elvaloy + %0.2 PPA + SG %0.2	E1.6-SL-0.2	%1.6 Elvaloy + %0.2 PPA + SL %0.2
E1.6-SG-0.3	%1.6 Elvaloy + %0.2 PPA + SG %0.3	E1.6-SL-0.3	%1.6 Elvaloy + %0.2 PPA + SL %0.3
E1.6-SG-0.4	%1.6 Elvaloy + %0.2 PPA + SG %0.4	E1.6-SL-0.4	%1.6 Elvaloy + %0.2 PPA + SL %0.4
E1.6-SG-0.5	%1.6 Elvaloy + %0.2 PPA + SG %0.5	E1.6-SL-0.5	%1.6 Elvaloy + %0.2 PPA + SL %0.5
E1.7-SG-0.1	%1.7 Elvaloy + %0.2 PPA + SG %0.1	E1.7-SL-0.1	%1.7 Elvaloy + %0.2 PPA + SL %0.1
E1.7-SG-0.2	%1.7 Elvaloy + %0.2 PPA + SG %0.2	E1.7-SL-0.2	%1.7 Elvaloy + %0.2 PPA + SL %0.2
E1.7-SG-0.3	%1.7 Elvaloy + %0.2 PPA + SG %0.3	E1.7-SL-0.3	%1.7 Elvaloy + %0.2 PPA + SL %0.3
E1.7-SG-0.4	%1.7 Elvaloy + %0.2 PPA + SG %0.4	E1.7-SL-0.4	%1.7 Elvaloy + %0.2 PPA + SL %0.4
E1.7-SG-0.5	%1.7 Elvaloy + %0.2 PPA + SG %0.5	E1.7-SL-0.5	%1.7 Elvaloy + %0.2 PPA + SL %0.5
E1.8-SG-0.1	%1.8 Elvaloy + %0.2 PPA + SG %0.1	E1.8-SL-0.1	%1.8 Elvaloy + %0.2 PPA + SL %0.1
E1.8-SG-0.2	%1.8 Elvaloy + %0.2 PPA + SG %0.2	E1.8-SL-0.2	%1.8 Elvaloy + %0.2 PPA + SL %0.2
E1.8-SG-0.3	%1.8 Elvaloy + %0.2 PPA + SG %0.3	E1.8-SL-0.3	%1.8 Elvaloy + %0.2 PPA + SL %0.3
E1.8-SG-0.4	%1.8 Elvaloy + %0.2 PPA + SG %0.4	E1.8-SL-0.4	%1.8 Elvaloy + %0.2 PPA + SL %0.4
E1.8-SG-0.5	%1.8 Elvaloy + %0.2 PPA + SG %0.5	E1.8-SL-0.5	%1.8 Elvaloy + %0.2 PPA + SL %0.5
Reference Samples			
B-SG-0.1	Pure bitumen + SG %0.1	B-SL-0.1	Pure bitumen + SL %0.1
B-SG-0.2	Pure bitumen + SG %0.2	B-SL-0.2	Pure bitumen + SL %0.2
B-SG-0.3	Pure bitumen + SG %0.3	B-SL-0.3	Pure bitumen+ SL %0.3
B-SG-0.4	Pure bitumen + SG %0.4	B-SL-0.4	Pure bitumen + SL %0.4
B-SG-0.5	Pure bitumen + SG %0.5	B-SL-0.5	Pure bitumen + SL %0.5
B-SMA		Pure bitumen (unmodified)-SMA	
E1.6-SMA		%1.6 Elvaloy + %0.2 PPA (unmodified)-SMA	
E1.7-SMA		%1.7 Elvaloy + %0.2 PPA (unmodified)-SMA	
E1.8-SMA		%1.8 Elvaloy + %0.2 PPA (unmodified)-SMA	

For each series given in the table, new specimens were prepared at the OBC and subjected to Indirect Tensile Strength (ITS), Tensile Strength Ratio (TSR), Schellenberg bitumen drainage, sand patch, and Cantabro tests. Through these tests, the mixtures were comprehensively evaluated in terms of their mechanical performance, resistance to moisture damage, bitumen drainage characteristics, surface texture, and resistance to particle loss.

The Marshall stability and flow test, as specified in ASTM D1559 [65], is conducted to determine the resistance of bituminous mixtures to plastic deformation. For the test, the prepared specimens are first measured and weighed, then conditioned in a water bath maintained at 60 ± 1 °C for 30–40 min. After conditioning, the specimens are removed from the bath, centered between the loading heads, and subjected to loading at a rate of 50 ± 2 mm/min. During the test, the stability at the moment of specimen failure and the corresponding flow value are recorded. Stability represents the maximum load the mixture can withstand before failure, indicating its resistance to deformation, while flow refers to the vertical deformation that occurs at the point of maximum load [66].

The ITS test is conducted to indirectly determine the tensile strength of asphalt mixtures by applying compressive loads along the vertical diameter of the specimens using a Marshall loading device. The ITS value is determined by calculating the maximum load the specimen can sustain before failure (Equation (1)). The test is performed in accordance with the ASTM D6931-17 standard [67], using a Marshall testing apparatus at a constant temperature of 25 °C and a loading rate of 50.8 mm/min. This test method is highly important for evaluating the resistance of bituminous mixtures to cracking and assessing their behavior under temperature variations [21].

$$\mathrm{ITS} = \frac{2\mathrm{Pmax}}{\pi \mathrm{td}} \tag{1}$$

Pmax represents the maximum applied load (kN), t denotes the specimen thickness (mm), and d refers to the specimen diameter (mm).

Moisture sensitivity is one of the key parameters that directly affects the performance of bituminous mixtures. The presence of water or moisture within the pavement weakens the bond between the bitumen and the aggregate, leading to adhesion loss, cracking, and surface deterioration. The AASHTO T283 standard [68] is used to determine the moisture sensitivity of bituminous mixtures, and according to this standard, the prepared specimens are divided into two groups: unconditioned and conditioned. To simulate real environmental conditions, the conditioned specimens are first subjected to vacuum treatment so that 60–80% of their air voids are filled with water. Then, the specimens are wrapped with stretch film and kept in a freezer at −18 °C for 16 h. After freezing, they are placed in a water bath at 60 °C for 24 h, and subsequently, both conditioned and unconditioned specimens are kept in a water bath at 25 °C for 2 h to equilibrate. After completing these procedures, both the unconditioned (ITSdry) and conditioned (ITSwet) specimens are tested using a Marshall loading device to determine ITS. The TSR of the specimens is then calculated using Equation (2). According to the standard, TSR values must be at least 80%, indicating sufficient resistance to moisture damage. Specimens with TSR values below this threshold are considered to have inadequate resistance to moisture-induced damage [69].

$$\mathrm{TSR} = \frac{\mathrm{ITSwet}}{\mathrm{ITSdry}} \times 100 \tag{2}$$

ITSwet indicates the indirect tensile strength of the soaked specimens (kPa), while ITSdry represents the indirect tensile strength of the dry specimens (kPa).

In the bitumen drain-down test, for conventional bituminous mixtures, 1000 g of SMA mixture prepared at 135 ± 5 °C, and for polymer-modified mixtures (PMB), at 145 ± 5 °C, is placed into a 1000 mL glass beaker that has been preheated to 110 °C. The beaker is weighed with a precision of 0.1 g. After covering the beaker, it is kept in an oven for 1 h ± 1 min at 175 °C for conventional mixtures and 185 °C for modified mixtures. At the end of this period, the beaker is carefully removed from the oven and emptied without shaking. The drained mixture is then weighed again with a precision of 0.1 g, and the weight loss is calculated as a percentage (Figure 7). The test is performed on three parallel mixture samples, and the average of the results is taken for evaluation [34].

The surface texture roughness of SMA mixtures is determined by measuring the texture depth using the Sand Patch test. In this study, the Sand Patch test was conducted in accordance with the ASTM E965 testing standard [70]. For the test, the average diameter of each SMA briquette was first measured and recorded using a digital caliper. Then, 100 g of sand (with a specific gravity of 1.476 g/cm^3) was poured onto the surface of the SMA briquette placed on a flat tray. The sand was spread evenly across the surface using a leveling tool to fill the surface voids of the briquette. The weight of the sand filling the surface voids was recorded, and the volume of sand applied to each specimen was calculated (Figure 8). The resulting mean texture depth was determined for each specimen using Equation (3) [53].

Figure 7. Stages of the bitumen drain-down test.

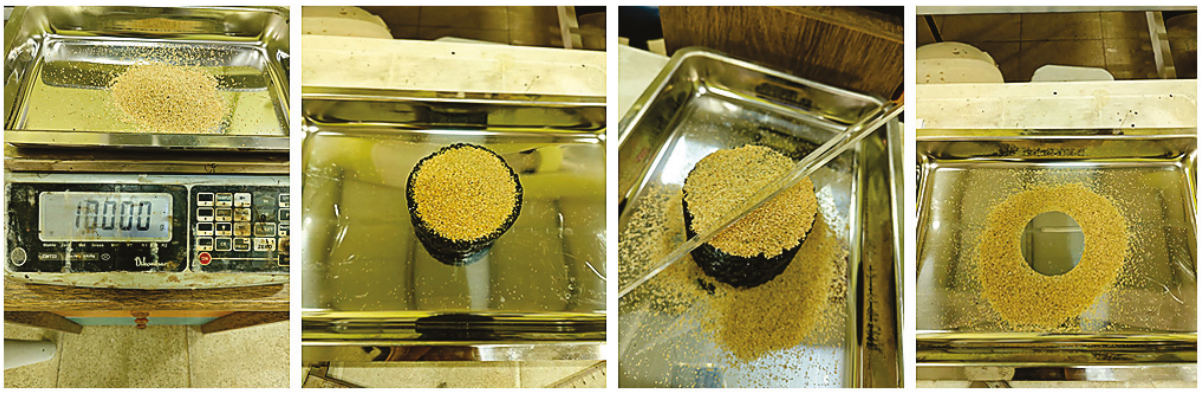

Figure 8. Stages of the sand patch test.

According to the HTS, the mean texture depth of the SMA Type-1A wearing course should be greater than 1.0 mm [34].

$$H = 4V/\pi D^2 \quad (3)$$

H represents the mean texture depth, V refers to the volume of sand used, and D denotes the mean diameter of the sand patch.

In order to evaluate the durability of the mixtures, the Cantabro test was performed. The purpose of this test is to determine the resistance of the mixture to raveling or particle loss. The specimens are placed in the Los Angeles abrasion machine without adding any abrasive load (such as steel balls) and subjected to a total of 300 revolutions (Figure 9). At the end of the test, the initial mass of the specimen is compared with the final mass obtained after the procedure to determine the mass loss [71].

This value is referred to as the Cantabro particle loss (PL) and is calculated using the following equation:

$$PL = 100 \times \frac{W_1 - W_2}{W_1} \quad (4)$$

where W_1 is the initial mass of the specimen and W_2 is the final mass after testing.

Figure 9. Cantabro test specimen.

4. Results

4.1. X-Ray Diffraction (XRD) Analysis Results of Modified Bitumen

The X-Ray Diffraction (XRD) analyses of bitumen modified with 1.7% and 1.8% Elvaloy RET + 0.2% PPA are presented together in Figure 10.

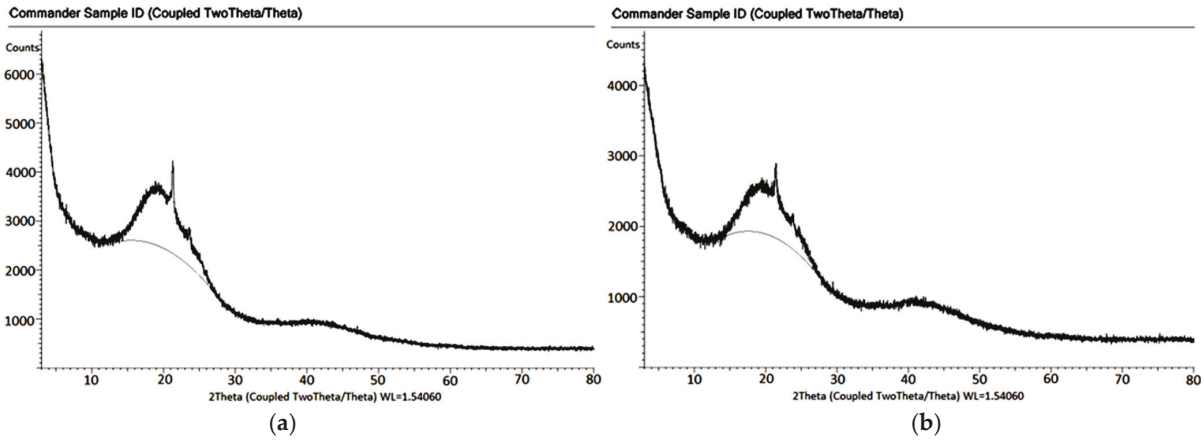

Figure 10. XRD patterns of bitumen modified with 1.7% Elvaloy RET + 0.2% PPA (**a**) and 1.8% Elvaloy RET + 0.2% PPA (**b**).

In both patterns, a broad peak is observed around 2θ = 20–22°, indicating that the samples largely retain their amorphous character. In both specimens, the intensity decreases significantly beyond 30°, and no strong peak is detected in the 40–80° range. Consequently,

it can be stated that neither the E1.7 nor the E1.8 bitumen samples exhibit the formation of a new crystalline phase; however, partial chain rearrangements likely occur, leading to improvements in the viscoelastic and mechanical properties of the material. Furthermore, previous research [10] has shown that Elvaloy RET interacts with the main macromolecular groups within bitumen and exhibits a homogeneous distribution throughout the bitumen phase, which supports the interpretation of the observed structural behavior in this study.

4.2. Bitumen Test Results

4.2.1. Conventional Bitumen Test Results

Penetration and softening point tests were performed for pure bitumen and modified bitumens containing different proportions of Elvaloy RET and PPA, and the results are presented in Table 7.

Table 7. Penetration and softening point values.

Sample	Elvaloy RET (%)	PPA (%)	Penetration (0.1 mm)	Softening Point (°C)
B	0.0	0.0	58	51.0
E1.6	1.6	0.2	45	60.0
E1.7	1.7	0.2	47	61.0
E1.8	1.8	0.2	48	62.4

The addition of Elvaloy RET and PPA significantly reduced the penetration value from 58 (for pure bitumen) to approximately 45–48 (a decrease of about 17–22%), indicating a noticeable increase in stiffness. However, further increases in modifier content beyond 1.6% caused only minor variations in penetration, suggesting that the bitumen had reached a relatively stable structure. Similarly, the softening point increased markedly from 51 °C to 60–62.4 °C (an increase of about 18–22%), confirming that Elvaloy RET and PPA substantially enhance the high-temperature stability of the bitumen. Overall, these results demonstrate that the modifiers effectively improve the bitumen's resistance to deformation and thermal susceptibility.

To determine the long-term stability of the interaction between the additives and the bitumen, storage stability tests were conducted. The softening point difference values are presented in Figure 11, and the penetration difference values are shown in Figure 12.

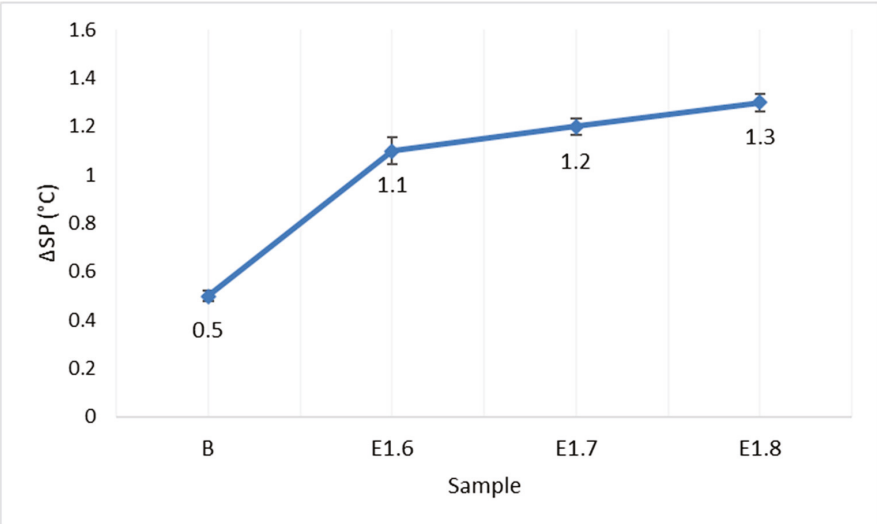

Figure 11. Softening point difference values.

According to the storage stability test, both pure and Elvaloy RET + PPA-modified bitumens did not undergo phase separation during the storage period. With increasing

Elvaloy RET content, the ΔSP and ΔP differences slightly decreased, indicating that the additives mixed compatibly with the bitumen and that the thermal stability of the system improved. The elastic recovery values are presented in Figure 13.

According to the results of the test conducted to determine the elastic recovery properties of bituminous binders, an increase in additive content in the modified bitumen leads to an increase in elastic recovery. This increase indicates that the Elvaloy RET additive promotes the development of an elastic network structure and enhances the material's ability to return to its original form after deformation.

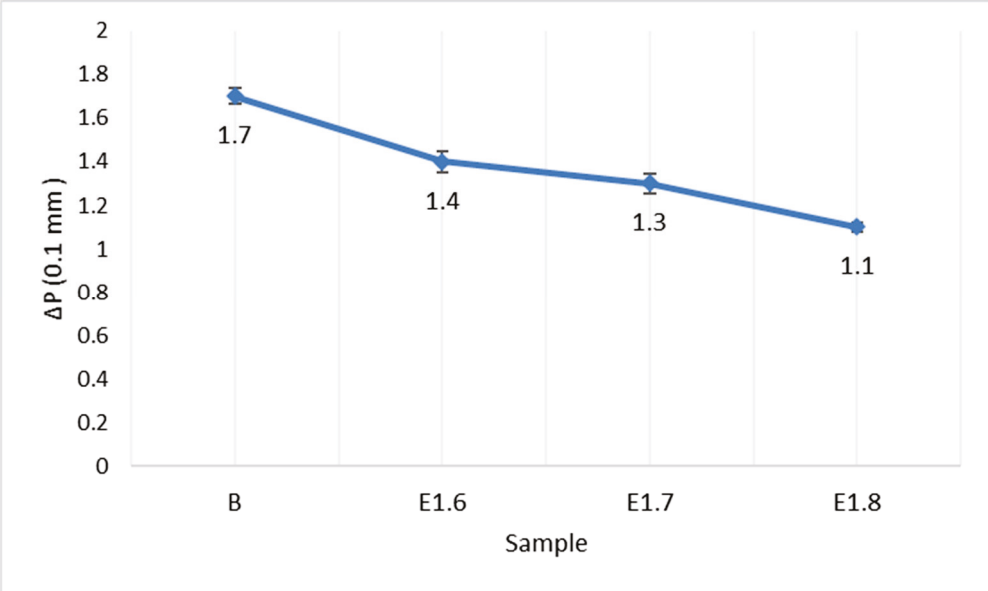

Figure 12. Penetration difference values.

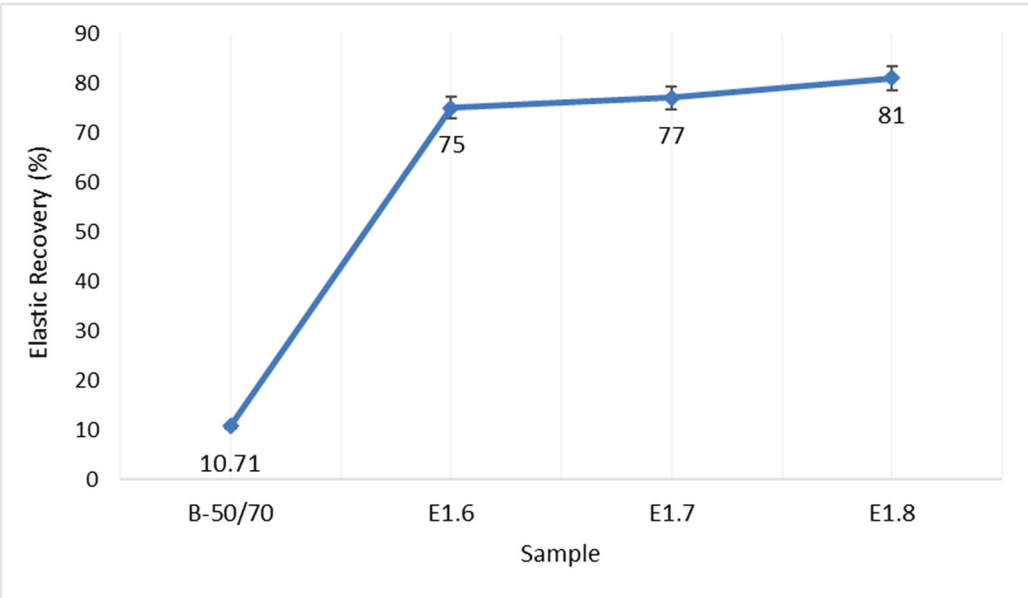

Figure 13. Elastic recovery values.

4.2.2. Results of Mass Loss After RTFOT, Residual Penetration, and Softening Point Tests of Bitumen Samples

To evaluate the short-term aging performance of the bitumens, mass loss, residual penetration, and softening point tests were conducted after the RTFOT procedure (Table 8).

Table 8. Test results of bitumen samples after RTFOT.

Sample Code	Mass Loss (%)	Residual Penetration (%)	Softening Point (°C)
B-50/70	0.11	81.2	53.8
E1.6	0.05	75.6	63.0
E1.7	0.03	70.2	64.0
E1.8	0.02	64.0	66.4

The pure bitumen showed the highest mass loss value of 0.11%, while this value gradually decreased with increasing additive content. In the bitumen modified with 1.8% Elvaloy RET + PPA, the mass loss decreased to 0.02%, indicating the highest short-term aging resistance. As the additive content increased, the penetration value decreased, showing stability in the viscoelastic behavior of the bitumens. The increase in softening point values indicated an improvement in the bitumen's resistance to heat.

4.2.3. Dynamic Shear Rheometer (DSR) and Bending Beam Rheometer (BBR) Test Results

The DSR tests were carried out on the bitumens in their unaged state, after short-term aging (RTFOT), and after long-term aging (PAV), and the results are presented in Figure 14.

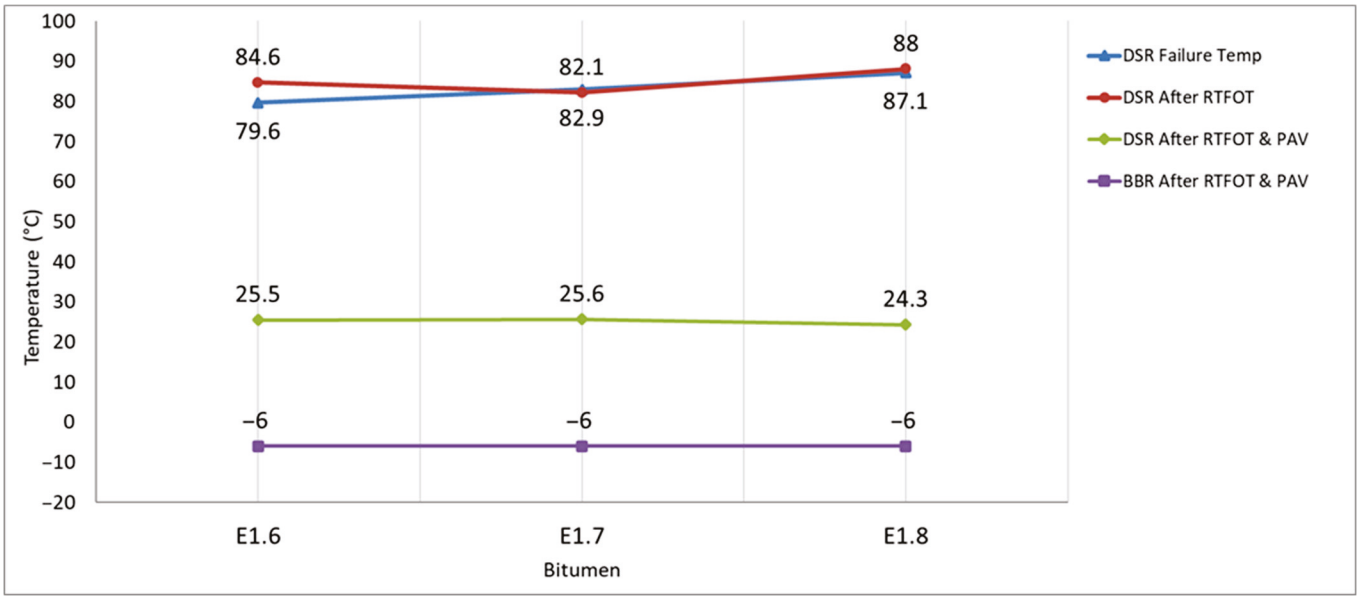

Figure 14. DSR and BBR test results.

According to the obtained results, the increase in DSR failure temperatures both before aging and after RTFOT indicates that the bitumens' deformation resistance at high temperatures has improved, and their resistance to rutting has been strengthened. After PAV aging, the DSR failure temperatures ranged between 24.3 and 25.6 °C, showing that the high-temperature performance was partially preserved and that the additives formed a polymeric network structure, enhancing the rheological strength of the bitumen.

4.3. Mixture Test Results

4.3.1. Marshall Stability, Flow and Marshall Quotient Results

In order to determine the Optimum Bitumen Content (OBC), the Marshall Stability (MS) test was performed, and the corresponding values of air voids (Vh), voids filled with bitumen (Vfa), voids in mineral aggregate (VMA), and bulk specific gravity (Dp) were obtained for each specimen. Each data point represents the average of three replicate measurements. Standard deviations were calculated and found to be small, indicating high repeatability of the results. Therefore, only mean values are displayed in the figures

to enhance visual clarity. In SMA mixtures, the optimum bitumen content is generally determined based on the Vh value. In the specification, the air void limits for hot climate regions are in the range of 3–4% [34]. A target value of 3.5% was adopted, and the optimum bitumen content for each series was determined based on the condition of Vh = 3.5%. Therefore, the air void content at the optimum bitumen content is 3.5% for all series. Detailed air void data corresponding to each bitumen content level (5.0%, 5.5%, 6.0%, 6.5%, and 7.0%) used in determining the optimum binder content are presented in Table 9.

Table 9. Relationship between bitumen content and Vh.

Bitumen Content	Vh (%)									
	E1.6-SG-0.1	E1.6-SG-0.2	E1.6-SG-0.3	E1.6-SG-0.4	E1.6-SG-0.5	E1.6-SL-0.1	E1.6-SL-0.2	E1.6-SL-0.3	E1.6-SL-0.4	E1.6-SL-0.5
5%	4.84	5.05	6.07	6.42	6.68	4.83	4.97	7.03	7.82	7.78
5.5%	4.09	3.93	4.58	5.39	5.42	3.09	3.35	5.57	5.32	5.69
6%	2.71	3.01	2.97	4.28	3.25	1.53	1.50	4.30	4.24	4.19
6.5%	1.36	1.69	1.52	3.38	3.55	1.30	1.30	3.15	3.29	3.26
7%	1.11	1.32	1.23	3.04	3.71	1.00	1.00	2.74	2.76	2.92
	E1.7-SG-0.1	E1.7-SG-0.2	E1.7-SG-0.3	E1.7-SG-0.4	E1.7-SG-0.5	E1.7-SL-0.1	E1.7-SL-0.2	E1.7-SL-0.3	E1.7-SL-0.4	E1.7-SL-0.5
5%	5.09	5.99	7.51	7.71	6.78	5.89	5.93	7.30	7.47	7.55
5.5%	3.81	4.58	5.47	6.24	5.51	4.82	4.90	5.47	5.51	5.59
6%	2.97	3.16	3.71	5.02	3.34	3.71	3.79	4.12	3.99	4.08
6.5%	1.61	2.15	2.59	3.01	3.66	2.68	2.72	2.72	3.09	3.17
7%	1.32	1.85	2.35	3.67	3.80	1.89	1.94	2.43	1.40	1.48
	E1.8-SG-0.1	E1.8-SG-0.2	E1.8-SG-0.3	E1.8-SG-0.4	E1.8-SG-0.5	E1.8-SL-0.1	E1.8-SL-0.2	E1.8-SL-0.3	E1.8-SL-0.4	E1.8-SL-0.5
5%	5.06	5.58	6.88	7.19	6.89	6.21	6.29	7.40	7.27	7.35
5.5%	3.80	4.16	4.85	5.64	4.97	5.32	5.34	5.43	5.68	5.77
6%	2.71	3.01	3.31	4.45	3.81	4.39	4.43	3.91	4.13	4.22
6.5%	1.81	2.12	2.26	3.63	3.41	3.42	3.57	2.85	2.63	2.71
7%	1.08	1.50	1.69	3.17	3.77	2.43	2.77	2.26	1.16	1.24
	B-SG-0.1	B-SG-0.2	B-SG-0.3	B-SG-0.4	B-SG-0.5	B-SL-0.1	B-SL-0.2	B-SL-0.3	B-SL-0.4	B-SL-0.5
5%	4.61	4.72	4.60	5.17	5.01	4.62	6.52	6.74	5.29	6.90
5.5%	2.67	3.28	3.56	3.81	3.89	3.60	3.88	4.62	3.81	3.64
6%	2.03	2.15	2.40	2.60	2.97	2.38	2.78	2.69	2.40	2.52
6.5%	1.71	1.61	1.36	1.81	1.65	1.40	2.03	1.60	1.73	1.15
7%	0.99	1.23	1.07	1.27	1.27	1.02	0.85	0.77	1.40	1.73
				B-SMA	E1.6-SMA	E1.7-SMA	E1.8-SMA			
5%				4.04	3.89	4.60	4.91			
5.5%				2.87	3.14	3.56	3.49			
6%				1.87	2.46	2.40	2.35			
6.5%				0.85	1.73	1.36	1.48			
7%				0.36	1.30	1.07	0.89			

When all series are generally examined, it is observed that the Vh values decrease as the bitumen content increases. This trend indicates that the increasing amount of bitumen in the mixture fills the voids between the aggregates, resulting in a more compact structure. In mixtures with pure bitumen (B series), Vh values ranged between 4.61 and 6.90% at 5% bitumen content and decreased to 0.77–1.73% at 7% bitumen content. In the E1.6 series, the void ratios ranged from 4.83 to 7.82% at 5% bitumen content and declined to 1.00–3.71% at 7%. For the E1.7 series, these values were recorded as 5.09–7.71% at 5% bitumen content and 1.32–3.80% at 7%, while in the E1.8 series, they started from 5.06 to 7.40% and decreased to 1.08–3.77% at 7%. The SG fiber-modified mixtures generally exhibited higher void ratios than the SL fiber-modified ones due to the porous nature of the SG fibers. On the other hand, SL fiber-modified mixtures provided better interaction with bitumen, resulting in lower Vh values and a denser, more durable structure. In the SMA series (B-SMA, E1.6-SMA, E1.7-SMA, E1.8-SMA), void ratios ranged from 3.89 to 4.91% at 5% bitumen content and decreased to 0.36–1.30% at 7%. In Figure 15, the Marshall stability values at the optimum bitumen content for each series are presented, while Figure 16 shows the corresponding flow values.

According to the Marshall test results, a significant increase in the Marshall stability values of the mixtures was observed with bitumen modification and fiber additives. In the SMA (reference) series, the average stability value was approximately 1000 kg, while it increased by about 18–19% to 1185 kg in the E1.6 series, by approximately 22% to 1216 kg in the E1.7 series, and by around 19% to 1188 kg in the E1.8 series. These results indicate that the use of Elvaloy RET, PPA, and SG-SL additives significantly enhances the load-bearing

capacity of the mixtures. In particular, the E1.7 series achieved the optimum balance between high stability and workability, exhibiting the best overall performance among the fiber-modified mixtures.

As the modification ratio increases, a decrease in flow values is observed. In the SMA (pure bitumen) mixtures, the average flow ranged between 4.0 and 4.4 mm, while in the E1.6 series, it decreased to 3.1–3.9 mm; in the E1.7 series, to 3.1–4.1 mm; and in the E1.8 series, to around 3.3–3.8 mm. This indicates a 15–25% reduction in deformation due to bitumen modification. Mixtures containing SG additive exhibited lower flow values, indicating higher stiffness and deformation resistance compared to SL fiber-modified mixtures. In terms of modification level, the E1.7 modification provided the most suitable balance for achieving optimum performance. In Figure 17, the Marshall quotient (MQ) values obtained from the Marshall stability and flow results of the SMA series are presented.

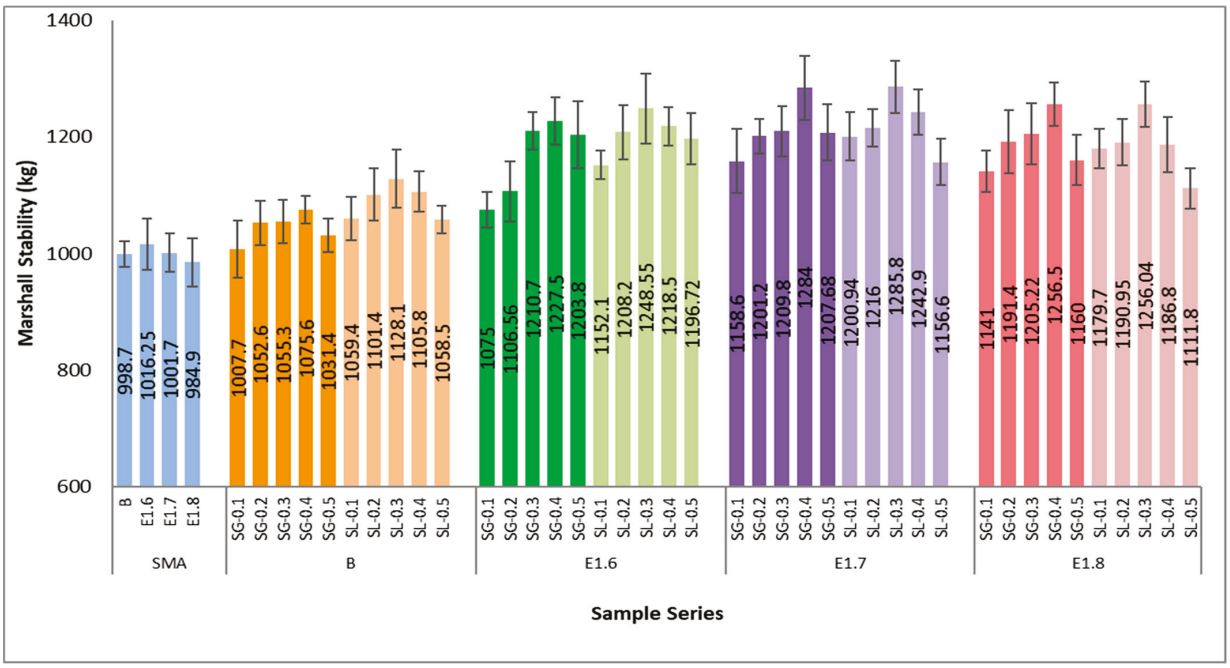

Figure 15. Marshall stability values of all SMA series.

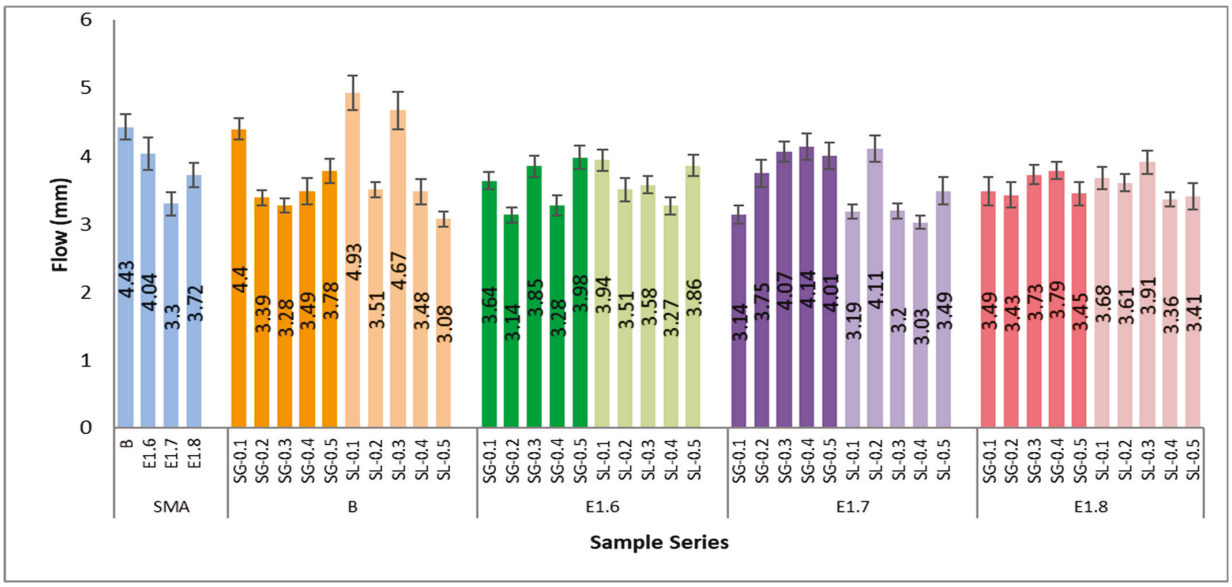

Figure 16. Flow values of all SMA series.

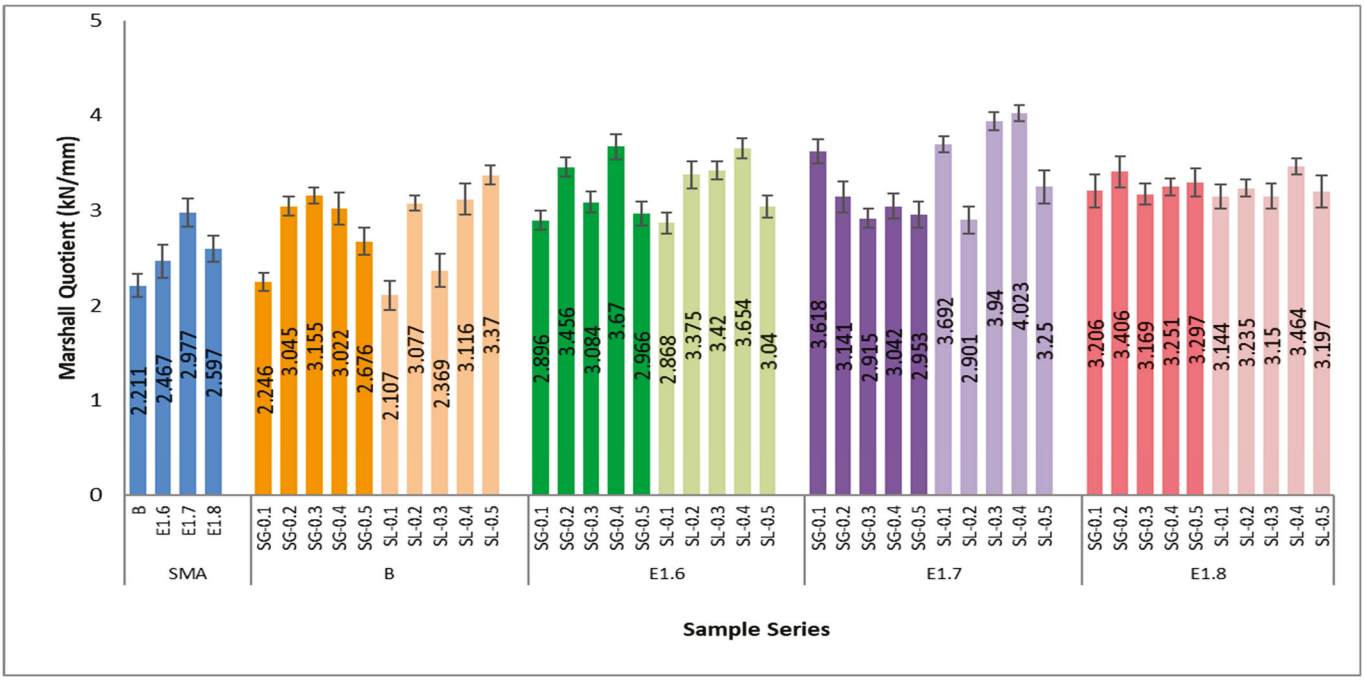

Figure 17. Marshall quotient values of all SMA series.

In the SMA series, the average Marshall quotient value ranged between 2.2 and 2.6 kN/mm, while in the E1.6–E1.8 series, these values increased to around 3.2–3.3 kN/mm, corresponding to an improvement of approximately 45–50% compared to the reference mixture. This increase indicates an improvement in both the load-bearing capacity and the resistance to permanent deformation of the mixtures. The rise in the Marshall quotient is directly associated with enhanced rutting resistance, as widely reported in the literature. It is observed that mixtures containing SG and SL additives exhibit a lower potential for permanent deformation compared to the reference mixtures prepared with pure bitumen. In particular, the E1.7 series achieved the optimum Marshall quotient, combining high stability with balanced flow values.

4.3.2. Indirect Tensile Strength and Moisture Damage Resistance Test Results

In the study, ITS tests were performed on both conditioned and unconditioned specimens to determine their resistance to moisture-induced pavement damage. ITS values of all series are presented in Figure 18, while the corresponding TSR values are shown in Figure 19.

A meaningful improvement in ITS values is observed with the increase in the modification rate. In the SMA series, the average dry ITS value was approximately 1012 kPa, while in the E1.6, E1.7, and E1.8 series, these values increased to 1043, 1087, and 1092 kPa, respectively. Similarly, the wet ITS values ranged between 870 and 1014 kPa, indicating that the mixtures retained about 91–93% of their strength. This enhancement can be attributed to the micro-reinforcement effect of fibers and the improved adhesion between bitumen and aggregate. The small difference between the dry and wet specimen results indicates that the modification reduced the moisture sensitivity of the mixtures, suggesting that they will be more resistant to moisture-induced stripping, rutting, and other forms of deterioration throughout their service life. The TSR values of the series are presented in Figure 19.

As the modification ratio increases, TSR values rise, indicating a reduction in moisture sensitivity. In the SMA series, the TSR values ranged between 81 and 88%, while in the modified mixtures, these values exceeded 90%, reaching approximately 93% in the E1.7 and E1.8 series. This increase corresponds to an improvement of about 12–14%. This result

demonstrates that the modification and fiber additives impart a hydrophobic character to the mixtures, preventing water from weakening the binder. Among the modified mixtures, SG-added mixtures exhibited higher stiffness and durability, whereas SL-added mixtures showed the best performance in terms of moisture resistance. In particular, the E1.7 series achieved the optimum performance level.

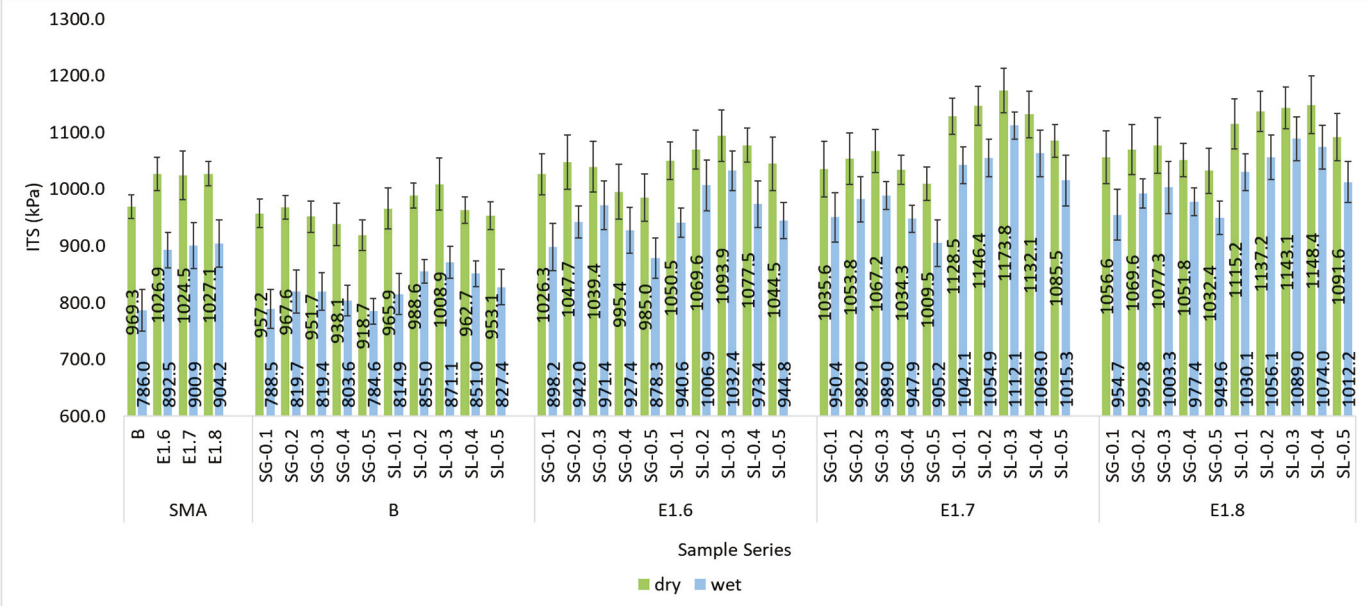

Figure 18. ITS values of all mixture series.

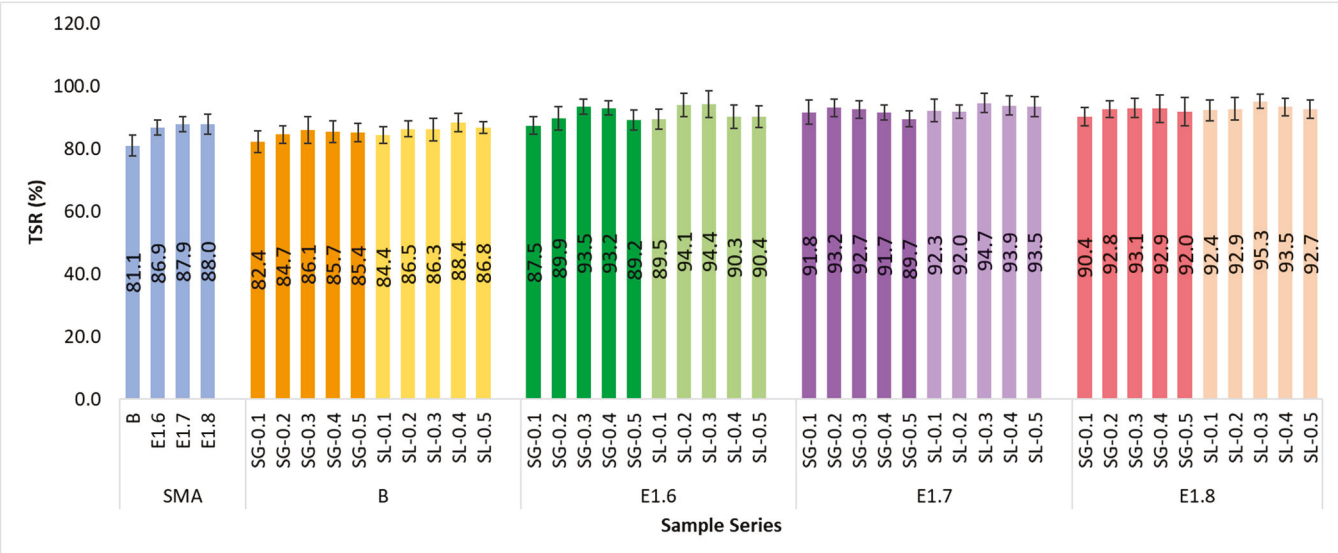

Figure 19. TSR values of all mixture series.

A paired *t*-test was applied to examine the difference between dry and wet samples, a one-way ANOVA with Tukey's test was used to compare modification levels, an independent *t*-test was conducted to evaluate the difference between fiber types, and a regression analysis was performed to determine the relationship between fiber content and TSR.

According to the analysis results, moisture conditioning caused an average decrease of approximately 10% (about 101 kPa) in ITS values, and this reduction was found to be statistically significant ($p < 0.001$). The Elvaloy RET + PPA modification significantly increased TSR values, raising the average TSR from 86% in the control mixtures to about 93% in the

modified mixtures ($p < 0.001$). No statistically significant difference was found between SG and SL fibers in terms of TSR (difference < 2%, $p > 0.05$). Although the effect of fiber content (0.1–0.5%) on TSR was not linearly significant, the highest values were obtained at approximately 0.3–0.4%. According to the regression analysis results, a slight increase in TSR was observed with increasing fiber content for both fiber types. For the SG fiber, the relationship was defined by the equation TSR = 85.42 + 16.23·(Fiber%), with $R^2 = 0.78$ ($p = 0.041$). For the SL fiber, the relationship was determined as TSR = 86.01 + 13.55·(Fiber%), with $R^2 = 0.72$ ($p = 0.056$). Although the increase was not completely linear, the highest TSR values were observed at a fiber content of 0.3–0.4%, indicating the occurrence of a saturation effect beyond this level. In conclusion, SMA mixtures modified with Elvaloy RET + PPA exhibited high resistance to moisture-induced damage, and the SG fiber performed as effectively as the SL fiber.

4.3.3. Bitumen Drain-Down Test Results

Figure 20 presents the bitumen drain-down percentages for all mixture series.

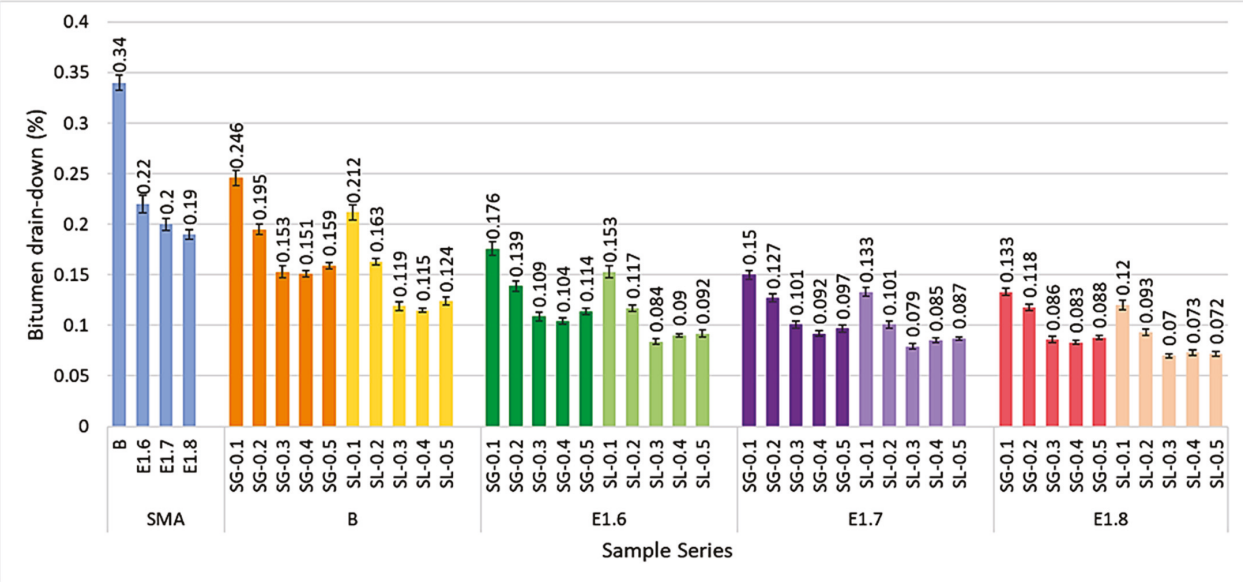

Figure 20. Bitumen drain-down percentage values for the mixture series.

In the test conducted to determine the amount of bitumen drainage from the mineral aggregate, it was generally observed that both SG and SL additives significantly reduced the bitumen drainage rate. While the SMA mixtures exhibited high drainage values of around 0.34%, the modified mixtures reduced this rate to below 0.1%. This difference can be attributed to the increased viscosity of the modified binder and the micro-porous structure of the fibers, which physically retain the bitumen. Furthermore, the bitumen drainage values of SL-modified mixtures were lower compared to those of the SG series. Due to their larger surface area, SL fibers effectively absorbed the bitumen phase and minimized drainage.

4.3.4. Sand Patch Test Results

In the test conducted to determine the surface texture roughness of the SMA mixtures, the surface texture depth values of all series are presented in Figure 21.

In the graph, it is observed that the surface texture depth (STD) values decrease with increasing fiber content and modification ratio. In the B-SMA series, the surface texture depth was 3.09 mm, and as the modification rate increased, this value gradually decreased to 2.30 mm in the E1.8 series, corresponding to a 26% reduction. In the fiber-modified

mixtures, both the SG and SL series exhibited lower surface roughness, with average values ranging between 1.6 and 1.8 mm. This represents a reduction of approximately 40–50% compared to the unmodified SMA mixture. This decrease in STD indicates that the voids between aggregates are reduced and the bitumen is distributed more uniformly on the surface. As the modification ratio increases, a reduction in STD values is observed for both fiber types, which can be explained by the densification of the mixture. The STD values of the SL fiber-modified mixtures are slightly lower compared to those of the SG series. This can be attributed to the more elastic structure of cellulose fibers, which creates a smoother surface texture within the mixture.

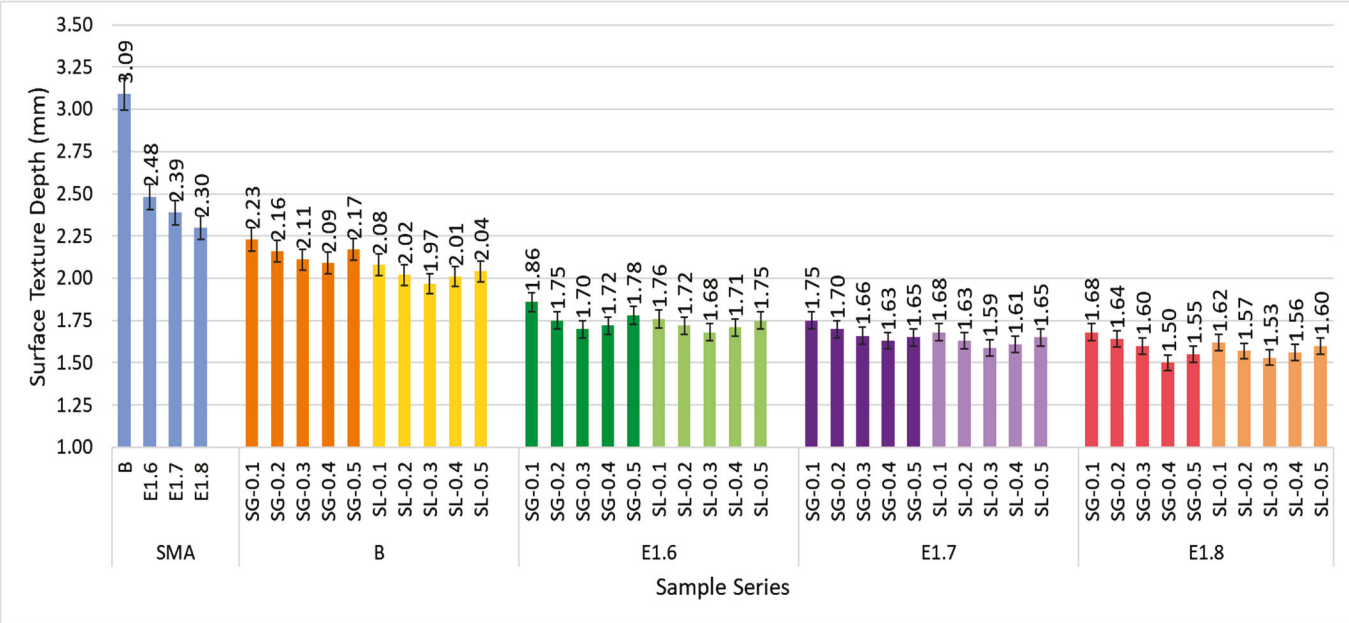

Figure 21. Sand Patch test results of all SMA series.

4.3.5. Cantabro Test Results

The test results obtained to measure the resistance of the SMA mixtures against fragmentation are presented in Figure 22.

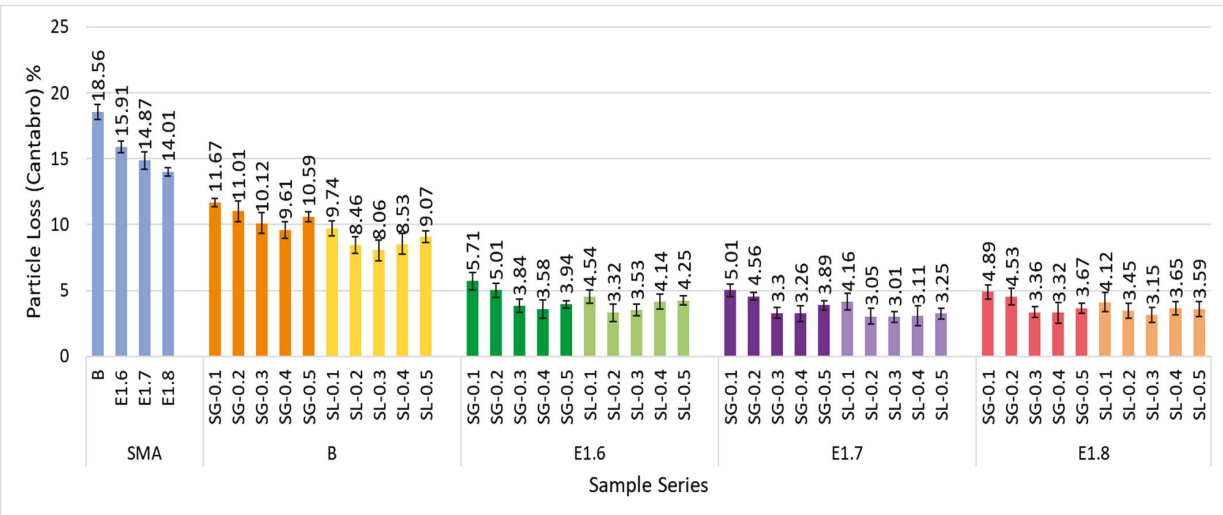

Figure 22. Cantabro test results of all SMA series.

When the mixtures are evaluated as a whole, it is observed that the amount of particle loss decreases with the increase in the modification ratio. This improvement can be

attributed to the enhanced viscosity of the modified bitumen and the better coating of aggregates due to the reinforcing effect of the fibers. The SL fiber-modified mixtures exhibited slightly lower particle loss compared to the SG fiber-modified mixtures, which can be explained by the micro-bonding reinforcement effect of cellulose fibers that enhances the cohesion within the mixture. Both types of additives provided more than a 70% improvement in abrasion resistance compared to the mixtures prepared with pure bitumen.

4.3.6. Cost Analysis

In this study, the cost analysis was conducted based solely on the bitumen, Elvaloy RET, and fiber components (either industrial cellulose or cellulose acetate fibers recovered from cigarette butts) contained in the mixtures. The unit prices were taken as follows: bitumen \$0.37/kg, Elvaloy RET \$6.01/kg, industrial cellulose fiber \$0.60/kg, and SG fiber recovered from cigarette waste \$0.29/kg. The SG fibers are produced through a chemical cleaning and recovery process; therefore, their pricing was determined based on the cleaning and processing costs. The cost analysis was performed by comparing each SMA series containing SG fibers with the corresponding SMA mixture containing the same amount of SL, which was taken as the reference. For each mixture ratio within the series, the optimum bitumen percentage, bitumen quantity (kg), bitumen cost, Elvaloy RET cost, fiber cost, and total cost were calculated. The average values of the five mixture ratios were then summarized and presented in the corresponding columns of the cost comparison tables for each series (Table 10).

Table 10. Average cost analysis of all SMA series.

Series	Opt. Bitumen (%)	Bitumen (kg)	Bitumen Cost ($)	Elvaloy Cost ($)	Fiber Cost ($)	Total ($/t)	Difference in SG Compared to SL ($)
B-SG	5.48	54.76	20.37	0	0.87	21.24	−1.68 (-cost saving)
B-SL	5.62	56.56	20.89	0	1.8	22.92	
E1.6-SG	6.02	59.46	22.16	5.73	0.87	28.76	−2.15 (-cost saving)
E1.6-SL	6.14	61.42	22.87	5.91	1.8	30.91	
E1.7-SG	6.08	60.82	22.63	6.21	0.87	29.8	−1.64 (-cost saving)
E1.7-SL	6.17	61.64	22.96	6.31	1.8	31.44	
E1.8-SG	6.04	60.78	22.46	6.65	0.87	30	−2.53 (-cost saving)
E1.8-SL	6.33	63.32	23.59	6.85	1.8	32.53	

In all series, the SG fiber-modified mixtures were found to be, on average, 1.7–2.5 \$/t less costly than the corresponding SL fiber-modified mixtures. The largest cost difference was observed in the E1.8 series (≈2.5 \$/t), while the smallest difference occurred in the E1.7 series (≈1.6 \$/t). Overall, the use of SG fibers in SMA mixtures provided a cost saving of approximately 6–8% compared to the use of conventional SL fibers.

5. Conclusions

In this study, the usability of cellulose acetate (SG) fibers recycled from cigarette butts as an alternative to the conventional cellulose (SL) fibers commonly used in the literature was investigated in Stone Mastic Asphalt (SMA) mixtures. In addition to the binder tests applied to neat and Elvaloy RET + PPA-modified bitumens, the performance tests carried out on SMA mixtures were also comprehensively evaluated, and significant improvements were obtained at both levels.

In terms of mixture performance, the combined use of fibers and modified bitumen provided notable improvements in Marshall stability, Marshall quotient, indirect tensile strength (ITS) and tensile strength ratio (TSR) values. Compared to SMA mixtures prepared with neat bitumen, stability performance increased significantly in the series where fibers and modified bitumen were used. Regarding ITS, the best results were obtained in the E1.6 series in mixtures where both SG and SL fibers were used; TSR values reached the highest levels, especially in the E1.6 and E1.7 mixtures.

Binder drainage decreased to the lowest levels in mixtures where fibers and modification were used together, and both fiber types effectively retained the bitumen, significantly reducing binder loss. Surface texture and Cantabro particle loss results showed that the fibers exhibited a homogeneous distribution within the mixture, reduced surface roughness, and significantly improved the mixture's particle loss resistance when used at certain proportions. The cost analysis revealed that SG fibers offer a generally more economical option compared to traditional SL fibers in terms of production and application.

As a result, recycled cellulose acetate fibers stand out as an additive that, when used at low dosages (0.3–0.4%), improves bitumen retention, reduces drainage, enhances the mechanical performance of the mixture, and provides cost advantages without adversely affecting the workability of SMA mixtures. However, for widespread industrial-scale use, the production process needs to be optimized, fiber properties need to be standardized, and the environmental impacts of the additive should be investigated within the scope of life-cycle assessment. In addition, considering the lack of literature on the recycling performance of SMA mixtures containing SG fibers, it is recommended that this issue be supported with more comprehensive studies in the future.

Author Contributions: Conceptualization, H.V.M. and C.Ö.; methodology, H.V.M. and C.Ö.; validation, C.Ö.; investigation, H.V.M.; resources, C.Ö.; data curation, H.V.M.; writing—original draft preparation, H.V.M.; writing—review and editing, H.V.M. and C.Ö.; visualization, H.V.M.; supervision, C.Ö. All authors have read and agreed to the published version of the manuscript.

Funding: This research received no external funding.

Data Availability Statement: The original contributions presented in this study are included in the article. Further inquiries can be directed to the corresponding author.

Acknowledgments: This study is derived from Hande Varol Morova's PhD thesis prepared at the Graduate Education Institute of Isparta University of Applied Sciences.

Conflicts of Interest: The authors declare no conflicts of interest. The funders had no role in the design of the study; in the collection, analyses, or interpretation of data; in the writing of the manuscript, or in the decision to publish the results.

References

1. Moghaddam, T.B.; Karim, M.R.; Syammaun, T. Dynamic properties of stone mastic asphalt mixtures containing waste plastic bottles. *Constr. Build. Mater.* **2012**, *34*, 236–242. [CrossRef]
2. Evirgen, B.; Çetin, A.; Karslıoğlu, A.; Tuncan, A. An evaluation of the usability of glass and polypropylene fibers in SMA mixtures. *Pamukkale Univ. J. Eng. Sci.* **2021**, *27*, 318–328. [CrossRef]
3. Keyf, S. Investigation of penetration and penetration index in bitumen modified with SBS and reactive terpolymer. *Sigma J. Eng. Nat. Sci.* **2010**, *28*, 26–34.
4. Seloğlu, M.; Geçkil, T. The effect of reactive terpolymer on the consistency and temperature susceptibility of bitumen. *Firat Univ. J. Eng. Sci.* **2019**, *31*, 203–213.
5. Şengöz, B.; Işıkyakar, G. Evaluation of the properties and microstructure of SBS and EVA polymer modified bitumen. *Constr. Build. Mater.* **2008**, *22*, 1897–1905. [CrossRef]
6. Kordi, Z.; Shafabakhsh, G. Evaluating mechanical properties of stone mastic asphalt modified with nano Fe_2O_3. *Constr. Build. Mater.* **2017**, *134*, 530–539. [CrossRef]
7. Arshad, A.K.; Shaffie, E.; Hashim, W.; Ismail, F.; Masri, K.A. Evaluation of nanosilica modified stone mastic asphalt. *Int. J. Civ. Eng. Technol.* **2019**, *10*, 1508–1516.
8. Gong, M.; Yang, J.; Yao, H.; Wang, M.; Niu, X.; Haddock, J.E. Investigating the performance, chemical, and microstructure properties of carbon nanotube-modified asphalt binder. *Road Mater. Pavement Des.* **2018**, *19*, 1499–1522. [CrossRef]
9. Irfan, M.; Saeed, M.; Ahmed, S.; Ali, Y. Performance evaluation of elvaloy as a fuel-resistant polymer in asphaltic concrete airfield pavements. *J. Mater. Civ. Eng.* **2017**, *29*, 04017163. [CrossRef]
10. Geçkil, T. Physical, chemical, microstructural and rheological properties of reactive terpolymer-modified bitumen. *Materials* **2019**, *12*, 921. [CrossRef]

11. Taciroğlu, M.V. Comparison of elvaloy and styrene-butadiene-styrene added polymer modified bitumen. *J. Innov. Transp.* **2023**, *4*, 25–32. [CrossRef]
12. Vachhani, K.K.; Mishra, C. Influence of VG30 grade bitumen with and without reactive ethylene terpolymer (Elvaloy® 4170) in short-term aging. *Int. J. Curr. Eng. Technol.* **2014**, *4*, 4206–4209.
13. Inocente Domingos, M.D.; Faxina, A.L. Accelerated short-term ageing effects on the rheological properties of modified bitumens with similar high PG grades. *Road Mater. Pavement Des.* **2015**, *16*, 469–480. [CrossRef]
14. Jasso, M.; Hampl, R.; Vacin, O.; Bakos, D.; Stastna, J.; Zanzotto, L. Rheology of conventional asphalt modified with SBS, Elvaloy and polyphosphoric acid. *Fuel Process. Technol.* **2015**, *140*, 172–179. [CrossRef]
15. Gedik, A. Utilising cellulose fibre in stone mastic asphalt. *Građevinar* **2023**, *75*, 775–784. [CrossRef]
16. Fauzi, N.M.; Masri, K.A.; Ramadhansyah, P.J.; Samsudin, M.S.; Ismail, A.; Arshad, A.K.; Hainin, M.R. Volumetric properties and resilient modulus of stone mastic asphalt incorporating cellulose fiber. In *IOP Conference Series: Materials Science and Engineering*; IOP Publishing: Bristol, UK, 2020; Volume 712, p. 012028. [CrossRef]
17. Gallo, P.; Valentin, J.; Mondschein, P. Asphalt concrete for binder courses with different jute fibre content. In *IOP Conference Series: Materials Science and Engineering*; IOP Publishing: Bristol, UK, 2021; Volume 1203, p. 032041. [CrossRef]
18. Shaffie, E.; Rashid, H.A.; Shiong, F.; Arshad, A.K.; Ahmad, J.; Hashim, W.; Masri, K.A. Performance characterization of stone mastic asphalt using steel fiber. *J. Adv. Ind. Technol. Appl.* **2021**, *2*, 22–33. [CrossRef]
19. Ma, R.; Haldenbilen, S.; Zengin, D. Investigation of usability of mineral fiber in stone mastic asphalt. *Rev. Constr.* **2023**, *22*, 569–580. [CrossRef]
20. Alonso-Troyano, C.; Llopis-Castelló, D.; Olaso-Cerveró, B. Incorporating recycled textile fibers into stone mastic asphalt. *Buildings* **2025**, *15*, 1310. [CrossRef]
21. Zoorob, S.E.; Suparma, L.B. Laboratory design and investigation of the properties of continuously graded asphaltic concrete containing recycled plastics aggregate replacement (Plastiphalt). *Cem. Concr. Compos.* **2000**, *22*, 233–242. [CrossRef]
22. Morova, N. Use of waste phonolite as filler material in flexible asphalt pavements. *Mater. Sci.* **2024**, *30*, 96–105. [CrossRef]
23. Rodríguez, W.; Rivera, J.; Sevillano, M.; Torres, T. Performance evaluation of stone mastic asphalt (SMA) mixtures with textile waste fibres. *Constr. Build. Mater.* **2024**, *455*, 139125. [CrossRef]
24. Ahlawat, Y.; Bhardawaj, A.; Bhardwaj, R. An experimental study on the stability and flow characteristics of mastic asphalt mix using cigarette butt additive. *Mater. Today Proc.* **2022**, *65*, 651–661. [CrossRef]
25. Farzadkia, M.; Yavary Nia, M.; Yavari Nia, M.; Shacheri, F.; Nourali, Z.; Torkashvand, J. Reduction of the environmental and health consequences of cigarette butt recycling by removal of toxic and carcinogenic compounds from its leachate. *Environ. Sci. Pollut. Res.* **2024**, *31*, 23942–23950. [CrossRef] [PubMed]
26. Rahman, M.T.; Mohajerani, A.; Giustozzi, F. Possible use of cigarette butt fiber modified bitumen in stone mastic asphalt. *Constr. Build. Mater.* **2020**, *263*, 120134. [CrossRef]
27. Mohajerani, A.; Kurmus, H.; Rahman, M.T.; Smith, J.V.; Woo, S.S.; Jones, D.; Calderón, C. Bitumen and paraffin wax encapsulated cigarette butts: Physical properties and leachate analysis. *Int. J. Pavement Res. Technol.* **2022**, *15*, 931–947. [CrossRef]
28. Gallo, P.; Valentin, J. Study on use of two types of waste cigarette filters in asphalt mixtures. In *International Conference Series on Geotechnics, Civil Engineering and Structures, Proceedings of the 7th International Conference on Geotechnics, Civil Engineering and Structures, CIGOS 2024, Ho Chi Minh City, Vietnam, 4–5 April 2024*; Springer Nature: Singapore, 2024; pp. 638–646.
29. Jin, J.; Wu, Z.; Song, J.; Liu, X. Research on the road performance of cigarette butts modified asphalt mixture. In *Journal of Physics: Conference Series*; IOP Publishing: Bristol, UK, 2019; Volume 1168, p. 022053. [CrossRef]
30. Tataranni, P.; Sangiorgi, C. A preliminary laboratory evaluation on the use of shredded cigarette filters as stabilizing fibers for stone mastic asphalts. *Appl. Sci.* **2021**, *11*, 5674. [CrossRef]
31. Guo, Y.; Tataranni, P.; Tarsi, G.; Sangiorgi, C. Performance evaluation of stone mastic asphalt reinforced with shredded waste e-cigarette butts. *Case Stud. Constr. Mater.* **2024**, *20*, e03126. [CrossRef]
32. Al-Ameri, N.A.H.; Ramadhansyah, P.J. Performance of asphalt mixture incorporated encapsulated cigarette butts as bitumen modifier. *Construction* **2022**, *2*, 10–21. [CrossRef]
33. Hu, X.; Chen, X.; Yu, J.; Cheng, G.; Yuan, Y.; Zhang, L. Physical properties and rheological characteristics of cigarette butt-modified asphalt binders. *Coatings* **2025**, *15*, 170. [CrossRef]
34. General Directorate of Highways. *State Highways Technical Specifications (HTS)*; General Directorate of Highways: Ankara, Turkey, 2013.
35. *TS EN 1097-6*; Tests for Mechanical and Physical Properties of Aggregates–Part 6: Determination of Particle Density and Water Absorption. Turkish Standards Institution (TSE): Ankara, Turkey, 2013.
36. *TS EN 1097-7*; Tests for Mechanical and Physical Properties of Aggregates–Part 7: Determination of the Particle Density of Filler–Pyknometer Method. Turkish Standards Institution (TSE): Ankara, Turkey, 2008.
37. *ASTM D2041*; Standard Test Method for Theoretical Maximum Specific Gravity and Density of Asphalt Mixtures (Rice Test). ASTM International: West Conshohocken, PA, USA, 2019.

38. *AASHTO T 96*; Standard Method of Test for Resistance to Degradation of Small-Size Coarse Aggregate by Abrasion and Impact in the Los Angeles Machine. American Association of State Highway and Transportation Officials (AASHTO): Washington, DC, USA, 2019.
39. *TS EN 1097-1*; Tests for Mechanical and Physical Properties of Aggregates–Part 1: Determination of the Resistance to Wear (Micro-Deval Test). Turkish Standards Institution (TSE): Ankara, Turkey, 2011.
40. *TS EN 1367-2*; Tests for Thermal and Weathering Properties of Aggregates–Part 2: Magnesium Sulfate Test. Turkish Standards Institution (TSE): Ankara, Turkey, 2010.
41. *BS 812*; Methods for Determination of Particle Shape: Flakiness Index. British Standards Institution (BSI): London, UK, 1989.
42. *ASTM D1664*; Standard Test Method for Coating and Stripping of Bitumen–Aggregate Mixtures. ASTM International: West Conshohocken, PA, USA, 2017.
43. *TS EN 933-9*; Tests for Geometrical Properties of Aggregates–Part 9: Assessment of Fines–Methylene Blue Test. Turkish Standards Institution (TSE): Ankara, Turkey, 2010.
44. *TS EN 12591*; Bitumen and Bituminous Binders–Specifications for Paving Grade Bitumens. Turkish Standards Institution (TSE): Ankara, Turkey, 2011.
45. *TS EN 14023*; Bitumen and Bituminous Binders–Framework Specification for Polymer Modified Bitumens. Turkish Standards Institution (TSE); Turkish and European Standard: Ankara, Turkey, 2006.
46. Anonim. What Is ELVALOY™ 5160 Copolymer? Available online: https://www.dow.com/en-us/pdp.elvaloy-5160-copolymer.1891824z.html#overview (accessed on 8 February 2025).
47. *ASTM D792*; Standard Test Methods for Density and Specific Gravity (Relative Density) of Plastics by Displacement. ASTM International: West Conshohocken, PA, USA, 2020.
48. *ISO 1183*; Plastics–Methods for Determining the Density of Non-Cellular Plastics. International Organization for Standardization (ISO): Geneva, Switzerland, 2019.
49. *ASTM D1238*; Standard Test Method for Melt Flow Rates of Thermoplastics by Extrusion Plastometer. ASTM International: West Conshohocken, PA, USA, 2020.
50. *ISO 1133*; Plastics–Determination of the Melt Mass-Flow Rate (MFR) and Melt Volume-Flow Rate (MVR) of Thermoplastics. International Organization for Standardization (ISO): Geneva, Switzerland, 2011.
51. *ASTM D3418*; Standard Test Method for Transition Temperatures of Polymers by Differential Scanning Calorimetry. ASTM International: West Conshohocken, PA, USA, 2015.
52. *ISO 3146*; Plastics–Determination of Melting Behaviour (Melting Temperature or Melting Range) of Semi-Crystalline Polymers by Differential Scanning Calorimetry. International Organization for Standardization (ISO): Geneva, Switzerland, 2000.
53. Kurt, Y. Experimental Investigation of the Use of Waste Paper Cups in Stone Mastic Asphalt Mixtures. Master's Thesis, Graduate Education Institute, Isparta University of Applied Sciences, Isparta, Turkey, 2025.
54. Blazejowski, K. *Stone Matrix Asphalt: Theory and Practice*; CRC Press: Boca Raton, FL, USA, 2016.
55. Herrera-Puerta, C.F.; Suspes-García, S.; Galindres-Jimenez, D.M.; Cifuentes-Galindres, D.; Tinoco, L.E.; Piraján, J.C.M.; Murillo-Acevedo, Y. Exploring the thermal decomposition of cigarette butts and its role in chromium adsorption processes. *Heliyon* **2025**, *11*, e42162. [CrossRef]
56. Rahman, M.T.; Mohajerani, A. Thermal conductivity and environmental aspects of cigarette butt modified asphalt. *Case Stud. Constr. Mater.* **2021**, *15*, e00569. [CrossRef]
57. Liu, H.; Chen, Y.; Xue, Y. Reutilization of Recycled Cellulose Diacetate from Discarded Cigarette Filters in Production of Stone Mastic Asphalt Mixtures. *Front. Mater.* **2021**, *8*, 770150. [CrossRef]
58. Zhang, H.; Yu, J.; Wu, S. Effect of montmorillonite organic modification on ultraviolet aging properties of SBS modified bitumen. *Constr. Build. Mater.* **2012**, *27*, 553–559. [CrossRef]
59. Mohammadiroudbari, M.; Tavakoli, A.; Aghjeh, M.K.R.; Rahi, M. Effect of Nanoclay on the Morphology of Polyethylene Modified Bitumen. *Constr. Build. Mater.* **2016**, *116*, 245–251. [CrossRef]
60. Ansar, M.; Sikandar, M.A.; Althoey, F.; Tariq, M.A.U.R.; Alyami, S.H.; Elsayed Elkhatib, S. Rheological, Aging, and Microstructural Properties of Polycarbonate and Polytetrafluoroethylene Modified Bitumen. *Polymers* **2022**, *14*, 3283. [CrossRef] [PubMed]
61. Yu, J.; Wang, L.; Zeng, X.; Wu, S.; Li, B. Effect of Montmorillonite on Properties of Styrene–Butadiene–Styrene Copolymer Modified Bitumen. *Polym. Eng. Sci.* **2007**, *47*, 1289–1295. [CrossRef]
62. *TS EN 13399*; Bitumen and Bituminous Binders–Determination of Storage Stability of Modified Bitumen. Turkish Standards Institution (TSE): Ankara, Turkey, 2018.
63. *TS EN 13398*; Bitumen and Bituminous Binders–Determination of Elastic Recovery. Turkish Standards Institution (TSE): Ankara, Turkey, 2010.
64. Sağlık, A.; Orhan, F.; Güngör, A.G. *BSK Kaplamalı Yollar Için Bitüm Sınıfı Seçim Haritaları*; Ulaştırma, T.C., Ed.; Denizcilik ve Haberleşme Bakanlığı Karayolları Genel Müdürlüğü: Ankara, Türkiye, 2012. (In Turkish)

65. *ASTM D1559*; Standard Test Method for Resistance to Plastic Flow of Bituminous Mixtures Using Marshall Apparatus. ASTM International: West Conshohocken, PA, USA, 1989.
66. Yalçın, E. The Assessment of the Effects of Hydrated Lime Usage as Filler on the Performance of Mixtures Prepared with Modified Bitumen. Master's Thesis, Graduate School of Natural and Applied Sciences, Fırat University, Elazig, Turkey, 2014.
67. *ASTM D6931-17*; Standard Test Method for Indirect Tensile (IDT) Strength of Bituminous Mixtures. ASTM International: West Conshohocken, PA, USA, 2017.
68. *AASHTO T 283*; Standard Method of Test for Resistance of Compacted Asphalt Mixtures to Moisture-Induced Damage. American Association of State Highway and Transportation Officials (AASHTO): Washington, DC, USA, 2014.
69. Durmaz, A.C.; Morova, N. Investigation of performance properties of milled carbon fiber reinforced hot mix asphalt. *Mater. Sci.* **2024**, *30*, 87–95. [CrossRef]
70. *ASTM E965*; Standard Test Method for Measuring Pavement Macrotexture Depth Using a Volumetric Technique (Sand Patch Test). ASTM International: West Conshohocken, PA, USA, 2015.
71. Özay, O.; Öztürk, E.A. Performance of modified porous asphalt mixtures. *J. Fac. Eng. Archit. Gazi Univ.* **2013**, *28*, 577–586.

Disclaimer/Publisher's Note: The statements, opinions and data contained in all publications are solely those of the individual author(s) and contributor(s) and not of MDPI and/or the editor(s). MDPI and/or the editor(s) disclaim responsibility for any injury to people or property resulting from any ideas, methods, instructions or products referred to in the content.

materials

MDPI

Article

Characterization of Viscoelastic Performance and VOC Emission of Warm-Mixed SBS Asphalt Binder Under Different Dosages of Warm-Mixed Additive

Wentao Wang [1], Yue Yang [1], Mengxue Xu [1], Xiangrui Han [1], Yinghao Miao [1,*] and Linbing Wang [2,*]

[1] National Center for Materials Service Safety, University of Science and Technology Beijing, Beijing 100083, China; wentaowang@ustb.edu.cn (W.W.)
[2] The Sensing and Perception Lab, School of Environmental, Civil, Agricultural and Mechanical Engineering, University of Georgia, Athens, GA 30602, USA
* Correspondence: miaoyinghao@ustb.edu.cn (Y.M.); linbing.wang@uga.edu (L.W.)

Abstract

Warm-mixed asphalt technology can significantly reduce the heating temperatures required for asphalt pavement construction, which makes it one of the crucial technical approaches in road engineering for achieving energy conservation and emission reduction, and carbon neutrality. Existing research often focuses on designing asphalt materials to ensure optimal service performance, but insufficient attention has been paid to the specific extent of reduction in asphalt fume emissions. However, the latter is a critical factor that cannot be neglected when constructing asphalt pavements in environmentally sensitive regions. Considering the environmental factor, this study systematically explores the comprehensive influence of different warm-mixed additive dosages on the viscoelastic properties and VOC emissions of warm-mixed SBS asphalt binder using rotational viscosity, bending beam rheometer (BBR), dynamic shear rheometer (DSR), and gas chromatography–mass spectrometry (GC-MS) test methods. The findings show that the application of warm-mixed additive does not compromise the comprehensive properties of SBS asphalt binder, but partially enhances its service performance instead. Due to the significant reduction in heating temperature, asphalt VOC emissions are indirectly reduced. Although the warm-mixed additive possesses a certain degree of volatility, its application still shows a significant trend toward emission reduction. Despite 0.4% being a relatively economical dosage of warm-mixed additive, a slight increase to 0.5% can achieve more pronounced environmental benefits in VOC emission reduction while maintaining comprehensive service performance that meets specification requirements. The findings can provide new insights for the application and decision-making of warm-mixed asphalt technology in environmentally sensitive regions.

Keywords: warm-mixed asphalt binder; rotational viscosity; viscoelastic performance; VOC emission; additive dosage

1. Introduction

Styrene–Butadiene–Styrene (SBS)-modified asphalt binder is commonly used in the middle and surface layers of asphalt pavements. During the construction process of asphalt pavement, raw materials such as asphalt and aggregate need to be heated and mixed at temperatures ranging from 150 °C to 180 °C, followed by processes of transportation, paving, and compaction at temperatures above 135 °C [1]. All these construction stages

involve high-temperature heating, which leads to significant energy consumption and noticeable asphalt volatile organic compound (VOC) emissions [2,3], as shown in Figure 1. Warm-mixed asphalt technology serves as one of the crucial technical approaches in road engineering [4–7] for achieving energy conservation and emission reduction, as well as carbon neutrality [8,9]. It enables a substantial reduction in the required heating temperature for asphalt binder, thereby significantly decreasing energy consumption and carbon emissions during the construction process.

(**a**) Mixing (**b**) Paving

(**c**) Compacting

Figure 1. Obvious asphalt VOC emissions during construction procedures of asphalt layers.

Warm-mixed asphalt technology is often applied to asphalt pavement, accompanied by environmentally friendly research topics. Li et al. [10] explored the effects of rubber absorption on the aging resistance of hot and warm asphalt rubber binders prepared with waste tire rubber. The warm-mixed additives were found to affect the asphalt rubber sample's rheological properties, but its aging resistance was not compromised. Doyle et al. [11] compared hot- and warm-mixed asphalt rutting performance, and found that a hot asphalt mixture was similar to or slightly better than a warm-mixed asphalt mixture. Abd El-Hakim et al. [12] also discussed the difference between the moisture susceptibility of hot and warm mix asphalts in two aspects of laboratory and field experimental methods. The findings in their study indicated that small differences in moisture susceptibility were found between these two asphalt materials. Thus, the warm-mixed asphalt technology can satisfy the technical requirements of asphalt pavement materials well under the background of being green and low-carbon, and providing environmental protection.

Attention has also been paid to asphalt VOC emissions recently. Borinelli et al. [13] investigated the VOC emission features of commercial base asphalt and crumb-rubber-modified asphalt binder with a fixed dosage of crumb rubber particles. In their study, the influence of two heating processes (step-by-step raising and incremental increase) on VOC emission rates were evaluated. Lei et al. [14] discussed VOC emission at three temperatures

https://doi.org/10.3390/ma19030485

with the rheological properties of different asphalt binder samples. They found that the complex-flow activation energy increased after VOC emission, while naphthalene content exhibited a better linear relation with activation energy. Mo et al. [15] found that hazardous potentials of asphalt fumes varied with asphalt source and mixing temperature. They suggested that proper material selection and construction strategies might be chosen for hazard mitigation.

Variable parameters concerning the VOC emissions of warm-mixed asphalt binder were often discussed, which mainly included categories of warm-mixed additive or base asphalt, warm-mixed additive dosages, heating duration, heating temperature values, stirring speed, and duration. However, these research studies did not explore the features of asphalt fume emissions from the perspective of engineering practice, but just discussed emission variation in variable parameters from an academic view. In the practical engineering application of warm-mixed asphalt technology, it is important to pay attention to how the service performance and emission characteristics of a warm-mixed asphalt mixture vary if the warm-mixed additive dosages are changed. Specifically, comprehensive effects of both heating temperature values and additive dosages should be taken into account to reach the same viscosity of warm-mixed asphalt binder for mixing, paving, and compacting processes, to ensure construction quality. Based on the analysis discussed above, research studies related to warm-mixed asphalt mixture primarily focused on designing asphalt materials to ensure optimal service performance, but insufficient attention has been paid to the specific extent of reduction in carbon-containing gas emissions, such as asphalt fumes. Yet, the latter is a crucial factor that must be considered for asphalt pavement construction in environmentally sensitive regions, such as urban residential zones, ecological reserves, and poorly ventilated (extra-long) tunnels [16–18]. As a result, warm-mixed asphalt technology often fails to deliver its full potential in terms of energy conservation, emission reduction, and environmental friendliness.

This study explored the comprehensive influence of different warm-mixed additive dosages on the viscoelastic properties and VOC emissions of warm-mixed SBS asphalt binder. Firstly, the viscosity–temperature characteristics of warm-mixed SBS asphalt binder were investigated using the rotational viscosity test method to establish experimental reference data for subsequent sample preparation. Subsequently, bending beam rheometer (BBR) and dynamic shear rheometer (DSR) test methods were employed to inspect the viscoelastic behaviors of asphalt materials at low and high temperatures, respectively. Finally, the gas chromatography–mass spectrometry (GC-MS) test method was applied to quantitatively analyze the composition of asphalt VOC emissions generated during the heating process, aiming to explore the emission characteristics associated with different warm-mixed additive dosages.

2. Materials and Sample Preparation

In this study, a typical SBS asphalt binder was selected to be the base material for warm-mixed modification with six additive dosages using a heating and stirring device, which include 0.0%, 0.2%, 0.3%, 0.4%, 0.5%, and 0.6% of the mass of the SBS asphalt binder, as shown in Figure 2. The warm-mixed additive applied in this study is a typical kind of surfactant admixture, which is developed by a local construction company in Beijing, China. Specifically, the 0.4% dosage is selected from the application of a warm-mixed asphalt mixture in an actual pavement constructing project. The basic physical properties of the SBS asphalt binder were inspected, and the relevant results are summarized in Table 1, which meet the requirements of the specification [19].

(**a**) Heating and stirring device (Lichen, Shaoxing, China) (**b**) Warm-mixed SBS asphalt binder with different additive dosages

Figure 2. Fabrication of the warm-mixed SBS asphalt binder.

Table 1. Physical properties of the SBS asphalt binder sample.

Items		Units	Requirements	Results
Penetration (25 °C, 100 g, 5 s)		0.1 mm	60–80	69
Softening point		°C	≥75	78.0
Ductility (5 cm/min)		cm	≥30 (5 °C)	39
Residue after rolling thin film oven test (163 °C, 85 min)	Mass loss	%	≤±1.0	−0.221
	Residual penetration ratio (25 °C, 100 g, 5 s)	%	≥60	68.1
	Residual ductility (5 cm/min)	cm	≥20 (5 °C)	23

The base material was first heated in an oven at 150 °C for about 3 h and melted into liquid state, which was then moved and mounted into the heating device for further modification. To reach the same viscosity of the mixing process in an asphalt layer construction, warm-mixed SBS asphalt binder with different additive dosages should need corresponding different heating and stirring temperatures. Therefore, the rotational viscosity test method was first applied in this study to characterize the viscosity–temperature relationship, and then to determine the relevant temperature values to fabricate warm-mixed SBS asphalt binder with different additive dosages. Accurately weighed additives were poured into the base SBS asphalt binder and continuously stirred with a speed of 500 r/min for about 20 min. Then, the fabricated warm-mixed SBS asphalt binder was poured into specific molds to prepare samples for rotational viscosity, BBR, DSR, and GC-MS experiments.

3. Test and Analysis Methods

3.1. The Rotational Viscosity Test Method

Asphalt materials should be heated and melted into liquid state with suitable viscosity values for both mixing and compacting stages to ensure good construction quality. The rotational viscosity test method was applied to measure the viscosities of the warm-mixed SBS asphalt binder with different additive dosages at 135 °C and 175 °C, respectively, as shown in Figure 3, and then the viscosity–temperature curve could be determined [20,21]. For pavement petroleum asphalt materials, the viscosity ranges suitable for mixing and compacting procedures are 0.17 Pa·s ± 0.02 Pa·s and 0.28 Pa·s ± 0.03 Pa·s, respectively [19]. Two parallel samples of each warm-mixed additive dosage were prepared for rotational viscosity evaluation. In this study, the additive dosage of 0.4% was selected as the reference

value due to its practical engineering application, and its viscosity value was thus referred to in order to determine the relevant heating temperatures for asphalt samples with different additive dosages.

Figure 3. The rotational viscosity device (Changji, Shanghai, China).

3.2. The BBR Test Method

The BBR method [22] was adopted to explore low-temperature viscoelastic properties of warm-mixed SBS asphalt binder with different additive dosages. As shown in Figure 4, a thin beam sample is located on two supports with a constant load of 980 mN ± 50 mN placed on its midspan, while the flexural deformation can be measured. The entire loading duration lasts about 240 s, while the BBR testing temperature was controlled at −12 °C in this study [23]. Three parallel samples of each warm-mixed additive dosage were prepared for BBR evaluation.

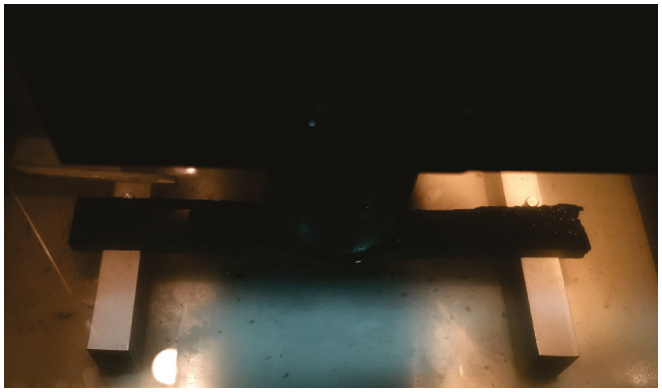

Figure 4. A sample of warm-mixed SBS asphalt binder in the BBR test.

The basic indicators of creep stiffness S and creep rate *m-value* can be calculated based on testing data measured at the 60th second, which mainly include creep mechanical stress and strain. The creep stiffness S reflects the magnitude of stress generated in the asphalt binder under thermal influence. A relative lower value of creep stiffness S indicates stronger resistance to stress variations induced by temperature, which means a better cracking resistance. The creep rate *m-value* reflects the relaxation capacity of asphalt binder and is positively correlated with the stress release rate. A relative higher value of the creep rate *m-value* denotes greater relaxation capacity and superior cracking resistance. Creep stiffness S and creep rate *m-value* can be further used to derive the index of m/S, which reflects the growth rate of creep compliance $D'(t)$, as shown in Equation (1). The detailed derivation processes of m/S can be found in the previous research [23,24]. A relative larger

value of m/S often indicates a larger value of $D'(t)$, which means a slower increase in creep stiffness S.

$$\frac{m(t)}{S(t)} \approx D'(t) \times t \tag{1}$$

The Burgers model, which contains characteristics of both the Maxwell and Kelvin models, can fit the creep compliance curve well in the BBR test. In the Burgers Equation (2) of creep compliance $D(t)$, E_1 and E_2 are the instantaneous elastic modulus and delayed elastic modulus, respectively, while both η_1 and η_2 are viscous coefficients. These viscoelastic parameters can be further used to derive indexes of relaxation time λ and the delay time τ, which are calculated by Equations (3) and (4). Relaxation time λ reflects the asphalt sample's ability to release internal stress, while delay time τ means creep and delayed elastic performance. A relative lower value of relaxation time λ indicates a better viscous performance, while a relative larger value of delay time τ usually means a much more viscous deformation, which means a better cracking resistance.

$$D(t) = \frac{\varepsilon(t)}{\sigma_o} = \frac{1}{E_1} + \frac{t}{\eta_1} + \frac{1}{E_2}\left(1 - e^{-t \cdot \frac{E_2}{\eta_2}}\right) \tag{2}$$

$$\lambda = \frac{\eta_1}{E_1} \tag{3}$$

$$\tau = \frac{\eta_2}{E_2} \tag{4}$$

3.3. The MSCR Test Method

The DSR device was applied to conduct the multiple stress creep and recovery (MSCR) test [25,26] to evaluate the high-temperature rheological behaviors of warm-mixed SBS asphalt binder with different additive dosages, as shown in Figure 5. The testing temperature was controlled at 64 °C in this study. Two parallel samples of each warm-mixed additive dosage were prepared for MSCR evaluation. A MSCR test often contains 30 cycles, which include the first 10 cycles for the 0.1 kPa preloading period, the subsequent 10 cycles for the 0.1 kPa formal loading stage, and the remaining 10 cycles for the 3.2 kPa formal loading duration. Every cycle includes a loading period of 1 s followed by a recovering period of 9 s, and the entire MSCR test lasts for 300 s. The 0.1 kPa is applied to simulate a typical light traffic loading and obtain performance of the asphalt binder within the linear viscoelastic range. The value of 3.2 kPa is designated to simulate representative heavy traffic loading and detect the asphalt material's nonlinear viscoelastic behaviors. The non-recoverable creep compliance J_{nr} for every creep recovery cycle can be determined based on Equation (5), where γ_{nr} and γ_0 are the initial strain and residual strain, respectively, for each cycle, and τ is the shear stress. A relative lower value of non-recoverable creep compliance J_{nr} means a stronger capacity of permanent deformation resistance. Meanwhile, a larger value of the creep recovery ratio R indicates a better ability of recovery resilience.

$$J_{nr} = \frac{\gamma_{nr} - \gamma_0}{\tau} \tag{5}$$

3.4. The VOC Emission Test Method

Asphalt fumes generated during constructing processes often contain small particulate matters and VOCs, which not only negatively impact air quality at construction sites but also pose potential irritation and health risks to workers. Asphalt VOCs mainly include aliphatic hydrocarbons (alkanes and alkenes), aromatic hydrocarbons, and oxygenated hydrocarbon derivatives, as well as CO_2, CO, NO_x, and SO_2. In this study, asphalt VOCs were generated and collected using the assembled test system, as shown in Figure 6.

https://doi.org/10.3390/ma19030485

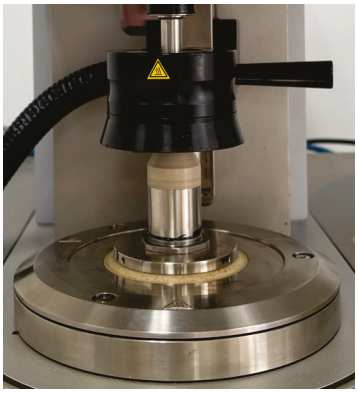

Figure 5. MSCR test using the DSR device (Anton Paar GmbH, Graz, Austria).

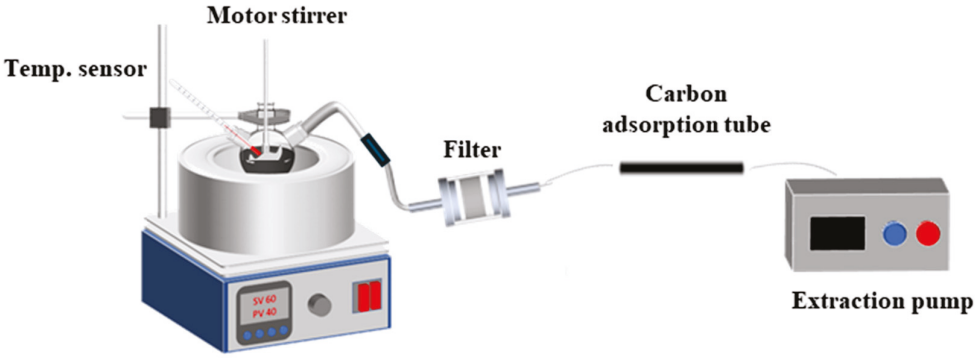

Figure 6. Schematic diagram of the asphalt VOC gas collection system.

For each group of warm-mixed SBS asphalt binder with different additive dosages, a 150 g sample was heated and maintained at its corresponding temperature for 30 min. The precision of temperature control is within 0.5 °C. To ensure a uniform heating effect, the asphalt sample was stirred at 1000 rpm throughout the process. An asphalt VOC sample of each warm-mixed additive dosage was prepared. The emitted asphalt fume was then drawn by an air pump at a flow rate of 0.5 L/min for 30 s and directed into an activated carbon adsorption tube for subsequent thermal desorption/purge-and-trap analysis using the GC-MS system, as shown in Figure 7. Specifically, small particulate matter present in the asphalt fumes was captured by the filter to prevent clogging the adsorption tube.

Figure 7. The GC-MS system (Agilent 7890B-5977B, Agilent Technologies Inc., Santa Clara, CA, USA).

4. Results and Discussions

4.1. Viscosity–Temperature Characteristics

The viscosities of warm-mixed SBS asphalt binder with different additive dosages were determined at both 135 °C and 175 °C using the rotational viscosity test method, as

shown in Figure 8. It is obviously proven that asphalt binder is a typical temperature-sensitive material. Compared with the control group of 0.0% warm-mixed additive dosage, the increase in dosages can significantly reduce the viscosities of SBS asphalt binder. At the relatively low temperature condition of 135 °C, the viscosities of warm-mixed asphalt binder show a clear decreasing trend as the additive dosages increase. In particular, when the dosage increases from 0.3% to 0.4%, a sharp and substantial drop trend in the viscosity curve is observed. At the relatively high temperature condition of 175 °C, although the control group's viscosity is already at a relative lower level, a further noticeable improvement in viscosity reduction is still evident with the increasing warm-mixed additive dosages. Therefore, the warm-mixed additive used in this study has a significant effect on reducing the viscosity of the SBS asphalt binder, while 0.4% is a relatively economical dosage with a good viscosity reduction.

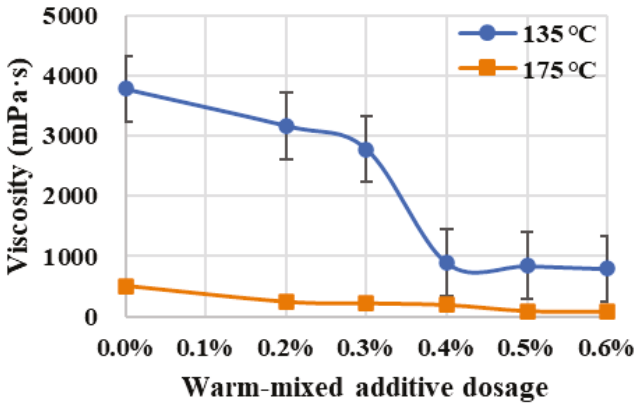

Figure 8. Viscosity variation in warm-mixed SBS asphalt binder with different additive dosages.

The viscosity–temperature curve is further applied to predict mixing and compacting temperatures according to the viscosity requirements of 0.17 Pa·s ± 0.02 Pa·s and 0.28 Pa· s ± 0.03 Pa·s, respectively [19], as shown in Figure 9. The predicted temperature curves exhibit decreasing trends with the increase in warm-mixed additive dosage. Specifically, the rate of temperature reduction slows within the dosage range of 0.2% to 0.4%. However, when the dosage is further increased from 0.4% to 0.5%, the mixing temperature still demonstrates a significant and substantial decrease. Therefore, the warm-mixed additive can effectively reduce the constructing temperatures of asphalt materials, and continually increasing the additive dosage from 0.4% to 0.5% yields a greater effect on temperature reduction.

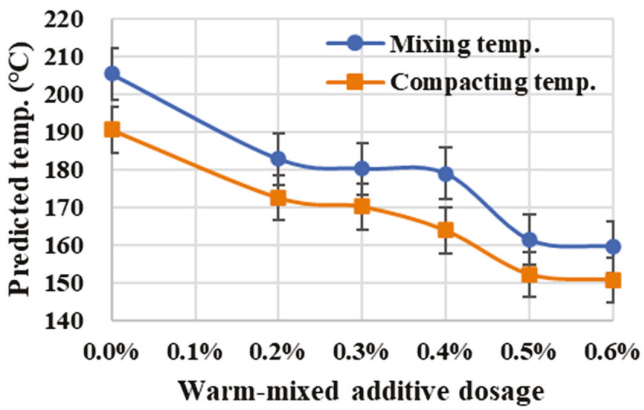

Figure 9. Predicted temp. variation in warm-mixed SBS asphalt binder with different additive dosages.

The warm-mixed SBS asphalt binder with 0.4% additive dosage was already applied in a practical engineering project of asphalt pavement construction. In this case, its viscosity value is thus selected as a reference in this study to determine relevant mixing temperatures for samples with other additive dosages. The viscosity–temperature curve was employed to predict heating temperatures required for warm-mixed SBS asphalt binder at other additive dosages to achieve the same viscosity, which is 269.1 mPa·s, as shown in Table 2. Specially, the 0.0% dosage group's temperature is predicted as 191.7 °C but exceeds the specification's requirement of 175 °C [19], thus its mixing temperature was directly determined at 175 °C with the viscosity of 512 mPa·s. The temperature values summarized in Table 2 establish the testing foundation of sample fabrication for subsequent performance evaluation.

Table 2. Suitable heating temperature values for warm-mixed SBS asphalt binder with different additive dosages to research the same viscosity (except for 0.0% dosage).

Warm-Mixed Additive Dosage	Viscosity	Heating and Stirring Temperature
0.0%	512 mPa·s	175.0 °C
0.2%	269.1 mPa·s	173.3 °C
0.3%		170.9 °C
0.4%		165.0 °C
0.5%		152.9 °C
0.6%		151.3 °C

4.2. Low-Temperature Viscoelastic Performance

The variation in the low-temperature creep stiffness *S* and the creep rate *m-value* of warm-mixed SBS asphalt binder with different additive dosages can be observed in Figure 10a. The values of creep stiffness *S* for all groups are measured within the range of 60–70 MPa, which are significantly lower than the upper limit of 300 MPa according to the specification [22]. It indicates that the application of warm-mixed additive does not cause the failure of asphalt materials. Compared with the control group, the application of warm-mixed additive resulted in slight increases in creep stiffness *S*. The values of creep stiffness *S* rise sharply to 69.3 MPa at the 0.2% dosage, then remain essentially stable within 0.3–0.5%, and finally increase to 69.8 MPa. The values of creep rate *m-value* for all groups are above 0.44, exceeding the standard requirement of 0.30 [22]. This implies that the warm-mixed SBS asphalt binder possesses a good capacity for rapid thermal stress dissipation induced by sudden temperature drops. The values of the creep rate *m-value* fluctuate slightly in the range of 0.2–0.4% relative to the control group, but show a slight upward trend at dosages of 0.5–0.6%.

The indicator of *m/S @ 60th* is positively related to the growth rate of creep compliance, but shares an opposite fluctuation with creep stiffness *S*. As shown in Figure 10b, the variation in *m/S @ 60th* for groups of warm-mixed SBS asphalt binder with different additive dosages exhibit an exactly one-to-one opposite relationship with the creep stiffness *S*. This indicates that the warm-mixed additive makes asphalt binder slightly stiffer with an increasing trend of creep stiffness *S* or a decreasing trend of *m/S @ 60th*, but it also increases or maintains the creep rate *m-value*, thereby improving its ability to withstand thermal stress.

The viscoelastic indicators of relaxation time λ and time τ are further determined to evaluate low-temperature viscoelastic behaviors of warm-mixed SBS asphalt binder with different additive dosages. As shown in Figure 10c, the values of relaxation time λ basically show a downwards trend, which means the viscous performance of warm-mixed SBS asphalt binder increases gradually with the additive dosage. The values of delay time τ are

https://doi.org/10.3390/ma19030485

slightly affected by the additive dosage. This indicates that higher additive dosages may help to add some viscous components of the asphalt binder, thereby further enhancing its cracking resistance.

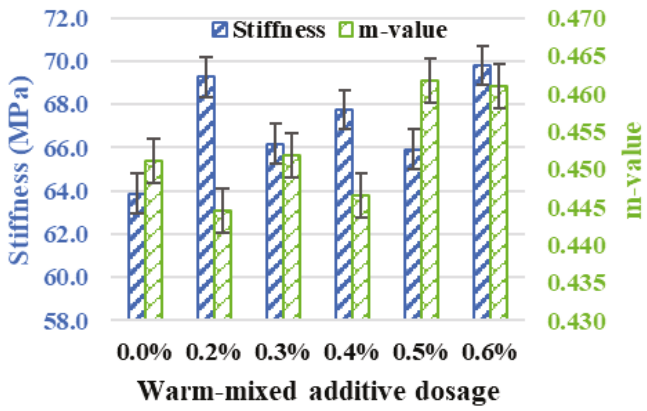

(**a**) Flexural creep stiffness *S* and creep rate *m-value*

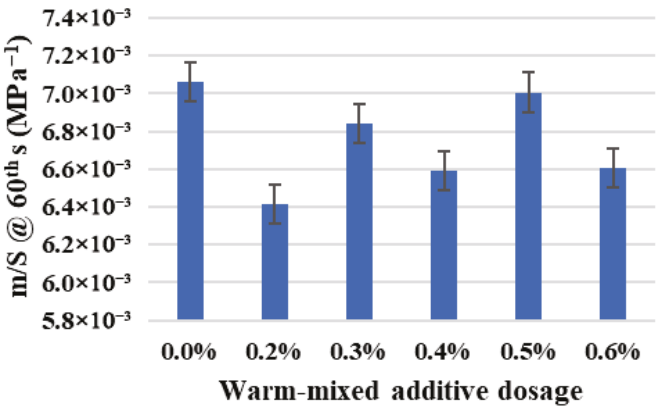

(**b**) m/S @ 60th s

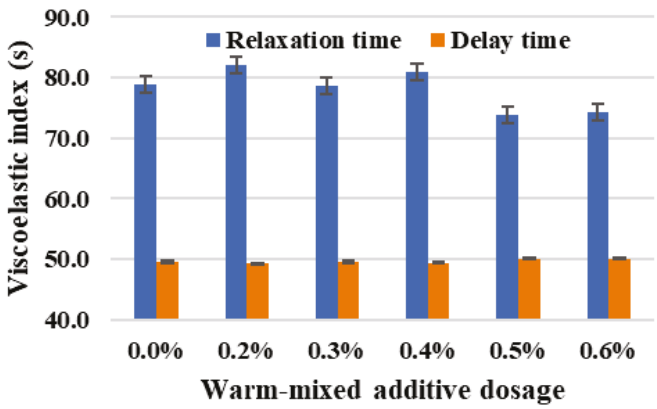

(**c**) Viscoelastic indicators

Figure 10. Variations in low-temperature indexes in BBR tests.

Taking the testing data of 0.4% additive dosage as the reference level, values of creep stiffness *S* and creep rate *m-value* for other groups fluctuate within ±5%. Given the normal variability of experimental data in scientific research, warm-mixed additive dosage has no significant impact on the low-temperature creep performance of warm-mixed SBS asphalt binder in this study. The application of warm-mixed additive leads to a slight

increase in low-temperature creep stiffness *S*, but the increase is limited and stabilizes with higher additive dosages. High dosages (>0.4%) further enhance the creep rate *m-value*, which improves the stress-relaxation capacity of asphalt binder. Taking the stability of low-temperature mechanical performance into account, the warm-mixed additive dosage range of 0.3–0.5% is strongly considered to be adopted.

4.3. High-Temperature Viscoelastic Performance

Variations in the high-temperature viscoelastic performance of warm-mixed SBS asphalt binder are determined using the MSCR method and presented in Figure 11. As shown in Figure 11a, creep-recovery shear-strain curves of different warm-mixed additive dosages are closely clustered in the 0.1 kPa loading period and visually illustrate no significant differences. This indicates that within the linear viscoelastic range under a relative light traffic loading, additive dosage has a minor effect on the high-temperature rheological properties of the warm-mixed SBS asphalt binder. However, the deformation resistance of different asphalt samples exhibits a notable difference when the MSCR test enters the 3.2 kPa heavy traffic loading stage. The control group shows a rapid growth in cumulative shear deformation with its curve positioned higher and limited recovery after unloading, which indicates a relatively weak high-temperature shear deformation resistance. In contrast, warm-mixed groups are tightly clustered near the bottom of the Figure, which exhibits relatively small peak values of shear strain and significant elastic recovery characteristics.

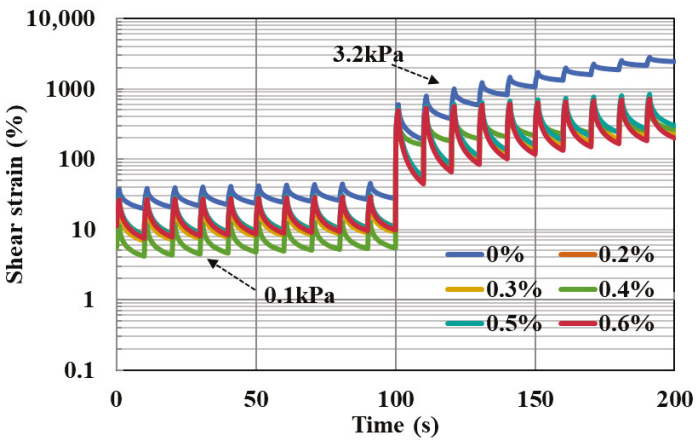

(**a**) Creep-recovery strain curves

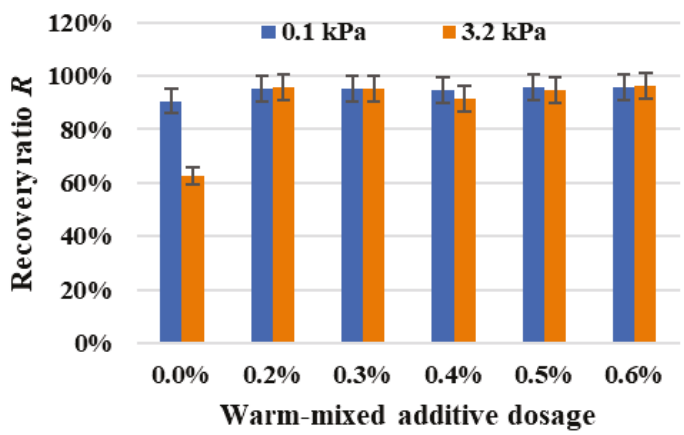

(**b**) Creep recovery ratio *R*

Figure 11. *Cont.*

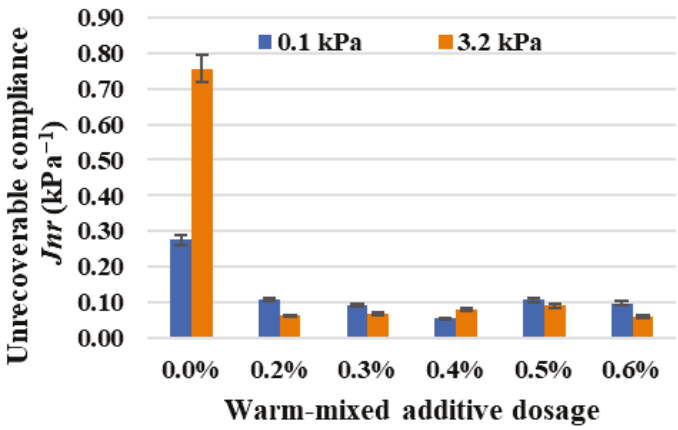

(**c**) Non-recoverable creep compliance J_{nr}

Figure 11. Variations in high-temperature indexes in MSCR tests.

The variations in non-recoverable creep compliance J_{nr} and creep recovery ratio R are shown in Figure 11b,c. In the 3.2 kPa heavy traffic loading stage, the control group without warm-mixed modification exhibits a high J_{nr} value of 0.76 kPa^{-1} and a low R value of 62.46%, but all modified groups show significant reductions in J_{nr} values to below 0.1 kPa^{-1} and obvious increases in R to above 91%. The J_{nr} values show a first increasing and then decreasing trend, and the R values exhibit the opposite trend to the additive dosage, while both the testing values of J_{nr} and R for all warm-mixed groups do not differ much. Specifically, both warm-mixed SBS asphalt binder samples with additive dosages of 0.4% and 0.5% show better relative high-temperature behaviors. The application of warm-mixed additive significantly enhances the high-temperature deformation resistance of SBS asphalt binder, while the improving effect is not obviously sensitive to the warm-mixed additive dosage.

4.4. VOC Emission Characteristics

The application of warm-mixed additive in SBS asphalt binder can decrease the heating temperature required to reach a certain viscosity. Quantitative analysis on asphalt VOCs using the GC-MS method can systematically reveal the coupling influence mechanism of temperature and warm-mixed additive dosage on asphalt VOC emissions. As shown in Figure 12, the GC-MS chromatograms indicate that the retention time ranges of chromatographic peaks generally remain stable under different temperature conditions. This means that the main volatile components possess relatively fixed molecular structures and diffusion characteristics. However, both chromatographic peaks' numbers and intensities rise significantly as the temperature increases, which means an increase in the variety of volatiles and a continuous enhancement in emission levels. The experimental analysis identifies nearly one hundred organic compounds from asphalt VOC emissions. These chemical compositions become more complex as heating temperatures increase. This is not only related to the accelerated diffusion rate of light fractions in asphalt VOCs but also potentially linked to partial thermal decomposition of both the SBS modifier and the warm-mixed additive at elevated temperatures. The warm-mixed additive itself contains a certain content of oxygenated components that are prone to volatilization upon the heating process. Its application increases the variety of volatile components at a relative lower temperature, such as 150 °C. When the warm-mixed additive dosage is reduced, a raised heating temperature is required for asphalt binder to achieve the same mixing viscosity. It often leads to a substantial release of hydrocarbon and aromatic components.

This indicates a clear indirect coupling effect between warm-mixed additive dosage and heating temperature.

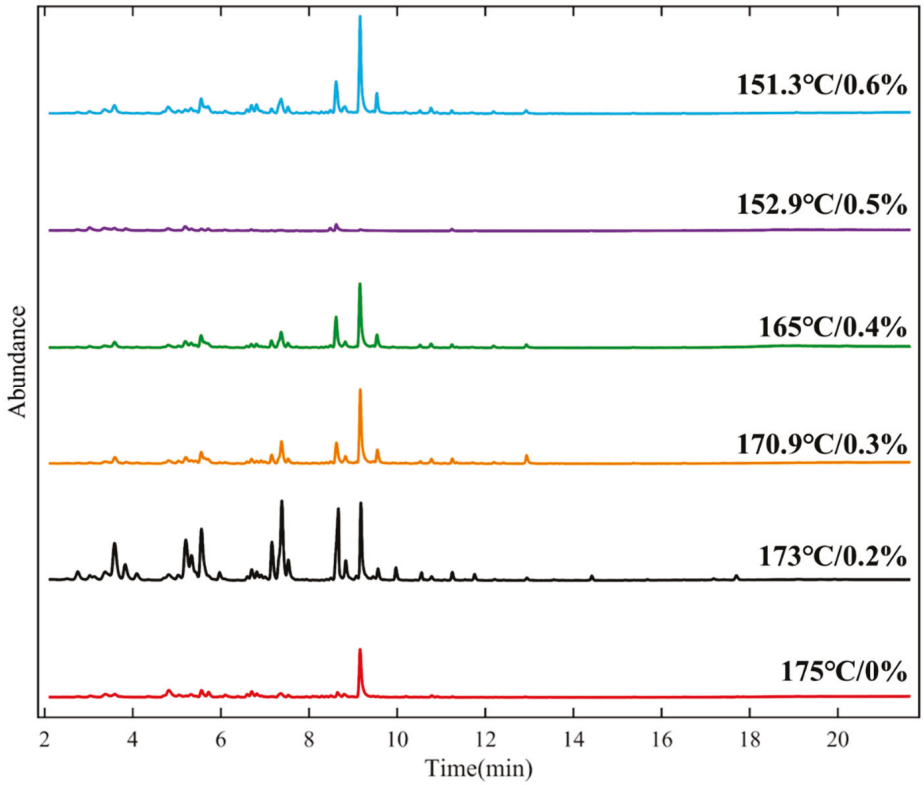

Figure 12. GC-MS chromatograms of warm-mixed SBS asphalt binder at different temperatures.

The proportion variation in different categories of VOCs exhibits significant selective release characteristics as temperature increases, as shown in Figure 13. This reflects the combined influence of activation energy differences and chemical structural variations on the volatilization behavior of each emission component. At relatively low temperatures, oxygenated hydrocarbons account for a notably higher proportion (70–80%). This can be attributed to their higher vapor pressure, weaker binding capacity, and contributions from the thermal decomposition products of warm-mixed additives. Simultaneously, the volatilization rates of hydrocarbons and aromatic hydrocarbons decline more rapidly at low temperatures, which leads to the proportional dominance of oxygenated hydrocarbons. As temperature increases, the release of aliphatic and aromatic hydrocarbons becomes more intense. This is primarily due to the promotion of the thermal cracking of light hydrocarbon fractions, the desorption and migration of aromatic ring structures under high-temperature conditions, and the reduction in diffusion resistance resulting from the decreased viscosity of asphalt [27–30]. The rapid increase in the proportion of aromatic hydrocarbons in the high-temperature range carries greater environmental and health risk implications. It indicates that elevated temperatures not only increase the total emission volume but also raise the relative proportion of highly toxic components. Under identical sampling conditions, the total VOC emissions show a clear mitigation trend relative to the hot-mix control (175 °C/0%). Specifically, total VOCs decrease by 45.9% at 170.9 °C (0.3%), 54.6% at 165 °C (0.4%), and 67.8% at 152.9 °C (0.5%). In contrast, 173 °C causes a 16.3% increase, whereas 151.3 °C achieves only a 33.5% reduction.

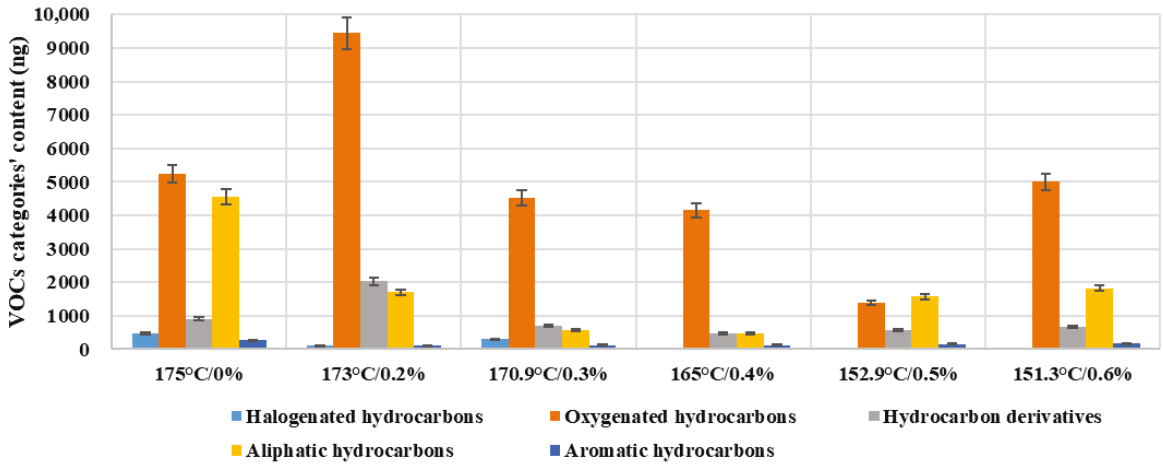

Figure 13. VOC categories' contents of warm-mixed SBS asphalt binder with different additive dosages.

Figure 14 exhibits content variation in several typical volatile components of warm-mixed SBS asphalt binder with different additive dosages. The total amount of VOC emission increases as temperature rises, while a concentrated emission peak was observed around 173 °C, which may be formed from the superposition of multiple mechanisms. Around the temperature range of 170 °C–180 °C, initial thermal decomposition may occur in the SBS modifier, partial surfactant-type components in the warm-mixed additive reach their volatilization peak, the vapor pressure of C_6–C_{12} hydrocarbons in the asphalt binder rises to a relative high level, and a significant drop in the asphalt binder's viscosity may lead to a sharp reduction in the internal diffusion resistance. These factors work together to make asphalt VOC emissions sensitive to a temperature around 173 °C, and prolonged exposure of asphalt to this temperature during construction should be avoided. Some individual compounds still exhibit relatively high concentrations at lower temperatures, such as 1-Butanol. This indicates that VOC emissions are not only a thermally controlled equilibrium process but may also involve secondary pathways, such as the structural breakdown of the warm-mixed additive and oxidative side-reactions of the asphalt binder. It reflects the multi-source, composite release characteristics of asphalt VOC emissions in this study.

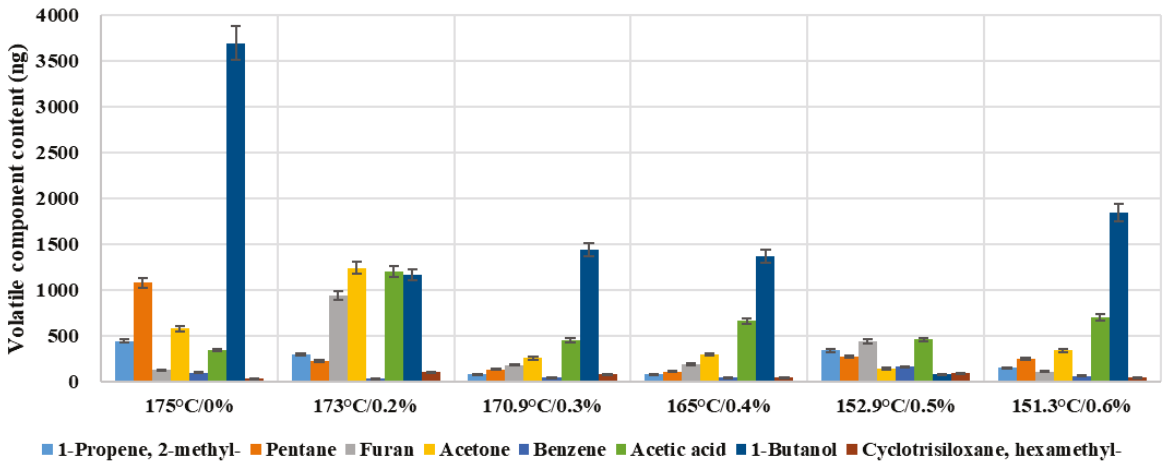

Figure 14. Typical volatile component contents of warm-mixed SBS asphalt binder with different additive dosages.

A data-driven assessment supports 0.3–0.5% as the optimal dosage. Compared with the control group of 0.0% dosage, the total emissions of the experimental group decreased by 45.9% (170.9 °C/0.3%), 54.6% (165 °C/0.4%), and 67.8% (152.9 °C/0.5%), respectively.

On the contrary, the 173 °C/0.2% condition increased by 16.3% compared with the control group, indicating that 173 °C is an emission-sensitive temperature. Furthermore, increasing the dosage to 0.6% does not lead to further mitigation; only a 33.5% reduction in total VOCs, and oxygenated VOCs remained at a high level. This means additional volatilization or decomposition products generated from the additive itself. Therefore, 0.3–0.5% provides substantial mitigation via temperature lowering while avoiding additive-driven emission rebound.

From an environmental and health perspective, the identified VOC spectrum covers light alkanes/alkenes (e.g., pentane and methylpropene), oxygenated VOCs (e.g., acetone, acetic acid, and 1-butanol), heteroaromatics (e.g., furan), and aromatics (e.g., benzene) (Figure 14). These species are not equivalent in risk: aromatics and heteroaromatics are typically associated with stricter occupational exposure limits and higher chronic health concern, whereas oxygenated VOCs often contribute to acute irritation and odor nuisance. In addition, both aliphatic and oxygenated VOCs are key precursors for photochemical ozone formation and secondary organic aerosol, implying that emission mitigation benefits extend beyond the work zone to the surrounding air quality.

Although the laboratory collection configuration is not intended to replicate onsite dilution or ventilation, the fixed sampling volume enables an upper-bound estimation of source-stream concentration. For priority toxicants, benzene remains at the sub-mg·m^{-3} level, while furan shows a stronger temperature and additive sensitivity, highlighting that risk management should consider toxicity-weighted species rather than only the total mass. Therefore, it is suggested to control dwell time within the emission-sensitive temperature range (170–180 °C), and to ensure local exhaust ventilation (especially in enclosed environments, such as tunnels). It is also recommended to facilitate compliance with workplace air-quality requirements and to support safer infrastructure construction.

Overall, temperature is the dominant factor influencing asphalt VOC emissions. Reducing heating temperature can decrease the total VOC emissions by 60–80% and significantly lower the proportion of high-risk components such as aromatic hydrocarbons. It thereby achieves dual mitigation of both emission volume and hazards. Warm-mixed additive indirectly reduces VOC emissions by lowering the heating temperature. Although the warm-mixed additive used in this study possesses a certain degree of volatility, its application still shows a significant trend toward emission reduction. Considering factors of emission volume, chemical composition, and construction performance, the warm-mixed additive dosage range of 0.3–0.5% demonstrates optimal performance. It not only significantly reduces the heating temperature but also avoids excessive volatile by-products from the warm-mixed additive itself. This study systematically validates the effectiveness of warm-mixed technology in suppressing asphalt VOC emissions during asphalt layer construction. By elucidating thermal action mechanisms and behavioral differences in various volatile components, it provides a more theoretically grounded scientific basis for green road construction.

5. Conclusions

This study explored the comprehensive influence of different warm-mixed additive dosages on the viscoelastic properties and VOC emissions of a warm-mixed SBS asphalt binder. Based on the analysis discussed above, the following conclusions can be obtained:

(1) The warm-mixed additive could effectively reduce viscosity and construction temperature of the SBS asphalt binder. A dosage of 0.4% was relatively economical with a good viscosity reduction, but continually increasing additive dosage from 0.4% to 0.5% yielded a greater effect on temperature reduction.

(2) Increasing trends of creep stiffness S and creep rate *m-value* were determined within ±5% fluctuation, which indicated no significant impact of additive dosage on low-temperature creep performance. Higher additive dosages might help to add some viscous components of the asphalt binder, thereby further enhancing its cracking resistance.
(3) All warm-mixed groups showed significant reductions in J_{nr} values to below 0.1 kPa^{-1} and obvious increases in R to above 91%. The improvement effect of high-temperature performance was not obviously sensitive to additive dosage. Dosage ranges from 0.4% to 0.5% showed better relative high-temperature behaviors.
(4) Temperature is the dominant factor influencing asphalt VOC emissions. Considering the factors of emission volume, chemical composition, and performance, the additive dosage range of 0.3–0.5% demonstrated optimal performance by reducing heating temperature and avoiding excessive volatile by-products from the additive itself.
(5) Despite 0.4% being a relatively economical dosage of warm-mixed additive, a slight increase to 0.5% could achieve more pronounced environmental benefits in VOC emission reduction while maintaining comprehensive service performance that met specification requirements.
(6) Asphalt VOC emissions are also affected by the aggregate gradation and the interaction between mixture and construction machinery, while these influential factors should be taken into account in future studies.

Author Contributions: Conceptualization, W.W.; methodology, W.W. and Y.Y.; resources, W.W. and Y.M.; data curation, W.W., M.X. and X.H.; writing—original draft preparation, W.W.; writing—review and editing, W.W.; and supervision, Y.M. and L.W. All authors have read and agreed to the published version of the manuscript.

Funding: The authors acknowledge the financial support of Beijing Natural Science Foundation (Project No. 8244054), the Interdisciplinary Research Project for Young Teachers of USTB (Fundamental Research Funds for the Central Universities) (Project No. FRF-IDRY-23-017), and China Postdoctoral Science Foundation (Project No. 2021M690356).

Institutional Review Board Statement: Not applicable.

Informed Consent Statement: Not applicable.

Data Availability Statement: The original contributions presented in this study are included in the article. Further inquiries can be directed to the corresponding authors.

Conflicts of Interest: The authors declare no conflicts of interest.

References

1. Abed, A.; Thom, N.; Grenfell, J. A novel approach for rational determination of warm mix asphalt production temperatures. *Constr. Build. Mater.* **2019**, *200*, 80–93. [CrossRef]
2. Cui, P.; Wu, S.; Li, F.; Xiao, Y.; Zhang, H. Investigation on Using SBS and Active Carbon Filler to Reduce the VOC Emission from Bituminous Materials. *Materials* **2014**, *7*, 6130–6143. [CrossRef] [PubMed]
3. Lin, S.; Hung, W.; Leng, Z. Air pollutant emissions and acoustic performance of hot mix asphalts. *Constr. Build. Mater.* **2016**, *129*, 1–10. [CrossRef]
4. Hettiarachchi, C.; Hou, X.; Wang, J.; Xiao, F. A comprehensive review on the utilization of reclaimed asphalt material with warm mix asphalt technology. *Constr. Build. Mater.* **2019**, *227*, 117096. [CrossRef]
5. Sobhi, S.; Yousefi, A.; Behnood, A. The effects of Gilsonite and Sasobit on the mechanical properties and durability of asphalt mixtures. *Constr. Build. Mater.* **2020**, *238*, 117676. [CrossRef]
6. Nazzal, M.; Qtaish, L.; Al-Hosainat, A.; Talha, S.; Kaya, S.; Abbas, A. Evaluation of Moisture Damage in Asphalt Mixtures at Macro- and Nanoscales. *J. Mater. Civ. Eng.* **2021**, *33*, 04021369. [CrossRef]
7. Izadi, A.; Motamedi, M.; Alimi, R.; Nafar, M. Effect of aging conditions on the fatigue behavior of hot and warm mix asphalt. *Constr. Build. Mater.* **2018**, *188*, 119–129. [CrossRef]

8. Peng, B.; Fan, X.; Wang, X.; Li, W. Key steps of carbon emission and low-carbon measures in the construction of bituminous pavement. *Int. J. Pavement Res. Technol.* **2017**, *10*, 476–487. [CrossRef]
9. Wang, W.; Wang, L.; Miao, Y.; Cheng, C.; Chen, S. A survey on the influence of intense rainfall induced by climate warming on operation safety and service life of urban asphalt pavement. *J. Infrastruct. Preserv. Resil.* **2020**, *1*, 4. [CrossRef]
10. Li, D.; Leng, Z.; Zou, F.; Yu, H. Effects of rubber absorption on the aging resistance of hot and warm asphalt rubber binders prepared with waste tire rubber. *J. Clean. Prod.* **2021**, *303*, 127082. [CrossRef]
11. Doyle, J.; Sefidmazgi, N.; Mejías-Santiago, M.; Rushing, J. Relationship of field versus laboratory compaction to hot- and warm-mixed asphalt rutting performance. *J. Transp. Eng. Part B Pavements* **2021**, *147*, 04021014. [CrossRef]
12. Abd El-Hakim, R.; Epps, J.; Martin, A.; Arámbula-Mercado, E. Laboratory and field investigation of moisture susceptibility of hot and warm mix asphalts. *Int. J. Pavement Eng.* **2021**, *22*, 1389–1398. [CrossRef]
13. Borinelli, J.; Blom, J.; Portillo-Estrada, M.; Maeijer, P.; Van den bergh, W.; Vuye, C. VOC Emission Analysis of Bitumen Using Proton-Transfer Reaction Time-Of-Flight Mass Spectrometry. *Materials* **2020**, *13*, 3659.
14. Lei, M.; Wu, S.; Liu, G.; Amirkhanian, S. VOCs characteristics and their relation with rheological properties of base and modified bitumens at different temperatures. *Constr. Build. Mater.* **2018**, *160*, 794–801. [CrossRef]
15. Mo, S.; Wang, Y.; Xiong, F.; Ai, C. Effects of asphalt source and mixing temperature on the generated asphalt fumes. *J. Hazardous Mater.* **2019**, *371*, 342–351.
16. Qiu, J.; Yang, T.; Wang, X.; Wang, L.; Zhang, G. Review of the flame retardancy on highway tunnel asphalt pavement. *Constr. Build. Mater.* **2019**, *195*, 468–482. [CrossRef]
17. Xiao, F.; Guo, R.; Wang, J. Flame retardant and its influence on the performance of asphalt—A review. *Constr. Build. Mater.* **2019**, *212*, 841–861. [CrossRef]
18. Yang, X.; Shen, A.; Su, Y.; Zhao, W. Effects of alumina trihydrate (ATH) and organic montmorillonite (OMMT) on asphalt fume emission and flame retardancy properties of SBS-modified asphalt. *Constr. Build. Mater.* **2020**, *236*, 117576. [CrossRef]
19. *JTG F40-2004*; Technical Specifications for Construction of Highway Asphalt Pavements. China Communication Press: Beijing, China, 2004; pp. 9–15.
20. *JTG 3410-2025—T0625-2011*; Asphalt Rotational Viscosity Test (Rotational Viscometer). China Communication Press: Beijing, China, 2025; pp. 146–152.
21. Wang, W.; Luo, R.; Feng, G.; Wang, L. Impact factors in rotational viscosity tests. *J. Wuhan Univ. Technol. (Transp. Sci. Eng.)* **2016**, *40*, 514–518.
22. *ASTM D6648-08*; ASTM Standard Test Method for Determining the Flexural Creep Stiffness of Asphalt Binder Using the Bending Beam Rheometer (BBR). ASTM International: West Conshohocken, PA, USA, 2016.
23. Wang, W.; Luo, R.; Yan, G.; Wang, L. Evaluation on moisture sensitivity induced by dynamic pore water pressure for asphalt mixture and its components using the bending beam rheometer method. *Constr. Build. Mater.* **2020**, *251*, 118942. [CrossRef]
24. Wang, W.; Luo, R.; Li, J.; Wang, L. Evaluation on the influence of dynamic water pressure environment on viscoelastic mechanical performance of asphalt mixture using the bending beam rheometer method. *Constr. Build. Mater.* **2022**, *321*, 126428. [CrossRef]
25. *JTG 3410-2025—T0647-2025*; Multiple Stress Creep and Recovery Test of Asphalt Binder (MSCR Test). China Communication Press: Beijing, China, 2025; pp. 185–189.
26. *ASTM D7405-20*; ASTM Standard Test Method for Multiple Stress Creep and Recovery (MSCR) of Asphalt Binder Using a Rheometer. ASTM International: West Conshohocken, PA, USA, 2020.
27. Wang, M.; Li, P. An overview of studies on the hazards, component analysis and suppression of fumes in asphalt and asphalt mixtures. *Constr. Build. Mater.* **2021**, *35*, 10189–10196.
28. Jiang, Q.; Li, N.; Yang, F.; Ren, Y.; Wu, S.; Wang, F.; Xie, J. Rheology and volatile organic compounds characteristics of warm-mix flame retardant asphalt. *Constr. Build. Mater.* **2021**, *298*, 123691. [CrossRef]
29. Ma, W.; Niu, C.; Wang, Y.; Liang, X.; Guo, H. Research progress of asphalt fume concentration and composition detection technology. *Highw. Traffic Sci. Technol. (Appl. Technol. Ed.)* **2020**, *16*, 155–157.
30. Xue, Y.; Wei, X.; Zhao, H.; Wang, T.; Xiao, Y. Interaction of spent FCC catalyst and asphalt binder: Rheological properties, emission of VOCs and immobilization of metals. *J. Clean. Prod.* **2020**, *259*, 120830. [CrossRef]

Disclaimer/Publisher's Note: The statements, opinions and data contained in all publications are solely those of the individual author(s) and contributor(s) and not of MDPI and/or the editor(s). MDPI and/or the editor(s) disclaim responsibility for any injury to people or property resulting from any ideas, methods, instructions or products referred to in the content.

materials

MDPI

Article

Evaluation of the Crushing Characteristics of Slate Coarse Aggregate Used for Asphalt Mixture

Hao Huang [1], Yanfei Zhu [2], Kun Zhou [2], Yue Xiao [3] and Liantong Mo [1,*]

[1] State Key Laboratory of Silicate Materials for Architectures, Wuhan University of Technology, Wuhan 430070, China; 344828@whut.edu.cn
[2] Gezhouba Group No. 1 Engineering Co., Ltd., Yichang 443002, China; zhuyanfei5719@cggc.cn (Y.Z.); zhoukun0039@cggc.cn (K.Z.)
[3] School of Materials Science and Engineering, Chang'an University, Xi'an 710061, China; xiaoy@chd.edu.cn
* Correspondence: molt@whut.edu.cn

Abstract

The relict bedding and slaty cleavage structure in slate directly influences the crushing characteristics and strength properties of slate aggregates. When slate aggregates are used in asphalt concrete, it may have risks of insufficient resistance to crushing and uncertain long-term durability. In order to investigate the crushing behavior of slate coarse aggregates in asphalt mixtures, a comparative study was conducted using limestone and basalt aggregates as reference. Various tests were carried out including crushing value tests, single-particle compression crushing tests, Marshall compaction resistance tests, and gyratory compaction resistance tests. The crushing patterns, crushing strength, and gradation changes of slate aggregates after crushing were systematically examined. Based on the Weibull distribution function, the statistical distribution of single-particle crushing strength was analyzed. Additionally, the particle distribution patterns were studied for single-sized aggregates, blended aggregates, and asphalt mixtures after these were subjected to crushing under Marshall compaction and gyratory compaction. The test results indicated that the crushing value of slate coarse aggregates was 9.2%, which indicates superior crushing resistance compared to traditional limestone and basalt. After long-term exposure to water immersion at 60 °C, high-pressure steam treatment, and heating at 220 °C, the increase in crushing value of slate coarse aggregates was less than 1.5%, indicating excellent water and heat resistance. The two-point and four-point crushing strengths of single particles of slate coarse aggregates were higher than those of limestone and basalt coarse aggregates, and the single-particle compression crushing strength followed the Weibull distribution pattern. Both single-sized and blended slate aggregates exhibited lower proportions of crushing during Marshall and gyratory compaction compared to basalt and limestone aggregates. Asphalt mixtures prepared with slate coarse aggregates also demonstrated better crushing resistance than those made with basalt and limestone, confirming that the bedding structure of slate does not cause excessive crushing in asphalt mixture. The obtained findings were limited to the tested slate aggregates from a single quarry and thus necessary performance verification should be conducted on slate aggregates from other sources before practical engineering applications.

Keywords: asphalt mixture; slate; crushing characteristics; crushing strength

1. Introduction

The construction of asphalt concrete pavements for highways requires a large amount of high-quality aggregates such as limestone, diabase, and basalt. However, some regions lack these premium aggregate resources but have abundant slate deposits. Utilizing locally available slate aggregates can help reduce project costs and accelerate the construction progress. Compared to other types of rock, slate exhibits cleavage planes, giving it pronounced anisotropy. Under external loads, it tends to split along these planes into thin sheets or plate-like structures [1,2]. Due to its splitting property, slate is primarily used in traditional applications such as roofing, walling slabs, and paving stones [3]. However, research on processing slate into aggregates for engineering applications remains limited. The main reasons are that slate's relict bedding structure directly affects its crushing characteristics and strength properties. Additionally, slate is prone to weathering, posing risks such as insufficient resistance to crushing, high flakiness content, and uncertain long-term durability when used as road aggregates. Nevertheless, if properly treated, slate has potential applications as an aggregate substitute in concrete, base or sub-base material in road construction [4]. For instance, the Qinzhou region of Guangxi, China has abundant slate deposits with good rock integrity, large block sizes, and poor splitting properties, making them unsuitable for traditional slate building materials. Instead, they are mainly processed into aggregates for road bases and low-grade cement concrete. Currently, due to concerns over the insufficient crushing resistance and weathering resistance combined with the dynamic loads from construction compaction and repeated tire loads during pavement service, there is a risk of excessive aggregate crushing if the slate's crushing strength is inadequate. Therefore, it is necessary to study the crushing resistance characteristics of slate aggregates used for asphalt concrete.

Currently, researchers have conducted a series of tests, including Brazilian splitting, uniaxial compression, and triaxial compression tests, to evaluate the mechanical properties of slate rock [5–8]. Numerous studies on the mechanics of slate rock have confirmed that its internal bedding structure significantly influences its strength and failure modes including shear failure deviating toward the bedding plane direction, slip failure along the bedding plane, and splitting failure along the bedding plane [9–12]. Additionally, slate faces issues related to water stability and weathering [13–15]. Water intrusion triggers physicochemical reactions that alter the mineral microstructure and composition [16–18]. Freeze–thaw cycles and water–rock interaction can lead to strength degradation in slate [19,20]. Slate's bedding structure has multiple adverse effects on its strength, along with issues such as strength degradation due to water immersion softening and weathering. However, there remain considerable doubts about whether slate aggregates, processed by crushing massive slate into smaller particles, suffer from insufficient crush resistance and weathering durability. As the fundamental building block of the skeletal structure in asphalt mixtures, the crush resistance of aggregate particles is a critical mechanical property. It is required to exhibit excellent compressive crushing resistance during laboratory preparation, construction compaction, and throughout the pavement's service life, thereby preventing particle breakage from compromising the mechanical performance of asphalt concrete. Consequently, the quality of crush resistance directly determines whether slate aggregates can be utilized in asphalt concrete pavements. Given the distinctive relict bedding structure of slate, the investigation of the crushing characteristics and strength properties of slate aggregates is particularly essential for their application in asphalt pavements.

Currently, the mechanical properties of slate rock have been well studied, while there are few studies on the mechanical properties of slate aggregate. It should be noted that slate rock and slate aggregate are in different scale of size and thus can have distinctly different mechanical properties with respect to crushing resistance. This is especially true when the

https://doi.org/10.3390/ma19030503

effects of the inherent bedding structure can be significant on the strength of slate rock, but not for slate aggregate. At present, there is no research on whether the inherent bedding structure of slate rock affects the mechanical properties of slate aggregate particles after the processing and crushing of slate rock into aggregate particles. Furthermore, the resistance to fragmentation in the complex stress environment of asphalt mixtures remains unknown. This knowledge gap makes it difficult to comprehensively and accurately evaluate the engineering suitability of slate aggregates based solely on the crushing behavior of slate rock. To address this research gap, this study aims to systematically evaluate the crushing characteristics of a specific slate coarse aggregate for use in asphalt mixtures. For the purpose of comparison, limestone and basalt aggregates commonly accepted and used in asphalt pavements were taken as references. Tests including the crushing value test, single-particle compression crushing test, Marshall compaction test, and gyratory compaction test were conducted on different aggregates to systematically study the crushing modes, crushing strength, and gradation changes of slate aggregate after crushing. The Weibull distribution function was employed to statistically analyze the distribution pattern of single-particle crushing strength. Additionally, the particle distribution patterns after crushing were analyzed for single-size aggregate, mixed aggregate, and asphalt mixtures subjected to Marshall compaction and gyratory compaction. Finally, by comparing with traditional limestone and basalt aggregates, this study verifies whether the relict bedding and slaty cleavage structure of slate would lead to excessive crushing and damage of the aggregate in asphalt mixtures, providing data support for the application of slate aggregate in asphalt mixtures.

2. Materials and Methods

2.1. Materials

The slate coarse aggregate used was obtained from the De'an Quarry in Qinzhou, China. Figure 1 presents the on-site mining diagram of the slate vein. The slate primarily formed from the Mesoproterozoic to the Lower Paleozoic. Its metamorphism mainly occurred during the Sibaoian and Caledonian periods, resulting from low-pressure, regional, low-temperature dynamic metamorphism. The slate processed for the aggregate belongs to low-grade metamorphic rock, with its parent rock appearing gray-black. Petrographic analysis as indicated in Figure 2 showed that the mineral composition of the slate mainly included quartz (55%), biotite (21%), chlorite (16%), pyrite (8%), and opaque minerals. X-ray fluorescence spectrometry determined that the primary chemical components of the slate were SiO_2 (53.36%), CaO (6.79%), Al_2O_3 (19.88%), Fe_2O_3 (5.92%), MgO (2.49%), K_2O (6.45%), and Na_2O (0.83%). The slate used in this study exhibited a characteristic cryptocrystalline texture and a dense massive structure. Its internal fabric was dominated by relict bedding inherited from the protolith, rather than a slaty cleavage formed by tectonic stress. In terms of mineral composition, quartz, accounting for up to 55% of the content, formed the rigid framework of the rock as cryptocrystalline grains, establishing a matrix of exceptionally high mechanical strength. During microstructural evolution, extremely fine cryptocrystalline minerals filled inter-granular spaces through recrystallization, enhancing the overall integrity of the matrix. More critically, these randomly distributed rigid grains effectively impeded the extensive, oriented, and continuous alignment of platy minerals (e.g., biotite, chlorite), thereby suppressing the development of a penetrative slaty cleavage at the microscopic scale. Although banded relict bedding formed by compositional differentiation was observable under the microscope, the high-strength cementation provided by the cryptocrystalline matrix prevented these bedding planes from evolving into mechanically weak parting surfaces.

https://doi.org/10.3390/ma19030503

Figure 1. The on-site mining diagram of the slate vein.

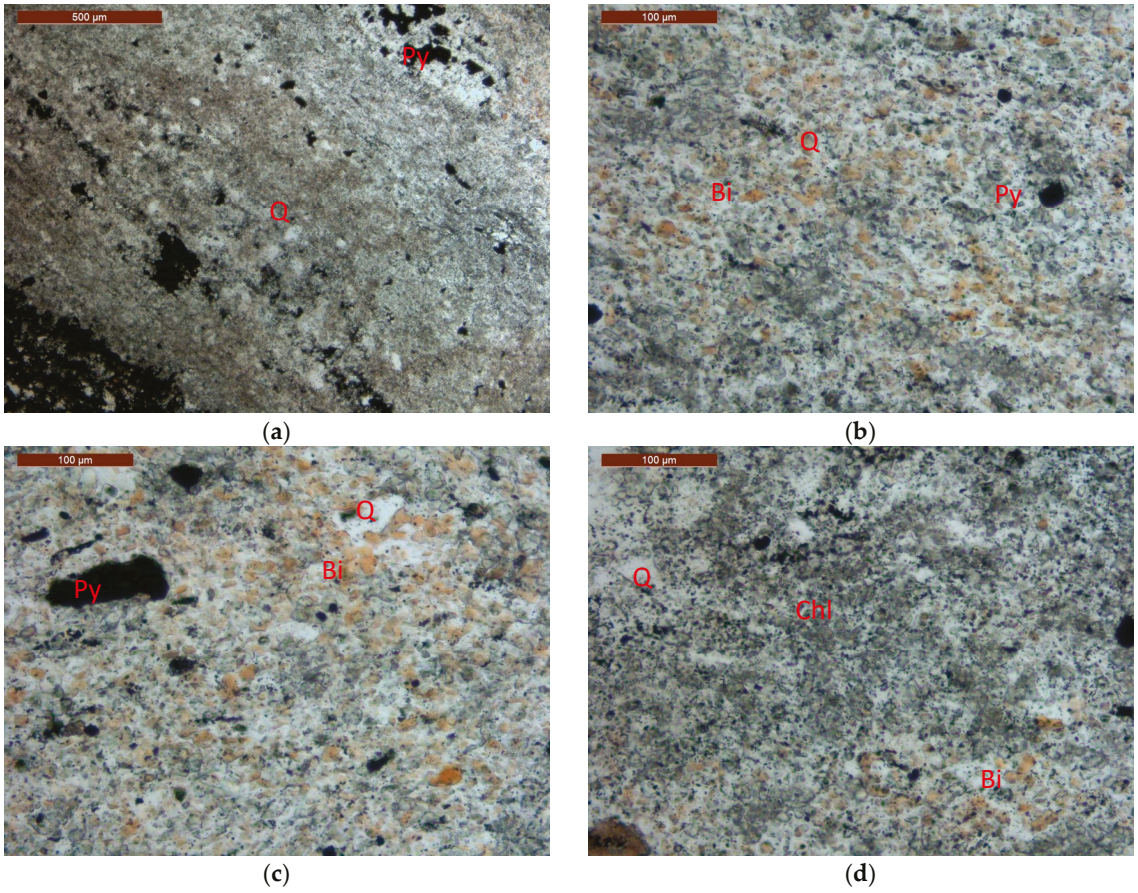

Figure 2. Petrographic analysis micrographs (**a**) Quartz (Q), opaque minerals (Py), and the banded structure of the rock; (**b**) Quartz (Q), biotite (Bi), and opaque minerals (Py); (**c**) Quartz (Q), biotite (Bi), and opaque minerals (Py); (**d**) Quartz (Q), chlorite (Chl), and biotite (Bi).

As shown in Figure 3, the slate coarse aggregate consisted of three fractions: 2.36–4.75 mm, 4.75–9.5 mm, and 9.5–16 mm. For comparative analysis, high-quality limestone and basalt coarse aggregates commonly used in asphalt mixtures were selected for experimental study. Basalt is considered the high-quality aggregate for asphalt concrete, offering excellent crushing and wear resistance, while limestone is the most representative alkaline aggregate, with moderate crushing resistance. Furthermore, to compare the compressive crushing resistance of asphalt mixtures containing different rock types, asphalt mixtures were prepared using slate, limestone, and basalt coarse aggregates, respectively. In all three asphalt mixtures, limestone fine aggregate (0–2.36 mm) was used, the filler was mineral powder produced by grinding limestone, and the asphalt binder was penetration 70 paving asphalt with a penetration of 68 (0.1 mm), a softening point of 47.5 °C, and a ductility at 10 °C of 47 cm.

Figure 3. The coarse slate aggregates with different sizes.

2.2. Test Methods

Regarding the study of aggregate crushing characteristics, the aggregate crushing value is commonly used to characterize aggregates in asphalt mixtures [21]. Furthermore, the compaction methods such as Marshall compaction, gyratory compaction, and wheel rolling can also be used to examine the crush resistance of aggregates during the compaction process [22]. The mechanical properties of coarse granular materials are largely constrained by the compressive strength of single particles [23,24]. Therefore, the single-particle crushing strength test is an effective method for analyzing the crushing patterns and strength of aggregates. Figure 4 shows the research methodology flowchart. As shown in Figure 4, different crushing tests were considered including the crushing value test, single-particle compression crushing test, Marshall compaction test, and gyratory compaction test. Different material scales were also involved including single particle, single-grade aggregate, mixed aggregates and asphalt mixture. The test plan was aimed at getting insight into the resistance to fragmentation in the complex stress environment of asphalt mixtures ranging from single-particle loading to multi-scale aggregate skeleton compaction.

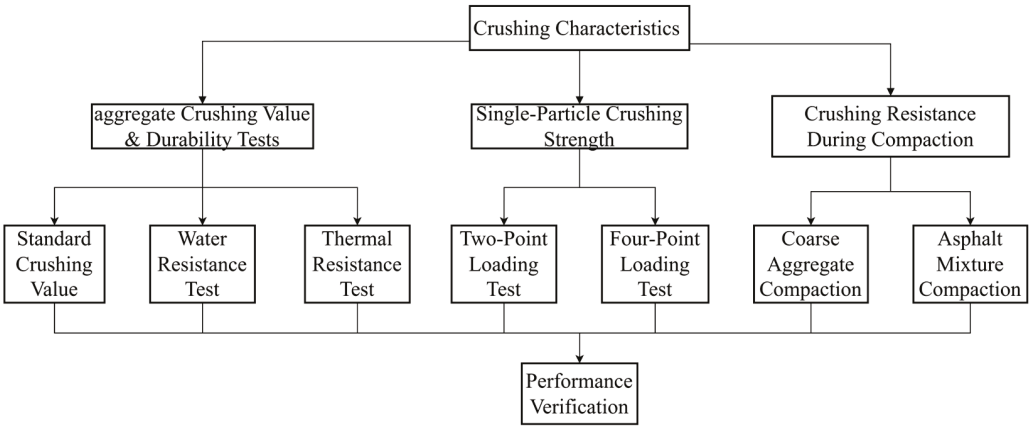

Figure 4. Research methodology flowchart.

2.2.1. Coarse Aggregate Crushing Test

To analyze the compressive resistance of slate aggregate and evaluate its suitability for asphalt mixtures, a crushing value test was conducted on coarse aggregates of three rock types including slate, limestone, and basalt in accordance with T0316-2024 Test Procedures for Highway Engineering Asphalt Aggregates [25]. The test utilized single-sized aggregates ranging from 9.5 to 13.2 mm. After applying a 400 kN load, the proportion of crushed material smaller than 2.36 mm was defined as the coarse aggregate crushing value. Since the crushing value alone is a single indicator and can not fully capture the crushing

characteristics of different aggregates, the crushed material obtained from the test was further sieved to analyze its particle size composition after crushing.

The unique bedding structure and metamorphic characteristics of slate determine the risk of weathering and alteration of slate aggregate during long-term service. Therefore, tests were conducted to evaluate the water resistance and heat resistance of slate aggregate. The degradation of its compressive crushing resistance after long-term (21 days) immersion in water at high temperature (60 °C) was characterized using the coarse aggregate crushing value test. Meanwhile, an accelerated high-temperature and high-pressure test was performed to further examine its long-term water resistance. The slate aggregate was subjected to high-temperature autoclaving (autoclave steam pressure: 0.14–0.16 MPa, temperature: 126–128 °C, duration: 9 h), after which the change in the coarse aggregate crushing value was measured. The above-mentioned long-term immersion and high-temperature autoclaving tests were primarily designed to simulate whether slate aggregate would experience weathering and strength deterioration under long-term water immersion conditions during service in asphalt pavements.

During the production of asphalt mixtures, aggregates were heated to 170~190 °C in the drying drum of an asphalt mixing plant. To ensure the stability of the mechanical properties of aggregates after high-temperature heating, a high-temperature crushing value test was conducted on slate coarse aggregate. For the test, the slate coarse aggregate was first placed in the crushing value test mold, then put into an oven at 220 °C and kept at that temperature for 4 h. After removal, the loading test was carried out immediately as required, i.e., loading to 400 kN within 10 min to determine its crushing value. The slate aggregate, after being heated to 220 °C and held for 4 h, was directly subjected to the high-temperature compressive crushing test. This was intended to simulate the impact of high-temperature mixing, paving, and compaction of asphalt mixtures on the thermal stability of the slate aggregate.

The crushing value tests were conducted in triplicate, with the reported result being the average value of the three replicate tests.

2.2.2. Single Particle Compression Crushing Test

To analyze the single-particle compressive crushing strength of different coarse aggregates, single-particle two-point and four-point compression crushing tests were conducted. The loading methods are illustrated in Figure 5. In the single-particle two-point compression crushing test, an individual aggregate particle was placed between the base and the loading head, equivalent to the particle being crushed under two-point force. In contrast, the single-particle four-point compression crushing test employed three tangent steel balls arranged as a base, with the individual aggregate placed on the steel ball base to form three supporting points. The loading head applied pressure to create a four-point force mode. The size of the steel balls matched the particle size of the aggregates. For example, when conducting single-particle crushing tests for particles in the 4.75~9.5 mm range, steel balls with a diameter of 7 mm were used as the base. For particles in the 9.5~13.2 mm range, steel balls with a diameter of 12 mm were used. Compared to the single-particle two-point compression crushing test, the four-point compression crushing test involves more contact points and more complex force distribution on the aggregate, making it more effective for examining the influence of the inherent bedding structure of slate on the aggregate crushing strength. For the tests, 50 particles each of slate, limestone, and basalt in two size ranges including 4.75~9.5 mm and 9.5~13.2 mm, were selected. Since particle shape significantly affects crushing characteristics, particles with regular shapes and non-flaky, non-elongated forms (with a length-to-diameter ratio less than 1.3:1) were chosen for the compressive crushing strength tests. Before testing, the largest surface of each particle was placed in

https://doi.org/10.3390/ma19030503

contact with the base. Loading was performed at a rate of 1 mm/min and stopped when the load dropped sharply to half of the maximum load. Some typical load-displacement curves are presented in Figure 6. During the loading process, the instrument automatically recorded the load and displacement and plotted the load-displacement curve.

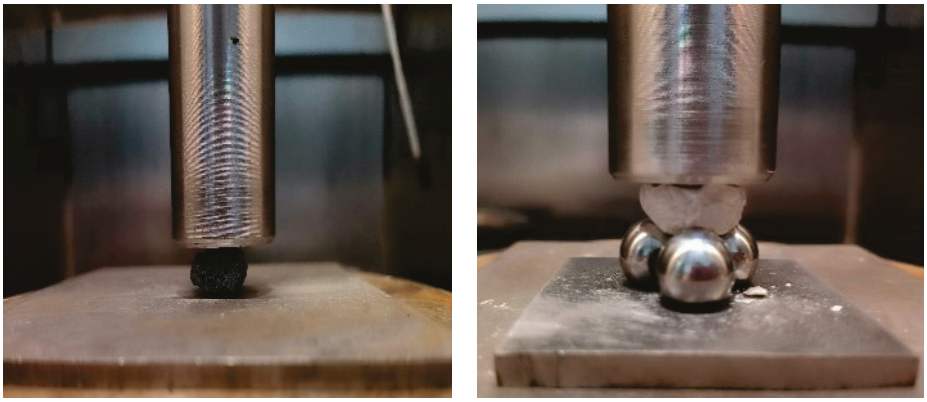

(**a**) (**b**)

Figure 5. Single-particle compression crushing test ((**a**): two-point test; (**b**): four-point test).

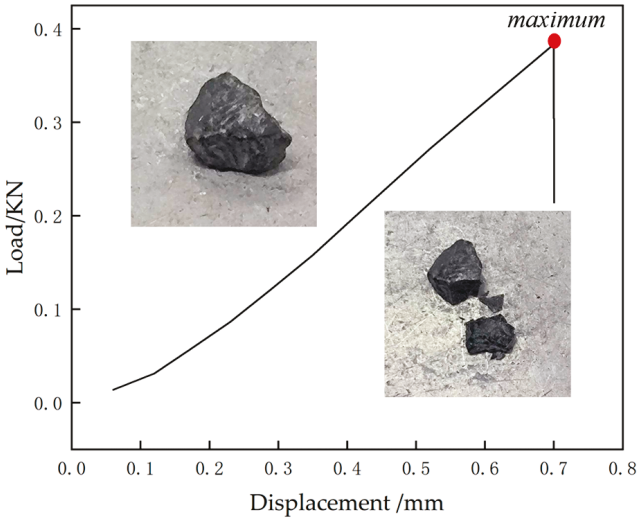

(**a**)

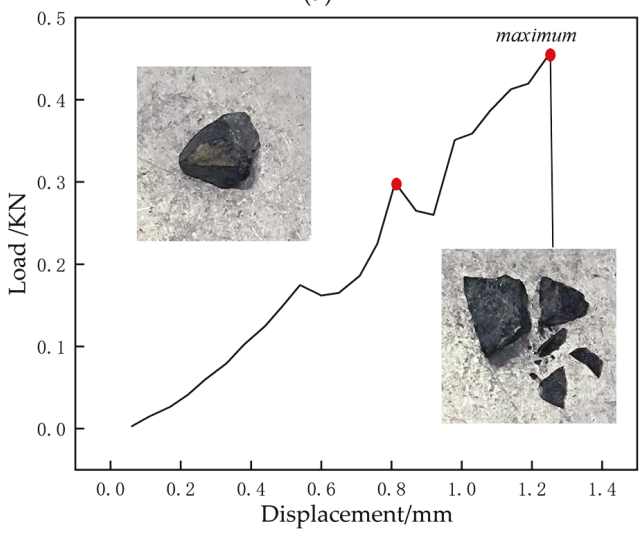

(**b**)

Figure 6. *Cont.*

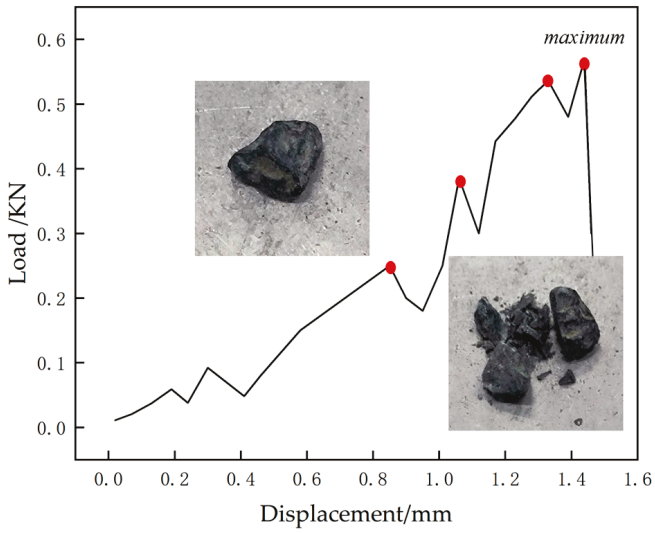

(**c**)

Figure 6. Typical load-displacement curves of slate single-particle compression crushing ((**a**): Single-peak curve; (**b**): Double-peak curve; (**c**): Multi-peak curve; red dots: maximum).

The single-particle two-point compressive crushing strength can be calculated using the particle crushing strength formula proposed by Jaeger [26]:

$$\sigma_f = \frac{F}{d^2} \tag{1}$$

where F is the crushing load force, and d is the particle diameter.

However, particles of the same size can have varying shapes, ranging from flaky to blocky. Simply using the average particle diameter to calculate the crushing strength may introduce bias. To analyze the influence of particle shape, this study employed a modified formula proposed by Afshar et al. [27], which incorporates the particle aspect ratio parameter to calculate the crushing strength of aggregate particles:

$$\sigma_f = \frac{F \times AR}{d^2} \tag{2}$$

where AR is the particle aspect ratio.

For the single-particle four-point compressive crushing test, the compressive crushing strength is simplified using Equation (3) [28]:

$$\sigma_f = \frac{F}{\pi\left(\frac{d_{\text{int}}}{2}\right)\left(\frac{d_{\text{min}}}{2}\right)} \tag{3}$$

where d_{int} and d_{min} are the intermediate diameter and minimum diameter of the aggregate particle, respectively.

2.2.3. Coarse Aggregate Compaction Crushing Test

Currently, Marshall compaction tests and gyratory compaction tests are primarily used for laboratory compaction of asphalt mixtures. Both Marshall compaction and gyratory compaction can cause crushing damage to aggregates, thereby affecting the gradation and mechanical properties of asphalt concrete. To evaluate the crushing resistance of different coarse aggregates during the compaction process, Marshall compaction tests and gyratory compaction tests were conducted using single-sized and combined-sized coarse aggregates.

For the Marshall compaction test with single-sized coarse aggregates, around 800 g of aggregates with a particle size of 9.5–13.2 mm were selected. After washing, the aggregates

were dried in an oven at 105 °C for 4 h, cooled to room temperature, and then placed into a Marshall mold. A Marshall electric compactor (Shanghai Changji Geological Instrument Co., Ltd., Shanghai, China) was used to apply 75 blows on one side. After compaction, the aggregates were removed and sieved to analyze particle breakage.

For the Marshall compaction test with combined-sized coarse aggregates, three fractions of coarse aggregates including 2.36–4.75 mm, 4.75–9.5 mm, and 9.5–16 mm, were used. Their proportions corresponded to the coarse aggregate gradation in AC-13 asphalt mixtures, representing a mineral aggregate composition without fine aggregates and mineral filler, consisting only of coarse aggregates larger than 2.36 mm to form an aggregate skeletal structure. The selected proportions for the 9.5–16 mm, 4.75–9.5 mm, and 2.36–4.75 mm coarse aggregates were 36.1:43.1:20.8. The passing percentages of the mixed aggregates through sieve sizes of 13.2 mm, 9.5 mm, 4.75 mm, and 2.36 mm were 91.7%, 63.9%, 20.8%, and 0%, respectively. After uniformly mixing the three coarse aggregates in the specified proportions, they were placed into a Marshall mold. Following 75 blows on one side, the crushed aggregates were removed and sieved to compare and analyze the changes in gradation before and after the compaction test.

The gyratory compaction test for coarse aggregate crushing resistance was similar to the Marshall compaction test. For the single-sized gyratory compaction test, aggregates with a particle size of 9.5–13.2 mm were washed, dried, and cooled, then carefully placed into a steel mold with an inner diameter of 150 mm in three layers, with the filling height controlled at approximately 115 mm. The gyratory compaction test was conducted with a compaction pressure of 600 kPa, a rotation speed of 30 r/min, and a constant rotation angle of 1.25 degrees. To simulate the effects of heavy traffic (equivalent to the maximum number of gyrations (N_{max}) of 205 corresponding to a design traffic load of more than 30 million equivalent single axle loads (ESALs)), the number of gyrations was set to 205. After 205 gyrations, the test aggregates were removed from the mold and sieved to analyze the particle composition after crushing.

For the gyratory compaction test with combined-sized aggregates, the aforementioned mixed aggregates of 2.36–4.75 mm, 4.75–9.5 mm, and 9.5–16 mm were used. After 205 gyratory cycles, the crushed aggregates were removed and sieved to examine the changes in gradation before and after gyratory compaction.

2.2.4. Asphalt Mixture Compaction Crushing Test

The aforementioned tests are conducted solely on aggregates to evaluate their crushing resistance, which differs somewhat from the actual preparation and formation of asphalt mixtures. Therefore, asphalt mixtures were prepared using coarse aggregates of slate, limestone, and basalt, respectively. During the preparation process, in addition to the coarse aggregates, fine aggregates of 0–2.36 mm were uniformly made of limestone fine aggregate; the filler was limestone mineral powder, the asphalt binder was penetration 70 paving asphalt, and the asphalt-to-aggregate ratio was 4.7%. All three asphalt mixtures prepared from the different rock types used the same mineral gradation of AC-13 asphalt mixture as listed in Table 1. To minimize gradation deviations, manually and strictly sieved single-sized coarse and fine aggregates were used for batching. To compare and analyze the potential crushing of the skeletal structures formed by different coarse aggregates during the compaction process, Marshall compaction tests and gyratory compaction tests were conducted on the asphalt mixtures. During the mixing of the AC-13 asphalt mixture, the aggregate heating temperature was 175 °C, and the asphalt heating temperature was 160 °C. The mixing temperature for the asphalt mixture was 160 °C, and the specimen compaction temperature ranged from 150–155 °C. When using the Marshall method for compaction, a Marshall electric compactor was used to apply 75 blows on each side. After

https://doi.org/10.3390/ma19030503

compaction, the specimen was demolded while hot and the asphalt mixture was separated and placed in a combustion furnace to burn off the asphalt binder. After combustion, it was cooled to room temperature and sieved to examine the aggregate gradation. When using the gyratory compaction method, a gyratory compactor was used for 205 compaction cycles. After gyratory compaction, the specimen was similarly demolded while hot and the asphalt mixture was separated and placed in a combustion furnace to burn off the asphalt. After combustion, it was cooled to room temperature and sieved to examine the aggregate gradation. By comparing the changes in the aggregate gradation of the asphalt mixtures before and after compaction using the two methods, the crushing behavior of the different rock coarse aggregates was analyzed.

Table 1. The mineral gradation of AC-13 asphalt mixture.

Type of Gradation	Passing Percentage at Different Sieve Sizes									
	16	**13.2**	**9.5**	**4.75**	**2.36**	**1.18**	**0.6**	**0.3**	**0.15**	**0.075**
Upper limit	100	100	75	39	30	22	18	14	11	8
Lower limit	100	80	62	25	18	14	8	6	5	5
Designed gradation	100	94	74	43	26	17.9	11.7	8.0	6.4	5.8

The Marshall compaction test and gyratory compaction test were conducted in triplicate, with the reported result being the average value of the three replicate tests.

3. Results

3.1. Coarse Aggregate Crushing Value

Tables 2 and 3 present the crushing value test results and the particle size distribution after crushing for the three types of rock coarse aggregates, respectively. The test results showed that the crushing value for slate was 9.2%, for basalt 11.4%, and for limestone 19.8%. It should be noted that basalt is considered the high-quality aggregate that has excellent crushing and wear resistance, while limestone is the most representative alkaline aggregate with moderate crushing resistance. Overall, slate had the lowest crushing value, outperforming traditional limestone and basalt, indicating that slate coarse aggregate possessed excellent resistance to crushing. After 21 days of immersion in water at 60 °C, the crushing value of slate was 10.2%; after high-temperature autoclaving, it was 10.6%; and after heating at 220 °C for 4 h, it was also 10.6%. Compared to the conventional crushing value, the effects of high-temperature water immersion, high-temperature autoclaving, and high-temperature heating on the crushing value of slate were minimal. Reference [22] reported that the crushing values of basalt, steel slag, limestone, recycled aggregate, and marble aggregate were 9.6%, 16.8%, 20.2%, 22.6%, and 26.7% respectively. Compared with these aggregates, the slate used in this study exhibits a crushing value comparable to that of basalt and superior to those of the other aggregates.

The crushing value test used single-sized aggregates of 9.5–13.2 mm, while the aggregates showed significant crushing after the test. As shown in Table 3, the crushing characteristics of the coarse aggregates were significantly related to their rock type. For example, the particle size distribution of limestone in the 9.5–13.2 mm range was 22.9%, indicating that nearly 77% of the 9.5–13.2 mm aggregate particles were crushed into smaller aggregates. In contrast, the distributions for basalt and slate in the 9.5–13.2 mm range were 46.4% and 44.8%, respectively, indicating that approximately 55% of the 9.5–13.2 mm aggregate particles were crushed into smaller aggregates. For other smaller particle size ranges, limestone consistently showed higher values than basalt and slate, while the particle size distributions for slate and basalt were generally similar. Slate did not exhibit excessive fragmentation issues due to its inherent bedding rock structure. After high-temperature water

immersion, high-temperature autoclaving, and high-temperature heating, the particle size distribution of crushed slate aggregate showed little difference from that after conventional crushing test.

Table 2. Crushing value test results of different coarse aggregates.

Aggregate	Limestone	Basalt	Slate	Slate (Soaked in Water at 60 °C for 21 Days)	Slate (Autoclaved at High Temperature)	Slate (Heated at 220 °C for 4 h)
Crushing value (%)	19.8	11.4	9.2	10.2	10.6	10.6

Table 3. Particle size distribution of crushed aggregates after the crushing value test.

Aggregate Particle Size	9.5–13.2	4.75–9.5	2.36–4.75	1.18–2.36	0.6–1.18	0–0.6
Limestone	22.9	40.0	17.3	7.5	5.6	6.7
Basalt	46.4	33.2	9.0	3.5	3.0	4.9
Slate	44.8	35.0	11.1	3.4	2.7	3.1
Slate (soaked in water at 60 °C for 21 days)	41.1	36.8	11.9	3.8	3.0	3.4
Slate (autoclaved at high temperature)	41.4	36.9	11.1	4.2	3.1	3.3
Slate (heated at 220 °C for 4 h)	39.3	38.2	11.9	4.2	3.1	3.3

Overall, the used slate aggregate exhibited good water resistance and heat resistance. The low crushing value also indicated that its resistance to crushing was comparable to that of traditional basalt and superior to that of limestone aggregate. Furthermore, slate coarse aggregate demonstrated good thermal stability, with no severe strength degradation after high-temperature heating. It had good resistance to crushing during the high-temperature production and construction compaction of asphalt mixtures. All of these results on high crushing resistance and durability could have contributed to the lack of slaty cleavage structure, and the cryptocrystalline matrix prevented these bedding planes from evolving into mechanically weak parting surfaces.

3.2. Single-Particle Compression Crushing Strength

The crushing modes of individual aggregate particles were found to be diverse. Taking slate coarse aggregate as an example, typical load-displacement curve results are shown in Figure 6. Overall, the crushing modes of individual particles can be categorized into three types: (1) Single-peak curve: In this crushing mode, the load-displacement curve has only one peak point. The coarse aggregate typically fractures into two pieces with neat fracture surfaces, producing very few fines or small fragments. (2) Double-peak curve: In this crushing mode, the load-displacement curve has two peak points. The main body of the coarse aggregate generally fractures into two pieces, generating a small amount of fines and small fragments. (3) Multi-peak curve: In this crushing mode, the load-displacement curve exhibits multiple peak points. The coarse aggregate usually fractures into multiple fragments, producing a large amount of fines and small fragments.

The statistical results of single-particle crushing modes for a total of 600 aggregate particles from three rock types including limestone, basalt, and slate, are presented in Table 4. For limestone coarse aggregate, regardless of changes in particle size or the number of loading contact points, its load-displacement curves were predominantly characterized by the multi-peak crushing mode, accounting for nearly 50%. The proportions of the other two modes were both close to 26–28%.

For basalt coarse aggregate, during the single-particle two-point compression crushing test, the load-displacement curves were mainly characterized by the double-peak crushing mode, accounting for 40%. The other two modes each accounted for approximately 30%, and particle size had no significant effect on the crushing mode. During the single-particle four-point compression crushing test, the load-displacement curves were dominated by the

multi-peak crushing mode. In the 4.75–9.5 mm range, it accounted for 40%, with the other two modes each at 30%. In the 9.5–13.2 mm range, the proportion of the multi-peak crushing mode slightly increased to 44%, while the other two modes each accounted for 28%.

Table 4. Breakdown of fracture modes for single-particle compression crushing tests.

Aggregate	Loading Method	Particle Size Distribution	AR	Breakdown of Fracture Modes (%)		
				Single-Peak	Double-Peak	Multi-Peak
Limestone	Two-point crushing	4.75–9.5 mm	1.0–1.2	26	28	46
		9.5–13.2 mm	1.0–1.2	28	26	46
	Four-point crushing	4.75–9.5 mm	1.0–1.2	26	28	46
		9.5–13.2 mm	1.0–1.2	26	26	48
Basalt	Two-point crushing	4.75–9.5 mm	1.0–1.2	32	40	28
		9.5–13.2 mm	1.0–1.2	28	40	32
	Four-point crushing	4.75–9.5 mm	1.0–1.2	30	30	40
		9.5–13.2 mm	1.0–1.2	28	28	44
Slate	Two-point crushing	4.75–9.5 mm	1.0–1.2	28	46	26
		9.5–13.2 mm	1.0–1.2	28	44	28
	Four-point crushing	4.75–9.5 mm	1.0–1.2	40	44	16
		9.5–13.2 mm	1.0–1.2	44	40	16

For slate coarse aggregate, during the single-particle two-point crushing test, the load-displacement curves were primarily characterized by the double-peak crushing mode, accounting for about 45%, with the other two modes each around 28%. During the single-particle four-point compression crushing test, the double-peak and single-peak crushing modes were dominant, each accounting for about 40%, while the multi-peak crushing mode accounted for only 16% in both cases.

The presence of weak points on the surface of coarse aggregate particles can lead to poor contact, causing grinding or local fractures that occur before the main failure under load, thereby generating more fines and fragments.

To describe the distribution patterns of compressive crushing strength for the three types of aggregates, the Weibull theory was employed for analysis. Based on the Weibull distribution function, the survival probability of crushable particles is related to their crushing strength, which can be characterized by Equation (4) [17]:

$$P_s = \exp\left[-\left(\frac{\sigma_f}{\sigma_{f0}}\right)^m\right] \tag{4}$$

where P_s is the survival probability of the particle, which can be calculated using Equation (5). σ_{f0} is the scale parameter, corresponding to the strength at a survival probability of 37%, serving as an important location parameter of the distribution for comparing strength levels of different materials. m is the Weibull modulus (shape parameter). It quantifies the degree of dispersion or reliability of the strength data. A higher m value indicates a more homogeneous material with less scattered strength properties (higher reliability), whereas a lower m value suggests greater inherent variability and defect distribution within the material, leading to less predictable strength.

$$P_s = \frac{i}{n+1} \tag{5}$$

where n is the total number of test particles. Following conventions in particle crushing strength studies, 50 particles strike a good balance between statistical reliability and experimental effort, sufficient for Weibull distribution fitting. i is the rank of a particle's crushing strength in the sequence after arranging all particles' crushing strength data in descending order.

Figures 7 and 8 present the crushing strength test results for three types of aggregates with different particle sizes (4.75–9.5 mm and 9.5–13.2 mm) from the two-point crushing tests. In particular, the straight lines in Figures 7b and 8b represent the linear fits to the data points, and their slopes correspond to the Weibull modulus. The results showed that the ranking of crushing strength among the three aggregates was consistent with that of the crushing values: slate exhibited the highest crushing strength, followed by basalt, with limestone showing the lowest. In terms of particle survival probability (P_s), slate demonstrated the greatest variability in crushing strength, while basalt and limestone exhibited relatively smaller variations. The Weibull modulus and the characteristic crushing strength corresponding to a 37% survival probability for the different aggregates are listed in Table 5. The fitted correlation coefficients (R^2) in Table 5 were all greater than 0.98, indicating that the crushing strengths of particles for all three aggregate types followed a Weibull distribution. Overall, the characteristic crushing strength of slate (ranging from 39.77 MPa to 44.42 MPa) was higher than that of basalt (ranging from 20.43 MPa to 21.95 MPa) and limestone (ranging from 12.94 MPa to 17.00 MPa). As the particle size increased, the characteristic crushing strength of all three aggregates decreased. Additionally, the Weibull modulus (ranging from 2.04 to 2.79MPa) also decreased with increasing particle size, which can be attributed to the increase in internal defects within the aggregates as particle size grows, leading to a reduction in crushing strength and an increase in variability.

In terms of particle strength, Ref. [24] conducted single-particle two-point crushing tests on slate particles with different shapes and sizes. The characteristic strength σ_{f0} for regularly shaped slate particles ranged from 11.70 to 34.05 MPa, and the Weibull modulus m ranged from 2.026 to 2.697. A similar trend of decreasing characteristic strength and Weibull modulus with increasing particle size was also observed. By comparison, the slate aggregate used in the present study demonstrated a high strength while exhibiting a comparable level of Weibull modulus.

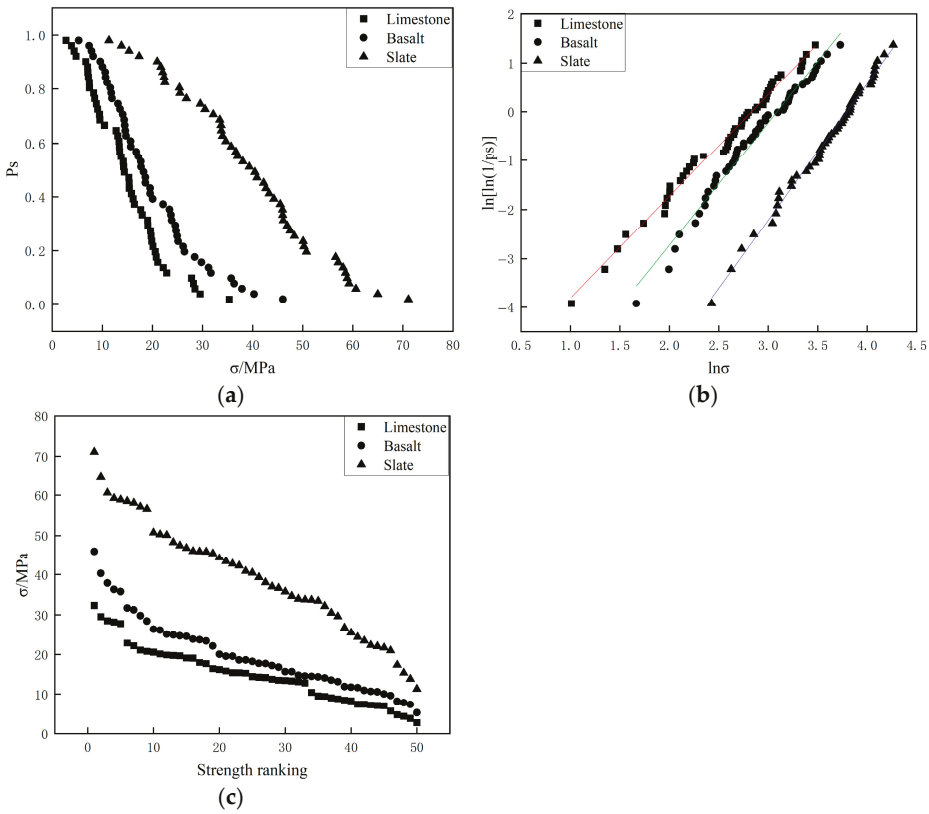

Figure 7. Two-point crushing test results of 4.75–9.5 mm particles for different aggregates ((**a**): Comparison of survival probabilities; (**b**) Weibull distribution of particle strength; (**c**) Single particle strength.).

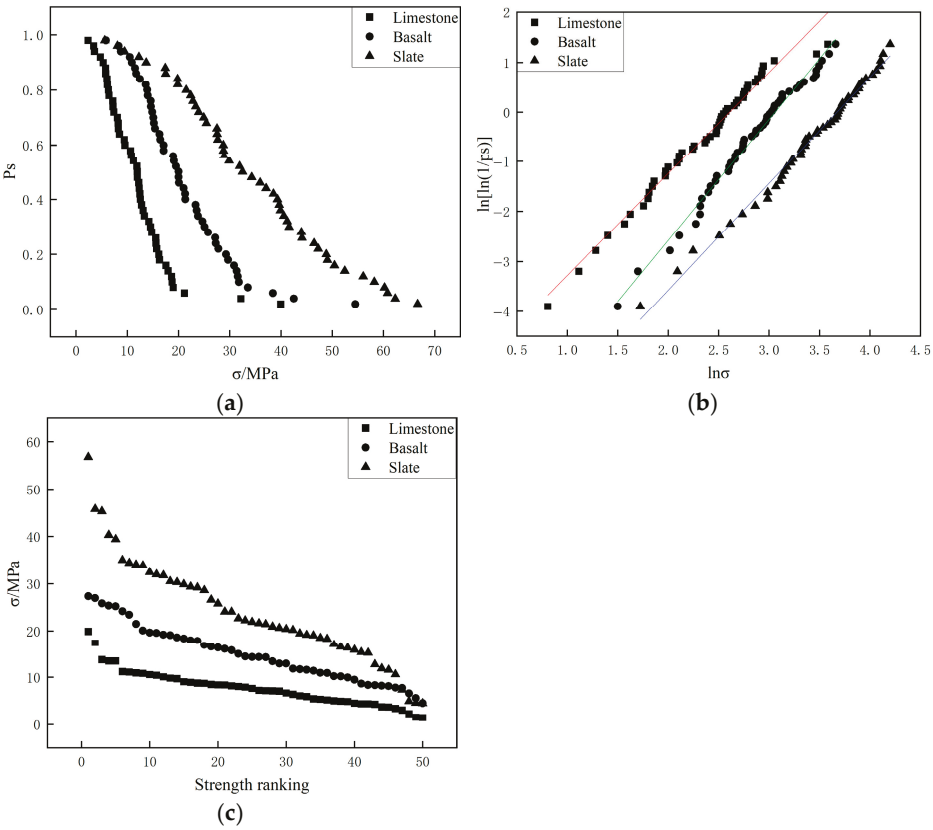

Figure 8. Two-point crushing test results of 9.5–13.2 mm particles for different aggregates ((**a**): Comparison of survival probabilities; (**b**) Weibull distribution of particle strength; (**c**) Single particle strength.).

Table 5. Statistical results of two-point crushing tests for different aggregates.

Aggregate	Aggregate Particle Size	Characteristic Compressive Strength/(MPa)	m	R^2
Limestone	4.75–9.5 mm	17.00	2.08	0.989
	9.5–13.2 mm	12.94	2.04	0.980
Basalt	4.75–9.5 mm	21.95	2.50	0.982
	9.5–13.2 mm	20.43	2.43	0.980
Slate	4.75–9.5 mm	44.42	2.79	0.993
	9.5–13.2 mm	39.77	2.14	0.990

Figures 9 and 10 present the results of four-point crushing tests for three types of aggregates with different particle sizes (4.75–9.5 mm and 9.5–13.2 mm), respectively. The results of the four-point crushing tests were similar to those of the two-point crushing tests. In the four-point crushing tests, In particular, the straight lines in Figures 9b and 10b represent the linear fits to the data points, and their slopes correspond to the Weibull modulus. the characteristic crushing strength of slate aggregate was consistently higher than that of basalt and limestone aggregates, indicating that slate aggregate exhibited superior crushing strength compared to basalt and limestone. Table 6 provides the Weibull modulus and the characteristic crushing strength corresponding to a 37% survival probability for the different aggregates. As the aggregate particle size increased from 4.75–9.5 mm to 9.5–13.2 mm, the characteristic compressive strength and Weibull modulus for the three types of aggregates in the four-point crushing tests showed minimal changes, indicating low sensitivity to variations in particle size.

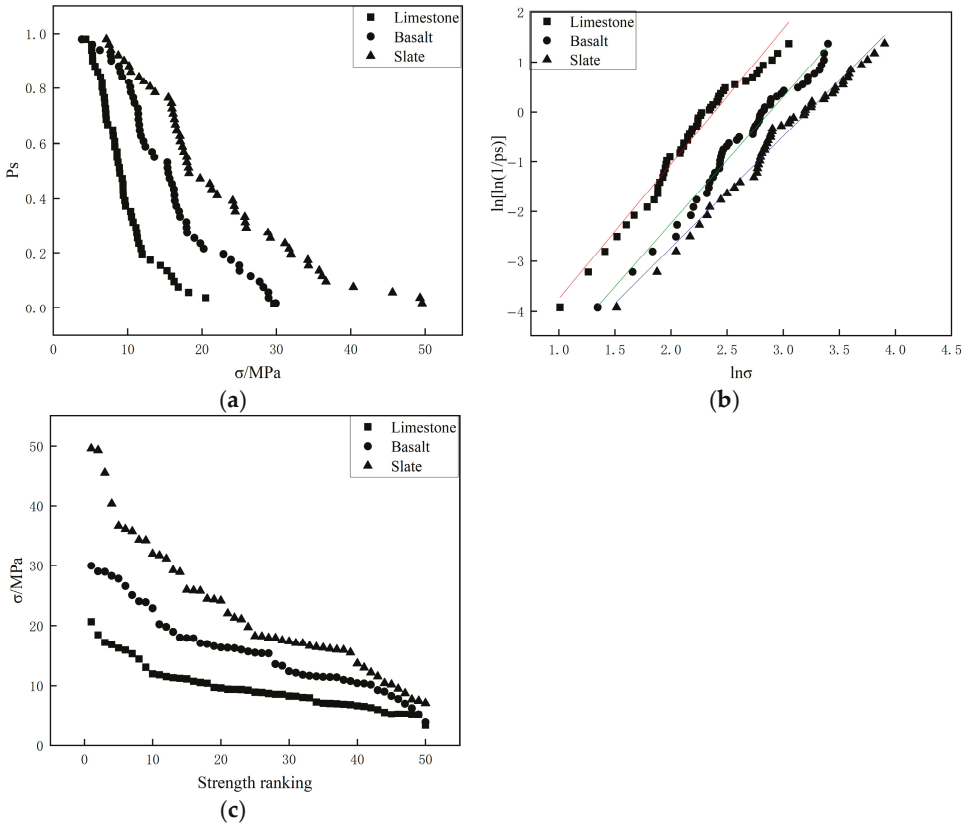

Figure 9. Four-point crushing test results of 4.75–9.5 mm particles for different aggregates ((**a**): Comparison of survival probabilities; (**b**) Weibull distribution of particle strength; (**c**) Single particle strength.).

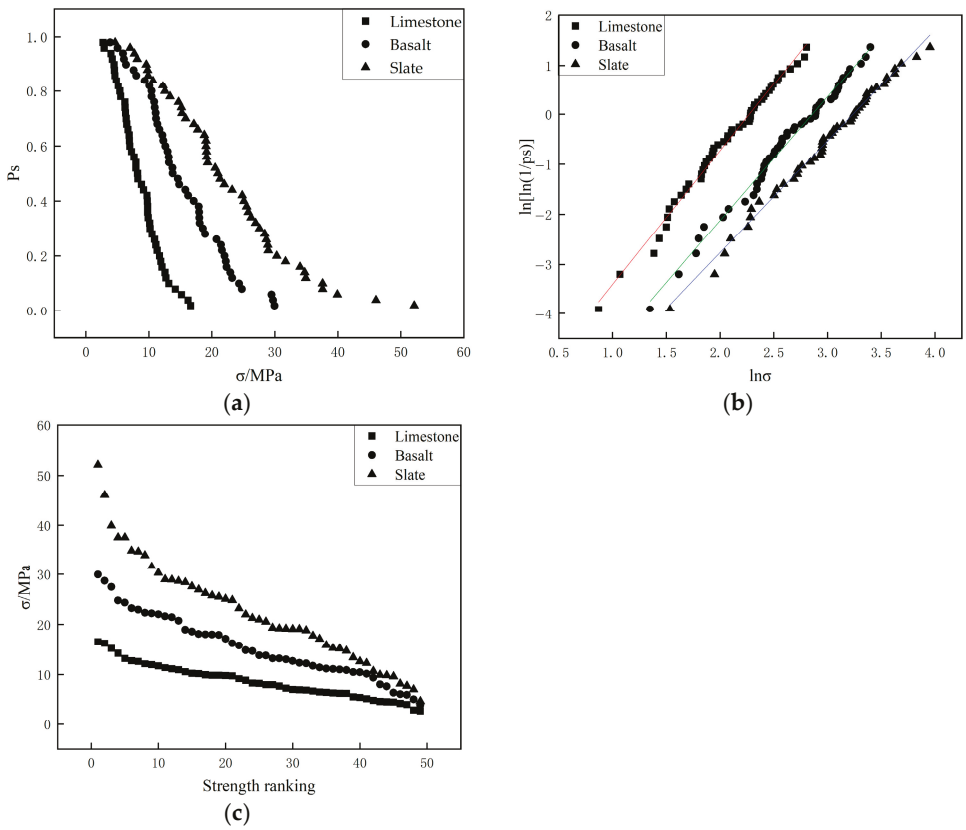

Figure 10. Four-point crushing test results of 9.5–13.2 mm particles for different aggregates ((**a**): Comparison of survival probabilities; (**b**) Weibull distribution of particle strength; (**c**) Single particle strength.).

Table 6. Statistical results of four-point crushing tests for different aggregates.

Aggregate	Aggregate Particle Size	Characteristic Compressive Strength/(MPa)	m	R^2
Limestone	4.75–9.5 mm	9.71	2.72	0.975
	9.5–13.2 mm	9.81	2.67	0.989
Basalt	4.75–9.5 mm	17.70	2.53	0.980
	9.5–13.2 mm	17.97	2.48	0.989
Slate	4.75–9.5 mm	24.33	2.24	0.983
	9.5–13.2 mm	25.65	2.23	0.993

The stress states and failure modes of aggregate particles differed between the two-point and four-point crushing tests. Compared to the two-point crushing test, the characteristic crushing strength in the four-point crushing test showed a significant decrease, with a reduction ranging from 20% to 40%, indicating that the stress conditions in the four-point crushing test were more demanding. Overall, the characteristic crushing strengths and Weibull modulus for the four-point crushing tests across different particle sizes were more similar, tending toward a certain value. This suggested that the four-point crushing test was more suitable for evaluating the crushing strength of aggregates with different particle sizes, as it reduced the influence of particle size. Additionally, whether in the two-point or four-point crushing tests, the Weibull modulus for the crushing strength of particles of different sizes for all three aggregates fail within the range of 2.0–3.0. This indicated a relatively dispersed distribution of aggregate crushing strength. The particle size and the number of contact points had a significant influence on the crushing strength.

A comparison of the Weibull modulus for these three types of aggregate (Tables 5 and 6) revealed that the m values for slate generally ranged from 2.14 to 2.79 across different particle sizes and loading methods. This range partially overlapped with those of limestone (2.04–2.72) and basalt (2.43–2.53) but exhibited a broader variation. This indicated that the dispersion of single-particle crushing strength for slate was at a moderate level, yet its variability is more sensitive to different conditions, such as changes in particle size. A similar Weibull modulus indicates that the tested slate aggregate had a similar variability in the single-particle strength when compared with limestone and basalt.

3.3. Coarse Aggregate Compaction Crushing Test

Table 7 presents the results of the crushing resistance tests for single-sized coarse aggregates (9.5–13.2 mm) during compaction. After 75 blows on one side using the Marshall compactor, significant crushing was observed for all aggregate types. For instance, the particle size distribution of limestone aggregates in the 9.5–13.2 mm range was 65.8%, indicating that nearly 34% of the 9.5–13.2 mm aggregate particles were crushed into smaller aggregates. In contrast, the distributions for basalt and slate aggregates in the same size range were 80.6% and 81.0%, respectively, indicating that approximately 20% of the 9.5–13.2 mm aggregate particles were crushed into smaller aggregates. After 75 Marshall compaction blows, limestone aggregates exhibited higher proportions in all smaller particle size ranges compared to basalt and slate aggregates, while the particle size distributions of slate aggregates closely resembled those of basalt.

Compared to the Marshall compaction method, gyratory compaction is another common laboratory compaction method for asphalt mixtures. The gyratory compaction pressure is relatively lower than the Marshall compaction energy, which is reflected in its reduced crushing effect on aggregates. After 205 cycles of gyratory compaction, the particle size distributions of limestone, basalt, and slate aggregates in the 9.5–13.2 mm range were 89.3%, 96.4%, and 94.4%, respectively. This indicated that only about 5% to 10% of the 9.5–13.2 mm aggregate particles were crushed into smaller aggregates, with relatively

minimal proportions in other smaller size ranges. These results suggested that the shearing action of gyratory compaction had a less destructive effect on aggregates, primarily causing wear and shearing of aggregate edges and corners. In contrast, Marshall compaction exerted a greater crushing effect, leading to a higher proportion of aggregates in the 4.75–9.5 mm range.

Table 7. Crushing resistance test results of single-sized 9.5–13.2 mm aggregates under Marshall and gyratory compaction.

Aggregate	Compaction Method	9.5–13.2	4.75–9.5	2.36–4.75	1.18–2.36	0.6–1.18	0–0.6
Limestone	Marshall compaction	65.8	24.8	4.9	1.7	1.2	1.6
	Gyratory compaction	89.3	7.0	1.4	0.6	0.6	1.1
Basalt	Marshall compaction	80.6	14.3	2.4	0.8	0.6	1.3
	Gyratory compaction	96.4	2.5	0.5	0.1	0.1	0.5
Slate	Marshall compaction	81.0	15.4	2.1	0.7	0.5	0.5
	Gyratory compaction	94.4	4.4	0.4	0.2	0.2	0.4

Overall, whether subjected to Marshall compaction or gyratory compaction, slate aggregates demonstrated excellent resistance to crushing. Their particle size distributions across different ranges closely resembled those of basalt, with no evidence of excessive damage due to the inherent bedding structure of slate.

Table 8 presents the results of the crushing resistance tests for mixed coarse aggregates under Marshall compaction and gyratory compaction. The mixed coarse aggregates were composed of three coarse aggregate sizes including 9.5–16 mm, 4.75–9.5 mm, and 2.36–4.75 mm, blended in specific proportions to simulate the skeletal structure formed by all coarse aggregates in asphalt mixtures. After 75 blows on one side using Marshall compaction or 205 cycles of gyratory compaction, the skeletal structures formed by the different coarse aggregates exhibited significant damage, leading to notable changes in their gradation and individual sieve residues. Before testing, the passing percentages of the different mixed aggregates through the 13.2 mm, 9.5 mm, 4.75 mm, and 2.36 mm sieves were 91.7%, 63.9%, 20.8%, and 0%, respectively. After testing, the passing percentages through these sieves increased significantly, with the effect of 75 blows on one side using Marshall compaction being noticeably greater than that of 205 cycles of gyratory compaction.

Table 8. Crushing resistance test results of mixed aggregates under Marshall and gyratory compaction.

Sieve Size/mm	Limestone		Basalt		Slate		Designed Gradation
	Marshall Compaction	Gyratory Compaction	Marshall Compaction	Gyratory Compaction	Marshall Compaction	Gyratory Compaction	
13.2	91.9	92.8	91.8	92.2	91.7	92.1	91.7
9.5	72.5	67.8	67.2	65.6	68.8	66.0	63.9
4.75	31.1	26.5	27.7	23.2	24.3	22.1	20.8
2.36	8.2	5.6	5.2	2.2	3.0	1.6	0.0
1.18	4.3	3.3	3.1	1.3	1.5	0.8	0.0
0.6	2.2	2.0	2.0	0.9	0.7	0.5	0.0
0.3	1.4	1.3	1.1	0.6	0.4	0.3	0.0

After 75 blows using Marshall compaction, the limestone mixed aggregates experienced a higher degree of crushing compared to the basalt and slate mixed aggregates, while the passing percentages of the slate mixed aggregates across different sieve sizes closely resembled those of the basalt mixed aggregates. After 205 cycles of gyratory compaction, the differences in passing percentages among the limestone, basalt, and slate mixed aggregates across various sieve sizes were relatively small. This further indicated that the shearing action of gyratory compaction had a less destructive effect on aggregates,

whereas Marshall compaction was more demanding and better distinguished the crushing resistance of different aggregates.

Figure 11 presents the comparative analysis of the differences in individual sieve residues after the crushing of mixed aggregates. It was evident that the skeletal structures composed of different coarse aggregates experienced the most significant crushing in the 9.5–13.2 mm size fraction. For example, after Marshall compaction, the individual sieve residues of the limestone, basalt, and slate mixed aggregates decreased by 8.4%, 3.2%, and 4.9%, respectively. Subsequently, the limestone and basalt mixed aggregates also underwent considerable crushing in the 4.75–9.5 mm fraction, resulting in reductions of 1.7% and 3.6% in their individual sieve residues, respectively. In contrast, the slate mixed aggregates did not experience excessive crushing in the 4.75–9.5 mm fraction; instead, their individual sieve residue increased by 1.4%. Overall, the Marshall compaction process produced the highest amount of fine aggregates in the 1.18–2.36 mm range. For instance, the individual sieve residues of the limestone, basalt, and slate mixed aggregates increased by 3.9%, 2.1%, and 1.5%, respectively.

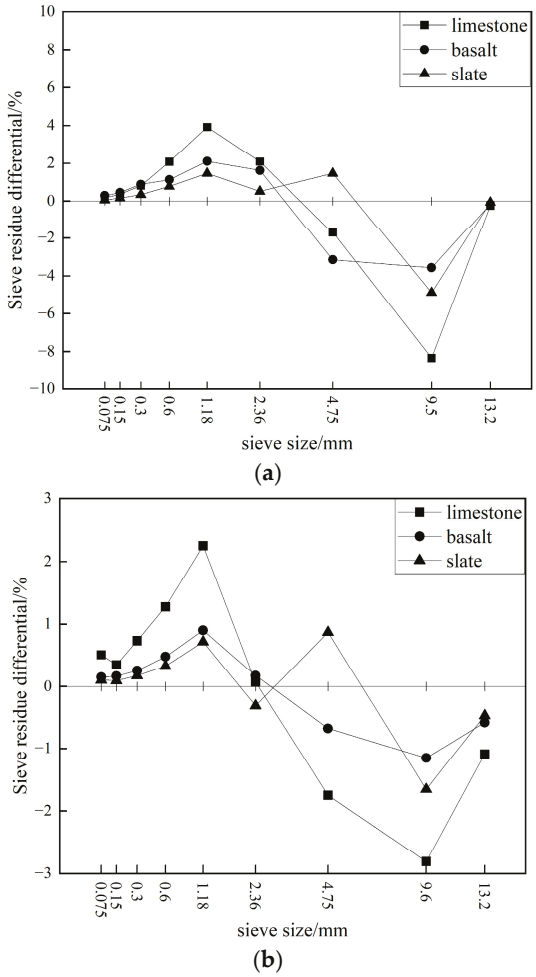

Figure 11. Difference in sieve residue fractions of mixed aggregates after crushing: ((**a**): Marshall compaction; (**b**): gyratory compaction.).

Compared to Marshall compaction, gyratory compaction had a similar effect on the limestone, basalt, and slate mixed aggregates, with the most significant crushing also occurring in the 9.5–13.2 mm coarse aggregate skeletal structure, and the highest production of fine aggregates in the 1.18–2.36 mm range. However, the magnitude of these changes was relatively smaller. For example, in the 9.5–13.2 mm range, the individual sieve residues of the limestone, basalt, and slate mixed aggregates decreased by 2.8%, 1.2%, and 1.7%,

respectively, while in the 1.18–2.36 mm range, they increased by 2.3%, 0.9%, and 0.8%, respectively. This indicated that the damage to the skeletal structure was concentrated in the 9.5–13.2 mm aggregates.

Compared to limestone and basalt, the slate mixed aggregates showed a positive difference in individual sieve residue at the 4.75 mm sieve, indicating that the damage to the skeletal structure of slate coarse aggregates was concentrated only in the 9.5–13.2 mm fraction, demonstrating better skeletal resistance to crushing.

A comparison with the results of the earlier Marshall and gyratory compaction tests on single-sized 9.5–13.2 mm aggregates showed that, for single-sized aggregates, approximately 20% to 34% were crushed after Marshall compaction, while about 5% to 10% were crushed after gyratory compaction. For mixed aggregates, the proportion of crushed aggregates can be characterized by the sum of the differences in individual sieve residues for the three aggregate sizes (9.5–16 mm, 4.75–9.5 mm, and 2.36–4.75 mm). This yielded approximate crushing proportions of 3.0% to 8.0% after Marshall compaction and 1.2% to 4.5% after gyratory compaction. These results indicated that Marshall compaction caused a greater degree of crushing than gyratory compaction, and the skeletal structure formed by mixed aggregates exhibited better resistance to crushing than that of single-sized aggregates. Since Marshall compactors are widely used in laboratories, while gyratory compactors are primarily employed for research purposes, the Marshall compaction test on single-sized aggregates can serve as a rapid and effective method for evaluating the crushing resistance of coarse aggregates.

In the compaction tests on coarse aggregates (both single-size and blended gradation), although minor deviations existed among different replicate tests, the range of variation was normal and controllable, and the exhibited trends in gradation evolution were highly consistent. Comparisons with reference aggregates clearly show that under both Marshall impact and gyratory shear compaction, the degree of breakage and gradation curves of slate aggregate were very close to those of basalt aggregate. These results demonstrate, from the scale of a pure aggregate skeleton, that slate aggregate can form a stable skeletal structure under compaction energy simulating construction. Its relict bedding structure did not lead to abnormal or excessive breakage of the skeleton, indicating excellent resistance to compaction-induced crushing.

3.4. Asphalt Mixture Compaction Crushing Test

Table 9 presents the results of the crushing resistance tests for different asphalt mixtures under Marshall compaction and gyratory compaction. In these tests, all asphalt mixtures used the same gradation to ensure a consistent aggregate skeletal structure. After 75 blows on each side using Marshall compaction or 205 cycles of gyratory compaction, significant changes were observed in the gradation and individual sieve residues of the different asphalt mixtures. Before testing, the passing percentages of the different asphalt mixtures through the key sieve sizes of 9.5 mm, 4.75 mm, 2.36 mm, and 0.075 mm were 74.0%, 43.0%, 26.0%, and 5.8%, respectively. After testing, the passing percentages through these key sieve sizes increased noticeably, with the effect of 75 blows on each side using Marshall compaction being significantly greater than that of 205 cycles of gyratory compaction.

While minor deviations exist among the replicate test data in Table 9, the overall trends indicated that the gradation changes of slate asphalt mixture after Marshall and gyratory compaction closely overlapped with the distribution range of basalt asphalt mixture. Their variation was distinctly different from the change curve of limestone asphalt mixture. This clear data distribution and evolution trend indicated that the compaction-induced breakage behavior of slate aggregate in asphalt mixtures is fairly consistent with that of basalt aggregate.

https://doi.org/10.3390/ma19030503

Table 9. Crushing resistance test results of asphalt mixture under Marshall and gyratory compaction.

Sieve Size/mm	Limestone		Basalt		Slate		Designed Gradation
	Marshall Compaction	Gyratory Compaction	Marshall Compaction	Gyratory Compaction	Marshall Compaction	Gyratory Compaction	
13.2	94.7	94.1	94.4	94.1	94.3	94.1	94.0
9.5	78.3	74.6	76.6	74.2	77.0	74.2	74.0
4.75	49.4	45.0	46.6	43.7	44.8	43.4	43.0
2.36	31.4	28.6	30.3	27.5	28.8	27.1	26.0
1.18	25.0	22.0	24.5	21.4	23.1	21.0	17.9
0.6	16.7	14.5	16.4	14.1	15.3	13.7	11.7
0.3	11.8	10.6	11.3	10.4	10.1	10.1	8.0
0.15	8.7	8.8	8.3	8.6	7.6	8.4	6.4
0.075	6.4	8.1	6.0	7.6	6.0	7.5	5.8

After 75 blows on each side using Marshall compaction, the limestone asphalt mixture experienced slightly more crushing compared to the basalt and slate asphalt mixtures, with increases in passing percentages across different sieve sizes ranging from 2% to 4%. In contrast, after 205 cycles of gyratory compaction, the differences in passing percentages among the limestone, basalt, and slate asphalt mixtures across various sieve sizes were minimal, all within 2%.

Figure 12 presents the comparative analysis of the differences in individual sieve residues among the different asphalt mixtures; it was evident that the effects of Marshall compaction and gyratory compaction on asphalt mixtures differed significantly. For example, Marshall compaction primarily caused the most significant crushing in the 9.5–13.2 mm aggregates, followed by the 1.18–2.36 mm aggregates. In contrast, gyratory compaction resulted in the most significant crushing in the 1.18–4.75 mm aggregates. In terms of the increase in individual sieve residues, Marshall compaction mainly led to an increase in fine materials within a broader range of 0.075–0.6 mm, while gyratory compaction primarily caused an increase in materials smaller than 0.075 mm (filler) and fine materials in the 0.6–1.18 mm range. This indicated that, under standard laboratory compaction conditions for asphalt mixtures, the destructive effects of Marshall compaction and gyratory compaction on aggregates were entirely different. The former primarily involved the crushing and refinement of coarse aggregates due to impact, while the latter mainly involved the grinding and shearing of 1.18–4.75 mm aggregates under rotational shear forces.

Based on a comparative analysis with the results of the crushing resistance tests on mixed aggregates under gyratory compaction, the findings described above were related to the fact that the asphalt mixture used limestone for the 0–2.36 mm fine aggregates, while basalt and slate, which are harder, were used for the coarse aggregates. The limestone fine aggregates filled the gaps in the skeletal structure formed by the basalt and slate coarse aggregates, making them more prone to breakage under compression and grinding. Overall, after adding asphalt binder, mineral filler, and fine aggregates, the degree of crushing of each type of aggregate in the asphalt mixture was significantly lower than that observed in the aforementioned mixed aggregates.

Similarly, the proportion of crushed coarse aggregate skeletal structure in the asphalt mixture can also be characterized by the sum of the residual differences for the three aggregate sizes: 9.5–16 mm, 4.75–9.5 mm, and 2.36–4.75 mm. Based on this, the proportion of aggregates crushed after Marshall compaction was approximately 2.5% to 4.7%, whereas after gyratory compaction was about 1.0% to 2.5%. These results further indicated that the degree of crushing caused by Marshall compaction was much greater than that caused by gyratory compaction, which can easily lead to internal structural damage in the specimen and affect its mechanical properties.

https://doi.org/10.3390/ma19030503

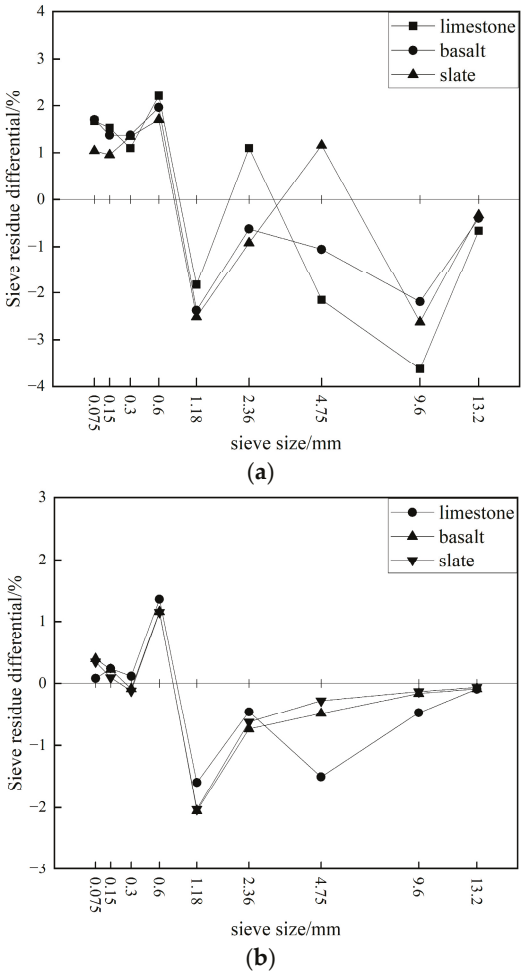

Figure 12. Difference in sieve residue fractions of asphalt mixture after crushing: (**a**) Marshall compaction; (**b**) gyratory compaction.

Whether under Marshall compaction or gyratory compaction, the resistance to crushing progressively improved from the skeletal structure formed by single-sized aggregates to that of mixed aggregates and further to the skeletal structure of asphalt mixtures. This also underscored that when designing asphalt mixtures with a high-skeletal structure, high-quality, crush-resistant aggregates should be selected, while excessive compaction that could cause aggregate breakage should be avoided. Slate asphalt mixtures demonstrated excellent resistance to crushing, comparable to basalt asphalt mixtures, which further confirms that the metamorphic bedding structure of slate did not lead to excessive aggregate crushing in its asphalt mixtures.

In the compaction tests on all asphalt mixtures, all results point to a clear trend that the degree of compaction-induced breakage in slate asphalt mixture was at the same level as that of basalt asphalt mixture and significantly lower than that of limestone asphalt mixture. This result further confirms, from the engineering scale of a complete asphalt mixture, that the internal structure of slate aggregate skeleton can withstand complex multi-directional stresses during actual mixture formation and compaction. No excessive breakage due to potential weak planes in slate aggregate occurred. It should be noted that an asphalt mixture is a multi-particle system where inter-particle interlocking is more sensitive to weaker particles, which are prone to be crushing under compaction. The compaction tests done on mixed aggregates and asphalt mixtures in this study showed that the tested slate aggregate did not exhibit excessive crushing in the stone skeleton, confirming the reliability of its overall performance at the engineering scale.

4. Conclusions

A series of crushing resistance tests was conducted on slate, limestone, and basalt aggregates. The crushing modes, crushing strength, and gradation changes of slate aggregates and its asphalt mixture was analyzed, and the main conclusions are as follows:

(1) The tested slate coarse aggregate exhibits a low crushing value, with its resistance to crushing comparable to that of traditional basalt and superior to limestone aggregate. The slate aggregate demonstrates good water resistance and thermal stability, meeting the requirements for resistance to crushing during high-temperature production and construction compaction of asphalt mixtures, as well as the demands for weathering resistance during service.

(2) For the tested slate coarse aggregate, the load-displacement curves from single-particle two-point compression crushing tests are primarily characterized by a double-peak crushing mode. In single-particle four-point compression crushing tests, the dominant modes are double-peak and single-peak crushing. The single-particle compressive crushing strength of slate coarse aggregate is greater than that of limestone and basalt aggregates, and the compressive crushing strength of individual particles follows the Weibull distribution pattern. Aggregate particle size and the number of force contact points significantly influence its characteristic crushing strength and Weibull modulus. The four-point crushing test is more suitable than the two-point crushing test for evaluating the crushing strength of aggregates with different particle sizes, as it reduces the influence of particle size.

(3) Marshall compaction causes a greater degree of crushing in different aggregates compared to gyratory compaction. Additionally, single-sized aggregates experience 2–3 times higher crushing levels than mixed aggregates. Therefore, the Marshall compaction test on single-sized aggregates can be used to rapidly evaluate the crushing resistance of aggregates from different rock types.

(4) Both the tested single-sized and mixed slate aggregates exhibit lower proportions of aggregate breakage during Marshall compaction and gyratory compaction processes compared to basalt and limestone aggregates. Asphalt mixtures prepared using slate coarse aggregate also demonstrate excellent resistance to crushing compared to basalt asphalt mixtures. This further confirms that the inherent bedding structure of the tested slate does not lead to excessive aggregate crushing and damage in its asphalt mixtures.

This study only focused on one type of slate, limestone, and basalt, and only one type of asphalt mixture was considered. The obtained findings were limited to the tested slate aggregates from a single quarry and thus necessary performance verification should be conducted on slate aggregates from other sources before practical engineering applications. In order to further validate the results of this study, a test section of 300 m of asphalt concrete containing the slate coarse aggregates obtained from the De'an Quarry in Qinzhou was constructed in the Qinzhoubei Freeway, April, 2025. The tracking observation results of the test section will further verify the long-term service performance of asphalt concrete with slate aggregates.

Author Contributions: Conceptualization, H.H. and L.M.; data curation, H.H., Y.Z. and K.Z.; formal analysis, H.H., Y.Z. and K.Z.; investigation, H.H., Y.Z. and K.Z.; methodology, Y.X. and L.M.; resources, L.M.; software, Y.X. and L.M.; supervision, L.M.; validation, H.H., Y.Z. and K.Z.; visualization, Y.X. and L.M.; writing—Original draft, H.H.; writing—Review and editing, L.M. All authors have read and agreed to the published version of the manuscript.

Funding: This research was supported by China Gezhouba Group No. 1 Engineering Co., Ltd. Research project (YGS-QZB-2024-FW-002).

https://doi.org/10.3390/ma19030503

Institutional Review Board Statement: Not applicable.

Informed Consent Statement: Not applicable.

Data Availability Statement: The original contributions presented in this study are included in the article. Further inquiries can be directed to the corresponding author.

Acknowledgments: The authors are grateful for the financial support of the research project of CCCC-SHB Fourth Engineering Co., Ltd. (No. G19SLLX030-QT083) and the research project of Handan Binjiang Environmental Protection Technology Group Co., Ltd. (No.202501xh0015).

Conflicts of Interest: Author Yanfei Zhu and Kun Zhou were employed by the China Gezhouba Group No. 1 Engineering Co., Ltd. The funder was not involved in the study design, collection, analysis, interpretation of data, the writing of this article or the decision to submit it for publication. The remaining authors declare no conflicts of interest.

References

1. Ikari, M.J.; Niemeijer, A.R.; Marone, C. Experimental investigation of incipient shear failure in foliated rock. *J. Struct. Geol.* **2015**, *77*, 82–91. [CrossRef]
2. Bahaaddini, M.; Hagan, P.C.; Mitra, R.; Khosravi, M.H. Scale effect on the shear behaviour of rock joints based on a numerical study. *Eng. Geol.* **2014**, *181*, 212–223. [CrossRef]
3. Wenk, H.-R.; Yu, R.; Cárdenes, V.; López-Mungira, A.; Briers, N. Fabric and anisotropy of slates: From classical studies to new results. *J. Struct. Geol.* **2020**, *138*, 104051. [CrossRef]
4. Oti, E.J. Engineering properties of concrete made with slate waste. *Proc. Inst. Civ. Eng.-Constr. Mater.* **2010**, *163*, 131–142. [CrossRef]
5. Chen, Y.; Wei, K.; Liu, W.; Yang, C.H.; Zhou, J.W. Experimental characterization and micromechanical modelling of anisotropic slates. *Rock Mech. Rock Eng.* **2016**, *49*, 3541–3557. [CrossRef]
6. Ding, C.-D.; Zhang, Y.; Hu, D.-W.; Zhou, H.; Shao, J.-F. Foliation effects on mechanical and failure characteristics of slate in 3D space under Brazilian test conditions. *Rock Mech. Rock Eng.* **2020**, *53*, 3919–3936. [CrossRef]
7. Weng, M.-C.; Lin, S.-S.; Lee, C.-S.; Jeng, F.-S. An anisotropic thermal–mechanical coupling failure criterion for slate. *Rock Mech. Rock Eng.* **2024**, *57*, 8157–8177. [CrossRef]
8. Weng, M.-C.; Li, H.-H.; Fu, Y.-Y.; Fang, C.-H.; Chen, H.-R.; Chang, C.-Y. A failure criterion for foliation and its application for strength estimation of foliated metamorphic rock. *Int. J. Rock Mech. Min. Sci.* **2022**, *153*, 105086. [CrossRef]
9. Weng, M.-C.; Chang, C.-Y.; Jeng, F.-S.; Li, H.-H. Evaluating the stability of anti-dip slate slope using an innovative failure criterion for foliation. *Eng. Geol.* **2020**, *275*, 105737. [CrossRef]
10. Wu, H.; Ma, T.; Li, Y.; Yang, T.; Zhang, G. Numerical and experimental investigation of the anisotropic tensile behavior of layered rocks in 3D space under Brazilian test conditions. *Int. J. Rock Mech. Min. Sci.* **2023**, *170*, 105558.
11. Debecker, B.; Vervoort, A. Experimental observation of fracture patterns in layered slate. *Int. J. Fract.* **2009**, *159*, 51–62. [CrossRef]
12. Hong, R.-C.; Yu, R.; He, T.; He, M.-C. Failure and mechanical behavior of transversely isotropic rock under compression-shear tests: Laboratory testing and numerical simulation. *Eng. Fract. Mech.* **2020**, *238*, 107389.
13. Xu, Y.-P.; Cheng, Q.-N.; Huang, X.-C.; Yang, G.-S.; Zhou, L.-F. An experimental study of microstructure and uniaxial compression test of carbonaceous slate in a deep buried tunnel. *Hydrogeol. Eng. Geol.* **2020**, *47*, 96–102. (In Chinese)
14. Jiang, H.; Jiang, A.; Zheng, F. Creep mechanical behavior and damage model of layered slate under combined thermal-hydraulic-mechanical action. *Case Stud. Therm. Eng.* **2024**, *55*, 104137. [CrossRef]
15. Yang, C.-H.; Mao, H.-J.; Wang, H.-L.; Li, S.-C. Study on variation of microstructure and mechanical properties of water-weakening slates. *Rock Soil Mech.* **2006**, *27*, 2090–2098. (In Chinese)
16. Li, E.; Feng, J.; Zhang, L.; Chen, Q.; Wang, P. Brazilian tests on layered carbonaceous slates under water-rock interaction and weathering. *Chin. J. Geotech. Eng.* **2021**, *43*, 329–337. (In Chinese)
17. Li, G.; Tang, C. A statistical meso-damage mechanical method for modeling trans-scale progressive failure process of rock. *Int. J. Rock Mech. Min. Sci.* **2015**, *74*, 133–150. [CrossRef]
18. Xiang, H.; Zhang, W.; Liu, P.; He, Z. Fatigue–Healing Performance Evaluation of Asphalt Mixture Using Four-Point Bending Test. *Mater. Struct.* **2020**, *53*, 47. [CrossRef]
19. Zheng, P.; Tan, X.; Du, Z.; Chen, L.; Liu, H.; Wang, D. Microscopic damage and deterioration of carbonaceous slate in cold region subjected to freeze-thaw cycles. *J. Rock Mech. Geotech. Eng.* **2025**, *18*, 113–128. [CrossRef]
20. Zheng, P.; Tan, X.; Xie, Y.; Wang, F.; Liu, H. Study on the tensile strength and fracture characteristics of interlayer mineral grain interfaces in slate exposed to water–rock interaction. *Rock Mech. Rock Eng.* **2025**, *58*, 9801–9824. [CrossRef]

21. Liu, H.; Qin, H.; Gao, Y.; Zhou, Y. Experimental study on particle breakage of rockfill and coarse aggregates. *Rock Soil Mech.* **2005**, *26*, 562–566. (In Chinese)
22. Jiang, S.; Yan, H.; Mo, L. Crushing characteristics of coarse aggregates for asphalt mixtures under simulated laboratory compaction loads and repeated traffic loads. *Materials* **2022**, *15*, 5865. [CrossRef] [PubMed]
23. Shen, C.; Liu, S.; Wang, L.; Li, X.; Xu, W. Micromechanical modeling of particle breakage of granular materials in the framework of thermomechanics. *Acta Geotech.* **2019**, *14*, 939–954. [CrossRef]
24. Gao, Y.; Mao, H. Impacts of slow-rate cyclic loading on the crushing of single rockfill particles. *Rock Mech. Rock Eng.* **2025**, *58*, 4791–4808. [CrossRef]
25. *JTG E42-2024*; Test Methods of Aggregate for Highway Engineering. Research Institute of Highway Ministry of Transport: Beijing, China, 2025; pp. 1–137. (In Chinese)
26. Jaeger, J.C. Failure of rocks under tensile conditions. *Int. J. Rock Mech. Min. Sci. Geomech. Abstr.* **1967**, *4*, 219–227. [CrossRef]
27. Afshar, T.; Disfani, M.M.; Arulrajah, A.; Narsilio, G.A. Impact of particle shape on breakage of recycled construction and demolition aggregates. *Powder Technol.* **2017**, *308*, 1–12. [CrossRef]
28. Todisco, M.C.; Wang, W.; Coop, M.R.; Senetakis, K. Multiple contact compression tests on sand particles. *Soils Found.* **2017**, *57*, 126–140. [CrossRef]

Disclaimer/Publisher's Note: The statements, opinions and data contained in all publications are solely those of the individual author(s) and contributor(s) and not of MDPI and/or the editor(s). MDPI and/or the editor(s) disclaim responsibility for any injury to people or property resulting from any ideas, methods, instructions or products referred to in the content.

https://doi.org/10.3390/ma19030503

materials

MDPI

Article

Evaluation of Moisture Damage in Asphalt Mixtures Under Dynamic Water Pressure Using 3D Laser Scanning

Wentao Wang [1], Hua Rong [2], Yinghao Miao [1] and Linbing Wang [3,*]

[1] National Center for Materials Service Safety, University of Science and Technology Beijing, Beijing 100083, China; wentaowang@ustb.edu.cn (W.W.)
[2] Wuzhou Engineering Group Corporation Ltd., Beijing 100083, China
[3] The Sensing and Perception Lab, School of Environmental, Civil, Agricultural and Mechanical Engineering, University of Georgia, Athens, GA 30602, USA
* Correspondence: linbing.wang@uga.edu

Abstract

Under continuous erosion of dynamic water pressure generated by vehicle–water–pavement coupling interaction, asphalt mixture will gradually deteriorate and severe moisture damage finally emerges. The fine aggregate mixture (FAM) component is notably eroded and stripped, while the aggregate component even cracks sometimes. Sufficient attention has not been paid to these critical phenomena. This study employed the 3D laser scanning technique to detect changes in surface roughness of the asphalt mixture before and after it was eroded by dynamic water pressure. The degree of erosion of the asphalt mixture, FAM component, and aggregate component were thereby evaluated. The influences of experimental parameters such as water temperature and pore water pressure magnitude, as well as variable parameters including lithology and asphalt type, were also taken into account. By integrating the detection of physical and mechanical properties evolution of aggregates, the mechanism of moisture damage was comprehensively illustrated from the perspectives of both components of FAM and aggregate. The findings revealed that the 3D laser scanning technique could clearly detect and quantitatively assess the morphological changes on the asphalt mixture surface after been eroded in dynamic water pressure. Both types of asphalt mixtures exhibited varying degrees of erosion and wear, and obvious increases in surface unevenness were observed in each case. Variations in either temperature or pore water pressure magnitude showed limited influence on moisture damage in basalt-based asphalt mixture. In contrast, moisture damage sustained by limestone-based asphalt mixture was notably sensitive to temperature changes but remained largely insensitive to fluctuations in pore water pressure magnitude. The increase in surface roughness of asphalt mixture was primarily attributed to the scouring action of dynamic water pressure, which removed the FAM component surrounding coarse aggregate particles. Degradation in coarse aggregate particles would lead to the deterioration of the entire asphalt mixture. The compatibility between the stripping rate of FAM component and the deterioration rate of coarse aggregate governed the macroscopic manifestation of overall moisture damage in the asphalt mixture.

Keywords: asphalt mixture; moisture damage; dynamic pore water pressure; 3D laser scanning technique; erosion mechanism

1. Introduction

Under continuous erosion of dynamic water pressure generated by vehicle–water–pavement coupling interaction, asphalt mixture will gradually deteriorate and severe moisture damage will finally emerge [1]. Asphalt mixture mainly comprises a coarse aggregate skeleton, fine aggregate mixture (FAM) component, and air void component. The FAM component is notably eroded and stripped away after asphalt mixture is conditioned in a dynamic water pressure environment. Conditioning a sample of asphalt mixture with a polished surface in a dynamic water pressure environment will often observe significant surface roughening, as shown in Figure 1. Obvious cracks sometimes even occurred in aggregate particles of asphalt mixture specimens after being eroded by dynamic water pressure, as shown in Figure 2. This typical phenomenon proved that moisture damage of asphalt mixture related to dynamic water pressure exhibited a totally different damage mechanism compared with damage forms related to traditional water environments like static water immersion and freeze–thaw.

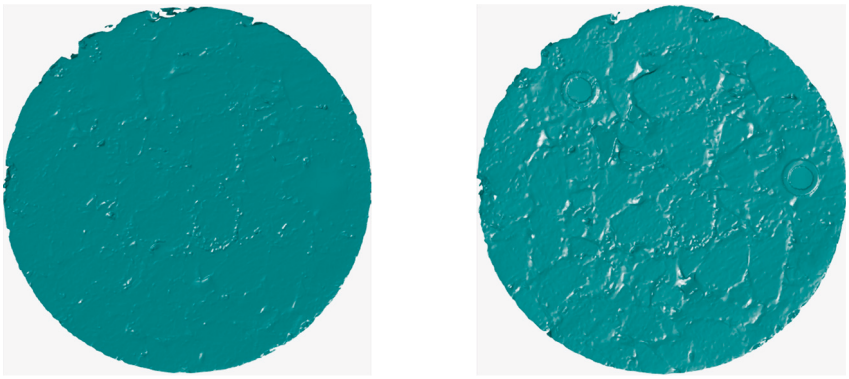

(**a**) Before conditioning: smooth surface. (**b**) After conditioning: rough surface and cracks.

Figure 1. Comparison on asphalt mixture's surface before and after being conditioned in dynamic water pressure environment.

Figure 2. Obvious cracking occurred in aggregate of Marshall specimen after being eroded by dynamic water pressure.

After being eroded by dynamic water pressure, comprehensive performance of the asphalt mixture inevitably deteriorated to a certain extent. Multi-scale testing techniques could be employed to evaluate the degradation characteristics of asphalt material properties. Chen and Huang [2] employed dynamic modulus tests and Superpave indirect tensile tests to evaluate the moisture damage resistance of asphalt mixture specimens subjected to dynamic water pressure. They also assessed the influence of factors such as anti-stripping agents, coarse aggregate angularity, and the number of dynamic water pressure cycles on the test results. Weldegiorgis and Tarefder [3,4] utilized dynamic modulus tests and a newly proposed index to evaluate the moisture damage resistance of specimens

https://doi.org/10.3390/ma19081514

subjected to dynamic water pressure and proposed corresponding test procedures. Varveri et al. [5] conducted a comparative study on the differences between long-term and short-term moisture damage using water bath immersion and dynamic water pressure erosion. They found that the former primarily involved moisture diffusion, while the latter was characterized by cyclic pore water pressure, which could effectively accelerate the water environment action process. Tarefder and Ahmad [6] applied dynamic water pressure conditioning to field core specimens and conducted indirect tensile tests for performance evaluation. They found that penetrating and terminal voids had little effect on moisture damage resistance of asphalt mixture. Xu et al. [7] investigated the influence of test parameters and specimen diameter on the accuracy of internal hydraulic characteristic measurements in asphalt mixture specimens after dynamic water scour, using relative error indicators to identify the optimal combination of test parameters that maximize image resolution and contrast. Varveri et al. [8] employed CT scanning and image analysis techniques to analyze the damage mechanisms induced by dynamic water pressure. Their study revealed that strength degradation was related to the state and duration of dynamic water pressure action, as well as the type of raw materials. Image analysis techniques visually revealed the mechanism by which dynamic water pressure affected air void content and connectivity inside asphalt mixture. Faisal et al. [9] conducted tests on asphalt mixture specimens subjected to dynamic water conditioning and found that the modulus of FAM decreased by 60% compared to dry conditions after water action, which led to a 70% reduction in the overall indentation modulus of asphalt mixture. Khorasani and Al-Rub [10] employed nanoindentation to investigate the local nanoscale mechanical properties of the FAM, aggregate, and their interaction zone within asphalt mixture. They found that the modulus and hardness values of the interaction zone fell between those of the aggregate and FAM. Yao et al. [11] utilized atomic force microscope (AFM) and nanoindentation to quantitatively determined the strength loss and damage types (adhesive or cohesive failure) of asphalt materials after moisture damage, and validated the nanoscale test results through surface energy techniques and freeze–thaw splitting tests.

Based on the above research, it is evident that employing a variety of testing techniques could effectively characterize the multi-scale performance degradation patterns of asphalt-related materials subjected to moisture damage. These studies exhibited the following characteristics: Firstly, the associated testing costs were relatively high, particularly for micro- and nano-scale techniques such as CT and AFM. Systematic testing of a large number of moisture-damaged asphalt-material specimens required careful consideration of the experimental expenses beforehand. Secondly, many of these tests were destructive, such as mechanical strength and dynamic modulus tests, making it difficult to characterize the performance degradation of the same specimen before and after moisture damage. Thirdly, there was a lack of standardized image-based methods for directly observing and analyzing the morphological changes associated with the damage and deterioration of asphalt mixture specimens. Direct photography could capture apparent changes on the specimen surface, as illustrated in Figures 1 and 2. However, more precise quantitative analysis of surface variations required the use of more sophisticated techniques. CT technology could effectively acquire images of internal damage characteristics within asphalt mixtures [12–14]. Considering that the erosive effect of dynamic water pressure on an asphalt mixture specimen was a dynamic process progressing from the surface inward, CT scanning was highly effective for characterizing changes in internal pore channels after a certain degree of internal damage had developed. Nevertheless, its ability to assess morphological changes on the specimen surface during the initial stage of damage was limited. 3D laser scanning technology, on the other hand, could effectively measure and quantify the roughness characteristics of the macroscopic surface texture of

asphalt pavements [15,16]. It was particularly well-suited for the quantitative analysis of surface roughening induced by erosion and scouring from dynamic water pressure on asphalt mixture.

While the aforementioned studies primarily focused on the overall performance changes exhibited by entire asphalt mixture, several critical phenomena associated with the stepwise erosion process of FAM component induced by dynamic water pressure, as well as the direct development of visible cracks in coarse aggregate particles, have not received adequate attention and investigation. The observations of Figures 1 and 2 strongly demonstrated the importance of fundamental components such as the FAM component and coarse aggregate particles in determining the overall moisture damage resistance of an asphalt mixture. Furthermore, compared with conducting complicated mechanical tests to evaluate changes in the comprehensive properties of eroded asphalt mixture, it is more straightforward and effective to directly observe and assess its surface erosion changes, which can be well achieved by the 3D laser scanning technique.

This study employed the 3D laser scanning technique to detect changes in surface roughness of asphalt mixture before and after it was eroded by dynamic water pressure. The degree of erosion of the asphalt mixture, FAM component, and aggregate component were thereby evaluated. The influence of evaluating dimension on surface erosion degree was discussed. The impacts of experimental parameters such as water temperature and pore water pressure magnitude, as well as variable parameters including lithology and asphalt type, were also taken into account. By integrating the detection of physical and mechanical properties evolution of aggregates, the mechanism of moisture damage was comprehensively illustrated from the perspectives of both components of FAM and aggregate.

2. Materials and Sample Preparation

In this study, two types of typical asphalt mixture samples were fabricated for comprehensive evaluation. A base asphalt binder labeled 70# and a styrene–butadiene–styrene (SBS)-modified asphalt binder were selected. The asphalt binder samples' physical properties were inspected, and their testing results are summarized in Table 1, both of which satisfied the technical requirements of the specification [17]. Limestone and basalt aggregate were adopted with two different gradations of AC-20 and SMA-16 respectively, as shown in Figure 3. AC-20 and SMA-16 were usually applied to construct the middle layer and top surface layer of asphalt pavement, respectively. Therefore, these two types of typical asphalt mixture were selected to comparatively evaluate moisture damage resistance induced by dynamic pore water pressure. For AC-20, the 70# base asphalt binder was applied to fabricate hot mix asphalt (HMA) samples with the asphalt content of 3.94% and the air void content of 4.7%. For SMA-16, the SBS-modified asphalt binder was used to prepare asphalt mixture samples with the asphalt content of 5.57%, the fiber content of 0.3%, and the air void content of 3.8%. Specifically, the lithology of the fine aggregate in SMA-16 was limestone. Basic service properties of asphalt mixture samples were tested, as shown in Table 2, both of which met the requirements of the specification [17].

Table 1. Physical properties of asphalt binder.

Items	Units	Base 70# Asphalt Binder		SBS Modified Asphalt Binder	
		Requirements	Results	Requirements	Results
Penetration (25 °C, 100 g, 5 s)	0.1 mm	60–80	64	60–80	74
Softening Point	°C	≥46	48	≥75	77.5
Ductility (5 cm/min)	cm	≥20 (10 °C)	42	≥30 (5 °C)	35

https://doi.org/10.3390/ma19081514

Table 1. *Cont.*

Items		Units	Base 70# Asphalt Binder		SBS Modified Asphalt Binder	
			Requirements	Results	Requirements	Results
Residue after rolling thin film oven test (163 °C, 85 min)	Mass Loss	%	≤±0.8	−0.177	≤±1.0	−0.204
	Residual Penetration Ratio (25 °C, 100 g, 5 s)	%	≥61	65.4	≥60	65.6
	Residual ductility (5 cm/min)	cm	≥6 (10 °C)	9.8	≥20 (5 °C)	21.2

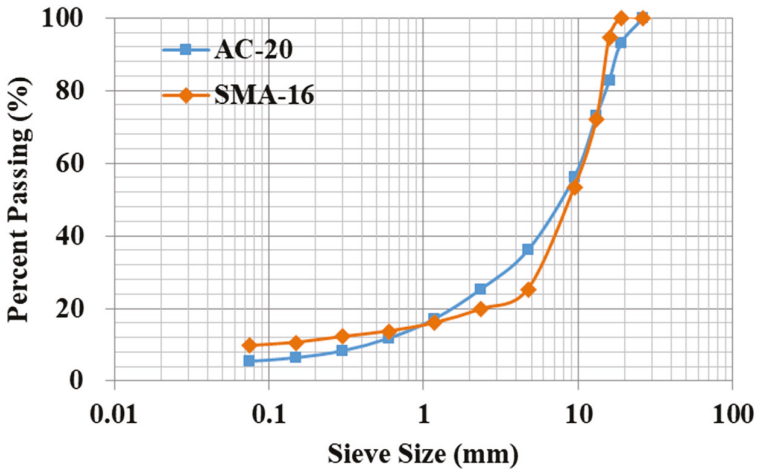

Figure 3. Two types of aggregate gradations.

Table 2. Mechanical properties of the asphalt mixture.

Items	Units	AC-20-Limestone-70#		SMA-16-Basalt-SBS	
		Requirements	Results	Requirements	Results
Marshall stability	kN	≥8	11.25	≥6	9.06
Flow value	mm	1.5–4	2.8	–	–
Residual Marshall stability of water immersion	%	≥80	84.7	≥80	84.7
Tensile strength ratio of Freeze–thaw	%	≥75	79.6	≥80	83.8
Rutting dynamic stability	Cycle/mm	≥1000	1539	≥4000	4385

Asphalt mixture samples were fabricated at relevant suitable temperatures according to the requirements of the specification [18]. The mixing temperatures for AC-20 and SMA-16 were 160 °C and 170 °C respectively, and their compacting temperatures were 150 °C and 160 °C individually. The Superpave Gyratory Compactor (SGC) device (Controls, Aosta, Italy) was applied to compact specimens of asphalt mixture. The cylindrical sample's dimensions were 150 mm in diameter and 150 mm in height. The core drilling machine (Cayken, Shanghai, China) and the auto saw device (Zhongdeshenke, Beijing, China) were applied to extract a core sample with a uniform distribution of air voids from a SGC specimen, while the dimensions of the core sample were 100 mm in diameter and 100 mm in height. The core specimen of the asphalt mixture was further divided uniformly into three pieces along the height direction, and thus the dimensions of the final sample of asphalt mixture were 100 mm in diameter and 30 mm in height. The circular cross-sections of the asphalt mixture sample's top and bottom sides were polished successively using 100-, 240-, 400-, 600-, 800-, 1000-, 1200-, and 1500-grid sandpapers. A smooth cross-section

with enough representative coarse aggregates was selected for further erosion by different dynamic pore water pressure environments. Typical examples of fabricated asphalt mixture samples for AC-20-Limestone-70# and SMA-16-Basalt-SBS are shown in Figure 4. Each group of dynamic water pressure conditioning was prepared with one HMA specimen.

(**a**) AC-20-Limestone-70# (**b**) SMA-16-Basalt-SBS

Figure 4. Typical examples of fabricated asphalt mixture samples.

3. Test and Analysis Methods

3.1. Dynamic Pore Water Pressure Conditioning Method

The Moisture Induced Sensitivity Tester (MIST) device (Hangtianhangyu, Beijing, China) was applied to provide dynamic pore water pressure environment for stripping effect on the asphalt mixture and aggregate. This kind of dynamic water was formed by the repeat process of inflation and restitution of a bladder inside the device [19]. Three variable parameters could be adjusted to simulate different dynamic water environments, which included water temperature, magnitude of pore water pressure, and conditioning duration. In this study, the parameter of conditioning duration was fixed at 4000 cycles for every water-conditioning environment, while the influential degrees of water temperature and pore water pressure magnitude were evaluated at three levels respectively. Five environments of dynamic pore water pressure were taken into account in this study, and the proposal was summarized in Table 3. In particular, the expression of 60 °C—0.4 MPa represented that a sample of asphalt mixture or aggregate was conditioned in a dynamic water environment for 4000 cycles, in which the water temperature was 60 °C and the pore water pressure magnitude was 0.4 MPa.

Table 3. The proposal of dynamic pore water pressure environment conditioning.

No.	Water Temperature (°C)	Water Pressure Magnitude (MPa)	Duration (Cycles)
1	40	0.4	4000
2	50		
3	60		
4		0.3	
5		0.2	

3.2. The 3D Laser Scanning Technique

The 3D laser scanning technique was applied to measure the surface roughness of asphalt mixture samples, as shown in Figure 5. A sample was placed on the horizontal test bench with a series of reflective marking points being pasted around the sample and on its surface. As the FAM component was easily eroded and scoured away by dynamic water pressure, the pasted place of the reflective marking points on the sample's surface

https://doi.org/10.3390/ma19081514

was chosen within coarse aggregate particles. These scan-blank points on the sample's surface would be auto-filled by the algorithm during the analysis process. The obtained points were presented by x-y-z coordinates, and the scanning accuracy was set at 0.1 mm.

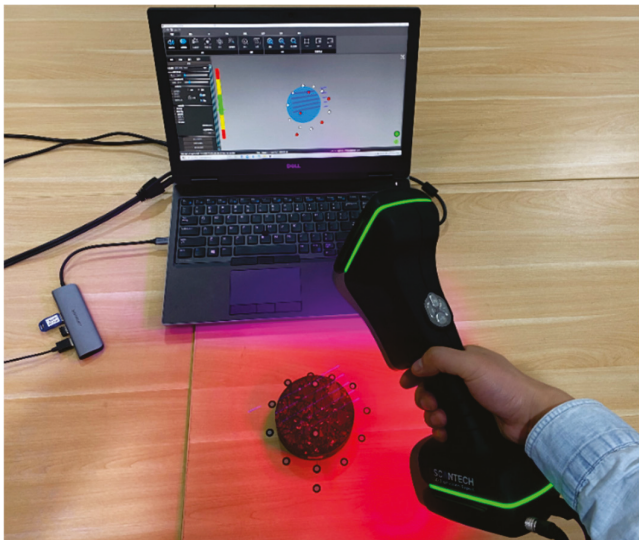

Figure 5. Measuring a sample's surface roughness using the 3D laser scanning technique.

The edge of the asphalt mixture sample might be deformed and become irregular due to stripping. Therefore, the central circular cross-section with the 90 mm diameter was selected from the sample's 100 mm diameter range to ensure uniformity and integrity of 3D scanning data distribution. The variation in surface roughness for asphalt mixture could be evaluated based on the measured 3D scanning data from this 90 mm diameter central circular cross-section. In addition, the central square cross-section with 60 mm side length was also chosen from the sample surface to compare the influence of evaluating dimension on roughness assessment. Two representative coarse aggregate particles with their surrounded FAM component for each group were selected for further analysis and discussion. To evaluate changes in the interface between the aggregate and FAM component, a rectangle cross-section with a 15~22 mm side-length range was selected for 3D scanning data analysis. The rectangle cross-section with a 4~8 mm side-length range was further determined within the chosen representative coarse aggregate particle to discuss changes in aggregate surface roughness. Different evaluating dimensions for surface erosion degree analysis based on 3D scanning are shown in Figure 6.

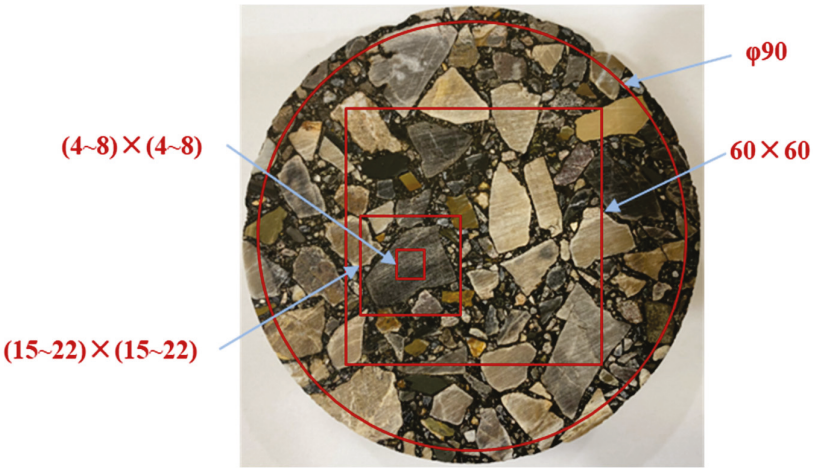

Figure 6. Different evaluating dimensions during 3D laser scanning (Unit: mm).

Both statistical, fractal, and entropy indicators were calculated based on the laser-scanned data of each point within the selected cross-section region mentioned above to analyze surface texture variation in asphalt mixture samples [20–22]. The statistical indicators of R_a and R_q were effective to evaluate surface roughness of asphalt mixture, and were thus selected in this study to characterize texture elevation values. R_a represented the arithmetic mean deviation of asphalt mixture surface points' elevations from the mean elevation within the selected region. R_q quantified the root mean square deviation of asphalt mixture surface points' elevations relative to the mean elevation across the analyzed region. R_a and R_q were determined according to the Formulas (1) and (2), in which R_c was the mean elevation within the selected region and z_i was each point's elevation.

$$R_a = \frac{1}{n}\sum_{i=1}^{n}|z_i - R_c| \tag{1}$$

$$R_q = \sqrt{\frac{1}{n-1}\sum_{i=1}^{n}(z_i - R_c)^2} \tag{2}$$

The fractal dimension D was a scaling exponent that quantitatively characterized the roughness or structural complexity of the sample's surface. D reflected the non-integer dimensional properties of the sample's morphology as a function of measurement scale, and the detailed description can be referred to in the previous study [21]. Entropy E was a thermodynamic state function that quantified the degree of disorder or randomness in a system; in this study, it meant the uncertainty or average information content of a random variable. E was determined based on the Formula (3), in which p_i was the probability of grey level i and N_g meant an image had the maximum grey level. Detailed illustration of E can be found in the previous study [22].

$$E = \sum_{i=1}^{N_g} p_i \log_2\left(\frac{1}{p_i}\right) \tag{3}$$

3.3. Aggregate Crushing Value Testing Method

For limestone and basalt, aggregates with particle size within 9.5 mm–13.2 mm were cleaned firstly and then conditioned in dynamic water pressure environments. Each group contained a mass of about 3000 g, and two parallel samples were considered. The physical properties of mass loss and water absorption rate for aggregate samples before and after being conditioned were evaluated, while the mechanical property of crushing value was assessed. In the aggregate crushing value test, aggregate particles were firstly poured into a fixture and then evenly applied by a gradual increasing load using a Material Testing System (MTS). The loading procedure should be as follows: ramped the force to 400 kN over a period of 10 min, held the constant load for 5 s, and subsequently performed unloading. The crushed aggregate sample was then sieved using the 2.36 mm sieve. The process of the aggregate crushing value test is shown in Figure 7. The crushing value was defined as the ratio of the mass passing the 2.36 mm sieve to the total mass of the crushed aggregate sample. A higher crushing value indicated weaker mechanical performance of the aggregate in this study.

https://doi.org/10.3390/ma19081514

(**a**) Aggregate fixture

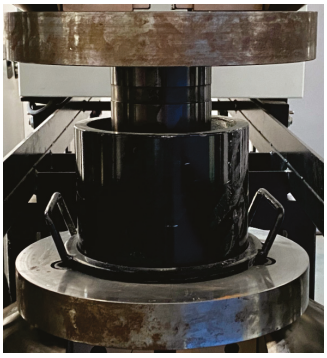

(**b**) Loading process

(**c**) Crushed aggregate

Figure 7. Aggregate crushing value test.

4. Results and Discussions

4.1. Surface Erosion Degree Based on 3D Scanning

4.1.1. Evaluating Dimension: Asphalt Mixture Specimen

After being conditioned in dynamic water pressure environments with different contents of severity, the FAM component on the surface of an asphalt mixture specimen was eroded and scoured away. The surfaces of coarse aggregate particles also endured the erosion effects. Therefore, these eroding actions would alter the surface texture of an asphalt mixture specimen and make its surface rougher. The 3D laser scanning technology was adopted to acquire elevation data of testing points spaced at 0.1 mm intervals on the specimen surface. By selecting an appropriate cross-sectional area, the changes in surface roughness of a sample before and after erosion within this region could be calculated and characterized. The erosion degree of the sample within the selected region could thus be evaluated.

Figures 8 and 9 illustrated surface texture variations within a 90 mm diameter circular cross-section at the center of specimens for two typical asphalt mixtures, AC-20-Limestone-70# and SMA-16-Basalt-SBS, before and after erosion, respectively. It could be observed that the outer contours of coarse aggregate particles on the HMA specimen surface became distinctly visible after erosion under various conditions of dynamic water pressure. The phenomena were attributed to the erosion and significant stripping of the FAM component filling within the coarse aggregate skeleton by dynamic water pressure. The areas between coarse aggregate particles which were the locations of the FAM component showed dark color. After stripping, the dark coloration would be intensified, as shown in Figure 8a,b compared to Figure 9c,d. Alternatively, the number of dark areas increased markedly, as shown in Figure 8c,d versus Figure 9a,b. In other cases, originally isolated small dark areas might coalesce into a continuous larger dark region following erosion, as demonstrated in Figure 8g,h compared to Figure 9g,h. These observations indicated that dynamic water pressure induced significant erosion effects on both AC-20-Limestone-70# and SMA-16-

Basalt-SBS asphalt mixture specimens. Comparing two types of asphalt mixture after stripping, it revealed that the AC-20-Limestone-70# specimens exhibited larger continuous dark areas between coarse aggregate particles, e.g., Figure 8b,h, whereas the SMA-16-Basalt-SBS specimens predominantly displayed scattered and isolated dark areas, e.g., Figure 9h. This finding also suggested that the resistance of the FAM component to erosion by dynamic water pressure was weaker for the base 70# asphalt binder compared to the SBS-modified asphalt binder.

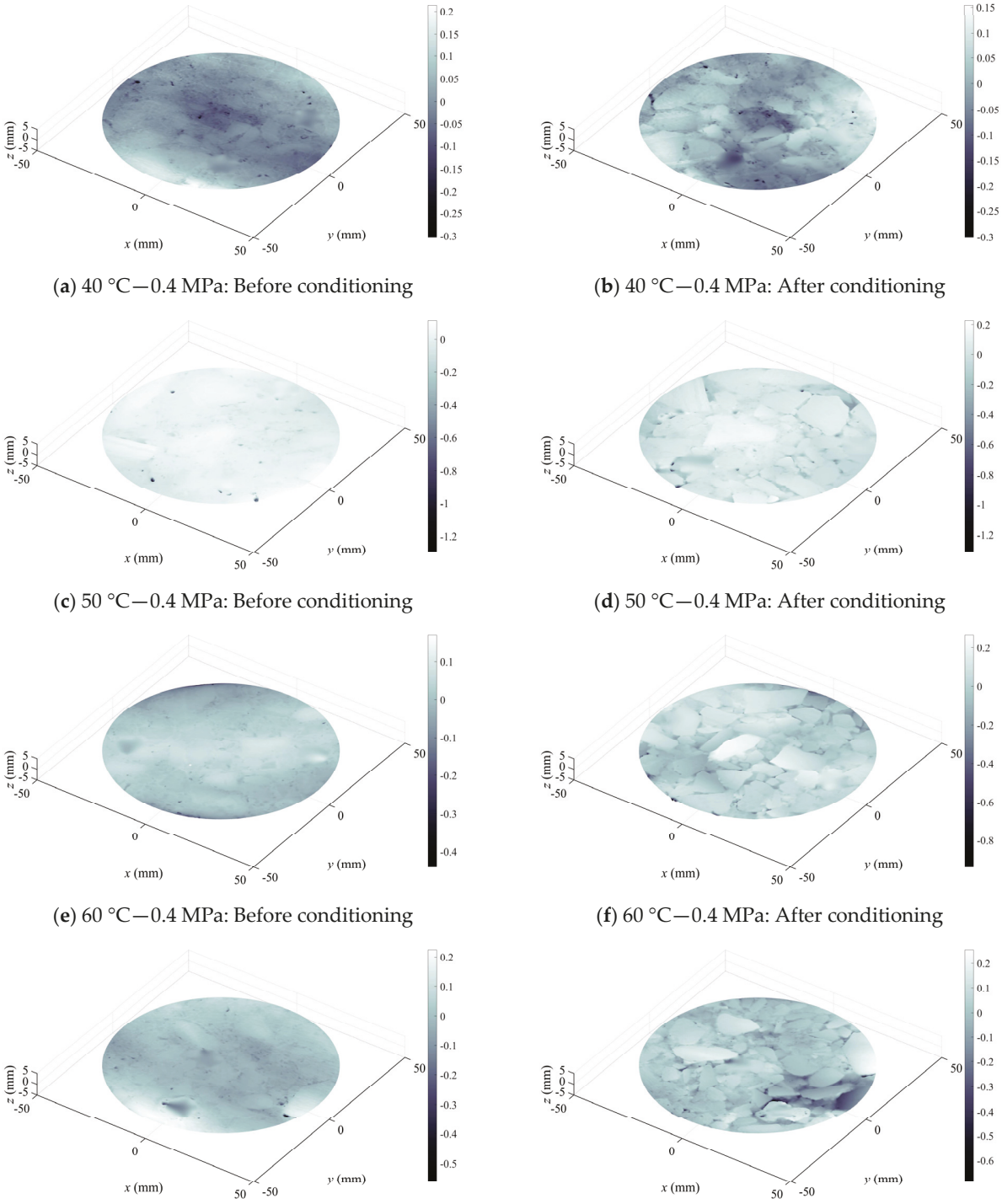

(**a**) 40 °C—0.4 MPa: Before conditioning

(**b**) 40 °C—0.4 MPa: After conditioning

(**c**) 50 °C—0.4 MPa: Before conditioning

(**d**) 50 °C—0.4 MPa: After conditioning

(**e**) 60 °C—0.4 MPa: Before conditioning

(**f**) 60 °C—0.4 MPa: After conditioning

(**g**) 60 °C—0.3 MPa: Before conditioning

(**h**) 60 °C—0.3 MPa: After conditioning

Figure 8. *Cont.*

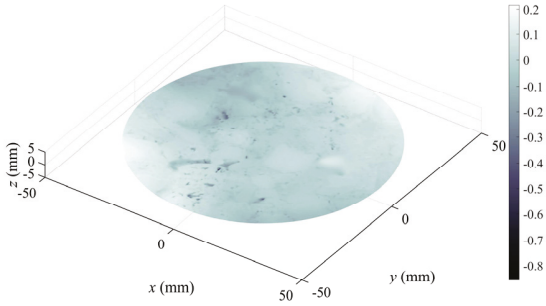

(**i**) 60 °C—0.2 MPa: Before conditioning

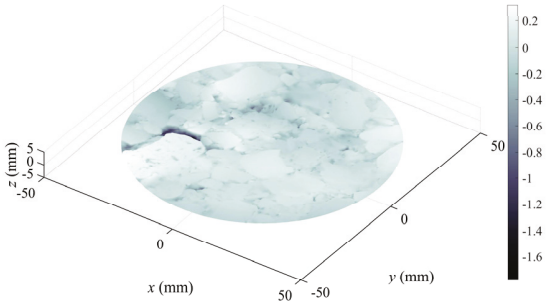

(**j**) 60 °C—0.2 MPa: After conditioning

Figure 8. Variation in surface roughness AC-20-Limestone-70# HMA samples before and after being conditioned in dynamic water pressure environment.

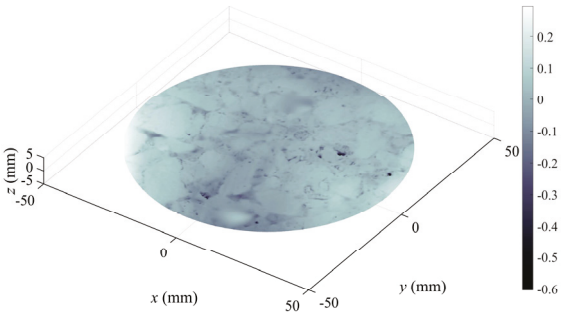

(**a**) 40 °C—0.4 MPa: Before conditioning

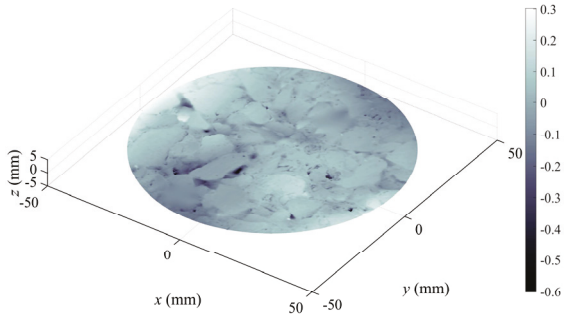

(**b**) 40 °C—0.4 MPa: After conditioning

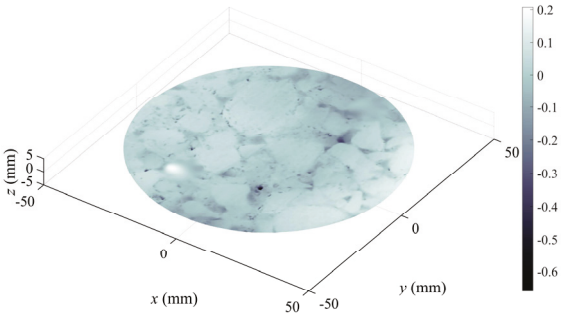

(**c**) 50 °C—0.4 MPa: Before conditioning

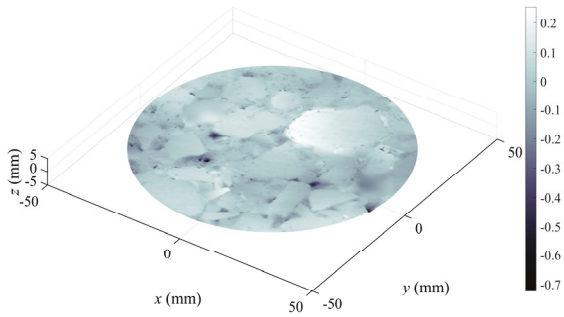

(**d**) 50 °C—0.4 MPa: After conditioning

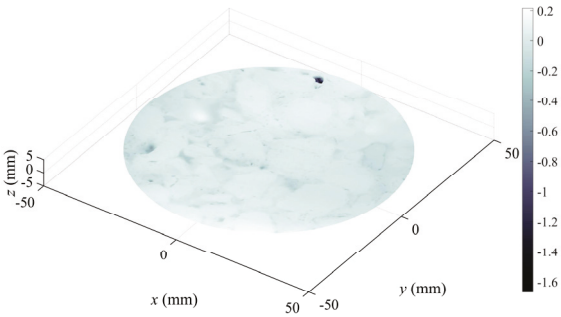

(**e**) 60 °C—0.4 MPa: Before conditioning

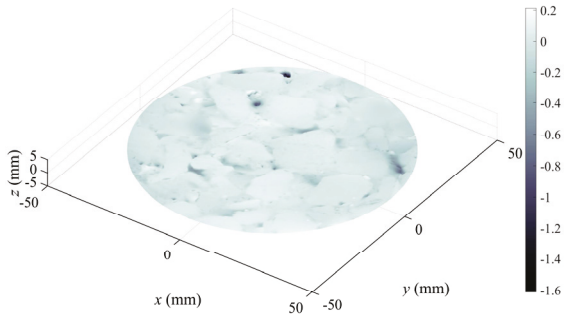

(**f**) 60 °C—0.4 MPa: After conditioning

Figure 9. *Cont*.

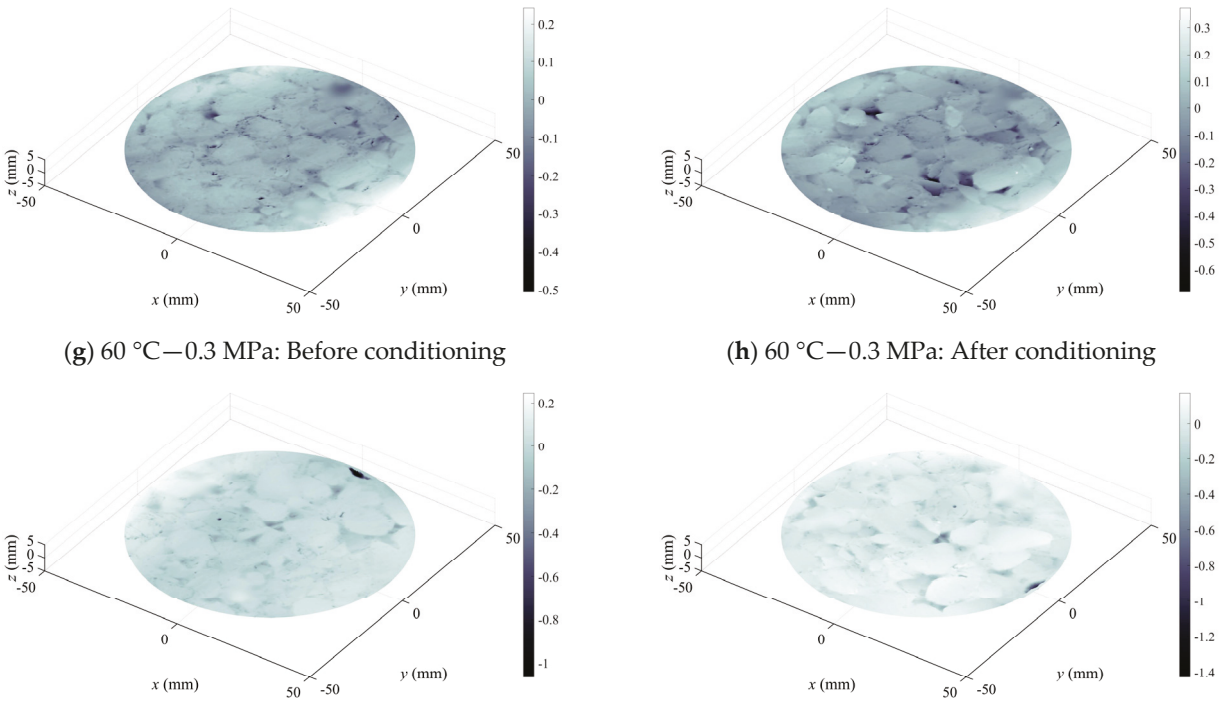

(**g**) 60 °C—0.3 MPa: Before conditioning

(**h**) 60 °C—0.3 MPa: After conditioning

(**i**) 60 °C—0.2 MPa: Before conditioning

(**j**) 60 °C—0.2 MPa: After conditioning

Figure 9. Variation in surface roughness SMA-16-Basalt-SBS HMA samples before and after being conditioned in dynamic water pressure environment.

After being eroded by dynamic water pressure, the surface roughness indicators of both types of asphalt mixture specimens exhibited significant changes, as shown in Figure 10 with percentage error bars. Figure 10a,b reveals that statistical indicators, including the arithmetic mean deviation R_a and the root mean square deviation R_q, increased across all experimental groups. It indicated an obvious rise in surface unevenness of all HMA specimens. However, an opposite trend was observed under the 40 °C water condition. This might be attributed to the relatively mild environment of the 40 °C water temperature in this study, resulting in no significant difference in erosion degrees between the two types of asphalt mixture. When the water pressure magnitude was maintained at 0.4 MPa, the change rate in roughness indicators for the limestone-based asphalt mixture gradually increased with a rising water temperature. It suggested that the damage degree sustained by the limestone-based asphalt mixture under dynamic water pressure erosion intensified with increasing water temperature. Under the harsh conditions of 60 °C water temperature, an increase in water pressure magnitude did not induce a clear change in the erosion degree of the limestone-based asphalt mixture. This indicated that the erosion effect of water pressure magnitude on a HMA specimen might be related to the distribution of its various components on the contact surface.

Figure 10c,d demonstrates that indicators such as the fractal dimension D and the entropy E increased for all experimental groups after being eroded by dynamic water pressure. For the limestone-based asphalt mixture, the fractal dimension D increased with a rising water temperature but decreased with an increasing water pressure magnitude. Furthermore, the entropy E for the limestone-based asphalt mixture also increased with a rising water temperature, while it exhibited an increasing trend with the elevation of water pressure magnitude. The overall variation in the fractal dimension D for the basalt-based asphalt mixture was relatively small. It also increased slowly with a rising water temperature, but gradually increased with the magnitude of water pressure, while the later phenomenon was converse to that of the limestone-based asphalt mixture. The changes

in the entropy *E* for the basalt-based asphalt mixture did not show a clear pattern with variations in parameters such as water temperature and water pressure magnitude.

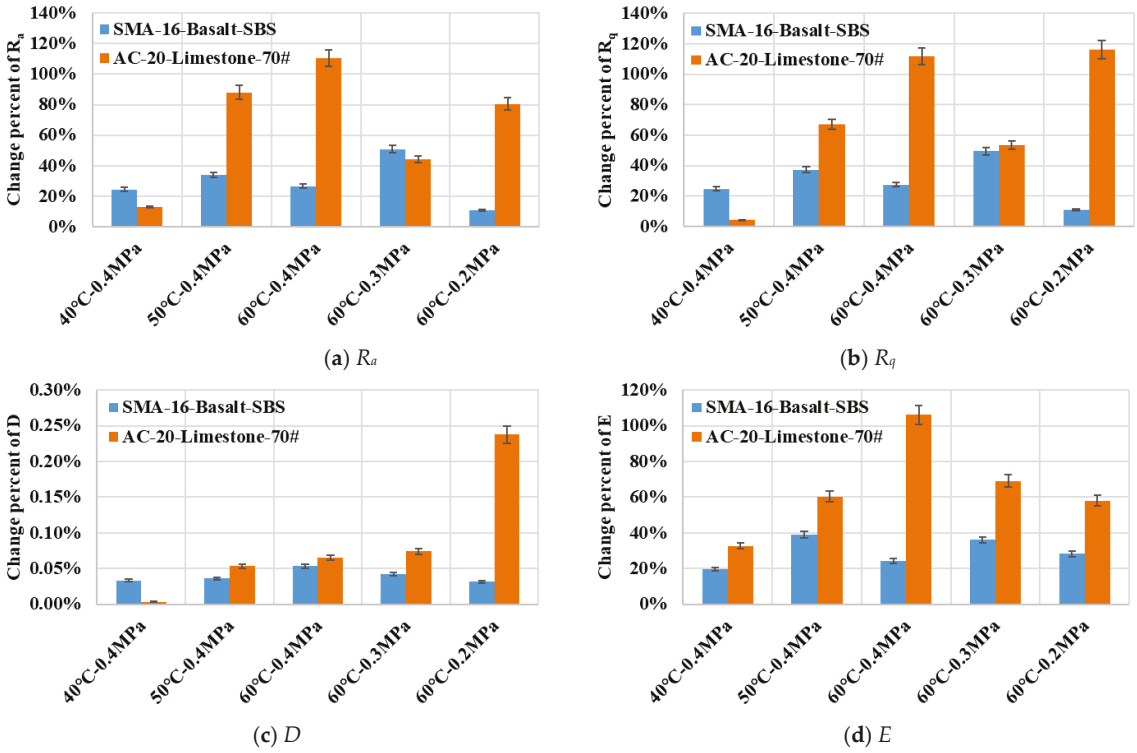

Figure 10. Variations in surface roughness indicators for HMA samples with different severities of dynamic water pressure.

All roughness indicators for the limestone-based asphalt mixture increased significantly with a rising water temperature, whereas the changes in surface roughness indicators for the basalt-based asphalt mixture did not exhibit a clear pattern with dynamic water pressure conditions. Compared to the statistical indices, parameters such as fractal dimension *D* and entropy *E* could better reflect the fluctuating pattern of asphalt mixture's erosion degree with changes in water pressure magnitude. Overall, the change degree in roughness indices for the limestone-based asphalt mixture exceeded that of the basalt-based asphalt mixture. It indicated that the basalt-based asphalt mixture possessed relative superior resistance to erosion by dynamic water pressure. This phenomenon was closely related to the types of asphalt binder used in the fabrication of asphalt mixture specimens. Although the basalt-based asphalt mixture was also eroded under different water pressure environments, the fluctuations in its surface roughness indices did not display a clear pattern and were relatively small in overall magnitude. It implied that the basalt-based asphalt mixture exhibited more stable service performance in a dynamic water pressure environment compared to the limestone-based asphalt mixture.

4.1.2. Evaluating Dimension: Aggregate Considering the FAM Component Interface

The asphalt mixture of AC-20-Limestone-70# was characterized as a suspension-dense structure, wherein the limestone coarse aggregate particles were encapsulated by the FAM component and air void component. In contrast, the asphalt mixture of SMA-16-Basalt-SBS was featured as a stone-on-stone skeleton interlocking structure, wherein the basalt coarse aggregate particles were also surrounded by the FAM component and air void component, but these particles were additionally in direct contact and interlock with one another. An extracted image depicting a single coarse aggregate particle along with its surrounded FAM component was presented in Figure 11. This allowed for direct observation of the erosion

characteristics of the fundamental constituent components of asphalt mixture under the erosion of dynamic water pressure. Although the aforementioned analysis also pertained to the air void component, the 3D laser scanning technique employed in this study could not precisely identify microscopic air voids. Therefore, the air void component of asphalt mixture was collectively incorporated into the FAM component for a holistic analysis.

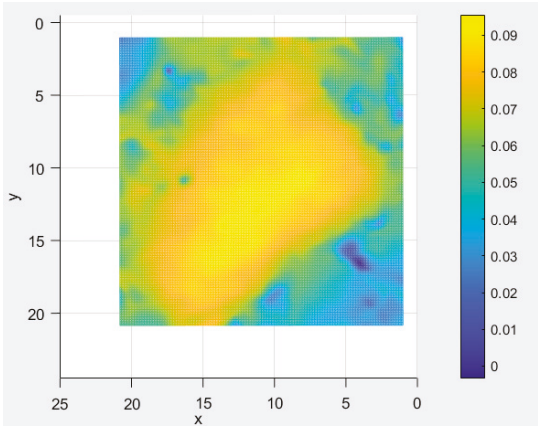

Figure 11. A typical coarse aggregate particle with surrounded FAM component.

Figure 12 illustrates the variations in surface roughness indices for coarse aggregate particles and their surrounded FAM components with erosion under different dynamic water pressure conditions. It could be observed that after being eroded in dynamic water pressure, statistical indicators such as the arithmetic mean deviation R_a and the root mean square deviation R_q for both types of asphalt mixture increased significantly. It indicated a rise in surface unevenness within the dimensional scale of the coarse aggregate particles and their surrounded FAM components. For the limestone-based FAM component, R_a and R_q exhibited clear increasing trends with a rising water temperature, but their variations with water pressure magnitude were less systematic. The increases in R_a and R_q for the basalt-based FAM component were considerably smaller than those observed for the limestone-based FAM component. Furthermore, the magnitude of these increases did not fluctuate significantly across different dynamic water pressure conditions. It suggested that the service behavior of the basalt-based FAM component was relatively stable. The greatest increase in roughness indices for both types of asphalt mixture occurred in the most severe dynamic water pressure condition (60 °C—0.4 MPa). Figure 12 clearly presented the stability characteristics of the base 70# asphalt mortar and the SBS-modified asphalt mortar when subjected to the erosion by dynamic water pressure.

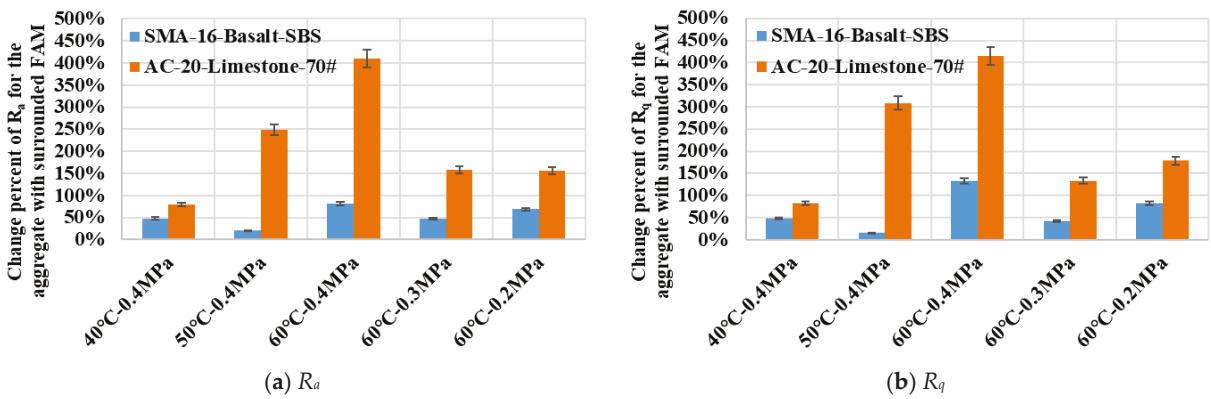

(**a**) R_a (**b**) R_q

Figure 12. Variations in surface roughness indicators for aggregates and surrounded FAM components with different severities of dynamic water pressure.

4.1.3. Evaluating Dimension: Aggregate

Under different service environments, coarse aggregate particles in asphalt mixture were conventionally considered to function primarily in bearing vehicle loads. However, these particles themselves were also susceptible to performance degradation due to environmental influences. In this study, suitable coarse aggregate particles were selected from cross-sections of asphalt mixture specimens, and small local areas within these particles were chosen for further analysis. Utilizing data acquired via 3D laser scanning, the evolution of surface roughness characteristics of coarse aggregate particles before and after erosion by dynamic water pressure was investigated.

As illustrated in Figure 13, the surface roughness of limestone exhibited a clear increasing trend with a rising water temperature. The most pronounced increase in surface roughness after erosion occurred under the most severe dynamic water pressure condition of 60 °C and 0.4 MPa. In contrast, the change percent in surface roughness for basalt subjected to dynamic water pressure was smaller than that observed for limestone. Furthermore, the change percent for basalt showed a greater dependency on variations in water temperature than on the magnitude of dynamic water pressure. Under the dynamic water pressure environment of 50 °C and 0.4 MPa, the surface roughness of both limestone and basalt was noticeably affected by dynamic water erosion. Notably, a decrease in surface roughness was observed for both rock types, with basalt exhibiting a relatively more pronounced reduction. This phenomenon might be attributed to the presence of micropores or microcracks on the coarse aggregate surfaces. Under the sustained erosion of dynamic water pressure, these superficial imperfections underwent continuous abrasion, leading to the detachment of finer particles and resulting in a relatively smoother surface. Additionally, the continuous erosion and stripping of the FAM component surrounding the coarse aggregate particles might induce displacement and rotation of the coarse aggregate particles within asphalt mixture. This could contribute to a relative decrease in the roughness values derived from the 3D laser scanning data of the eroded aggregate surfaces.

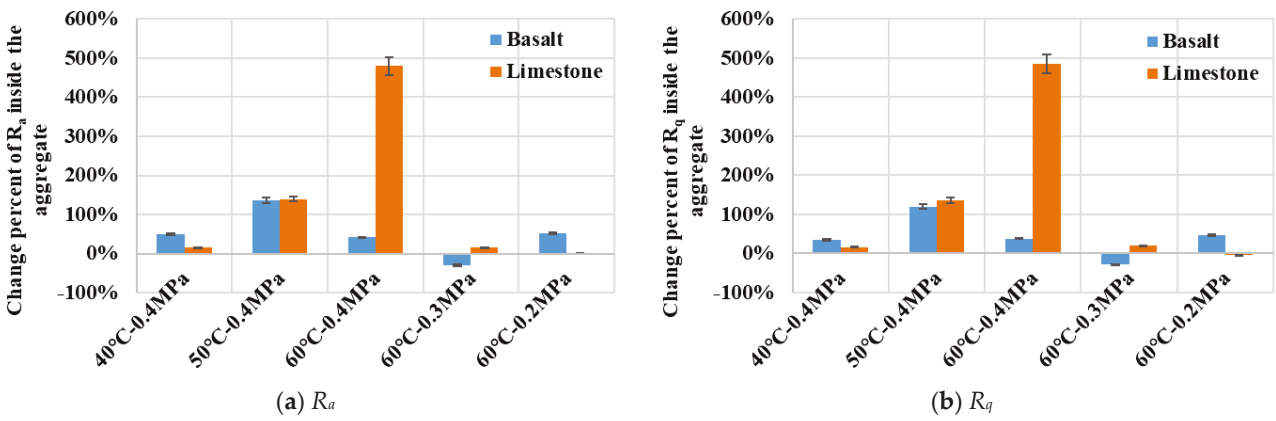

(**a**) R_a (**b**) R_q

Figure 13. Variations in surface roughness indicators for aggregates with different severities of dynamic water pressure.

4.1.4. Influence of Evaluating Dimension on Surface Erosion Degree

The values of the arithmetic mean deviation R_a and the root mean square deviation R_q presented in Figure 10 represent the roughness of the entire cross-section of asphalt mixture, which essentially integrated the areas encompassing multiple individual coarse aggregate particles and their surrounded FAM components shown in Figure 12. It could be observed that the trends in the indicators of R_a and R_q for AC-20-Limestone-70# with varying parameters of dynamic water pressure are broadly consistent between Figures 10 and 12.

However, differing trends were noted for the indicators of R_a and R_q of SMA-16-Basalt-SBS between these two figures. This suggested that for a base 70# asphalt mortar FAM, which was susceptible to erosion by dynamic water pressure, the region comprising a single coarse aggregate particle and its surrounded FAM component could basically characterize the degree of stripping affecting the asphalt mixture specimen. Selecting a small evaluation area encompassing several coarse aggregate particles appeared sufficient to effectively represent the overall roughness change characteristics of the entire asphalt mixture. Conversely, for an SBS-modified asphalt mortar FAM that exhibited good resistance to the erosion of dynamic water pressure, a larger evaluation area was necessary to effectively characterize the overall roughness change in the entire asphalt mixture.

The R_a and R_q values in Figure 12 quantify the roughness within the region encompassing a single coarse aggregate particle and its surrounded FAM component. This region included the smaller intra-particle area analyzed in Figure 13. Although the percentage changes in the indices shown in Figure 13 are relatively large, the absolute magnitudes of these indices are considerably smaller than those presented in Figure 12. A combined examination of Figures 12 and 13 reveals that, within the evaluation scale of a single coarse aggregate particle and its surrounded FAM component, the change degree of roughness originating from the intra-aggregate region is substantially less than the roughness increase caused by the erosion and denudation of the FAM component. Consequently, under the erosion duration of 4000 cycles of dynamic water pressure applied in this study, although some surface erosion and roughening of the coarse aggregate particles occurred, the erosion and stripping effect on the FAM component within the specimen cross-section was significantly more pronounced. A further increase in the erosion duration would likely induce more extensive erosion of coarse aggregate particles, potentially revealing more substantial changes in their surface roughness.

4.2. Physical and Mechanical Properties of Aggregates

Coarse aggregates of limestone and basalt both were conditioned in dynamic water pressure environments, and their physical and mechanical properties were evaluated. Figure 14 shows the small granular debris detached from limestone and basalt aggregates after being subjected to erosion in a dynamic water pressure environment of 60 °C and 0.4 MPa. It was clearly observed that the number of debris detached from limestone was relatively small, whereas basalt shed considerably more debris. This phenomenon was consistently observed following erosion under various dynamic water pressure environments. As illustrated in Figure 15a, the mass loss of limestone was typically around 2 g, demonstrating relative stability and greater resistance to erosion by dynamic water pressure. In contrast, the mass loss of basalt approached 20 g, with substantial variation between different experimental groups. This variability might be attributed to the presence of surface imperfections such as microcracks or micropores on the aggregate particles. Erosion by dynamic water could lead to the detachment of larger particles from these flawed areas, resulting in the observed randomness and lack of a clear trend in basalt mass loss. The phenomenon of basalt shedding more granular debris after erosion provided indirect support for the explanation regarding the decrease in basalt surface roughness.

As shown in Figure 15b, the percentage change in aggregate water absorption rate was influenced by erosion in a dynamic water pressure environment. Basalt exhibited a higher absolute water absorption rate value compared to limestone, although the overall range of variation was not substantial. The water absorption rate of limestone varied between 0.04% and 0.17%, while that of basalt ranged from 0.37% to 0.42%. For both aggregate types, water absorption rate increased with greater severity of water temperature and dynamic water pressure magnitude, with temperature exerting a more pronounced influence than

https://doi.org/10.3390/ma19081514

water pressure magnitude [23]. The increase in aggregate water absorption rate might be attributed to the erosion and detachment of surface debris under dynamic water pressure conditions, leading to a slight increase in surface porosity.

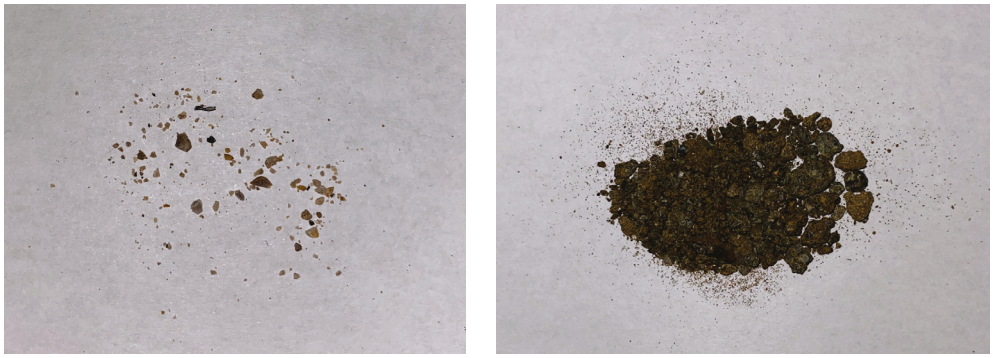

(**a**) Limestone (**b**) Basalt

Figure 14. Small particles scoured away from coarse aggregates after being conditioned in dynamic water pressure.

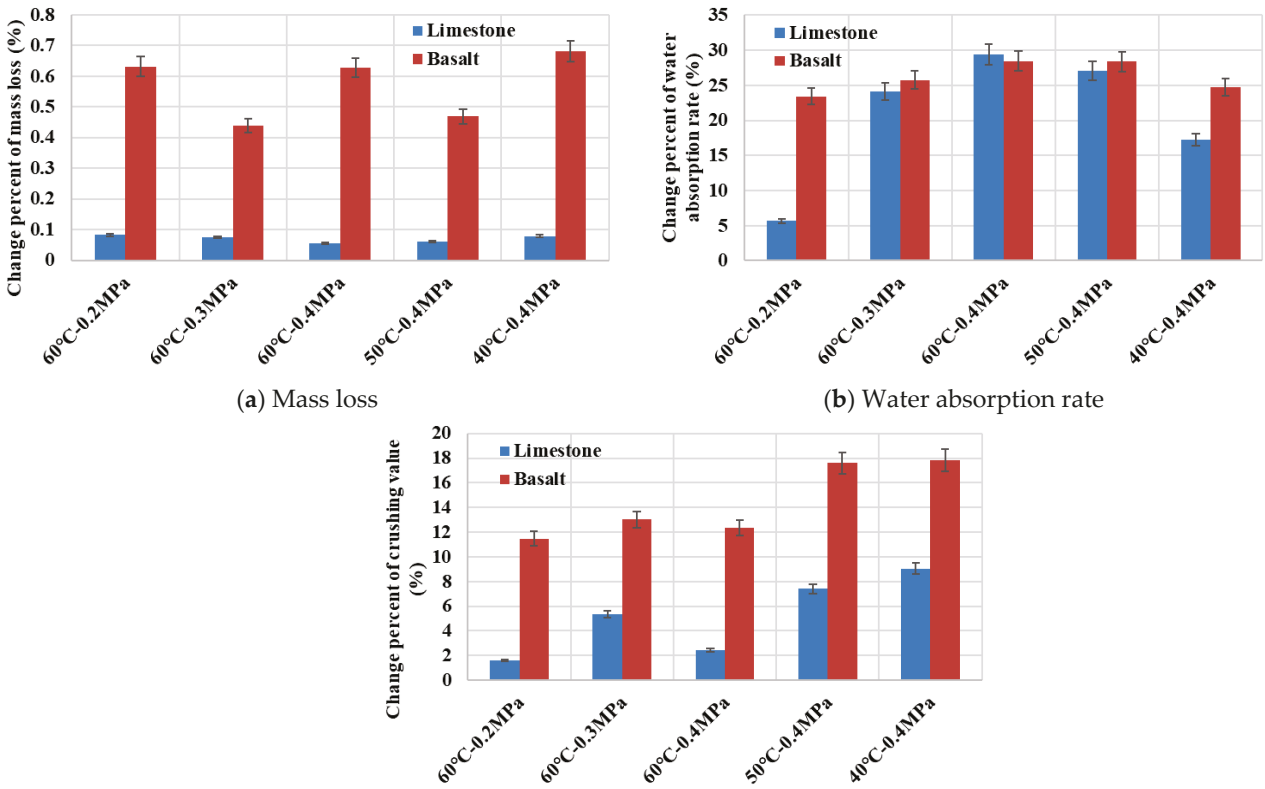

(**a**) Mass loss (**b**) Water absorption rate

(**c**) Crushing value

Figure 15. Physical and mechanical properties of aggregates.

Figure 15c illustrated the percentage change in aggregate crushing value resulting from erosion in dynamic water pressure. Under identical test conditions, the absolute crushing value of basalt was 3.5% to 4.5% lower than that of limestone, and it indicated that basalt possessed superior mechanical properties. However, the extent of change in the crushing value was generally smaller for limestone than for basalt, and it suggested that limestone exhibited greater stability under dynamic water erosion. The influence of water temperature variations on the crushing value was consistently more significant than that of water pressure magnitude variations [23], with limestone showing an increase of 0.24% to 1.35% and basalt showing an increase of 1.22% to 1.89%. Notably, as the

severity of the dynamic water pressure intensified, the aggregate crushing value tended to decrease. This phenomenon might be attributed to the detachment of weaker surface debris from aggregate particles, leaving behind a more robust and resilient remaining structure. In summary, while the basalt selected for this study demonstrated superior mechanical properties compared to limestone, it possessed a greater abundance of surface micropores or microcracks. This characteristic made the physical and mechanical performance of basalt more susceptible to fluctuations under the erosive action of dynamic water pressure.

4.3. Discussion on Moisture Damage Mechanism of Asphalt Mixture

Moisture damage in asphalt mixtures induced by erosion from dynamic water pressure was typically accompanied by significant stripping of the asphalt mortar FAM component. Following the conclusion of experiments, a substantial quantity of eroded fine aggregate was commonly observed within the vessels of environmental simulation equipment. The moisture damage mechanism exhibited by this characteristic phenomenon was fundamentally distinct from that associated with traditional water environments, such as static water immersion or freeze–thaw conditions.

When an asphalt mixture specimen was placed in a dynamic water pressure environment, the asphalt binder endured the erosion action of coupled multi-physical fields. This progressively reduced its internal cohesive energy and its adhesive energy with the aggregate. Consequently, cracks initiated either within the asphalt mastic or at the asphalt–aggregate interface. The adhesion between the asphalt binder and fine aggregate weakened, which led to stripping, and even small fragments of the asphalt mortar FAM could be directly eroded away. This manifested globally as the pronounced stripping of the asphalt mortar FAM component within an asphalt mixture. The coarse aggregate component inside the asphalt mixture was also subject to erosion. Micropores or microcracks on the surfaces of coarse aggregate particles would serve as initiation points for erosion by dynamic water pressure, and it would result in the detachment of weak surface layers. The morphological characteristics of the coarse aggregate particles were altered, such as surface roughness, and their physical and mechanical properties correspondingly deteriorated.

The variation in surface roughness indicators of asphalt mixture samples in this study directly reflected the stripping degrees of asphalt-material components. A larger value of surface roughness indicated the more severe moisture damage for asphalt mixture. The stripping of FAM components allowed water to more readily penetrate the interior of asphalt mixture specimens with higher surface roughness. The deterioration of coarse aggregate particles affected the load transfer path within the coarse aggregate skeleton of the asphalt mixture when subjected to external mechanical loads. This created weak points in the force chain of asphalt mixture specimens, leading to a reduction in the overall mechanical performance. The FAM component of asphalt mixtures played a direct and critical role in moisture damage resistance. An increase in roughness signified the loss of the FAM component, which facilitated moisture intrusion into the asphalt–aggregate interface and induced stripping. Furthermore, the depletion of the FAM led to dislodging around coarse aggregate particles, altering the pathway of moisture infiltration and exacerbating the overall moisture damage of the asphalt mixture. In this case, the roughness indicators were directly and positively correlated with the degree of moisture damage in the asphalt mixture induced by dynamic water pressure.

The deterioration rates of the FAM component and the coarse aggregate component under erosion by dynamic water pressure differed. The erosion duration of dynamic water pressure conditioning was set at 4000 cycles in this study, and the stripping of the FAM component was more pronounced and significant. This often led to the fact that the concurrent erosion of coarse aggregate particles receives less attention. If the erosion

duration of dynamic water pressure was to be further extended, the deterioration of coarse aggregate particles would likely become more evident. Furthermore, the progressive stripping of the FAM component also impacted the coarse aggregate skeleton of the asphalt mixture. As established in the preceding analysis, the spaces surrounding coarse aggregate particles were filled with the FAM component. Continued disintegration of the FAM component allowed for the displacement, rotation, and loosening of coarse aggregate particles, ultimately leading to the collapse of the entire aggregate skeleton. Therefore, the mode of overall moisture damage manifestation in asphalt mixture was governed by the compatibility between the stripping rate of FAM component and the deterioration rate of coarse aggregate particles.

In this study, the asphalt mortar FAM fabricated with SBS-modified asphalt binder demonstrated significantly greater resistance to erosion and stripping by dynamic water pressure compared to that made with base 70# asphalt binder. Although the mechanical strength property of basalt was higher than that of limestone, the porous surface characteristics of basalt rendered its physical and mechanical properties more susceptible to the influence of dynamic water pressure. This could potentially make the coarse aggregate skeleton within basalt-based asphalt mixture relatively more prone to destabilization. Consequently, under the sustained erosion of dynamic water pressure in this study, the asphalt mixture AC-20-Limestone-70# might experience loosening and disintegration of its limestone coarse aggregate skeleton due to the stripping and breakdown of its base asphalt mortar FAM component. For the asphalt mixture SMA-16-Basalt-SBS, fluctuations in the compatibility between the deterioration rate of the basalt aggregate and the stripping rate of the SBS-modified asphalt mortar FAM could lead to an overall reduction in asphalt mixture performance, ultimately dictating the mode of failure. In this case, the deterioration of the basalt aggregate would undoubtedly contribute significantly to the moisture damage of the asphalt mixture. Due to the presence of multiple variables (e.g., water temperature and water pressure magnitude), the comprehensive analysis in this study basically focused on qualitative trends rather than absolute quantitative predictions, while relevant discussions are concluded on the basis of the previous study [23].

5. Conclusions

This study explored the moisture damage of asphalt mixture and its components induced by dynamic water pressure using the 3D laser scanning technique. Based on the analysis discussed above, the following conclusions can be obtained:

(1) All roughness indices for limestone-based asphalt mixture increased significantly with a rising water temperature, but these indices for basalt-based samples did not exhibit a clear pattern with dynamic water pressure conditions. Compared to statistical indices, fractal dimension and entropy better captured fluctuating patterns of erosion degree as water pressure magnitude.

(2) The resistance of base asphalt FAM to erosion by dynamic water pressure was weaker than that of SBS-modified asphalt FAM, which resulted in greater changes in roughness indices for limestone-based asphalt mixture.

(3) Limestone's surface roughness exhibited a clear increasing trend with a rising water temperature, while basalt had relatively smaller change degree in these indices, and their percentage changes showed a greater dependency on variations in water temperature than on water pressure magnitude.

(4) Basalt demonstrated superior mechanical properties compared to limestone, but it possessed a greater abundance of surface micropores or microcracks, which made basalt particles more susceptible to fluctuations under the erosive action of dynamic water pressure.

https://doi.org/10.3390/ma19081514

(5) Compared to water pressure magnitude, water temperature exerted a more significant impact on asphalt mixture and its constituents. The compatibility between the stripping rate of FAM component and the deterioration rate of coarse aggregate governed the macroscopic manifestation of overall moisture damage in asphalt mixture.
(6) Efforts can be made in the future study to link material deterioration and surface roughness features together, which can be helpful to deeply illustrate moisture damage of asphalt materials related to dynamic water pressure.

Author Contributions: Conceptualization, W.W.; methodology, W.W.; resources, W.W.; data curation, W.W., H.R. and Y.M.; writing—original draft preparation, W.W.; writing—review and editing, W.W.; and supervision, Y.M. and L.W. All authors have read and agreed to the published version of the manuscript.

Funding: The authors acknowledge the financial support of Fundamental Research Funds for the Central Universities (Project No. FRF-TP-26-086), Beijing Natural Science Foundation (Project No. 8244054), the Interdisciplinary Research Project for Young Teachers of USTB (Fundamental Research Funds for the Central Universities) (Project No. FRF-IDRY-23-017), and China Postdoctoral Science Foundation (Project No. 2021M690356).

Institutional Review Board Statement: Not applicable.

Informed Consent Statement: Not applicable.

Data Availability Statement: The original contributions presented in this study are included in the article. Further inquiries can be directed to the corresponding author.

Conflicts of Interest: Author Hua Rong was employed by the company Wuzhou Engineering Group Corporation Ltd. The remaining authors declare that the research was conducted in the absence of any commercial or financial relationships that could be construed as a potential conflict of interest. All authors declare no conflicts of interest.

References

1. Wang, W.; Wang, L.; Xiong, H.; Luo, R. A review and perspective for research on moisture damage in asphalt pavement in-duced by dynamic pore water pressure. *Constr. Build. Mater.* **2019**, *204*, 631–642. [CrossRef]
2. Chen, X.W.; Huang, B.S. Evaluation of moisture damage in hot mix asphalt using simple performance and Superpave indirect tensile tests. *Constr. Build. Mater.* **2008**, *22*, 1950–1962. [CrossRef]
3. Tarefder, R.A.; Weldegiorgis, M.T.; Ahmad, M. Assessment of the effect of pore pressure cycles on moisture sensitivity of hot mix asphalt using MIST conditioning and dynamic modulus. *J. Test. Eval.* **2014**, *42*, 1530–1540. [CrossRef]
4. Weldegiorgis, M.T.; Tarefder, R.A. Towards a mechanistic understanding of moisture damage in asphalt concrete. *J. Mater. Civ. Eng.* **2015**, *27*, 04014128. [CrossRef]
5. Varveri, A.; Avgerinopoulos, S.; Scarpas, A.; Collop, A.; Erkens, S. On the combined effect of moisture diffusion and cyclic pore pressure generation in asphalt concrete. In Proceedings of the Transportation Research Board 93rd Annual Meeting, Washington, DC, USA, 12–16 January 2014.
6. Tarefder, R.A.; Ahmad, M. Evaluation of pore structure and its influence on permeability and moisture damage in asphalt concrete. *Int. J. Pavement Eng.* **2017**, *18*, 274–283. [CrossRef]
7. Xu, H.; Tan, Y.; Yao, X. X-ray computed tomography in hydraulics of asphalt mixtures: Procedure, accuracy, and application. *Constr. Build. Mater.* **2016**, *108*, 10–21. [CrossRef]
8. Varveri, A.; Avgerinopoulos, S.; Scarpas, A. Experimental evaluation of long- and short-term moisture damage characteristics of asphalt mixtures. *Road Mater. Pavement Des.* **2016**, *17*, 168–186. [CrossRef]
9. Faisal, H.; Tarefder, R.; Weldegiorgis, M. Nanoindentation characterization of moisture damage in different phases of asphalt concrete. *Adv. Civ. Eng. Mater.* **2015**, *4*, 31–46. [CrossRef]
10. Khorasani, S.; Masad, E.; Kassem, E.; Abu Al-Rub, R.K. Nano-mechanical characterization of mastic, aggregate, and interfacial zone in asphalt composites. *J. Test. Eval.* **2013**, *41*, 924–932. [CrossRef]
11. Yao, Z.; Zhu, H.; Gong, M.; Yang, J.; Xu, G.; Zhong, Y. Characterization of asphalt materials' moisture susceptibility using multiple methods. *Constr. Build. Mater.* **2017**, *155*, 286–295. [CrossRef]

12. Lv, Q.; Huang, W.; Bahia, H.; Tang, N.; Zhu, T. Three-stage damage evolution of asphalt mixture in the wet hamburg wheel tracking device test using X-Ray computed tomography. *J. Mater. Civ. Eng.* **2018**, *30*, 04018138. [CrossRef]
13. Jin, C.; Zou, F.; Yang, X.; Liu, K. 3-D virtual design and microstructural modeling of asphalt mixture based on a digital aggregate library. *Comput. Struct.* **2021**, *242*, 106378. [CrossRef]
14. Plessis, A.; Boshoff, W. A review of X-ray computed tomography of concrete and asphalt construction materials. *Constr. Build. Mater.* **2019**, *199*, 637–651. [CrossRef]
15. Luo, W.; Li, L. Estimation of water film depth for rutting pavement using IMU and 3D laser imaging data. *Int. J. Pavement Eng.* **2021**, *22*, 1334–1349. [CrossRef]
16. Li, L.; Wang, K.; Li, Q. Geometric texture indicators for safety on AC pavements with 1mm 3D laser texture data. *Int. J. Pavement Res. Technol.* **2016**, *9*, 49–62. [CrossRef]
17. *JTG 3410-2025*; Standard Test Methods of Asphalt and Asphalt Mixture for Highway Engineering. China Communication Press: Beijing, China, 2025.
18. *JTG F40-2004*; Technical Specifications for Construction of Highway Asphalt Pavements. China Communication Press: Beijing, China, 2004.
19. *ASTM D7870-20*; Standard Practice for Moisture Conditioning Compacted Asphalt Mixture Specimens by Using Hydrostatic Pore Pressure. ASTM: West Conshohocken, PA, USA, 2020.
20. Miao, Y.; Song, P. Multifractal characteristics of asphalt concrete pavement macrotexture. *Highway* **2013**, *4*, 71–75.
21. Miao, Y.; Song, P.; Gong, X. Fractal and multifractal characteristics of 3D asphalt pavement macrotexture. *J. Mater. Civ. Eng.* **2014**, *26*, 04014033. [CrossRef]
22. Miao, Y.; Wu, J.; Hou, Y.; Wang, L.; Yu, W.; Wang, S. Study on asphalt pavement surface texture degradation using 3-D image processing techniques and entropy theory. *Entropy* **2019**, *21*, 208. [CrossRef] [PubMed]
23. Wang, W.; Wang, L.; Yan, G.; Zhou, B. Evaluation on moisture sensitivity of asphalt mixture induced by dynamic pore water pressure. *Int. J. Pavement Res. Technol.* **2020**, *13*, 489–496. [CrossRef]

Disclaimer/Publisher's Note: The statements, opinions and data contained in all publications are solely those of the individual author(s) and contributor(s) and not of MDPI and/or the editor(s). MDPI and/or the editor(s) disclaim responsibility for any injury to people or property resulting from any ideas, methods, instructions or products referred to in the content.

MDPI AG
Grosspeteranlage 5
4052 Basel
Switzerland
Tel.: +41 61 683 77 34

Materials Editorial Office
E-mail: materials@mdpi.com
www.mdpi.com/journal/materials

Disclaimer/Publisher's Note: The title and front matter of this reprint are at the discretion of the Guest Editors. The publisher is not responsible for their content or any associated concerns. The statements, opinions and data contained in all individual articles are solely those of the individual Editors and contributors and not of MDPI. MDPI disclaims responsibility for any injury to people or property resulting from any ideas, methods, instructions or products referred to in the content.

Academic Open
Access Publishing

mdpi.com

ISBN 978-3-7258-9128-3